



AD-A212 314

AL-CP-89-002

AD:

Proceedings of the High Energy Density Matter (HEDM) Conference held 12-15 March 1989 in New Orleans LA

July 1989

Editors:
T. G. Wiley
R. A. van Opijnen

Approved for Public Release

Distribution is unlimited. The AL Technical Services Office has reviewed this report, and it is releasable to the National Technical Information Service, where it will be available to the general public, including foreign nationals.

Astronautics Laboratory (AFSC)

Air Force Space Technology Center
Space Systems Division
Air Force Systems Command
Edwards Air Force Base, California 93523-5000

DTIC
ELECTE
AUG 24 1989
S B D

89 8 04 071

This conference proceedings has been reviewed and is approved for distribution in accordance with the distribution statement on the cover and on the DD Form 1473.

Roeland A. van Opijnen

ROELAND A. VAN OPIJNEN, 2Lt, USAF
Project Manager

FOR THE DIRECTOR

Robert C. Corley

ROBERT C. CORLEY
Deputy Director, Astronautical
Sciences Division

NOTICE

When U.S. Government drawings, specifications, or other data are used for any purpose other than a definitely related government procurement operation, the government thereby incurs no responsibility nor any obligation whatsoever, and the fact that the government may have formulated, furnished, or in any way supplied the said drawings, specifications, or other data is not to be regarded by implication or otherwise, as conveying any rights or permission to manufacture, use, or sell any patented invention that may in any way be related thereto.

REPORT DOCUMENTATION PAGE

Form Approved
OMB No. 0704-0188

1a. REPORT SECURITY CLASSIFICATION Unclassified			1b. RESTRICTIVE MARKINGS		
2a. SECURITY CLASSIFICATION AUTHORITY			3. DISTRIBUTION/AVAILABILITY OF REPORT Approved for public release. Distribution is unlimited.		
2b. DECLASSIFICATION/DOWNGRADING SCHEDULE					
4. PERFORMING ORGANIZATION REPORT NUMBER(S) AL-CP-89-002			5. MONITORING ORGANIZATION REPORT NUMBER(S)		
6a. NAME OF PERFORMING ORGANIZATION Astronautics Laboratory		6b. OFFICE SYMBOL (if applicable) LSX		7a. NAME OF MONITORING ORGANIZATION	
6c. ADDRESS (City, State, and ZIP Code) Edwards Air Force Base, CA 93523-5000			7b. ADDRESS (City, State, and ZIP Code)		
8a. NAME OF FUNDING/SPONSORING ORGANIZATION		8b. OFFICE SYMBOL (if applicable)		9. PROCUREMENT INSTRUMENT IDENTIFICATION NUMBER	
8c. ADDRESS (City, State, and ZIP Code)			10. SOURCE OF FUNDING NUMBERS		
			PROGRAM ELEMENT NO. 62302F	PROJECT NO. 5730	TASK NO. 00
11. TITLE (Include Security Classification) (U) Proceedings of the High Energy Density Matter (HEDM) Conference Held 12-'15 Mar 89 in New Orleans, LA					
12. PERSONAL AUTHOR(S) Wiley, Timothy G., and van Opijnen, Roeland A., Editors					
13a. TYPE OF REPORT Special		13b. TIME COVERED FROM 88/3 TO 89/3		14. DATE OF REPORT (Year, Month, Day) 89/07	
15. PAGE COUNT 338					
16. SUPPLEMENTARY NOTATION Extended abstracts from the third annual High Energy Density Matter Contractors Conference					
17. COSATI CODES			18. SUBJECT TERMS (Continue on reverse if necessary and identify by block number)		
FIELD	GROUP	SUB-GROUP	HEDM; high energy density matter; propulsion; ab initio configuration interaction; H ₄ ; tetrahydrogen; molecular beam; crossed beam;		
19. ABSTRACT (Continue on reverse if necessary and identify by block number) This report documents presentations given at the third annual High Energy Density Matter (HEDM) Contractors Conference held 12-15 March 1989 in New Orleans, LA. Presentations were given by HEDM contractors funded by the Air Force, as well as in-house researchers from the Astronautics Laboratory (AL) and the Wright Research and Development Center (WRDC). This document consists of extended abstracts from each of the presentations.					
20. DISTRIBUTION/AVAILABILITY OF ABSTRACT <input checked="" type="checkbox"/> UNCLASSIFIED/UNLIMITED <input checked="" type="checkbox"/> SAME AS RPT. <input type="checkbox"/> DTIC USERS			21. ABSTRACT SECURITY CLASSIFICATION Unclassified		
22a. NAME OF RESPONSIBLE INDIVIDUAL Lt Roeland A. van Opijnen			22b. TELEPHONE (Include Area Code) (805) 275-5725		22c. OFFICE SYMBOL LSX

18. metastable, excited state, dynamics, H_2 , hydrogen, He_2 , spin-orbit, spin-spin, multi-configuration self-consistent field, MCSCF, condensed phase, metastability, quantum Monte Carlo, trial function, polyatomic hydrogen, ions, charge transfer, D_3^+ , SiH_4 , fluorine azide, FN_3 , laser initiated decomposition, IR, UV-Vis, ultraviolet, visible, spectroscopy, H_3O , N_2O_2 , dinitrogen dioxide, CO, carbon monoxide, CH, high spin states, spin forbidden, radiative transition, electronic structure, molecular geometry, rare gas fluorides, NF_5 , nitrogen pentafluoride, high oxidation state, rhombic structure, tetratomics, Si_2C_2 , disilicon dicarbide, zintl, photoexcitation, metastable metals, atomic metals, metal dimers, matrix isolation, matrix, rare gas matrix, theoretical, H_3 , trihydrogen.



Accession For	
NTIS GRA&I	<input checked="" type="checkbox"/>
DTIC TAB	<input type="checkbox"/>
Unannounced	<input type="checkbox"/>
Justification	
By	
Distribution/	
Availability Codes	
Dist	Avail and/or Special
A-1	

TABLE OF CONTENTS

Executive Summary.....	vii
Technical Program Agenda.....	viii
Extended Abstracts of Presentations	
"Propellant Payoff from a Classical Perspective" G. Nordley, Astronautics Laboratory (AFSC).....	1
"New High Energy Oxidizer Systems for Propellant and Energy Storage Applications" S. A. Kinkead, P. G. Eller, J. B. Nielsen, Los Alamos National Laboratory.....	9
"Synthesis and Structural Characterization of New High-Valent Inorganic Fluorine Compounds and their Oxidizing Properties" A. A. A. Emara, D. Hutchinson, A. Paprica, J. C. P. Sanders, G. J. Schrobilgen, J. Valsdottir, McMaster University.....	15
"Experimental Studies on the Synthesis of New Noble Gas Fluorides and High Oxidation State Energetic Fluorine Compounds involving Unusual Bonding Situations" W. W. Wilson, K. O. Christe, Rocketdyne.....	21
"Computational Studies of Tetrahedrane, some Azatetrahedranes, and their Nitro Derivatives" P. Politzer, J. M. Seminario, University of New Orleans.....	25
"The Synthesis of Nitrocyclopropanes using Nitrodiazomethanes" W. P. Dailey, University of Pennsylvania.....	43
"Dynamic Constraints on Stochastic Behavior in the Chemistry of Highly Excited Molecules" B. K. Carpenter, J. R. Wiesenfeld, Cornell University.....	49
"Theoretical Study of Ion-Pair States" R. P. Saxon, D. Talbi, SRI International.....	55
"Theoretical Investigation of Energy Storage in Atomic and Molecular Systems" H. H. Michels, J. A. Montgomery, Jr., United Technologies Research Center.....	61
"Spectroscopy of Hydrogenic (Ionic) Species in Hot Plasmas and Cryogenic Solids" T. Oka, The University of Chicago.....	73
"Photoionization and Dissociation of the Triatomic Hydrogen Molecule" H. Helm, L. J. Lembo, P. C. Cosby, D. L. Huestis, SRI International.....	79

"Ionic Solid Hydrogen Fuel: Production and Properties of Cluster Ions"	
Y. K. Bae, P. C. Cosby, D. C. Lorents, SRI International.....	91
"Experimental and Theoretical Studies of the Properties of Trihydrogen"	
A. Kuppermann, California Institute of Technology.....	97
"Two Dimensional Potential Energy Surfaces of Pyramidal Tetrahydrogen near a Three-Fold Seam"	
S. Huang, W. A. Lester, Jr., University of California, Berkeley.....	109
"Quenching Measurements of Electronically Excited Hydrogen"	
C. D. Pibel, A. H. Kung, C. B. Moore, University of California, Berkeley.....	113
"Further Investigations of the Infrared Absorption Spectra of the Ionic Clusters of Hydrogen"	
M. W. Crofton, J. M. Price, G. Niedner-Schatteburg, Y. T. Lee, University of California, Berkeley.....	121
"(NH) ₆ : The Amino-analogue of Cyclohexane. A Laboratory for the Understanding of Lone-pair Effects on Molecular Geometry."	
C. P. Blahous, H. F. Schaefer, University of Georgia.....	129
"Metastability in Molecules Metastability in Excited States: The ⁴ II _g State and its Autodetachment Spectrum"	
T. Pluta, R. J. Bartlett, L. Adamowicz, University of Florida.....	139
"Theoretical Studies of Bridged Structures of Be ₂ H ₂ and B ₂ H ₂ "	
B. H. Lengsfeld, Lawrence Livermore National Laboratory.....	147
"New High Energy Density Small Ring Systems"	
K. Lammertsma, University of Alabama at Birmingham.....	153
"Computational Studies of Metal Clusters"	
G. F. Adams, U. S. Army Ballistic Research Laboratory.....	159
"Theoretical and Experimental Investigations of Dications"	
W. C. Lineberger, S. R. Leone, S. V. O'Neil, University of Colorado/National Institute for Standards and Technology.....	165
"Investigations of Hypervalent Compounds as High Energy Compounds"	
P. Engelking, T. Dyke, J. Farley, University of Oregon and University of Nevada at Las Vegas.....	169
"Laser and Fourier Transform Spectroscopy of Novel Propellant Molecules"	
P. F. Bernath, University of Arizona.....	177
"Production of the CH Radical with an Ion Gun"	
P. Bletzinger and M. E. Ruark.....	183

"Ab Initio Study of the Energetics of the Decomposition of HN ₃ and N ₃ "	
M. H. Alexander, University of Maryland.....	189
"Experimental Study of the H+N ₃ Reaction and the Photodissociation of HN ₃ "	
P. J. Dagdigian, The Johns Hopkins University.....	195
"Time and State Resolved Studies of the Overtone-Pumped Photodissociation of HN ₃ (X ¹ A')"	
M. P. Casassa, B. R. Foy, D. S. King, J. C. Stephenson, National Institute of Standards and Technology.....	201
"Model Studies of CBES Decomposition"	
T. A. Seder, D. J. Benard, Rockwell International.....	205
"Theoretical Studies of Highly Energetic CBES Materials"	
N. E. Brener, J. Callaway, N. R. Kestner, H. Chen, Louisiana State University.....	211
"Theoretical Studies of Spin-Forbidden and Electronically Nonadiabatic Processes: Decay Processes in Energetic Materials"	
D. R. Yarkony, The Johns Hopkins University.....	217
"High Energy Density Systems in Cryogenic Media: The Production and Reaction of Atoms and Radicals"	
E. Weitz, Northwestern University.....	223
"Chemically Bound Excited Clusters"	
C. A. Nicolaides, National Hellenic Research Foundation.....	229
"Limitations on Atom Densities in Cryogenic Matrices"	
A. T. Pritt, Jr., N. Presser, R. R. Herm, The Aerospace Corporation.....	245
"Weak Interactions"	
D. D. Konowalow, Astronautics Laboratory (UDRI).....	251
"Matrix Isolation Spectroscopy of Metal Atoms Generated by Laser Ablation: the Li/Ar System"	
M. E. Fajardo, Astronautics Laboratory (UDRI).....	259
"Metastable Metals in Matrix Materials"	
N. Presser, A. T. Pritt, Jr., R. R. Herm, The Aerospace Corporation.....	267
"Energy Transfer Processes in Rare Gas Solids"	
H. Helvajian, L. Wiedeman, B. Koffend, The Aerospace Corporation.....	271
"Rydberg Holes and Solid State Exciplex Lasers"	
V. A. Apkarian, University of California, Irvine.....	281

"Ab Initio Study of ArH, ArH ⁺ , Ar ₂ H, Ar ₂ H ⁺ , and Ar ₄ H ⁺ Molecules"	
M. E. Rosenkrantz, Astronautics Laboratory (UDRI).....	291
"The Interaction of Hydrogen Chloride with Rare Gas Atoms"	
C. F. Chabalowski, G. F. Adams, D. R. Yarkony, U.S. Army Ballistic Research Laboratory, The Johns Hopkins University..	301
"Experimental Probes of Coupling between Elementary Limits in the Higher Excited States of HCL"	
K. S. Haber, E. Patsilinaou, Y. Jiang, E. R. Grant, Purdue University.....	307
"Gas Phase Production of Energetic Species for Cryogenic Trapping"	
P. G. Carrick, Astronautics Laboratory (UDRI).....	315
"Dynamics of Atomic Hydrogen Trapped in Crystal Lattices"	
B. C. Garrett, Chemical Dynamics Corporation.....	321
"Energy Storage in Solid Molecular Hydrogen due to Trapped Atoms"	
J. R. Gaines, University of Hawaii at Manoa.....	327
"Photoinitiated Chain Reactions in Low Temperature Solids"	
C. A. Wight, University of Utah.....	333
"Dynamics of Metastables in the Condensed Phase"	
P. K. Swaminathan, Chemical Dynamics Corporation.....	339
"Specific Impulse Enhancement via Pressure Stabilized Excited Electronic States of High Energy Density Propellants"	
J. W. Kenney III, Eastern New Mexico University.....	345
"Theoretical Studies of Metastable Molecular Systems"	
K. Kirby, Harvard-Smithsonian Center for Astrophysics.....	347
"The Stability of N ₂ (A' ⁵ Σ _g ⁺)"	
W. J. Marinelli, W. J. Kessler, A. M. Woodward, Physical Sciences Inc.....	353
"The Phase Diagram of Hydrogen: Prospects for Metallization"	
I. F. Silvera, Harvard University.....	363

Non-Speaking Abstracts

"The <i>ab initio</i> Determination of the Damped Dispersion Energy of Interaction between an Atom and a Diatomic Molecule"	
J. E. Bohr, Astronautics Laboratory (AFSC).....	369
"Synthesis of Novel, Substituted Polycyclic Cage Systems"	
A. P. Marchand, University of North Texas.....	371
"Research Opportunities in the Field of Energetic Materials"	
R. L. McKenney, Jr., Air Force Armament Laboratory.....	373

EXECUTIVE SUMMARY

In 1985, Air Force Project Forecast II identified 70 technology areas whose research and development would greatly enhance the Air Force mission in the future. The High Energy Density Matter (HEDM) program was initiated as a result of this effort.

The HEDM program is specifically targeted at identifying and developing new high energy molecular systems which will substantially exceed the energetics of current propulsion systems. Such systems must have a large ratio of energy to molecular weight (energy density). Molecular systems that are currently being examined include chemically bound excited states (CBES), high energy ground states, hypervalent molecules and strained compounds. The goal of the program is to develop these and other chemical systems as propellants resulting in increased specific impulse, with a concomitant increase in payload, and more versatile space capability. Other Air Force payoffs from the HEDM program's investigation of energetic molecules include spinoffs in lasers, explosives, and power generation.

The HEDM program is guided through an Air Force joint Steering Panel consisting of the Astronautics Laboratory (AL) as the lead organization, the Air Force Office of Scientific Research (AFOSR), and the Wright Research and Development Center (WRDC). A Technical Panel, administered by the National Research Council, affords a scientific review during proposal selection and provides technical insight to the Air Force Steering Committee.

Technical issues facing both the theoretical and experimental researchers include identification of high energy density systems, formation mechanisms, energy efficiency, lifetimes, methods of stabilization and storage, novel bonding structures, and decay mechanisms. Theorists are performing quantum mechanical calculations to determine energy states and predict possible decomposition pathways while experimentalists are working to verify theory, characterize species and investigate stability. In order to maintain a synergistic environment between HEDM researchers, a HEDM Contractors Conference is held annually.

These proceedings document the most recent results of the projects funded through the HEDM program as presented at the Third HEDM Contractors Conference. Progress is continually being made in these areas of high energy molecular systems. While the main goal of the program is to identify and develop these high energy systems, a consequent result is the significant scientific advancements in chemistry and chemical physics.

High Energy Density Materials Contractors Conference

Technical Program

Sunday, 12 March 1989

5:00 - 7:00 p.m.: Reception, Home of Rep. Lindy Boggs, 623 Bourbon Street

Monday, 13 March 1989

7:00 a.m. - Registration and Continental Breakfast, St. Charles Foyer

Meeting Session, St. Charles A & B
Chairman - Larry P. Davis, AFOSR

8:00 - Administrative Announcements

8:05 - Welcome - Donald L. Ball, AFOSR

8:10 - "AFAL Perspective of HEDM Research," Stephen Rogers, AFAL

8:20 - "The AFOSR High Energy Density Materials Program," Larry P. Davis and Frank J. Wodarczyk, AFOSR

8:30 - "Propellant Payoff from a Classical Perspective," Gerald Nordley, AFAL

9:00 - "Complex Chemical Reactions Mechanisms and Efficiency," John Ross, Stanford University.

9:30 - Break

9:50 - "Studies on Advanced Oxidizer Systems Containing the Fluoroperoxide and Fluorodiazine Moiety," S.A. Kinkead, P.G. Eller, and J.B. Nielsen, Los Alamos National Laboratory.

10:15 - "Synthesis and Structural Characterization of New High-Valent Inorganic Fluorine Compounds and Their Oxidizing Properties," A.A.A. Emara, D. Hutchinson, A. Paprica, J.C.P. Sanders, G.J. Schrobilgen, and J. Valsdottir, McMaster University.

10:40 - "Experimental Studies on the Synthesis of New Noble Gas Fluorides and High Oxidation State Energetic Fluorine Compounds Involving Unusual Bonding Situations," W.W. Wilson and K.O. Christie, Rocketdyne Division, Rockwell International Corporation.

11:05 - "Computational Studies of Tetrahedrane, Some Azatetrahedranes, and Their Nitro Derivatives," Peter Politzer and Jorge M. Seminario, University of New Orleans.

11:30 - "The Synthesis of Nitrocyclopropanes using Nitrodiazomethanes," William P. Dailey, University of Pennsylvania.

11:55 - "Dynamic Constraints on Stochastic Behavior in the Chemistry of Highly Excited Molecules," Barry K. Carpenter and John R. Wiesenfeld, Cornell University.

12:20 - Lunch, Rhythms Room

Meeting Session, St. Charles A & B

Chairman - Alan Garscadden, AF Wright Aeronautical Laboratories

1:30 - "Theoretical Study of Ion-Pair States," Roberta P. Saxon and Dabbia Talbi, SRI International.

1:55 - "Theoretical Investigation of Energy Storage in Atomic and Molecular Systems," H.H. Michels and J.A. Montgomery, Jr., United Technologies Research Center.

2:20 - "Spectroscopy of Hydrogenic Species in Hot Plasmas and Cryogenic Solids," Takeshi Oka, University of Chicago.

2:45 - "Photoionization and Dissociation of the Triatomic Hydrogen Molecule," H. Helm, L.J. Lembo, P.C. Cosby, and D.L. Huestis, SRI International.

3:10 - "Ionic Solid Hydrogen Fuel: Production and Properties of Hydrogen Clusters," Young K. Bae and Philip C. Cosby, SRI International.

3:35 - Break

4:00 - "Experimental and Theoretical Studies of the Properties of Trihydrogen," Aron Kuppermann, California Institute of Technology.

4:25 - "Two Dimensional Potential Energy Surfaces of Pyramidal Tetrahydrogen Near a Three-Fold Seam," Sheng-yu and William A. Lester, Jr., University of California, Berkeley.

4:50 - "Electronic Quenching of B-State H_2 (v,J)," Charles D. Pibel, Andrew H. Kung and C. Bradley Moore, University of California, Berkeley.

5:15 - "Further Investigations of Infrared Absorption Spectra of Ionic Clusters of Hydrogen," M. Crofton, J.M. Price, and Y.T. Lee, University of California, Berkeley.

5:40 - Adjourn

Tuesday, 14 March 1989

7:00 - Continental Breakfast, St. Charles Foyer

Meeting Session, St. Charles A & B
Chairman - Daniel D. Konowalow, AFAL

8:00 - "(NH)₆: The Amino-analogue of Cyclohexane. A Laboratory for the Understanding of Lone-pair Effects on Molecular Geometry," Charles P. Blahous III and Henry F. Schaefer III, University of Georgia.

8:25 - "Metastable He₂⁻ and Its Autodetachment Spectra: An Accurate Coupled-Cluster Study," Tadeusz Pluta and Rodney J. Barlett, University of Florida, and Ludwik Adamowicz, University of Arizona.

8:50 - "Theoretical Studies of Bridged Structures of Be₂H₂ and B₂H₂," Byron H. Lengsfeld III, Lawrence Livermore National Laboratory.

9:15 - "New High Energy Density Small Ring Systems," Koop Lammertsma, University of Alabama at Birmingham

9:40 - "Molecular Structures and Heats of Formation for Light Metal Atom Clusters." George F. Adams, US Army Ballistic Research Laboratory.

10:05 - Break

10:25 - "Theoretical and Experimental Investigations of Dications," W.C. Lineberger, S.R. Leone, and S.V. O'Neil, JILA, University of Colorado.

10:50 - "Investigations of Hypervalent Compounds as High Energy Materials," Paul Engelking, University of Oregon.

11:15 - "Laser and Fourier Transform Spectroscopy of Novel Propellant Molecules," Peter F. Bernath, University of Arizona.

11:40 - "Production of the CH Radical With an Ion Gun," P. Bletzinger and M. E. Ruark, Aero Propulsion and Power Laboratory, Air Force Wright Aeronautical Laboratories.

12:05 - Lunch (Participants on their own)

Meeting Session, St. Charles A & B
Chairman - Frank J. Wodarczyk, AFOSR

1:30 - "Ab Initio Study of the Energetics of the Decomposition of HN₃ and N₃," Millard H. Alexander, University of Maryland.

1:55 - "Experimental Study of the $H + N_3$ Reaction and the Photodissociation of HN_3 ," Paul J. Dagdigan, The Johns Hopkins University.

2:20 - "Time and State Resolved Studies of the Overtone-Pumped Photodissociation of HN_3 (X^1A')," M.P. Casassa, B.R. Foy, D.S. King, and J.C. Stephenson, National Institute of Standards and Technology.

2:45 - "Model Studies of CBES Decomposition," T.A. Seder and D.J. Benard, Rockwell International Science Center.

3:10 "Theoretical Studies of Highly Energetic CBES Materials," N.E. Brener, J. Callaway, and N.R. Kestner, Louisiana State University.

3:35 - Break

4:00 - "Decay Processes in Energetic Species: Theoretical Studies of the Electronic Structure Aspects of $He(2^3S)$ Quenching and the Azide Decomposition Reaction $N_3H \rightarrow NH(X^3\Sigma^-) + N_2$," David R. Yarkony, The Johns Hopkins University.

4:25 - "High Energy Density Systems in Cryogenic Media: The Production and Reaction of Atoms and Radicals," Eric Weitz, Northwestern University.

4:50 - "Chemically Bound Excited Clusters," C.A. Nicolaides, National Hellenic Research Foundation.

5:15 - Adjourn

7:00 p.m. - Mixer with No-host Bar, Lagniappe Room

8:00 p.m. - Banquet, Rhythms Room

Guest Speaker: Don Hart, Don Hart & Associates
Former Director, AF Rocket Propulsion Laboratory

Wednesday, 15 March 1989

7:00 - Continental Breakfast, Pontchartrain B Foyer

Meeting Session, Pontchartrain B

Chairman - Stephen Rodgers, AFAL

8:00 "Limitations on Atom Densities in Cryogenic Matrices," A.T. Pritt, Jr., N. Prosser, and R.R. Herm, The Aerospace Corporation.

8:25 - "Weak Interactions," Daniel D. Konowalow, Air Force Astronautics Laboratory.

8:50 - "Matrix Isolation Spectroscopy of Metal Atoms Generated by Laser Ablation," Mario E. Fajardo, Air Force Astronautics Laboratory.

9:15 - "Metastable Metals in Matix Materials," N. Presser, A.T. Pritt, Jr., and R.R. Herm, The Aerospace Corporation.

9:40 - "Energy Transfer Process in Rare Solids," H. Helvajian, L. Wiedeman and J.B. Koffend The Aerospace Corporation.

10:05 - Break

10:25 - "Rydberg Holes and Solid State Exciplex Lasers," V.A. Apkarian, University of California, Irvine.

10:50 - "Ab Initio Study of ArH , ArH^+ , Ar_2H , Ar_2H^+ , Ar_4H , and Ar_4H^+ Molecules," Marcy E. Rosenkrantz, Air Force Astronautics Laboratory.

11:15 - "The Interaction of Hydrogen Chloride with Rare Gas Atoms," Cary F. Chabalowski and George F. Adams, US Army Ballistic Research Laboratory, and David R. Yarkony, The Johns Hopkins University.

11:40 - "Production and Characterization of High-Energy Hypervalent Hydrides," Edward R. Grant, Purdue University.

12:10 - Lunch (Participants on their own)

Meeting Session, Pontchartrain B

Chairman - Larry W. Burggraf, AFOSR

1:30 - "Gas Phase Production of Energetic Species for Cryogenic Trapping," Patrick G. Carrick, Air Force Astronautics Laboratory.

1:55 - "Dynamics of Atomic Hydrogen Trapped in Crystal Lattices," Bruce C. Garrett, Chemical Dynamics Corporation.

2:20 - "Energy Storage in Solid Molecular Hydrogen Due to Trapped Atoms," James R. Gaines, University of Hawaii at Manoa.

2:45 - "Photoinitiated Chain Reactions in Low Temperature Solids," Charles A. Wight, University of Utah.

3:10 "Dynamics of Metastables in the Condensed Phase," P.K. Swaminathan, Chemical Dynamics Corporation.

3:35 - Break

4:00 - "Specific Impulse Enhancement via Pressure Stabilized Excited Electronic States of High Energy Density Propellants," John W. Kenney, III, Eastern New Mexico University.

4:25 - "Theoretical Studies of Metastable Molecular Systems," K. Kirby, Harvard-Smithsonian Center for Astrophysics.

4:50 - "High-Spin Nitrogen: The $A'^5\Sigma_g^+$ State," William J. Marinelli and Anne M. Woodward, Physical Sciences Inc.

5:15 - "A Phase Diagram for Hydrogen: Prospects for Metallization," Isaac Silvera, Harvard University.

5:40 - Adjourn

NON-SPEAKING ABSTRACTS

"The Ab Initio Determination of the Damped Dispersion Energy of Interaction Between an Atom and a Diatomic Molecule." James E. Bohr, Air Force Astronautics Laboratory.

"Synthesis of Novel, Substituted Polycyclic Cage Systems," Alan P. Marchand, University of North Texas.

"Research Opportunities in the Field of Energetic Materials," Robert L. McKenney, Jr., Air Force Armament Laboratory.

PROPELLANT PAYOFF FROM A CLASSICAL PERSPECTIVE

Maj Gerald Nordley
Astronautics Laboratory (AFSC)
Edwards AFB CA

Abstract

The problem facing the Air Force and the rest of the space community is the extremely high cost of access to space. No reusable single stage vehicle can currently achieve low earth orbit, and multistage vehicles deliver only a percent or two of their initial mass as payload. The payoff for higher energy propellants is to increase the payload of a rocket stage for a given mission and liftoff mass. The ratio of the initial mass (including propellants) to the final mass (initial mass minus propellant exhausted) for a rocket stage increases exponentially with the velocity change needed and decreases exponentially with the exhaust velocity, or, equivalently, specific impulse. The exhaust velocity is proportional to the square root of its kinetic energy. This kinetic energy must be some dimensionless fraction of the chemical energy available from the propellant, typically about .8. Engine, propellant, tankage and structure masses can be estimated from exhaust velocity and mission. What remains of the initial mass is payload. For exhaust velocities in the regime of interest for high energy chemical propellants, roughly 4 to 9 km/s, payload increases rapidly from zero and then less rapidly. When significant payload can be achieved, other considerations, such as shelf life or environmental impact also play an important role in propellant choice.

1. BACKGROUND

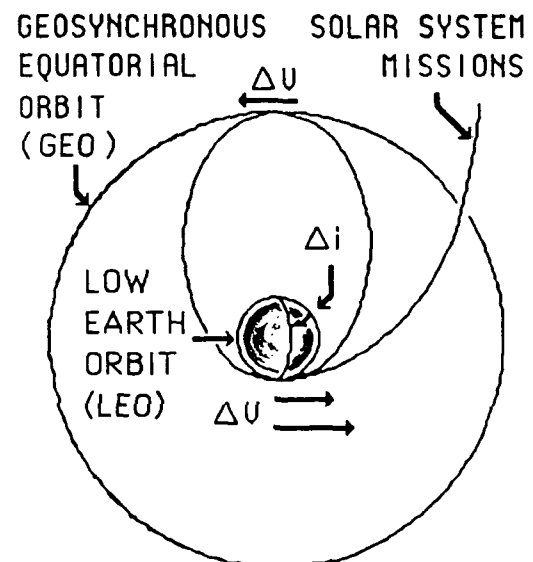
Recurring costs for launching a Space Shuttle are subject to debate, but a reasonable estimate would be about \$100 M for a flight delivering about 20 metric tons to low earth orbit (LEO), or roughly \$5000/kg. Recurring costs for a large airliner, which need be only checked out and fueled for most missions are on the order of \$100,000 for a 100 metric ton payload. That's \$1/kg or about \$100 for most of us. The main differences are that the space launch vehicle requires more care between missions and needs to carry so much fuel.

There are two main approaches to trying to achieve airline type access to space. The first is to push technology to its limit with conventional fuels with clever ways to recycle parts, reduce tankage, structure and engine mass, and/or make use of the atmosphere for some initial reaction mass and lift. The Space Shuttle, the future "Advanced Launch System" (ALS) and the partially airbreathing aerospace vehicle (ASV) concepts are examples of this approach.

Alternatively, one can try to increase the exhaust velocity of a rocket, thus providing thrust per unit mass of propellant exhausted. Less propellant mass would be needed and more of the vehicle could then be devoted to payload and other hardware to make the system fully reusable. Everything else being roughly equal, increasing exhaust velocity requires more chemical energy per unit mass of propellant, and thus needs what we call "high energy density matter", or HEDM.

2. MISSION REQUIREMENTS

The mission required of a rocket can be described by the "Mission Equivalent Velocity Change", usually shortened to "delta V" or ΔV . This is the velocity a given rocket would achieve if fired in free space, with no losses due to gravity or air resistance. Gravity losses can be comprehended by visualizing a rocket lifting slowly off the pad: a large amount of fuel is being expended to support the rocket and very little to gain velocity. Air resistance is self explanatory. A rocket going from earth to Low Earth Orbit (LEO) thus must carry enough fuel to achieve a burn out velocity of about 10 km/s, even though final orbital velocity is only about 8 km/s. This is a very large velocity increment, about half of what is needed to escape the solar system entirely! The late engineer and science fiction author Robert A Heinlein often said that earth orbit was "halfway to anywhere".



MISSION EQUIVALENT VELOCITY CHANGE (km/s)

Earth to LEO	10
LEO to GEO and Return	8.4
60° Plane Change (Δi)	8
In LEO	
LEO to GEO and Return	6
(Aerobrake)	
LEO to GEO one way	4.2
LEO to Mars (Aerobrake)	3.3 - 6
LEO to Moon's Orbit	3.1

Figure 1. Mission Requirements

Figure 1 illustrates several mission categories of interest to NASA and the Air Force. Inclination change is a particularly difficult mission because it requires changing an already very large velocity vector. Aerobraking means using friction with a planetary atmosphere instead of rockets to slow a spacecraft. Large orbital transfer maneuvers deep within a gravitational field often require more velocity change than simply achieving escape velocity. The details of these mission requirements may be found in astrodynamics texts, such as Bates, Mueller and White.

3. BASIC ROCKET MECHANICS

The principal of the reaction engine was described by Isaac Newton, and is simply an application of the law of conservation of momentum. In the case of the rocket in free space, the gain in momentum of the rocket and its remaining propellant in one direction must equal the gain of momentum of an increment of exhaust mass in the other direction. Thus:

$$m dV = -v_x dm \quad (1)$$

where m is the instantaneous mass of the rocket, dV is the increase in its free space velocity, V , v_x is the velocity with which the exhaust increment, dm , is ejected (considered here to be constant, a fair assumption for most chemical rocket designs). Separating the variables and integrating from initial to final velocity and initial mass, m_0 , to final mass, m_f , leads to:

$$\Delta V = v_x \ln(m_0/m_f) \quad (2)$$

This is the classic "rocket equation" derived by Tsiolkovsky, Goddard, Oberth and others in the early 20th century. It applies to all free space reaction engines with constant exhaust velocities; for example electromagnetic accelerators (mass drivers) which exhaust pellets and ion rockets as well as thermal expansion nozzle rockets. In the exponential form:

$$m_0/m_f = e^{(\Delta V/v_x)} \quad (3)$$

This equation is plotted in figure 2 for two different exhaust velocities. The quantity, m_0/m_f is known as the "mass ratio" of a rocket. The more fuel one can carry with a given rocket mass, the higher its mass ratio. It is very difficult to build a rocket that carries six to eight times its empty mass in propellant, and still have mass for engines and payload. The solid rocket indicated toward the top of the graph was a simple ground test item: it contained no guidance system or payload.

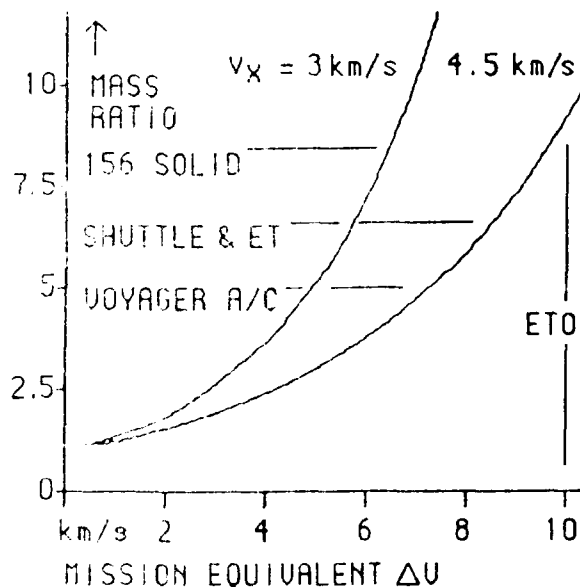


Figure 2. The Basic Rocket Equation

4. EXHAUST VELOCITY AND SPECIFIC IMPULSE

In figure three we consider the rocket engine as a "black box" into which go energy and reaction mass and from which emerges an exhaust with kinetic energy in the desired direction and various forms of waste energy, which depend on the type of rocket and propellant.

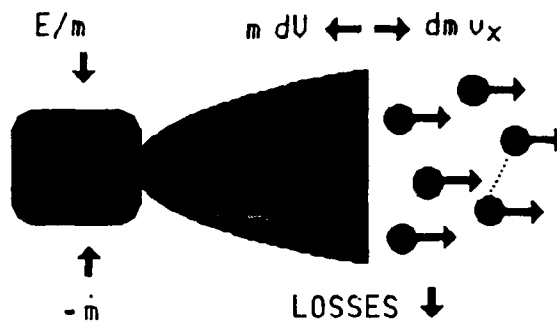


Figure 3. "Black Box" Rocket Engine

From the non-relativistic definition of kinetic energy, the exhaust power is:

$$P_x = (dm/dt) v_x^2 / 2 \quad (4)$$

Because of conservation of energy, this power must be some fraction, η , of the power available to accelerate the exhaust, dE/dt , so that:

$$(dm/dt) v_x^2 / 2 = \eta dE/dt \quad (5)$$

$$\text{thus: } v_x = \sqrt{2 \eta dE/dm} \quad (6)$$

The force or thrust imparted by an exhaust is the rate of momentum (p) change so that:

$$F = dp/dt = -v_x dm/dt \quad (7)$$

Equations (7) and (4) can be combined so that:

$$P_x = F v_x / 2 \quad (8)$$

Specific impulse (I_{sp}) was originally defined as impulse per unit mass, or equivalently, thrust over mass flow rate (Hart, 1989). From equation (7), it is obvious that specific impulse in rationalized units is simply the exhaust velocity. Engineers used to dealing with English units, however, tended to think of mass in pounds (metric culture engineers have been just as guilty of thinking of force in kilograms!) and thus expressed mass flow rate in pounds per second, resulting in specific impulse values in seconds. Texts such as Sutton and Ross (1976) now define specific impulse as thrust over (planet earth) weight flow rate, dw/dt , possibly because I_{sp} in seconds has become too ingrained in rocket culture to consider overturning at this point. Thus (neglecting the minus sign):

$$I_{sp} = F / (dw/dt) = F / g (dm/dt) = v_x / g$$

$$\text{and, } v_x = g I_{sp} \quad (9)$$

Because exhaust velocity is so important to reducing mass ratio, and because it is proportional to the square root of input energy per unit mass of propellant, it seems logical to consider lowering the average molecular weight of the exhaust stream by diluting it with a light exhaust specie such as hydrogen. In nuclear, solar thermal, and electric rockets where the energy supply is separate from the propellant, lowering the dm part of dE/dm produces significant increases in v_x . Hydrogen is better than water. In Chemical rockets, however, the energy supply is itself proportional to the mass of the reacting propellants. Adding inert mass of any molecular weight *lowers* total E/m .

Consider figure 3. In equilibrium thermal expansion nozzle rockets, exhaust particles generally share the same exhaust velocity regardless of mass (consider dust in a windstorm). If all the exhaust products are moving at the same velocity, then one could connect any two or three particles, creating larger particles, without changing the velocity or momentum of the exhaust. (Galileo used a similar argument in the leaning tower of Pisa thought experiment) Indeed, one would get exactly the same ΔV if the entire propellant mass were ejected at once, as long as it was ejected at v_x ! Thus mass drivers ejecting pellets weighing grams at 10 km/s will perform just as well as hydrogen propelled nuclear rockets with the same mass ratio and exhaust velocity.

Suppose, however, that there were a way to take a little energy from the higher mass particles and use it to give the lower mass particles a greater velocity. Something like this might happen in an explosive pellet rocket (figure 4). What would be the optimum distribution of exhaust velocities under these circumstances?

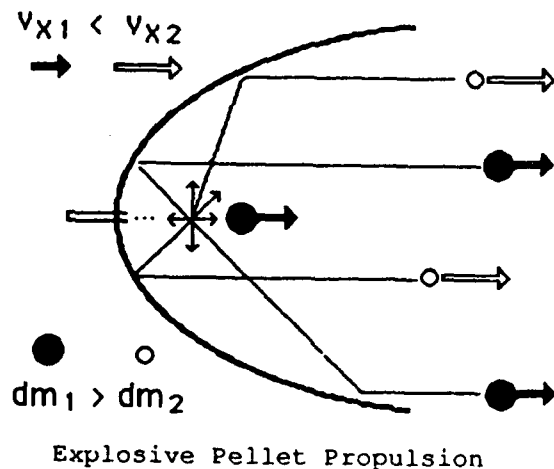


Figure 4. A Two Exhaust Component Rocket

Consider a two component system as illustrated in figure 4; from equation (7) the total thrust will be:

$$F = -v_{x1} \, dm_1/dt - v_{x2} \, dm_2/dt \quad (10)$$

$$\text{and } \langle v_x \rangle = F/(dm_1 + dm_2) \quad (11)$$

The subscripts refer to the two exhaust components.

We want to maximize effective exhaust velocity, $\langle v_x \rangle$, subject to the law of conservation of energy:

$$2 \eta \, dE = dm_1 v_{x1}^2 + dm_2 v_{x2}^2 \quad (12)$$

where the left side of the equation is constant. Figure 5 is a computer plot of these equations showing that the optimum condition occurs for v_{x2} to equal v_{x1} . This can also be shown analytically. Noting that $dm = dm_1 + dm_2$, one can substitute and collect terms so that:

$$\langle v_x \rangle \, dm = v_{x1} \, dm + (2 \eta \, dE - dm v_{x1}^2)/(v_{x1} + v_{x2})$$

For a maximum:

$$\frac{\partial \langle v_x \rangle \, dm}{\partial v_{x2}} = (-1) \frac{2 \eta \, dE - dm v_{x1}^2}{(v_{x1} + v_{x2})^2} (1) = 0$$

$$\text{Thus: } 2 \eta \, dE = dm v_{x1}^2$$

If one exchanges subscripts and follows the same procedure, it is also true that:

$$2 \eta \, dE = dm v_{x2}^2$$

So that for maximum I_{sp} :

$$v_{x1} = v_{x2}$$

From figure 5 we see that the maximum is very broad. Therefore, while explosive pellet rockets might operate off the maximum, the penalty is relatively small unless there are very great disparities in the distribution of exhaust velocity components.

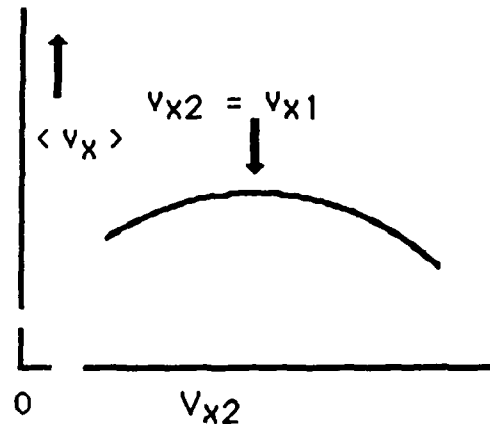


Figure 5. Two Component Exhaust Equivalent Velocity.

(After I had gone through all this, Bill Haloulakos of McDonnell Douglas observed that the problem was very similar to the one solved by the ancient Greeks some two thousand years ago to find the maximum area for a given perimeter. This problem is also the subject of a famous story concerning Aeneas' sojourn in Carthage, wherein he needed to mark out the maximum amount of Carthage real estate possible with one cowhide. He cut it into very thin strips and made a big circle. My literature didn't go back that far.)

If there were n components to the exhaust we could follow this procedure: select two components and get the maximum thrust contribution from those two by making them equal. Now, considering that first set as a single component, we can optimize the contribution of a third element by setting it equal to the first two, and so on. Thus the optimum condition for an exhaust is for all the components to have equal v_x .

In chemical rocket practice, adding a small amount of hydrogen to a given propellant mixture will often allow a higher I_{sp} . (Hart 1989) If the total theoretical energy supply stays fixed, this result is mathematically equivalent to increasing η . This increase might be attributed to improved combustion efficiency, higher chamber pressure, optimization at a different nozzle design, or some combination of the above.

Thus far we have considered equations which would apply to any rocket regardless of how its exhaust velocity is generated. In chemical rockets, the source of energy is the net heat of formation of the reactants, so that $dE/dm = \Delta H_f$. ΔH_f should include heats of vaporization of reactants and so forth so that it represents the total energy ideally available from the propellants.

There are several programs available which calculate a specific impulse for propellant mixtures based on rocket engine design parameters supplied by the user. The values calculated are thus as much a result of the user's rocket engineering as they are of the propellant mixture. These programs embody several decades of experience with rocket engine combustion and thermodynamics. They can provide the user much information about the mixture ratios, combustion chamber conditions, exhaust conditions, temperatures, expansion ratios and so on needed to get optimum performance from a given propellant combination.

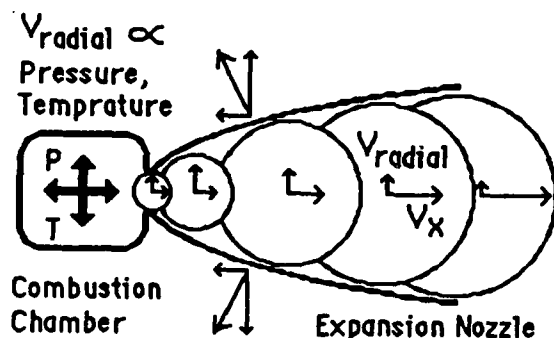


Figure 6. Thermal Expansion Rocket

Some observations can be made about the conditions in the combustion chamber and nozzle of a standard chemical/thermal rocket, such as illustrated in figure 6. The combustion chamber is typically very well insulated or regeneratively cooled, thus the only way for a significant amount of energy to escape the chamber is through its throat. The combustion gases reside in the chamber long enough, and at high enough density and ionization that any energy released within is readily thermalized. Any photons released from chemical processes are absorbed by chamber walls as heat which is passed to the propellant circulating through walls before injection or by the gases themselves.

The gases move through the throat at high density and pressure and then pick up additional lateral velocity in bulk as they expand and cool, losing perpendicular velocity. Some exhaust may be diverted to turbines to run propellant pumps. Energy release from chemical reactions which continue in the nozzle and help drive the expansion are increasingly less effective at getting rid of non-translational energy as the density of the gas in the nozzle decreases. Eventually, photons are lost as brilliant light, and high energy states and incomplete reactions become "frozen" in the exhaust flow. Thus when the gases leave the nozzle, any thermal and chemical energy remaining in the gases is lost. Other loss mechanisms are minor in comparison.

The I_{sp} programs model many of these interesting processes in detail with thermodynamic equations found in most standard rocket references, (for instance: Clarke, Sutton and Ross, Barrere). The net result of these equations and models is the prediction of an exhaust velocity which is some fraction of the exhaust velocity which would be obtained if all the available energy were converted to exhaust kinetic energy.

A useful thing to do with I_{sp} programs is to manipulate the input parameters until they give an answer of about 450 s for a 6:1 LO₂-LH₂ mixture. There are two such engines currently flying, the space shuttle main engine (SSME) which gets 453.5 s in vacuum and the older RL-10 which gets 444 s according to manufacturer's data. Then use these same input conditions (chamber pressures, expansion ratios, external pressure, and so forth) for the new propellant combination.

If the only thing needed is an I_{sp} estimate, since I_{sp} is proportional to $\sqrt{\Delta H_f}$, it is just as valid to do a good job of calculating ΔH_f ($\approx dE/dm$) for all the reactants and products and put the result into equation (6) using $\eta = 0.8$. ΔH_f should be expressed in Joules/kg to get an exhaust velocity in m/s. Divide by g for I_{sp} .

$$v_x = \sqrt{2\eta \Delta H_f} = g I_{sp} \quad (13)$$

Use of this formula is equivalent to saying that whatever design difficulties need to be overcome in using the candidate propellant, rocket engineers will eventually find a way to get 80% of the available energy into the kinetic energy of the exhaust. The result does not depend on any assumptions of the type of rocket technology used other than the assumption of a ballpark value for η . Table 1 is an example worked for LO₂/LH₂.

Table 2 is taken from a JPL study of advanced concepts by Frisbee (1983). The tri-propellants in Table 2 will probably require a hybrid rocket. In hybrid rockets, liquid propellant(s) may be injected into a solid grain, allowing greater flexibility in propellant combinations and thrust control with solid propellant.

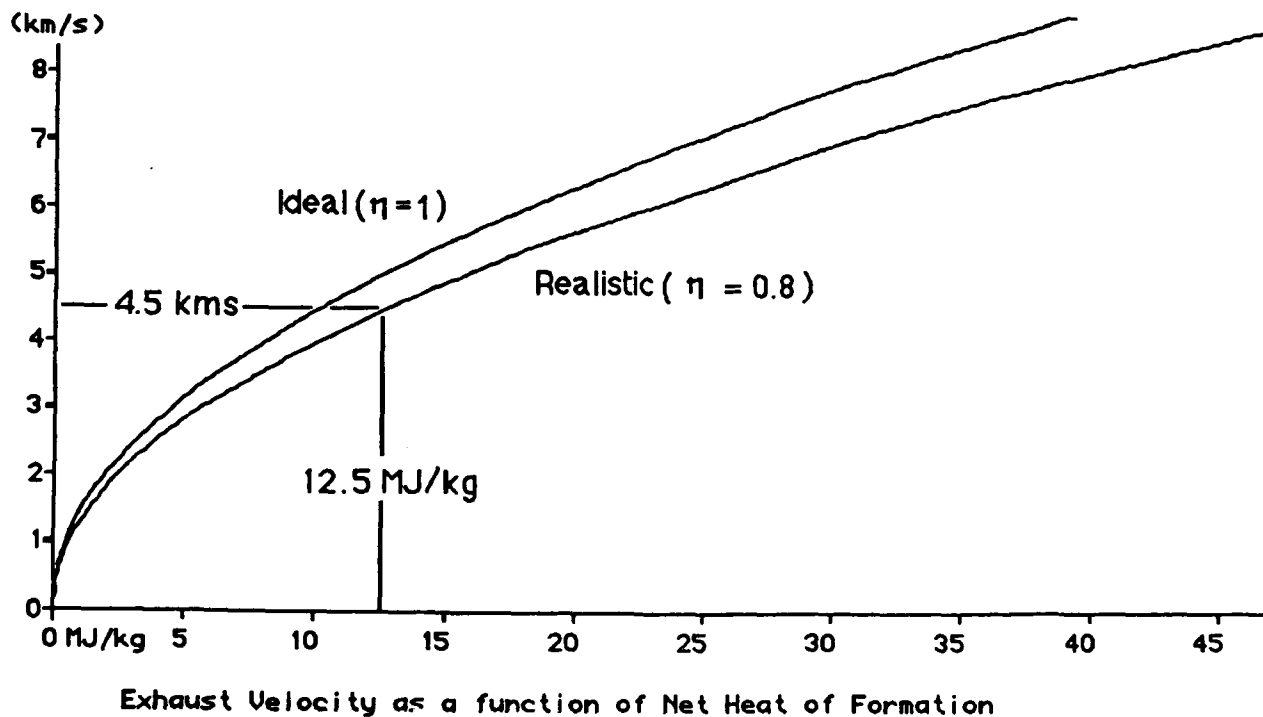
Figure 7 is a graph of equation (13) with exhaust velocity and I_{sp} on the vertical axis and ΔH_f on the horizontal axis. For propellant combinations that may not be amenable to treatment with standard liquid rocket engine technology, reading the I_{sp} off this graph is probably as useful as anything else one might try at this stage of HEDM propellant research.

Table 1. SSME LOx-LH2 Isp Calculation Example

<u>REACTION</u>				
$1/2 \text{ O}_2(\text{L}) + 4/3 \text{ H}_2(\text{L}) = \text{H}_2\text{O}(\text{g}) + 1/3 \text{ H}_2(\text{g})$				
<u>MASS</u>				
16	+ 2.695	= 18.015	+ 0.68	
			= 18.695 g	
<u>HEATS</u>				
$H_f(\text{CRC})$	$H_f(\text{CRC})$	$H_f(\text{CRC})$	$H_f(\text{CRC})$	
0	0	-57.1 kcal/mol	0	
		(13,285 J/g)		
H Vap.	H Vap			
213 J/g	452 J/g			
<hr/>				
3.40 kJ	+ 1.20 kJ	- 238.9 kJ	+ 0	
<hr/>				
Net $\Delta H_f = -234.3 \text{ kJ}$				
<hr/>				
$\Delta H_f = -234.3 \text{ kJ} / 18.7 \text{ g} = 12.53 \text{ MJ/kg}$				
Let $\eta = 0.8$ and $g = 9.8 \text{ m/s}^2$				
$I_{sp} = (1/g) \sqrt{2 \eta \Delta H_f}$				
$= 456.9 \text{ s}$ versus 453.5 s from ref.				

Table 2. Isp For Various Propellants (Frisbee, 1983)

PROPELLANT	CALCULATED I_{sp} , s	
	IDEAL	ODE (1000 psia \rightarrow 0.2 psia)
<u>SOLIDS</u>		
$10\text{CH}_2/72\text{NH}_4\text{C}_{10}\text{H}_8\text{Al}$	($\eta = 1$)	340
$10\text{CH}_2/52\text{NH}_4\text{C}_{10}\text{H}_8\text{Al}$		347 <u>IUS</u>
$14\text{CH}_2/72\text{NH}_4\text{C}_{10}\text{H}_8\text{Al}$		370 $I_{sp} = 306 \text{ s}$
<u>MONOPROPELLANTS</u>		
H_2O_2	265	192
N_2H_4	269	264
<u>BIPROPELLANTS</u>		
$\text{ClF}_3/\text{N}_2\text{H}_4$	386	372
$\text{N}_2\text{O}_4/\text{N}_2\text{H}_4$	404	354
$\text{O}_2/\text{RP-1}$	461	380
$\text{F}_2/\text{N}_2\text{H}_4$	-	436
F_2/H_2	528	489 <u>SSME</u>
O_2/H_2	507	470 $I_{sp} = 460 \text{ s}$
O_3/H_2	607	501
<u>TRIPROPELLANTS</u>		
$\text{F}_2/\text{Li-H}_2$	703	-
$\text{O}_2/\text{Be-H}_2$	705	-
<u>FREE RADICALS</u>		
$\text{H}+\text{H} \rightarrow \text{H}_2(100\%)$	2130	-

Figure 7. Exhaust Velocity Versus ΔH_f , Net Heat of Formation of the Exhaust Products

5. PAYLOAD PAYOFF ESTIMATION

The actual payoff for increasing exhaust velocity is a lower cost for delivering a given payload to a given mission equivalent velocity. This cost generally scales with the initial mass of the rocket stage. This is easy enough to see for an orbit transfer vehicle, given the cost of delivering any mass to LEO. It is as well a given in the aerospace industry that the costs associated with most pieces of comparable hardware scale with their mass. If we accept this, then the problem of minimizing cost becomes one of maximizing the fraction of a rocket stage which consists of payload.

From the above review, we can calculate the mass ratio of a rocket stage from the mission equivalent velocity and the energy content of the propellants. This gives the burnout mass of the rocket including guidance and control systems, structure, engines, and propellant tankage as well as payload. To estimate the payoff in payload fraction for increased propellant energy, one must make allocations for these masses.

Guidance, control and structural masses can be modeled as a fraction of the initial mass. This seems intuitively reasonable in that it should take more hardware to support and control the movements of a large rocket than a small one. Accurate assessment of this requires a detailed design for a specific mission, but for the purposes of evaluating the relative benefits of various propellants, an allocation of 5-10% for guidance control and structural mass will be realistic. Thus:

$$M_S \approx m_0 Gf \quad (14)$$

where M_S is the mass of the guidance, control and structural systems, m_0 is the initial mass and Gf is the "Guidance control and structural fraction", ≈ 0.05 .

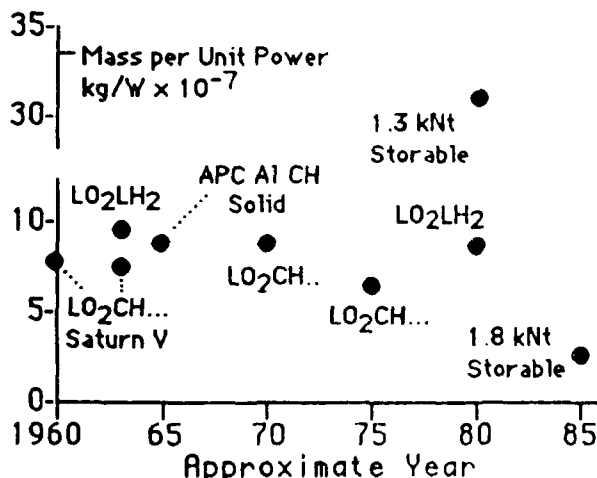


Figure 8. Specific Masses of Various Engines

Engine mass tends to scale as the power of the engine. This seems intuitively obvious as well; in our experiences with other kinds of engines, the more powerful ones weigh more. It is, however, somewhat surprising to see how closely the disparate kinds of rocket engines track in terms of mass per unit power. Figure 8 graphs data on a number of engines taken from various sources versus the approximate year of the engine technology.

The engines range from about 7 million newtons (1.6 M lbf) to around 1 thousand newtons. The only really disparate point was for relatively small engines. These were the subject of a successful strategic defense initiative technology program at the astronautics laboratory. The state of the art is now such that these engines can be made lighter per unit power than their larger brothers. For analysis purposes, we will assume that rocket engines weigh 7×10^{-7} kg per watt of exhaust power. This is called the "specific power" of the engine, represented by α .

The engine power required depends on the acceleration required for the type of mission considered. A rocket taking off vertically from the surface of the earth must obviously have a thrust greater than the weight of the rocket. This means a "thrust to weight ratio" greater than 1. A rocket taking off horizontally can get by with less, perhaps as little as 0.5. Orbit transfer, in theory, could be done with vanishingly small thrust, and in fact has been accomplished, under dire circumstances, with 10 Nt attitude control thrusters. That procedure requires either many separate firings or an inefficient trajectory because a rocket in orbit does not spend enough time near its desired firing point for a 10 Nt thruster to deliver much velocity change. In practice, a thrust to weight ratio of at least 0.1 is desired for earth orbit transfer missions. Because the most difficult mission to be addressed by high energy propellants is the earth to orbit mission, the model used here assumes a thrust to weight ratio, "T" of 1.0. By definition, $T = F / (g m_0)$. Using the above with equation (8) we get:

$$M_e \approx \alpha P_x = \alpha F v_x = \alpha g m_0 T v_x \quad (15)$$

where M_e is the mass of the engines. This means that, for a given thrust to weight ratio, the weight of the engine scales directly with its exhaust velocity.

The mass of the propellant, M_p , can be taken from the basic rocket equation (3) as follows:

$$M_p = m_0 - m_f = m_0 (1 - m_f/m_0) = m_0 (1 - e^{(-\Delta V/v_x)}) \quad (16)$$

The mass, M_t , of propellant tanks sufficiently strong to retain their propellants when subject to several gravities of acceleration can be modeled as a fraction "b" of the propellant mass, so that:

$$M_t = b M_p \approx b m_0 (1 - e^{(-\Delta V/v_x)}) \quad (17)$$

Liquids and solids which approximate water in density require a tankage fraction, of about .05. Low density liquid hydrogen may have tankage fractions from 0.15 to .5 depending on how long the hydrogen must be stored in the tank. The Space Shuttle external tank, containing mostly liquid hydrogen by volume and mostly liquid oxygen by mass, has a tankage fraction of about .08. If the payload is very small and the tanks very big, small changes in the tankage fraction can result in large percentage changes in payload.

Thus, dense propellants with respectable exhaust velocities may compete with more energetic propellants requiring heavier tanks. In marginal circumstances, one has to work out the numbers carefully to choose between alternative propellants.

The initial mass of the rocket stage is the sum of the masses described above:

$$m_0 = M_I + M_S + M_E + M_P + M_t \quad (18)$$

Using equations (14) - (17) and solving for M_I / m_0 yields the following equation for payload fraction, PF, in terms of ΔV , v_x , and the parameters Gf , α , T , and b :

$$PF = 1 - Gf - \alpha g T v_x - (1 - e^{(-\Delta V/v_x)})(1 + b) \quad (19)$$

Equation (19) is plotted in figure 9 for mission requirements of 4.2, 6.0 and 10 km/s. The curves are steep and linear in the region of the zero payload axis intercept meaning that: 1) for a given set of parameters there exists an exhaust velocity below which a rocket will be unable to deliver a payload, and, 2) in this region there is a significant payoff for small increases in v_x .

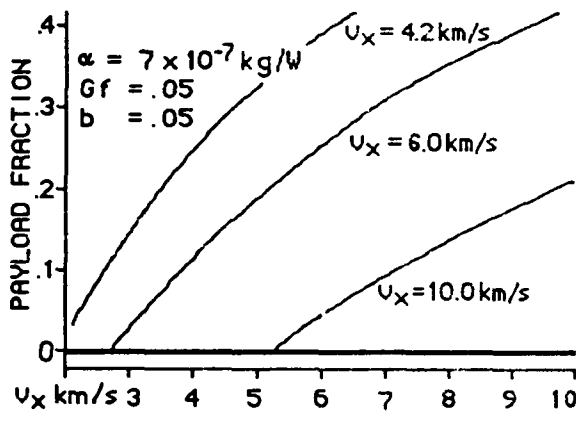


Figure 9. Payload Fraction as a Function of V_x

In figure 10, the intercept region for the 10 km/s mission is expanded and two curves are plotted based on different assumption for specific power of the rocket engine. While the mass of the engine can clearly make the difference between some payload and no payload near the intercept, the slope of the curves is not sensitive to assumptions about α . This is also true of Gf , T and b . We can thus say with some confidence that, for a single stage earth to orbit (10 km/s) mission near the intercept, an increase in exhaust velocity of about 200 m/s (20 s Isp) should yield a gain in payload equal to about 1% of the gross liftoff weight. The percentage of payload increase, of course, depends on where one is on the curve initially.

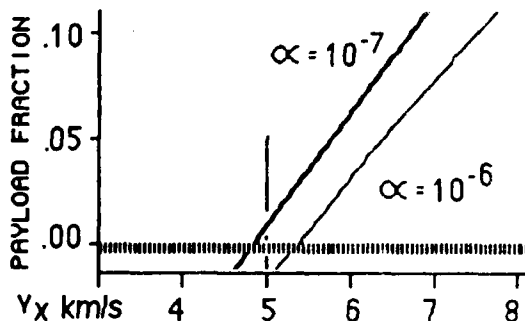


Figure 10. Sensitivity of Payload Fraction to α .

6. SUMMARY

The following should be kept in mind: Everything else being held constant, exhaust velocity and specific impulse are proportional to $\sqrt{\Delta H_f}$ as used above. This net ΔH_f should be expressed as energy per unit mass, not energy per mole. There is no trick in the classical mechanics of rocket propulsion known to this author which allows deviation from this result.

Parametric analysis of payload payoff relies on estimates for the various parameters and can provide only an approximate absolute payload fraction estimate. It is, however, a fairly powerful tool for estimating the relative merit of particular propellant combinations, particularly if parameters such as tankage fraction and specific power can be adjusted based on knowledge of propellant specific storage requirements. Mission requirements (ΔV , T) and assumptions about engine internal efficiency (η) and specific power (α) should be held constant for comparisons.

If first order analysis shows the difference in payoff of two candidates is relatively small, the choice between them may hinge on other considerations such as low tankage fraction, storability, development cost, producibility, safety, environmental impact and so forth of the candidate. For example, a room temperature, dense, stable, solid propellant with a specific impulse of 400 seconds would be revolutionary compared to existing 300 s class solid propellants and might even be preferred to volatile LOx-Hydrogen.

7. ACKNOWLEDGEMENTS

I would like to express my thanks to Dr Marcy Rosenkrantz for her most helpful comments, to Don A. Hart for illuminating the history of the definition of Isp and on how engine design parameters may change with mixture ratios to optimize efficiency, and to Bill Haloulakos for his perspective on the mathematics of exhausts with different velocity components.

8. BIBLIOGRAPHY

Barrere, M., et al., Rocket Propulsion, Elsevier, Princeton, 1960

Clarke, Arthur C., Ascent to Orbit, Wiley & Sons, New York 1984. This is a compilation of Clarke's technical writing going back to 1938, including tutorials.

Frisbee, Robert, Ultra High Performance Propulsion for Planetary Spacecraft, JPL D-1184, Pasadena CA, 1983

Haloulakos, V. E., Personal Communication, 15 Mar 89

Hart, Don A. Personal Communication, 13 Mar 89

Ley, Willy, Rockets, Missiles, and Men into Space, Viking, New York, 1968. This is the final edition by the author of the classic history of this field, originally published as simply Rockets in 1944 and revised until the author's death days before the first moon landing.

Sutton, and D. Ross, Rocket Propulsion Elements, Wiley & Sons, New York, 1976.

NEW HIGH ENERGY OXIDIZER SYSTEMS FOR PROPELLANT AND ENERGY STORAGE APPLICATIONS

Scott A. Kinkead, P. Gary Eller, Jon B. Nielsen

MS-C346

Los Alamos National Laboratory

Los Alamos, New Mexico 87545

The objective of our program is to provide basic research involving the syntheses, characterization, and application of inorganic compounds potentially useful for advanced rocket propulsion and energy storage applications. The initial emphasis for this program has been in two areas: the synthesis of inorganic starting materials for reactions with O_2F_2 and testing of our non-equilibrium or "hot wire" reactor.

Initially we intended to prepare several halogen oxyfluorides for our reaction studies with O_2F_2 . However, our method using $P(O)F_3$ as an oxygen transfer agent did not proceed as we had planned. The reaction of $P(O)F_3$ with the halogen fluorides ClF_5 and ClF_3 proceeds in a nearly quantitative fashion to give PF_5 and the oxyfluoride $FClO_2$. The reagent stoichiometry does not have any apparent effect on the product distribution for these reactions since it was found that all ratios of reactants used gave $FClO_2$ and PF_5 . The reaction of ClF_5 with $P(O)F_3$ presumably proceeds by first forming ClF_3O . However, ClF_3O is known to be a stronger fluorinating agent than ClF_5 and thus it should react faster with phosphoryl fluoride than will ClF_5 to give chloryl fluoride.¹

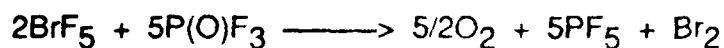


The reaction of ClF_3 with $P(O)F_3$ also gave chloryl fluoride. This reaction most likely proceeds as follows.



Disproportionation of the unstable intermediate FClO is presumed to give the product FClO₂.

On the other hand, the reaction of BrF₅ and P(O)F₃ produced the following products:



Here, like the ClF₅ reaction with P(O)F₃, it is probable that BrF₃O is the initial product formed. The BrF₃O then can continue to react with the P(O)F₃, eventually resulting in the formation of oxygen, bromine, and PF₅ through a complex series of reactions. The oxygen formed was volatilized at -183 °C and the gases quantitated by PVT techniques along with the weight loss of the reaction vessel. These reactions and products are very similar to the work published recently by Christie and co-workers in which they were able to prepare the compounds of interest by reaction of LiNO₃ with the appropriate halogen fluoride.²

The reaction of XeF₆ with P(O)F₃ was found to be a very effective method for the formation of xenon oxyfluorides. When XeF₆ and P(O)F₃ are reacted at room temperature, XeOF₄ is formed in an essentially quantitative yield. (CAUTION: use an excess of XeF₆ to prevent the formation of XeO₃). This is an advantage over published procedures which involve the controlled hydrolysis of XeF₆.³

Since the chemistry of phosphoryl fluoride with strong fluorinating agents had proven interesting, we followed the reactivity further by studying its reactions with transition metal fluorides and actinide hexafluorides. For example, phosphoryl fluoride reacted cleanly with MoF₆ to give PF₅ and MoOF₄. The reaction products are easily separated since PF₅ is quite volatile whereas MoOF₄ is a nonvolatile solid at room temperature.⁴

The actinide hexafluorides UF₆, PuF₆, and NpF₆ also reacted with P(O)F₃. The reaction of UF₆ and P(O)F₃ was carried out in a glass vessel over a period of several days. The products isolated were PF₅ and orange-yellow UOF₄. Attempts to obtain UV-vis absorption spectrum were unsuccessful. However, a Raman spectrum of the solid confirmed the identity of the solid as UOF₄ with the U=O

stretching frequency being observed at 893.4 cm^{-1} . The reaction of NpF_6 with P(O)F_3 gave a mixture of NpOF_4 and NpO_2F_2 , as confirmed by infrared analysis of the solid. The PuF_6 reaction with P(O)F_3 gave PF_5 and a tan residue but characterization is still incomplete. The work on the P(O)F_3 reactions is currently being completed for publication.

We have also initiated a study of the reaction of FOOF with perfluoroalkenes. Some time ago, it was found that FOOF reacted with SO_2 and $\text{CF}_3\text{CF}=\text{CF}_2$ to give FSO_2OOF and $\text{C}_3\text{F}_7\text{OOF}$ and we felt that it might be possible to use FOOF to add the fluoroperoxy group to other olefins.^{5,6} In our experiments we have found that FOOF reacts violently with $\text{CF}_3\text{CF}=\text{CF}_2$ and $\text{CF(H)}=\text{CF}_2$ even at -196°C . The only products isolated from these reactions were perfluorobutane and HF respectively, and both reactions produced some CF_4 and unidentified fluorocarbon compounds.

In addition to the above results, we have been completing the final tests of our "hot wire" reactor. In this reactor we are now able to safely and conveniently prepare and transfer FOOF at sustained rates approaching 0.5 mole per hour, much greater than by any other method. KrF_2 can be prepared in this same reactor at the rate of tens of grams per day, again at a rate and level of convenience and safety unsurpassed by other methods. We are thus well positioned to prepare large quantities of these powerful oxidizers for subsequent reaction chemistry and to use the reactor for other novel syntheses.

Another experiment which we have completed with the hot wire reactor is the preparation of XeF_6 , which in our reactor can be prepared XeF_6 at much lower pressures than by published methods. The accepted method of preparing XeF_6 is to heat a 20:1 mixture of F_2 and Xe at 300°C and 50 atm pressure.⁷ In our experiment, 70 mmoles of xenon was condensed onto the walls of the reactor at -196°C and treated with a tenfold excess of fluorine at a pressure of 40-80 torr, without gas circulation. During this treatment the filament temperature was in excess of 700°C (by calculation and observation). Over a period of 6 hours, all of the xenon was converted to fluorides and approximately 2 grams of XeF_6 was obtained. The remainder of the material, a white solid with a vapor pressure of 2-4 torr at 25°C , is believed to be a mixture of XeF_2 and XeF_4 . Repeated fluorinations

of the remaining material in the reactor produced only small additional amounts of XeF_6 , probably due to surface effects. However, this method does have advantages over the existing methods of producing XeF_6 and it is likely that we can improve the synthesis by varying the temperature of the reactor and by varying the thickness of the xenon layer condensed on the reactor walls.

In a similar fashion we attempted to prepare N_2F_2 in our hot wire reactor. In this experiment a 50:50 mixture of F_2 and N_2 was circulated in the flow loop of the thermal reactor at 3-5 l/min and 140-160 torr. After 250 torr of gas was consumed (in 10 liters) a small amount of white solid was collected at -196°C in a trap fitted with a sapphire viewport. Infrared analysis of this gas showed it to be mainly CF_4 and a trace of NF_3 . The quantity of gaseous products collected by no means correlated with the amount of F_2 and N_2 consumed. However, upon disassembling the reactor, a solid was found in the bottom of the reactor, which evolved a large quantity of fumes on exposure to air. When the solid was contacted with water, the solid detonated. There are at least two possible explanations for these observations. First, we may have prepared a powerfully oxidizing complex salt of the type $(\text{NF}_4^+)_2\text{NiF}_6^{2-}$ or $(\text{N}_2\text{F}^+)_2\text{NiF}_6^{2-}$. Since the reactor is constructed only of nickel, Monel, and copper in the heated zone, there are only a limited number of possibilities for the composition of the solid. Second, but less likely, it is conceivable that residual XeF_2 and XeF_4 was not thoroughly removed from a prior run with the reactor, which would explain the violent explosions (formation of XeO_3) upon hydrolysis of any XeF_6 formed. This point is currently under further investigation.

REFERENCES

1. Pilipovich, D.; Lindahl, C. B.; Schack, C. J.; Wilson, R. D.; Christie, K. O.
Inorg. Chem. **1972**, *6*, 2189.
2. Alexander, L. E.; Beatie, I. R.; Bukovsky, A.; Jones, P. J.; Marsden, C. J.; Van
Schalkwyk, G. J. *J. Chem. Soc., Dalton Trans.* **1974**, 81.
3. Paine, R. T.; Ryan, R. R.; Asprey, L. B. *Inorg. Chem.* **1975**, *14*,
1113.(And references within)
4. Christie K. O.; Wilson W. W.; Wilson, R. D. *Inorg. Chem.* **1989**, *28*, 675.
5. Solomon, I. J.; Kacmarek, A. J.; Keith, J. N.; Raney, J. K. *J. Am. Chem.*
Soc. **1968**, *90*, 6557.
6. Solomon, I. J.; Kacmarek, A. J.; Raney, J. K. *Inorg. Chem.* **1968**, *7*, 1221
7. Chernick, C. L.; Malm, J. G. *Inorg. Synth.* **1966**, *8*, 258.

SYNTHESIS AND STRUCTURAL CHARACTERIZATION OF NEW HIGH-VALENT INORGANIC FLUORINE COMPOUNDS AND THEIR OXIDIZING PROPERTIES

A.A.A. Emara, D. Hutchinson, A. Paprica, J.C.P. Sanders, G.J. Schrobilgen* and J. Valsdóttir

Department of Chemistry, McMaster University, Hamilton, Ontario L8S 4M1, Canada

KRYPTON-NITROGEN AND XENON-NITROGEN BONDS

We are currently in a much better position to understand the factors underlying noble gas compound formation. This has been accomplished by synthesizing over two dozen new noble-gas (xenon and krypton) compounds bonded to organic fragments through nitrogen. The ligand groups consist of perfluoropyridines,¹ nitriles² and s-trifluorotriazine³ adducted to the Lewis acid cations XeF^+ and KrF^+ .



where $\text{R} = \text{H}, \text{CH}_3, \text{C}_2\text{H}_5, \text{n-C}_3\text{H}_7, (\text{CH}_3)_2\text{CH}, (\text{CH}_3)_3\text{C}, \text{CH}_2\text{X}$ ($\text{X} = \text{F}, \text{Cl}$), $\text{CH}_3\text{CH}_2\text{ClCH}, \text{C}_3\text{F}_5$, etc.; $\text{R}_r = \text{CF}_3, \text{C}_2\text{F}_5, \text{n-C}_3\text{F}_7$; $\text{R}_r' = \text{F}, 2\text{-CF}_3, 3\text{-CF}_3, 4\text{-CF}_3$; $\text{Ng} = \text{Xe}$ or Kr .

The chemistry represents the first time the highly oxidizing XeF^+ and KrF^+ cations have been bonded to organic ("fuel") moieties. These species are therefore of interest as high energy density materials as is most evident in the preparation of the hydrocyano cations, $\text{HC}\equiv\text{N}-\text{XeF}^+$ and $\text{HC}\equiv\text{N}-\text{KrF}^+$. The formation of the xenon analog and several organic nitrile cations ($\text{RC}\equiv\text{N}-\text{XeF}^+$) led to successful attempts to bond one of the best fuels known, $\text{HC}\equiv\text{N}$, to what is one of the strongest oxidants known, KrF^+ .⁴ As a result, the $\text{HC}\equiv\text{N}-\text{KrF}^+\text{AsF}_6^-$ salt is a violent detonator in the solid state at ca. -60°C .

Noble-gas nitrogen bonds were rare until these recent discoveries and, in fact, $\text{HC}\equiv\text{N-KrF}^+$ represents the first example of a Kr-N bond and, moreover, the first example of krypton bonded to an element other than fluorine. The only previously known krypton species were KrF_2 , KrF^+ and Kr_2F_3^+ . Since the discovery of the $\text{HC}\equiv\text{N-KrF}^+$ cation four more examples of Kr-N bonds have been prepared, namely, $\text{R}_x\text{C}\equiv\text{N-Kr-F}^+\text{AsF}_6^-$ ($\text{R}_x = \text{CF}_3, \text{C}_2\text{F}_5, \text{n-C}_3\text{F}_7$).³

In collaboration with Prof. R.F.W. Bader and P.J. MacDougall at McMaster University, single determinantal SCF calculations with linearly constrained geometry optimizations using the program GAMESS were performed for ArF^+ , KrF^+ , XeF^+ , KrF_2 , XeF_2 , $\text{HC}\equiv\text{N-Kr-F}^+$ and $\text{HC}\equiv\text{N-Xe-F}^+$.⁵ The findings are discussed in terms of Bader's theory of atoms in molecules and support the experimental findings relating to the strong Lewis acid behaviors of KrF^+ and XeF^+ .

While we have previously demonstrated the existence of fluoro(alkylnitrile)xenon(II) cations, many of these species have not been isolated as solid compounds, but have been characterized unambiguously in solution by multi-NMR spectroscopy. Previous to this we have only reported on the isolation of $\text{HC}\equiv\text{N-NgF}^+\text{AsF}_6^-$ ($\text{Ng} = \text{Kr}, \text{Xe}$) and $\text{CH}_3\text{C}\equiv\text{N-XeF}^+\text{AsF}_6^-$ in the solid state. The salts have been characterized in the solid state by Raman spectroscopy and, most recently, by ^{129}Xe Mössbauer spectroscopy. We have now isolated further examples of fluoro(alkylnitrile)xenon(II) cations in the solid state; these include $(\text{CH}_3)_3\text{CC}\equiv\text{N-XeF}^+\text{AsF}_6^-$, $(\text{CH}_3)_2\text{CHC}\equiv\text{N-XeF}^+\text{AsF}_6^-$, $\text{CH}_3\text{CH}_2\text{C}\equiv\text{N-XeF}^+\text{AsF}_6^-$ and $\text{CH}_2\text{XC}\equiv\text{N-XeF}^+\text{AsF}_6^-$ ($\text{X} = \text{F}, \text{Cl}$). The salts have all been characterized by low-temperature Raman spectroscopy and have also been studied, along with further examples, by ^{129}Xe Mössbauer spectroscopy. The $\text{CH}_2\text{FC}\equiv\text{N-XeF}^+\text{AsF}_6^-$ salt is stable at room temperature for up to several hours. A low temperature X-ray crystal structure determination is currently underway.

THE KRYPTON-OXYGEN BOND

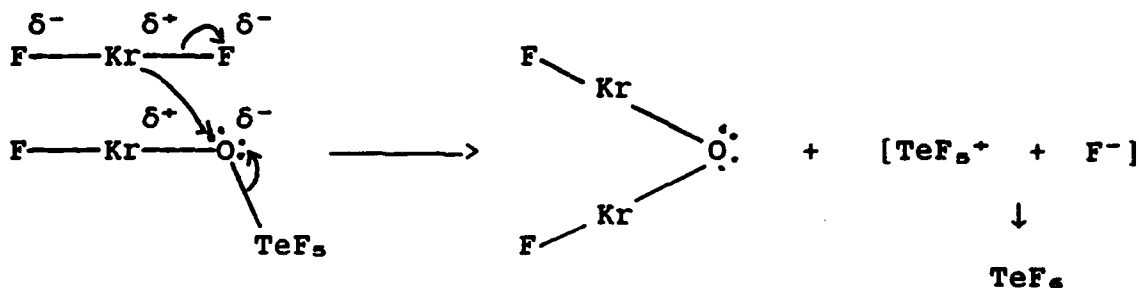
Our recent discovery of the first krypton-nitrogen bond, i.e., $\text{HC}\equiv\text{N-KrF}^+$, and the previous existence of Kr-F bonded species have served to underscore the apparent anomalous non-existence of the Kr-O bond.

We have recently put a considerable amount of effort into trying to synthesize the first such example of a Kr-O bond and have evidence for what appears to be the first Kr-O bonded species, $\text{O}(\text{KrF})_2$. The latter is postulated to arise from the following metathesis and fluorination reactions:





The proposed novel Kr-O bonded species is isoelectronic with its V-shaped, fluorine-bridged analog, Kr_2F_3^+ , and isovalent with Xe_2F_3^+ . The mechanism of the reaction could be represented as follows:

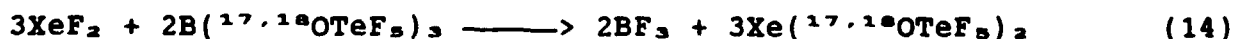
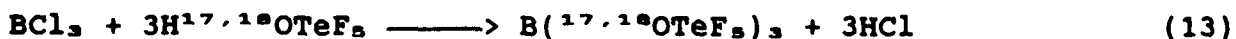
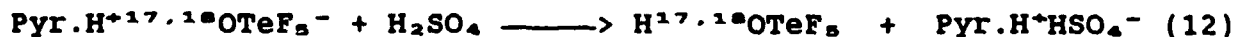
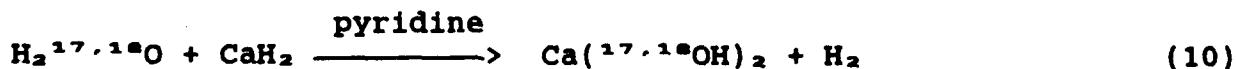


In addition, a number of side reactions, such as those proposed in equations (8) and (9), occur leading to FOTeF_5 and $\text{F}_5\text{TeOOTeF}_5$



The evidence that has thus far accrued for $\text{O}(\text{KrF})_2$ is based on exhaustive high-field ^{19}F and ^{17}O NMR studies of $\text{KrF}_2/\text{Xe}(\text{OTeF}_5)_2$ mixtures in SO_2ClF solvent.

In order to conclusively establish the presence of oxygen in the proposed new species, we have enriched the xenon precursor, $\text{Xe}(\text{OTeF}_5)_2$, with ^{18}O and in a separate preparation, with ^{17}O . The enrichments have allowed us to obtain ^{17}O NMR evidence for $\text{O}(\text{KrF})_2$, while both ^{17}O and ^{18}O enrichments should allow us to identify the Kr-O stretching frequencies and Kr-O-Kr bend in the low-temperature vibrational Raman spectrum. The following synthetic route to the oxygen enriched xenon precursors has recently been carried out in our laboratory:

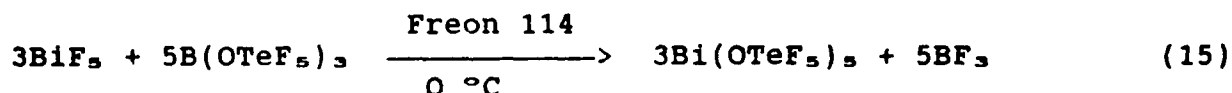


We have also obtained the ^{17}O NMR spectra for the ^{17}O -enriched precursor, $\text{Xe}(\text{OTeF}_5)_2$, and all side reaction products identified previously by high-field ^{19}F NMR spectroscopy, namely, FXeOTeF_5 , FOTeF_5 , $\text{Xe}(\text{OTeF}_5)_2$ and $\text{F}_5\text{TeOOTeF}_5$ as well as a new ^{17}O environment. The study represents the first ^{17}O NMR study of OTeF_5 derivatives and is crucial to gaining an understanding of the $\text{Xe}(\text{OTeF}_5)_2/\text{KrF}_2$ system. The new ^{17}O environment is assigned to $\text{O}(\text{KrF})_2$ which has been identified and assigned in the ^{19}F NMR spectrum by means of its natural abundance krypton primary isotopic shift pattern. These findings bode well for the ultimate definitive characterization of $\text{O}(\text{KrF})_2$ which is presently also being studied by low-temperature Raman spectroscopy.

MAIN-GROUP HIGH-OXIDATION STATE DERIVATIVES OF THE OTeF_5 LIGAND

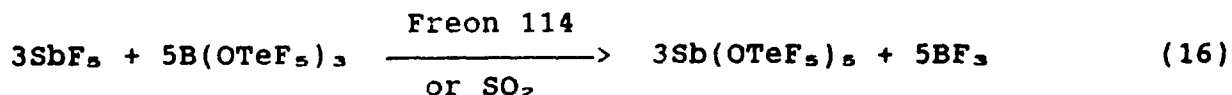
The syntheses and characterization of OTeF_5 analogs of strong fluoride ion acceptors and the hexafluoro-anions, $\text{Bi}(\text{OTeF}_5)_5$, $\text{Bi}(\text{OTeF}_5)_6^-$, $\text{Sb}(\text{OTeF}_5)_5$ and $\text{Sb}(\text{OTeF}_5)_6^-$ have been undertaken. The hexakis anions are large and of low basicity making their syntheses of particular interest for stabilizing strongly oxidizing cations.

The synthesis of $\text{Bi}(\text{OTeF}_5)_5$ yields a product of greater than 95% purity, as described by equation (15).



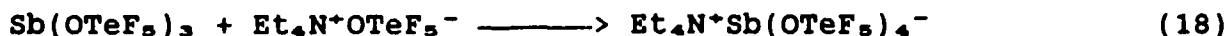
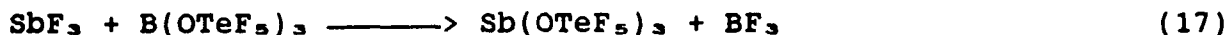
The compound is a yellow powder which is marginally stable at room temperature.

Attempts to prepare the analogous antimony derivative $\text{Sb}(\text{OTeF}_5)_5$ according to equation (16)



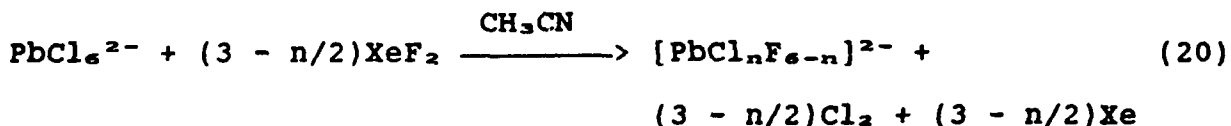
have confirmed reports that this compound is unstable above 0°C . This instability renders the compound difficult to isolate and inconvenient to use in the synthesis of other derivatives.

The $\text{Sb}(\text{OTeF}_5)_6^-$ anion was synthesized by reacting $\text{Et}_4\text{N}^+\text{OTeF}_5^-$ directly with the crude $\text{Sb}(\text{OTeF}_5)_5$ product from equation (16). However, this method invariably gave an impure product, as demonstrated by ^{19}F NMR spectroscopy. In view of this, a new strategy for the synthesis of $\text{Sb}(\text{OTeF}_5)_6^-$ has been adopted and is outlined in equations (17) - (19).



This method, starting from the stable antimony(III) derivative, $\text{Sb}(\text{OTeF}_5)_3$, avoids having to prepare $\text{Sb}(\text{OTeF}_5)_5$ as an intermediate and yields $\text{Et}_4\text{N}^+\text{Sb}(\text{OTeF}_5)_6^-$ cleanly. Evidence for the new Sb(III) anions $\text{Sb}(\text{OTeF}_5)_4^-$, $\text{Sb}(\text{OTeF}_5)_5^{2-}$ and possibly $\text{Sb}(\text{OTeF}_5)_6^{3-}$ has also been obtained from ^{19}F NMR spectroscopic data.

Although an extensive range of organo-lead(IV) compounds is known, the inorganic chemistry of powerfully oxidizing Pb(IV) is limited to a few compounds (e.g., PbF_4 , PbCl_4 and PbCl_6^{2-}) and is virtually unexplored. As a necessary preliminary to the synthesis of the Pb(IV) derivatives of the OTeF_5 group, we have now extended the inorganic chemistry of Pb(IV) by synthesizing mixtures of the previously unknown anions $[\text{PbCl}_n\text{F}_{6-n}]^{2-}$, $n = 1-5$, according to equation (20).



The anions have been characterized in CH_3CN solution by ^{19}F and ^{207}Pb NMR spectroscopy.

Work is underway to isolate a pure sample of $(\text{Et}_4\text{N}^+)_2\text{PbF}_6^{2-}$ and to synthesize $\text{Pb}(\text{OTeF}_5)_6^{2-}$ as well as the mixed anions $[\text{PbF}_n(\text{OTeF}_5)_{6-n}]^{2-}$, where $n = 1 - 5$.

REFERENCES

1. A.A.A. Emara and G.J. Schrobilgen, J. Chem. Soc., Chem. Commun., 1988, 257.
2. A.A.A. Emara and G.J. Schrobilgen, J. Chem. Soc., Chem. Commun., 1987, 1644.
3. G.J. Schrobilgen, J. Chem. Soc., Chem. Commun., 1988, 1506.
4. G.J. Schrobilgen, J. Chem. Soc., Chem. Commun., 1988, 863.
5. P.J. MacDougall, G.J. Schrobilgen and R.F.W. Bader, Inorg. Chem., in press.

EXPERIMENTAL STUDIES ON THE SYNTHESIS OF NEW NOBLE GAS FLUORIDES AND HIGH OXIDATION STATE ENERGETIC FLUORINE COMPOUNDS INVOLVING UNUSUAL BONDING SITUATIONS

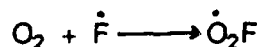
W. W. Wilson and K.O. Christe

Rocketdyne Division of Rockwell International Corporation, Canoga Park, California 91303

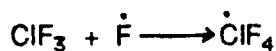
The primary objective of this program is the synthesis of new "super oxidizers" based on hypervalent or high oxidation state fluorides of nitrogen, oxygen, chlorine, and the noble gases. The target compounds include NF_5 , ClF_5O , ClF_6^- , NF_2^- , catenated nitrogen fluorides, and ArF^+ which are among the most challenging synthetic problems encountered in high energy chemistry.

During the past year, our efforts were concentrated on three areas: (i) $\dot{\text{F}}$ atom reactions in Ar and mixed Ar/ N_2 matrices, (ii) the coupling of halogen fluoride anions with organic counterions, and (iii) the study of the steric activity of the free valence electron pairs on the central atoms in BrF_6^- and IF_6^- .

In the area of $\dot{\text{F}}$ atom reactions, we have studied the reactions of either microwave or photolytically generated $\dot{\text{F}}$ atoms with ClF_3O in either Ar or mixed Ar/ N_2 matrices. No evidence was obtained for a stepwise fluorine addition with either $\dot{\text{ClF}}_4\text{O}$ or ClF_5O formation. Model reactions of F atoms with either ClF or O_2 proceeded, as expected, according to:



For ClF_3 , however, no $\dot{\text{F}}$ addition according to

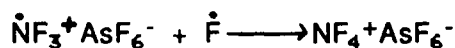
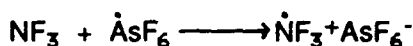


was observed. Instead, $\dot{\text{F}}$ abstraction occurred.



It thus appears that $\dot{\text{F}}$ atom addition proceeds well with low oxidation state molecules, but for higher oxidation states the preferred pathway is fluorine abstraction.

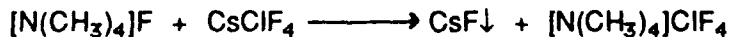
The reaction of $\dot{\text{F}}$ atoms with AsF_3 was also studied in Ar and Ar/ N_2 matrices. The desired $\dot{\text{AsF}}_6$ radical has been proposed as the crucial intermediate in the favored formation mechanism for NF_4^+ salts.



Recent calculations of electron affinities of numerous fluorine compounds by Gutsev and Boldyrev have indicated that the electron affinity of $\dot{\text{AsF}}_6$ is 0.2eV higher than that of PtF_6 and, therefore, $\dot{\text{AsF}}_6$ should easily oxidize NF_3 to $\dot{\text{NF}}_3^+$. However, all attempts to observe $\dot{\text{AsF}}_6$ radicals in the reactions of AsF_3 with $\dot{\text{F}}$ atoms were unsuccessful.

A major breakthrough in oxidizer chemistry was achieved by successfully combining the ClF_4^- anion with the tetramethylammonium cation in the form of a salt which is stable up to 100°C and, most surprisingly, is not shock-sensitive. The ClF_4^- anion is an excellent incendiary for almost all hydrocarbons and many halocarbons. For example, tests recently carried out under separate Air Force and Army contracts have demonstrated that KClF_4 is an excellent incendiary for Diesel fuel which is very difficult to ignite by conventional incendiaries.

The $[\text{N}(\text{CH}_3)_4]\text{ClF}_4$ salt was prepared in high yield and purity by the following metathetical reaction in CH_3CN at room temperature:



It was characterized by Raman, infrared and NMR spectroscopy and DSC. A few single crystals were isolated after numerous recrystallizations from CH_3CN solution. However, an x-ray diffraction study, carried out by Prof. Bau at USC, showed them to be $[\text{N}(\text{CH}_3)_4]\text{HF}_2$, formed by the hydrolysis of some $[\text{N}(\text{CH}_3)_4]\text{ClF}_4$ with traces of moisture. The crystal structure of

$[\text{N}(\text{CH}_3)_4]\text{HF}_2$ is quite remarkable and shows an unusual packing for the HF_2^- anions. In addition to $[\text{N}(\text{CH}_3)_4]^+\text{ClF}_4^-$, the new $[\text{N}(\text{CH}_3)_4]^+\text{BrF}_4^-$ and the known $[\text{N}(\text{CH}_3)_4]^+\text{BrF}_6^-$ salts were also synthesized and characterized.

In connection with our work on $[\text{N}(\text{CH}_3)_4]^+\text{BrF}_6^-$, we became interested in the structure of the BrF_6^- anion and its implications for the possible existence of ClF_6^- . The HalF_6^- anions belong to the interesting class of AX_6E structures where E represents a free valence electron pair. Based on Gillespie's VSEPR rules, E should be sterically active, and the AX_6 part should be non-octahedral. If, however, the maximum coordination number of A toward X equals six, then the free valence electron pair E cannot be any longer sterically active and must occupy a centrosymmetric s-orbital. Since from their reaction chemistry we know that I has a maximum coordination number of 8 toward F, while that of Br is only six, it was interesting to compare the structures of BrF_6^- and IF_6^- . It is shown that for the study of highly fluxional moieties, such as the HalF_6^- anions, it is important to investigate the free ions and not the solids to eliminate the influence of crystal field effects, and to use structural techniques operating on a very fast time scale, such as vibrational spectroscopy. Raman polarization measurements combined with ^{19}F NMR data for CH_3CN solutions of $\text{Cs}^+\text{BrF}_6^-$ and Cs^+IF_6^- show that on the time scale of vibrational spectroscopy BrF_6^- is octahedral and IF_6^- is distorted, while on the slower NMR time scale both anions are fluxional. Since chlorine has also a maximum coordination number of six toward fluorine, the nonexistence of a stable ClF_6^- anion is attributed to the weak Lewis acidity of ClF_3 and not to steric effects.

COMPUTATIONAL STUDIES OF TETRAHEDRANE, SOME AZATETRAHEDRANES,
AND THEIR NITRO DERIVATIVES.

Peter Politzer and Jorge M. Seminario
Department of Chemistry
University of New Orleans
New Orleans, Louisiana 70148

Introduction

We are conducting a computational study and evaluation of certain nitro, nitro/amino and nitro/methyl derivatives of the highly-strained tetrahedrane and azatetrahedrane molecules I-III [1-4]. Our objective is to identify systems that show particular promise as potential high energy density materials. The derivatives investigated so far are IV-IX.



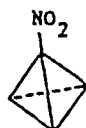
I



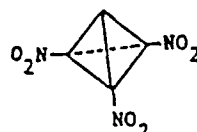
II



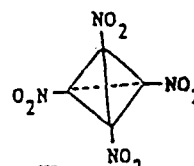
III



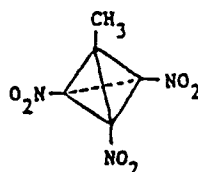
IV



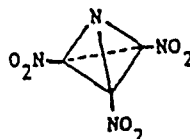
V



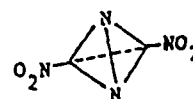
VI



VII



VIII



IX

In Figures 1 and 2 are shown the predicted detonation properties and relative specific impulse values of some nitrotetrahedranes and nitroazatetrahedranes [5]. A comparison of these data with the corresponding ones for HMX, also given in these figures, is very encouraging with regard to the potential importance of the former.

Methods

Our computational analyses have been carried out with the ab initio SCF-MO GAUSSIAN 86 program [6]. For each molecule, the first step is to compute its optimized structure at the 3-21 G level. This is subsequently used in calculating the following key molecular properties.

(a) Electrostatic Potential

The electrostatic potential $V(\vec{r})$ that is created in the space around a molecule by its nuclei and electrons is given rigorously by eq. (1):

$$V(\vec{r}) = \sum_A \frac{Z_A}{|\vec{R}_A - \vec{r}|} - \int \frac{\rho(\vec{r}') d\vec{r}'}{|\vec{r}' - \vec{r}|} \quad (1)$$

Z_A is the charge on nucleus A, located at \vec{R}_A . $\rho(\vec{r})$ is the molecular electronic density function, which we compute.

The electrostatic potential is well-established as a means for interpreting and predicting reactive behavior [7-9]. For example, an approaching electrophile will initially be attracted to those regions in which $V(\vec{r})$ is negative, where the effects of the molecule's electrons are dominant, and in particular to those points at which $V(\vec{r})$ reaches its most negative values (the local minima). The electrostatic potential is a real physical property, which can be determined experimentally as well as computationally [9].

(b) Bond Deviation Index:

The "bond path" is the ridge of maximum electronic density linking two chemically-bonded nuclei [10]. It often lies along the internuclear axis, as in the C-C bonds in cyclohexane and propane; in some instances, however, as in strained bonds, it is curved [10-16]. We have introduced the "bond deviation index", λ , as a measure of the degree of this curvature [12].

$$\lambda = \frac{\left[\frac{1}{N} \sum_i^N r_i^2 \right]^{1/2}}{R} \quad (2)$$

The r_i are the lengths of N equally-spaced lines drawn between the actual bond path and the reference path defined by the superposed electronic densities of the corresponding free atoms placed at the same positions as in the molecule. We set N to 320, well beyond the point at which further increases in its magnitude produce no significant change in λ . The inclusion of the internuclear distance R permits the comparison of λ values for bonds of different lengths.

The bond deviation index provides a basis for characterizing and comparing strained chemical bonds [12-16]. It focuses specifically upon individual bonds, rather than reflecting the molecule as a whole.

(c) **Bond Order:**

We have shown that bond orders obtained with eq (3) correlate well with experimentally-determined dissociation energies [17, 18], and are therefore an effective measure of relative bond strengths, especially for comparing bonds between the same atoms in different chemical environments.

$$\text{Bond Order} = 0.55747 \sqrt{\frac{k}{R_e}} \quad (3)$$

In eq (3), k is the force constant in mdyne/A and R_e is the equilibrium bond length in Å.

Results

(a) **Electrostatic Potentials:**

Tetrahedrane shows (Figure 3) the characteristic feature that we have found to be associated with the C-C bonds in strained hydrocarbons: a negative electrostatic potential near the middle of the bond, to the outside of the molecule [11, 13-16, 19]. Thus the bond itself can serve as an initial site for electrophilic attachment, as has been observed for some strained hydrocarbons [11, 13, 16]. The strongly electron-withdrawing nitro group eliminates these negative bond potentials (Figure 4), so that the only negative regions around IV - VII are those near the nitro oxygens (Figure 5), which can be attributed to the effects of their lone pairs.

There are also strong negative potentials associated with the aza nitrogens, as shown in Figure 6. These are characteristic of trivalent nitrogens, reflecting their lone pairs, and are indicative of the basic natures of these sites. The aza nitrogen lone pair potentials (and basicities) become weaker as the number of aza nitrogens increases, since they are all competing for the same polarizable charge, and as nitro substituents are introduced. Thus the value at the most negative points in III is -48.6 kcal/mole (compared to -60.6 in II, as shown in Figure 6), while in IX it is -13.6 kcal/mole.

(b) Bond Properties:

The bond deviation indices and bond orders in Figures 7 and 8 show that the introduction of aza nitrogens into tetrahedrane leads to a marked relaxation of bond strain and strengthening for both the C-C and C-N bonds. The substitution of nitro groups, on the other hand, produces only small changes (increases) in bond strain.

The effect of nitro groups upon C-C bond strengths (as measured by their bond orders) is more complex, but very interesting and significant. The overall effect of NO₂ substitution is to slightly strengthen the C-C bonds, but there are some exceptions, which show a definite pattern. This pattern is illustrated in Figure 9, which shows an NO₂ bonded to C₁. When the O-N-O and N-C₁-C₂ planes are perpendicular to each other, then the C₁-C₂ bond is slightly weakened; when O-N-O and N-C₁-C₂ are coplanar, the C₁-C₂ bond is slightly strengthened.

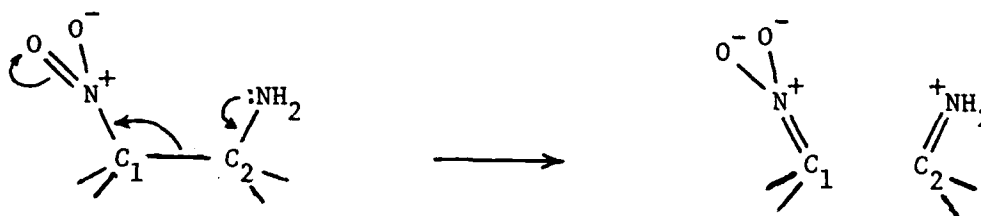
A rather extreme consequence of this is observed in the case of aminonitrotetrahedrane, X.



When the O-N-O plane is perpendicular to the N-C₁-C₂, the molecule actually undergoes a rearrangement! Both the C₁-C₂ and the C₃-C₄ bonds break, and 1-nitro-3-aminocyclobutadiene, XI, is formed (Figure 10). However when the O-N-O and N-C₁-C₂ planes are coplanar, the tetrahedrane framework is retained and the C-C bonds are even slightly strengthened.

An explanation of the striking effect that NO_2 rotation has upon the adjacent C-C bond can be obtained by looking at individual molecular orbitals. Tetrahedrane has three degenerate doubly-occupied t_2 molecular orbitals. When an NO_2 substituent replaces a hydrogen on C_1 , the degeneracy is removed and the orbitals assume the forms shown in Figure 11. The t_2^z , shown in the bottom portion of the figure, is seen to be a $\text{C}_1\text{-C}_2$ bonding orbital. The NO_2 has a π -type $1b_1$ molecular orbital which has predominantly the character of a nitrogen 2p orbital perpendicular to the O-N-O plane. Thus, when the O-N-O and N- $\text{C}_1\text{-C}_2$ planes are perpendicular to each other, this orbital is properly oriented to mix with the t_2^z and to accept electronic charge from it [Figure 11, bottom], thus weakening the $\text{C}_1\text{-C}_2$ bond. When O-N-O and N- $\text{C}_1\text{-C}_2$ are coplanar, these orbitals are orthogonal; the $t_2^z \rightarrow 1b_1$ charge shift cannot occur, and the $\text{C}_1\text{-C}_2$ bond is not weakened.

The complete rupture of the C-C bond that occurs in the case of $\underline{\text{X}}$ can be interpreted by suggesting that the process described above is now reinforced by the charge redistribution shown below:



The possibility of the formation of the $\text{H}_2\text{N}^+=\text{C}^-$ double bond evidently allows the C-C bonding electrons to respond completely to the attraction exerted by the NO_2 . However this only happens when the O-N-O and N- $\text{C}_1\text{-C}_2$ planes are perpendicular.

In view of the important effect that the NO_2 conformation has upon C-C bond properties, it is interesting to note that we find NO_2 rotation to have virtually no energy barrier at the 3-21 G level. According to the hypothesis that such rotation dissipates energy and stabilizes the system [20], this may mean that nitrotetrahedranes would have low impact sensitivities.

Acknowledgement

We greatly appreciate the support on this work by the Air Force Office of Scientific Research, through grant #AFOSR-88-0068.

REFERENCES

1. Politzer, P.; Seminario, J. M.; J. Phys. Chem. **1989**, 93, 588.
2. Politzer, P.; Seminario, J. M.; Struct. Chem., in press.
3. Politzer, P.; Seminario, J. M.; J. Phys. Chem., in press.
4. Politzer, P.; Seminario, J. M.; submitted to Chem. Phys. Lett.
5. Sanders, O., predicted detonation properties Working Group Meeting on Synthesis of High Density Energetic Materials, Alster, J.; Iyer, S. and Marchand, A. P., eds., U. S. Army ARDC, May, 1984, Dover, N. J. The experimental data for HMX are from Meyer, R., Explosives, Chemie, V., Weinheim, 1977, and from LASL Explosive Property Data, Gibbs, T. R. and Popolato, A., eds., University of California Press, Berkeley, CA, 1980. The relative specific impulse values were computed using a program written in our laboratory by Sjoberg, P. and tested against programs used elsewhere.
6. Frisch, M. J.; Binkley, J. S.; Schlegel, H. B.; Raghavachari, K.; Melius, C. F.; Martin, R. L.; Stewart, J. P.; Bobrowicz, F. W.; Rohlfing, C. M.; Kahn, L. R.; Defrees, D. J.; Seeger, R.; Whiteside, R. A.; Fox, D. J.; Fleuder, E. M.; and Pople, J. A. GAUSSIAN 86, Carnegie-Mellon Quantum Chemistry Publishing Unit, Pittsburgh, PA, 1984.
7. Scrocco, E.; Tomasi, J. Adv. Quantum Chem. **1978**, 11, 115.
8. Politzer, P.; Daiker, K. C. The Force Concept in Chemistry; Deb, B. M., Ed.; Van Nostrand-Reinhold; New York, 1981; Chapter 6.
9. Politzer, P.; Truhlar, D. G., Eds.; Chemical Applications of Atomic and Molecular Electrostatic Potentials; Plenum: New York, 1981.
10. Bader, R. F. W.; Tang, T.-H.; Tal, Y.; Biegler-Konig, F. W. J. Am. Chem. Soc. **1982**, 104, 940, 946.
11. Politzer, P.; Domelsmith, L. N.; Sjoberg, P.; Alster, J. Chem. Phys. Lett. **1982**, 92, 366.
12. Politzer, P.; Abrahmsen, L.; Sjoberg, P.; Laurence, P. R. Chem. Phys. Lett. **1983**, 102, 74.

13. Politzer, P.; Domelsmith, L.N.; Abrahmsen, L. J. Phys. Chem. 1984, 88, 1752.
14. Politzer, P.; Jayasuriya, K.; Zilles, B. A. J. Am. Chem. Soc. 1985, 107, 121.
15. Politzer, P.; Jayasuriya, K. J. Mol. Struct. (THEOCHEM) 1986, 135, 245.
16. Politzer, P.; Murray, J. S. Structure and Reactivity (Molecular Structure and Energetics); Liebman, J. F.; Greenberg, A.; Eds.; VCH Publishers; New York, 1988, Ch. 1.
17. Politzer, P. J. Chem. Phys. 1969, 50, 2780; 51, 459.
18. Politzer, P.; Ranganathan, S. Chem. Phys. Lett. 1986, 124, 527.
19. Politzer, P.; Kirschenheuter, G. P.; Alster, J. J. Amer. Chem. Soc. 1987, 109, 1033.
20. Kamlet, M. J. and Adolph, H. G., Proceedings Seventh Symposium International on Detonations; Anapolis MD; June, 1981; NSWCMP-82-334, Naval Surface Weapons Center, 84.

FIGURE 1. COMPARISON OF PREDICTED NITROPOLYHEDRANE PROPERTIES TO THOSE OF HMX.
(EXPERIMENTAL HMX PROPERTIES ARE IN PARENTHESES.)

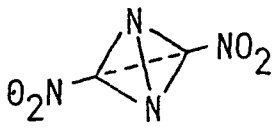
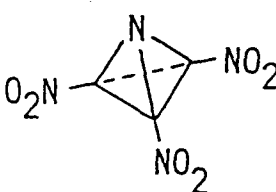
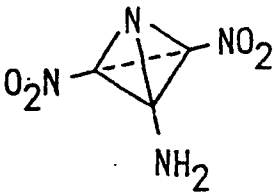
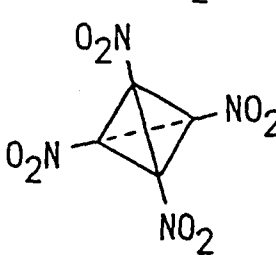

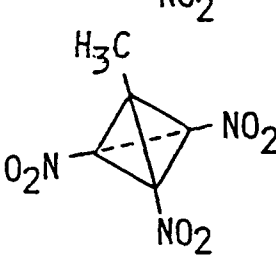
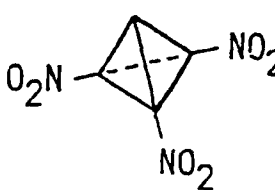
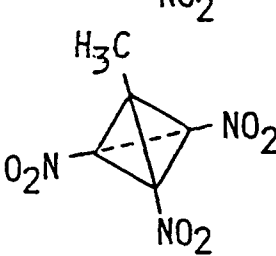
MOLECULE	DENSITY (G/CC)	HEAT OF FORMATION (KCAL/MOLE)	DETONATION VELOCITY (MM/MSEC)	DETONATION PRESSURE (KBAR)
	1.90 (1.96)	17.4 (17.9)	9.12 (9.10)	382 (395)
	2.14	88.0	10.20	512
	2.14	80.0	10.04	493
	2.19	133.5	10.91	590

FIGURE 2. ESTIMATES OF RELATIVE SPECIFIC IMPULSE VALUES.

A PROPELLANT DEVELOPS THRUST (RECOIL FORCE) DUE TO THE DISCHARGE OF GASEOUS PRODUCTS WHEN IT UNDERGOES COMBUSTION. THE SPECIFIC IMPULSE, I_s , IS THE INTEGRAL OF THE THRUST, PER UNIT WEIGHT PROPELLANT, OVER THE TIME OF COMBUSTION; IT IS GIVEN BY:

$$I_s \sim N^{1/2} T^{1/2}$$

N = MOLES OF GASEOUS PRODUCTS PER UNIT WEIGHT PROPELLANT; T = COMBUSTION TEMPERATURE, $^{\circ}\text{K}$, ESTIMATED FROM HEAT CAPACITIES AND HEAT OF COMBUSTION. LATTER CALCULATED FROM HEATS OF FORMATION COMPUTED WITH SEMI-EMPIRICAL AM1 PROCEDURE.

MOLECULE	RELATIVE I_s	MOLECULE	RELATIVE I_s
	1.32		1.24
	1.26		1.20
	1.25		1.20
	1.25		1.00

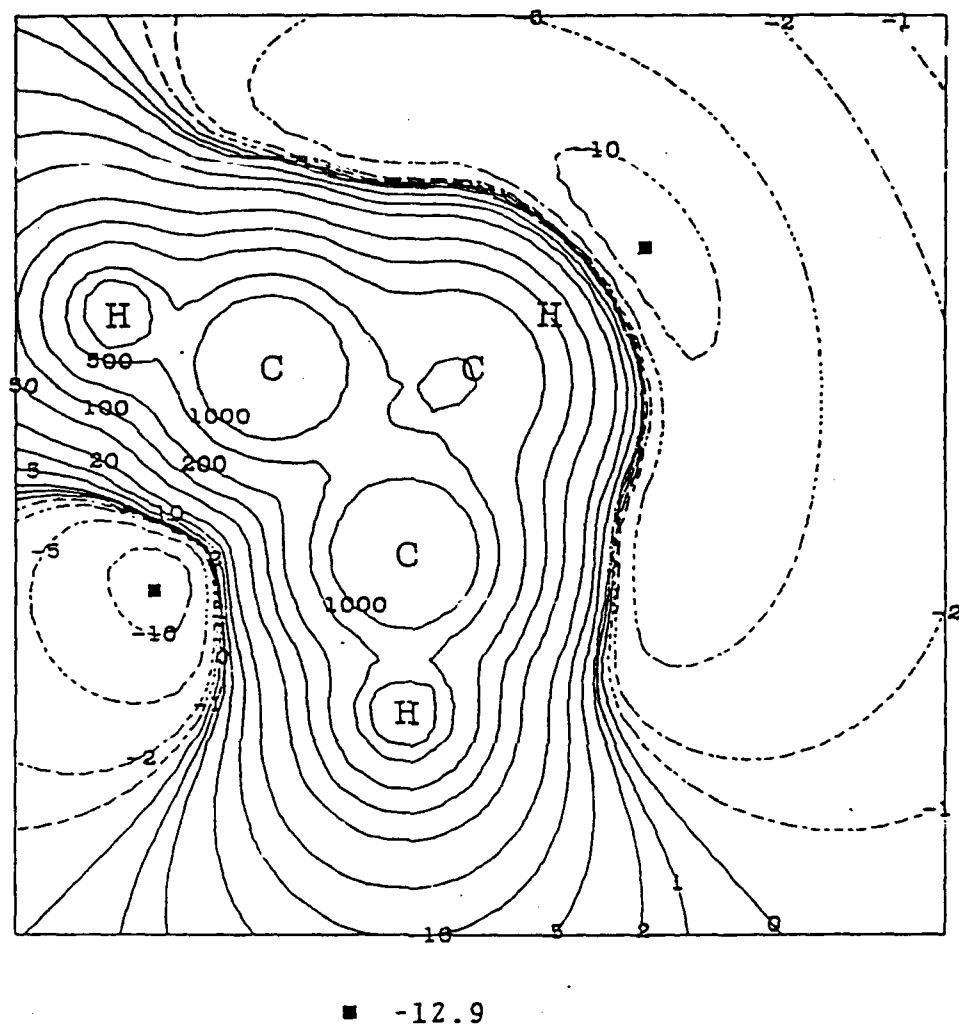


FIGURE 3. ELECTROSTATIC POTENTIAL OF TETRAHEDRANE, IN KCAL/MOLE, IN THE MIRROR PLANE PASSING THROUGH ONE C-C BOND AND THE MIDPOINT OF THE OPPOSITE ONE. DASHED CONTOURS CORRESPOND TO NEGATIVE POTENTIALS.

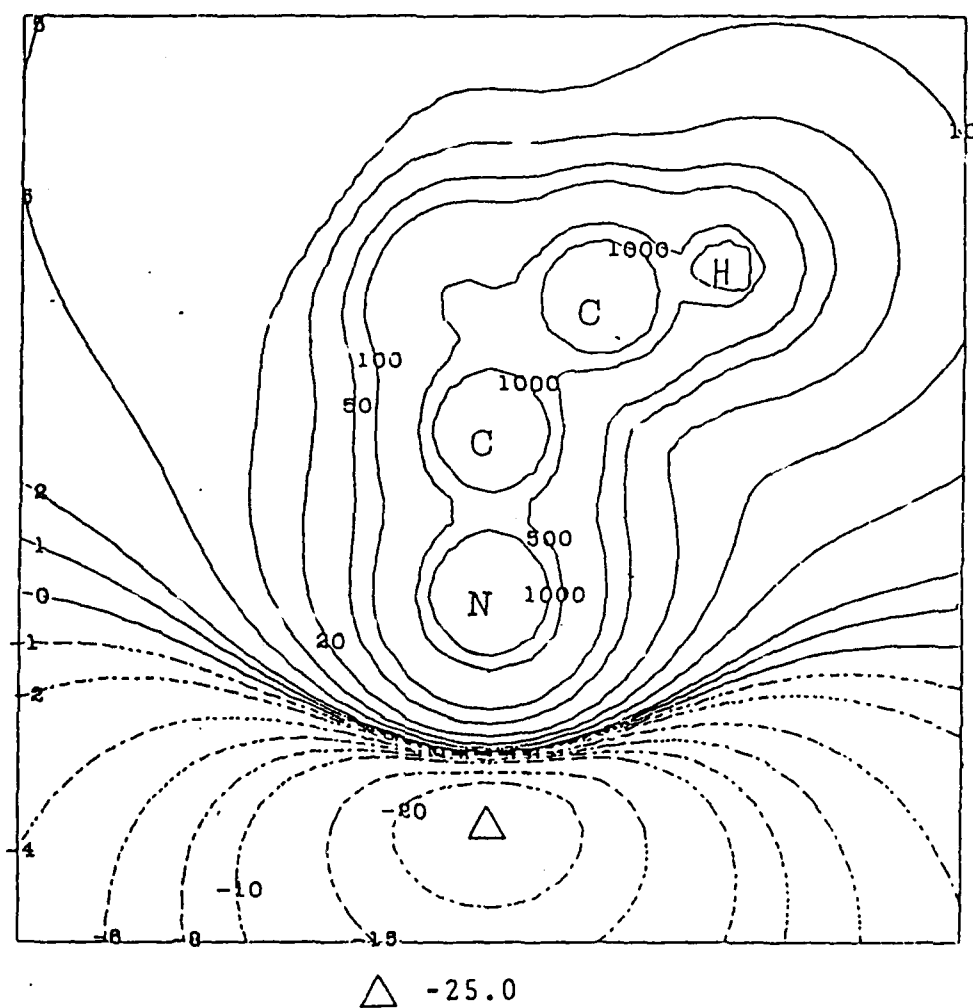


FIGURE 4. ELECTROSTATIC POTENTIAL OF NITROTETRAHEDRANE, IN KCAL/MOLE, IN PLANE BISECTING THE O-N-O ANGLE AND PASSING THROUGH THE NUCLEI INDICATED. DASHED CONTOURS CORRESPOND TO NEGATIVE VALUES.

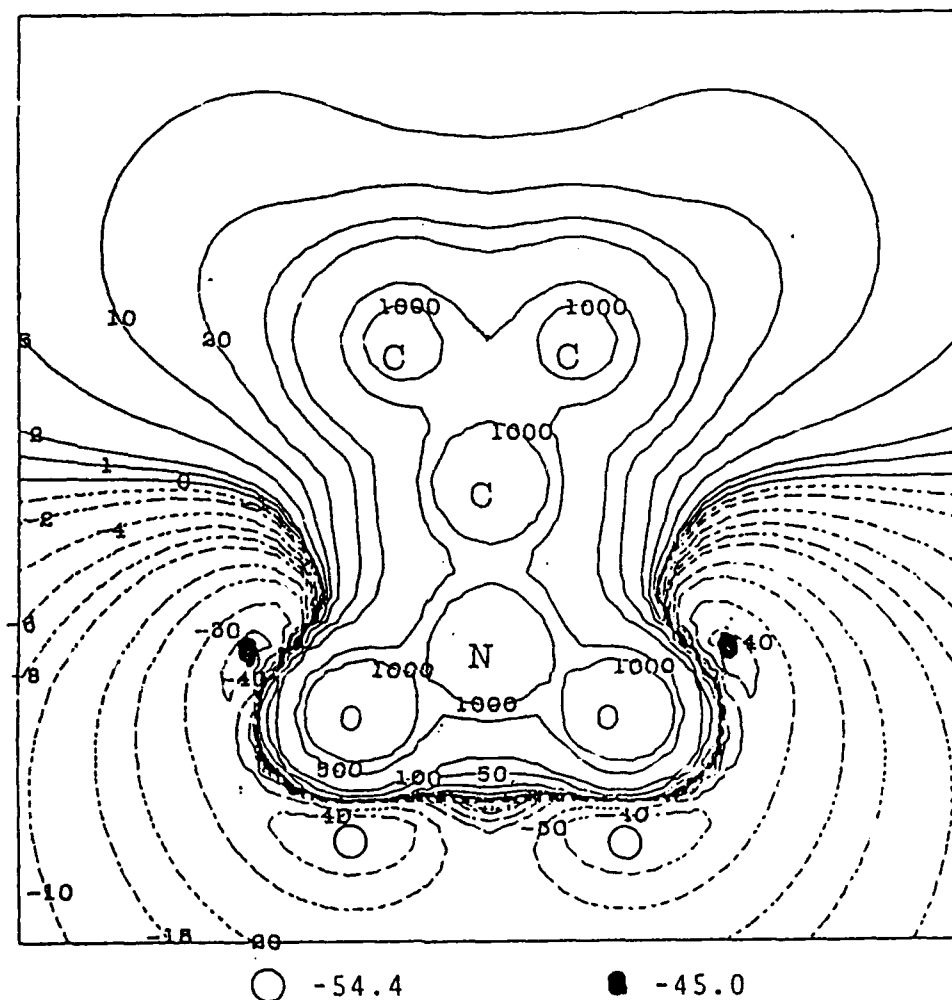
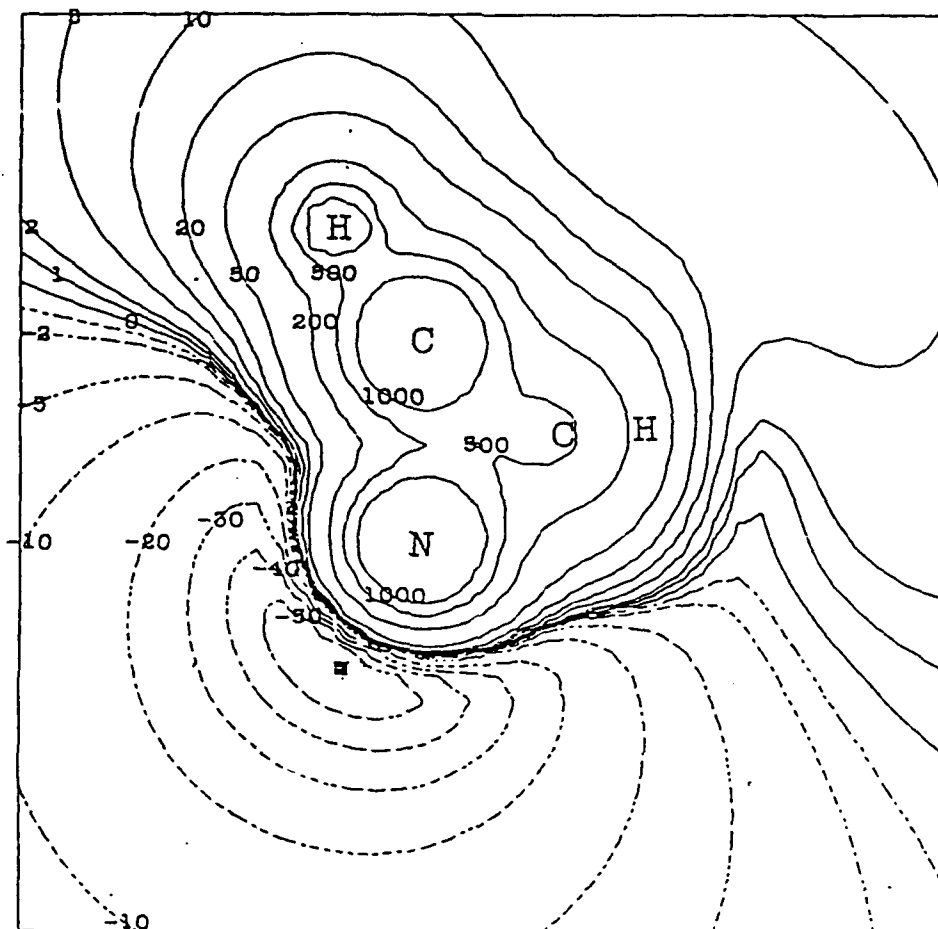


FIGURE 5. ELECTROSTATIC POTENTIAL OF NITROTETRAHEDRANE, IN KCAL/MOLE, IN PLANE PASSING THROUGH THE ATOMS INDICATED. DASHED CONTOURS CORRESPOND TO NEGATIVE POTENTIALS.



■ -60.6

FIGURE 6. ELECTROSTATIC POTENTIAL OF AZATETRAHEDRANE, IN KCAL/MOLE, IN THE PLANE PASSING THROUGH THE C-N BOND AND THE MIDPOINT OF THE OPPOSITE C-C BOND. DASHED CONTOURS CORRESPOND TO NEGATIVE POTENTIALS.

FIGURE 7. CALCULATED BOND DEVIATION INDICES AND BOND ORDERS FOR MOLECULES I AND IV - VII.

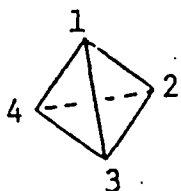
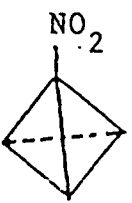
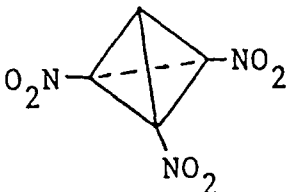
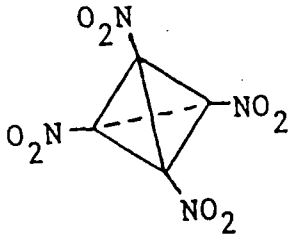
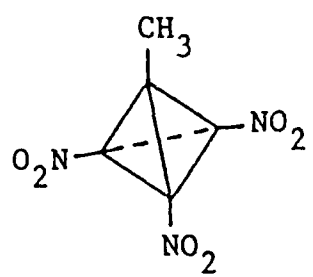
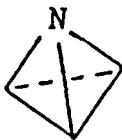
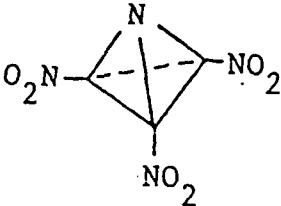
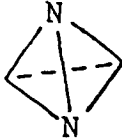
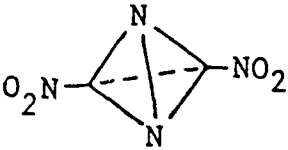
Molecule	Bond Deviation Indices	Bond Orders
	C-C: 0.114	C-C: 1.25
	C_1-C_3 : 0.118 C_1-C_4 : 0.112 C_2-C_4 : 0.120 C_2-C_3 : 0.113	C_1-C_3 : 1.18 C_1-C_4 : 1.31 C_2-C_4 : 1.21 C_2-C_3 : 1.27 C-N: 1.48 N-O: 1.91
	C_1-C_2 : 0.116 C_2-C_3 : 0.117	C_1-C_2 : 1.23 C_2-C_3 : 1.30 C-N: 1.44 N-O: 1.93
	C-C: 0.118	C-C: 1.26, 1.29 C-N: 1.42 N-O: 1.94
	C_1-C_2 : 0.117 C_2-C_3 : 0.116	C_1-CH_3 : 1.37 C_1-C_2 : 1.23 C_2-C_3 : 1.28 C-N: 1.44 N-O: 1.95, 1.91

FIGURE 8. CALCULATED BOND DEVIATION INDICES AND BOND ORDERS FOR
MOLECULES II, III, VIII AND IX.

Molecule	Bond Deviation Indices	Bond Orders
	C-N: 0.105 C-C: 0.101	C-N: 1.07 C-C: 1.35
	C-N ₁ : 0.109 C-C: 0.106	C-N ₁ : 1.05 C-C: 1.40 C-N: 1.43 N-O: 1.93
	C-N: 0.091 C-C: 0.087 N-N: 0.109	C-N: 1.16 C-C: 1.48 N-N: 0.93
	C-N ₁ : 0.096 C-C: 0.090 N-N: 0.108	C-N ₁ : 1.15 C-C: 1.57 C-N: 1.44 N-O: 1.94 N-N: 0.96

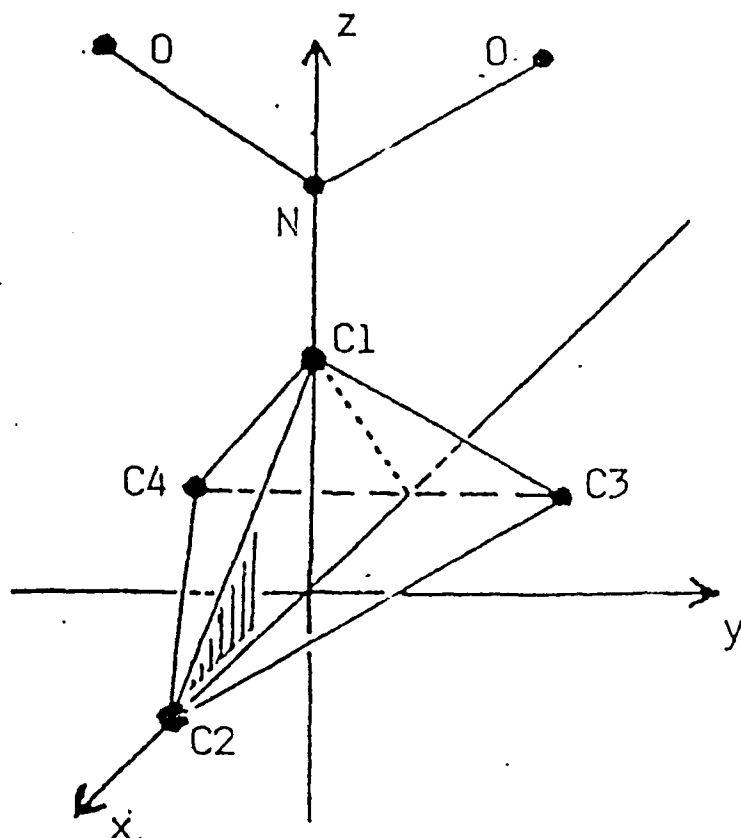
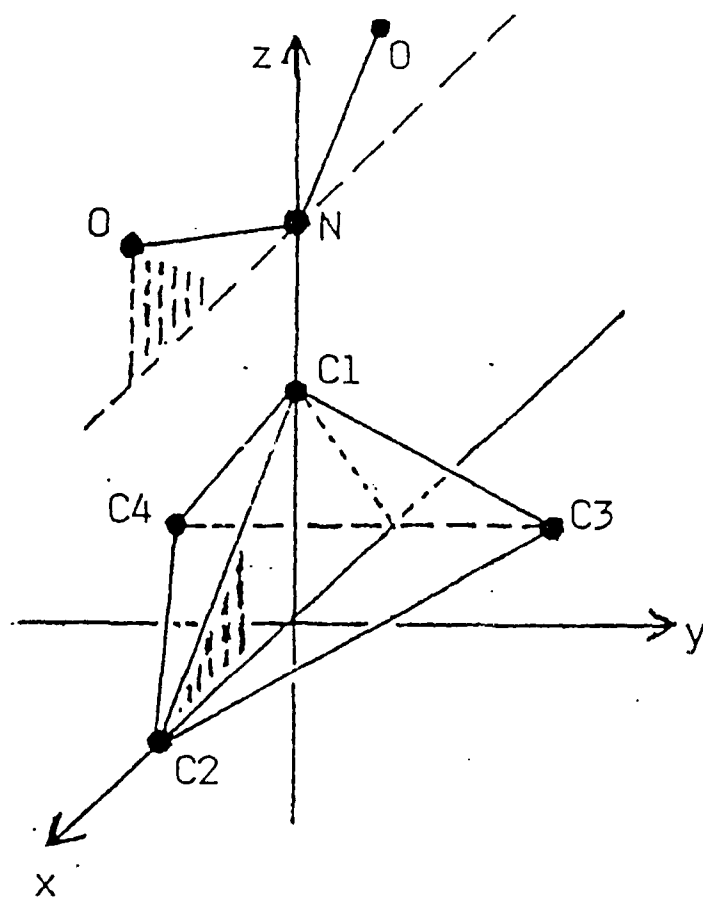


FIGURE 9.

O-N-O PLANE PERPENDICULAR
TO N-C₁-C₂ PLANE.

C₁-C₂ BOND WEAKENED.



O-N-O PLANE COPLANAR
WITH N-C₁-C₂ PLANE.

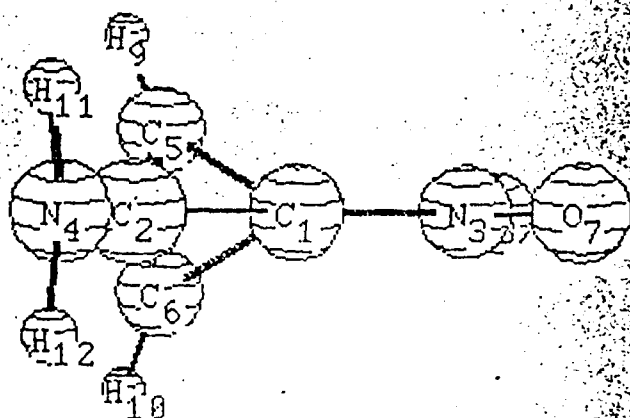
C₁-C₂ BOND STRENGTHENED.

FIGURE 10.

RELATIVE ENERGY

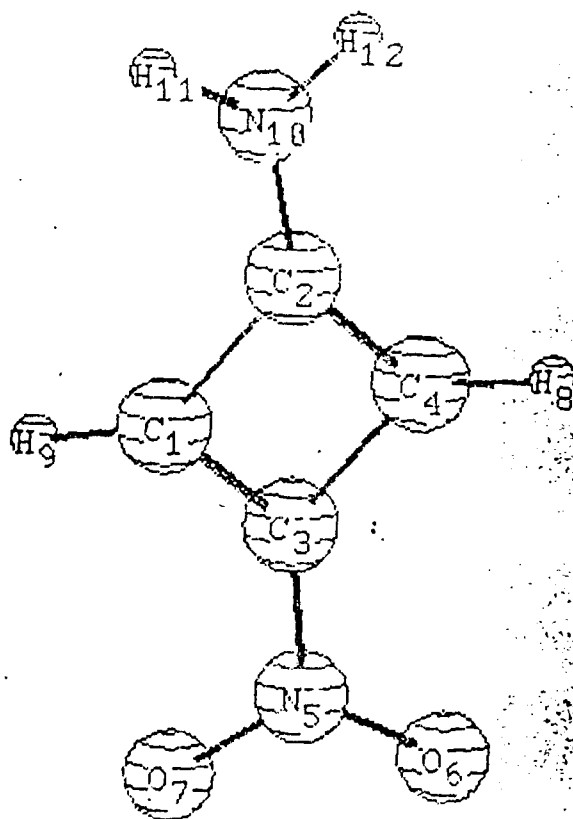
57 KCAL/MOLE

(NON-REARRANGED
AMINONITROTETRA-
HEDRANE, X.)



0 KCAL/MOLE

(1-NITRO-3-AMINO-
CYCLOBUTADIENE, XI.)



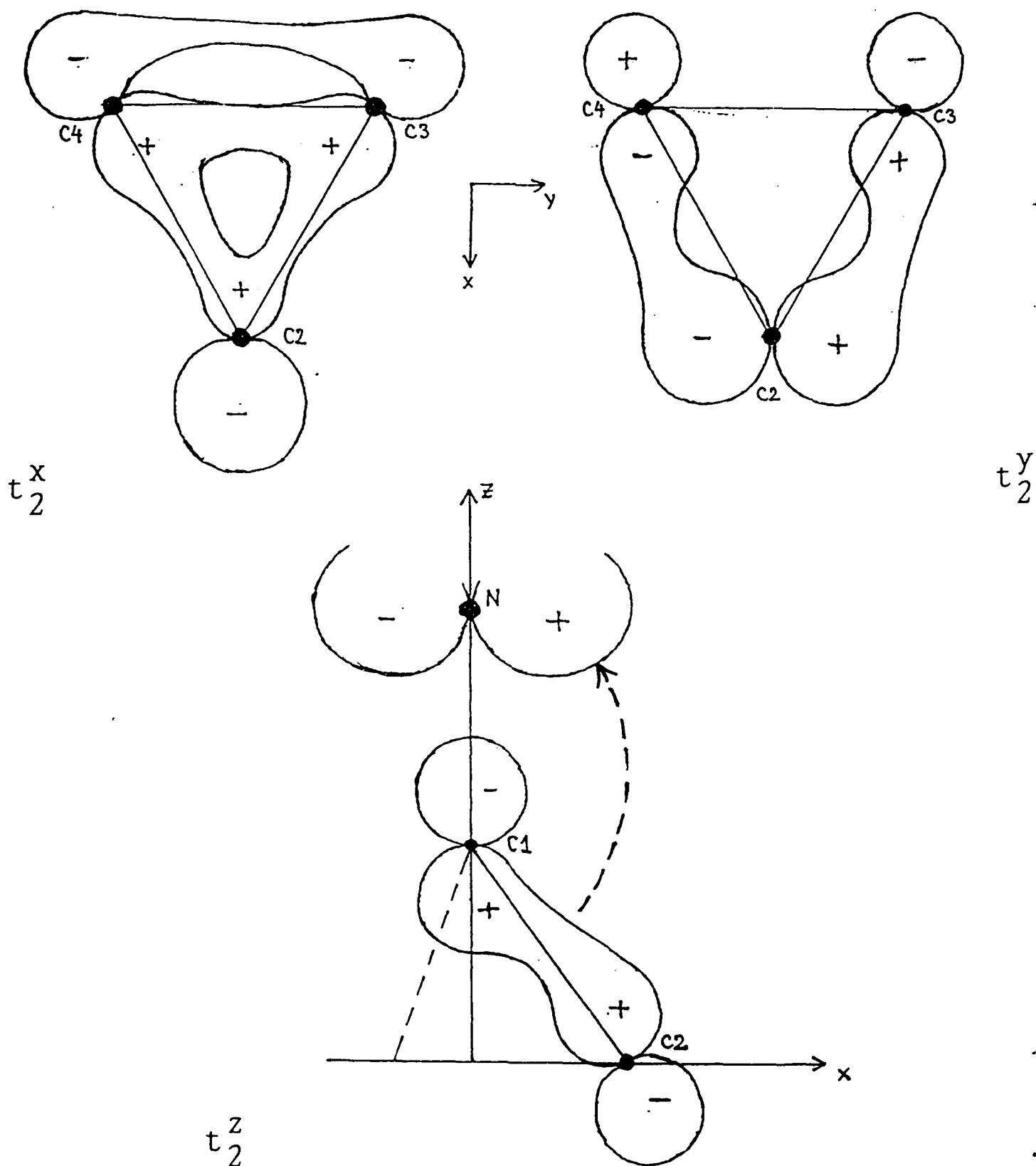


FIGURE 11.

The Synthesis of Nitrocyclopropanes using Nitrodiazomethanes

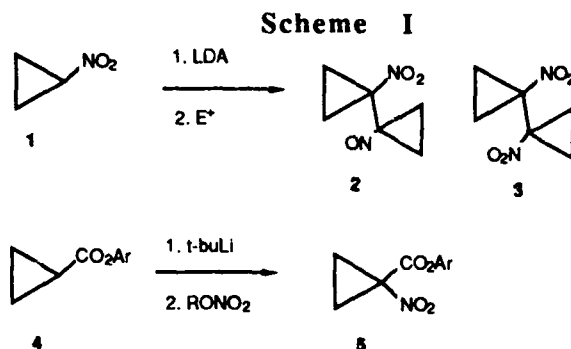
William P. Dailey
Department of Chemistry
University of Pennsylvania
Philadelphia, Pennsylvania 19104-6323

There has recently been considerable effort directed at the synthesis and study of strained ring nitro compounds as high energy density materials.¹ Nitrocyclopropanes are the simplest members of this class of compounds. Although there are several preparative methods for nitrocyclopropanes,² an obvious choice, the addition of nitrocarbene to an alkene, has only recently been described by us.³ In fact, despite the wealth of information on carbenes,⁴ only a handful of publications pertaining to nitrocarbenes exist.⁵ The most significant of these are from Schöllkopf and co-workers. They developed syntheses for nitrodiazomethane and nitrodiazoesters.^{5a,c} Although diazo compounds are ideal precursors to carbenes, photolysis or thermolysis of ethyl nitrodiazoacetate or nitrodiazomethane in the presence of 2,3-dimethyl-2-butene afforded no cyclopropanes and no other products that would indicate formation of the nitrocarbene.^{5b} Despite this seemingly bleak outlook for nitrocarbene chemistry, we found that rhodium(II) acetate⁶ will transfer nitrocarbene from nitrodiazomethane to electron rich alkenes.³

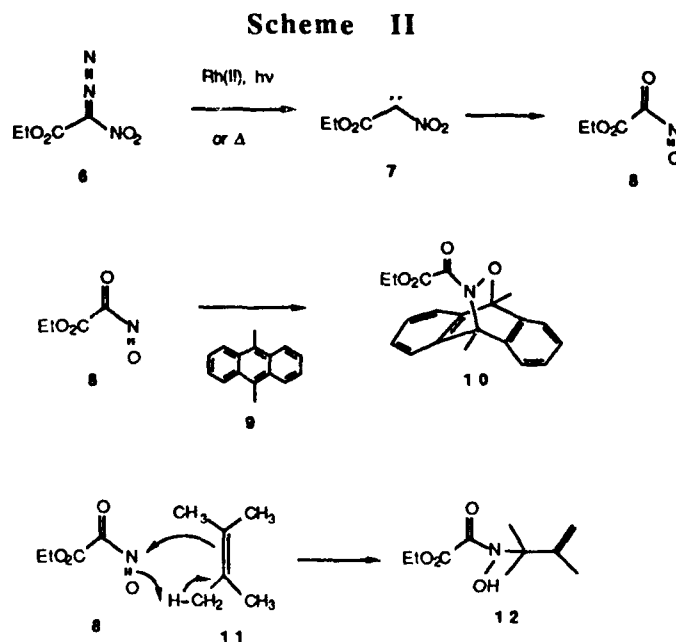
While this method provides an entry to nitrocyclopropanes that are otherwise inaccessible, the reaction has several drawbacks. The yields of cyclopropanes range from poor to moderate, and, importantly, there is an ever present danger of explosion when working with nitrodiazomethane and its precursor, nitrodiazoacetic acid.⁷ On the other hand, ethyl nitrodiazoacetate may be prepared in decagram quantities by nitration of ethyl diazoacetate and stored for months at 5°C without danger of explosion or decomposition.

We sought to extend this cyclopropanation reaction to ethyl nitrodiazoacetate (6). This would provide access to 1-nitrocyclopropane carboxylates. Subsequent saponification and decarboxylation would provide a roundabout route to nitrocyclopropanes. Moreover, 1-substituted nitrocyclopropanes are not easily prepared.⁸ Seebach and coworkers have shown that deprotonation of nitrocyclopropane (1) with LDA and subsequent addition of an electrophile does not result in capture of the nitrocyclopropyl anion. Instead, only coupled products (2

and 3) could be isolated.⁹ To circumvent this, they have developed methodology for the low temperature nitration of cyclopropyl aryl ester enolates (4) (Scheme I).¹⁰

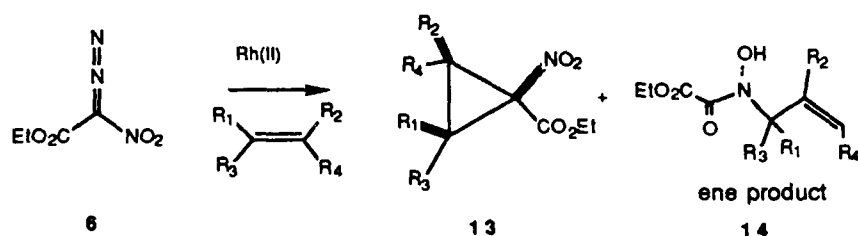


Our attempted cyclopropanation of 2,3-dimethyl-2-butene with ethyl nitrodiazoacetate (6) and catalyst afforded no cyclopropane. Instead, ethyl oxo[hydroxy(1,1,2-trimethyl-2-propenyl)amino]acetate (12) was obtained in good yield.¹¹ This is the same product that Schöllkopf obtained when ethyl nitrodiazoacetate was pyrolyzed in the presence of the same alkene.^{5a} Apparently, ethyl nitrodiazoacetate (6) undergoes nitrogen extrusion to form a nitrocarbene (7) which rearranges to an acyl nitroso compound (8) that reacts as an enophile with the alkene. For nitrocarbene itself, this rearrangement is calculated to have no activation barrier and to be exothermic by 100 kcal/mol.³ The intermediate acyl nitroso compound (8) can also be trapped as the Diels-Alder adduct 10 with 9,10-dimethyl-anthracene (Scheme II).¹¹



Since our foiled attempt to cyclopropanate 2,3-dimethyl-2-butene with ethyl nitrodiazoacetate (6) in the presence of a catalytic amount of $\text{Rh}_2(\text{OAc})_4$, we have carried out the reaction on a variety of alkenes and find that certain alkenes can be successfully cyclopropanated (Scheme III). Cyclopropanes 13 are formed in yields ranging from 0 to 75 percent. Yields of ene products 14 span the same range. The course of the reaction is highly dependent on the substitution pattern of the alkene. Electron rich and sterically undemanding alkenes give the best yields of cyclopropane products. As the alkene becomes more crowded, the yield of cyclopropanes decreases, and there is a concomitant increase in ene product.

Scheme III



We desired to quantify these observations and correlate the yield of cyclopropane formation with alkene reactivity. A series of competition studies to determine the relative reactivities of several alkenes were performed. In Figure 1 percent yield of cyclopropane is plotted against the log of the relative reactivity of the alkenes. The degree of correlation is remarkable. Those alkenes with the highest relative rates give the best yields of cyclopropanes, and the least reactive give the poorest yield.

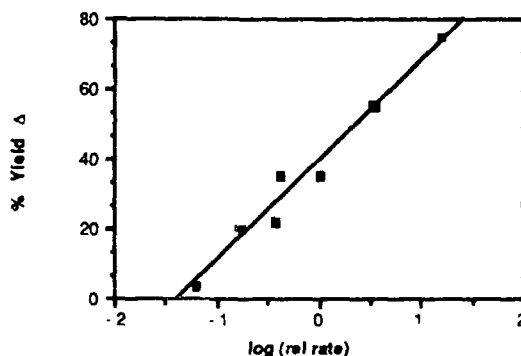
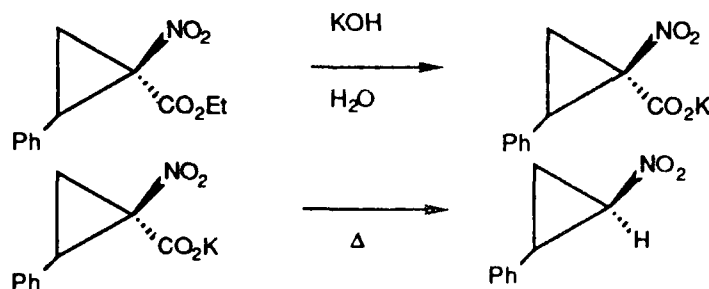


Figure 1. Percent yield of cyclopropane formation using catalytic rhodium(II) acetate and ethyl nitrodiazoacetate vs. log(relative rate) of alkene based on 1-hexene.

The ethyl 1-nitrocyclopropanecarboxylates can be converted to nitrocyclopropanes in high yield by saponification in refluxing aqueous ethanol.

This two step method is more efficient for the preparation of nitrocyclopropanes than catalytic cyclopropanation using nitrodiazomethane.



References

- (a) Wade, P. A.; Dailey, W. P.; Carroll, P. J. *J. Am. Chem. Soc.* **1987**, *109*, 5452.
 (b) Eaton, P. E.; Ravi Shankar, B. K.; Price, G. D.; Pluth, J. J.; Gilbert, E. E.; Alster, J.; Sandus, O. *J. Org. Chem.* **1984**, *49*, 185. (c) Archibald, T. G.; Baum, K. *J. Org. Chem.* **1988**, *53*, 4645. (d) Waycole, L. M.; Shen, C.; Paquette, L. A. *J. Org. Chem.* **1988**, *53*, 4969. (e) Review: Marchand, A. P. *Tetrahedron*, **1988**, *44*, 4645.
- (a) Asunskis, J.; Shechter, H. *J. Org. Chem.* **1968**, *33*, 1164. (b) Parham, W. E.; Braxton, H. G.; Serres, C. *J. Org. Chem.* **1961**, *26*, 1831. (c) Kuwajima, I.; Ryochi, A.; Tomsu, S. *Tetrahedron Lett.* **1983**, *24*, 4429. (d) Valades, L.; Siminez, M.; Rodriguez-Hahn, L. *Rev. Latinoam. Quim.* **1975**, *6*, 152. (e) Russell, G. A.; Makosza, M.; Hersherberger, J. *J. Org. Chem.* **1979**, *44*, 1195. (f) Lampman, G. M.; Horne, D. A.; Hager, G. D. *J. Chem. Eng. Data* **1969**, *14*, 396.
- O'Bannon, P. E. and Dailey, W. P. *Tetrahedron Lett.* **1988**, 987.
- Moss, R. A. and Jones, M., eds., *Carbenes*, Vol. II, Wiley, New York, 1975; Vol I, 1973; Kirmse, W. *Carbene Chemistry*, 2nd ed., Academic Press, New York, 1971.
- (a) Schöllkopf, U. and Tonne, P. *Ann. Chem.* **1971**, 753, 135. (b) Schöllkopf, U. and Markus, P. *Ann. Chem.* **1971**, 753, 143. (c) Schöllkopf, U.; Tonne, P.; Schaefer, H.; Markus, P. *Ann. Chem.* **1969**, 722, 45. (d) Frank-Neumann, M. and Miesch, M. *Tetrahedron Lett.* **1984**, 2909. (e) Rahman, A. and Clapp, L. *J. Org. Chem.* **1976**, *41*, 122. (f) Coutouli-Argyropoulou, E. and Alexandrou, N. E. *J. Org. Chem.* **1980**, *45*, 4158.
- For a review of metal carbene transformations, see: Doyle, M. P. *Chem. Rev.* **1986**, *86*, 919.
- O'Bannon, P. E.; Carroll, P. J.; Dailey, W. P. *Tetrahedron Lett.* **1988**, 6031.

8. 1-alkylnitrocyclopropanes can be prepared by the methods of Shechter and Russell. See ref 2a and 2e.
9. Kai, Y.; Knochel, P.; Kwiatkowski, S.; Dunitz, J. D.; Oth, J.F.M.; Seebach, D.; Kalinowski, H-O. *Helv. Chim. Act.* **1982**, *65*,137.
10. Haener, R.; Maetzke, T.; Seebach, D. *Helv. Chim. Act.* **1986**, *69*, 1655.
11. O'Bannon P. E. and Dailey, W. P. *Tetrahedron Lett.* **1988**, 5719.

ABSTRACT FOR CONTRACTORS MEETING 3/12/89-3/15/89
AFOSR-87-0165

January 30, 1989

*Dynamic Constraints on Stochastic Behavior
in the Chemistry of Highly Excited Molecules*

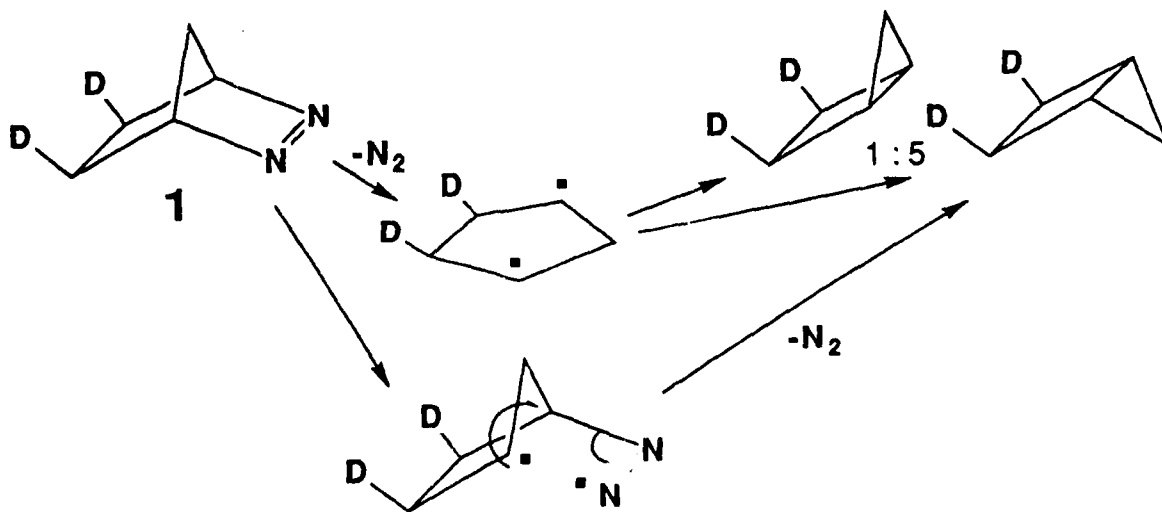
Barry K. Carpenter and John R. Wiesenfeld

Department of Chemistry, Baker Laboratory
Cornell University, Ithaca, NY 14853-1301

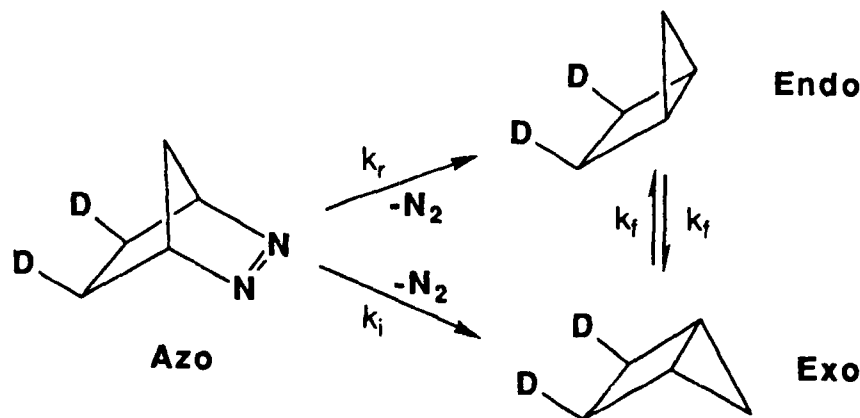
Two topics will be discussed in this summary. First, evidence will be presented that the thermal deazetization of 2,3-diazabicyclo[2.2.1]heptene-*exo,exo*-5,6-*d*-2 (1) exhibits a ratio of stereoisomeric products that is determined by dynamic phenomena rather than by exit-channel effects, as had previously been assumed. The ratio of stereoisomeric products is found to be temperature independent. A difference is observed in gas-phase and solution-phase product ratios. The significance of these observations for the dynamic interpretation will be discussed.

The second topic will involve discussion of the synthesis of high-energy molecule 2 which is expected to exhibit profound effects of non-statistical intramolecular dynamics in its thermal reactions.

The thermal extrusion of nitrogen from compound 1 occurs with a preference for inversion, as shown below. The mechanism proposed by W.R. Roth et al. to explain this result is also shown.



If this were the correct explanation, one would expect the ratio of apparent rate constants for formation of the stereoisomeric products to be temperature dependent, since only by highly improbable coincidence would the formation of the two different biradicals occur with the same activation energy. In fact, the ratio shows no temperature dependence within our experimental error.



$$[\text{Exo}] = 0.5 + \{(k_i - k_r)/D\}e^{-2k_r t} + \{2(k_f - k_i)/D\}e^{-(k_i + k_r)t}$$

$$[\text{Endo}] = 0.5 - \{(k_i - k_r)/D\}e^{-2k_r t} + \{2(k_f - k_r)/D\}e^{-(k_i + k_r)t}$$

$$D = 2(k_i + k_r - 2k_f)$$

T °C	k_i/k_r (gas phase)
129.8	4.6 ± 0.5
140.0	5.0 ± 0.6
150.1	5.4 ± 0.6
160.0	5.1 ± 0.5
170.0	4.5 ± 0.6
182.5	5.4 ± 0.6

Furthermore, as shown on the next page, the ratio is found to be different in dibenzyl ether solution than it is in the gas phase. It is still temperature independent in solution, though. This is consistent with a dynamic explanation wherein the preference for inversion is due to conservation of momentum of the nuclei as the reaction proceeds. The ability to conserve

momentum is reduced in solution where energy exchange with solvent molecules adds a randomizing component to the reaction trajectories.

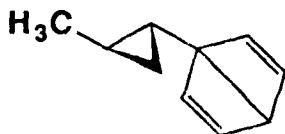
T °C	k_i/k_r (soln phase)
130.8	1.68 ± 0.05
140.0	1.76 ± 0.05
150.5	1.64 ± 0.06
159.8	1.63 ± 0.04
170.1	1.79 ± 0.06
182.5	1.73 ± 0.06

Future studies on this system will focus on pressure dependence in the gas phase, dependence on solvents in the solution phase, and dependence on moment of inertia of the atom groups (adjustable through isotopic substitution) in both phases.

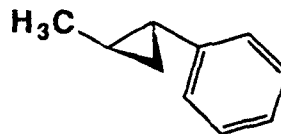
The thermal reactions of optically active compound **2** are expected to be distinguishable from those of optically active 1-methyl-2-phenylcyclopropane (**3**), despite the fact that **3** is expected to be a formal intermediate in the reactions of **2**. This should not be possible according to the statistical theories of unimolecular kinetics, such as RRKM theory. The argument is that the **3** formed by ring opening of **2** should be non-statistically activated, with the phenyl ring having, initially, a much higher effective temperature than the rest of the molecule. The ring opening of the cyclopropane moiety of **3** will be detectable by racemization and *trans* - *cis* isomerization. Our expectation is that the branching ratio among these processes will be different when starting with **2** or **3**, in contradiction to the prediction of the statistical theories.

The synthesis of **2** is difficult, but has now just been completed. It is shown on the next page.

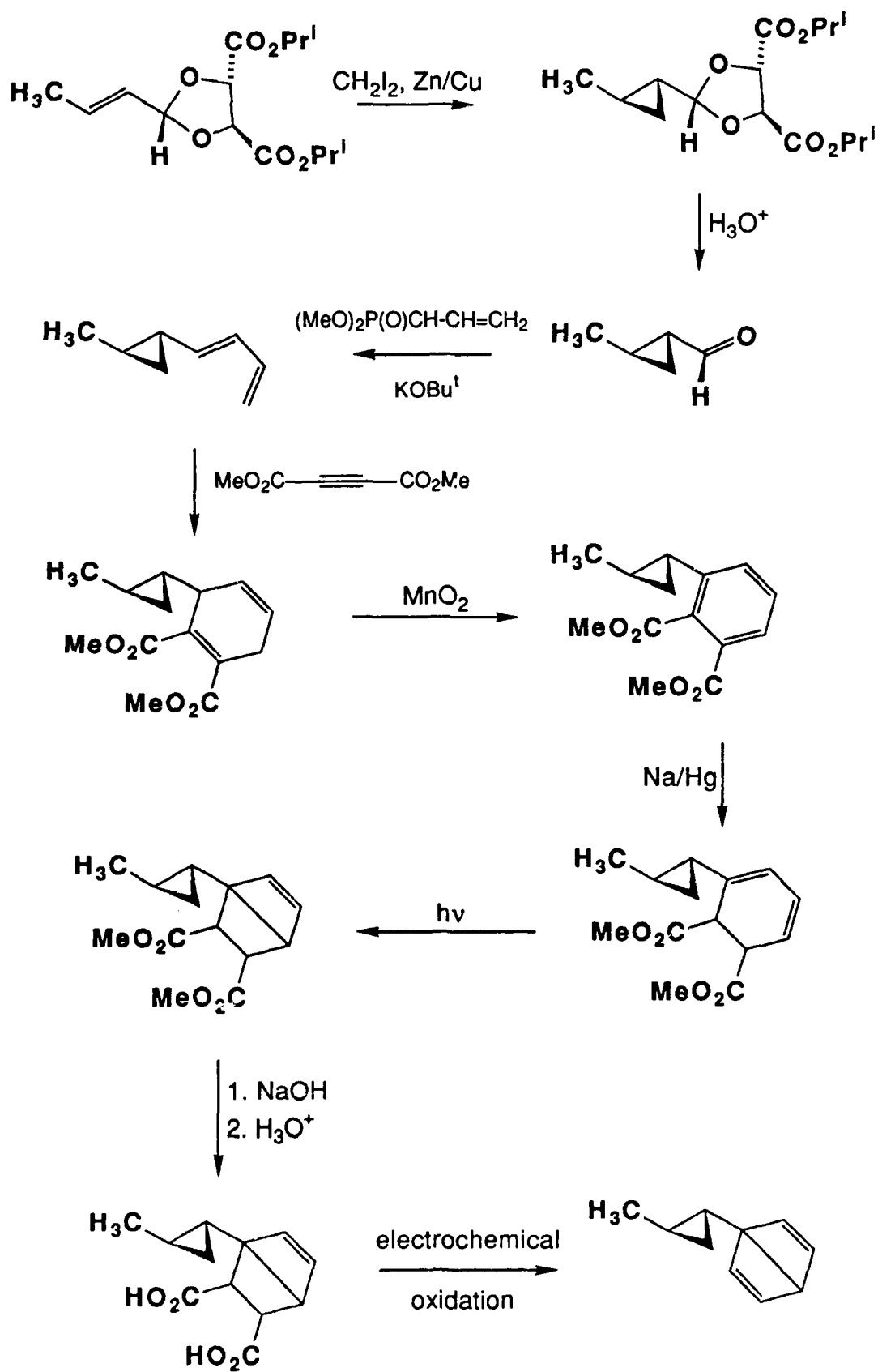
Studies comparing the behavior of **2** and **3** are just commencing.



2



3



If the results of these studies confirm our expectations, it will apparently be necessary to consider the possibility of significant contributions from non-statistical dynamics in a variety of thermal processes. The implications for unimolecular kinetics of high-energy processes, such as those involved in the reactions of high energy density materials, would be profound. Right now the only way to deal with such a system theoretically is by way of trajectory calculations, which are impossibly demanding on computational capacity (even for modern supercomputers) when one is dealing with molecules of more than about a dozen atoms. The long-term aspects of this research will thus be involved with the development of alternative theoretical models that are capable of including non-statistical dynamics without the need for a full scale simulation.

In the shorter term, we expect soon to begin marrying the current "physical organic" approach to the problem to a more hardware-oriented study. Specifically we expect to induce non-statistical excitation of molecules that will then dissociate to small fragments whose energy distributions can be determined by multiphoton ionization or laser-induced fluorescence. The results from these studies will be of crucial importance for the calibration of new theories.

THEORETICAL STUDY OF ION-PAIR STATES†

Roberta P. Saxon and Dahbia Talbi*
Molecular Physics Laboratory, SRI International
Menlo Park, California 94025

Metastable molecular fuels, high-energy, long-lived species, that do not decay when isolated in vacuum have been proposed as the basis of new propulsion schemes. This theoretical program, based on the premise that Coulombic attraction between a stable positive ion and a stable negative ion may lead to a stable energetic species, has proceeded by detailed examination of particular examples of ion-pair states. We summarize here our completed studies of H_3O and Li_3H .

H_3O

Based on the significant electron affinity (1.46 eV) of the oxygen atom, H_3O was selected as an interesting candidate system. Furthermore, there is substantial theoretical¹ and experimental² interest in the existence of stable or metastable H_3O , in its spectroscopy as an example of a Rydberg molecule,³ and in the potential surface for the hydrogen abstraction reaction⁴ $\text{OH} + \text{H}_2 \rightarrow \text{H}_2\text{O} + \text{H}$. In our calculations,⁵ geometries have been optimized by MCSCF analytic gradient techniques, and large-scale multi-reference CI calculations have been used to obtain energy separations. The Gaussian basis set included two sets of diffuse s and p functions on oxygen to describe the negative ion or Rydberg character.

Minima and transition states on the two lowest doublet potential surfaces of H_3O are shown in Figure 1. Energies of the minima are given in Table 1. While there exists a region of the lowest energy surface that may be described as an ion-pair, our results have shown that the ion-pair is not even a local minimum on that surface. The ion-pair minimum that has been identified (dashed line in Figure 1) is a local minimum on the excited 1^2E surface in C_{3v} geometry. It is, however, not stable in lower symmetry and is predicted to dissociate without an energy barrier to $\text{H}_2 + \text{H} + \text{O}$.

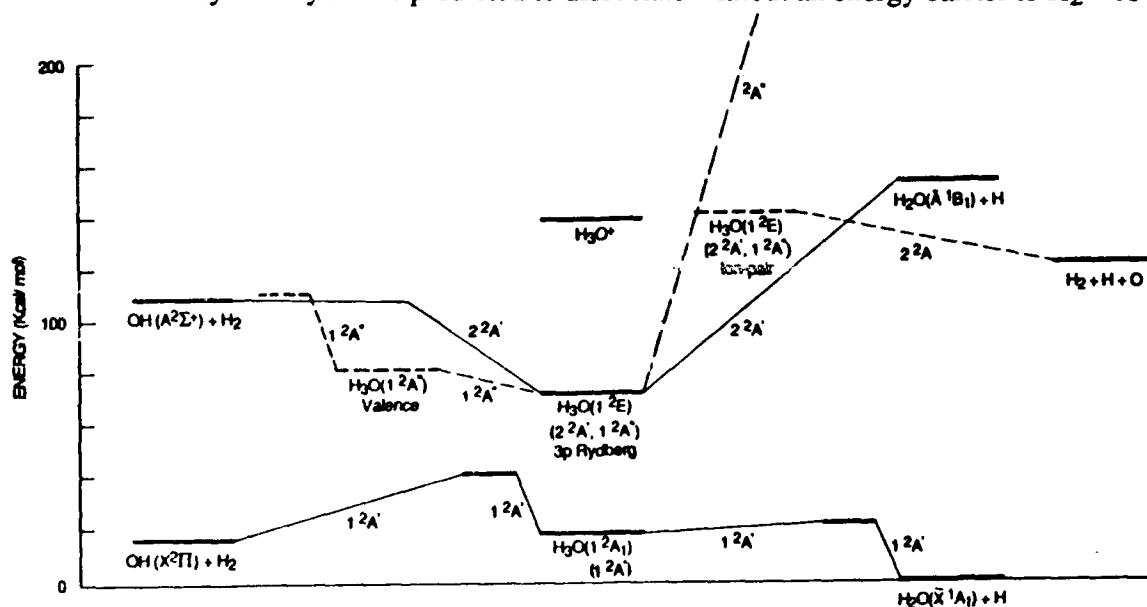


Figure 1. Minima and transition states on the lowest two doublet surfaces of H_3O .

Table 1. Minima on first two doublet surfaces of H₃O

State	Symmetry	Relative Energy ^a (kcal/mol)	Zero pt Energy (kcal/mol)	Relative Energy ^a with zero pt (kcal/mol)
1 ² A ₁ (1 ² A')	C _{3v} (C _s)	17.93	18.08	23.14
1 ² E(2 ² A', 1 ² A'')	C _{3v} (C _s)	71.94		
1 ² A'' (3p Rydberg)	C _s	73.77	23.49	84.39
1 ² A'' (Valence)	C _s	80.65	17.65	85.14
1 ² E(2 ² A', 1 ² A'') (ion-pair)	C _{3v}	141.57		

^aWith respect to H₂O + H.

Principal features of the H₃O potential surfaces are summarized below. In agreement with previous work,¹ we find the lowest state (1²A') of H₃O, which lies 18 kcal/mol above H₂O + H, may be characterized as an H₃O⁺ core surrounded by an oxygen 3s Rydberg electron. The metastability of the species depends on the barriers to dissociation which have been determined with care. A very low barrier, 3.58 kcal/mol, is found for dissociation to H₂O + H, which has a conventional transition state with one imaginary frequency (2310i cm⁻¹). Including the vibrational energies, a barrier height of 0.4 kcal/mol is predicted. Scaling the vibrational energies at the minimum and the barrier gives a barrier height including vibration for D₃O of 1.32 kcal/mol. These predictions may be consistent with the report² of metastability of D₃O but not of H₃O.

The transition state identified for dissociation of the 1²A' state to OH + H₂, with a calculated barrier height of 25.3 kcal/mol, will not limit the stability of H₃O but has the curious property of being characterized by two imaginary frequencies. Following the geometric distortions associated with the two imaginary modes, indicates this double transition state leads in addition to formation of H₂O + H in two different ways. There are a total of three ways to form H₂O + H from H₃O.

The second doublet state of H₃O (1²E in C_{3v} symmetry, 2²A', 1²A'' in C_s symmetry) is a 3p Rydberg state with, however, an admixture of valence antibonding character in the wavefunction. There also exists a minimum of completely valence character on the 1²A'' surface. The dissociation of the second state and the relationship between the minima on the 1²A'' surface have also been considered. The stability of the second state will be limited, in any event, by the calculated 18 ns radiative lifetime.

While the metastability of H₃O (D₃O) as an example of a hypervalent hydride has proven to be of great interest, the postulated ion-pair state of this system was not found to be stable. Similarly, a predicted⁶ pyramidal minimum on the lowest surface of H₄ has also been shown⁷ to

be unstable with respect to geometric perturbations. Back charge transfer from O^- or H^- to H_3^+ appears to lead to ground state H_3 which is unstable with respect to $H_2 + H$.

Li_3H

In contrast to systems with H_3^+ as the positive ion, as suggested by Michels, the Li_3H molecule may be more likely to exist as a stable ion-pair because both Li_3^+ and Li_3 are bound species. Therefore, the $1^1A'$, $1^1A''$, $1^3A'$, and $1^3A''$ states of Li_3H have been investigated⁸ at the MCSCF/Second Order CI level. The Gaussian basis set was chosen to be sufficiently diffuse to describe the hydrogen anion. Energies of the dissociation fragments have also been determined within a consistent computational model.

In agreement with the report of Michels and Montgomery,⁹ we find a local minimum with all real vibrational frequencies on the lowest potential surface of Li_3H at the C_{3v} symmetry pyramidal geometry anticipated for the ion-pair state. The geometry of the minima are illustrated in Figure 2. Analysis of the wavefunction indicates substantial mixing of ion-pair and covalent bonding character. The Li-Li bond length is 0.36 Å shorter than the corresponding bond length in Li_3^+ , in contrast to the case of H_3O where the ion-pair local minimum was found at the H-H separation of H_3^+ . Both Li-Li bond lengths in the C_{2v} structure of $Li_3(^2A_1)$ to which this state correlates are longer as well.

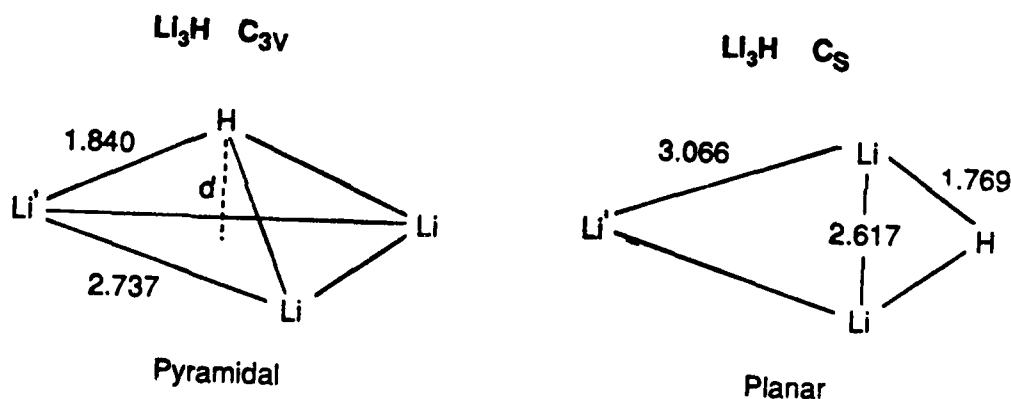


Figure 2. Optimized geometries for the pyramidal (local) minimum and planar (global) minimum on the $1^1A'$ potential surface of Li_3H .

The global minimum, however, on the lowest singlet potential surface is a planar conformation 20.3 kcal/mol lower in energy. The transition state for conversion of the pyramidal form to the planar geometry is predicted to have a very low imaginary frequency ($120i \text{ cm}^{-1}$). The transition occurs at a modest geometrical distortion from the pyramid, with a calculated barrier height of 1.3 kcal/mol. The stability of the Li_3H ion-pair should be considered to be problematical.

Energetic results and correlations for the lowest singlet and triplet surfaces of Li_3H are illustrated graphically in Figure 3. In contrast to the case for H_3O , the lowest state of each symmetry is clearly bound with respect to all possible separated fragment asymptotes. The diagram also includes the second state of each symmetry at the geometry of the ground state. The excitation energies are of qualitative reliability only but the excited states are also predicted to be bound with respect to the $LiH + Li_2$ asymptotes to which they correlate.

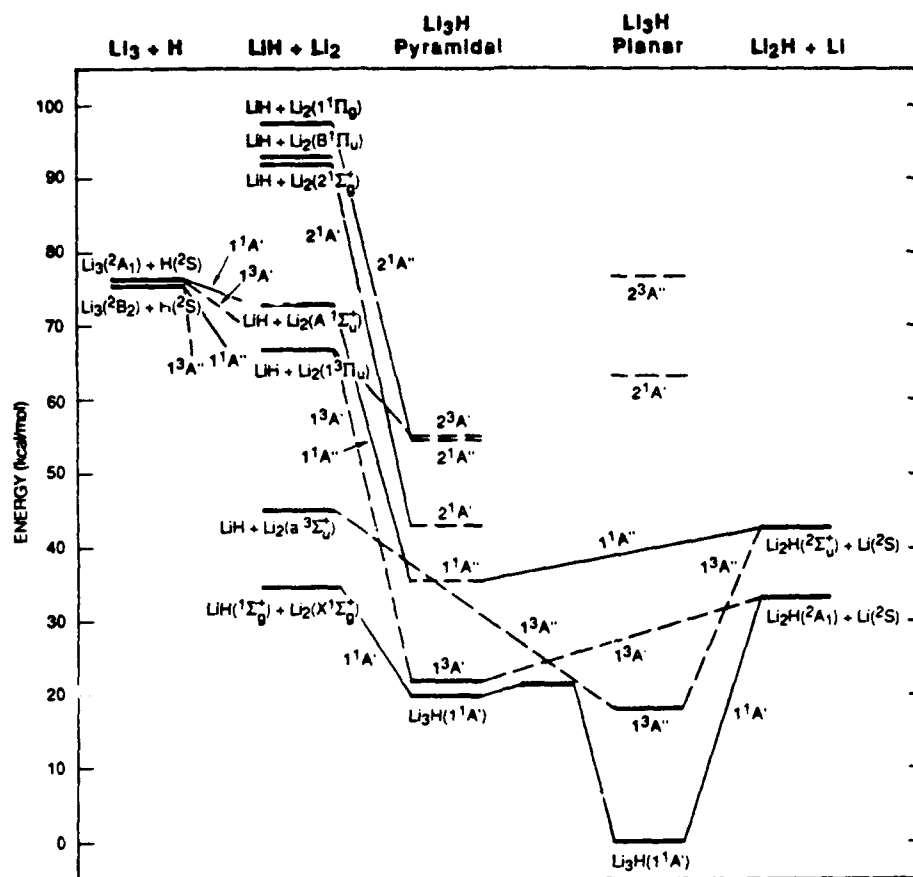


Figure 3. Correlation diagram for the Li_3H system, drawn in C_s symmetry. The second state of each symmetry (dashed line) has been calculated at the geometry of the lower state.

Predicted Specific Impulse

The NASA-Lewis code for prediction of rocket performance has been used to calculate specific impulse without extensive optimization for the species considered here. From our calculated energies and literature values for the fragments, the heat of formation of the Li_3H $1A'$ pyramidal and planar forms is calculated as 71.36 and 51.06 kcal/mol, respectively. The heat of formation of the $3A''$ state is predicted to be 69.62 kcal/mol. In Table 2, we list the specific impulse calculated for heats of formation approximating these values for combinations of Li_3H , O_2 , and H_2 . Combinations of Li_3H and H_2 were investigated following the suggestion of Rodgers¹⁰ who pointed out the improvement in predicted performance of $\text{H}_2\text{-O}_2$ with addition of small amounts of Li. Ratios have been only approximately optimized.

Even assuming the lowest energy planar form of Li_3H , taking the molar ratio $\text{Li}_3\text{H}:\text{H}_2:\text{O}_2$ of 5:30:4 results in a predicted I_{sp} of 429 sec, an increase of 16% over the $\text{H}_2\text{-O}_2$ value of 369 sec calculated under these conditions. From our calculated results, we estimate the heat of formation of Li_2H to be 50 kcal/mol. Use of Li_2H as an additive is estimated to be even more favorable, with a calculated specific impulse of 445 sec. Li_3H was not found to be an energetic species; combustion of Li_3H by itself, as expected, provides a low I_{sp} . Finally, in Table 2 we have also included specific impulse predictions for H_3O and D_3O assuming sufficient metastability. D_3O considered as a monopropellant is predicted to provide a modest improvement over the $\text{H}_2\text{-O}_2$ system.

While ion-pair metastability is proving a somewhat illusive goal, general features of these light atom systems highlighted by our detailed studies of H_3O and Li_3H is leading to improved insight in evaluating candidate systems.

Table 2. Estimated I_{sp} (NASA-Lewis Code)

Molar Composition			I_{sp} (sec)	
	<u>H_2</u>	<u>O_2</u>		
	2	1	369	
Li_3H	<u>H_2</u>	<u>O_2</u>	<u>$\Delta H_f = 68^a$</u>	<u>$\Delta H_f = 50^a$</u>
5	---	2	352	331
5	20	2	416	
5	30	4	438	429
Li_3H	<u>H_2</u>	<u>O_2</u>		
5	---	2	361	
5	30	4	445	
	<u>H_3O</u>	<u>O_2</u>		
	3	1	373	
	1	---	427	
	<u>D_3O</u>	<u>O_2</u>		
	3	1	355	
	1	---	396	

^aEnergies in kcal/mol.

†Supported by AFAL contract F04611-86-C-0070

*Present address Ecole Normale Supérieure, 75005 Paris, France

1. K. S. E. Niblaeus, B. O. Roos, and P. E. M. Siegbahn, *Chem. Phys.* 25, 207 (1977).
2. G. I. Gellene and R. F. Porter, *J. Chem. Phys.* 81, 5570 (1984).
3. G. Herzberg, *Ann. Rev. Phys. Chem.* 38, 27 (1987).
4. S. P. Walch and T. H. Dunning, *J. Chem. Phys.* 72, 1303 (1980); H. B. Schlegel and C. Sosa, *Chem. Phys. Lett.* 145, 329 (1988).
5. D. Talbi and R. P. Saxon, to be published *J. Chem. Phys.* (1989).
6. C. A. Nicolaides, G. Theodorakopoulos and I. D. Petsalakis, *J. Chem. Phys.* 80, 1705 (1984).
7. J. A. Montgomery and H. H. Michels, *J. Chem. Phys.* 86, 5882 (1987); A. Metropoulos and C. A. Nicolaides, *J. Phys. B: At. Mol. Opt. Phys.* 21 L77 (1988).
8. D. Talbi and R. P. Saxon, to be published, *Chem. Phys. Lett.* (1989).
9. H. H. Michels and J. A. Montgomery, in "Proceedings of the Air Force High Energy Density Materials Contractors Conference," p. 93 (1988).
10. S. Rodgers, personal communication.

Theoretical Investigation of Energy Storage
in Atomic and Molecular Systems*

H. H. Michels and J. A. Montgomery, Jr.
United Technologies Research Center
East Hartford, CT 06108

ABSTRACT

Theoretical electronic structure calculations are being carried out for several high energy species that are attractive candidates for advanced chemical propulsion systems. Using deliverable specific impulse and storability as the major criteria for the evaluation of new oxidizers or fuels, primary consideration is being given to ground state molecular structures, of low molecular weight, which exhibit a high positive heat of formation. Calculations to date have been carried out on: 1) light element C_{3v} and C_{2v} structures (H_4 , Li_3H , LiH_3 , Li_4); 2) azide-like structures (FN_3 , $a-N_2O_2$, $FNCO$, CO_3 , HN_3 , $FNBF$); 3) cyclic boron structures (B_3H_3 , B_2H_2NH); and 4) hypervalent structures (NF_5 , PF_5).

We have studied the Li_3H system in both C_{3v} (trigonal pyramid) and C_{2v} (planar kite-like) symmetries. Both structures are vibrationally stable, with the C_{2v} symmetry lower in energy at the MP2/6-311G** level of theory. Using either O_2 or F_2 as an oxidizer, Li_3H appears to give about 10% improvement in I_{sp} over LiH .

The energies and pathways for decomposition of FN_3 have been studied. Our calculations, carried out to compliment the experimental studies of FN_3 at Rockwell Science Center, indicate that $NF[a^1\Delta]$ should be efficiently produced by the thermal decomposition of FN_3 . The structure of this molecule, its predicted vibrational spectrum and the role of low-lying triplet states have been examined. A parallel study of the isoelectronic $FNCO$ molecule is in progress.

Further studies of the hypervalent NF_5 molecule indicate vibrational stability only in D_{3h} symmetry. A comparison of the bonding in NF_5 and PF_5 is currently in progress.

A preliminary experiment has shown evidence for formation of $a-N_2O_2$ from the reaction of $O[1D]$ with N_2O in a neon matrix on a window cooled to $\sim 10K$. A complete vibrational characterization, to positively identify that $a-N_2O_2$ has been formed, is in progress.

A discussion of our theoretical calculations on particular species is given below.

*Supported in part under AFAL Contract F04611-86-C-0071

DISCUSSION

Light Element Fuels

The C_{3v} structure of Li_3H , which is the analog of tetrahydrogen with a Li_3^+ base, was examined using several basis sets and at the SCF and MP2 levels of theory. Calculations at both the SCF and MP2 levels of theory, using several basis sets including diffuse orbitals, are given in Table 1. These data, which were previously reported at the Second AF HEDM meeting held in Newport Beach, indicate that this species is stable in all approximations that were examined. A diffuse basis (6-31++G*) was examined at the SCF level to insure that Li^- and H^- were accurately represented. However, the diffuse functions appear to have little effect on the optimized geometries. The results for this basis were essentially the same as those with the double-zeta plus polarization basis sets. The optimized structure for Li_3H has a short pyramid height (~ 1.1 Å) for the H^- anion above the Li_3^+ base. The structure thus somewhat resembles the NH_3 molecule. The basic reason that Li_3H is stable, while H_4 is a saddle geometry, is that the back charge transfer of an electron from H^- into the Li_3^+ base does not create an instability. Li_3 as a neutral species has stability relative to $Li + Li_2$ whereas H_3 is unstable relative to $H + H_2$.

Recently Cardelino, et al¹ have shown that a kite-like C_{2v} structure for Li_3H is the ground state at the SCF level of theory. Calculations of this structure were carried out at both the SCF and MP2 level of theory, using 6-31G* and 6-311G** basis sets. The data are shown in Table 2 where the C_{2v} planar kite-like structure is, in fact, found to be lower in energy than the trigonal C_{3v} structure at both the SCF and MP2 level of theory. A harmonic frequency analysis indicates vibrational stability for this C_{2v} structure, which appears to be a Li atom bridged across the known, stable Li_2H molecule. A Mulliken population analysis indicates that the ionicity on the H atom is $\sim 18\%$ in this conformation as compared with $\sim 29\%$ for the trigonal C_{3v} structure. Since both of these structures exhibit stable vibrational frequencies, they represent different local minima on the same ground state surface. Preliminary studies of the transition state connecting these two structures have been carried out which indicate a slightly distorted (C_s) trigonal bipyramid, with nearly the same energy as the C_{3v} structure. Further detailed calculations of Li_3H are in progress, including an analysis of the transition state between the C_{2v} and C_{3v} structures.

Azides and Azide-Like Structures

Calculations of hydroazoic acid (HN_3), fluorine azide (FN_3), fluorine isocyanate ($FNCO$), asymmetric dinitrogen dioxide ($a-N_2O_2$) and difluoraminoborane ($FNBF$) have been carried out at several levels of theory to determine the most stable geometries of these azides and azide-like compounds. The results are summarized in Table 3 which indicate

that a stable C_s structure exists for each of these compounds. A vibrational frequency analysis has also been carried out for each of these compounds. The results indicate a stable structure in $^1A'$ symmetry. A comparison with experimentally determined structures for HN_3 ², FN_3 ³ and $FNCO$ ⁴ has been made. It is clear that very good agreement has already been achieved at the MP2 level of theory.

FN_3

Calculations of the potential energy surfaces for FN_3 , both ground and excited states, have been initiated to compliment the experimental studies of this system currently being undertaken at Rockwell Science Center. The energies and pathways for decomposition, and the prediction of emission/absorption wavelengths are being studied both theoretically and experimentally. Studies of the FN_3 system as a HEDM material and as a possible chemical source for $NF[a^1\Delta]$, with potential laser applications, are being pursued.

A detailed analysis of FN_3 has been carried out at geometries relevant to: a) the equilibrium ground $^1A'$ state, b) the transition state for decomposition to $NF[a^1\Delta] + N_2[X^1\Sigma_g^+]$, and c) the region of singlet-triplet crossing. The details of these studies are outlined below:

a) Equilibrium Calculations

Ab initio theoretical calculations of the equilibrium structure and properties of fluorine azide (FN_3) have been performed using several standard basis sets and theoretical methods. Gradient-optimized structures and the corresponding harmonic vibrational frequencies have been calculated. Comparisons are made with the recent experimental results of Christen, Mack, Schatte, and Willner³. Good agreement with the experimental structure is found, with the correlated methods tending to correct the short SCF bond lengths. The harmonic vibrational frequencies are well described by MP2, except for the highest frequency mode, the terminal N-N stretch, which is predicted to be over 300 cm^{-1} too large. Systematic studies have shown MP2 vibrational frequencies are usually within 5% for small molecules.

b) Transition State Calculations

Calculations have been performed to locate the transition state for the decomposition of FN_3 into N_2 and NF . Transition state gradient optimizations were performed at the RHF/6-31G* and MP2/6-31G* levels of theory. To ensure that stationary points of the correct curvature have been found, harmonic vibrational frequencies have been computed for the transition structures. At the MP2/6-31G* optimized transition state, the RHF wavefunction is unstable with respect to a broken-symmetry UHF solution, and therefore the MP2 results may not be meaningful (for example, the extended central N-N bond

length). Multireference calculations are required to reliably describe the effects of electron correlation on the transition state. Therefore, the transition state was also located using a 6-in-6 CAS MCSCF wavefunction. MP3 and coupled cluster calculations were also performed at the SCF geometries to assess the effects of a more complete treatment of electron correlation on the barrier height. These results suggest a barrier height of about 0.5 - 0.7 eV, including correction for vibrational zero-point motion.

c) Singlet-Triplet Splitting

The location of the FN_3 $^1\text{A}' - ^3\text{A}''$ crossing determines the singlet-triplet distribution of the $\text{FN}_3 \rightarrow \text{N}_2 + \text{NF}$ products. Experimental evidence⁵ suggests that the crossing is on the product side of the barrier. *Ab initio* SCF calculations have therefore been performed to predict this crossing point from theory. These are UHF triplet calculations done at the RHF/6-31G* $^1\text{A}'$ optimized equilibrium and transition states. The UHF spin contamination was low, indicating that UHF is an acceptable level of theory for an initial approach to this problem. In order to locate the singlet-triplet crossing, the dissociative reaction path (intrinsic reaction coordinate) from the RHF/6-31G* $^1\text{A}'$ transition state was computed. At selected points on the reaction path, the singlet-triplet gap was calculated. We find the singlet-triplet crossing at an FN-NN distance of 1.78 Å, on the outside of the activation barrier of the ground state surface and close to the corresponding geometry predicted by Alexander and Dagdigan for HN_3 .⁶

FNCO

The synthesis of fluorine isocyanate (FNCO) was first reported by Gholivand, et al⁴ using photolysis of F-CO-N₃ in an argon matrix. This azide-like compound is predicted to be thermodynamically more stable than the isoelectronic FN_3 molecule. Our calculated equilibrium geometry is given in Table 3 which again indicates that the MP2/6-31G* level of theory gives good agreement with the experimentally determined structure. Harmonic vibrational frequencies are also well described at the MP2 level, except for the terminal C-O stretch.

Despite the greater thermodynamic stability of FNCO, this molecule shows a similar dissociation pathway to that found for the halogen azides. We find the transition state at an FN-CO bond length of ~ 2.0 Å. The barrier height relative to the decomposition products $\text{NF}[a^1\Delta] + \text{CO}[X^1\Sigma^+]$ is calculated to be ~ 0.7 eV at the GVB(1)/6-31G* level of theory. RHF calculations are unreliable in this region since a multiconfiguration representation is required to achieve proper dissociation to the $a^1\Delta$ state of NF. Additional calculations of both FNCO and the NCO radical are in progress.

Hypervalent Compounds

A category of compounds which may represent energetic molecular conformations are those resulting from orbital hybridization to a high valence state of the central coordinating atom in the molecule. Conventional wisdom is that hypervalent molecules, such as NF_5 , formed from first row atoms are not stable since the required hybridization energy is too large. In recent years, however, quantum mechanical studies have revealed that the bonding in a hypervalent structure such as PF_5 is much more complicated than the simple Pauling hybridization model. In fact, detailed calculations⁷ reveal that PF_5 is vibrationally stable, even if the d-orbital participation is set to zero. The bonding appears to be better described by hybridization to form the trigonal PF_3 ring, with the axial fluorines in a 3-center bond. Such a structure can be further stabilized by back-bonding contributions of the normally unoccupied d-orbitals. This interpretation of the bonding of hypervalent compounds revives the possibility of forming such structures from first row atoms. Compounds such as NF_5 , NH_3F_2 , OF_4 , ClF_5O and ClF_5 represent hypervalent, high oxidation state structures which represent a new class of possible oxidizers for chemical propulsion systems. For example, Christie⁸ has estimated that theoretical performance calculations for H_2/NF_4 yield a vacuum I_{sp} of 505 sec.

The synthesis of such strong oxidizers is an obvious experimental challenge. Christie and collaborators⁹ have succeeded in the synthesis of the adduct tetrafluoronitronium (V) hexafluoroarsenate (NF_4AsF_6) but all attempts to date to synthesize NF_5 have failed. The structure of NF_4AsF_6 has been confirmed by spectroscopy and magnetic resonance measurements and is known to be ionic, $\text{NF}_4^+\text{AsF}_6^-$. The hybridization of the N atom in NF_4AsF_6 is thus sp^3 , forming the stable tetrahedral NF_4^+ cation, rather than a true pentavalent structure. Further, semi-quantitative arguments by Kutzelnigg¹⁰ suggest that NF_5 or NH_3F_2 structures will not exist for steric reasons; the charge distribution in the NF_3 planar ring excludes the formation of a short axial N-F bond.

In an effort to more fully understand the competition between steric factors, which might prevent axial bond formation, and the strengths of 3-center bonds, an analysis of NF_5 structures was carried out at both the SCF and MP2 levels of theory using several basis sets. An ionic NF_4^+F^- structure was first examined in light of the stability of Christie's $\text{NF}_4^+\text{AsF}_6^-$ structure. No stable minimum could be located starting the geometry search along the $\text{NF}_4^+ + \text{F}^-$ reaction path. This structure simply decomposes to $\text{NF}_3 + \text{F}_2$. However, two stable covalently bonded structures (D_{3h} and C_{3v}) were found for NF_5 at the SCF level. These calculations were reported at the Second AF HEDM meeting held at Newport Beach. The D_{3h} (trigonal bipyramid) structure was found to be lower in energy than the C_{3v} structure at the SCF/6-31G* level of theory. Further MP2 calculations later indicated that the C_{3v} structure (inverted umbrella) probably represents a saddle point. The calculated geometry and vibrational frequencies for the D_{3h} structure are

given in Tables 4 and 5, respectively, at several levels of theory. These calculations clearly indicate that careful optimization of the basis set and a correlated level of theory will be required to positively identify the structure and vibrational modes. Introduction of diffuse basis functions and optimization of the d-orbital exponents have a small but important effect on the thermochemistry. Calculations at the MP2 level of theory clearly show a different vibrational pattern owing to the lengthening of the planar NF bond. The most significant observation, however, is that NF₅ is predicted to be vibrationally stable without incorporation of d-orbitals. The classical model of sp³d bonding is thus clearly inadequate for this system.

- ¹ B. H. Cardelino, W. H. Eberhardt and R. F. Borkman, JCP, 84, 3230 (1986).
- ² Tables of Interatomic Distances and Configurations in Molecules and Ions, L. E. Sutton, ed., Chemical Society, London (1985).
- ³ D. Christen, H. G. Mack, G. Schatte and H. Willner, J. Am. Chem. Soc., 110, 707 (1988).
- ⁴ K. Gholivand, H. Willner, D. B. Bielefeldt and A. Haas, Z. Naturforsch, 39b, 1211 (1984).
- ⁵ B. K. Winker, D. J. Benard and T. A. Seder, Quarterly Report No. 8, Contract F04611-86-C-0072, Rockwell International (1988).
- ⁶ M. H. Alexander and P. I. Dagdigian, Proc. Second HEDM Conf., L. P. Davis and F. J. Wodarczyk, ed. (1988).
- ⁷ A. Strick and A. Veillard, J. Amer. Chem. Soc. 95, 5574 (1973).
- ⁸ W. W. Wilson and K. O. Christe, Proceedings of the HEDM Conference, Editors - W. S. Lauderdale and W. A. Sowell, Rosslyn, VA, p.287 (1987).
- ⁹ J. P. Guerten, K. O. Christe and A. E. Pavlath, Inorganic Chemistry, 5, 1921 (1966).
- ¹⁰ W. Kutzelnigg, Journal de Chimie Physique, 78, 2 (1981).

Table 1. *Ab Initio* Structure and Calculated Energy for Li_3H in C_{3v} Symmetry

Theory	h	r	Energy	Frequencies			
				e	a_1	e	a_1
SCF/6-31G*	1.1992	2.6461	-22.857226	247	400	344	821
SCF/6-31++G*	1.1895	2.6563	-22.859319	258	389	349	809
SCF/6-311G**	1.1422	2.5993	-22.867477	291	390	421	837
MP2/6-31G*	1.1786	2.6391	-22.901463	259	389	454	848
MP2/6-311G**	1.1104	2.5768	-22.958672	280	387	511	853

Energies (hartrees), distances (\AA), frequencies (cm^{-1})
h = distance of the hydrogen atom above the Li_3 plane
r = length of the side of the Li_3 ring

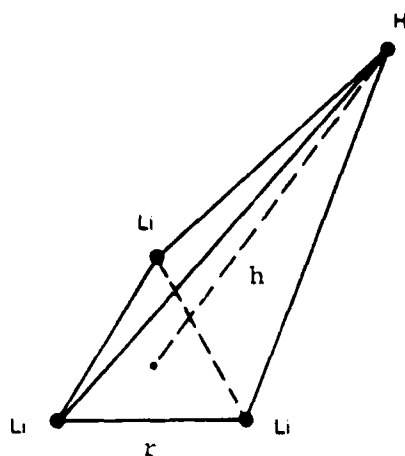


Table 2. *Ab Initio* Structure and Calculated Energy for Li₃H in C_{2v} Symmetry

Theory	r_s	r_b	r_t	Energy	Frequencies					
					b ₂	a ₁	b ₁	a ₁	a ₂	b ₂
SCF/6-31G*	3.1923	2.5310	1.7741	-22.896763	177	269	382	396	1039	1041
SCF/6-311G**	3.1703	2.4832	1.7327	-22.906001	178	263	385	399	1063	1092
MP2/6-31G*	3.1092	2.5129	1.7761	-22.936496	190	283	369	379	1054	1036
MP2/6-311G**	3.0688	2.4596	1.7164	-22.992986	192	279	377	398	1050	1105

Energies (hartrees), distances (Å), frequencies (cm⁻¹)

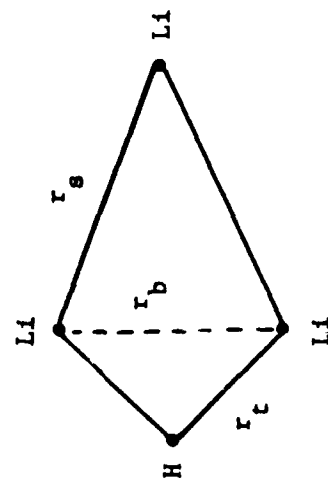
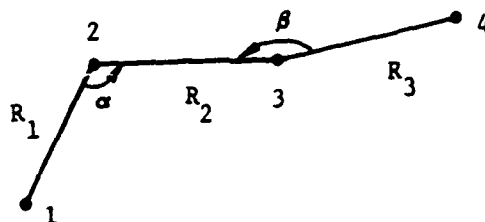


Table 3. Optimized Geometries of Azides



Compound	Theory	$R_1(\text{\AA})$	$R_2(\text{\AA})$	$R_3(\text{\AA})$	a (deg)	b (deg)
HN ₃	SCF	1.0055	1.2381	1.0987	108.181	173.815
	MP2	1.0182	1.2502	1.1583	109.946	171.209
	Exp. ²	1.012	1.240	1.134	112.65	(180.0)
FN ₃	SCF	1.3820	1.2536	1.0995	104.315	174.108
	MP2	1.4309	1.2799	1.1521	103.765	171.803
	Exp. ³	1.444	1.253	1.132	103.8	170.9
FNCO	SCF	1.3737	1.2387	1.1354	109.846	173.235
	MP2	1.4185	1.2622	1.1765	110.717	168.914
	Exp. ⁴	1.39	1.28	1.18	114.0	(180.0)
a-N ₂ O ₂	SCF	1.7574	1.2024	1.0844	103.966	179.506
	[MP2	1.5305	1.2272	1.1548	103.591	179.488]
	CISD	1.5817	1.2240	1.1072	102.867	179.344
FNBF	SCF	1.2993	1.2068	1.2871	180.000	180.000
	MP2	1.3394	1.2491	1.3069	154.650	169.291

() Assumed

[] ψ_0 is UHF unstable

Table 4. *Ab Initio* Structure and Calculated Energy for NF₅ in D_{3h} Symmetry

Theory	d-exponent		r _p	r _h	Energy
	N	F			
SCF/6-31G	-	-	1.3860	1.5926	-550.936601
SCF/6-31G*	0.80	0.80	1.3267	1.5312	-551.103856
SCF/6-31G(d)	0.94	0.76	1.3260	1.5310	-551.104823
SCF/6-31+G*	0.80	0.80	1.3223	1.5473	-551.126800
SCF/6-311G	-	-	1.3765	1.5978	-551.116124
SCF/6-311G*	0.91	1.75	1.3132	1.5457	-551.249831
SCF/6-311G(d)	0.94	0.76	1.3260	1.5310	-551.274677
SCF/6-311G(2d)	1.63	1.32	1.3148	1.5429	-551.292792
	0.54	0.44			
MP2/6-31G*	0.80	0.80	1.4098	1.5472	-552.228780
MP2/6-31G(d)	0.93	1.47	1.3962	1.5538	-552.302405

Energies (hartrees), distances (Å)

r_p = N-F bond length in the plane

r_h = N-F axial bond length

Table 5. Calculated Harmonic Frequencies for NF₅ as a D_{3h} Structure

Theory	Frequencies (cm ⁻¹)									
	a ₁ ' axial stretch	e' axial bend	a ₁ ' axial stretch	e' axial bend	e'' asym. bend	a ₂ ' planar bend	a ₁ ' sym. stretch	e' axial bend		
SCF/6-31G	574	235	480	560	568	743	744	1184		
SCF/6-31G*	459	276	509	656	663	828	857	1352		
SCF/6-31G(d)	452	277	509	656	664	828	858	1351		
SCF/6-31+G*	155	284	489	649	652	802	855	1353		
SCF/6-311G	472	243	442	566	574	718	762	1230		
SCF/6-311G*	50	288	481	659	669	829	868	1373		
SCF/6-311G(d)	377	278	507	657	666	822	860	1349		
SCF/6-311G(2d)	233	286	499	656	664	821	863	1354		
MP2/6-31G*	614	173	426	551	578	936	690	969		
MP2/6-31G(d)	603	187	394	552	587	922	692	975		

Spectroscopy of Hydrogenic (Ionic) Species in Hot Plasmas and Cryogenic Solids

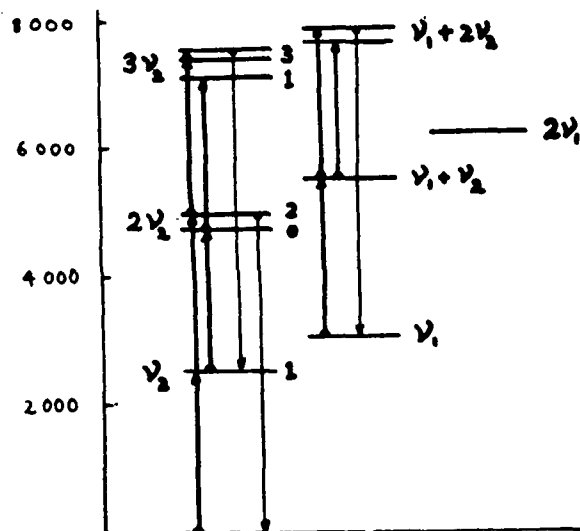
Takeshi Oka

Department of Chemistry and
Department of Astronomy and Astrophysics
The University of Chicago
Chicago, Illinois 60637

We have observed infrared spectra of (a) vibrationally hot H_3^+ in hot plasmas and (b) H_3^+ surrounded by solid para ($J=0$) - H_2 at cryogenic He temperature. These results are novel but were more or less anticipated in my proposal to AFOSR three years ago (May 2, 1986). The most exciting development related to these experiments, however, came totally unexpected, i.e., (a) the discovery by astronomers of an emission spectrum from vibrationally hot H_3^+ in Jupiter corresponding to the overtone $2\nu_2 \rightarrow 0$ transitions and (b) observation of extremely narrow infrared spectral lines in solid H_2 .

1. Vibrationally Hot H_3^+

The vibrational energy levels of H_3^+ are shown in Fig. 1.

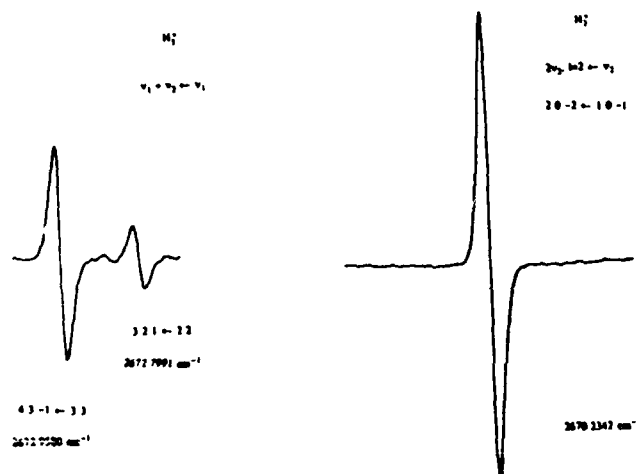


They are composed of excitations of the totally symmetric (breathing) ν_1 band (fundamental at 3179 cm^{-1}) and the degenerate (deformation) ν_2 band (2521 cm^{-1}).

We have observed and characterized three hot bands $2\nu_2(l=2) \leftarrow \nu_2$, $2\nu_2(l=0) \leftarrow \nu_2$, and $\nu_1 + \nu_2 \leftarrow \nu_1$.¹

In order to produce vibrationally hot H_3^+ , we used discharges with $\text{He}:\text{H}_2$ mixtures with the total pressure of ~ 10 Torr and the mixing ratios of 10:1. He has the unique quality that (1) because of the exceptionally high ionization potential (24.6 eV), He^+ or metastable He^* are very efficient and energetic ionizers making both the electron temperature of plasmas and the vibrational temperature of H_3^+ very high and (2) because of the exceptionally low proton affinity (1.9 eV), HeH^* gives the proton away to H_2 to form H_3^+ . The plasma tube was dipped in liquid nitrogen so that we have vibrationally hot but rotationally cold H_3^+ .

High resolution - high sensitivity spectroscopy has been conducted using our difference frequency spectrometer with LiNbO_3 and LiIO_3 as mixers. The resolution is Doppler limited $\Delta\nu/\nu \sim 10^{-6}$ and the sensitivity is $\Delta I/I \sim 5 \times 10^{-7}$. The hot band lines have been observed with good signal to noise ratios as shown in Fig. 2.



One major problem in the analysis of the spectrum was the observed chaotic vibration-rotation patterns which did not show simple regularity or symmetry. Here we have been helped by the timely first principle calculation communicated to us by Miller and Tennyson.² They treat the problem as that of

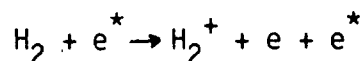
global motion of the three protons in ab initio potential potential field rather the traditional perturbational approach after separation of vibration and rotation.

It has been the general concensus among molecular astrophysicists that H_3^+ is the most important molecular species yet to be detected in interstellar space. Ever since the initial discovery of the H_3^+ spectrum in 1980, I have been attempting its detection in molecular clouds with Tom Geballe.³ In December 1988, Jim Watson of the Herzberg Institute of Astrophysics informed me that a novel emission spectrum had been observed in the Jupiter hot spot by the Canada-French-Hawaii telescope.⁴ I sent the list of our observed hot band frequencies and this led to the definitive identification of the emission spectrum as due to H_3^+ . After the fact, I learned that Jupiter is a gigantic dynamo surrounded by enormous amount of plasmas but it had never occurred to me to look at Jupiter.

2. Ionic Species in Solid Para- H_2

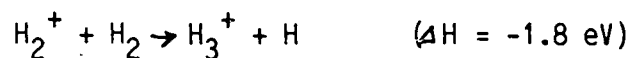
We have studied infrared spectrum of ionized solid para- H_2 at 4K. We make a transparent para- H_2 (99.8%) crystal in a copper vessel of $\sim 2 \text{ cm} \times 2 \text{ cm}$ and ionize by high energy ($\sim 2\text{MeV}$) electrons. The van de Graaf accelerator in the Argonne National Laboratories has been used. The electron beam enters into the crystal cell through a thin ($50 \mu\text{m}$) Al-alloy foil. The absorption spectroscopy was conducted using a blackbody infrared beam which was passed through the cell in the direction perpendicular to the electron beam through two sapphire windows. The radiation is then analyzed by a Bomem DA-2 FTIR spectrometer.

The sequence of reactions begin with the ionization.

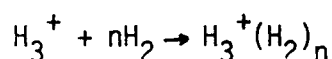


where e^* is the high energy electron. The secondary electron e flies away

with sufficient excess energy leaving H_2^+ behind. The H_2^+ ion immediately reacts with one of the neighboring H_2 through a proton hop reaction

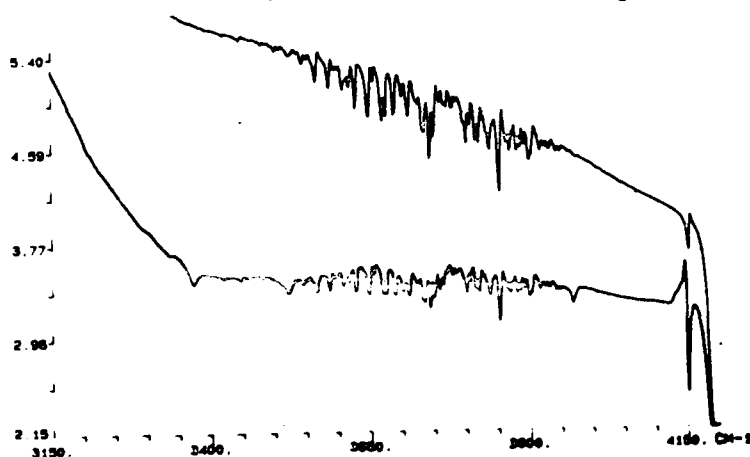


where the excess energy of 1.8 eV makes the resultant H atom to fly away leaving H_3^+ . The H_3^+ ion then attract neighboring H_2 molecules to form clusters. The excess energy for the first clustering to form H_5^+ is $\sim 0.25 \text{ eV}$



and the intermolecular distance reduces from 3.8 \AA to $\sim 2 \text{ \AA}$ according to theory.⁵ How much the clustering proceeds remains to be seen.

An example of the observed spectrum is shown in Fig. 3.⁶

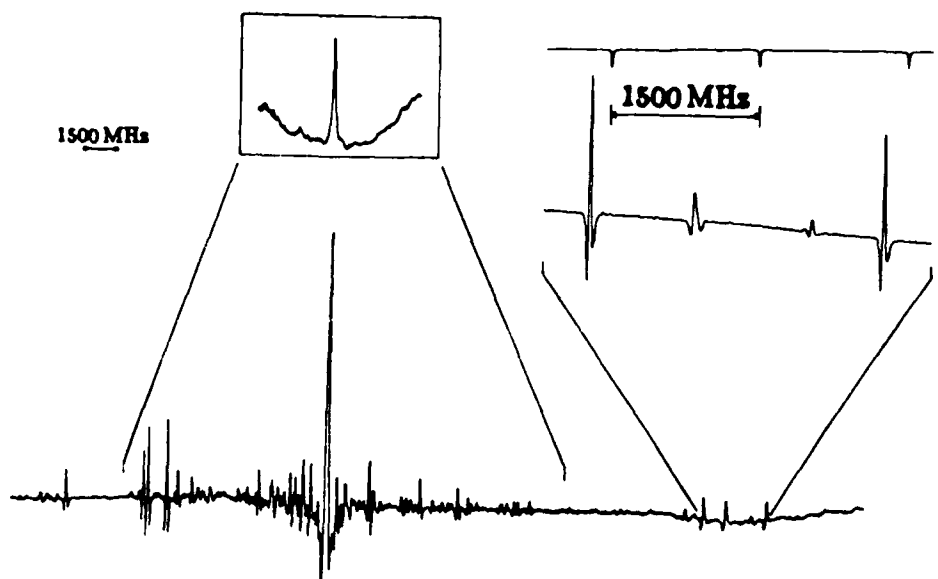


The upper trace is the FTIR spectrum of solid $p\text{-H}_2$. The complicated structure in the center is due to the extremely strong OH stretching vibration of atmospheric air. The lower trace gives infrared spectrum after electron bombardment. Three new features appearing in the range are marked with arrows. Three other new features have been observed in the region of $2100\text{--}2250 \text{ cm}^{-1}$. They are listed below together with their tentative assignments.

Observed Frequencies (cm^{-1})	Tentative Assignments
3967.8	H_2 stretch
3514.5	H_3^+ symmetric stretch
3372.9	
2230.2	H_3^+ antisymmetric stretch symmetric stretch
2132.9	
2109.7	

The highest line is very close to the absorption line of gaseous H_5^+ (3910 cm^{-1} and 3532 cm^{-1}) reported earlier by Okumura, Yeh, and Lee,⁷ and tentatively assigned accordingly. The lines around 2100 cm^{-1} are close to the H_3^+ stretching vibrations originating from the ν_2 degenerate vibration of free H_3^+ . More work is in progress. It is remarkable that all the features last very long time of $\sim 1 \text{ hr}$.

An unexpected result were obtained when we studied infrared spectrum of solid hydrogen under high resolution using our laser spectrometers. The tetrahexacontapole (2^6) induced $J = 6 \leftarrow 0$ rotational spectrum appeared as a very narrow spectral line with the linewidth of $\sim 90 \text{ MHz}$ (hwhm).⁸ This prompted us to observe the vibration rotation $\nu = 1 \leftarrow 0$ $J = 1 \leftarrow 1$ impurity ortho- H_2 spectrum. Back in our mind was the remarkable microwave spectrum observed by Hardy and Berlinsky.⁹ The observed spectrum is shown in Fig. 4.¹⁰ The complicated structure is due to the electric quadrupole interactions between $J = 1 \text{ H}_2$ molecules. The linewidth has been observed to be on the order of $\sim 10 \text{ MHz}$ for the sharpest lines. This opens up the new possibility of high resolution spectroscopy in solid and storing radiative energy in solid H_2 .



References.

1. M. Bawendi, B.D. Rehfuss, and T. Oka, manuscript in preparation.
2. S. Miller and J. Tennyson, *J. Mol. Spectrosc.* 128, 530 (1988) private communication.
3. T.R. Geballe and T. Oka, *Astrophys. J.*, in press.
4. J.P. Maillard and P. Drossant, *CFHT Bulletin* 20, 13 (1989).
5. Y. Yamoguchi, J.F. Gaw, R.B. Remington, and H.F. Schaefer III, *J. Chem. Phys.* 86, 5072 (1987).
6. M.C. Chan, M. Okumura, and T. Oka, *The 44th Symposium on Molecular Spectroscopy*, Ohio State University (1989) submitted.
7. M. Okumura, L.I. Yeh, and Y.T. Lee, *J. Chem. Phys.* 88, 79 (1988).
8. M. Okumura, M.C. Chan, and T. Oka, *Phys. Rev. Lett.* 62, 32 (1989).
9. W.N. Hardy and A.J. Berlinsky, *Phys. Rev. Lett.* 34, 1520 (1975).
10. M. Okumura, M.C. Chan, B.D. Rehfuss, and T. Oka, manuscript in preparation.

PHOTOIONIZATION AND DISSOCIATION OF
THE TRIATOMIC HYDROGEN MOLECULE

H. Helm, L. J. Lembo, P. C. Cosby and D. L. Huestis
Molecular Physics Laboratory
SRI International, Menlo Park, CA 94025

ABSTRACT

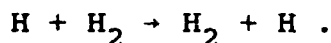
Rotationless triatomic hydrogen molecules are synthesized in a fast molecular beam. Laser excitation of the molecules allows study of electric field induced ionization as well as autoionization of the ns, np, nd, and nf Rydberg series of H_3 . Two photon ionization and double resonance techniques are applied to determine vibrational frequencies of trihydrogen.

Experimental analysis of the electron-core interaction shows that selective optical excitation of core rotation and core vibration can be achieved concurrent with excitation of the Rydberg electron.

Predissociation of low principal quantum number Rydberg states is observed to lead to the formation of both $H_2 + H$ as well as $H + H + H$ fragments.

INTRODUCTION

Triatomic hydrogen presents topics for experimental and theoretical investigation that are interesting from a variety of points of view. As the simplest polyatomic molecule it should have received extensive experimental attention, yet its electronic emission spectrum was first identified only ten years ago [He79]. From a chemist's perspective H_3 consists of H_2 with an extra hydrogen atom, or the unstable transition state in the most fundamental of chemical reactions,



The unstable nature of the ground state of H_3 easily explains the difficulties in its quantitative experimental investigation.

From a physicist's perspective we might think of H_3 as the combination of the exceptionally stable molecular ion H_3^+ with an extra electron. In our investigations we take this perspective literally. We begin with a beam of H_3^+ molecular ions, to which we attach a single electron by charge transfer in a Cs vapor cell. Most of the resulting H_3 neutrals are predissociated by the vibrational continuum of the ground electronic state. The few that remain are in a single rotational level of a single electronic state and survive only because they have a symmetry that is not present in the ground-state continuum [GP83,He86]

We detect the existence of these levels by laser photoabsorption, leading either to photodissociation, in which case the $\text{H}_2 + \text{H}$ or $\text{H} + \text{H} + \text{H}$ fragments are detected in coincidence by a position-sensitive detector, or by reionization, in which case reformed H_3^+ ions are detected. The resulting spectra are remarkably simple, appearing more like that of the hydrogen atom, than that of the hydrogen molecule. The objective of our studies is to quantitatively investigate the interactions among the relatively uncoupled electronic, vibrational, and rotational motions of H_3 .

EXPERIMENTAL RESULTS

Formation of H_3^*

We form the metastable species of H_3 by electron transfer from a stationary alkali target (Cs or Rb) to a mass selected H_3^+ ions in a fast beam. As mentioned above only a small fraction of charge transfer products are metastable [JB84]. Typically 10^7 to 10^9 metastable molecules are produced per second in a 1 mm diameter beam traveling at energies of several keV. Experimental schematics for the laser photoionization and photodissociation

spectrometers have been presented in recent publications [LHH89a,HC87].

Photodissociation in the Visible

The lowest photoexcitations transitions from the $\tilde{B} 2p \ ^2A_2''$ are to the $3s \ ^2A_1'$ and $3d \ E''$ states at 16694 and 17297 cm^{-1} respectively, as reported by Herzberg et al. [DH80,HHW82]. In our experiments, the initial state is unique, having $N''=0$, thus the one-photon absorption spectrum can have only a single rotational branch with $N'=1$. These same transitions are easily observed by collecting $H_2 + H$ photodissociation products, as shown as peaks labeled $3s\nu_0$ and $3d\nu_0$ in Figure 1 [CH88]. The energy analysis capability of the position-sensitive detector allows us to show that predissociation of these two states leads to substantially different distributions of vibrational energy in the H_2 fragment. For the $3s$ state, H_2 is observed in vibrational levels from $v=0$ to $v>12$. For the $3d$ state, however, a significance preference is observed for the formation of H_2 with $v=5-9$. In addition to predissociation to $H_2 + H$ products, both the $3s$ and $3d$ states are observed to predissociate into three atoms, $H + H + H$. Also shown in Figure 1 are transitions from vibrationally excited $\tilde{B} 2p \ ^2A_2''$ initial states to $3s$ and $3d$ states with the corresponding vibrational excitation (labeled $3s\nu_1$, $3s\nu_2$, $3d\nu_1$, $3d\nu_2$). These indicate that vibrationally excited metastables are present in the beam (their relative abundance depends on the ion source conditions) and provides the first direct information about the vibrational frequencies of the excited states of H_3 .

Field Ionization in the Ultraviolet

The vibrational structure described above provides an indication of the role to be played by the H_3^+ core in making more interesting the pseudo-atomic H_3^* absorption spectrum. We can explore this core structure in somewhat more detail by gradually promoting the outer electron to higher principal quantum numbers in the Rydberg series $nd + 2p$, and detecting the photoabsorption

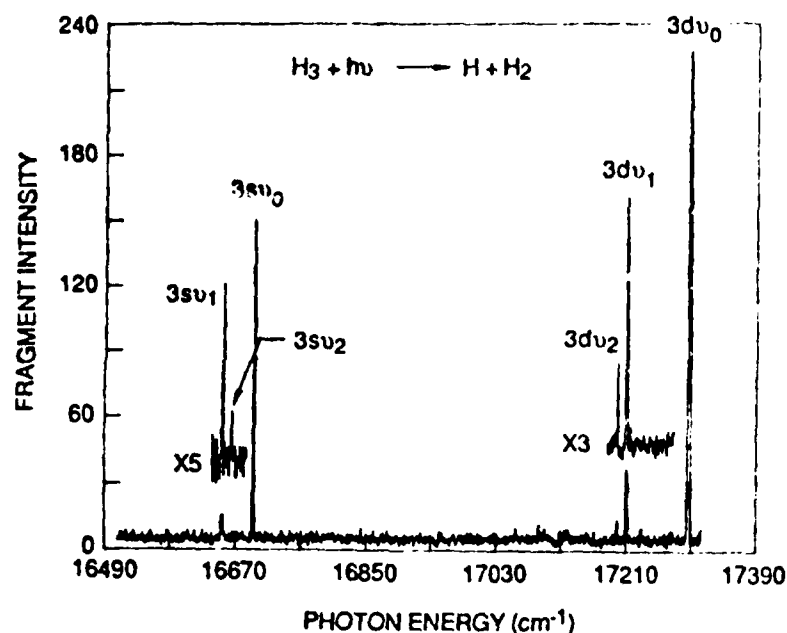


Figure 1: Observed production of photofragments from H_3 as a function of the photon energy of the exciting laser. Only photofragments produced with center-of-mass energies $W > 4$ eV are recorded for this spectrum. The spectrum at other energy releases is similar, but with a substantial background due to spontaneous dissociation fragments.

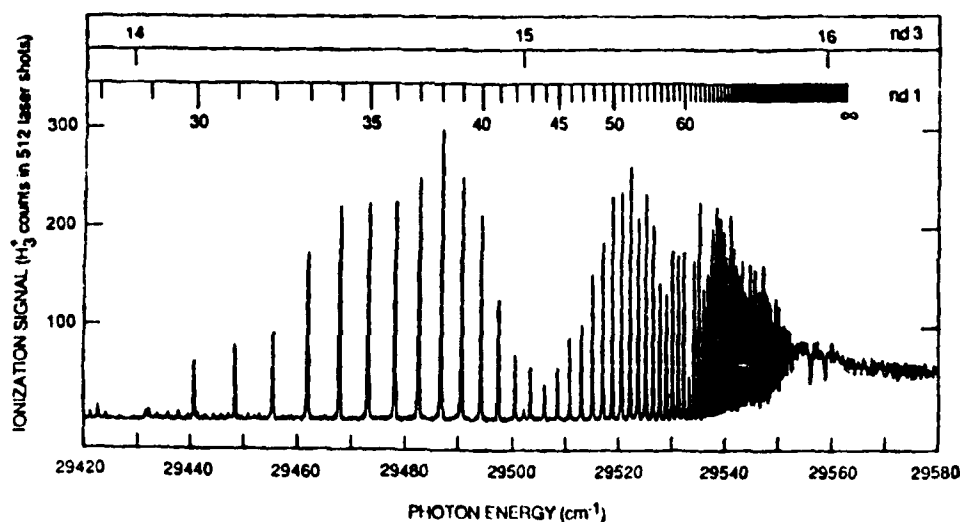


Figure 2: Photoabsorption of the lowest metastable level of H_3 , detected by field ionization of the excited d-electron Rydberg series. Series members converging to the $N^+=1, K^+=0$ level of H_3^+ are marked at the top of the figure as nd1. A series of interlopers, nd3, converging to the rotational level $N^+=3, K^+=0$ is also indicated. Three additional window resonances appear within 30 cm^{-1} of the threshold.

by field ionization. The resulting spectrum is shown in Figure 2, in which nd levels from $n = 28$ to $n = 100$ have been assigned [He88]. Field ionization has also been used by Dodhy *et al.* [DKM89] to detect nd states for n as low as 14. All n values from $n = 3$ to $n = 100$ have been detected by double-resonance ionization-depleting spectroscopy [LHH89b]. Extrapolation of this series has enabled the accurate determination of the ionization potential of the rotationless $\tilde{B} 2p^2 A_2''$ state as $29562.58 \pm 0.5 \text{ cm}^{-1}$. The intensity modulations shown in Figure 2 are significant, although weakly dependent on laser power, and show the influence of having multiple Rydberg series converging to different rotational states of the H_3^+ core. A particular example is the broad dip in signal near $n = 42$, which appears to correspond to an $n = 15$ interloper from the $N^+ = 3$ level of H_3^+ . Attempts to model this spectrum suggest that the actual situation is not quite so simple.

Vibrational Autoionization

Just to the red of the spectrum shown in Figure 2, additional photoionization peaks appear that reveal photoabsorption into levels that ionize spontaneously without an external field. These are shown in Figure 3, and as indicated by the labels, are the higher members of the $ns + 2p$ and $nd + 2p$ Rydberg series from the vibrationally excited metastables. These peaks appear in the ionization spectrum because the upper levels lie energetically above that of the vibrationless H_3^+ core plus a free electron. The autoionization mechanism is depicted in Figure 4. Note that $n = 6$ in the symmetric-stretch (ν_1) series and $n = 7$ in the bending vibration (ν_2) series are the lowest members that are subject to vibrational autoionization.

Two-Photon Excitation of np and nf Rydberg Series

The great strength of the $3s + 2p$ and $3d + 2p$ transitions suggests using these transitions in double-resonance experiments. In this paragraph we discuss the use of the $3s$ and $3d$ states as intermediates for two-photon excitation of the np and nf Rydberg

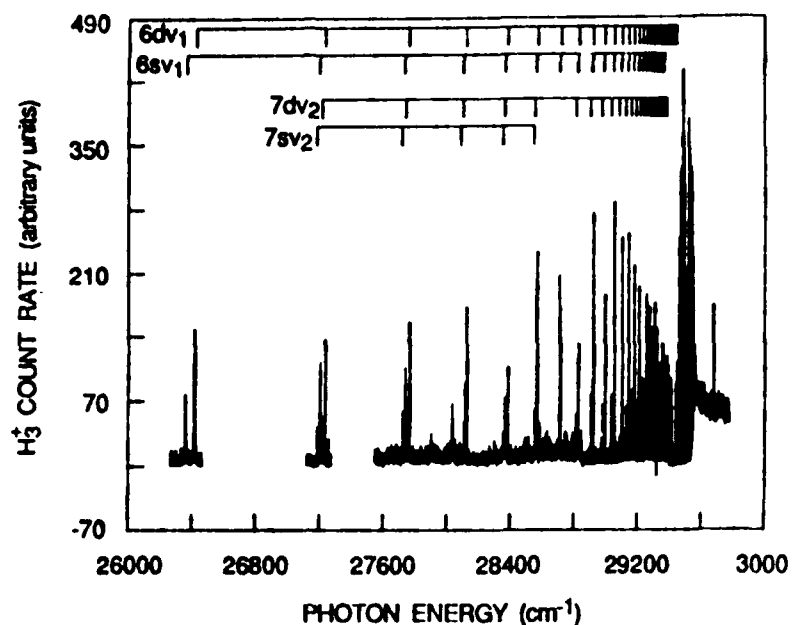


Figure 3. Vibrational autoionization of s- and d-electron Rydberg series converging to the bending excited core level (ν_2) and symmetric stretch excited core level (ν_1) of H_3^+ .

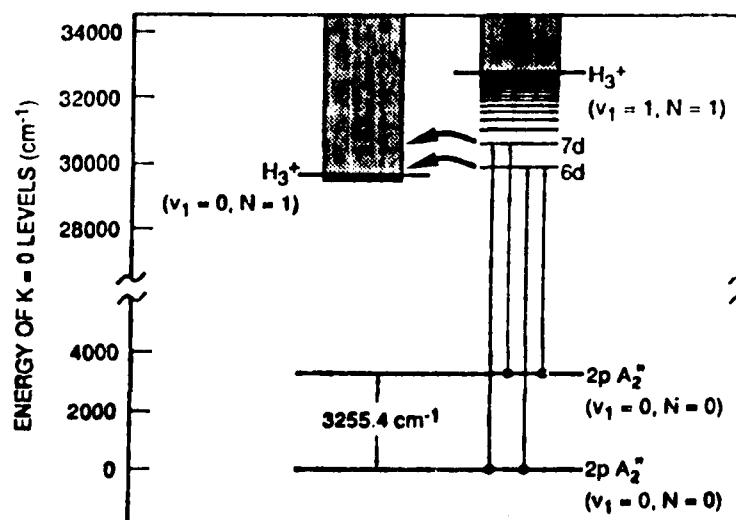


Figure 4. Energy level diagram of H_3 showing diagonal and off-diagonal excitation to the vibrationally autoionizing 6d and 7d Rydbergs with symmetric stretch excitation.

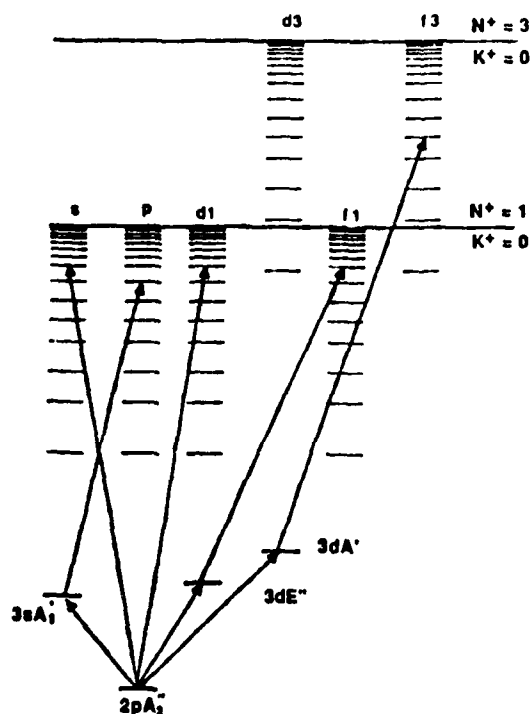


Figure 5. Energy level diagram of $N=1$ Rydbergs built on the lowest rotational cores of ortho- H_3 . Direct and stepwise excitation paths to these Rydbergs from the metastable $\tilde{B} 2p^2A_2^-$ state are indicated.

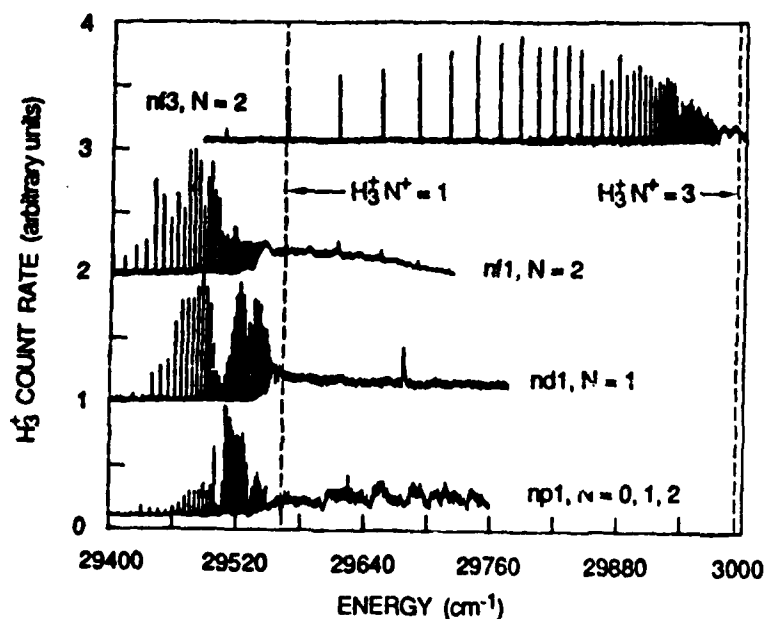


Figure 6. Excitation spectra into the field-ionized and rotationally-autoionized regions of the lowest p-, d-, and f- Rydberg series.

series that are of the same symmetry as the 2p initial state. Two-step excitation also allows us to reach higher total angular momentum, i.e. $N=0,1,2$, and to influence the relative strengths of the transitions by choosing intermediate states with different core properties. In Figure 5 we indicate schematically the excitation pathways used. The 3s intermediate state favors excitation of np final states. The resulting field-ionization spectrum is shown in the lower trace in Figure 6. Since there are two one-photon accessible 3d states, called $3dE''$ and $3dA_1'$, and since these two states have core rotational character of predominantly $N^+ = 1$ and $N^+ = 3$, respectively, we can bias the absorption spectrum. As shown in the upper two traces in Figure 6, choosing the $3dE''$ intermediate leads to a field-ionization spectrum labeled nf1, by which we mean an nf Rydberg orbital outside an $N^+ = 1$ H_3^+ core. Similarly, choosing the $3dA_1'$ intermediate leads to a substantially different spectrum, called nf3. Interestingly, some of the peaks appear in both spectra. The narrow peaks in the right hand part of the trace labeled nf1, above the $N^+ = 1$ ionization limit (dashed line), agree in position with the peaks in the nf3 trace and manifest the weak admixture of the $N^+ = 3$ core in the $3dA_1'$ intermediate state. Above the $N^+ = 1$ threshold the spectra result as a consequence of rotational autoionization.

Vibrationally Off-Diagonal Transitions

Finally, we have examined the spectral region between the $n = 3$ and $n = 4$ members of the Rydberg series. Absorptions are detected by one- or two-color photoionization, or by ionization depletion of another transition. Some of the transitions observed are shown schematically in Figure 7 and as a spectrum in Figure 8. The peaks labeled "G" and "I" correspond to simultaneous excitation of the electron, $3s \leftarrow 2p$ or $3d \leftarrow 2p$, and of the symmetric vibration mode, ν_1 . Peaks "D", "E", "F", and "H" result from excitation of the bending vibrational mode, ν_2 . But here the simultaneous electronic excitation is unusual. Only electronic transitions that previously were forbidden by parity,

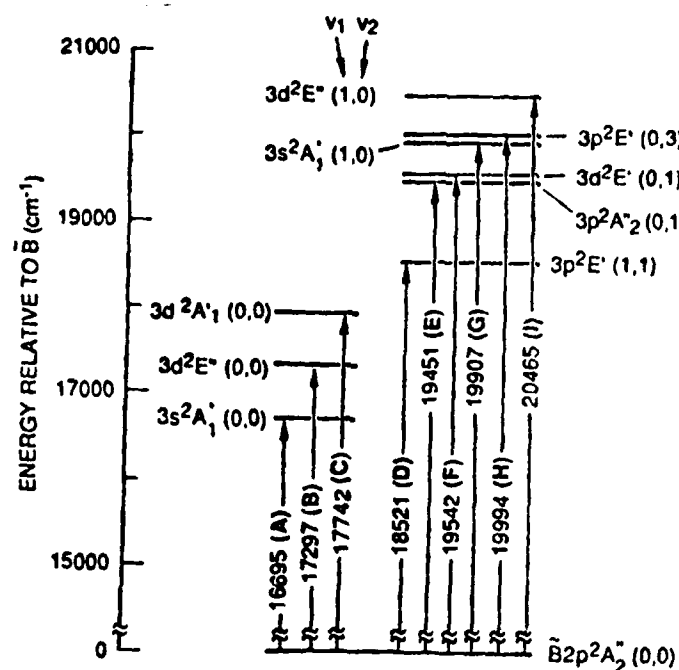


Figure 7: A selection of diagonal and off-diagonal excitations observed into the $n=3$ manifold of H_3

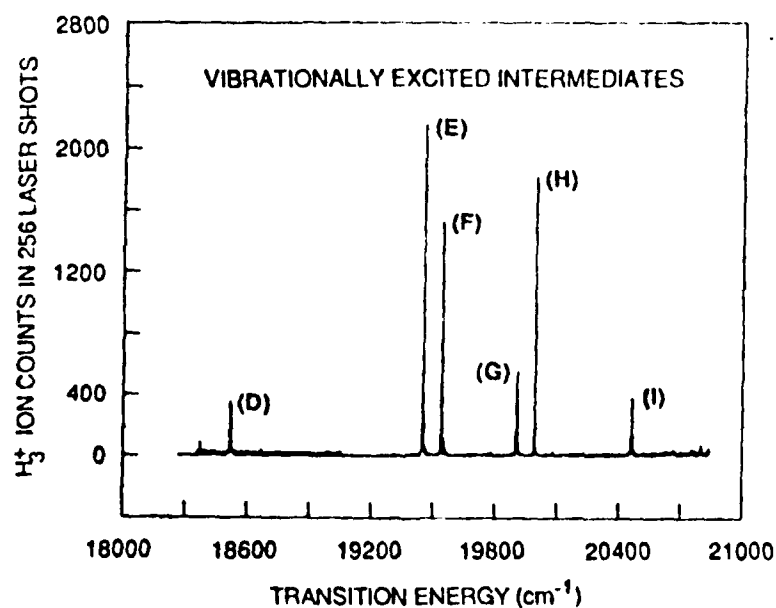


Figure 8: One-photon resonant two-photon ionization spectra involving rovibronic transitions marked in Figure 7.

i.e. $3p \leftarrow 2p$, are now possible. This is because the bending vibrational wavefunction changes the overall parity of the state. Such vibronically allowed transitions have also been observed in other polyatomic molecules and provide a detailed and specific probe of the electron-core interactions.

Summary

We have seen that the $\tilde{B} 2p \ ^2A_2''$ state of H_3 is metastable only for $N = 0$, but for any v . It is easily produced by charge transfer and is straightforward to investigate using photodissociation and photoionization. It shows a very simple, atomic-like absorption spectrum, with relatively weak, but revealing, interactions between the outer Rydberg electron and the vibrational and rotational motions of the underlying H_3^+ core.

Acknowledgments

This research was supported by the Air Force Office of Scientific Research.

References

- CH88 P. C. Cosby and H. Helm, Phys. Rev. Lett. 61, 298 (1988).
- DH80 I. Dabrowski and G. Herzberg, Can. J. Phys. 58, 1238 (1980).
- DKM88 A. Dodhy, W. Ketterle, H.-P. Messmer, and H. Walther, Chem. Phys. Lett. 151, 133, (1988).
- GP83 G. I. Gellene and R. F. Porter, J. Chem. Phys. 79, 5975 (1983).
- HC87 H. Helm and P. C. Cosby, J. Chem. Phys. 86, 6813 (1987).
- He79 G. Herzberg, J. Chem. Phys. 70, 4806 (1979).
- He86 H. Helm, Phys. Rev. Lett. 56, 42 (1986).
- He88 H. Helm, Phys. Rev. A 38, 3425 (1988).
- HHW82 G. Herzberg, J. T. Hougen, and J.K.G. Watson, Can. J. Phys. 60, 1238 (1982).
- JB84 J. R. Peterson and Y. K. Bae, Phys. Rev. A 30, 2807 (1984).

- LHH89a L. J. Lembo, H. Helm, and D. L. Huestis, J. Chem. Phys.
(in press).
- LHH89b L. J. Lembo, D. L. Huestis, and H. Helm, to be published.
- LPH89 L. J. Lembo, A. Petit, and H. Helm, Phys. Rev. A (in
press).
- TS55 C. H. Townes and A. L. Schawlow, Microwave Spectroscopy
(McGraw Hill, NY, 1955; Dover, NY, 1975).

IONIC SOLID HYDROGEN FUEL: PRODUCTION AND PROPERTIES OF CLUSTER IONS

Y. K. Bae, P. C. Cosby, and D. C. Lorents
Molecular Physics Laboratory
SRI International, Menlo Park, CA 94025

We are studying possible storage of stable positive and negative ions separately in hydrogen matrix for the high energy density materials. Figure 1 shows the estimated I_{sp} as a function of % molar concentration of H_3^+ and H^- ions. Pertinent questions needed to be answered are:

- 1) What kind of ions can we store stably in hydrogen matrix?
- 2) What are the association mechanisms and lifetimes of these ions?
- 3) What is the maximum storable ion density?
- 4) How can we mass produce the identified material?

In the first order approximation, these questions can be answered by studying ionic clusters. For example, the information on geometry and stability of H_{2N+1}^+ cluster ions indicate that one of the best candidate positive ions would be H_3^+ . However, the stability of similar negative ions is not well understood. We have carried out various experiments to address these questions.

1) STRUCTURES OF POSITIVE CLUSTER IONS

In the course of characterizing the ion source that we built to produce intense cluster ions, we have observed shell structures manifested in the size distributions of various cluster ions. The data suggest the identification of the core ion and the placement of equivalent moieties about the core during the embryonic stages of cluster growth. The cluster ion current, I_n^+ , observed as a function of mass for H_2 gas is shown on a logarithmic intensity scale in Figure 2. Two distinct regions are observed, and they include the clusters $H_3^+(H_2)_n$ ($n=1-3$) and ($n=4-6$). To understand this observation, first, we have

generated $\text{H}_3\text{O}^+(\text{H}_2)_n$ clusters of which size distribution is also shown in Figure 2. The core ion H_3O^+ is known to have a pyramidal structure with O atom attached to the apex.¹ If the H_3^+ ion can attach three H_2 molecules to its apexes, then so can H_3O^+ because it has H_3^+ characteristics. Indeed the first shell of H_3O^+ accommodates three H_2 molecules similar to H_3^+ . This observation is in agreement with the picture that H_9^+ has H_3^+ core ion with three H_2 molecules attached to the apexes of H_3^+ triangle. However, it is hard to understand the reason why the intensity distribution of $\text{H}_3\text{O}^+(\text{H}_2)_n$ cluster ions shows a break between $n=3$ and 4, but that of $\text{H}_3^+(\text{H}_2)_n$ does not. Furthermore, it is interesting to note that current theory predicts² that H_{13}^+ ($n=5$) forms the second closed shell with two H_2 molecules are attached to the top and bottom of the H_9^+ ($n=3$) plane, while our results and those of other researchers indicate H_{15}^+ ($n=6$) is the second closed shell.

To understand these features of the cluster intensity distributions, we have studied details of cluster growth mechanisms in our source we have generated $(\text{CO}_2)_n^+$ which is known to show no structure in the intensity distribution. The result is shown in Figure 3. The logarithmic distribution is very linear and nearly featureless, thus, indicates that the features are not artifacts. To characterize the growth mechanism in our source, we have generated other clusters such as $(\text{CO})_n^+$ (Figure 4), $(\text{N}_2)_n^+$ (Figure 4) and Xe_n^+ clusters. (Figure 5) Both $(\text{CO})_n^+$ and $(\text{N}_2)_n^+$ distributions show evident first shell structures with five fold symmetry. Thus, the most suggestive structure for $(\text{CO})_7^+$ and $(\text{N}_2)_7^+$ is a pentagonal bipyramid shown in Figure 6. Similar five fold symmetry has been seen in Xe_n^+ intensity distribution. (Figure 5) In this case it was predicted that Xe_3^+ from the core for $n=4-13$, and this prediction is in agreement with the absence of structure at $n=7$. The suggested structures for Xe_{13}^+ , Xe_{19}^+ , and Xe_{25}^+ are linear core ions surrounded by five-fold rings in agreement with recent theoretical predictions.³ (Figure 7) Apparently five-fold rings are very common in the cluster ion structures. From these findings one might speculate that the extra stability of the H_{15}^+ might be resulted from possible existence of the pentagonal bipyramid structure with H_5^+ core ion surrounded by five H_2 molecules.

2) PRODUCTION OF NEGATIVE CLUSTER IONS

After significantly improving our apparatus, now we can generate relatively intense beams of negative ions simply by reversing the polarity of the source potential. As an example we have generated $(\text{CO}_2)_n^-$ clusters. (Figure 8) The theoretical and experimental evidences on the existence of H_3^- are still contradictory. Although Bae et al.⁴ ruled out the existence of triangular H_3^- and its isotope ions, experimental searches for the linear geometry

have not been carried out. In their recent systematic theoretical studies Michels and Montgomery Jr.⁵ have found that the linear H_3^- is not thermodynamically stable relative $\text{H}^- + \text{H}_2$ upon consideration of the zero-point vibrational contribution to the dissociation energy. However, they found that D_3^- is bound by as much as 7 meV and suggested that it may be possible to produce it by colliding D^- with D_2 in a cooled jet. The suggested experimental scheme is identical to ours, and thus, if the linear D_3^- exists we should be able to generate it. So far we are still optimizing conditions for producing negative ions in our source. The obtained upper limit of the intensity ratio between H_3^- and H^- is 0.5 % and that of D_3^- to D^- is 1.0 %.

3) OBSERVATION OF BOUND-FREE TRANSITION OF H_3^+

Although the predissociation of H_3^+ was observed,⁶ there has been no report on direct excitation involving electronic excitation. Recently Talbi and Saxon⁷ have calculated the transition dipole moments connecting ground state ($1^1\text{A}'$) and the first excited state of C_s geometry ($2^1\text{A}'$). They found that the electronic excitation of highly vibrationally-rotationally excited $1^1\text{A}'$ states near the asymptote requires the excitation energy only 3-4 eV with significant dipole transition moments. The bound-free transition occurs between these states in which the proton moves far away ($4-5 a_0$) from the H_2^+ . We have first observed photofragmentation transition of H_3^+ into $\text{H}_2^+ + \text{H}$ near UV with an apparent threshold energy 2.5 eV (Figure 9). We interpret the observed transition as the predicted electronic excitation between the highly excited $1^1\text{A}'$ and $2^1\text{A}'$ states. The fact that the observed onset is about 0.3 eV lower than theoretically predicted value (2.8 eV) might be resulted from the excitation of states above the asymptote similar to the observation of Carrington and Kennedy.⁶

REFERENCES

1. D. J. Liu and T. Oka, Phys. Rev. Lett. **54**, 1787 (1985).
2. K. Hirao and S. Yamabe, Chem. Phys. Lett. **80**, 237 (1983).
3. M. Amarouche, G. Durand, and J. P. Malieu, J. Chem. Phys. **88**, 1010 (1988).
4. Y. K. Bae, M. J. Coggiola, and J. R. Peterson, Phys. Rev. A **29**, 2888 (1984).
5. H. H. Michels and J. A. Montgomery Jr., Chem. Phys. Lett. **139**, 535 (1987).
6. A. Carrington and R. A. Kennedy, J. Chem. Phys. **81**, 91 (1984).
7. D. Talbi and R. Saxon, J. Chem. Phys. **89**, 2235 (1988).

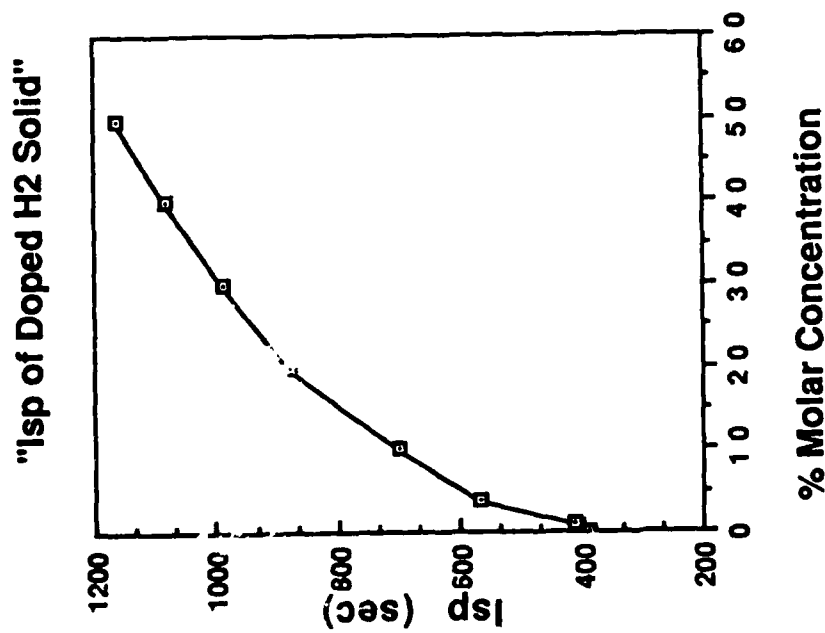


Figure 1

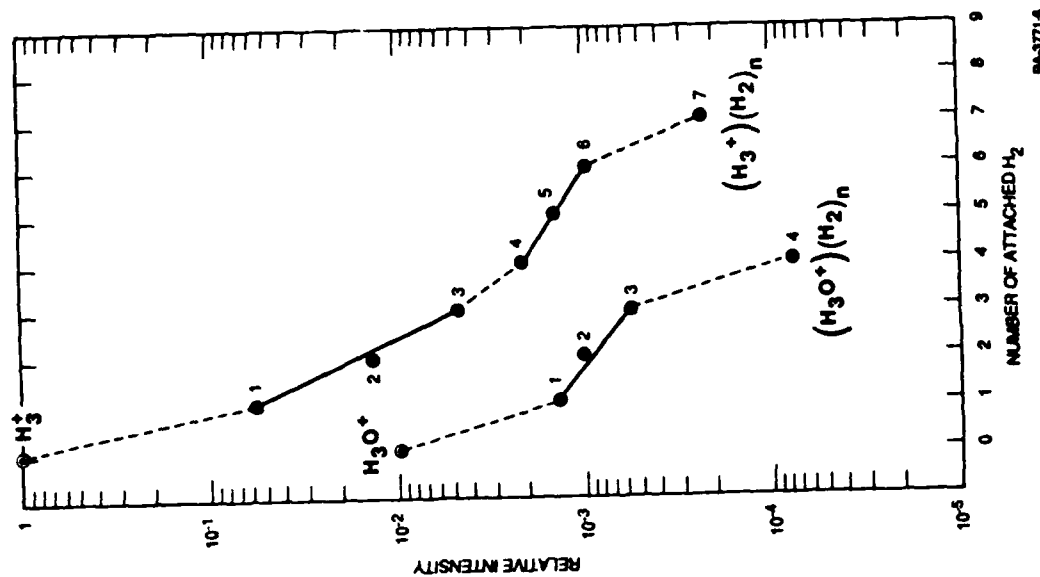


Figure 2

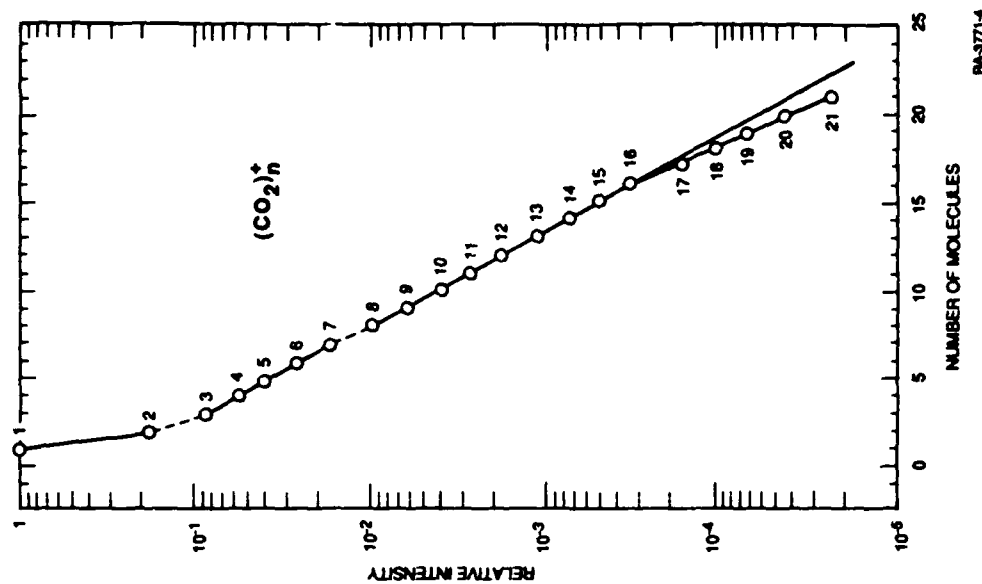


Figure 3

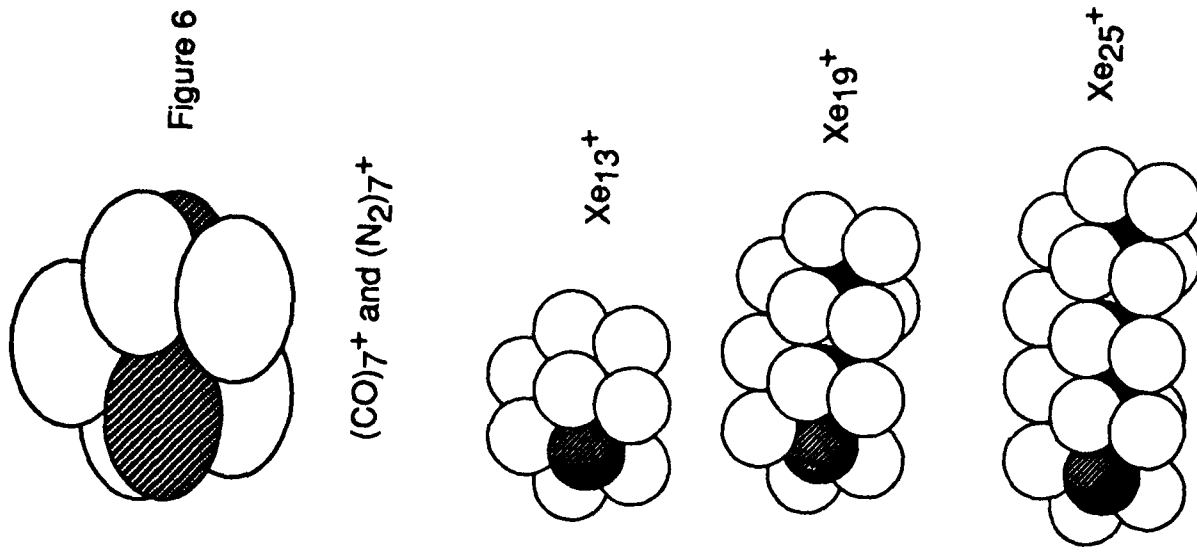


Figure 7

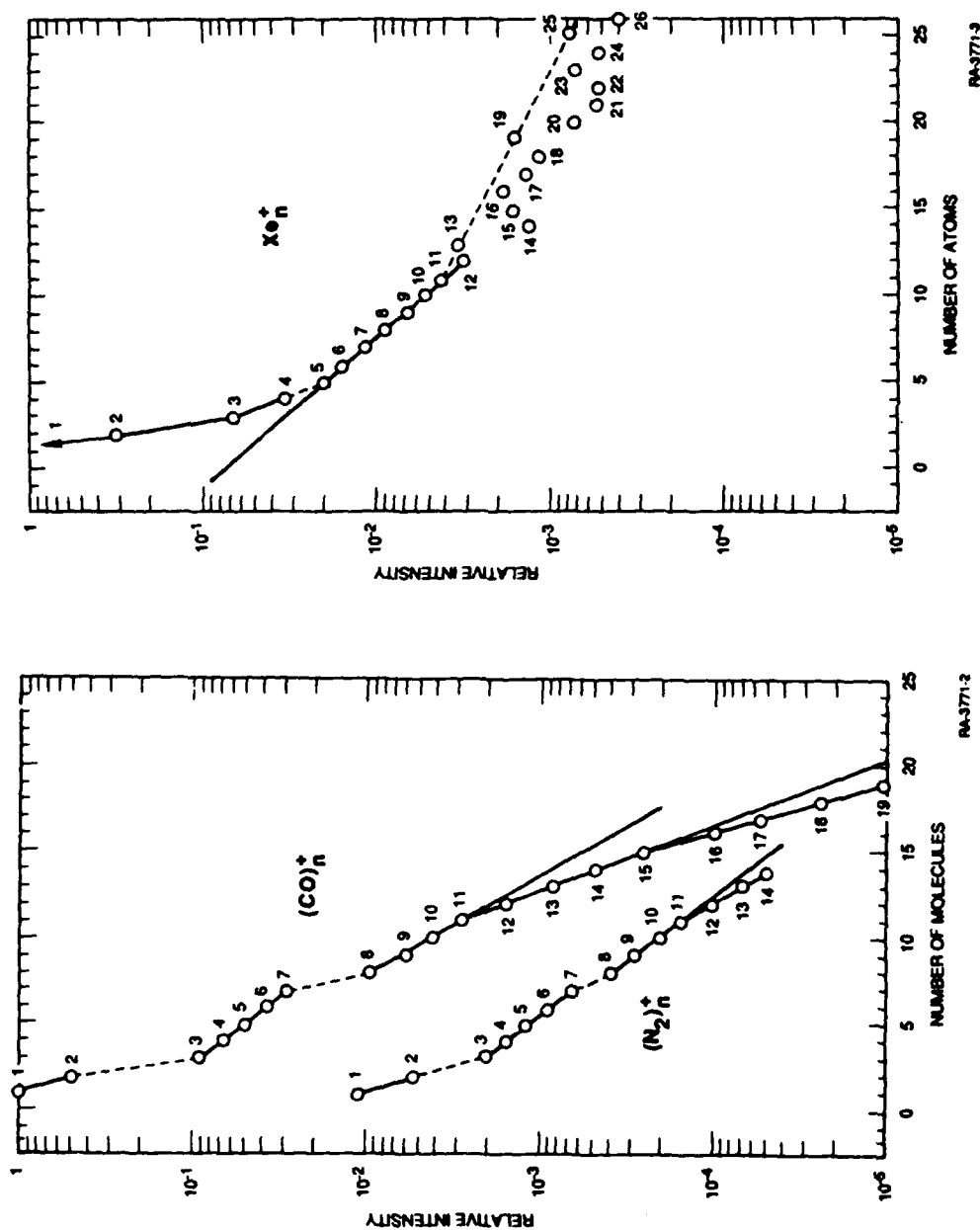


Figure 4

Figure 5

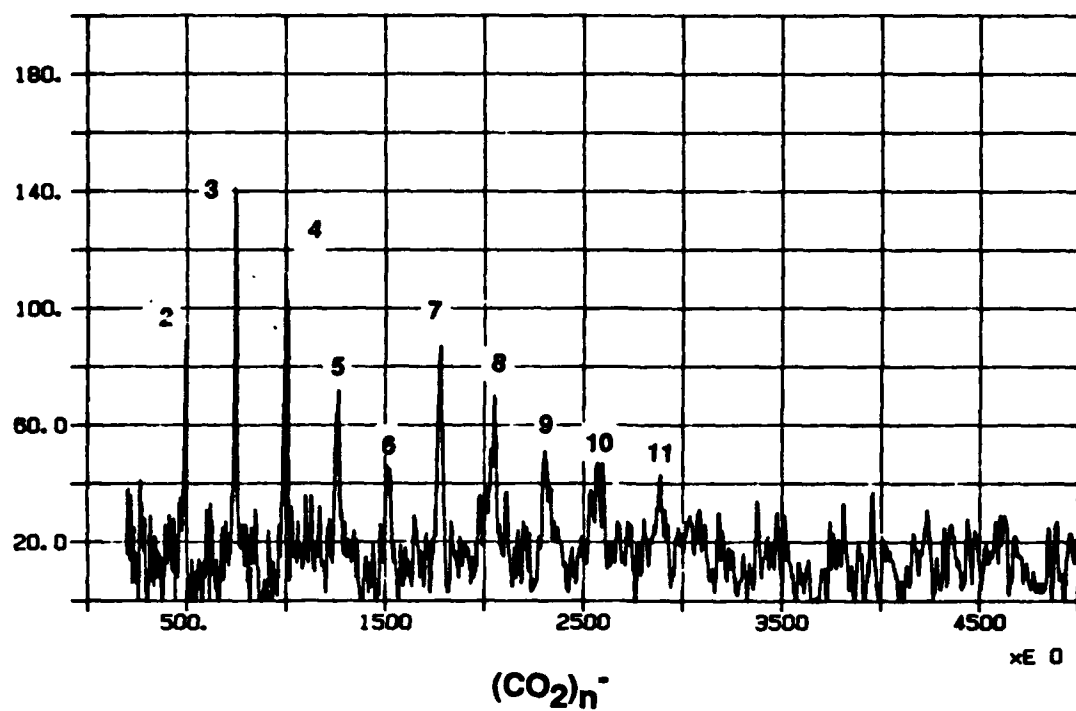


Figure 8

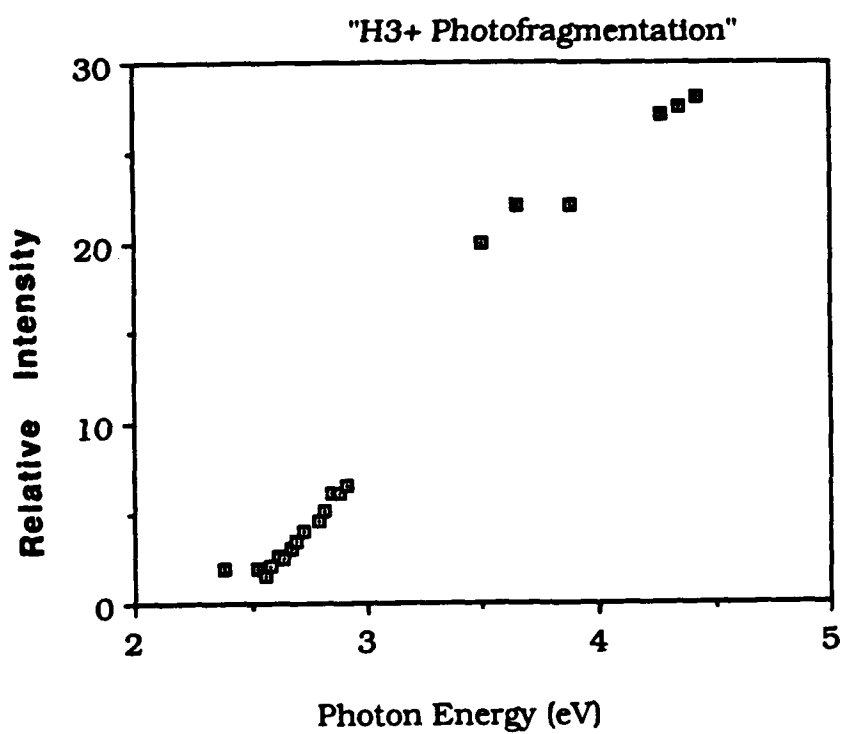


Figure 9

High Energy Density Materials Conference

13 - 15 March 1989

EXPERIMENTAL AND THEORETICAL STUDIES OF THE PROPERTIES OF TRIHYDROGEN

Aron Kuppermann

Division of Chemistry and Chemical Engineering, California Institute of Technology,
Pasadena, CA 91125

1. Background.

In studies of the emission spectroscopy from a hollow cathode discharge through 1 torr of H_2 , Herzberg and coworkers¹ detected emission bands at 560nm and 710nm comprised of broad lines, which they attributed to transitions from higher Rydberg states of H_3 to the $2s \ ^2A'_1$ state. This state can predissociate to the ground $2p_x \ ^2E'$ state by vibronic coupling to e' vibrations, and has a short life-time. They also found a band at 602.5nm formed of narrow lines, which they attributed to transitions from higher Rydberg states to the $2p_x \ ^2A''_2$. This state can only predissociate to the $^2E'$ one via rovibronic coupling, and the $J = 0$ state of $2p_x \ ^2A''_2$ is expected to be long lived, with a lifetime of the order of 40 μ sec or longer²⁻⁴. This state has since been detected by laser absorption to high Rydberg states followed by field ionization by Helm⁵. Figure 1 depicts some of the Rydberg energy levels of H_3 and their correlations to $H_2 + H$ states.

Previously we had produced a beam of metastable H_3 ,⁴ whose state we identified as $2p_x \ ^2A''_2$, and measured its total collision cross section, surface ionization and photoionization properties⁶. The internal energy content of this species, with respect to $\frac{3}{2}H_2$ ($X \ ^1\Sigma_g^+$) is 7.8 eV and its specific impulse 2050 s. This makes it an interesting high energy density species, whose properties should be further investigated. The objective of the present research is to measure the life-time of the $2p_x \ ^2A''_2$ state and its internal vibrational state composition in the beam in which it is produced using an arc-heated source, and to make life-time calculations of the excited states of H_3 .

2. Measurement of the ro-vibrational population of a beam of metastable H_3 .

We have previously produced a beam of metastable $2p_x \ ^2A''_2$ molecules^{4,6} using a high temperature arc-heated source similar to the one developed by Stwalley and coworkers⁷.

The intensity of that beam was estimated at 10^{20} molecules \times s $^{-1}$ \times sterad $^{-1}$, and it had a broad translational energy distribution from 0.1 eV to 13 eV, with a maximum at about 8 eV. Using an electron bombardment quadrupole mass spectrometer detector with an acceptance solid angle of about 10^{-5} sterad, the detected flux was 10^{15} molecules \times s $^{-1}$, corresponding to a current density of 10^{16} molecules \times cm $^{-2}$ \times s $^{-1}$. Since this flux and current density are appreciable, such a beam seems adequate for performing more detailed studies than the semi-quantitative ones conducted initially⁶, and mentioned above.

It is important to initially determine the ro-vibrational composition of that beam. A method for making such measurements has been developed by Helm⁵. It involves photo-excitation of the $2p_x, {}^2A_2''$ state by a pulsed laser to a high Rydberg state, followed by field ionization and mass analysis. This and subsequent experiments to be performed with the beam require more stages of differential pumping and a better alignment than previously used. When we interfaced the H₃ beam with a crossed molecular beam apparatus, we found that its angular position drifted with time by about 0.1° or more. The mechanical alignment of the apertures in the system was constant, and the drift was diagnosed as being due to slight time variations of the pinch magnetic field placed around the high temperature arc discharge source in which the H₃ was formed. On the other hand, the experiments to be performed require a directional stability of the beam of the order of 0.01°. In order to achieve this stability, the arc source support system was totally redesigned. Its central feature is an optical gimble mount having two electrically controlled angular degrees of freedom with a resolution of 0.001° each. This mount is supported by two orthogonal translational motion stages, which allow electrically controlled lateral and longitudinal translational motions (with respect to the beam axis), while the arc is on. This will permit maintenance of beam alignment during operation.

Figure 2 displays an overall view of the apparatus designed for these measurements. Construction of this apparatus has been completed over the last year. All three vacuum chambers were tested, as well as the corresponding pumping systems, and vacuum integrity has been achieved. The new arc source mount was tested and modified to accommodate tensions created by electrical and water connections. It is now operating properly. The arc was turned on and put into operational condition. The whole system has been aligned. The computer control system, as well as the signal electronics were made operational. The mass spectrometer detector is in final stages of debugging, and as soon as it is operational the experiments will be started.

3. Life-time calculations

The transition of the $2p_x \ ^2A_2''$ state to the ground $2p_x \ ^2E'$ state is radiatively electric-dipole forbidden as well as predissociatively vibronically forbidden. In order to calculate its predissociative life-time by a ro-vibronic coupling mechanism, we need the nuclear wave function of the ground and excited states as well as the coupling between these two states.

The ground state potential energy surface of H_3 is well known. Since it is not a bound state, its nuclear motion wave function is comprised of continuum scattering states. Using the method of symmetrized hyperspherical coordinates⁸, we have been able to calculate these states up to 2.1 eV for total angular momentum $J = 0$, and up to 1.75 eV for $J = 1$. Some of these results have been recently published⁹.

The potential energy surface for the $2p_x \ ^2A_2''$ state has not yet been calculated. However, a recent calculation of the excited state of H_3 which has an avoided conical intersection with the ground state has been calculated by a double many-body expansion method¹⁰. We have previously used that surface as a testing ground for calculating the ro-vibrational wave functions of a bound excited state of H_3 . We did so using a code developed by Tennyson¹¹, and calculated the energy levels and ro-vibrational wave functions of the $J = 0$ and 1 total angular momentum states of that excited potential energy surface. Between 1000 and 1400 variational wave functions were required to achieve convergence of those calculations. Unfortunately, the corresponding wave functions did not display the appropriate symmetry behavior of a system of three identical particles. Furthermore, the Tennyson code does not lend itself to the introduction of such symmetry. Since the calculation of the life-time of the upper state requires good ro-vibrational wave functions, we had to develop a new method for obtaining such functions. The rest of this report describes this method and the results obtained using it.

3.1 New method for calculating bound and scattering ro-vibrational wave functions having correct symmetry properties.

The hyperspherical method uses the hyper-radius ρ to describe the global size of the triatomic system and a set of five angles ζ to describe its shape and orientation in space. The Hamiltonian of the system on a given electronic Born-Oppenheimer potential V can be written as

$$H = -\frac{\hbar^2}{2\mu}\rho^{-\frac{5}{2}}\frac{\partial^2}{\partial\rho^2}\rho^{\frac{5}{2}} + \frac{\hat{\Lambda}^2}{2\mu\rho^2} + V + \frac{15\hbar^2}{8\mu\rho^2} \quad (1)$$

where μ is the three-body reduced mass, and $\hat{\Lambda}$ is the grand angular momentum⁹. Eigenfunctions of the Hamiltonian $\Psi^{JM\Pi\Gamma}$ are labelled by the total angular momentum J , its component M along a laboratory-fixed axis, the parity Π and the representation Γ of the permutation group of the system. They are expanded in a set of local hyperspherical surface functions (LHSF) $\Phi_n^{JM\Pi\Gamma}$, defined as eigenfunctions of the fixed hyper-radius Hamiltonian:

$$\Psi^{JM\Pi\Gamma}(\rho, \zeta) = \sum_n F_n^{J\Pi\Gamma}(\rho) \Phi_n^{JM\Pi\Gamma}(\zeta; \rho). \quad (2)$$

$$\left(\frac{\hat{\Lambda}^2}{2\mu\rho^2} + V \right) \Phi_n^{JM\Pi\Gamma}(\zeta; \rho) = \epsilon_n^{J\Pi\Gamma}(\rho) \Phi_n^{JM\Pi\Gamma}(\zeta; \rho) \quad (3)$$

The functions $F_n^{J\Pi\Gamma}$ are solutions of a set of coupled differential equations, which we solve using piece-wise diabatic bases.

In the present study, we use the Whitten-Smith¹² definition of the five angular coordinates, as modified by Johnson¹³. Three Euler angles (α, β, γ) specify the orientation of the body frame tied to the principal axes of inertia, and the two angles (θ, φ) describe the shape of the molecular triangle. The LHSF are variationally determined by expansion in products of simple analytical functions¹⁴:

$$\Phi_n^{JM\Pi\Gamma}(\zeta; \rho) = \sum_{K, n_\theta, n_\varphi} a_{Kn_\theta n_\varphi}^{J\Pi\Gamma}(\rho) D_{MK}^J(\alpha, \beta, \gamma) f_{n_\varphi}^{J\Pi K}(\varphi) g_{n_\theta}^{J\Pi K n_\varphi}(\theta) \quad (4)$$

K is the component of the total angular momentum along the body frame Z axis, D_{MK}^J are Wigner rotation matrices, $f_{n_\varphi}^{J\Pi K}$ and $g_{n_\theta}^{J\Pi K n_\varphi}$ are simple trigonometric sine and cosine functions, chosen such that the $\Phi_n^{JM\Pi\Gamma}$ LHSF satisfy appropriate boundary conditions for the system's collinear ($\theta = \frac{\pi}{2}$) and equilateral triangular ($\theta = 0$) configurations and have appropriate permutation symmetry properties.

The modified Whitten-Smith coordinates are specially suited for our present study. The excited state potential energy surface, which supports bound states, is nearly cylindrically symmetrical in internal configuration space (as defined in Ref.15) around the axis along which the conical intersection occurs. Therefore, very few $f_{n_\varphi}^{J\Pi K}(\varphi)$ are necessary to be included in the expansion of the LHSF to reach convergence of the bound states.

A further consideration is that in the vicinity of a conical intersection, the Born-Oppenheimer real electronic wavefunctions undergo a sign change when one follows a

closed path in nuclear configuration space around the curve along which the two states conically intersect¹⁶. Since the total electronuclear wavefunction is continuous and single valued, there is a compensating sign change on the nuclear part of the wavefunction¹⁷ (this is the molecular Aharonov-Bohm effect, referred to as the MAB effect in the following). This effect modifies the energies of the bound ro-vibrational states on the upper electronic state and the reaction probabilities on the lower one.

Wavefunctions $\Psi^{JM\Pi\Gamma}(\rho, \zeta)$ with correct permutation symmetries can be easily built by an adequate choice of the functions $f_{n_\varphi}^{J\Pi K}$. Let us suppose for instance we want to build A_1 spatial electro-nuclear wavefunctions for $J = 0$. If the MAB effect is ignored, the spatial part of the electronic wavefunction as well as the spatial part $\Psi^{JM\Pi\Gamma}$ of the nuclear wavefunction each transform as the A_1 irreducible representation. Therefore, the $f_{n_\varphi}^{J\Pi K}$ have to be of the A_1 type also (ie $\cos(n_\varphi\varphi)$, $n_\varphi = 3n$, n integer). If now the MAB effect is taken into account, the lower(upper) electronic state behaves like $\cos(\frac{3\varphi}{2})$ and $\sin(\frac{3\varphi}{2})$ under the symmetry operations of the permutation group, and one has to choose $f_{n_\varphi}^{J\Pi K}$ functions of the type $\cos(n_\varphi\varphi)(\sin(n_\varphi\varphi))$, with $n_\varphi = \frac{3n}{2}$, n odd integer, to obtain spatial electro-nuclear wavefunctions of the A_1 type.

3.2 Results

3.2.1 Bound state calculation on the upper electronic surface.

a) MAB effect neglected. Table 1 compares the energies of the bound states obtained with the present hyperspherical method and with the variational method of Tennyson¹¹. Although the hyperspherical calculation uses few $f_{n_\varphi}^{J\Pi K}$ functions and LHSF (8 and 5 respectively for $J = 0$, E symmetry), the energies are converged within 1 cm^{-1} approximately. On the other hand, although about 1300 basis functions are used in Tennyson's method, convergence of the energy is achieved only for the lowest states. In addition, this latter method permits introduction of the P_2 permutation symmetry of molecules of A_2B type, but not of the P_3 symmetry of A_3 -type systems. As a result, even the low energy bound states are distorted from their correct shape.

b) MAB effect included. Table 2 gives the energies of the bound states when the effect of the conical intersection is included. Only the hyperspherical method has been used, since it is cumbersome to take this effect into account in Tennyson's approach. Comparison with table 1 and examination of figure 3 shows that the spectrum is completely modified, so that the MAB effect cannot be neglected in the calculation of the bound state energies.

Table 1 : Comparison of the energies (in eV) of the bound states obtained with the hyperspherical method (left column for each value of the total angular momentum J and parity) and Tennyson's method (right column) when the MAB effect is neglected. The spatial symmetry (electronic and nuclear) is indicated in the central columns (only A2 and E states exist because of the Pauli principle). The zero in energy is the bottom of the H₂ well at infinite atom-diatom separation.

J=0			J=1 even parity			J=1 odd parity		
4.2886	E	4.2886	3.7283	A2	3.7294	3.7264	E	3.7275
4.4533	E	4.4533	3.9284	A2	3.9296	3.9266	E	3.9281
4.5980	E	4.5983	4.1130	A2	4.1145	4.1114	E	4.1133
4.7211	E		4.2817	A2	4.2838	4.2803	E	4.2831
			4.2955	E	4.2956	4.2904	E	4.2908
			4.4336	A2	4.4387	4.2969	A2	4.2972
			4.4595	E	4.4598	4.4323	E	4.4398
			4.5665	A2	4.5803	4.4549	E	4.4557
			4.6036	E	4.6047	4.4608	A2	4.4615
			4.6872	A2	4.6894	4.5657	E	4.5893
			4.7261	E	4.7349	4.5995	E	4.6027
						4.6047	A2	4.6093
						4.6842	E	4.6878
						4.7225	E	
						4.7270	A2	4.7355

Table 2 : Same as table 1, but with the MAB effect included, and for the hyperspherical method only.

J=0		J=1 even parity		J=1 odd parity	
4.0215	E	4.0286	E	4.0243	A2
4.2050	E	4.2114	E	4.0284	E
4.3710	E	4.3770	E	4.2076	A2
4.5189	E	4.5071	A2	4.2113	E
4.5700	A2	4.5243	E	4.3734	A2
4.6469	E	4.6484	A2	4.3768	E
4.7178	A2	4.6517	E	4.5050	E
				4.5210	A2
				4.6466	E
				4.6487	A2
				4.6516	E
				4.7224	E

3.2.2 Scattering state calculation on the lower electronic surface.

We have studied the influence of the MAB effect on the reaction dynamics of the H_3 system for the simple case $J=0$. The new boundary conditions on the LHSF imposed by the sign change of the electronic wavefunction as one follows a closed loop around the conical intersection axis drastically modify their nodal structures and their energies (fig. 4). As a result, the irreducible representation transition probabilities are also completely changed (fig. 5). The effect of these results on the Pauli-antisymmetrized transition probabilities are currently under investigation.

References

1. G. Herzberg, J. Chem. Phys. **70**, 4806 (1979); I. Dabrowski and G. Herzberg, Can. J. Phys. **58**, 1238 (1980); G. Herzberg and J. K. G. Watson, Can. J. Phys. **58**, 1250 (1980); G. Herzberg, H. Lew, J. J. Sloan and J. K. G. Watson, Can. J. Phys. **59**, 428 (1981); G. Herzberg, J. T. Hougen and J. K. G. Watson, Can. J. Phys. **60**, 1261 (1982)
2. H. R. King and K. Morokuma, J. Chem. Phys. **71**, 3213 (1979)
3. G. I. Gellene and R. F. Porter, J. Chem. Phys. **79**, 5975 (1983)
4. J. F. Garvey and A. Kuppermann, Chem. Phys. Lett. **107**, 491 (1984); Rev. Sci. Instr. **57**, 1061 (1986)
5. H. Helm, Phys. Rev. Lett. **56**, 42 (1986)
6. J. F. Garvey and A. Kuppermann, J. Chem. Phys. **86**, 6766 (1987)
7. K. R. Way, S. -C. Yang and W. C. Stwalley, Rev. Sci. Instr. **47**, 1049 (1976)
8. P. G. Hipes and A. Kuppermann, Chem. Phys. Lett. **133**, 1 (1987)
9. S. A. Cucaro, P. G. Hipes and A. Kuppermann, Chem. Phys. Lett. **154**, 155 (1989)
10. A. J. C. Varandas, F. B. Brown, C. A. Mead and D. G. Truhlar, J. Chem. Phys. **86**, 6258 (1987)
11. J. Tennyson, Comp. Phys. Comm. **42**, 1 (1986)

12. R.C. Whitten and F.T. Smith, J. Math. Phys. **9** 1103 (1968)
13. B.R. Johnson, J. Chem. Phys. **79** 1916 (1983)
14. J.M. Launay, private communication
15. A. Kuppermann, Chem. Phys. Lett. **32** 374 (1975)
16. G. Herzberg and H.C. Longuet-Higgins, Disc. Faraday Soc. **35** 77 (1963)
17. C.A. Mead and D.G. Truhlar, J. Chem. Phys. **70** 2284 (1979)

Figure Captions

Figure 1. Energy level diagram of some Rydberg states of H_3 and their correlation with the states of $H_2 + H$.

Figure 2. Sketch of the apparatus for characterizing the H_3 beam. VC1 is the vacuum chamber for the arc source, which is evacuated by the Roots pumping system depicted at the right of the figure. VC2 is a differential pumping chamber, pumped by the diffusion pump DP, and VC3 is the chamber containing the mass spectrometer detector, pumped by the turbomolecular pump TMP. The laser beam is coaxial with the H_3 beam and enters the apparatus from the left.

Figure 3. $J=0$ rovibrational energy levels for the first excited electronic state of H_3 . The full (dashed) horizontal lines depict the levels obtained including (not including) the MAB effect. The curve represents the potential energy at which the conical intersection occurs (i.e., the equilateral triangle configurations) as a function of the hyper-radius.

Figure 4. Energies (in electron-volts) of the LHSF as a function of the hyper-radius (in Bohr), for $J=0$ and A1 permutation symmetry of the electronuclear wavefunction; left: neglecting the MAB effect, right : including this effect. The zero in energy is the bottom of the H_2 well at infinite atom-diatom separation.

Figure 5. Transition probability as a function of energy from the state $H_2(v=0, j=0)$ to the same final state, for $J=0$ and A1 permutation symmetry of the electronuclear wavefunction. The lower abscissa is the total energy defined in figure 4 and the upper abscissa is the reagent translational energy. The vertical arrows on the upper abscissa denote the energies at which the $H_2(v, j)$ states open up. The length of the arrows decreases as v spans the values 0,1,2. Left : without MAB, right : with MAB.

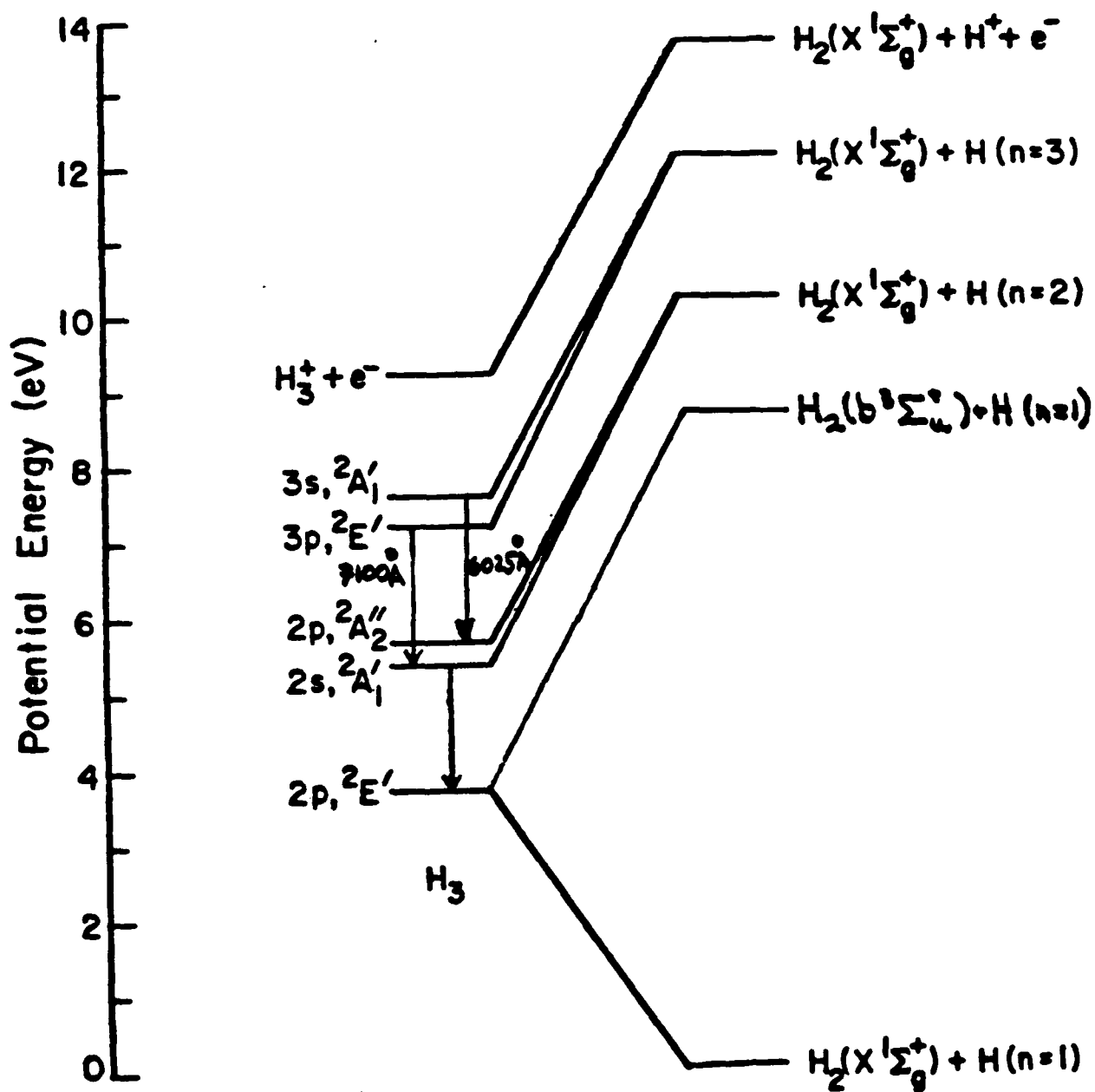


Figure 1

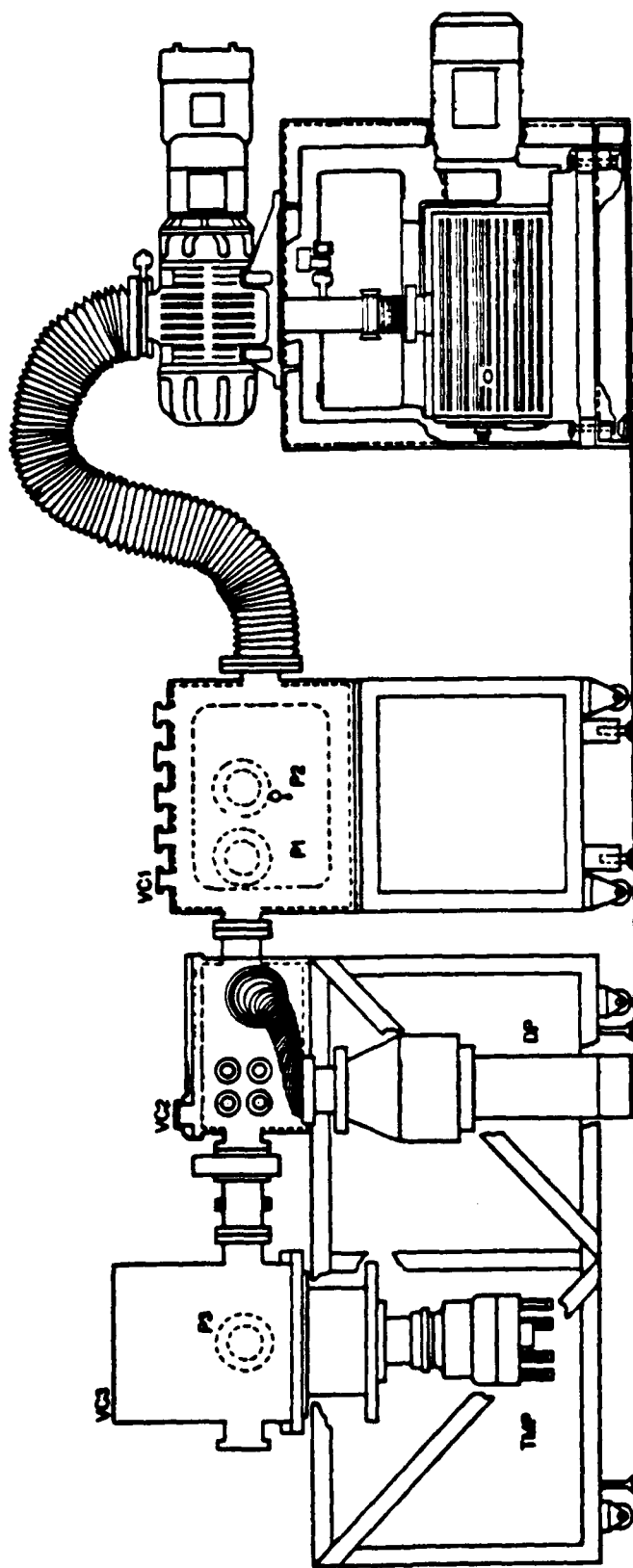


Figure 2

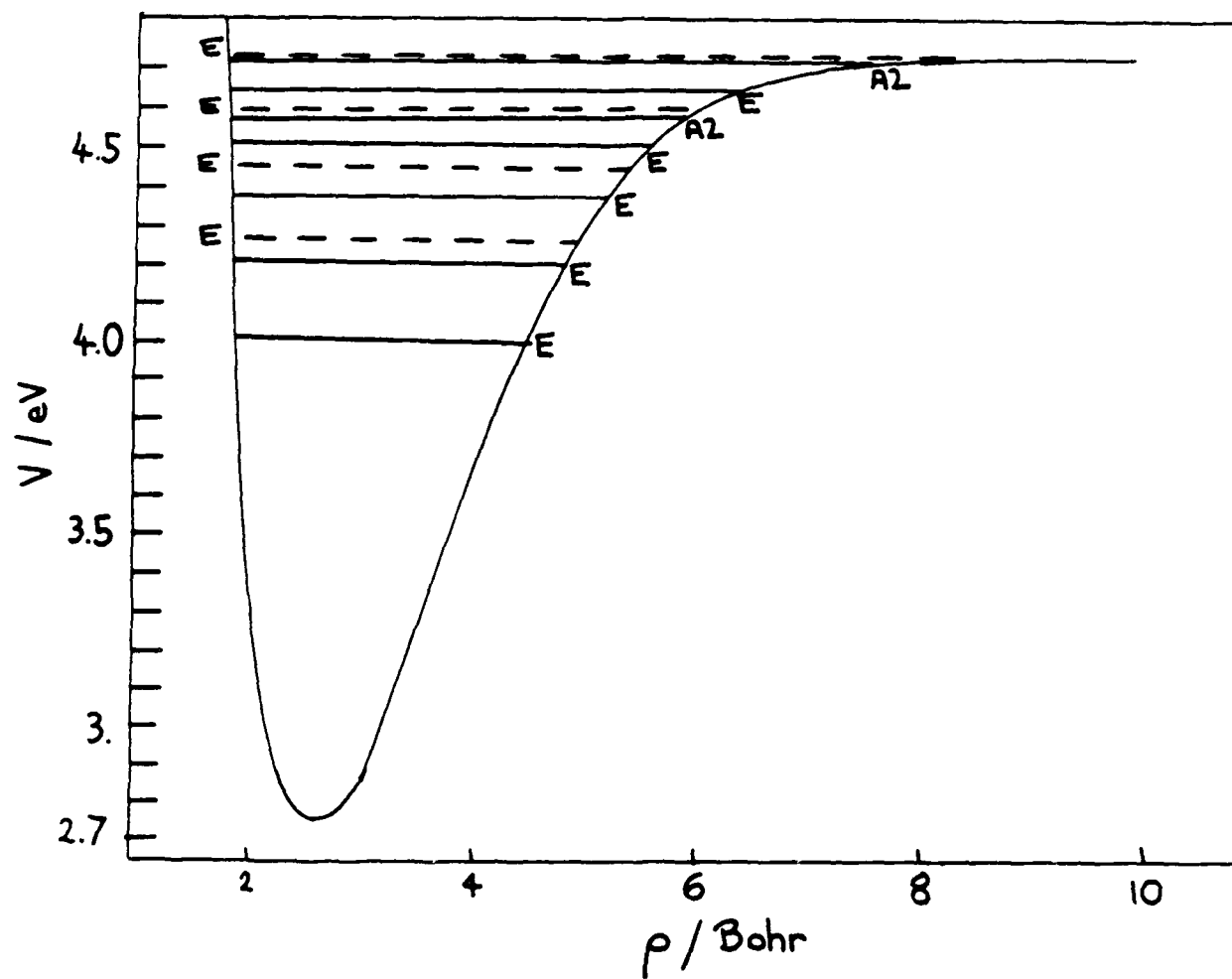


Figure 3

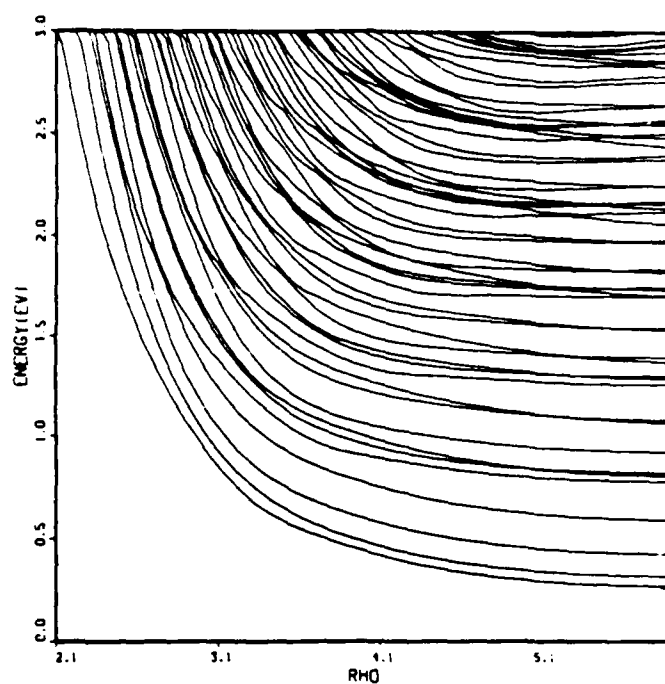
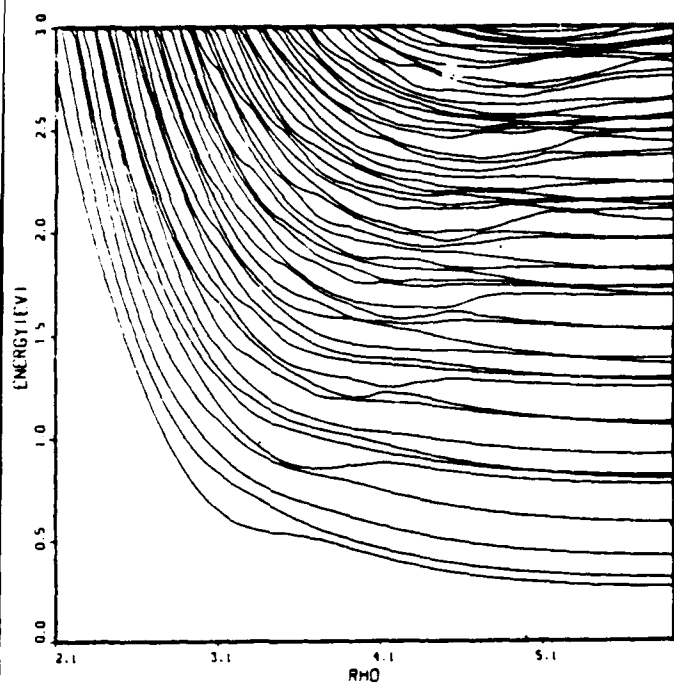


Figure 4

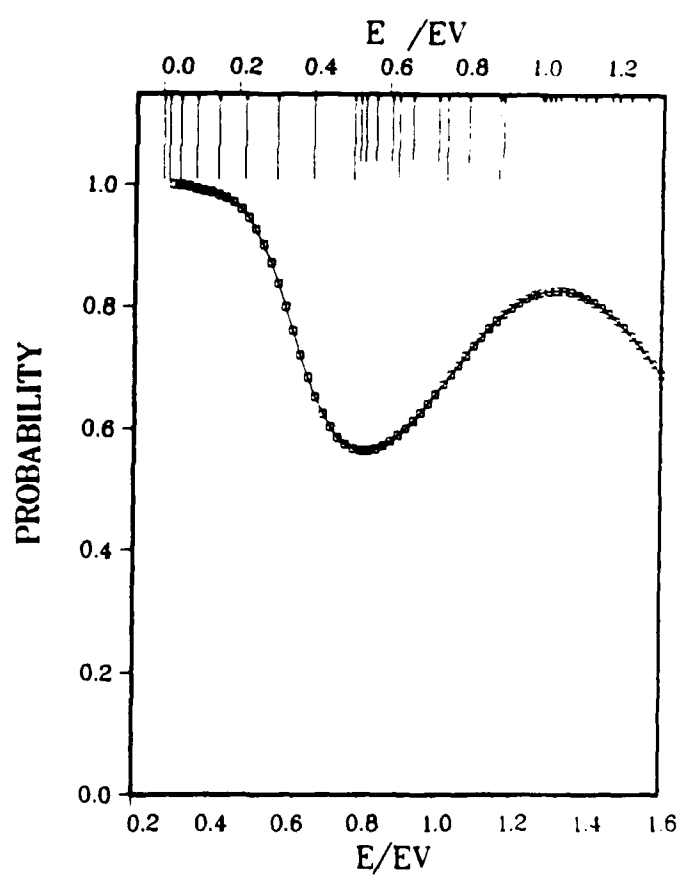
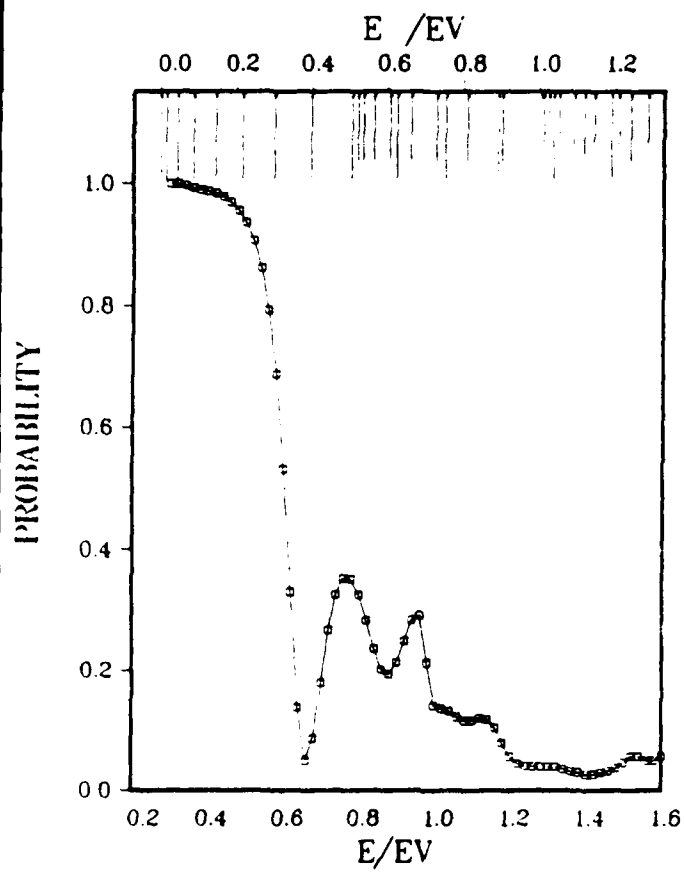


Figure 5

Two Dimensional Potential Energy Surfaces of Pyramidal Tetrahydrogen Near a Three-Fold Seam

Sheng-yu Huang and William A. Lester, Jr.

Department of Chemistry
University of California, Berkeley
Berkeley, California 94720

Because of its simplicity, four electrons and four nuclei, H_4 provides an excellent test for theoretical studies of processes that can occur in more complex systems. Present interest is focused on an indepth study of the lowest-lying excited states that correlate with $H_2(X^1\Sigma_g^+)$ and $H_2(B^1\Sigma_u^+)$. Background and initial motivation for the study of this system have been presented earlier.¹⁻³

Our recent efforts have entailed further study of the crossing region in r - R space. Here r is the side length of H_3 and R is the separation between the apex H and H_3 triangular base. Multiconfiguration Hartree-Fock (MCHF) calculations at 105 points and quantum Monte Carlo (QMC) computations using a new trial function optimization procedure at 49 points, for $r = 1.55 - 2.00$ a.u. and $R = 3.0 - 5.0$ a.u., have been carried out to obtain the two-dimensional potential energy surfaces. The seam arising from the crossing of the three states that correlates with the above-mentioned asymptotes for C_{3v} symmetry has been determined and characterized; see Figs. 1 and 2. The region of the seam at lower symmetry has also been studied and provides further insight on the decomposition pathways in the system. The minimum along the seam for C_s symmetry occurs at $r = 1.80$ a.u. and $R = 4.145$ a.u. The QMC energy obtained at this geometry is $-2.0634(43)$ a.u. and is 1.70 eV below a MCHF result obtained with a triple-zeta plus polarization basis set.

References

1. C. A. Nicolaides, G. Theodorakopoulos, and I. D. Petsalakis, *J. Chem. Phys.* **80**, 1705 (1984).
2. J. A. Montgomery, Jr. and H. H. Michels, *J. Chem. Phys.* **86**, 5882 (1987).
3. W. A. Lester, Jr., "Quantum Monte Carlo Study of the MIES Associated with $H_2(X^1\Sigma_g^+)$ and $H_2(B^1\Sigma_u^+)$," Final Report, Air Force Astronautics Laboratory, AFRPL 69022, October 1987.

Figure Captions

1. Potential energy surface for 1A state (C_{3v} symmetry) showing surface crossing seam.
2. Potential energy surface for 1E state (C_{3v} symmetry) showing surface crossing seam.

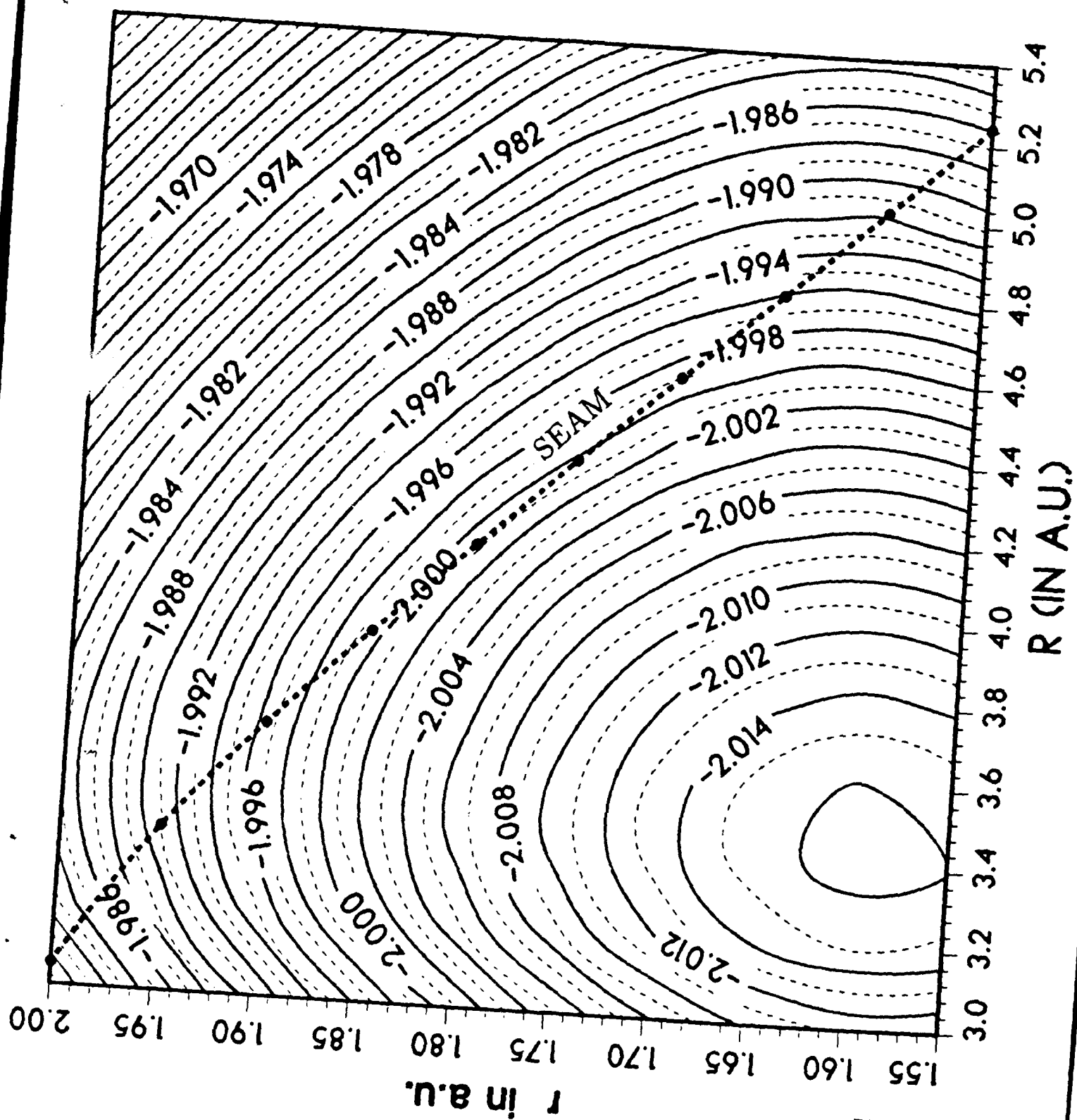


Fig. 1

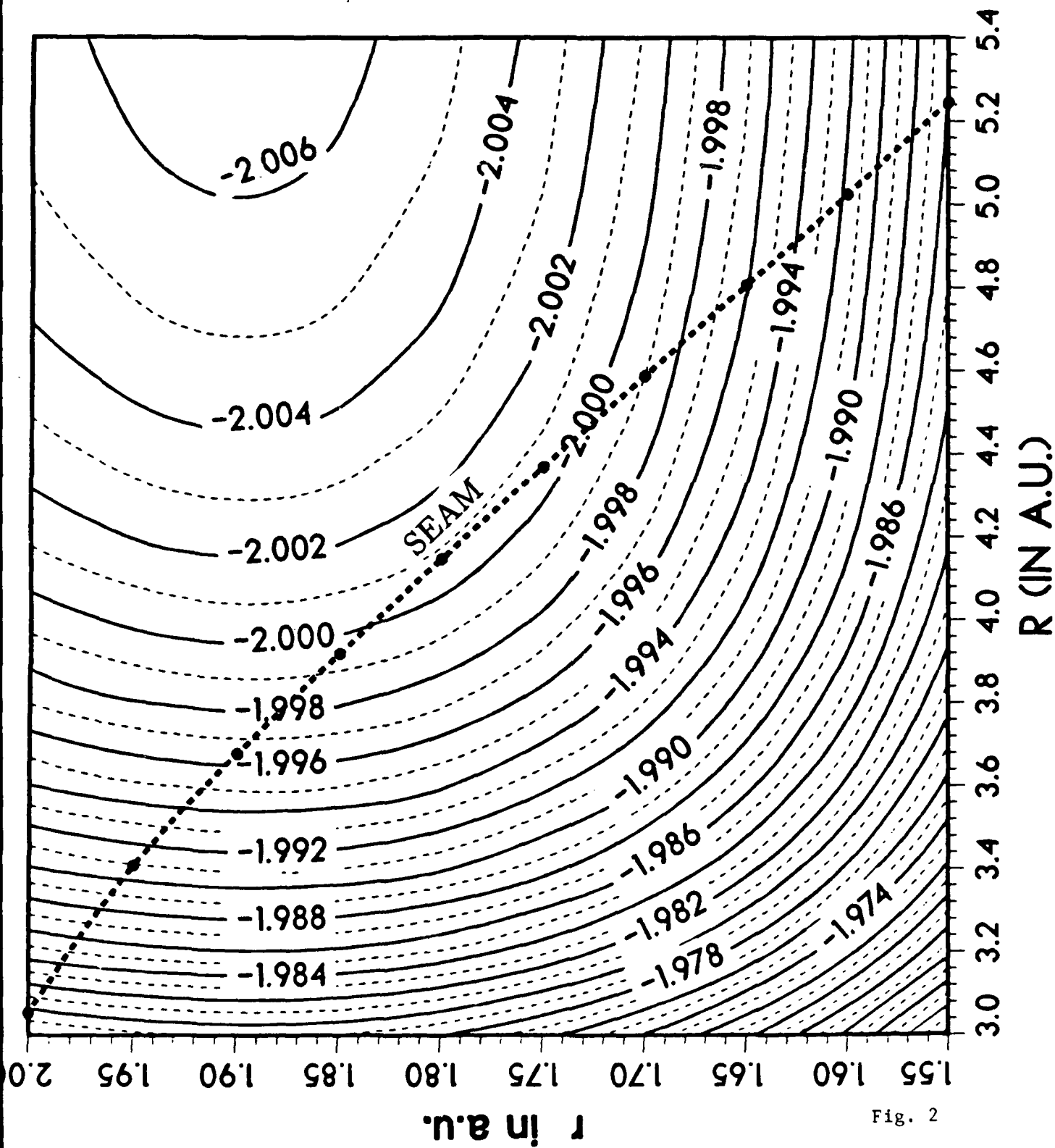
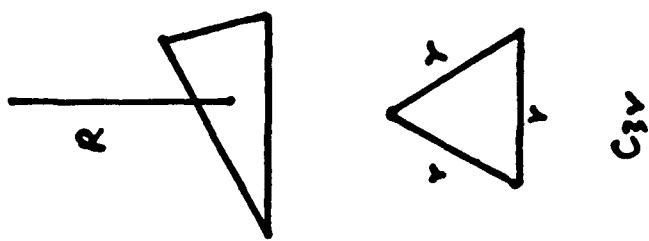


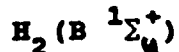
Fig. 2

Abstract: Air Force Contractors Meeting

March 11, 1988

C.D. Pibel, A.H. Kung, C.B. Moore, Univ. of California, Berkeley

Quenching Measurements of Electronically Excited Hydrogen



Measurements of the cross sections for the quenching of the fluorescence from the B - state of H_2 , HD, and D_2 by He have been completed for the first three vibrational states of each isotope. The results indicate that the vibrational states change adiabatically from separated $\text{H}_2(\text{B})$ and He to the transition state of the reaction that is responsible for the quenching, and the observed enhancement in the quenching cross section with vibrational excitation is due to a smaller H-H vibrational frequency at the transition state than in free $\text{H}_2(\text{B})$. In addition, the vibrationally adiabatic model predicts a difference in vibrational frequencies between the free diatom and the H_2 stretching mode in the transition state that is in fair agreement with recent theoretical work.¹

The lack of any rotational state dependence on the quenching rate suggests that the reactive collisions occur without sampling the rotationally anisotropic part of the $\text{H}_2(\text{B})$ -He potential energy surface. The $\text{H}_2(\text{B})$ -He potential surface is rotationally anisotropic, though, as shown by the large probability for ΔM_J collisions.

(I) Experimental Results

The experimental apparatus used is shown in Figure 1. Some sample quenching data is shown in Figure 2. All of the experimental results for the He quenching are shown in Table I. The quenching cross sections are seen to increase with increasing vibrational energy, as evidenced by the larger values for smaller reduced masses and larger vibrational quantum numbers. The $J'=0$ values in the ground vibrational states are also about 80% of the values for higher J's in each of the three isotopes. The single value for $v'=3$ in HD from previous work² agrees in magnitude with

the present results.

The value of the quenching cross section is seen to remain fairly constant with the rotational level excited for J' between 1 and 6 in the ground vibrational state of D_2 , but $J'=7$ is smaller by about 10%. This decrease in the cross section for high J 's could also be responsible for the smaller-than-expected cross sections measured with $v'=2$ (all of the levels excited with $v'=2$ also had large J 's.) The $v'=2$ quenching data for H_2 (shown in Figure 2) also shows positive deviations from linearity at high He pressures, suggesting that rotational relaxation followed by quenching may be occurring.

(II) Vibrationally Adiabatic Model

A schematic diagram of the potential energy surfaces involved in the quenching is shown in Figure 3. The barrier to quenching is small, and if vibrational energy can be siphoned into the reaction coordinate, enhanced quenching should be seen with very little vibrational excitation. If the vibrational motion is separable from the reaction coordinate, then the only enhancement in quenching with vibrational excitation will be due to a decrease in the frequency of the H-H stretching vibration in the transition state compared with the separated H_2 and He. If the reaction occurs with unit probability once the reactants reach the transition state, then the reaction cross section may be expressed as

$$\sigma = \sigma_{\text{crit}} \exp[-V_b(\rho, v)/kT],$$

where

$$\rho = [\mu(H_2)/\mu(XX)]^{\frac{1}{2}},$$

where $\mu(XX)$ is the reduced mass of HD or D_2 ($\rho(\text{HD}) = 0.866$, $\rho(D_2) = 0.707$;) v is the vibrational quantum number, and σ_{crit} is determined by the position of the barrier. If the vibrational

energy in both the separated reactants and the transition state is expanded out in the usual manner, one gets

$$\ln(\sigma/\sigma_{\text{crit}}) = -(V_0/kT) + (\Delta\omega_e/kT)(v+\frac{1}{2})\rho - \dots$$

The term $\Delta\omega_e$ is the difference in the vibrational frequency between free $\text{H}_2(\text{B})$ and the transition state, and V_0 is the barrier on the electronic PES. A plot of $\ln(\sigma)$ vs $(v+\frac{1}{2})\rho$ is shown in Figure 3. The slope of the line gives $\Delta\omega_e = 130 \pm 20 \text{ cm}^{-1}$. The magnitude of the intercept agrees with a zero-point barrier height near the calculated value of 1.5 kcal/mole.¹

(III) Future Work

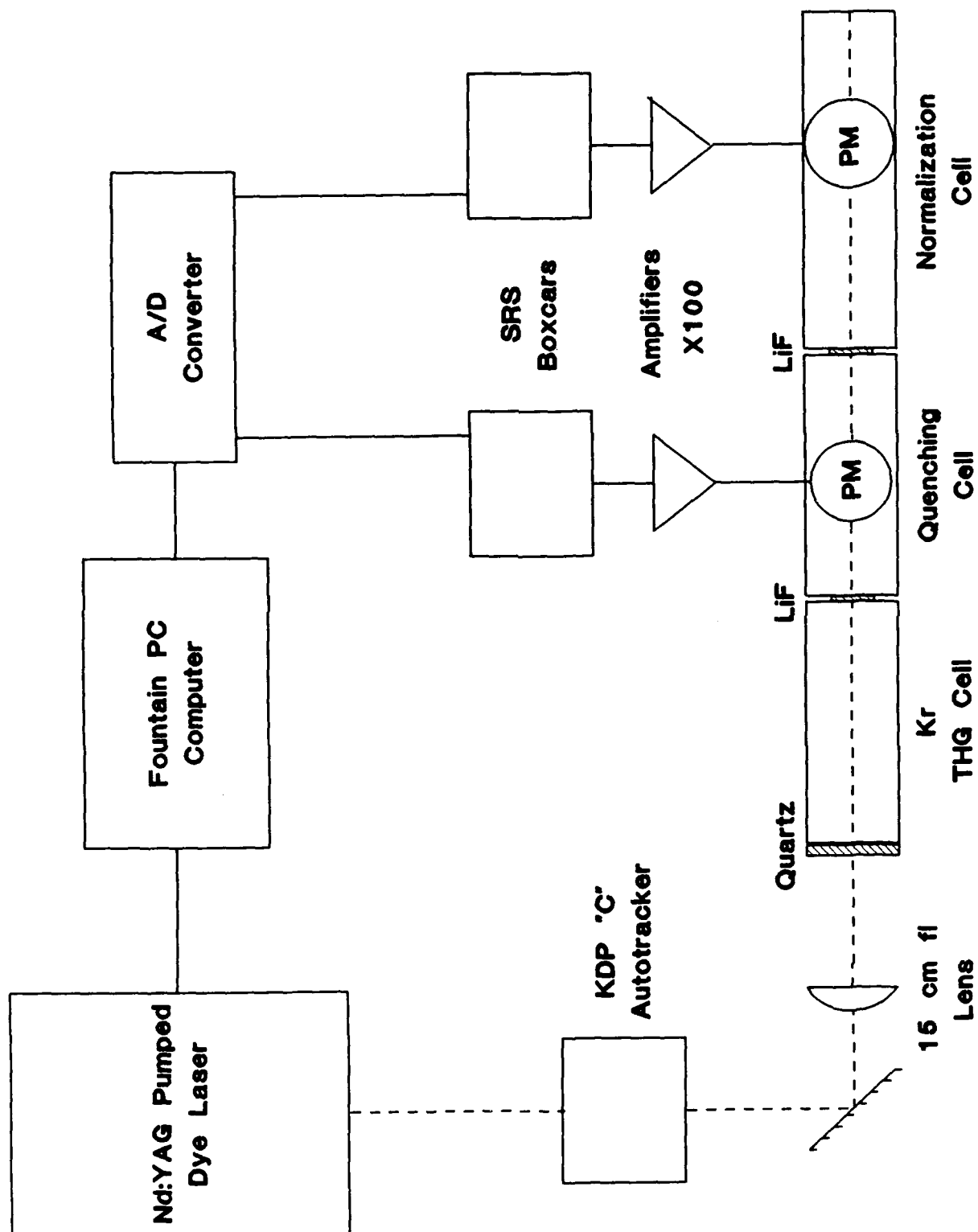
Future work will concentrate on looking for the products of the quenching reaction. Recent theoretical work¹ suggests that both $\text{H}_2(\text{X})$ and H atoms can be formed from the quenching process. A second VUV laser system will be used to look for H atoms. The ground state H_2 molecules from quenching will most likely be rotationally and vibrationally hot; either LIF or other techniques could be used to look for these products.

Past experiments indicate that there is little dependence of the quenching cross section for $\text{D}_2(\text{B})$ being quenched by $\text{H}_2(\text{X})$ on the vibrational or rotational level excited. The quenching products of this reaction will also be studied and compared with the products from the $\text{H}_2(\text{B}) - \text{He}$ quenching experiments. In the $\text{H}_2(\text{B}) - \text{He}$ case, presumably all of the quenching products exit on the ground-state $\text{H}_2(\text{X}) - \text{He}$ surface. In H_4 there is the possibility of quenching on the excited state surface through dissociation in different channels.

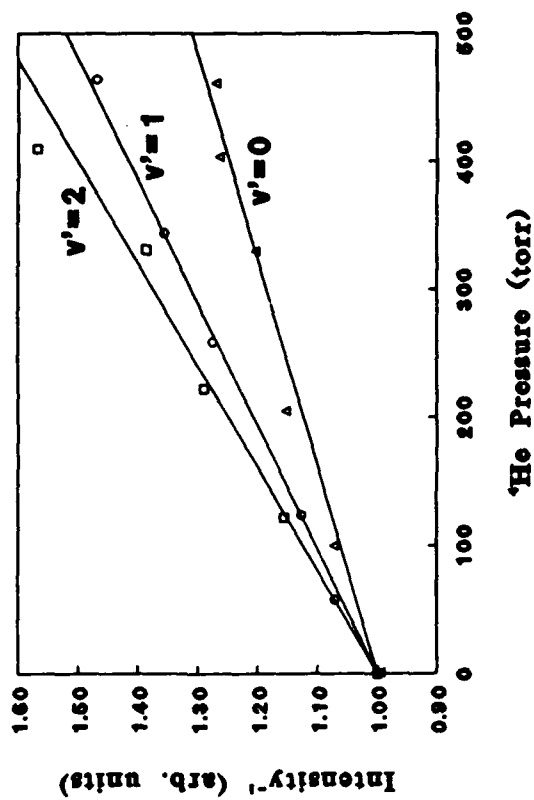
¹ J. K. Perry and D. R. Yarkony, J. Chem. Phys. **89**, 945 (1988). D. R. Yarkony (personal communication).

² E. H. Fink, D. L. Akins and C. B. Moore, J. Chem. Phys. **56**, 900 (1972).

Figure 1: This Figure is a schematic diagram of the experimental apparatus used in the quenching Experiments.



D_2 : Vibrational Dependence



$v'=2$: Isotopic Dependence

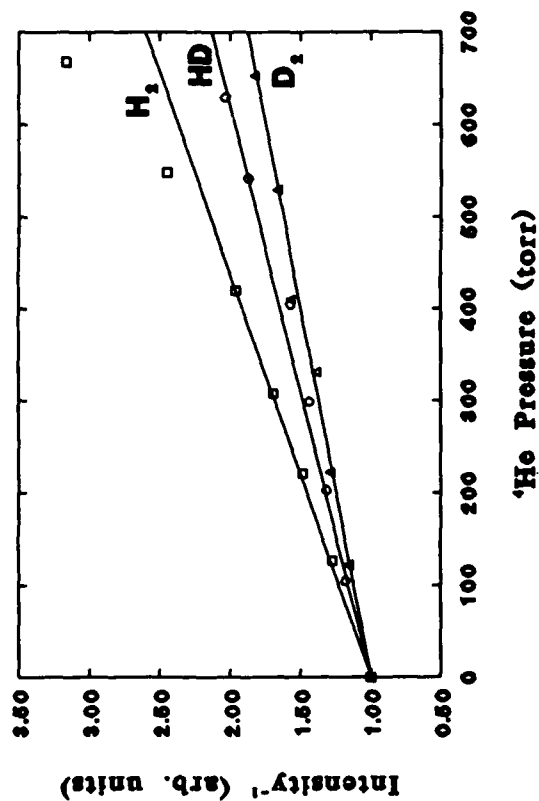


Figure 2: Sample kinetic data for electronically excited hydrogen quenched by 4He .

Figure 3: This figure is a schematic of the potential surfaces involved in the quenching of $\text{H}_2(\text{B})$ by He.

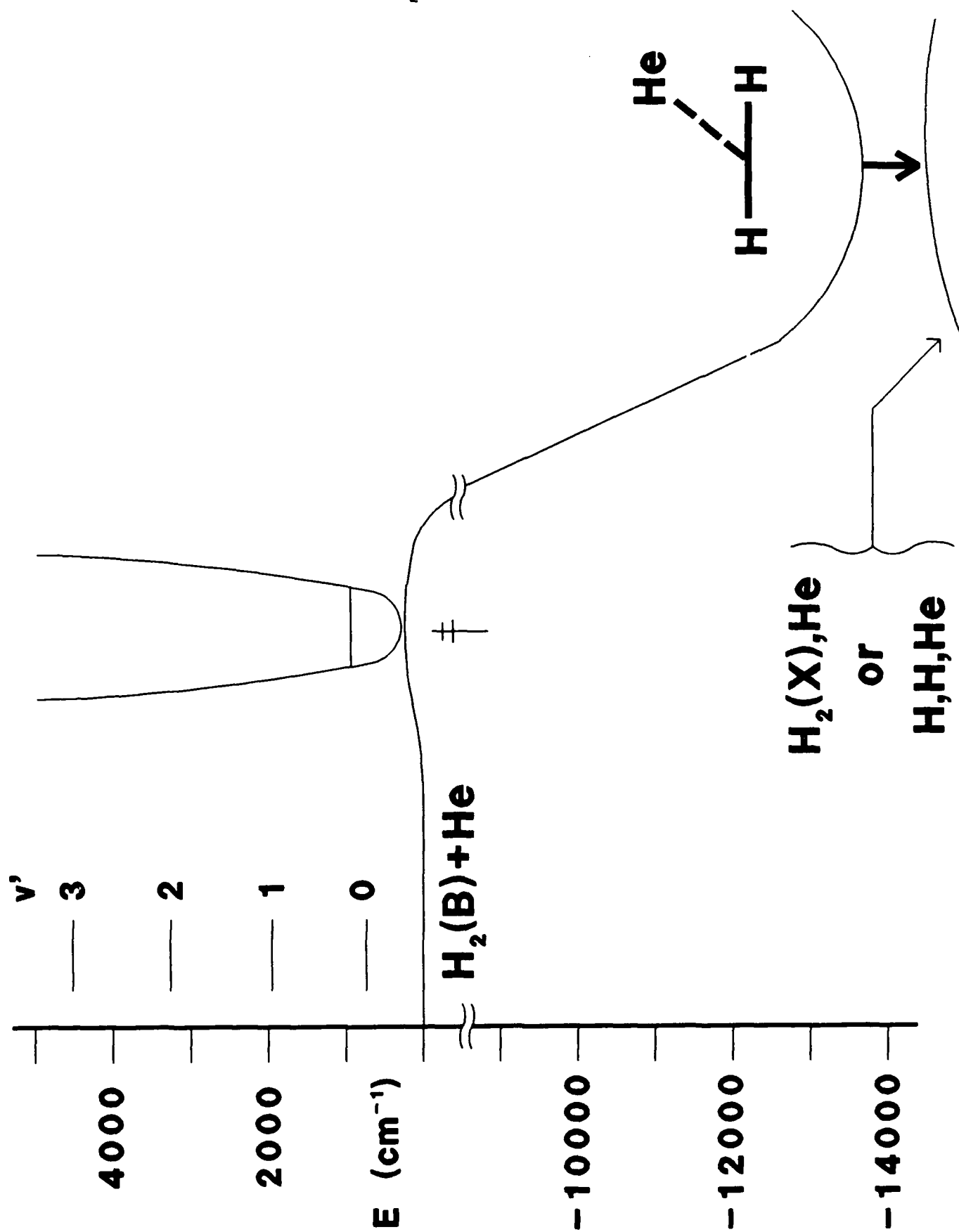


Table I: Experimental Results

Isotope	$ v,J\rangle$	k_Q^a (10^{-11} cc/mol-sec)	$\langle\langle\sigma\rangle\rangle^a$ (\AA^2)
D ₂	$ 0,0\rangle$	2.51 ± 0.09	1.42 ± 0.05
D ₂	$ 0,1\rangle$	3.52 ± 0.39	1.99 ± 0.22
D ₂	$ 0,2\rangle$	3.43	1.94
D ₂	$ 0,3\rangle$	3.70 ± 0.35	2.10 ± 0.20
D ₂	$ 0,4\rangle$	3.53 ± 0.25	2.00 ± 0.14
D ₂	$ 0,5\rangle$	3.43	1.94
D ₂	$ 0,6\rangle$	3.56	2.02
D ₂	$ 0,7\rangle$	3.09	1.75
D ₂	$ 1,3\rangle$	5.72	3.24
D ₂	$ 1,4\rangle$	5.83	3.30
D ₂	$ 2,6\rangle$	6.10	3.46
HD	$ 0,0\rangle$	3.94	2.07
HD	$ 0,3\rangle$	4.85	2.00
HD	$ 1,2\rangle$	7.50	3.94
HD	$ 2,5\rangle$	8.21	4.31
H ₂	$ 0,0\rangle$	4.10	1.90
H ₂	$ 0,3\rangle$	5.09	2.36
H ₂	$ 1,1\rangle$	9.30	4.31
H ₂	$ 2,5\rangle$	12.0	5.54
HD	$ 3,2\rangle$		9.9 ± 1.3^b

^a Uncertainties ($\pm 2\sigma$) are 15%, unless given.

^b E. H. Fink, D. L. Akins, and C. B. Moore, J. Chem. Phys. 56, 900 (1972).

**Further Investigations of the Infrared
Absorption Spectra of the Ionic Clusters of Hydrogen**

M.W. Crofton, J.M. Price, G. Niedner-Schatteburg
and Y.T. Lee

Department of Chemistry
University of California, Berkeley, California 94720

Previous studies in our laboratory of the vibrational predissociation spectra of mass selected ionic clusters of hydrogen, $H_3^+(H_2)_n$ (for $n=1-6$), have yielded only vibrational information about these systems.¹ Vibrational transitions were observed and assigned to motions of the clusters associated with both the H_3^+ ion core of these systems and the H_2 solvent molecules. This vibrational structure demonstrated convergence at high n to values close to that known for the vibrational frequency of H_2 in a solid hydrogen matrix.² Although no rotational structure in this early work was observed, the data were consistent with *ab initio* results for the structures consisting of an H_3^+ core solvated by H_2 molecules.

The fact that no rotational structure was observed was particularly surprising as theoretical predictions for the rotational constants of the smallest cluster, H_5^+ , have values of $A = 27 \text{ cm}^{-1}$, $B = 3.21$ and $C = 3.18 \text{ cm}^{-1}$ for the C_{2v} structure, considerably larger than the resolution of the laser system used.³ Possible explanations suggested for the unexpected result were homogeneous broadening of the transitions due to a particularly fast vibrational predissociation lifetime, or, spectral congestion due to high

levels of internal excitation in the clusters being probed. This latter possibility was investigated by changing the means of generating the clusters from an electron impact ionization source to a high pressure corona discharge source, known to produce vibrationally and rotationally colder clusters.

In our studies, ions are produced in a high pressure (150-300 torr) discharge region and then undergo a supersonic expansion through a $70\mu\text{m}$ nozzle for the formation of ionic clusters. A weak field (< 6 Volts/cm) was found to be needed between the nozzle and skimmer in order to transport ionic clusters through the skimmer. The ionic cluster of interest is selected by means of a mass spectrometer and is held in a radio frequency ion trap while it interacts with a pulsed infrared laser (QuantaRay IR WEX). If the cluster ion absorbs sufficient energy from the laser, vibrational predissociation can take place, resulting in the loss of one or more solvent molecules. Spectra are obtained by using a second mass spectrometer to monitor the number of daughter ions produced as a function of laser wavelength.

Recent work on the H_5^+ system which is intended to reduce the internal excitation differs from earlier work in the character of the corona discharge environment. Instead of running the discharge with pure H_2 as was done previously, Helium was used as a carrier gas, seeded with $\approx 35\%$ H_2 . This resulted in the formation of cooler H_5^+ than previously obtained. Based on fits of the rotational band contours of

other ionic cluster systems, we estimate the rotational temperature of the hydrogen cluster ions as near 20K. The source body itself was cooled to $\sim 40^{\circ}\text{C}$ to reduce the amount of vibrational excitation.

Figure 1 shows a recent infrared vibrational predissociation spectrum for the H_5^+ cluster ion in the region near 3535cm^{-1} that was previously assigned to the symmetric stretching vibration ν_2 of the H_3^+ core. This particular plot represents approximately 20 hours of signal averaging time and shows statistically significant variation in the product signal on the low frequency side of the band. Spectral resolution is $\approx 0.3\text{ cm}^{-1}$. Separation of the features denoted by the arrows averages about 7 cm^{-1} or roughly twice the B and C rotational constants for the cluster.

This work represents the first direct observation of rotational structure in the hydrogen cluster ion systems. The separation of spectral features is in reasonable agreement with the predicted value of $\approx 6.4\text{ cm}^{-1}$ based on the rotational constants from *ab initio* structural calculations. In spite of the superior rotational cooling, one still expects a substantial amount of spectral congestion for this system due to extensive tunneling splittings.

Work is underway now to improve the power of the excitation source using an optical parametric amplification scheme. This extra laser power will allow for even further dilution of the H_2 in the He expansion to give even better

rotational cooling and improved signal to noise on these weak transitions.

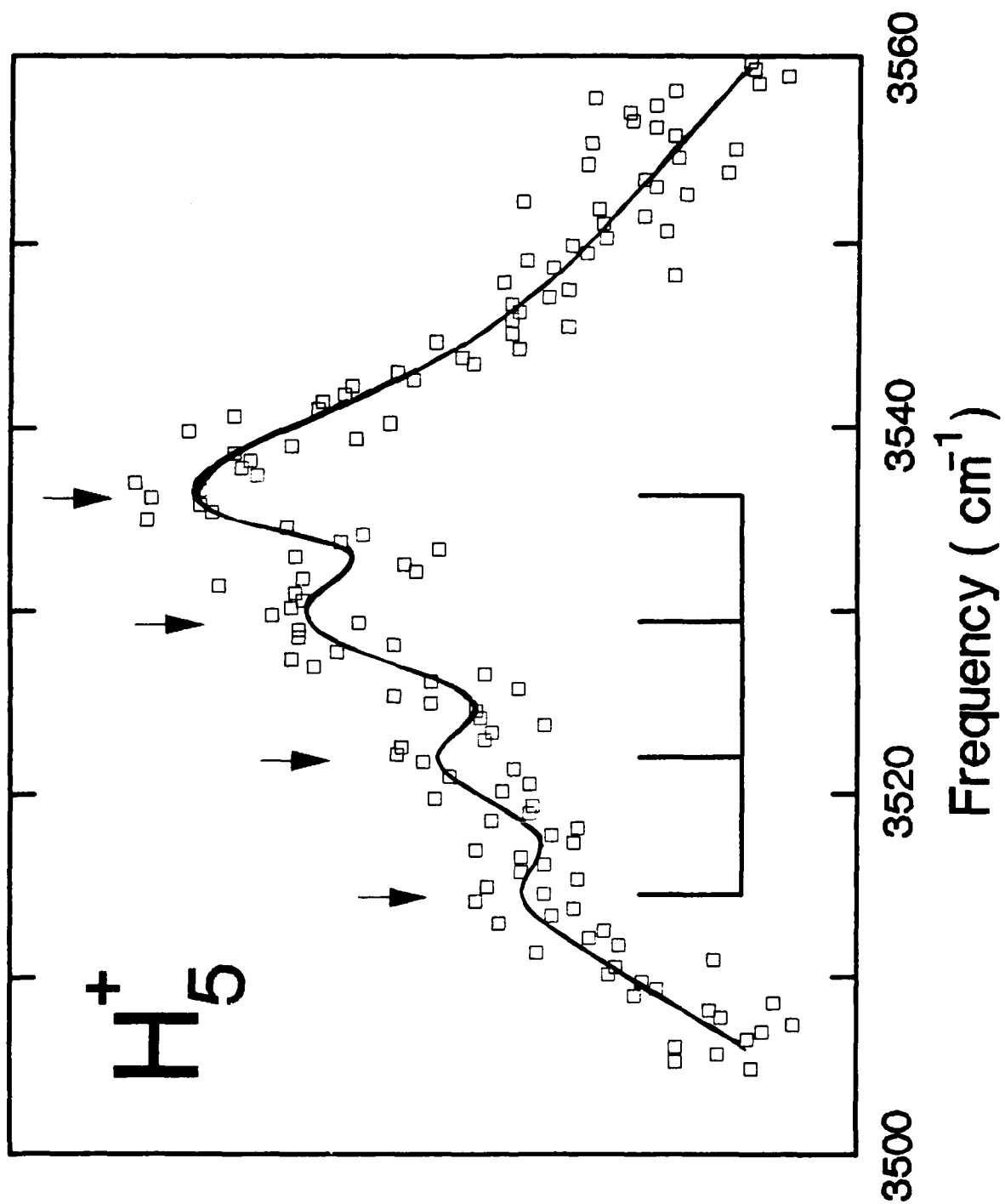
Acknowledgement

This work was supported by the Air Force Rocket Propulsion Laboratory under contract No. AFOSR F014611-87-K.

References:

1. M. Okumura, L.I. Yeh, and Y.T. Lee, submitted to J. Chem. Phys. (1989).
2. M. Okumura, M-C. Chan, T. Oka, Phys. Rev. Lett. 62, 32, (1989).
3. Y. Yamaguchi, J.F. Gaw, R.B. Remington, and H.F. Schaefer III, J. Chem. Phys. 78, 4074 (1983).

Figure 1. Infrared vibrational predissociation spectrum of H_5^+ .
Points represent H_3^+ counts at a given wavelength.
Solid curve is hand-drawn line representing a high
order average of the data showing the fluctuation in
product signal as a function of wavelength.



(NH)₆ : The Amino-analogue of Cyclohexane. A Laboratory for the Understanding of Lone-pair Effects on Molecular Geometry.

Charles P. Blahous III and Henry F. Schaefer III

Center for Computational Quantum Chemistry

School of Chemical Sciences

University of Georgia

Athens, GA 30602

Extended Abstract

The cyclohexane molecule has long been considered the supreme prototype for the understanding of conformational analysis. This is no mere accident of scientific history, but rather the direct consequence of saturated carbon's preference for arranging its bonds into a tetrahedron. Given the carbon bond's abhorrence¹ for large deviations from 109° 28', it follows that hydrocarbons of small size will be highly strained. Cyclopropane and cyclobutane are geometrically incapable of eliminating angular strain, and cyclopentane can do so only at the cost of eclipsing all hydrogens on adjacent carbons, thereby raising the energy considerably. In fact, this eclipsing of adjacent hydrogens is so unfavorable that cyclopentane accepts non-planarity in order to avoid the torsional strain, consequently increasing its angular strain.² Considering geometric limitations only, one therefore observes that cyclohexane is the smallest cyclic hydrocarbon which has an opportunity to exclusively contain unstrained carbon single bonds.

Eliel, Allinger, Angyal, and Morrison³ define conformations as "the non-identical arrangements of the atoms in a molecule obtainable by rotation about one or more

single bonds." This definition conveys a sense of why the cyclic hydrocarbon presents such an intriguing conformational problem to the chemist. If one considers strains only in terms of bond length, bond angle, torsional angle, and van der Waals forces, the conformational analysis of an acyclic hydrocarbon quickly becomes a series of quasi-separable problems, partitioned among the various bonds in the chain. Due to the limited effects they may have on one another, these local problems can only with great complexity be united into a comprehensive whole. On the other hand, cyclic hydrocarbons implicitly evaluate the consequences throughout the entire molecule of locally accepting a given type of strain. The nature of a ring is that no internal rotation across a single bond can be isolated; to leave the ring intact, it must always be accompanied by compensating rotations across the other bonds. Such internal rotations may alleviate one type of strain, but exacerbate another. In this way, each source of strain that would alter the torsional arrangements about a given bond must compete with other effectors at its own and other sites around the ring, and the local conformational problems assimilate into one general inclusive problem, within which they are inseparable and mutually affecting.

We have seen that cyclohexane is the smallest cyclic hydrocarbon wherein strain-reducing rotations may produce, in terms of bond length and angle, an "unstrained" species. In 1890, Sachse demonstrated⁴ that this could be accomplished in "symmetric" and "unsymmetric" forms (now known respectively as the "chair" and "flexible" conformations. Given little from which to choose in the two most obvious sources of strain (bond length and angle), it necessarily followed that the selection of a lowest energy shape be determined by other sources. It became apparent that cyclohexane could present a fundamental test for theories of the molecular geometries of organic species.

1936 witnessed the introduction of the hypothesis of Kemp and Pitzer⁵ that the discrepancy between the experimental heat capacity of ethane and that derived from

statistical mechanics calculations was due to a barrier to C-C bond rotation of approximately 3 kcal/mole. Although the connection was not then made, the eventual validation of this theory would have substantial ramifications for an experimental result published that same year. The Raman spectra of Kohlrausch et al.⁶ confirmed the results of a previous X-ray diffraction study⁷ that Sachse's "symmetric" structure was the energetically preferred conformation of cyclohexane. This was in perfect accord with the inferences of Kemp and Pitzer.⁵ Exploration of their idea eventually led to the conclusion¹ that rotation about the carbon-carbon single bond was not in fact free; that bonding regions about adjacent carbons preferred to be staggered rather than eclipsed, and that such eclipsing embodied another important type of molecular strain. The symmetric "chair" structure minimized this "torsional strain", a cyclic analogue of the C-H "staggering" which acyclic hydrocarbons were eventually seen to prefer.

The experiment by Kohlrausch et al.⁶ verified another postulate of Sachse, namely the existence of two symmetrically distinct types of hydrogen in chair cyclohexane. The maintenance of tetrahedral geometry at each carbon roughly fixed the angular positions of the hydrogens, with the result that one (the "axial") would be slightly more sterically crowded than the other (the "equatorial"). Perhaps also important, the axial hydrogen would be in a gauche position relative to an adjacent C-C bond, while the equatorial hydrogen would be antiperiplanar to it. That the chemical environments of the two types of hydrogen were different was eventually confirmed by their slightly differing bond lengths,⁸ but experimentalists had discovered long before then that substituents attaching to cyclohexane tended to prefer the roomier equatorial positions.⁹ Thus the effect of various ring-external substitutions upon the properties of cyclohexane became a practical test of the general responses of these substituents to varying steric pressures. Cyclohexane's contributions to the prediction of general conformational trends had increased still further.

To summarize cyclohexane's role in conformational analysis, it may be said that its strain-free bond lengths and angles permit such conformational determinants as torsional angle and steric factors to be isolated and evaluated. In moving from the "chair" to the "flexible" form of cyclohexane, the effects of torsional strain may be witnessed. Within the "chair" form, substitution at the different hydrogen sites exposes the steric requirements of a substituent and how steric strain may be alleviated.

As stated earlier, this analytical utility of cyclohexane is a consequence of the six-membered ring's suitability for the tetrahedral bond. As such, a six-membered ring provides a helpful analytical tool for any species which arranges its bonds in this way, including oxygen (with its two lone pairs and two bonded pairs) and nitrogen (with one lone pair and three bonded pairs).

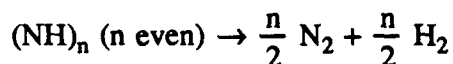
The data is available to begin an analysis of what torsional features to expect in six-membered oxygen and nitrogen rings. The barriers to rotation for hydrogen peroxide and hydrazine are quite large when moving to a geometry where lone pairs eclipse lone pairs (as in the *cis*-H₂O₂ and *cis*-hydrazine rotation barriers). The corollary of this is that the corresponding energy gaps between "chair" and "flexible" forms of the hypothetical isoelectronic oxygen (O₆) and nitrogen (N₆H₆) rings should be larger than in cyclohexane. Recent theoretical investigations by this group tentatively confirm that this is the case for O₆.¹⁵

One may demonstrate the analogous fact for N₆H₆, but doing merely that would leave unexplored the full potential of the molecule for contributions to conformational analysis. N₆H₆ lacks the enforced D_{3d} symmetry inherent in O₆ and cyclohexane, because of the presence at each nitrogen of one H-bonded and one lone electron pair. Consequently, it has no unique chair conformation, but rather several symmetrically distinct options. An exploration of the potential surface of only the chair conformations of N₆H₆ is akin to studying the 1,2,3,4,5,6-hexasubstituted cyclohexanes. As such, N₆H₆ may facilitate an understanding of the steric requirements of nitrogen's lone-pair

comparable to the understanding which cyclohexane and substituted cyclohexanes have fashioned for tetrahedrally bonded species.

N_6H_6 : A High Density Species?

Recent theoretical investigations^{15,16} of oxygen rings have advanced the notion that they may effectively store large amounts of energy (more than 40 kilocalories/mole O_2). The principles which engender this hypothesis, namely those of bond energy additivity, suggest that even more energy storage is possible in similar rings comprising nitrogen (N_nH_n). Consequently, a theoretical description of N_6H_6 may have worth extending beyond mere pedagogy; it may be of practical significance as well. The tremendous strength of the triple bond in N_2 (225.1 kcal/mole)¹⁷ in combination with standard values for the bond strengths of H_2 (103.3 kcal/mole), N-N single bonds (39 kcal/mole) and N-H bonds (93 kcal/mole),¹⁸ leads to the estimate that approximately 64 kcal of energy could be stored for each mole of N_2 released in the following reaction:



The problem is therefore presented: do these naive bond-energy estimates accurately reflect the energy of N_6H_6 relative to separated N_2 and H_2 ?

The question of N_6H_6 's energetics is intimately connected with the conformational concerns discussed in our Introduction. The lowest-energy structure of N_6H_6 needs to be identified, i.e., the conformation most effectively reducing strain from suboptimal torsional angles and lone-pair positioning.

The minimization of torsional strain in N_6H_6 is achieved in the "chair" structure,¹⁹ which is unique for cyclohexane and O_6 , but which in N_6H_6 appears in thirteen symmetrically distinct forms (see Figure 3). These forms correspond to the different permutations in which nitrogen's lone pairs may appear in the available axial and

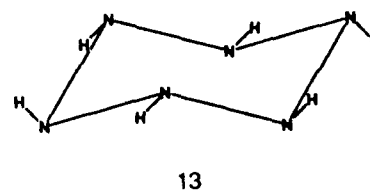
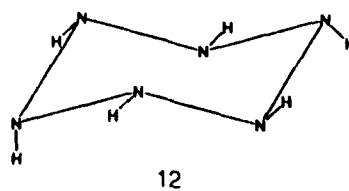
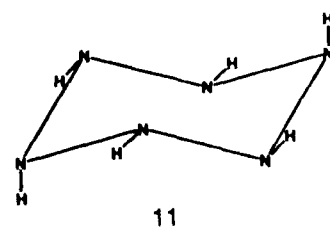
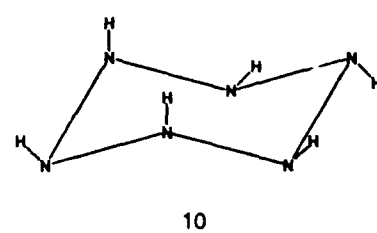
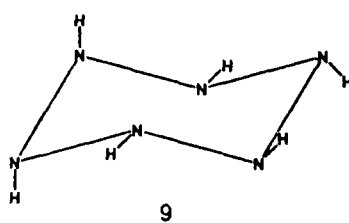
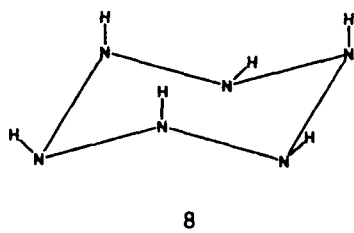
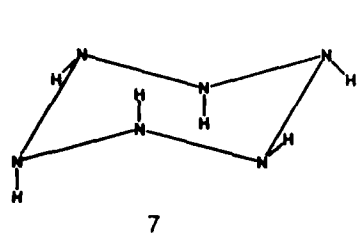
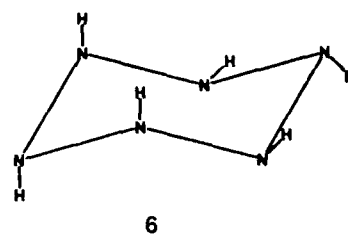
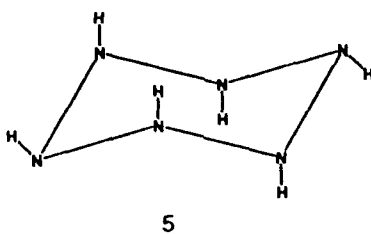
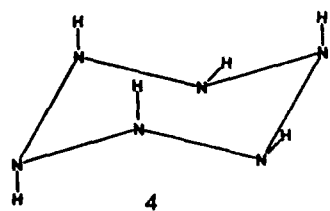
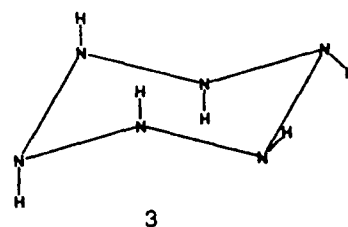
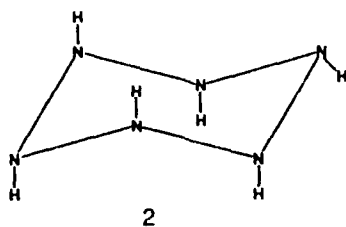
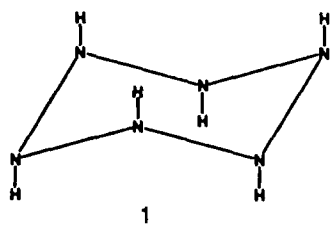
equatorial sites.

(Figure)

A first glance at these structures may prompt the conclusion that the one pictured first should be lowest in energy. The lone pairs on nitrogen, requiring more space than the electron pairs representing bonding with hydrogen, locate here in the roomier equatorial positions. Other preliminary conclusions might be drawn as well. For example, it is known that in cyclohexane the hydrogens in axial positions interact, in a van der Waals manner, as strongly with next-nearest neighbor hydrogens as they do with those on adjacent carbons.²⁰ This may imply that N_6H_6 conformations with "axial lone pairs" on the 1, 3, and 5 nitrogens (structure 8) might be particularly disfavored. We might also conjecture that axial and equatorial N-H bonds be of different lengths. Or, that the size or torsional angle of the ring may be strongly affected by the positioning of the lone pairs.

The expansive and thorough recent work of Lothar Schäfer and coworkers has convincingly demonstrated the value of *ab initio* investigations in testing these kinds of analyses.^{21,22} Their theoretical descriptions of cyclohexane and its derivatives have confirmed and helped to explain long acknowledged conformational trends²¹ as well as to establish new insights, as in their prediction that the axial C-H bonds of cyclohexane should be slightly longer than the equatorial C-H bonds.⁸ For this reason, we are satisfied that a theoretical study of the energies and structures of the various N_6H_6 chair conformations has much insight to offer into the conformational preferences of the lone-pair-bearing bonded species.

Figure : The thirteen symmetrically distinct conformations of chair - N_6H_6



References

- 1 E. L. Eliel, N. L. Allinger, S. J. Angyal, and G. A. Morrison, *Conformational Analysis*, p. 2, (Interscience Publishers, New York, 1965).
- 2 A. Almenningen, O. Bastiansen, and P. N. Skancke, *Acta. Chem. Scand.*, **15**, 711 (1961).
- 3 Reference 1, p. 1.
- 4 H. Sachse, *Ber.* **23**, 1363 (1890) *Z. Physik. Chem.* **10**, 203 (1892).
- 5 J. D. Kemp and K. S. Pitzer, *J. Chem. Phys.*, **4**, 749 (1936).
- 6 K. W. F. Kohlrausch, A. W. Reitz, and W. Stockmair, *Z. Physik. Chem.*, **B32**, 229 (1936).
- 7 R. G. Dickinson and C. Bolicke, *J. Amer. Chem. Soc.*, **50**, 764 (1928).
- 8 N. S. Chiu, J. D. Ewbank, L. Schäfer, *J. Mol. Struct.* **86**, 397 (1982).
- 9 Reference 1, Table, p. 44.
- 10 S. Weiss, G. Leroi, *J. Chem. Phys.*, **48**, 962-967 (1968).
- 11 D. R. Lide, Jr. *J. Chem. Phys.*, **27**, 343-352 (1941).
- 12 E. V. Ivash and D. M. Dennison, *J. Chem. Phys.*, **21**, 1804-1816 (1953).
- 13 W. H. Fink, D. C. Pan, and L. C. Allen, *J. Chem. Phys.*, **47**, 895-905 (1967).
Experimental data is available only for the cis-structure. We give theoretical values for both cis and trans to maintain internal consistency. The cis-value is roughly 0.5-0.6 kcal higher than experiment.
- 14 R. H. Hunt, R. A. Leacock, C. W. Peters, K. T. Hecht, *J. Chem. Phys.* **42**, 1931-1946 (1965).

- 15 C. P. Blahous and H. F. Schaefer, *J. Phys. Chem. Massimo Simonetta Memorial Issue*, **92**, 959 (1988).
- 16 E. T. Seidl and H. F. Schaefer, *J. Chem. Phys.* **88**, 7043 (1988).
- 17 K. Huber and G. Herzberg, *Constants of Diatomic Molecules* (Van Nostrand: Reinhold, New York, 1979).
- 18 S. H. Paie, J. B. Hendrickson, D. J. Cram, G. S. Hammond, *Organic Chemistry*, Fourth Edition, table, p. 85, (McGraw-Hill, New York, 1980).
- 19 C. P. Blahous and H. F. Schaefer, unpublished *ab initio* result.
- 20 Reference 1, p. 51.
- 21 L. Schäfer, J. D. Ewbank, V. J. Klimkowski, K. Siam, and C. Van Alsenoy, *J. Mol. Struct. (Theochem)*, **135**, 141-158 (1986).
- 22 K. Siam, J. D. Ewbank, L. Schäfer, C. Van Alsenoy, *J. Mol. Struct. (Theochem)*, **164**, 83-92 (1988).

Metastability in Molecules

Metastability in Excited States:

The ${}^4\Pi_g$ State and its Autodetachment Spectrum

T. Pluta, R.J. Bartlett and L. Adamowicz

Quantum Theory Project

University of Florida

Phys. Rev. A, submitted

ABSTRACT

The unusual autodetachment spectrum of metastable He_2^- is studied theoretically, using high level coupled-cluster methods and hybrid numerical and Slater orbital basis sets. By obtaining accurate curves for the repulsive wall of the ground He_2 ($X^1\Sigma_g^+$) state, the excited He_2 ($a^3\Sigma_u^+$) state and the metastable He_2^- (${}^4\Pi_g$) state, we are able to provide an alternative explanation for the experimental observations, which had cast doubt on the veracity of the accepted curve for the repulsive part of the $\text{He}_2(X^1\Sigma_g^+)$ potential. We attribute the experimental peak at 15.78 ± 0.13 eV to transitions of vibrationally excited states ($v=2$ and higher) of He_2^- to the $\text{He}_2(X^1\Sigma_g^+)$ continuum, since the $v=0$ transition would have a value 1 eV less. An error of this size is considered to be far outside the error bars for highly accurate correlated ab initio calculations. The electron affinity of the ${}^4\Pi_g$ state of the anion (measured relative to $a^3\Sigma_u^+$) is computed to be 0.201 and 0.212 eV for different basis sets, compared to an experimental value of 0.175 ± 0.032 eV; while predicted values for the vibrational detachment of the He_2^- (${}^4\Pi_g$) state are 3 to 15 meV, compared to an experimental value of 11.5 ± 2.6 meV.

Support: Air Force Office of Scientific Research, Chemistry and Atmospheric Sciences

Metastability in Excited States:

The $^4\Pi_g$ He_2^- State (See Fig. 1)

- He_2^- was discovered to exist in a metastable state by Bae, Coggiola and Peterson, PRL, 1984, with a lifetime of $>100 \mu\text{sec}$.
- Its "excimer" autodetachment spectrum was observed by Kvale, Compton, Alton, Thompson, and Pegg, PRL, 1986.
- Theoretical studies of He_2^- were done by Michels, PRL, 1984; CPL, 1986.
 - Concluded that observed state was $^4\Pi_g$ with the electronic configuration $(1\sigma_g^2 1\sigma_\mu 2\sigma_g 1\pi_\mu)$
 - That alternative $^4\Sigma_g (1\sigma_g^2 1\sigma_\mu 2\sigma_g 3\sigma_\mu)$ was a resonance state.
- Experimental results consist of these features:

- A peak at $15.78 \pm 0.13 \text{ eV}$ attributed to the transition from

$$^4\Pi_g \text{He}_2^- (v=0) \rightarrow X^1 \sum_g^+ \text{He}_2 + e^-$$

- A peak at $11.5 \pm 2.6 \text{ meV}$ attributed to the vibrational autodetachment

$$^4\Pi_g \text{He}_2^- (v=1) \rightarrow ^3 \sum_g^+ \text{He}_2 (v=0) + e^-$$

- A positive electron affinity of $0.175 \pm 0.032 \text{ eV}$ that corresponds to the transition

$$^3 \sum_g^+ \text{He}_2 (v=0) + e^- \rightarrow ^4\Pi_g \text{He}_2^- (v=0)$$

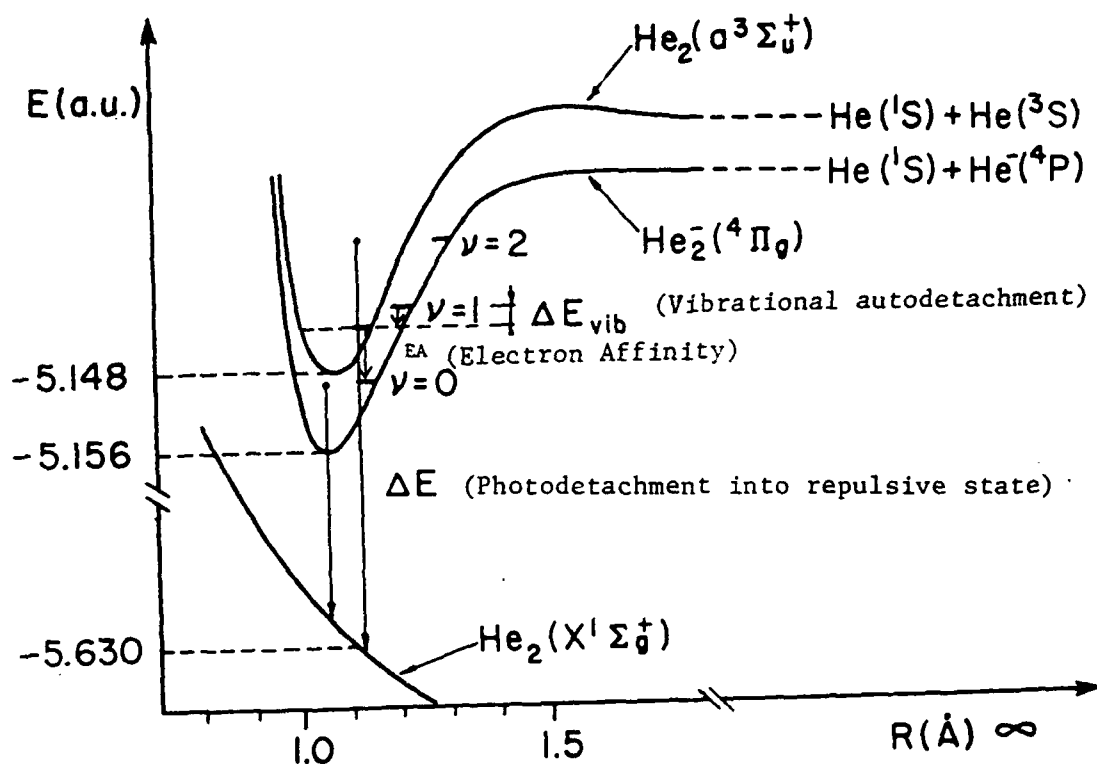
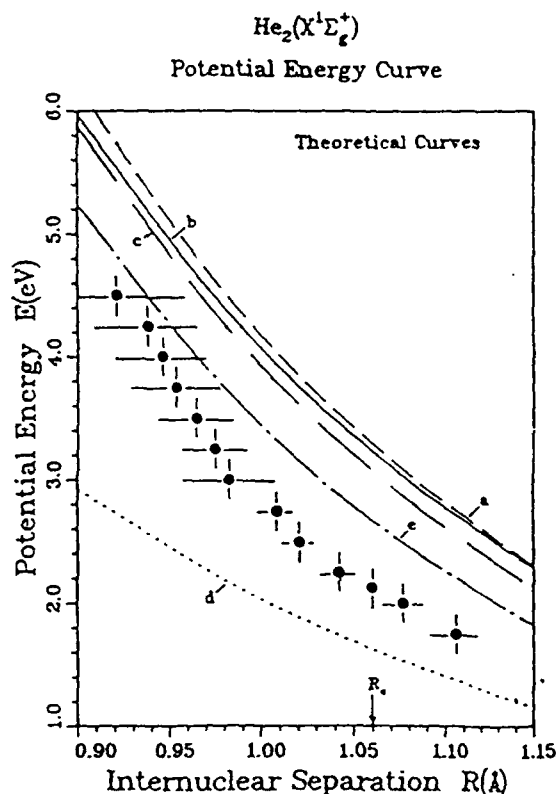


Fig.1. Total energy curves for He_2 and He_2^-

- Michels' theoretical results consist of these features:
 - Taking the CI results for the $^4\Pi_g He_2^-$ state, together with experimental curve for the $^3\Sigma_g^+ He_2$ excited state, the electron affinity was computed to be 0.233 eV, and 0.182 eV in good agreement with experiment 0.175 ± 0.032 eV.
 - Similarly, the vibrational autodetachment was computed to be 15 meV also in good agreement with 11.5 ± 2.6 meV
 - However, comparing the computed $^4\Pi_g He_2^-$ curve to the quantum Monte-Carlo results of Partridge and Ceperly for the $X^1\Sigma_g^+$ state gave a value of 15.2 eV; in error from experiment by 0.6 eV. Since even better calculations for He_2^- would likely *lower the energy of this state*, making the error greater, it was proposed by some that the accepted $X^1\Sigma_g^+ He_2$ curve was wrong.

Fig. 2. Predicted $X^1\Sigma_g^+ He_2$ Curve Based Upon Photodetachment
From $v=0$, $^4\Pi_g$ State of He_2^-



Experimental data and Figure taken from Kush, Compton, Alton, Thompson and Pegg
- unpublished.

^aKunk and Kaldor (SOSCF, 1972)

^bPhillipson (CI, 1962)

^cCeperly and Partridge (QMC, 1986)

^dYoung, et al. (Muffin tin electron based theory)

^eMatsumoto, Binder and Davidson (CI 1967)

Method of Calculation

- Treat all relevant electronic states at a consistent level of approximation
- Numerical (or hybrid) orbital coupled-cluster method
 - NHF solution augmented by numerical correlating orbitals obtained from series of Bethe-Goldstone optimizations
 - NHF solution augmented by Slater correlating orbitals obtained by hybrid Hartree-Fock solution
 - Introduce electron correlation to Φ_0 via CCSD+T(CCSD) for the three states

CCSD

G.D. Purvis and R.J. Bartlett, J. Chem. Phys., 1981

$$\begin{aligned}
 T_1 &= \sum_{i,a} t_i^a \{a^\dagger i\}; & T_1 \Phi_0 &= \sum_{i,a} t_i^a D_i^a \\
 T_2 &= \sum_{\substack{i < j \\ a < b}} t_{ij}^{ab} \{a^\dagger i b^\dagger j\}; & T_2 \Phi_0 &= \sum_{\substack{i < j \\ a < b}} t_{ij}^{ab} D_{ij}^{ab} \\
 \psi_{CCSD} &= \exp(T_1 + T_2) \Phi_0 \\
 E_{CCSD} &= \langle \Phi_0 | H \exp(T_1 + T_2) | \Phi_0 \rangle
 \end{aligned}$$

M. Urban, J. Noga, S.J. Cole and R.J. Bartlett, J. Chem. Phys. 1986

$$T(CCSD) = \langle \Phi_0 | T_2^\dagger T_2 | \Phi_0 \rangle D_3$$

CCSD has a mean absolute error compared to full CI (kcal/mol) of 1.9 at R_e ; 8.6 at 2 R_e .

CCSD +T(CCSD); 0.2 at R_e ; 3.2 at 2 R_e .

CURRENT WORK

Energy of He in Different Basis Sets

BASIS I. NHF + STO (Michels) (14σ6π2δ)

$$E_{\text{CCSD}}(\text{He}) = -2.8774 \text{ a.u.}$$

(Michels STO + CI -2.8738)

BASIS II. NHF + STO (Michels) + STO (16σ20π8δ2φ)

$$E_{\text{CCSD}}(\text{He}) = -2.9016 \text{ a.u.}$$

BASIS II*. Basis II + Michels 2s STO (20σ20π8δ2φ)

$$E_{\text{CCSD}}(\text{He}) = -2.9018 \text{ a.u.}$$

(-2.9032 Exp.)

Prediction of $X^1\Sigma_g^+$ He₂ Curve

Maximum Difference from Quantum Monte Carlo <0.05 eV

Absolute Energy Shift <0.08 eV

Equilibrium R_e for $^4\Pi_g$ State of He₂⁻

R_e = 1.056 Basis I

R_e = 1.053 Basis II

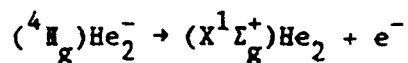
Excitation Energy $X^1\Sigma_g^+ \rightarrow ^3\Sigma_u^+$ for He₂

T₀₀ = 145548 cm⁻¹

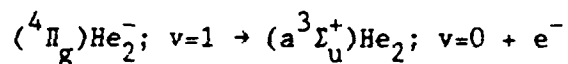
Exp = 144935 cm⁻¹

Calculated CCSD + T(CCSD) Photodetachment Energies for He₂ (eV)

A. Photodetachment into repulsive ground state

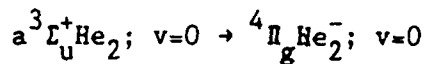


Vibrational level	Basis I	Basis II	Exp.
$v = 0$	14.1	14.8	
$v = 2$	15.2	15.7	15.78 \pm 0.13

B. Photodetachment into the $a^3\Sigma_u^+$ state of He₂

0.015	0.003	0.0115 \pm 0.0026
-------	-------	---------------------

C. Electron Affinity



0.201	0.212	0.175 \pm 0.032
-------	-------	-------------------

CONCLUSIONS

- I. The Quantum Monte Carlo Curve is for $X^1\Sigma_g^+ \text{He}_2$ is accurate
- II. On the basis of high accuracy CC calculations hot bands are required to explain observed experimental data.

Bae, et al., Phys. Rev. (1988) assumed a rotationally and vibrationally hot distribution and obtained suitable fits to their spectra.

But raises questions -

Competition between vibrational autodetachment and electronic autodetachment in $v=1$ and higher vibrational states.

Function of non-Born-Oppenheimer processes for $v > 1$.

Theoretical Studies of Bridged Structures of Be_2H_2 and B_2H_2

Byron H. Lengsfeld III

Theoretical Atomic and Molecular Physics Group, L-446

Lawrence Livermore National Laboratory

P.O. Box 808

Livermore, CA 94550

Abstract

These studies focus on enhancing the performance of energetic compounds by storing additional energy in bridged-bonding configurations. In the first phase of this work, three molecules were considered, Be_2H_2 , B_2H_2 and H_2O_2 . Preliminary studies of these dihydrides indicate that these molecules have stable isomers with hydrogen-bridged bonds. Propellants containing boron hydrides have been studied for some time as they yield a large specific impulse, I_{sp} , when burned with OF_2 [1]. Their yield is larger per unit weight than comparable fuels employing saturated hydrocarbons[2]. Propellants containing beryllium have also been extensively studied. The hybrid propellants, $\text{BeH}_2\text{-O}_2$, $\text{BeH}_2\text{-F}_2$, $\text{BeH}_2\text{-H}_2\text{O}_2$, and $\text{BeH}_2\text{-N}_2\text{O}_4$ have a large I_{sp} per unit weight and are superior to $\text{H}_2\text{-O}_2$ in some environments. The propensity of the hydrides of beryllium and boron to form stable hydrogen-bridged structures is well known[3]. In this effort, we have investigated hydrides of boron and beryllium whose lowest energy structures do not involve bridged bonds but may well possess stable energetic isomers which do involve bridged bonding and thus provide a mechanism for storing additional energy in these molecules. Studies of molecules such as BeBH_3 have also been proposed. We have also undertaken studies of the hydrogen-bridged structure of H_2O_2 . H_2O_2 is the oxidizer in a number of propellant formulations with a large I_{sp} , such as $\text{H}_2\text{O}_2\text{-H}_2$ and $\text{H}_2\text{O}_2\text{-AlH}_3$, in addition to the $\text{H}_2\text{O}_2\text{-BeH}_2$ formulation noted earlier. MCSCF studies of Be_2H_2 and B_2H_2 have been completed and the bridged structures of these molecules were found to be stable. Similar results were obtained in our SCF calculations of H_2O_2 .

In order to ascertain the lifetimes of these compounds additional calculations must be undertaken which locate the transition states on the potential energy surfaces and identify any surface crossings which occur. If a surface crossing occurs, nonadiabatic coupling terms will be

computed for input to dynamics calculations which will be undertaken at Livermore. Since the ground state of B_2H_2 is $^3\Sigma^-$ and our calculations indicate that the bridged structure is 1A_1 , the singlet-triplet surface crossing will be needed to determine the lifetime of the bridged isomer. The optimized geometries and relative energies obtained in our MCSCF calculations are reported in Table 1. and Table 2. for B_2H_2 and Be_2H_2 , respectively. We see that for B_2H_2 , the bridged structure is 40 kcal/mole higher than the lowest energy, linear structure. To assess the import of these calculations we compare the heat of formation, ΔH_f , of these molecules to those of the propellants discussed earlier. Page and Adams[4] have recently completed calculations of the heat of formation of a large number of boron hydrides. For linear ($^1\Delta$) B_2H_2 they find ΔH_f to be 117 kcal/mole and they compute a ΔH_f of 2.7 kcal/mole for B_2H_6 . The experimental values for ΔH_f of B_2H_6 range from 8–10 kcal/mole[5]. Using the values obtained by Page and Adams, ΔH_f of bridged B_2H_2 would be on the order of 140 kcal/mole. As I_{sp} goes as the square root of the heat of combustion, H_c , divided by the mean molecular weight of the exhaust gases[6], W,

$$I_{sp} = (\text{constant}) * \left[\frac{H_c}{W} \right]^{1/2} \quad (1)$$

then a propellant formulation containing B_2H_2 in place of B_2H_6 looks very promising. As the lifetime of the linear $^1\Delta$ state of B_2H_2 is on the order of a few seconds, when comparing the linear structure to bridged we should use the triplet state of the linear structure in which case an additional 16 kcal/mole is stored in the bridged bonds. If the singlet bridged structure is indeed long-lived, it may be less likely to polymerize than the linear triplet structure. Polymers of B_2H_2 are known and a large polymerization energy has been computed for this species[7].

In Table 2., we see that the bridged singlet isomer of Be_2H_2 is 30 kcal/mole above the linear isomer. Given the storage potential of the bridged isomer and the fact that the heat of the reaction, $Be(g) + BeH_2(g) \rightarrow Be_2H_2(g)$, is small, $\Delta H_f = -23$ kcal/mole[8], compared to the heat generated by the reactions which make BeH_2 a good propellant[1], the bridged structure of Be_2H_2 also bears further investigation. In this system, our future efforts will be focused on locating the barrier to isomerization as there is not a low-lying triplet state present.

Efforts to enhance the capabilities of the MESA[9] series of electronic structure codes will also be discussed. Recent work by Rice and Amos[10] has resulted in a more efficient method of obtaining an optimized structure from a configuration interaction, CI, wavefunction. This technique has only been applied to single reference methods to date. As we need to describe regions of the potential energy surface, such as a transition state, where bonds are being broken

or formed, multireference CI or multireference coupled-cluster techniques are generally required. So the development of a multireference optimization scheme based on the Rice-Amos algorithm will greatly improve our ability to rapidly characterize the potential energy surfaces of energetic molecules and thus ascertain their utility as propellants. Moreover, the method that we recently developed to evaluate derivative nonadiabatic coupling terms (d/dR , where R is a nuclear coordinate)[11] employs the same codes used to evaluate multireference CI energy derivatives[12]. Thus, both our ability to rapidly locate stationary points on a potential energy surface and to compute the coupling terms between potential energy surfaces will be enhanced by these developments.

I have also proposed that the capability of addressing spin-dependent interactions be added to the MESA package. There have been a number of recent advances in the techniques used to compute spin independent Hamiltonian matrix elements for Full-CI and MCSCF wavefunctions[13]. These techniques make it practical to employ CI expansions consisting of many thousands of configurations state functions in a MCSCF calculation. These techniques can also be applied to the computation of spin dependent matrix elements and I plan to implement such a scheme. The motivation for this development is that this code can be used to evaluate the nonadiabatic interactions that arise when singlet and triplet surfaces cross.

Finally, a new electron-molecule scattering package will be discussed. This code was recently developed at Livermore in collaboration with Bill McCurdy and Tom Rescigno and provides the first practical means of accurately studying nonlinear polyatomic systems. The important aspects of this work are as follows;

- 1) the Complex Kohn Variational Method[14] is used to obtain the scattering cross sections and this method is free of the spurious resonances which are present in other variational formulations of the scattering problem,
- 2) the bound-free and free-free integrals are efficiently computed with a novel adaptive quadrature scheme[15] and
- 3) the MESA electronic structure package is used to generate the optical potential employed in the Kohn method, so a correlated description of the target states can be used in the calculations.

This is an important development as we can now study the scattering processes used in such varied areas as the manufacture of semiconductors and in the design of short-wavelength chemical lasers.

References

1. R.T. Holzmann, "Chemical Rockets", Marcel Dekker, New York, 1969, pg 266
2. ibid, pg 400
3. W.N. Lipscomb, "Boron Hydrides", W.A. Benjamin, New York, 1963;
R. Cimiraglia, M. Persico, J. Tomasi and O. Charkin, J. Comp. Chem. 5,263(1984);
K. Hashimoto, Y. Osamura and S. Iwata, Chem. Soc. Japan 11,1377(1986)
4. M. Page, G.F. Adams, J.S. Binkley and C. Melius, J. Phys. Chem. 91,2675(1987)
5. J.P. Dill, P.v.R. Schleyer and J. Pople, J. Amer. Chem. Soc. 97,3402(1975)
6. N.H. Langton, "Rocket Propulsion", American Elsevier, New York, 1970, pg 46.
7. D. Armstrong, Theor. Chim. Acta 60,159(1981)
8. P.G. Jasien and C.E. Dykstra, J. Amer. Chem. Soc. 107,1891(1985)
9. MESA is a vectorized electronic structure package written by P. Saxe, B. Lengsfeld, M. Page and R. Martin
10. J. Rice and R. Amos, Chem. Phys. Letters 122,585(1985)
11. B.H. Lengsfeld III, P. Saxe and D.R. Yarkony, J. Chem. Phys. 81,4549(1984)
12. M. Page, P. Saxe, G. Adams and B.H. Lengsfeld III, J. Chem. Phys. 81,434(1984);
N.C. Handy and H.F. Schaefer III, J. Chem. Phys. 81,5031(1985)
13. J. Olsen, B. Roos, P. Jorgensen and H.J.A. Jensen, J. Chem. Phys. 89,2185(1988);
P.E.M. Seigbahn, Chem. Phys. Letters 109,417(1984);
P.J. Knowles and N.C. Handy, Chem. Phys. Letters 111,315(1984);
M.D. Gould and G.S. Chandler, Int. J. Quant. Chem. 25,1089(1984)
14. W.H. Miller and B.M.D.D. Jansen op der Haar, J. Chem. Phys. 86,6213(1987);
C.W. McCurdy, T.N. Rescigno and B.I. Schneider, Phys. Rev. A 36, 2061(1987)
15. C.W. McCurdy and T.N. Rescigno, Phys. Rev. A (in press)

Table 1. Summary of B_2H_2 MCSCF Results*

State	Total Energy atomic units	Relative Energy kcal/mole	Geometry
linear triplet $3\Sigma^-$	-50.5029	0.00	$R_{B-B}=1.528$ Å $R_{B-H}=1.192$ Å
linear singlet 1Δ	-50.4762	16.8	$R_{B-B}=1.548$ Å $R_{B-H}=1.190$ Å
bridged singlet $1A_1$	-50.4400	39.5	$R_{B-B}=1.524$ Å $R_{B-H}=1.382$ Å $\angle H-B-B = 56.53^\circ$ $\angle H-B-B-H = 104.4^\circ$

* Full Valence MCSCF (8 electrons in 10 orbitals)

Triplet: 20790 CSFs in C1 symmetry

Singlet: 13860 CSFs in C1 symmetry

A 4s3p1d basis was employed on B and a 2s1p basis on H

Table 2. Summary of Be_2H_2 MCSCF Results*

State	Total Energy atomic units	Relative Energy kcal/mole	Geometry
linear singlet $1\Sigma^+$	-30.4524	0.00	$R_{Be-Be}=2.065$ Å $R_{Be-H}=1.352$ Å
bridged singlet $1A_1$	-30.4040	30.5	$R_{Be-Be}=1.524$ Å $R_{Be-H}=1.382$ Å $\angle H-Be-Be = 56.53^\circ$ $\angle H-Be-Be-H = 104.4^\circ$

* Full Valence MCSCF (6 electrons in 10 orbitals)

Triplet: 6930 CSFs in C1 symmetry

Singlet: 4950 CSFs in C1 symmetry

A 4s3p2d basis was employed on Be and a 2s1p basis on H

NEW HIGH ENERGY DENSITY SMALL RING SYSTEMS*

Koop Lammertsma

*Department of Chemistry, University of Alabama at Birmingham
Birmingham, Alabama 35294*

.....

Theoretical ab initio MO calculations have been performed on small molecular clusters to identify candidates for advanced chemical propulsion systems. In the search for high energy density systems with high specific impuls we concentrate on new classes of tetraatomic compounds composed mainly of the light elements of the periodic table. In our studies the planar rhombic structure has a central place. These rhombic molecules are highly strained, have no hydrogens, and consequently are of high energy. We also concentrate on the differences between rhombic and tetrahedral species because of their structural properties. These atomic and molecular systems that are elemental, binary, and ternary clusters have important structural properties in the context of both densely packed high energy solid materials and fuel additives.

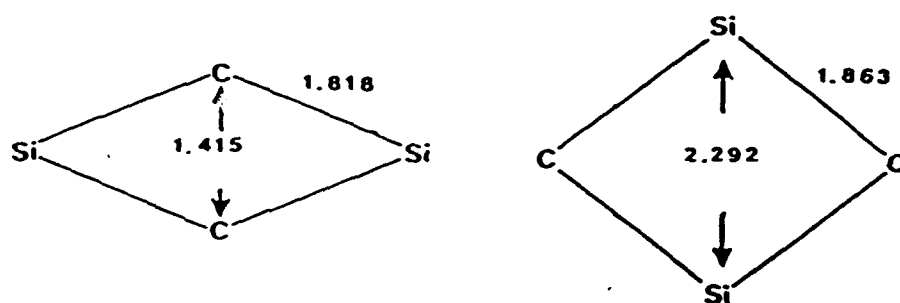
The calculations have been carried out using Pople's GAUSSIAN programs and Bader's topological electron density analysis on a cluster of VAX computers and a CRAY X-MP/24.

That the structural and electronic detail of rhombic structures is indeed special can be illustrated in a series of dicarbides and diborides. For example, in the rhombic (D_{2h}) structures. C_2Li_2 , C_2Be_2 , C_2B_2 , C_4 , $C_4H_2^{2+}$ the transannular bond steadily increases from 1.249Å in the ionically bonded C_2Li_2 to 1.593Å in diprotonated C_4 (HF/6-31G*). Analyses of the electron density and the topological features of C_4 reveal that the center of the short transannular C-C bond of 1.457Å in C_4 is close to a catastrophe point. Optimization at the MP2/6-31G* renders a slightly larger separation of 1.523Å and at this level of theory *the two carbons are*

* Supported under Contract F04611-86-K-0073

no longer directly bonded! This is shown by the gradient vector field and the Laplacian of the charge densities overlaid by the molecular graphs. (Figure 1) The lack of bonding despite the 1.523 Å short C-C separation results from 4c-2e π -bonding and a non-bonding σ -HOMO. From heats of hydrogenation a heat of formation of 228 kcal/mol is estimated for C_4 .

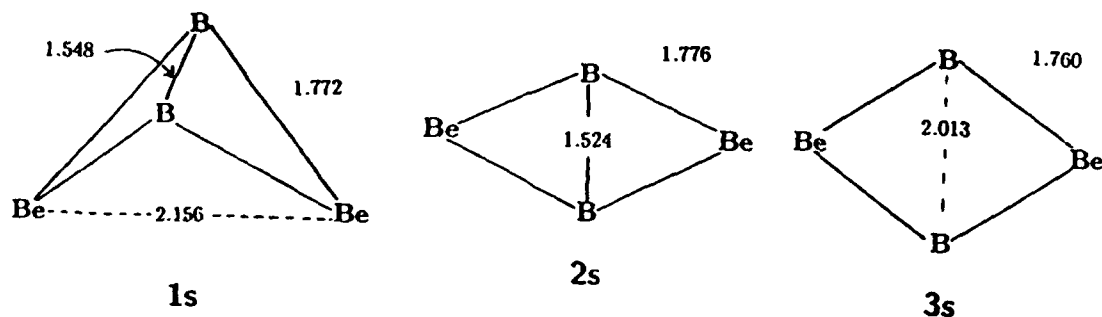
We revisited our earlier reported study on C_2Si_2 . For this system two D_{2h} structures were noted i.e., one with a short 1.415 Å C-C separation, the global C_2Si_2 minimum and a 84.5 kcal/mol (MP2/6-31G*) higher energy structure with a 2.292 Å large SiSi distance. It appears that these two structures are bond-stretch isomers that have forbidden interconversion pathways. Whereas the global minimum has a strong C-C bond this is not the case in the other isomer, which therefore is a high energy species.



Our study on 26 dicarbides show that all are equilibrium structures, although not necessarily the global minima. Interestingly, for these rhombics that have the ligands Li, Be, BeH^- , BH, C, CH^+ , AlH, and Si, the average C-C bond is only 1.449 Å. Similarly, we studied 28 rhombic diborides of which 21 are minima at HF/6-31G*. The average B-B bond is only 1.763 Å. Diborides have a tendency to form 'tetrahedral' structures only if light elements are involved. Thus, of 24 structures investigated three are minima and these have the ligands Li, Be, and BeH^- .

The structural and electronic detail of the electron deficient dicarbides is much more complex than that for the corresponding diborides like B_2Li_2 and B_2Be_2 . The study of the 10 valence electron diberyllium diboride (B_2Be_2) potential energy hypersurface yields a singlet tetrahedral-like form **1s** as the global minimum at the HF and MP2/6-31G* levels of theory. At MP4/6-31G* the energy difference of **1s** with any other isomer is at least 30 kcal/mol. The topological electron density analysis, based on the theory of atoms in molecules, shows **1s** to have its Be atoms polar π -complexed to the B-B bond with an angle of 80.1° between the π -planes.

The inversion barrier ($1s \rightleftharpoons 2s \rightleftharpoons 1s$) amounts to 11.7 (MP4 + ZPE) and 15.5 (MCSCF) kcal/mol. The 'bond-stretch' isomerism between the D_{2h} structures $2s$ and $3s$ reveals the topological feature of secondary 'ripple' bonds. (Figure 2) All B_2Be_2 structures show a short B-B bond that contains a non-nuclear attractor.



The rhombic and tetrahedral-like B_2Li_2 isomers are of similar energy. Interestingly, the topology of the rhombic form is more complex than is the case for B_2Be_2 . The observation of multiple bond paths between the two boron atoms even at MP2/6-31+G* may be due to the ionicity of the system.

We also investigated the hydrogenation of some of these systems by full potential energy surface scans. As may have been surmized from the Laplacian of B_2Be_2 the two tetrahedral-like or butterfly forms with the hydrogens on either both borons or on both berylliums as the most stable. The energy difference is 15.1 kcal/mol (MP4/6-31G*) is favor of the boron hydrogenated form.

Interaction of Si with the light elements Be and Mg gives stable triatomic system. The triangular isomers for Si_2Be , Si_2Mg , $SiBe_2$, $SiMg_2$, and $SiBeMg$ are energetically favored at the MP2/6-31G* over linear isomers, which in all cases have several close lying electronic states.

The study of the tetraatomic Li, Be, B, and C cluster was directed to obtain more insight in the elemental bonding. While three lithiums have bond paths to a common non-nuclear attractor, sets of both two berylliums and two borons share a pseudo-atom, but in the carbon based compounds the elements are directly bonded. This pattern remains in binary and ternary systems giving complex bonding patterns in the light clusters like B_2Li_2 .

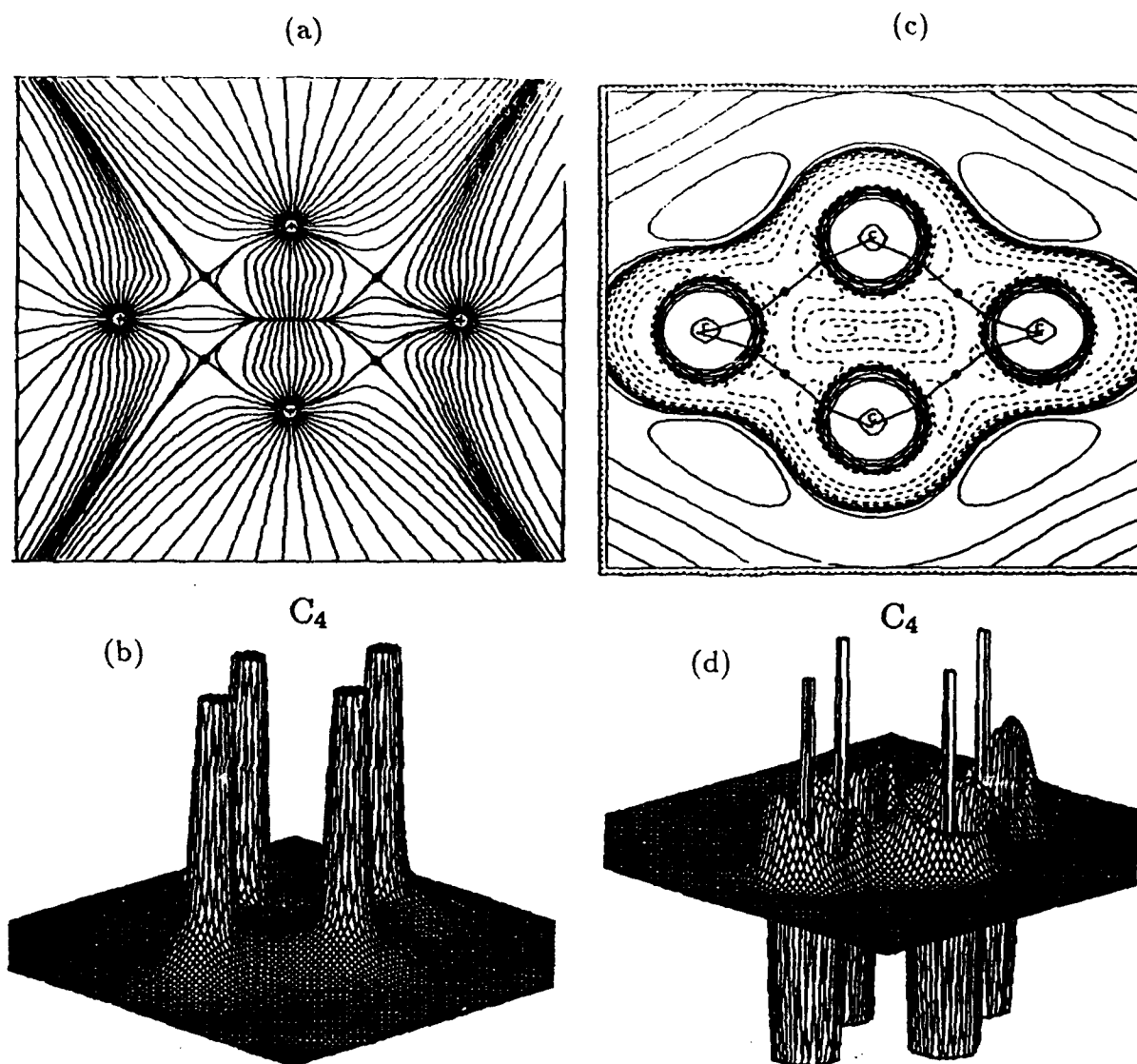


Figure 1. Display of (a) the gradient vector field $\nabla\rho$, (b) its relief map, (c) the contour map of the Laplacian $\nabla^2\rho$, and (d) its relief map at MP2/6-31G*.

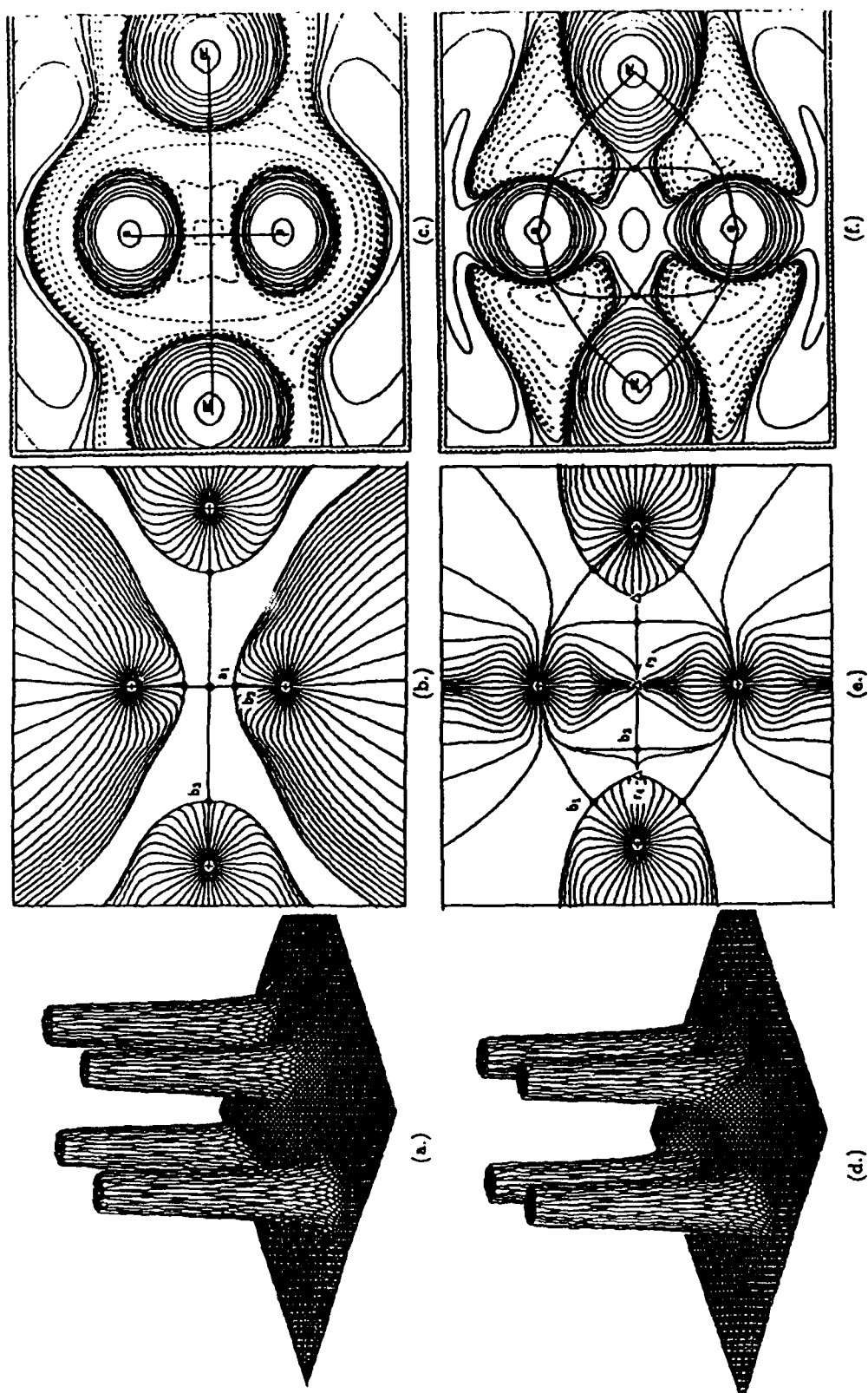


Figure 2. Display of (a) the relief map of ρ , (b) the gradient vector field $\nabla \rho$, and (c) the contour map of the Laplacian $\nabla^2 \rho$ of 2s at MP2/6-31G*. The corresponding displays of ρ , $\nabla \rho$, and $\nabla^2 \rho$ for 3s at HF/6-31G* are shown in (d), (e), and (f), respectively.

Computational Studies of Metal Clusters

George F. Adams

US Army Ballistic Research Laboratory

Aberdeen Proving Ground, MD

Introduction:

Lammertama and coworkers have reported at the last two technical meetings on high energy density materials results of computational studies on small molecular clusters, especially tetratomic clusters of low molecular weight. Structures for the clusters were predicted initially using Hartree-Fock methods, but structures computed using second-order perturbation theory methods have now been reported, as well. In addition, vibrational analyses were performed to determine the nature of the stationary points. While the calculations produced an enormous quantity of data on tetratomic clusters, especially rhombic structures, it was felt that a collaborative effort utilizing multiconfiguration methods would extend the database in a meaningful way. In addition, we felt that a perturbation theory technique used in our laboratory could provide accurate predictions of the cluster heats of formation.

With the results provided by Lammertama as a starting point, we have performed a series of ab initio calculations on the B_2Li_2 and B_2Be_2 molecules. These include SCF and CASSCF optimizations of the structures, determination of the Hessian matrix for each stationary point, and the computation of the heat of formation for several of the isomers. In the following sections we describe the third-order perturbation theory technique employed by Adams and Page to compute atomization energies for sigma-bonded systems, the results available from the CASSCF calculations, and some conclusions gleaned from the data presently available.

Methods and Facilities.

The Ballistic Research possesses outstanding computational facilities for the quantum chemical study of materials. Two Cray Computers are installed at the BRL: an X-MP/48 with 128-million words of SSD, and a Cray 2, with 256 million words of high-speed memory. In addition, the laboratory has acquired about a dozen supermini computers (Alliant FX8's and Convex C1's), one of which is dedicated to the quantum chemistry

research effort. The supercomputers are accessed via the BRLNET, currently being upgraded to an 80-megabit per second fiber-optic ring. The quantum chemical computations are performed using one of three software packages. Routine studies of structures and molecular properties are done with CADPAC (Version 4). Multiconfiguration structural studies, and more advanced computations, are performed using MESA, while studies of the properties of electronic excited states are performed using BROOKLYN (a tentative name). The computations described in this note were all performed with either CADPAC or MESA. In the following section, we describe the technique we've developed to estimate molecular energy storage using the (relatively) inexpensive third-order perturbation theory method, and we provide estimates of the heat of formation for several of the metal clusters. We then describe the results of the CASSCF computations on several of these clusters. For the most part, the calculations were performed using the 6-311G+ basis set. This set was substantially augmented for the perturbation theory calculations.

MP3 Atomization Energies.

With the development of software efficiently implementing quantum chemical techniques that employ energy gradient and Hessian data, and the concurrent access to modern supercomputers, systematic studies of molecular structures and properties have become routine. Recently several groups have reported efforts to compute accurate values of molecular heats of formation. Pople and coworkers described fourth-order perturbation theory calculations for a series of hydrides, attaining excellent agreement between the predicted and experimental atomization energies.⁽¹⁾ Subsequently, Page, et al, used fourth-order perturbation theory to compute the dimerization energy of borane, BH₃. Related to these efforts to compute accurate energies were computations by Handy and coworkers that used extended basis sets in a series of molecular property computations at various levels of theory. The rationale was to isolate basis set effects from the effect of method variation. We have adopted Handy's philosophy to study the effect of method on the prediction of atomization energies. In particular, we have investigated the use of the isogyric reaction technique described by Pople, et al, in reference 1. We compared the results with direct computation of the atomization process, with both a full correlation treatment, and using the frozen core approximation. Table 1 contains the data for the fourth-order perturbation theory results.

Table 1. MP4 Predictions of Atomization Energies (Units: Hartrees)

Molecule	Full MP4		Frozen Core MP4	
	Direct	Isogyric	Direct	Isogyric
BH	0.13336	0.13566
BH2	0.27064	0.27294
BH3	0.44674	0.45134	0.44425	0.44884
CH4	0.66233	0.66923	0.66201	0.66891
NH3	0.46822	0.47512	0.46538	0.47228
H2O	0.36937	0.37397	0.36755	0.37215
B2H6	0.95740	0.96660

In every case, the isogyric computation predicted a larger atomization energy than did the direct method. This is expected, since the isogyric method scales the computed reaction energy by substituting the known value of the hydrogen, it is expected that this should be the case. Further, as expected, the frozen core atomization energies are lower than those obtained using the full correlation treatment. The second table displays more atomization energy data, including the full fourth-order calculations, the results of an isogyric analysis using the results of third-order perturbation theory, and experimental data.

Table 2. Theoretical and Experimental Atomization Energies (kcal/mole)

Molecule	SDTQ-MP4		MP3	Experiment
	Direct	Isogyric		
BH	83.7	85.1	85.5	82.8
BH3	280.3	283.2	285.2	280.6
CH4	415.6	419.8	422.5	419.8
NH3	293.8	298.1	296.9	297.2
H2O	231.8	234.7	231.8	232.2
OH	106.2	107.6	106.9	106.6

The most obvious result of these computations is the systematic difference in predicted atomization energy at each level of theory. Isogyric analysis always predicts a larger atomization energy than does a direct computation. The magnitude of the difference scales with the number of hydrogen molecules needed to write the isogyric reaction. It is also true that the third-order results, obtained using the isogyric analysis, predict results that agree closely with the experimental results. This would not be the case, however, for molecules containing multiple bonds. Our results for the oxygen molecule and BO demonstrate this conclusively. Nonetheless, it is clear that the relatively inexpensive MP3 method is competitive with the full-fourth order result for sigma-bonded systems. While the test set is small, there is a strong indication that this technique should provide reasonably

accurate predictions for many molecular systems. We will address this point further in our discussion of metal clusters.

Small Metal Clusters.

Lammertsma and coworkers have identified stable structures for numerous small ring compounds. The tetratomic isomers of B_2Be_2 and B_2Li_2 are thought to be potentially useful in energetic materials applications. When dealing small boron containing compounds, however, one needs to be conscious of the possibility that even high-quality ab initio calculations based upon a single-reference function can predict stable structures for species that are, in fact, not stable when investigated with a multireference technique. At the 1988 symposium we reported two isomers of B_3H_3 which were predicted by large basis set SCF calculations to be stable isomers. Investigation with a complete active space SCF demonstrated that one of the isomers was, in fact, a transition state. In collaboration with Professor Lammertsma, we have performed a series of independent ab initio computations on several isomers of B_2Li_2 and B_2Be_2 . Using CADPAC (the Cambridge Analytical Derivatives Package), we have carried out SCF and MP2 optimizations of the isomers of the species. Our results agree extremely well with Lammertsma's results, although we used a slightly larger basis set than used in the previous calculations. We added a relatively diffuse function to the 631G* basis used in his initial work. We have also performed perturbation theory calculations using the extended basis sets used in our thermochemical studies described above.

We have also used the MESA codes to perform CASSCF computations on these isomers. At this writing, the data represent a potpourri of information, rather than a large systematic study. Our initial studies on B_2Li_2 were performed using a standard double zeta plus polarization basis set. For that basis, SCF calculations predicted that both the tetragonal and rhombic forms were stable minima. We then investigated the potential energy surfaces using 6-in-6 CASSCF wavefunctions. In each case, a stable structure was predicted, but the lowest vibrational eigenvalue was extremely small. There were two shortcomings of those computations. Both the basis set and the CASSCF expansion were too small. We have repeated these calculations using the 6-311G* basis set, and using both 6-in-8 and 8-in-8 CASSCF's. In each case, the tetragonal form is predicted to be stable, but the planar rhombic isomer is predicted to be a transition state. Unfortunately, the CASSCF force constant calculations used the finite-field technique rather than an analytic evaluation of the second derivatives, so we are not convinced that the rhombic form is an unstable isomer.

We have had computational problems with the B_2Be_2 isomers, especially with the larger basis set. We have verified that Lammertsma's characterization of the squashed rhombic isomer as a transition state is correct. It is also clear that the tetragonal isomer is more strongly bound than the rhombic

isomer. Both isomers are predicted to be stable structures by our large basis set SCF calculations.

Finally, we have performed third-order perturbation theory calculations using extended basis sets for the B₂Be₂ isomers. These data will provide the means to estimate the heats of formation of these novel species.

Theoretical and Experimental Investigations of Dications

W.C. Lineberger, S.R. Leone, S.V. O'Neil

Joint Institute for Laboratory Astrophysics
University of Colorado and
National Institute for Standards and Technology
Boulder, Colorado 80309-0440

In theoretical investigations of molecular dications, Jörg Senekowitsch and S.V. O'Neil have begun a systematic *ab initio* survey of the first and second row diatomic dications. These species are interesting because in the simplest picture the lowest potential curve, arising from the $A^+ + B^+$ asymptote, will be strongly repulsive, while a higher lying potential curve arising from the charge transfer asymptote $A + B^{++}$ is expected to be attractive, at least at long range, because of the polarization interaction. If the symmetry of these two states is the same, then we expect an avoided crossing, with the possibility of a well in the upper state and a lower state potential consisting of a local minimum, a barrier, and an asymptotically free region. In cases where the energy difference $E(A^+ + B^{++}) - E(A^+ + B^+)$ is large, these two potential minima might lie at energies high above the dissociated atom limit, and thus store substantial amounts of energy. The practical importance of this picture will depend upon the precise energetics and upon the details of the various destruction channels such as barrier tunnelling, radiative decay to any lower lying electronic states, or charge transfer with neutrals.

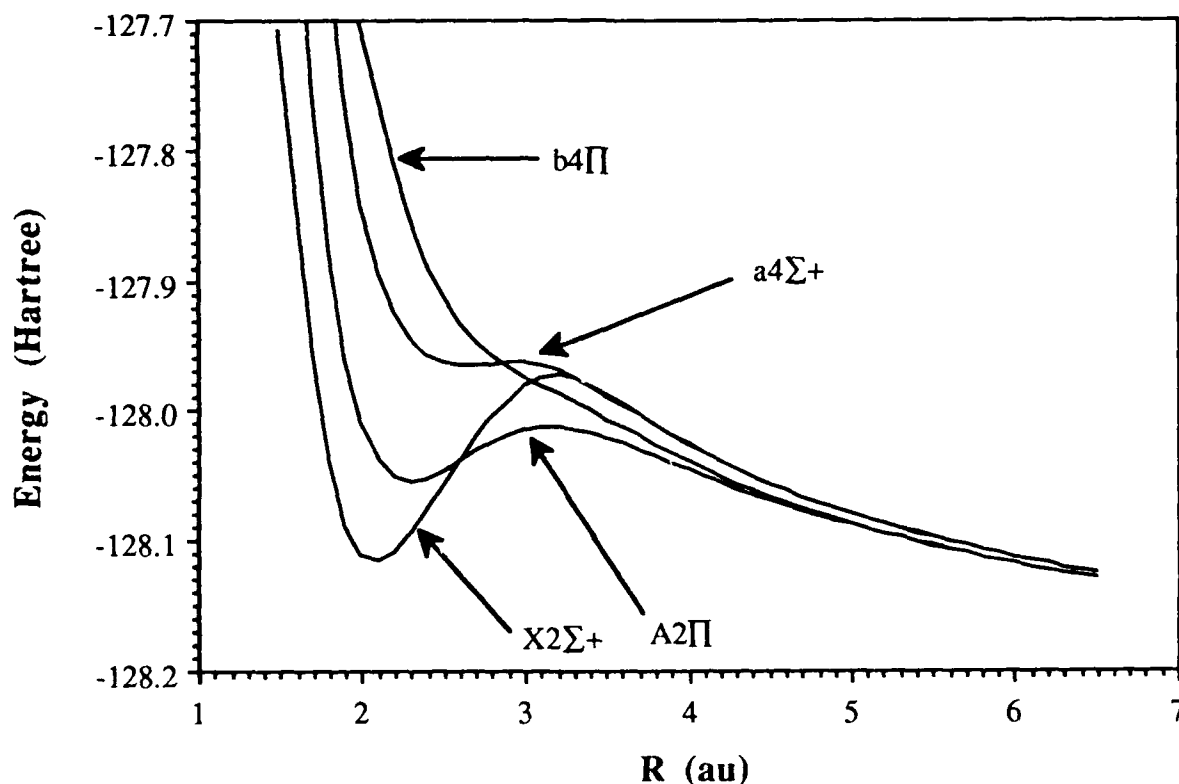
A first stage, focusing on the hydrides, employs a basis set flexible enough to describe the neutral atoms and their mono- and dications, and a state-averaged valence CAS-SCF wavefunction.¹ CAS is especially useful in this context because it automatically includes the most important configurations of all the low-lying electronic states, while the state averaging within each symmetry is essential because of the physical importance of avoided crossings in this problem. With these techniques we have mapped the general features of the lowest several electronic states of the relevant symmetries. Although in some cases details await verification at the CI level, results to date indicate that with one exception the low-lying potential curves of first row hydrides show no deep minima, while the second row hydrides such as MgH and SiH exhibit potential wells with a barrier to dissociation that is high and broad enough to support quasi-bound vibrational levels. In such favorable cases, we find the lowest vibrational levels to have long tunnelling lifetimes (years), while the higher vibrational levels tunnel free in $\leq 10^{-6}$ seconds.

One general conclusion from these early results is that for most hydrides, the picture of a potential well resulting from an avoided curve crossing of $H^+ + A^+$ and HA^{++} states is probably an oversimplification. For example, we have found that if the asymptotic energy difference $E(A + B^{++}) - E(A^+ + B^+)$ is too large, then even in the absence of intervening electronic states the anticipated curve crossing is so weak that the anticipated potential minima never develop.

Continuing the initial qualitative survey with similar techniques, we have found a number of first and second row oxides with long-lived quasi-bound vibrational levels, a result anticipated from isoelectronic arguments. Although a

number of these were previously characterized, several systems are accurately characterized for the first time. An example is NO^{++} , which should be an ideal candidate for study by the collaborating experimental groups. The CAS-SCF potential curves for this dication are shown below.

NO^{++} CAS-SCF Potential Curves



In related experimental investigations, the high resolution spectroscopic studies of dications will be carried out using a slightly modified version of the coaxial ion-laser beam spectrometer² used in Lineberger's laboratory. The instrument already contains the basic analyzing electric and magnetic fields required to identify dications unambiguously. Several substantial modifications required to make this instrument more suitable for dication spectroscopy are currently underway.

First, our neutral jet-electron beam ion source will be slightly modified to afford efficient productions of cations (and some dications) by electron impact. The major change is a significant improvement in pumping speed. Second, a gas charge-stripping cell is being added in the separately pumped region which provides angular collimation for the coaxial interaction region. When dications are produced by charge-stripping at this cell, then they can be unambiguously identified and

analyzed by the subsequent electric quadrupole deflector. Third, the detection systems, which had been optimized purely for photodetachment products, must be redesigned. The exit quadrupole deflector apertures, and a new ion detection system will replace the present Faraday cage. A smaller Faraday cage will collect unreacted dications, and separate particle multipliers will detect the ionic photodissociation products. The separate ion detectors permits the use of coincidence techniques to discriminate against stray unreacted dications. As in the case of negative ions, we continue to maintain the capability of detecting neutral products (should any be formed!) in the dication photoabsorption process.

Finally, many of the interesting experiments (and especially some of the first experiments planned) require intense laser radiation in the near infrared spectral region for which dye laser systems are difficult, inefficient or unavailable. A new Ti:sapphire laser will be utilized to fill this important spectral gap.

The systems to be studied first will be determined in part by the calculation of ONeil, *et al.* and the ion production and stability investigations of Leone. The first experiments to map out the potential energy surfaces for dications will be carried out on NO^{++} . This dication is isoelectronic with a well-studied favorite of the Lineberger group, C_2 . As Fig. 1 shows, the calculations of Senekowitsch and ONeil indicate that NO^{++} is an especially attractive target for first studies utilizing electronic excitation. The dication can be made in significant quantities by 100 eV electron impact on NO, and transitions from the ground $^2\Sigma$ to the excited $^2\Pi$ should be readily detectable and provide a direct mapping of the excited state potential energy surface. While the exact energies are not known, the studies by Hamdan and Brenton² and the calculations by Senekowitsch give a good guide to the location to the $^2\Pi$ state, and the availability of the Ti:sapphire laser ensures that we will have spectral coverage in the proper region. The studies of Hamdan and Brenton³ also indicate that NO^{++} is formed in at least seven vibrational states having up to 1.6 eV of internal excitation. We will be able to map out detailed vibrational levels of at least one, and possibly both, of these low lying states. We may be able to determine the structure of the $^2\Pi$ state by observing the predissociation from the quasibound levels. Alternately, if only the highest vibrational levels of the $^2\Pi$ state are sufficiently short lived to give a one-photon signal, then we can study transitions to that single state from a variety of initial levels of the $^2\Sigma$ state, providing a detailed mapping of the ground state. This is a situation very reminiscent of C_2 , in that it provides numerous opportunities for high resolution investigation. The next step in experimental sophistication will be to utilize a high intensity tunable infrared radiation in a double resonance experiment to obtain more information on the ground state potential surface. The double resonance experiments will require very high intensity infrared radiation, and will necessitate the use of an infrared buildup cavity in order to be successful. This buildup cavity is currently being designed. Finally, we plan to search for systems which are more likely to be stable against charge transfer in a rare gas environment, such as MgH^{++} .

S. Leone, together with P. Miller and S. Rogers, are developing two potential sources to form doubly charged molecular ions, which will then be used to study collisional processes of these species with other gases. First, a time-of-flight (TOF)

mass spectrometer has been constructed and made operational, in order to detect the doubly charged species after their formation. This TOF mass spectrometer is installed in a single collision ion apparatus, which will be used to study the collision dynamics of the doubly charge species.

One method of production of the doubly charged molecular ions centers on the use of high powered tunable pulsed lasers to strip electrons selectively from molecules by resonant multiphoton ionization (MPI). Two Nd:YAG lasers and three dye lasers, together with nonlinear frequency generation, are being made available for these experiments. Initial experiments designed to test the mass spectrometer and the electronics of the experimental system are concentrating on the MPI of benzene to form C^+ , which will then be resonantly ionized with another laser at 206 nm to form C^{++} . After these tests are completed successfully, we will first attempt to doubly ionize nitrogen molecules by a three laser scheme. A 3+1 resonant ionization will form N_2^+ , a second laser will pump this ion to the Rydberg-like molecular C state, and then a third laser will be used to doubly ionize the molecule. The use of the $^{15}N^{14}N$ isotope in the early stages of this work will be necessary to verify the production of the doubly charged ion, which will appear at the unique mass of 7.5. Rotational cooling of the nitrogen in a pulsed supersonic expansion will allow better definition of the initial energy in the doubly charge ion.

A second method of preparation of doubly charged molecular ions is based on the extensive experience of Prof. B. Brehm of Hannover, who is a Visiting Fellow in JILA this year. His group has shown that electrons of approximately 100 eV energy produce high percentages of doubly charged molecular ions when impacted on various precursor molecules. Together with Prof. Brehm, we are now designing an ion source to form, extract, and mass select with a quadrupole the doubly charged ions of interest. Reactive collisions and spectroscopy of these ions will then be studied by analysis with the TOF mass spectrometer or laser-induced fluorescence (or laser dissociation), respectively. The new ion source will be housed in a separate differentially pumped chamber of the apparatus, which connects to the main interaction region. This type of ion source has been extremely effective in producing doubly charged ions from stable molecules like ethylene or propene. Modifications to the voltages of the quadrupole mass spectrometer, recently demonstrated by D. Gerlich at Freiburg, will allow the doubly charge ions to be injected with low kinetic energies of a few 100 meV, so that near-thermal energy collision processes can be studied.

References

1. H.-J. Werner and P. Knowles, *J. Chem. Phys.*, **89**, 5803 (1988)
2. U. Hefter, R. D. Mead, P. A. Schulz and W. C. Lineberger, *Phys. Rev. A* **28**, 1429 (1983).
3. M. Hamdan and A. G. Brenton, *Chem. Phys. Lett.* **155**, 321 (1989).

INVESTIGATIONS OF HYPERVALENT COMPOUNDS AS HIGH ENERGY COMPOUNDS

Paul Engelking
Tom Dyke
University of Oregon

John Farley
University of Nevada at Las Vegas

Molecular ions with more bonds than "normal" chemistry allows are being studied spectroscopically. Species specifically targeted for research include SiH_5^- [refs 1-8], CH_5^- [refs 3,10,12,17-29], and NH_4^- [refs 8-16], along the lines which have proven successful [30] in studying HNO^- . Spectroscopic techniques include: visible and UV pulsed dye laser photodestruction spectrometry; IR F-center laser spectroscopy; and IR diode laser techniques. The results of this work will promote our understanding of the structure and energetics of these hypervalent species.

Currently, at the Univ. of Oregon, ions from a Roots-pumped, corona excited supersonic expansion [31] (CESE) produce a space-charge neutralized, molecular beam expansion of low velocity (0.1 eV) ions in the laser interaction region. These ions are monitored by a time-of-flight (TOF) mass spectrometer. At this experimental station, IR diode and UV/visible dye lasers on adjacent optical tables provide tunable photons for the photodissociation and photodetachment of the ions.

At UNLV, a high-velocity (3000 eV) coaxial ion beam photodetachment/photodestruction apparatus uses both F-center and visible lasers. Ions are prepared using either a duoplasmatron [30], electron impact [14], or, most recently, a CESE low temperature ion source.

An example of the type of data obtainable is afforded by the recently completed [30] work on HNO^- . Most of this work was done on the fast ion beam apparatus using a duoplasmatron type source (source temperature 430K). This ion was chosen for study since it could be produced with the existing source while cold sources were being developed for the more exotic SiH_5^- , CH_5^- , and NH_4^- ions, and since it had many of the properties of a true hypervalent species. Binding of H^- to an already stable molecule requires stabilization of the negative charge. This could be obtained by having the charge move away from the hydrogen onto another heavy atom in the molecule. In HNO^- , this may be achieved by having the electron move onto the oxygen. Thus, in bonding of the hydride, one might expect that the molecular ion adjusts towards the right on the continuum of charge reorganization:



The result would be manifest in a strengthening of the HN bond, weakening of the NO bond. This would be seen in the geometry, as obtained through the autodetachment spectrum of this anion.

The completed work on HNO^- confirms this very simple picture of stabilization of bonding by charge reorganization. Details are reported elsewhere [30]. In these studies, an F-center IR laser excites the NH stretch of the anion in the region between 2940 and 3150 cm^{-1} , which subsequently autodetaches. Seven branches are identified and analyzed, the lowest in the $K''=4$ subband, and extending up to the $K''=9$ subband. These transitions are summarized in the stick spectrum, Fig. 1. Two types of doubling occur: spin-rotation doubling apparent in the stick spectrum, and a much finer K-type doubling, shown for $K''=4$ subbands in Fig. 2. This latter, asymmetry doubling allows a measurement of the

difference of the B-C rotational inertial constants. The principal rotational constants for the ground state are $A''=15.233360(380)$, $(B''+B'')/2=1.096829(24)$ and $(B''-C'')/2=0.034424(900)$. The band origin is $2750.7827(53) \text{ cm}^{-1}$.

From the constants of rotation, constraints may be placed upon the possible geometries. There are three parameters: NO bond length, NH bond length, and the bond angle between the two bonds. Without isotopic substitution, the spectroscopic constants give two relations between the geometry constants. Fig. 3 indicates the NH and NO bond lengths that result as a function of assumed bond angle. Also plotted are the parameters for ground state HNO [32] and NO [33] itself, and the previous NO bond length in HNO^- obtained by Ellis and Ellison in fitting their photoelectron spectrum to a progression in O_2 [34]. Strikingly, the NO bond is much larger in the HNO^- anion than in either neutral. This supports the picture of the stabilization of H^- binding to NO by charge transfer to the oxygen, with an accompanying weakening of the NO bond. The second point observed is that the NH bond is also longer than that in HNO, regardless of any assumed bond angle. This would suggest that the charge reorganization is not complete. One more point relevant to the geometry is obtained from noticing that the vibrational frequency for the NH stretch in the ion is still close to that in the neutral (2684 cm^{-1}) [35], which would seem to argue for a short NH bond. From the graph, one sees that short NH bonds correspond to nearly right-angle bonding in the anion.

Line widths are able to give an indication of the lifetimes of the upper states, the upper vibrational levels of the anion. Figure 4 presents the measured linewidths as a function of rotational quantum numbers. As yet, no theory has been formulated to explain these results. This type of information could be very useful in exploring the relative stabilities of various vibrational levels in hypervalent anions.

Extension of the success with the anion HNO^- , which could be made in conventional ion sources, has required development of more exotic cold ion sources. Both the Nevada and the Oregon apparatuses have CESE type ion sources. This technology was originally developed for neutral spectroscopy; it is now being adapted for negative ion generation. Recent source modifications are being made to overcome the defects first seen in the original designs.

Figure 5 shows a mass spectrum from a nozzle expansion source, indicating the production of NH_4^- . We have been able to obtain this ion for about a year now, and it is a dominant ion in the mass spectrum. Unfortunately, total ions from the nozzle sources have been down by 2-3 orders of magnitude from those levels required for a working experiment. In the last six months, the cause of this problem was identified. This difficulty is inherent in all nozzle expansion type ion sources, regardless of the type of excitation.

As the ions and neutrals are skimmed from the expansion, entering the high vacuum region, the electrons are found to rapidly leave the mixture. This happens within 3 mm of the point of skimming. Within 1 cm, the resulting spacecharge expels the ions from the beam axis. This fact is confirmed in our work by observing the ions off-axis, and by careful measurements of the plasma characteristics on axis (Fig. 6). The energy source for the electrons appears to be electronically excited metastables in the neutral molecular beam emanating from the skimmer (emission from these metastables is observable by eye; there is no doubt of their presence). Electrons are ejected by superelastic scattering from the metastables, receiving on the order of 10 eV in a collision.

The solution to this problem is found in extracting ions within a centimeter after skimming. These design modifications are now being completed. A novel feature of the design is the use of a miniaturization of an existing design for a quadrupole ion-beam bender [36] to separate the ions from the background neutral molecular beam. Prelimi-

nary measurements with this new design indicate that ions have increased by 3 orders of magnitude; in the Oregon TOF, saturation of the ion detector occurs! The value of expansion sources for producing fragile negative ions is also confirmed: the negative ions are down by only a factor of five from the levels obtained for positive ions under similar conditions. These improvements now permit studies of NH_4^- , SiH_5^- , and possibly CH_5^- , along the paths shown for HNO^- .

References for "Investigations of Hypervalent Compounds as High Energy Compounds"

- [1] U. Brandemark and P. E. Sigbahn, *Th. Chem. Acta* **66**, 233 (1984).
- [2] P. Baybutt, *Mol. Phys.* **29**, 389 (1975).
- [3] N. M. Vitkovskaya, V. B. Mantsivoda, T. E. Moskovskaya, and M. G. Voronkov, *Int. J. Quantum Chem.* **17**, 299 (1980); Y. L. Frolov, S. G. Shevchenko and M. G. Voronkov, *J. Organometallic Chem.* **292**, 159 (1985).
- [4] M. S. Gordon, L. P. Davis, L. W. Burggraf, and R. Damrauer, *J. Am. Chem. Soc.* **108**, 7889 (1986).
- [5] F. Keil and R. Ahlrichs, *Chem. Phys.* **8**, 384 (1975).
- [6] D. L. Wilhite and L. Spialter, *J. Am. Chem. Soc.* **95**, 2100 (1973).
- [7] D. J. Hadjasz and R. R. Squires, *J. Am. Chem. Soc.* **108**, 3139 (1986).
- [8] J. A. Deiters and R. R. Holmes, *J. Am. Chem. Soc.* **109**, 1692 (1987).
- [9] J. V. Ortiz, *J. Chem. Phys.* **87**, 3557 (1987).
- [10] C. D. Ritchie and H. F. King, *J. Am. Chem. Soc.* **90**, 838 (1968).
- [11] J. Kalcher, P. Rosmus, and M. Quack, *Can. J. Phys.* **62**, 1323 (1984).
- [12] D. Cremer and E. Kraka, *J. Phys. Chem.* **90**, 33 (1986).
- [13] W. DeLange and N. M. Nibberling, *Int. J. Mass Spectr. Ion Phys.* **80**, 201 (1987).
- [14] J. V. Coc, J. T. Snodgrass, C. B. Freidhoff, K. N. McHugh, and K. H. Bowen, *J. Chem. Phys.* **83**, 3169 (1985).
- [15] M. Gutowski, J. Simons, R. Hernandez, and H. L. Taylor, *J. Phys. Chem.* **92**, 6179 (1988).
- [16] H. Cardy, C. Larrieu, and A. Dargelos, *Chem. Phys. Lett.* **131**, 507 (1986).
- [17] T. Yonezawa, H. Nakatsuji, and H. Kato, *J. Am. Chem. Soc.* **90**, 1239 (1968).
- [18] J. L. Gole, *Chem. Phys. Lett.* **3**, 577 (1969); **4**, 408 (1969).
- [19] W. T. Van der Lugt and P. Ros, *Chem. Phys. Lett.* **4**, 389 (1969).
- [20] N. L. Allinger, J. C. Tai, and F. T. Wu, *J. Am. Chem. Soc.* **92**, 579 (1970).

- [21] C. D. Ritchie and G. A. Chappell, *J. Am. Chem. Soc.* 92, 1819 (1970).
- [22] J. J. Mulder and J. S. Wright, *Chem. Phys. Lett.* 5, 445 (1970).
- [23] J. P. Lowe, *J. Am. Chem. Soc.* 93, 301 (1971).
- [24] K. Ishida, K. Moroi,uma, A. J. Komornicki, *J. Chem. Phys.* 66, 2153 (1977).
- [25] A. Dedieu and A. Veillard, *J. Am. Chem. Soc.* 94, 6730 (1972).
- [26] V. Dyczmons W. Kutzelnigg, *Theor. Chim. Acta (Berlin)* 33, 239 (1974).
- [27] P. Cremaschi and M. Simonetta, *Theor. Chim. Acta (Berlin)* 37, 341 (1975).
- [28] C. P. Dwivedi, *Ind. J. Phys.* 58B, 69 (1984).
- [29] G. D. Mahajan and B. M. Deb, *Ind. J. Pure and Appl. Phys.* 20, 453 (1982).
- [30] H. C. Miller, J. L. Hardwick and J. W. Farley, *J. Mol. Spect.* (Accepted).
- [31] A. T. Droege and P. C. Engelking, *Chem. Phys. Lett.* 96, 316 (1983); P. C. Engelking, *Rev. Sci. Instrum.* 57, 2277 (1986).
- [32] F. W. Dalby, *Can. J. Phys.* 36, 1336 (1958).
- [33] Johns, Reid, Lepard, *J. Mol. Spectr.* 65, 155 (1977); F. J. Lovas and E. J. Tiemann, *J. Phys. Chem. Ref. Data* 3, 609 (1974).
- [34] H. B. Ellis and G. B. Ellison, *J. Chem. Phys.* 78, 6541 (1983).
- [35] J. W. C. Johns, A. R. McKellar, and E. Weinberger, *Can. J. Phys.* 61, 1106 (1983).
- [36] J. W. Farley, *Rev. Sci. Instrum.* 56, 1934 (1985).

FIGURE 1

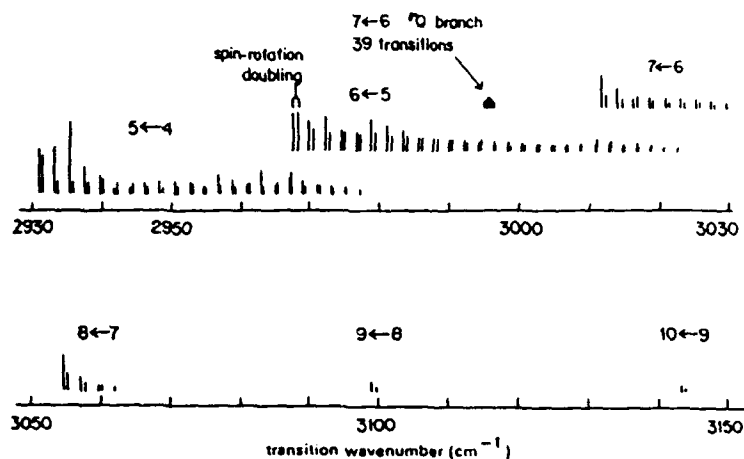


Figure 1. Stick spectrum of the measured transitions in the ν_1 band of HNO^- . The sub-bands are labeled with the appropriate K_a quantum numbers. All are R transitions except for the indicated Q sub-band.

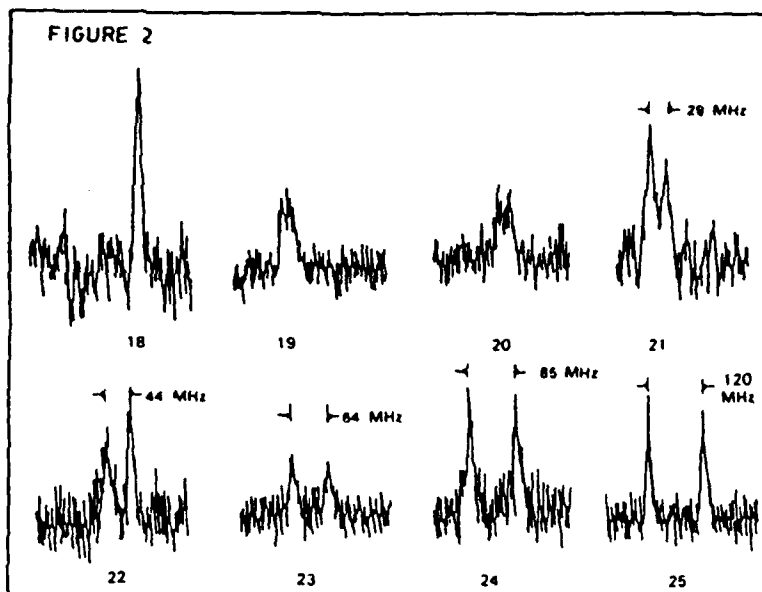


Figure 2. K-type doubling of the R_4 branch of HNO^- as a function of N . Only the F_1 branch is shown; the splitting of the F_2 branch is almost identical.

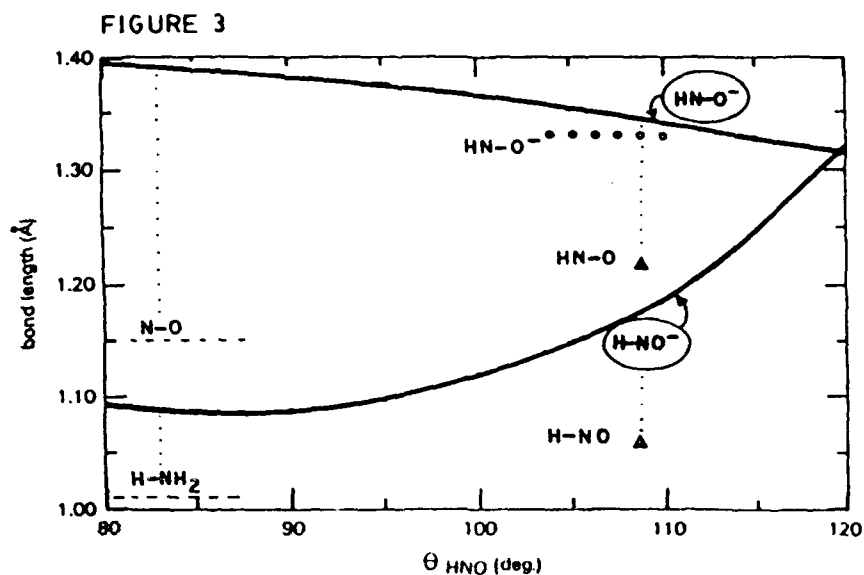


Figure 3. Permissible HNO^- geometries: bond lengths as a function of bond angle (heavy lines). Also shown are the HNO neutral bond lengths (triangles, ref. 32), the previous estimate of the N-O bond length in the anion (circles, ref. 34), along with typical bond lengths in neutral NH_3 and NO .

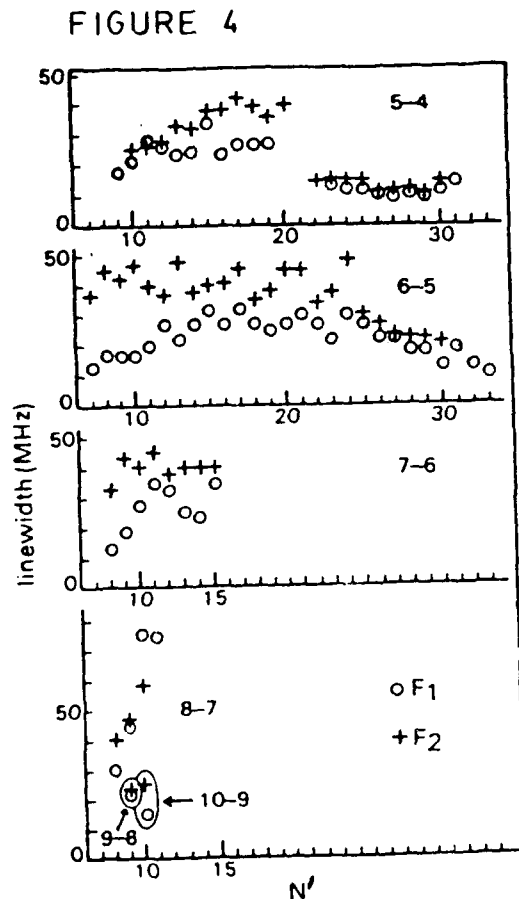


Figure 4. Autodetachment widths as a function of rotational quantum number N' . Lifetimes are obtained from inverse widths.

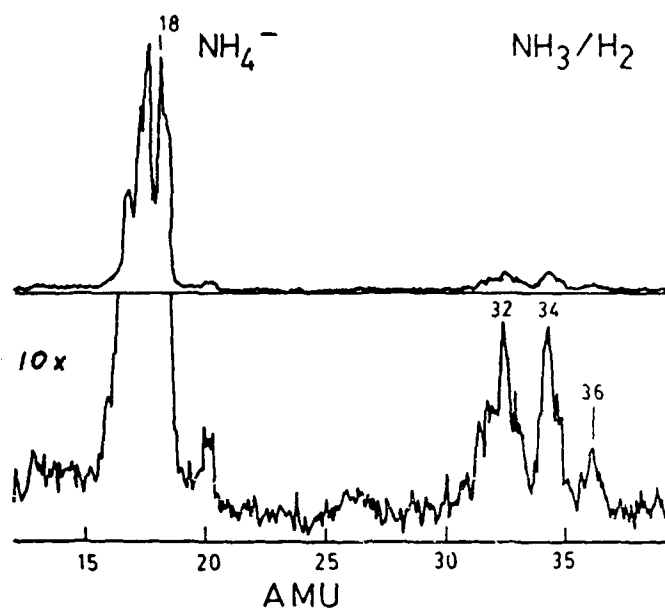


Figure 5. Mass spectrum showing NH_4^- anion (mass 18) prepared in a nozzle expansion of H_2 and ammonia.

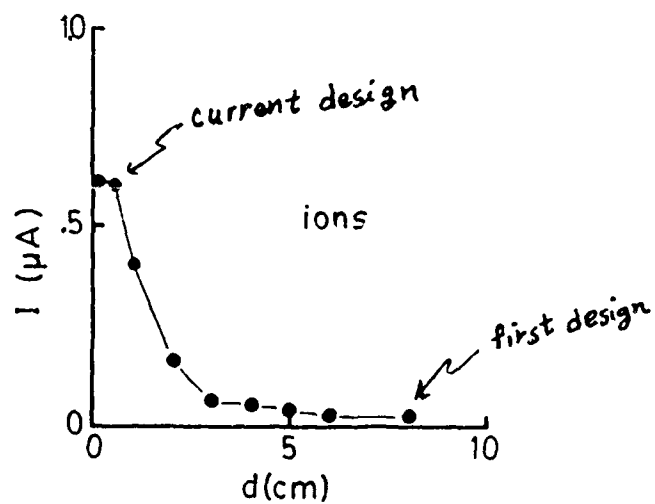


Figure 6. Ions found on axis in plasma beam, as a function of distance from skimmer, d . Measurements made with a plasma probe. Comparison of older and newer design points is shown.

Laser and Fourier Transform Spectroscopy
of Novel Propellant Molecules

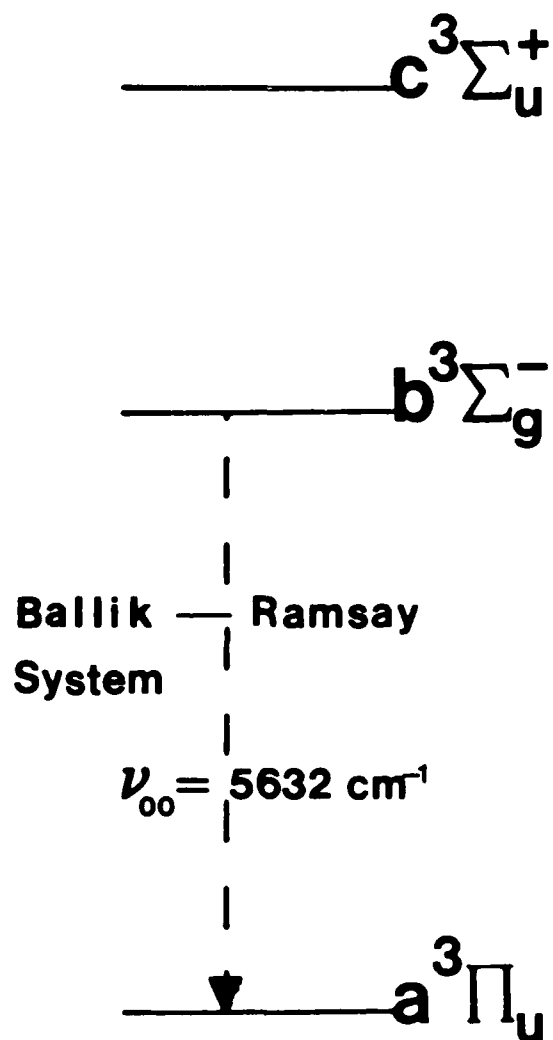
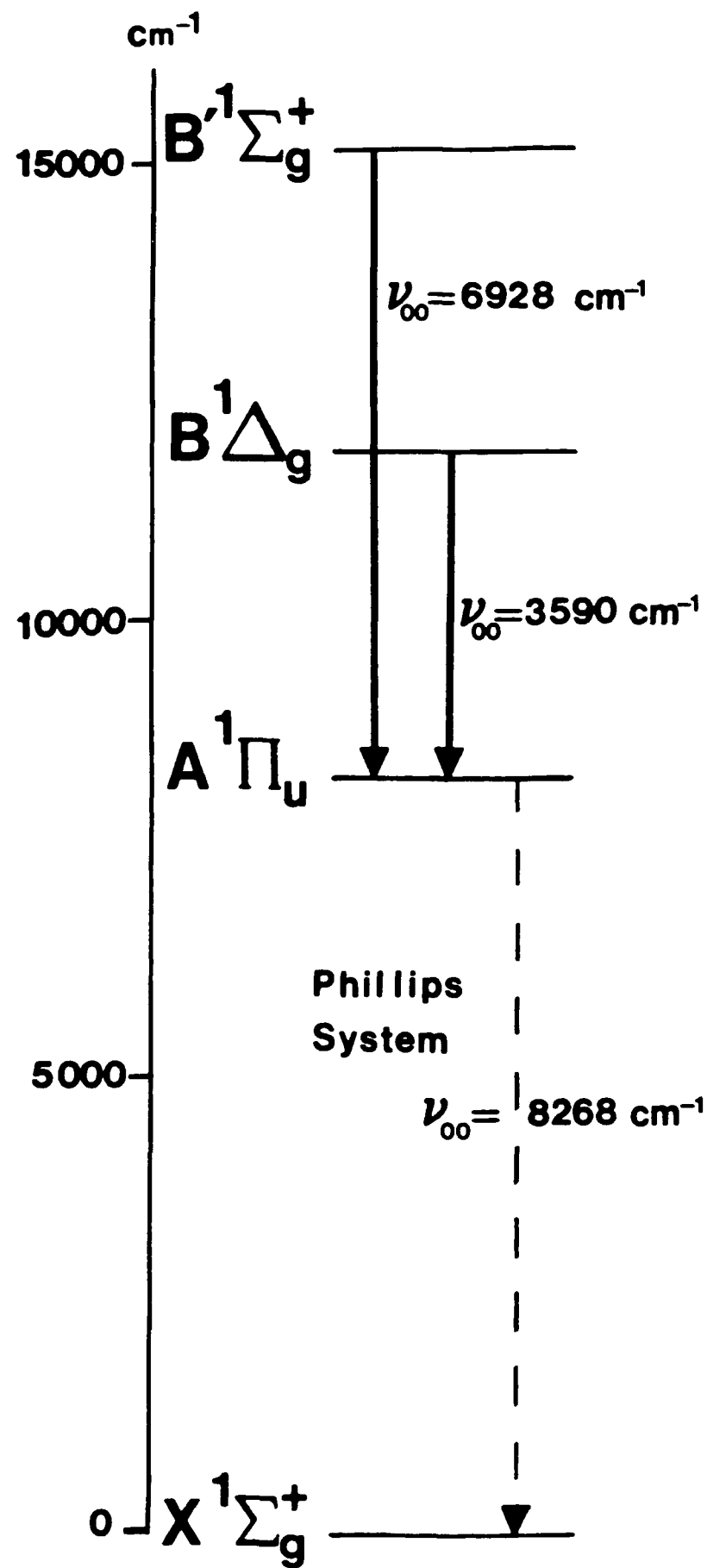
F 04611-87-K-2000

Peter F. Bernath
Department of Chemistry
University of Arizona
Tucson, AZ 85721

A. C_2

During the course of our spectroscopic observation of the $d^1\Sigma^+ - b^1\Pi$ transition of SiC^1 , A. D. McLean pointed out that the corresponding C_2 transition ($B'^1\Sigma_g^+ - A^1\Pi_u$) has not been reported. This was quite surprising because the C_2 molecule occurs in such a wide variety of sources and has been studied for many years. Examination of two previously recorded spectra disclosed the $B'^1\Sigma_g^+ - A^1\Pi_u$ and $B^1\Delta_g - A^1\Pi_u$ transitions² in addition to the well-known Phillips system, $A^1\Pi_u - X^1\Sigma_g^+$, and Ballik-Ramsay system, $b^3\Sigma_g^- - a^3\Pi_u$. We have also reanalyzed the Phillips system.³ Figure 1 shows an energy level diagram of the low-lying states of C_2 .

The $B^1\Delta_g$ and $B'^1\Sigma_g^+$ states of C_2 are predicted to be low-lying bound states by *ab-initio* calculation. These two states do not connect with the ground $X^1\Sigma_g^+$ state via one-photon electric dipole selection rules. The infrared electronic transitions $B^1\Delta_g - A^1\Pi_u$ and $B'^1\Sigma_g^+ - A^1\Pi_u$, however, are quite strong. The main difficulty is that the Ballik-Ramsay and Phillips systems (as well as the usual collection of impurities such as CO, CN, CH and ArH) make the infrared emission spectra of hydrocarbon discharges quite complex.



Strong emission spectra of the C_2 molecule were found in two data sets previously recorded for other purposes. These spectra were excited by an electrodeless microwave discharge of hydrocarbons in a quartz tube.

The emission from the discharge tube was observed with the McMath Fourier transform spectrometer of the National Solar Observatory at Kitt Peak. InSb detectors and a silicon filter limited the band pass to approximately $1800\text{--}9000\text{ cm}^{-1}$.

Our discovery of the $B^1\Delta_g$ and $B'^1\Sigma_g^+$ states completes the experimental detection of all of the low-lying states of C_2 . Two additional vibrational levels, $v=5$ and 6 , were observed in the ground $X^1\Sigma_g^+$ state. The transitions involve low-lying states, so they should be observable in comets, stellar atmospheres, flames and in the combustion of many propellants.

B. C_3 and C_5

Two additional members of the carbon chain series, C_3 and C_5 , were observed^{4,5} in the infrared absorption spectra of a carbon star, IRC+10216. This carbon star is the brightest source of radiation at 5μ in the sky. IRC+10216 is surrounded by a dusty carbon-rich envelope which is full of previously unobserved molecules. Many of these molecules, such as C_3 and C_5 , are possible advanced propellants.

For our C_3 work, the spectra of the prototypical obscured carbon star IRC+10216 and the moon were observed with an apodized resolution of 0.014 cm^{-1} by means of the Kitt Peak National Observatory 4-m telescope and the Fourier transform spectrometer located at the coudé focus. The spectrum was limited to $1975\text{--}2050\text{ cm}^{-1}$ by a cold blocking filter. After our discovery of C_3 , we recorded similar spectra in order to find C_5 .

The observed line positions of the antisymmetric stretching mode of C_3 were reduced to molecular constants (Table 1).

Table 1. Spectroscopic constants for the ν_3 vibrational mode of C_3 .

Constant	Value (cm^{-1})
ν_3	2040.02113(62)*
$B_{0,0,0}$	0.430557(37)
$D_{0,0,0}$	$1.415(79) \times 10^{-6}$
$B_{0,0,1}$	0.435654(39)
$D_{0,0,1}$	$3.937(88) \times 10^{-6}$

Similar constants were derived for the corresponding stretching mode of C_5 (Table 2).

Table 2. Spectroscopic constants for the ν_3 mode of C_5 .

Constant	Value (cm^{-1})
ν_3	2169.44205(40)*
B'' (ground state)	0.0853085(62)
B' (excited state)	0.0848879(60)

* One standard deviation uncertainty in parenthesis.

From the rotational constants of Table 1, an r_0 bond of 1.277Å can be derived for C_3 . If, as the *ab initio* calculations predict, all of the C-C bond lengths are nearly identical in C_5 , then an average r_0 bond length of 1.283Å can be derived from the data in Table 2.

Prior to our work, the high-resolution infrared spectra of C_3 and C_5 were unknown. Laboratory observations of C_3 and C_5 have occurred almost simultaneously with the astronomical detections. In the case of C_5 , the laboratory observations in two other research groups were guided by the astronomical C_5 results.

C. BC

Our production of BC was similar to our work with SiC. A composite wall (B_4C/Cu) hollow cathode discharge served as a light source for the Kitt Peak Fourier transform spectrometer.

The $B^4\Sigma^- - X^4\Sigma^-$ transition of BC was very weak and the first lines were not detected. Some evidence of spin-splitting was found in the lines. We hope to record better spectra in the future.

D. CH_3N and CCN

Electronic emission spectra of polyatomic free radicals are greatly simplified by cooling. We are using an Engelking-type of free radical jet source to record ultracold emission spectra at high-resolution with the Kitt Peak Fourier transform spectrometer. Our continuing work on the $\tilde{A}^3E - \tilde{X}^3A_2$ transition of CH_3N is described in the abstract by P. Carrick.

The $\tilde{A}^2\Delta - \tilde{X}^2\Pi$ transition of CCN was observed from diazoacetonitrile precursor ($HC(N_2)CN$) in a helium expansion. We observed the 000-000, 000-001, 000-002, 000-100 vibronic bands of this transition. Analysis of the spectra allows us to derive rotational constants and ground state fundamental vibrational frequencies of $\nu_1 = 1923.2502(74)$; $\nu_3 = 1050.7586(12)$ and $2\nu_3 = 2094.8153(16) \text{ cm}^{-1}$.

References

1. P.F. Bernath, S.A. Rogers, L.C. O'Brien, C.R. Brazier and A.D. McLean, *Phys. Rev. Lett.* **60**, 197 (1988).
2. M. Douay, R. Nietmann and P.F. Bernath, *J. Mol. Spectrosc.* **131**, 261 (1988).
3. M. Douay, R. Nietmann and P.F. Bernath, *J. Mol. Spectrosc.* **131**, 250 (1988).
4. K.H. Hinkle, J.J. Keady and P.F. Bernath, *Science* **241**, 1319 (1988).
5. P.F. Bernath, K.H. Hinkle and J.J. Keady, submitted to *Science*.

Production of the CH Radical with an Ion Gun

P. Bletzinger and M. E. Ruark

As noted at last year's HEDM contractor's conference [1], the CH radical is abundant and easily observed in diffusion flames and in afterglow plasmas where gases such as C_2H_2 or CH_4 are added to a flow of gases containing a large density of metastables. The dissociation of the added gases in the afterglow by collisional excitation by the metastables produces a fairly intense emission, for example the A-X transition of CH. On the other hand, the reaction rates for CH with a large number of other gases, including the generating gas, are in the order of $.5$ to $4 \times 10^{-10} \text{ cm}^3 \text{ molecule}^{-1} \text{ sec}^{-1}$, typical decay constants at low pressures are in the order of $5 \times 10^{-7} \text{ sec}$ (see references in [1]). Since the generation of CH in an afterglow plasma is very convenient and simple, we constructed a fast flow system with the upstream DC discharge section at about $.5$ - 1 Torr pressure followed by an orifice leading to a high vacuum section (10^{-5} Torr with flowing gas) incorporating a residual gas analyzer. Helium was used in the discharge section; at the injection point of C_2H_2 or CH_4 the flow speed was 10 m/sec or higher. Within the detection sensitivity of the RGA we did not detect any CH, probably since the gas residence time from injection to orifice was of the order of 1 msec . Injecting the gas into the low pressure section after the orifice produced a large background cracking pattern of the injected gas in the RGA. When switching the discharge on or off, the background mass peak at the CH position was large enough to mask any

changes in the abundance of CH. Investigating the cracking pattern produced by the RGA ionizer in more detail, we found that with an ionizer energy of 100 eV the yield of CH amounted to approximately 5% of the dissociation products of C_2H_2 (Fig. 1). Based on this finding we are now in the process of constructing a system using a commercial ion gun to produce CH^+ ions, which will be neutralized in a charge exchange chamber before deposition on the coldfinger of a cryostat.

Neutralized ion beams have been used extensively in collisional studies [2]. The neutralization of the ion beam requires a collision partner with an ionization energy not much lower than that of the ion to be neutralized. Gellene and Porter studied the case of CH_4 and its dissociation products and by analyzing the beam profiles after the charge exchange collision detected neutral dissociation products even in cases where the energy difference was only about 3 eV (Fig. 2) [3]. Their research suggests Zn as the optimum charge exchange collision partner. The charge exchange collision is a long range collision and causes little scattering of the beam. However, the density of the target species is critical. It has been found that the optimum neutral beam flux at minimum scattering occurs when the ion beam density as measured after the charge exchange cell has decreased to half its original value (Fig. 3) [4]. Another concern when using neutralized beams for the deposition of radicals is the requirement for very low beam velocity. For a decrease in beam energy from 3 keV to .5 keV Cisneros et. al. found very little increase in the width of a beam of D^+ ions converted to D^- ions in collisions with Cs [5]. When decelerating the ion beam, the influence of space charge has to be considered. Fig. 4 shows the space charge limited current for CH^+ ions with a distance of 10 cm using the classical Langmuir-Childs relation. Since in our application the ions are decelerated from a finite initial velocity, the actual current densities will be about a factor of eight larger. Also, we may be able to decrease the distance, resulting in another increase

in current density. Fig. 5 is a diagram of our experiment. The ion source is a hot filament low pressure discharge which provides a very low spread in ion energy but relatively low ion flux. After mass selection in the Wien filter, the ions can be decelerated in another series of lenses to an energy as low as 5 eV. Focussing can be checked by measuring the beam profile with the movable beam sensor before entering the 1mm diameter aperture of the charge exchange cell. Ions remaining in the beam after the charge exchange cell are being deflected out of the beam; also this provides a convenient means of measuring the total ion current. Presently the neutral beam will be analyzed by an RGA. Later, the neutral beam will be deposited unto the cold finger of the cryostat. A separate nozzle will deposit the matrix material. We have made initial measurements of the ions produced by dissociating CH_4 in the hot filament discharge (Fig. 6). At an energy of 5 keV, a flux of more than 10^{10} ions was measured with the beam sensor (.5mm diameter by 4mm length). From the isotopic abundance of C^{13} and the amplitude of the C^{12} peak we calculate about 2.8% impurities in the form of C^{13} atoms. At a beam energy of 50 eV the current is of course much lower, but we expect a considerable improvement with more careful focussing. Our ion beam currents appear to be considerably greater than those used in previous experiments and can be increased even further by using a more efficient ion source.

It is a pleasure to acknowledge the advice of Hans Peter Helm on the design of the charge exchange cell.

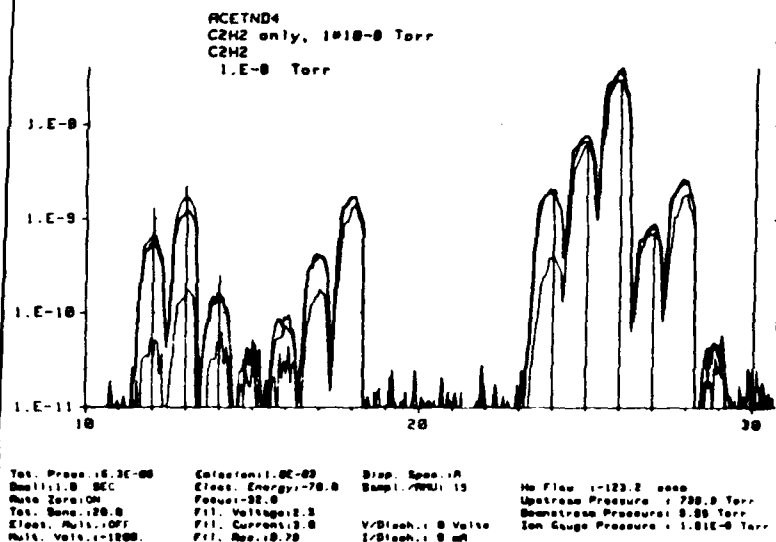
[1] P. Bletzinger and M. E. Ruark, 1988 HEDM Contractors Conference, Newport Beach CA.

[2] G. I. Gellene and R. F. Porter, Acc. Chem. Res. 16,200 (1983).

[3] G. I. Gellene, B. W. Williams and R. F. Porter, J. Chem. Phys. 74,5636 (1981).

[4] P. O. Danis, R. Feng and F. W. McLafferty, Anal. Chem. 58,355 (1986).

[5] G. Cisneros, I. Alvarez. G. F. Barnett, J. A. Ray and A. Russek, Phys. Rev. A14, 88 (1976).



Residual Gas Analyzer Spectrum of Acetylene

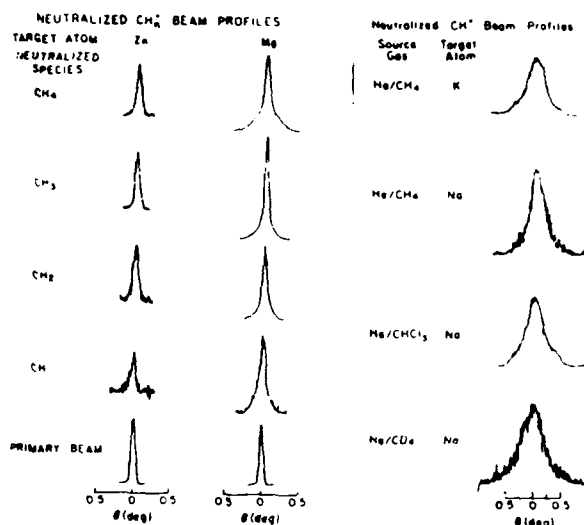
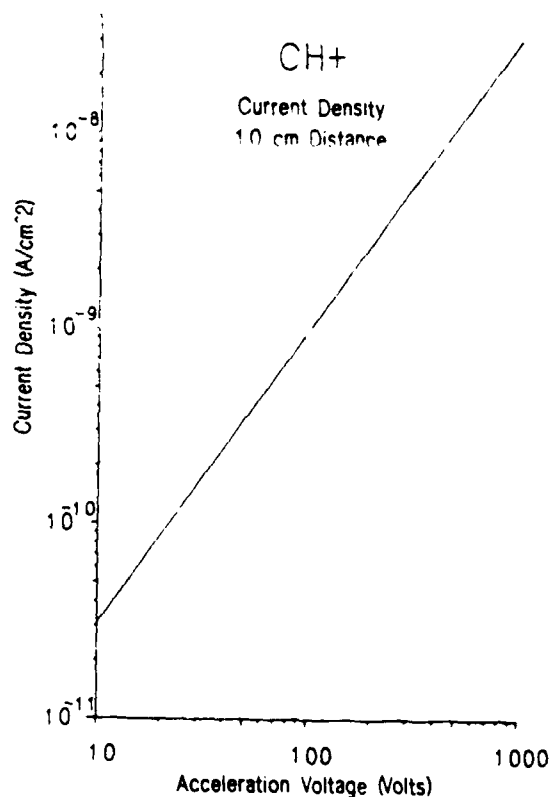


FIG. 3 Neutralized beam profiles for CH_n⁺ ions, target atoms Zn, Mg

Beam Profiles of CH_n⁺ (3)



Space Charge Limited Ion Current Density

350 • ANALYTICAL CHEMISTRY, VOL. 58, NO. 2, FEBRUARY 1986

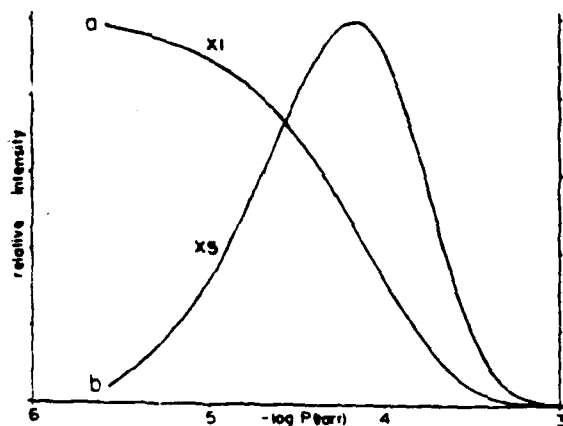
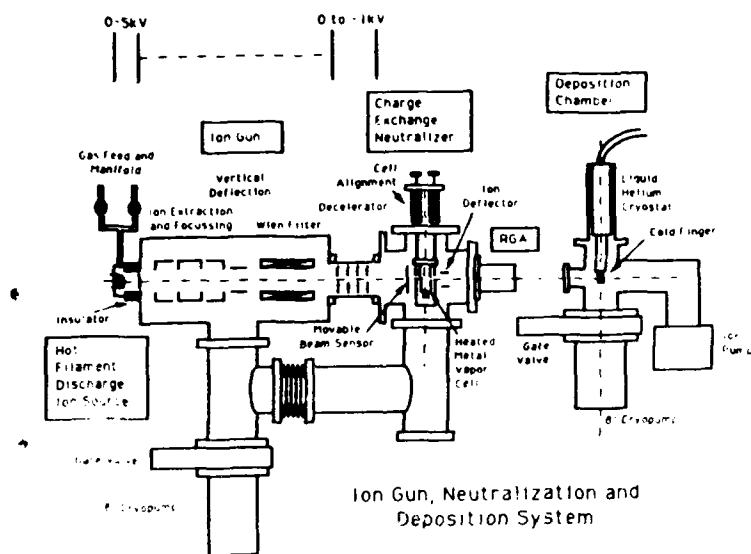
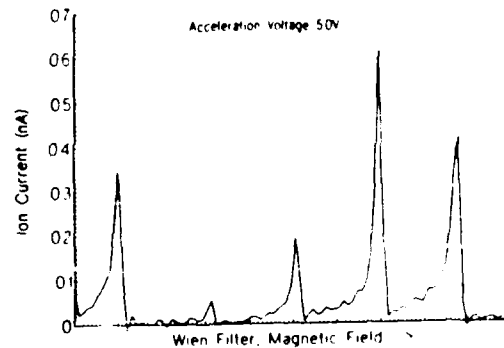
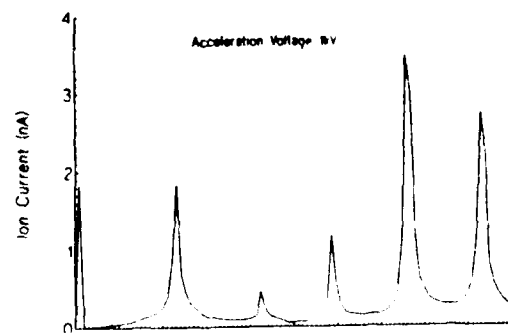
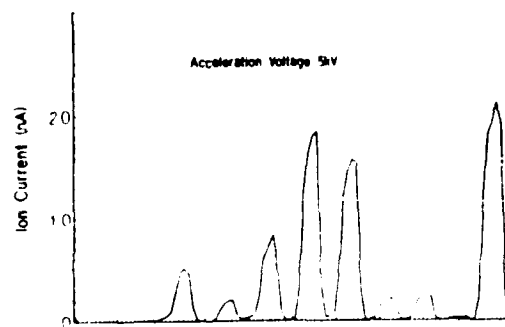


Figure 3. (a) Transmittance of Ar⁺ and (b) production of Ar²⁺, as a function of Ar target gas pressure for collisions at C1a-1 and detection at M1-1.

Yield of Charge Exchange Reaction vs. Target Pressure (4)



System Diagram



Measured Ion Currents From
A CH_4 Discharge

(First Mass Peak is Mass 12)

AB INITIO STUDY OF THE ENERGETICS OF THE DECOMPOSITION OF HN₃ AND N₃

Millard H. Alexander

Department of Chemistry, University of Maryland, College Park, MD 20742

From a theoretical point of view the mechanism of ground state decomposition is easier to characterize than photodissociation from an electronically excited state, since it is easier to determine good *ab initio* descriptions of the relevant potential energy surfaces. Ground state decomposition can be probed most selectively by narrow band overtone pumping followed by time resolved product detection. Particularly noteworthy to the present paper is the work of Stephenson, Casassa, Foy, and King on the decomposition of HN₃.^{1,2}

At the 1988 HEDM contractors meeting and in a previous paper³ we investigated the origin of preferential population of fine-structure levels in the NH products formed both in the spin-forbidden decomposition of HN₃:



as well as in the spin-allowed process



Decomposition according to Eq. (1) occurs by a spin-orbit induced crossing between the singlet surface, which correlates asymptotically to N₂(X¹Σ_g⁺) + NH(a¹Δ), and the lowest triplet surface. As illustrated schematically in Fig. 1, the triplet asymptote lies below the singlet asymptote by

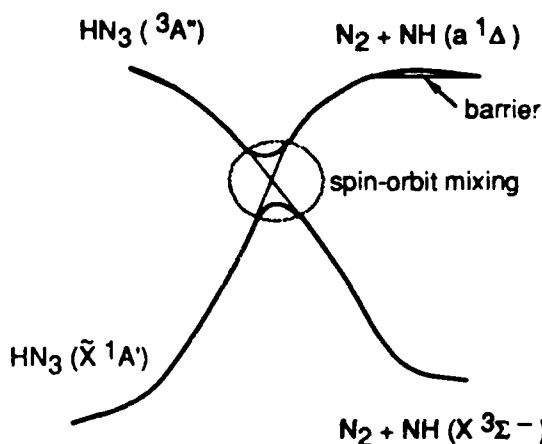


Fig. 1. Schematic reaction coordinate diagram for the energetics of the spin-forbidden dissociation of HN₃ on the ground electronic surface. Also indicated is the barrier in the NH(a¹Δ) – N₂ channel. A qualitatively similar diagram pertains to the spin-allowed and spin-forbidden decomposition of N₃.

$12,718\text{ cm}^{-1}$, the splitting between the splitting between the $X^3\Sigma^-$ and $a^1\Delta$ states of NH. In the molecular region the triplet surface correlates with an electronically excited triplet state of HN_3 . In this previous work³ we estimated of the height of the barrier for the spin-forbidden decomposition to be $12,500\text{ cm}^{-1}$, to which zero point corrections were not added. This value agreed well with the estimate⁴ $E_a \equiv 150\text{ kJ/mol} = 12,700\text{ cm}^{-1}$ from thermal dissociation studies in a shock tube, although other shock tube studies^{5,6} have yielded considerably different activation energies

In the impd study of Stephenson, Casassa, and King² the NH fragments in the spin-allowed $[\text{NH}(a^1\Delta)]$ channel were found to be translationally excited ($E_{tr} \approx 1700\text{ cm}^{-1}$). This implies the existence of a barrier in the singlet exit channel, the potential energy of which is subsequently released into the translational recoil energy of the dissociating fragments. A barrier in the exit channel for dissociation could also explain the low rate constant for quenching of $\text{NH}(a^1\Delta)$ by N_2 ($k_q = 6.8 \cdot 10^{-14}\text{ cm}^3/\text{s}$)⁷ as well as the sizeable activation energy for this quenching reaction.⁸ In the absence of a barrier, quenching should be efficient, mediated by approach on the singlet surface followed by crossing to the triplet surface, as proposed some time ago by Bauer and Fisher,⁹ for the isoelectronic system $\text{O}(^1\text{D}) + \text{N}_2$. Here the quenching rate constant is much faster ($k_q = 5.5 \cdot 10^{-11}\text{ cm}^3/\text{s}$).¹⁰

The ground state decomposition of the azido radical $[\text{N}_3(\tilde{X}^2\Pi_g)]$ is also a spin-forbidden process, since the spin-allowed asymptote $[\text{N}_2(X^1\Sigma_g^+) + \text{N}(^2\text{D})]$ lies $19,226\text{ cm}^{-1}$ higher than the spin forbidden asymptote $[\text{N}_2 + \text{N}(^4\text{S})]$

In its ground (X^1A') electronic state the HN_3 molecule is planar with a nearly linear N_3 moiety and the H-N bond strongly bent with respect to the N_3 backbone.¹¹ At large NN - NH distances the molecular orbitals of HN_3 become associated with either the N_2 or NH fragment. In particular, the degenerate N π orbitals correlate with the $10a'$ and $2a''$ orbitals, in c_s geometry. As the fragments approach, the energy of the in-plane $10a'$ orbital increases, due to Pauli repulsion between this in-plane orbital and the σ lone pair orbital on each of the N atoms in the N_2 molecule. It is for this reason that the energy of the triplet state of HN_3 , in which both the $10a'$ and $2a''$ orbitals are singly occupied and triplet coupled, increases strongly with decreasing NN - NH distance (Fig. 1). The lowest singlet asymptote $[\text{N}_2 + \text{NH}(a^1\Delta)]$, is doubly degenerate. In c_s geometry the symmetric (a') component of this degenerate pair corresponds to the electron occupancy $\dots 9a'^2 10a'^2 1a'^2 - \dots 9a'^2 1a'^2 2a'^2$, while the antisymmetric (a'') component corresponds to the electron occupancy $\dots 9a'^2 10a' 1a'^2 2a''$.

This latter is the same electron occupancy as the triplet state, except that here the singly filled orbitals are singlet coupled. Exactly as in the case of the triplet state, as the NN – NH distance decreases the energy of the singlet state of A" symmetry will increase. In the case of the singlet state of A' symmetry, Pauli repulsion can be minimized by orienting the NH fragment perpendicular to the N–N bond and by confining the two non-bonding NH π orbitals to the out-of-plane 2a" orbital. In a simplistic analysis the bonding in HN₃ is due to the slight stabilization of this 2a" orbital, which is non-bonding at large NN – NH distances. The confinement of the two NH π electrons, which, asymptotically, can occupy either the π_x or π_y orbitals, to a single orbital (2a") is the origin of the barrier in the exit channel of the singlet surface.

The qualitative description of the N₃ radical is similar. In *c_{∞v}* geometry, Pauli repulsion between the p_z orbital of the N atom and the lone pair σ orbitals of the N₂ molecule can be minimized by restricting the three *p* electrons of the N atom to either a p_x²p_y or p_xp_y² occupancy. These correspond to the the degenerate (Renner-Teller) states of the linear ² Π ground state of N₃. The quartet state correlates asymptotically with N₂ + N(p_xp_yp_z), which becomes energetically unfavored as the NN – N distance decreases. Also confining the three *p* electrons of the N atom to an occupied space which no longer includes the p_z orbital results in an energetic barrier in the spin-allowed (doublet) decomposition channel.

We have used complete active space self-consistent field (CASSCF)¹² and multireference configuration-interaction (MCSCF-CI)^{13,14} techniques to characterize quantitatively the energetics of the N₃ and HN₃ decomposition, in particular in the region of the spin forbidden crossings. The dominant configurations from the CASSCF calculations were selected as input into subsequent MCSCF–CI calculations. All the calculations described here were restricted to coplanar geometries for HN₃ and collinear geometries for N₃. Calculations were carried out with a large basis set including three *d* and one *f* polarization functions for N and 3 *p* polarization functions for H. In most of the HN₃ CASSCF calculations the active space included all the valence orbitals with the exception of the two highest sigma antibonding orbitals. The subsequent, "internally contracted,"¹³ CI calculations included all single and double excitations out of a reference space, built from the CAS reference by including all csf's with coefficient greater than (typically) 0.04 in the CAS wavefunction. This selection criterion gave rise typically to a reference space of 10-20 csf's. The CI calculations involved up to a total of ~ 500,000 contracted (7,000,000 uncontracted)

configurations.

The locus of crossings between the $1A'$ and $3A''$ surfaces of the HN_3 molecule is a five dimensional hypersurface. Our earlier, less sophisticated calculations³ established that at the point of the minimum crossing, the terminal N—N bond distance and the N—H bond distance were very close to the equilibrium internuclear separations in the ground electronic states of these two molecules [2.074 bohr for N_2 and 1.958 bohr for $\text{NH} (X^3\Sigma^-)$]. We subsequently carried out a series of larger MCSCF-CI calculations in the region of the lowest singlet-triplet crossing. While the NN and NH bond distances were held to the values in the isolated molecules, a full variation was made in the two polar angles and the NN—NH distance. Although only planar geometries were considered, a crude estimate of the dependence of the energy on the NN—NH dihedral angle was obtained by calculations for cis and trans geometries with the same NNN and NNH polar angles.

In the region of the minimum on the singlet-triplet crossing seam the singlet and triplet surfaces were fit to a multidimensional polynomial expansion. With this fit the minimum crossing point was found to occur at a NN—NH distance of 3.354 bohr, an NNH angle of 88.7° and a trans NNN angle of 161° . The dependence of the energy of these surfaces on the NN—NN distance and on the NNH and NNN angles is depicted in Fig. 2

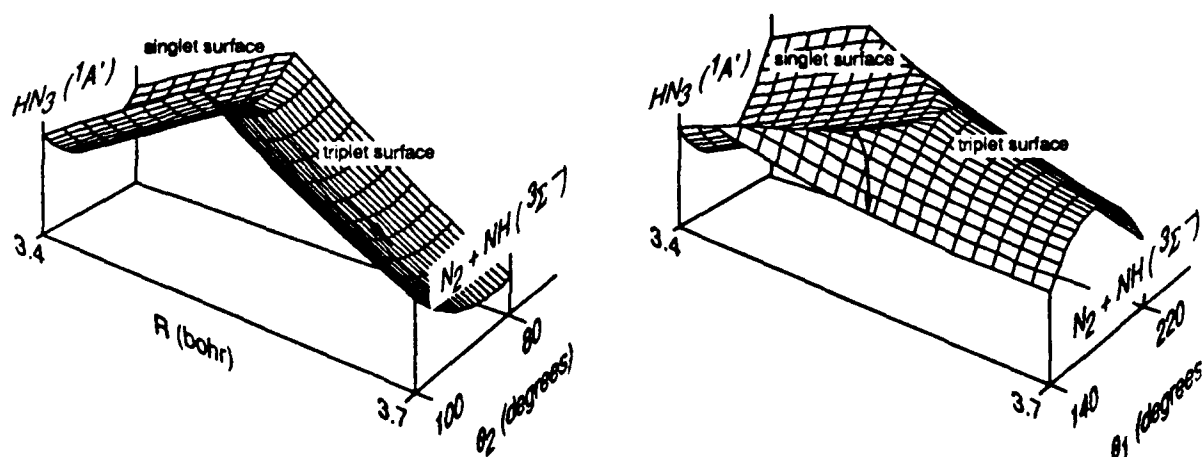


Fig. 2. Contour plot illustrating the region of crossing between the lowest singlet ($1A'$) and lowest triplet ($3A''$) surfaces of HN_3 as a function of the NN—NH distance and the NNH angle. The zero of energy refers to the minimum singlet-triplet crossing. The singlet surface is energetically lower to the left of the seam; the triplet surface, to the right.

At and near the crossing the two singlet and triplet wavefunctions will be mixed by the small spin-orbit term in the Hamiltonian, estimated by Yarkony to be 37 cm^{-1} .¹⁵ Significant mixing

of the two states can thus occur only when the energy gap between them is $\leq 100 \text{ cm}^{-1}$ which, we see from Fig. 2, is limited to just the region of the seam.

The saddle point on the adiabatic surface, with respect to the energy of the $\text{HN}_3 \text{ X}^1\text{A}'$ ground state, will define the height of the barrier for spin-forbidden decomposition (Fig. 1). Our best estimate of the height of this barrier is $17,130 \text{ cm}^{-1}$. This value is considerably larger than that predicted by our smaller calculations,³ most likely because the addition of f functions on N allows a more complete description of electron correlation on the HN_3 molecule at its equilibrium separation, relative to the more diffuse electron distribution at the singlet-triplet crossing. Using our polynomial fit to the singlet and triplet surfaces in the region of the barrier we estimate the zero point correction to this activation energy to be $\cong -1000 \text{ cm}^{-1}$, leading to an estimate for the activation energy of $E_a \cong 16,100 \text{ cm}^{-1} = 46.1 \text{ kcal/mol}$. This value is considerably higher than the earlier shock tube estimates⁴⁻⁶.

The product internal energy distributions of the nascent N_2 and NH molecules will be sensitive to the forces exerted while the system separates on the $^3\text{A}''$ surface. As is obvious in Fig. 2, recoil will be virtually uncoupled from the NNH angle, so that the large energy release which occurs as the $\text{N}_2\text{-NH}$ system falls down the triplet surfaces (Fig. 1) will not lead to rotational excitation of the NH fragment. This is consistent with experiment^{1,2} as well as with the conclusions of our previous study.³ By contrast, product recoil will be coupled with the NNN angle, so that considerable rotational excitation of the N_2 products might be expected.

In the case of N_3 , which has a symmetric linear structure at equilibrium with N-N bond distance of 2.22 bohr, at the minimum doublet-quartet crossing one of the N-N bonds is shortened to 2.085 bohr, very close to the equilibrium bond distance of N_2 (2.074 bohr), while the other N-N bond is lengthened to ~ 3.36 bohr. The barrier height is $\cong 18,500 \text{ cm}^{-1}$ which yields an activation energy of $E_a \cong 18,000 \text{ cm}^{-1} = 51.4 \text{ kcal/mol}$ when zero point corrections are included. Note that this value is $\sim 2000 \text{ cm}^{-1}$ higher than the comparable barrier for HN_3 , and considerably higher than the early literature estimate,¹⁶ derived from the experimental study of the isotopic $^{15}\text{N} + \text{N}_2$ exchange reaction.

The barrier in the $\text{NH}(a^1\Delta)$ exit channel (Fig. 1) is predicted by our calculations to lie $\cong 1,800 \text{ cm}^{-1}$ above the $\text{NH}(a^1\Delta) + \text{N}_2$ asymptote. This value, which includes zero-point corrections, is consistent with the value of $\sim 1,700 \pm 500 \text{ cm}^{-1}$, estimated by King and co-workers from the product translational energy in their impd experiments,² but considerably higher than the value of 440 cm^{-1} , estimated by McDonald and co-workers from the

temperature dependence of the rate constant for the quenching of $\text{NH}(a^1\Delta)$ by N_2 .⁸ A slightly higher barrier height ($E_a = 2,100 \text{ cm}^{-1}$) is predicted for the $\text{N}(^2\text{D}) + \text{N}_2$ exit channel.

REFERENCES

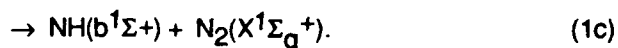
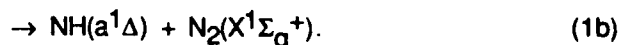
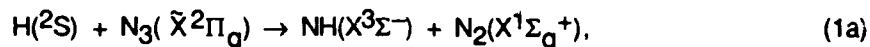
1. B. R. Foy, M. P. Casassa, J. C. Stephenson, and D. S. King, *J. Chem. Phys.*, **89**, 608 (1988); B. Foy, M. P. Casassa, J. C. Stephenson, and D. S. King, *J. Chem. Phys.*, submitted.
2. J. C. Stephenson, M. P. Casassa, and D. S. King, *J. Chem. Phys.* **89**, 1378 (1988).
3. M. H. Alexander, H.-J. Werner, and P. J. Dagdigan, *J. Chem. Phys.* **89**, 1388 (1988).
4. O. Kajimoto, T. Yamamoto, and T. Fueno, *J. Phys. Chem.* **83**, 429 (1979).
5. C. Paillard, G. Dupré, and J. Combourieu, *J. Chim. Phys.* **82**, 489 (1985).
6. A. I. Demin, I. S. Zaslonko, S. M. Kogarko and E. V. Mozzukhin, *Kinet. Katal.* **14**, 283 (1973) (as cited in Ref. 5).
7. F. Freitag, F. Rohrer, and F. Stuhl, *J. Phys. Chem.*, submitted.
8. H. H. Nelson, M. Hanratty, and J. R. Macdonald, work in progress.
9. E. R. Fisher and E. Bauer, *J. Chem. Phys.* **57**, 1966 (1972).
10. T. G. Slanger and G. Black, *J. Chem. Phys.* **60**, 468 (1974).
11. B. P. Winnewiser, *J. Molec. Spectrosc.* **82**, 220 (1980).
12. P. J. Knowles and H.-J. Werner, *Chem. Phys. Lett.* **115**, 259 (1985).
13. H.-J. Werner and E. A. Reinsch, *J. Chem. Phys.* **76**, 3144 (1982); in *Advanced Theories and Computational Approaches to the Electronic Structure of Molecules*, edited by C.E. Dykstra (D. Reidel, 1984), p. 79.
14. H.-J. Werner and P. J. Knowles, *J. Chem. Phys.*, **89**, 5803 (1988).
15. D. R. Yarkony, abstracts, USAF High Energy Density Materials Contractors Conference, New Orleans, LA, 1989.
16. R. A. Back and J. Y. P. Mui, *J. Phys. Chem.* **66**, 1364 (1962).

EXPERIMENTAL STUDY OF THE H + N₃ REACTION AND THE PHOTODISSOCIATION OF HN₃

Paul J. Dagdigan, Department of Chemistry, The Johns Hopkins University, Baltimore, MD 21218.

We report on the results from three separate experiments which probe the dynamics of processes involving potential energy surfaces of HN₃. These studies involve the determination of the internal state distribution of the products of various collisional processes, namely (1) the NH product from the H + N₃ chemical reaction, (2) the N₂ photofragment from the uv photodissociation of HN₃, and (3) NH(X³Σ⁻) from the electronic quenching of NH(a¹Δ) by N₂.

There are three possible NH product electronic states energetically accessible in the H + N₃ reaction:



As indicated in Fig. 1, four potential energy surfaces arise from the interaction between H and N₃. If this reaction proceeds through the lowest surface, which includes the potential well corresponding to hydrazoic acid, HN₃($\tilde{\text{X}}^1\text{A}'$), then we would expect preferential formation of NH(a¹Δ) through pathway

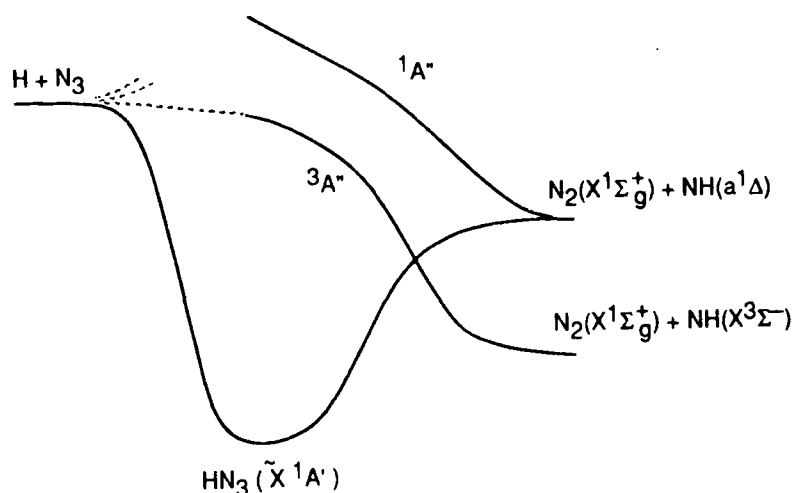


Fig. 1. Schematic diagram of the HN₃ potential energy surfaces connecting H + N₃ reactants and NH + N₂ products.

(1b). If singlet-triplet mixing occurs in the exit channel, then we would also expect formation of ground state $\text{NH}(X^3\Sigma^-)$, as has been seen in the ir dissociation experiments of the NIST group.¹ Alternatively, $\text{NH}(X^3\Sigma^-)$ could be formed directly on the $^3A''$ surface if the barrier in the entrance channel were low enough. The production of $\text{NH}(b^1\Sigma^+)$ is approximately thermoneutral.

We have set up an apparatus, illustrated in Fig. 2, to determine the nascent internal state distribution of NH products from the $\text{H} + \text{N}_3$ reaction. Here, hydrogen atoms are prepared in a supersonic microwave discharge source. Azide radicals are prepared by the reaction of fluorine atoms, produced in a CF_4/Ar microwave discharged flow, with hydrazoic acid and flow into the scattering chamber. We found that our previously employed source of azide radicals, namely the thermal decomposition of lead azide, was not sufficiently intense, stable, or long-lived to be suitable for these studies. Thus far, we have observed NH products in the ($a^1\Delta$) state, by laser fluorescence excitation in the $c^1\Pi \leftarrow a^1\Delta$ band system.

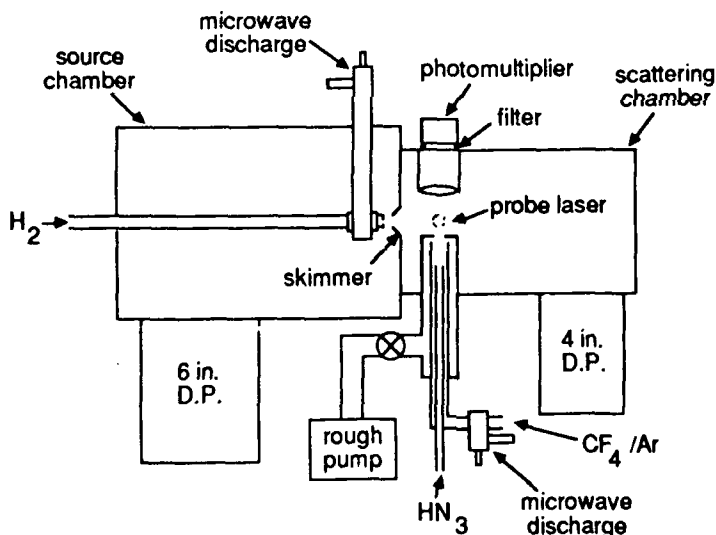


Fig. 2. Molecular beam apparatus for the study of the $\text{H} + \text{N}_3$ reaction.

$\text{NH}(a^1\Delta)$ product in its $v=0$ and 1 vibrational levels have been detected through excitation of both the (0,0) and (0,1) $c - a$ bands. Figure 3 presents the fluorescence excitation spectrum for the (0,1) band, which we have studied most extensively. The rotational state distribution can be characterized by a Boltzmann distribution with a temperature of 750 ± 100 K. From experiments at a differing scattering chamber pressures, we believe that this represents the nascent distribution from the reaction.

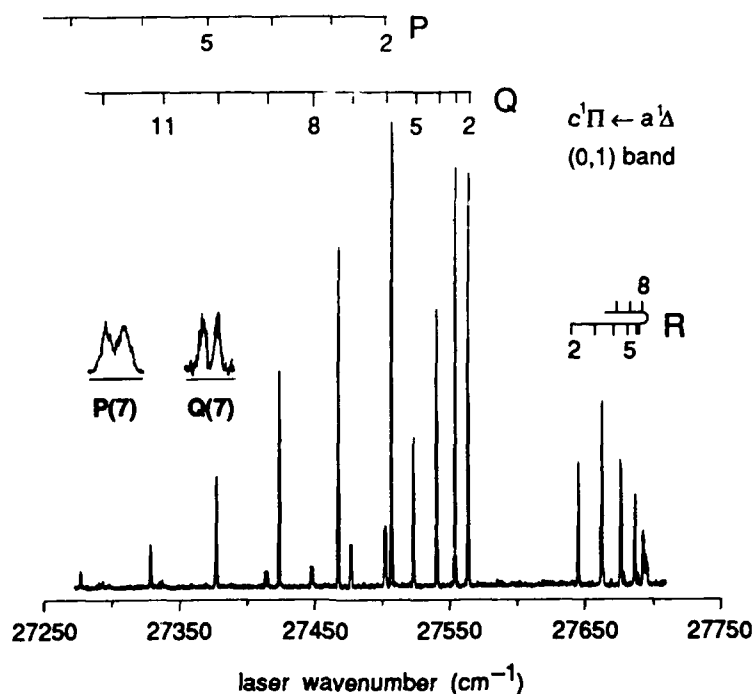


Fig. 3. Fluorescence excitation spectrum of the $\text{NH } c^1\Pi - a^1\Delta (0,1)$ band from the $\text{H} + \text{N}_3$ reaction. Insets show scans over resolved Λ doublets. The scattering chamber pressure was 0.4 mTorr.

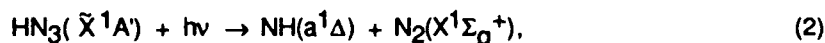
A preliminary report on this experiment has recently been submitted for publication.³

It is interesting to compare this rotational distribution with that reported² for the uv photodissociation of HN_3 . The total energy available in the photolysis at 248 nm is significantly larger than that available to the products of the $\text{H} + \text{N}_3$ reaction [$E_{\text{av}} = 2.92$ and 1.82 eV, respectively, for formation of $\text{NH}(a^1\Delta)$]. The rotational distribution of NH from photodissociation found to be only somewhat hotter, being characterized by $T = 1140 \pm 120$ K for $v=1$.² In the photodissociation process, the breakup occurs along a different HN_3 potential energy surface [$^1A'$, see Fig. 1] than does the chemical reaction. Perhaps it is perhaps more relevant that our reactive distribution is hotter than that observed¹ in the ir photodissociation of $\text{HN}_3(\tilde{X}^1A')$ since both this process and the $\text{H} + \text{N}_3$ chemical reaction proceed along the $^1A'$ surface.

As the insets in Fig. 3 show, the relative populations of the Λ doublet levels of a given J are equal to

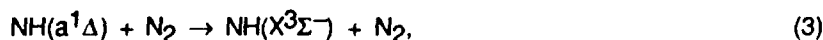
within experimental error. A similar lack of Λ doublet specificity in the $\text{NH}(a^1\Delta)$ product was observed in the uv photodissociation,² but a slight preference for $\Delta(A')$ levels⁴ was found in the ir dissociation experiments.¹ If the reaction proceeds along the $^1A'$ surface through a planar intermediate, then formation of $\Delta(A')$ is expected over $\Delta(A'')$.⁵ Our present efforts will be centered on the determination of the $\text{NH}(a)$ vibrational state distribution and observation of the $\text{NH}(X^3\Sigma^-)$ product.

We have also set up a time-of-flight mass spectrometer to determine the internal state distribution of $\text{N}_2(X^1\Sigma_g^+)$ products from the uv photodissociation of HN_3 by resonant-enhanced multiphoton ionization (REMPI) detection:



The calculations of M. H. Alexander⁶ suggest that the N_2 photofragment could be formed with considerable rotational excitation. We have obtained preliminary results for one-laser photodissociation/detection at the wavelength (283 nm) of the $\text{N}_2 a^1\Pi_g \leftarrow X^1\Sigma_g^+ (1,0)$ band, which is used for the 2+2 REMPI process. These suggest that the N_2 product possesses significant rotational excitation. Further experiments are required in order to characterize quantitatively the N_2 internal state distribution.

The *ab initio* calculations of Alexander⁶ and the study of infrared multiphoton dissociation of HN_3 by King, Stephenson, and coworkers at NIST¹ suggest that there is a barrier of height ca. 1500 cm^{-1} in the spin-allowed decomposition channel, which yields $\text{NH}(a^1\Delta)$. This is also consistent with the recently measured⁷ small thermal rate constant for quenching of $\text{NH}(a^1\Delta)$ by N_2 [$k_q = (6.8 \pm 0.5) \times 10^{-14} \text{ cm}^3 \text{ s}^{-1}$]:



By contrast, the quenching of $\text{NH}(a^1\Delta)$ by the isoelectronic CO molecule has been found⁷ to be fast [$k_q = (1.35 \pm 0.07) \times 10^{-11} \text{ cm}^3 \text{ s}^{-1}$].

In our laboratory, we have set up a crossed beam apparatus for the measurement of state-to-state inelastic cross sections involving small free radicals. Here, rotationally cold free radicals are prepared in their lowest rotational states by photolysis of a suitable precursor diluted in a seed gas at the tip of the nozzle of a pulsed beam. The free radical beam is crossed with a pulsed target beam, and the rotational

states of the former are interrogated by laser fluorescence detection. We have previously used this arrangement to determine rotationally inelastic cross sections for $\text{NH}_2(\text{X}^2\text{B}_1)\text{-He}^8$ and $\text{NH}(\text{X}^3\Sigma^-)\text{-Ar}$ collisions.⁹ More recently, we have prepared rotationally cold beams of $\text{NH}(\text{a}^1\Delta)$ by photolysis of HN_3 . We have thus far measured pure rotationally inelastic cross sections for excitation out of the ground $J=2$ level of $\text{NH}(\text{a}^1\Delta)$ by various collision partners. We will be shortly turning to the study of the quenching process, Eq. (3). By seeding both $\text{NH}(\text{a}^1\Delta)$ and the N_2 target in He seed gas, it is possible to reach a collision energy of 2000 cm^{-1} , which should be sufficient to overcome the expected barrier in the entrance channel.

-
1. B. R. Foy, M. P. Casassa, J. C. Stephenson, and D. S. King, *J. Chem. Phys.* **89**, 608 (1988); J. C. Stephenson, M. P. Casassa, and D. S. King, *ibid.* **89**, 1378 (1988); B. Foy, M. P. Casassa, J. C. Stephenson, and D. S. King, *ibid.* (submitted).
 2. F. Rohrer and F. Stuhl, *J. Chem. Phys.* **88**, 4788 (1988).
 3. J. Chen, E. Quiñones, and P. J. Dagdigan, *J. Chem. Phys.* (submitted).
 4. M. H. Alexander, P. Andresen, R. Bacis, R. Bersohn, F. J. Comes, P. J. Dagdigan, R. N. Dixon, R. W. Field, G. W. Flynn, K.-H. Gericke, E. R. Grant, B. J. Howard, J. R. Huber, D. S. King, J. L. Kinsey, K. Kleinermanns, K. Kuchitsu, A. C. Luntz, A. J. McCaffery, B. Pouilly, H. Reisler, S. Rosenwaks, E. W. Rothe, M. Shapiro, J. P. Simons, R. Vasudev, J. R. Wiesenfeld, C. Wittig, and R. N. Zare, *J. Chem. Phys.* **89**, 1749 (1988).
 5. M. H. Alexander, H.-J. Werner, and P. J. Dagdigan, *J. Chem. Phys.* **89**, 1388 (1988).
 6. M. H. Alexander, abstract at this meeting.
 7. F. Freitag, F. Rohrer, and F. Stuhl, *J. Phys. Chem.* (submitted).
 8. P. J. Dagdigan, *J. Chem. Phys.* **90**, 2617 (1989).
 9. P. J. Dagdigan, *J. Chem. Phys.* **90**, XXXX (1989).

TIME- AND- STATE RESOLVED STUDIES OF THE OVERTONE-PUMPED PHOTODISSOCIATION OF HN_3 ($\bar{X}^1\text{A}'$)

M.P.Casassa, B.R.Foy, D.S.King, and J.C.Stephenson
Molecular Spectroscopy Division
National Institute of Standards and Technology
Gaithersburg, Md. 20899

INTRODUCTION

Vibrational overtone excitation of molecules offers a powerful means of studying ground-electronic state unimolecular fragmentation. Reactants may be prepared in a highly state-specific manner, and time- and state-resolved analysis of the products reveals important details of the dissociation dynamics. Experiments by Crim and co-workers on HOOH illustrate these advantages well.¹ We have recently described similar experiments² on hydrazoic acid, HN_3 , in which the $\nu_{\text{NH}} = 5$ and 6 levels, populated by direct overtone pumping from the ground vibrational state, yield NH and N_2 fragments by the spin-forbidden process $\text{HN}_3(\bar{X}^1\text{A}') \rightarrow \text{NH}(\text{X}^3\Sigma^-) + \text{N}_2(\text{X}^1\Sigma_g^+)$. Here we report new overtone photodissociation data for HN_3 cooled in a supersonic expansion. Results include overtone photodissociation spectra of $5\nu_{\text{NH}}$ and $6\nu_{\text{NH}}$, a picosecond measurement of the $6\nu_{\text{NH}}$ dissociation lifetime, and product state distributions.

PHOTODISSOCIATION SPECTRA

Overtone photodissociation spectra enable us to examine the degree of vibrational level mixing at high vibrational energy in the ground electronic state (\bar{X}). Figure 1 shows the photodissociation spectrum of the $5\nu_{\text{NH}}$ band. This was obtained by scanning the frequency of the overtone-pump laser near $15,121 \text{ cm}^{-1}$ and monitoring fluorescence (LIF) excited by a probe laser tuned to a NH fragment transition ($\text{A}^3\Pi-\text{X}^3\Sigma^-$, $\text{R}_1(1)$ line near 336 nm). The HN_3 is cooled to a rotational temperature of $\approx 8 \text{ K}$ in the free-jet expansion (5% HN_3 in Ar, 1 atm backing pressure), eliminating the rotational congestion that dominates the 300 K spectra of the overtone bands.³ Linewidths in the spectrum are determined by the 0.03 cm^{-1} bandwidth of the pump laser. As expected, we observe the simple P,R-branch structure for a parallel band of a near-prolate top. Unexpectedly, though, the $(J,K=0)$ transitions appear as multiplets of up to three features rather than as single peaks. These features are separated by $0.02\text{-}0.18 \text{ cm}^{-1}$, and the patterns of the multiplets vary erratically with J . Identical patterns show up in the P and R branches for transitions with a common upper state J' . The combination-differences of these lines are consistent with the known

rotational constants of the ground vibrational state.⁴ Possible causes of the extra lines such as $K>0$ transitions, hot-band transitions, and absorptions of van der Waals clusters can all be excluded by known spectroscopic data³ and the fact that similar spectra are obtained in different expansion gases. These sets of transitions can only arise by mixing of the $(n\nu_{\text{NH}}, J, K=0)$ rovibrational levels of HN_3 with other rovibrational states of the molecule.

The photodissociation spectrum of the $6\nu_{\text{NH}}$ overtone ($17,671 \text{ cm}^{-1}$) is similarly perturbed by neighboring vibrational states.⁵ More components (from three to five) appear in this spectrum than in $5\nu_{\text{NH}}$, reflecting the increase in the density of background states with vibrational energy. Separations of features are larger, up to 0.39 cm^{-1} , indicating an increase in the coupling matrix elements between the vibrational states. In both the $5\nu_{\text{NH}}$ and $6\nu_{\text{NH}}$ spectra, the $J'=0$ levels are perturbed to the same extent as higher J , suggesting that the mixing is principally anharmonic (Fermi) in nature. We have estimated the size of the coupling matrix elements by performing a deperturbation of the patterns of mixing in Fig. 1,⁵ and we find that these matrix elements are in the range $0.010\text{--}0.065 \text{ cm}^{-1}$ for $5\nu_{\text{NH}}$, and up to 0.1 cm^{-1} for $6\nu_{\text{NH}}$. In both the $5\nu_{\text{NH}}$ and $6\nu_{\text{NH}}$ levels, the density of features that appear in the spectrum is comparable to the calculated density of vibrational states ($\rho_{\text{vib}} = 7$ and $13 \text{ states/cm}^{-1}$ for $\nu_{\text{NH}} = 5$ and 6 , respectively). This remarkable comparison suggests that the NH stretching overtones can couple to any neighboring states that fall within the coupling strength of $\approx 0.1 \text{ cm}^{-1}$, regardless of the type of motion involved.

VIBRATIONAL PREDISSOCIATION LIFETIMES

We previously reported the vibrational predissociation lifetime (τ_{vp}) of the $5\nu_{\text{NH}}$ level at 300 K , at which a broad distribution of rotational levels was excited.² Lifetimes were measured by varying

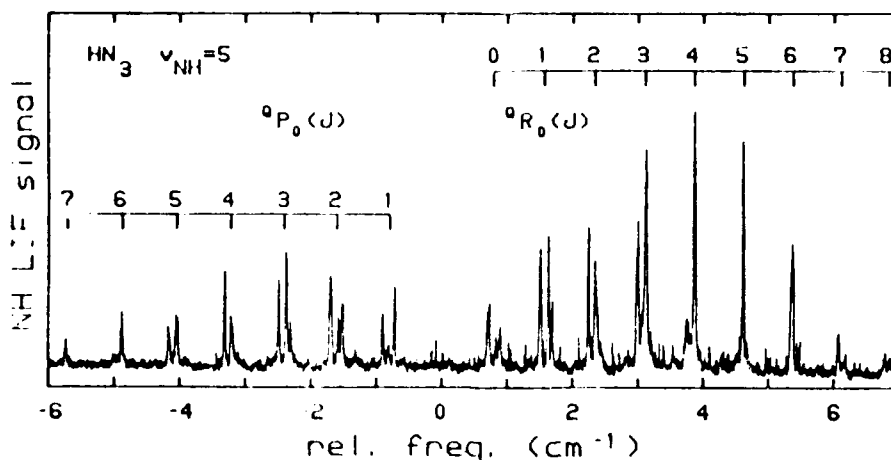


Figure 1. Photodissociation spectrum of HN_3 ($5\nu_{\text{NH}}$). Fragment LIF signal plotted vs. pump laser frequency; $\nu_0 = 15121.23 \text{ cm}^{-1}$.

the pump-probe time delay and monitoring the increase of fragment LIF. In molecular beam experiments, one can measure the lifetimes of individual (J,K) levels of $5\nu_{\text{NH}}$, and of the Fermi resonance components of those rotational levels. For the spectral features shown in Fig. 1, we find dissociation lifetimes on the order of 210 nsec. Surprisingly, a few particular Fermi resonance components have lifetimes that differ by as much as a factor of two.⁵ Aside from this deviation, however, τ_{vp} is not strongly dependent on rotational level at these low J values (J = 0-7, K=0).

The $6\nu_{\text{NH}}$ overtone state dissociates much more rapidly, and picosecond pump and probe pulses are required to measure its lifetime. Our apparatus consists of independently tunable picosecond lasers that generate pulses of duration ≤ 15 psec.⁶ Figure 2 shows the time evolution of the NH product generated from beam-cooled HN_3 pumped to the $6\nu_{\text{NH}}$ level. The exponential product appearance function corresponds to a dissociation lifetime of 950 ± 150 psec for $6\nu_{\text{NH}}$, with no rotational state dependence at low J. This represents about a 200-fold increase in the vibrational predissociation rate for a 17% increase in vibrational energy. Statistical theory predicts a less dramatic increase in the rate with energy and ρ_{vib} : RRKM calculations give only a factor of 4 increase at these energies.⁵ *Ab initio* calculations by M. Alexander indicate that the large ratio of the rates arises because the $5\nu_{\text{NH}}$ level dissociates by tunneling through a potential energy barrier.⁷

PRODUCT STATE DISTRIBUTIONS

The distribution of population over translational, rotational, vibrational, and spin-rotation states of the NH fragment in molecular beam photodissociation was found to be similar to our previous determinations in 300 K experiments.² Those experiments showed that most of the available energy (>96%) is converted into

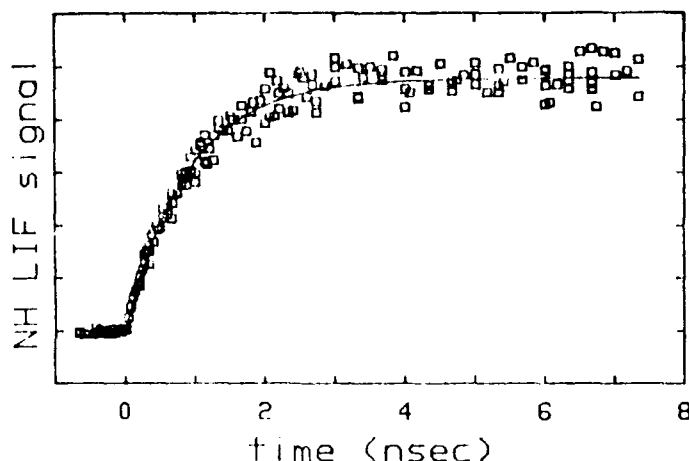


Figure 2. Photofragment appearance curve for the $6\nu_{\text{NH}}$ level. The pump laser spanned several lines ($J' \approx 1-4$) in the Q_{R0} branch. The fitted curve is of the form $1 - \exp(-t/\tau_{\text{vp}})$ with $\tau_{\text{vp}} = 0.95\text{ns}$.

fragment translational energy. The Fermi resonance components of given rotational levels of HN_3 each gives rise to fragments with the same degree of rotational excitation ($T_{\text{rot}} = 280 \pm 50$ K for $5\nu_{\text{NH}}$ dissociation, $T_{\text{rot}} = 570 \pm 60$ K for $6\nu_{\text{NH}}$). The selective population of fragment spin-rotation states that was noted in our earlier work was borne out in experiments in which we excited several individual vibrational components of transitions appearing in Fig. 1. Dissociation via the $5\nu_{\text{NH}}$ level gives no measurable population (i.e., $\leq 3\%$) in the F_2 spin-rotation states. For $6\nu_{\text{NH}}$ photodissociation, however, we found a small but measurable population in F_2 states, $P(F_2)/P(F_1, F_2, F_3) = 3(\pm 1)\%$. This was determined by tuning the probe laser to the $R_2(3)$ transition and observing the rise time of the LIF signal. The F_2 fragment population rises promptly, as do the populations of the F_1 and F_3 states. The prompt rise is too rapid to be attributed to collisional redistribution from the F_1 and F_3 states. Unfortunately, collisional effects make it more difficult to provide an absolute determination of the F_2 population fraction from $5\nu_{\text{NH}}$ photodissociation due to the long lifetime of this vibrational level. The observations that products are formed with high kinetic energies, little internal excitation, and a pronounced spin-rotation state selectivity are in accord with predictions based on theoretical calculations⁸ of the HN_3 potential energy surface.

REFERENCES

1. F.F. Crim in *Molecular Photodissociation Dynamics*, M.N.R. Ashfold and J.E. Baggott eds., (Royal Society of Chemistry, London, 1987); X. Luo, P.T. Rieger, D.S. Perry, and T.R. Rizzo, *J. Chem. Phys.* **89**, 4448 (1988).
2. B.R. Foy, M.P. Casassa, J.C. Stephenson, and D.S. King, *J. Chem. Phys.* **89**, 608 (1988); see also the Proceedings of the 1988 HEDM Conference, p.169.
3. D.T. Halligan, Ph.D. Thesis, Rice University (1988).
4. J. Bendtsen and F.M. Nicholaisen, *J. Mol. Spectrosc.* **119**, 456 (1986).
5. B.R. Foy, M.P. Casassa, J.C. Stephenson, and D.S. King, *J. Chem. Phys.*, in press.
6. M.P. Casassa, J.C. Stephenson, and D.S. King, *J. Chem. Phys.* **89**, 1966 (1988).
7. M.H. Alexander, T. Hemmer, H.J. Werner and P.J. Knowles, to be published.
8. M.H. Alexander, H.J. Werner, and P.J. Dagdigian, *J. Chem. Phys.* **89**, 1388 (1988).

Model Studies of CBES Decomposition

T. A. Seder and D. J. Benard
Rockwell International Science Center
Thousand Oaks, CA 91360

Fluorine azide, FN_3 , is a chemically bound excited state (CBES) material. CBES materials are so named because electronically excited species are produced via dissociation along the ground state potential surface. For instance, the products of the thermal dissociation of FN_3 have been shown to be excited state $\text{NF}(a)$ and ground state N_2 (1). Since CBES materials are essentially stabilized complexes containing electronically excited state species, they are high energy content molecules. Indeed, the heat of formation of FN_3 is ca. +130 kcal/mol. As this corresponds to a specific impulse of approximately 500 sec, fluorine azide is an attractive advanced propellant material. It represents a vast improvement in performance over the flight tested hydrazine monopropellant (240 sec), and even exceeds the performance of the H_2/O_2 system (400 sec).

The difficulty preventing utilization of fluorine azide is that it releases energy explosively. It is the goal of our research to find methods to moderate the decomposition process. To intelligently choose additive moderators, knowledge of the combustion mechanism is required. The research ongoing at Rockwell Science Center addresses the issues of identification of the intermediates and combustion products, characterization of energy pathways which may inhibit propellant performance and characterization of the burn rate of the material. These issues have been addressed via emission spectroscopy, schlieren photography, and an optical scattering technique following ignition of cryogenic films of FN_3 . The results of several studies which utilize these techniques will be presented following a brief experimental discussion.

The generation of FN_3 for use in these experiments has been described in previous technical reports to the Air Force Astronautics Laboratory (2). Cryogenic films were prepared by spraying the material through a nozzle onto a CaF_2 substrate which was maintained at 77 K. The polycrystalline FN_3 films were effective scatterers of optical radiation. A visible absorption spectrum revealed the presence of only a 425 nm absorption band which was attributed to FN_3 . The films were ignited with a ca. 100 μJ , 420 nm pulse from an N_2 pumped dye laser which was focused to a spot size of ca. 0.5 mm diameter. Following ignition, the films burned from the ignition site along the

surface of the substrate in a radial direction. A gaseous plume concurrently developed and was propelled from the surface.

The spectral and temporal behavior of the emissions which appeared subsequent to ignition were characterized using an optical multichannel analyzer and a bandpass-filtered photomultiplier tube, respectively. No emission by either $\text{NF}(a^1\Delta)$ or $\text{NF}(b^1\Sigma)$ was observed. These species are apparently rapidly quenched in the high density- high temperature combustion environment. This result is significant because it indicates that a substantial fraction of the combustion energy is not disposed of into these metastable energy "sinks" and is thus available to translational modes. The only emission band observed upon ignition is a complex feature centered at 450 nm. This emitter has not as yet been identified, although the emission has been temporally characterized. As the emission appears on a significantly delayed time scale (ca. 10 μs), it is attributed to a secondary reaction product of the plume gases.

Using emission spectroscopy we have been unable to identify any intermediate or product of FN_3 combustion. This task will be more properly addressed in the future using a time resolved mass spectrometric technique. Although we are presently unsure of the identity of important combustion intermediates we can construct a combustion mechanism on the basis of what is known for HN_3 combustion (3) and the result that $\text{NF}(a)$ is rapidly quenched. The important feature in the previously described mechanism (4) is that the 65 kcal/mole released upon decomposition of fluorine azide to ground state NF and N_2 greatly exceeds the activation energy for FN_3 dissociation (ca. 15 kcal) (5). Thus a thermal decomposition wave (detonation wave) can develop and be supported by the reaction enthalpy. The burn rate is likely to be dominated by this mode of decomposition unless the rate is moderated. We have qualitatively shown that the burn rate of the material can be moderated by increasing the heat capacity by incorporating additives such as SF_6 or NF_3 (4). Measurement of the effectiveness of these moderators requires the ability to accurately monitor the burn rate of the material.

We have characterized the burn velocity of pure fluorine azide using an optical scattering probe. In these experiments the time delay between absorption of the ignition laser pulse and the arrival of the combustion wave to a site probed at a known distance from the ignition site is measured. The degree of scattering of a c. w. HeNe laser beam by the FN_3 film is monitored at the probed site. The results of these experiments for the ignition of 20 films of various thickness are displayed in figure 1. The data indicate an insignificant dependence of

burn rate upon the thickness of the azide film. From the average of the delay time for these 20 ignitions, and the known ignition site- probe site separation, the burn velocity of the pure material has been determined to be (0.9 ± 0.2) mm/ μ s.

A series of experiments to determine the cause for the scatter in the data of figure 1 were also conducted. In the above experiments the measured delay time is comprised of both the ignition delay time and the time required for propagation of the combustion wave from the ignition site to the probed site. Ignition delay time, which can be defined as the time between absorption of the ignition laser energy and development of the combustion wave, is a function of ignition energy and can be affected by pulse to pulse instabilities in the ignition laser. The relationship between ignition energy and ignition delay was examined by both igniting and probing the same site on the film for several ignition laser energies. The significant results of this study were that the ignition delay under our experimental conditions was less than 1 μ s and that ignition delay was relatively invariant over a range of ignition energies which spanned from ca. 50 to 100 μ J. The scatter in the data of figure 1 cannot be attributed to ignition delay variations and is thus attributed to propagation time variations. Propagation time can likely be affected by a variety of factors such as film morphology and changes in the levels of trace impurities. We are currently incorporating an FTIR into our film combustion apparatus to more closely monitor the concentration of foreign species such as N_2F_2 (N_2F_2 is known to be a product of the slow thermal decomposition of FN_3).

Experiments to record and monitor the evolution of the gaseous plume via time resolved schlieren photography have also been performed in our laboratory. This two laser technique (6) captures on photographic film the image of the refractive index change resulting from the density changes which occur upon plume development. The schlieren image of the dimensions of the plume at various times following ignition of the azide film are shown in figure 2. The wrinkled nature of the images is indicative of a high degree of turbulence in the plume gases. This turbulence may arise from the polycrystalline film structure: the plumes of amorphous films may exhibit less turbulence behavior. By plotting one-half the plume diameter against the time following ignition for several schlieren experiments, we have determined a burn velocity of 1.6 mm/ μ s. The burn velocity as measured by this technique is substantially different from that determined via the optical scattering technique. This may indicate that the velocity of the plume exceeds the burn velocity of the condensed phase material.

In the future we will use the schliern and optical scattering probe to evaluate the burn rate of moderator doped azide films. We intend to also implement a time resolved mass spectrometry technique to fully identify the products and intermediates of FN_3 combustion.

References

1. Benard, D. J., et al, accepted for publication, J. Phys. Chem. (1989).
2. Benard, D. J. and Cohen, R. H. Quarterly Prog. Report No. 4, Dec. (1987).
3. Thrush, B. A., Proc. Roy. Soc. 235, 143 (1956).
4. Benard, D. J., et al Quarterly Prog. Report No. 10, Feb (1989).
5. Michels, H., United Technologies Research Center, private communication.
6. Lewis, B. and von Elbe, G. Combustion Flames and Explosions of Gases, Academic Press, New York (1961).

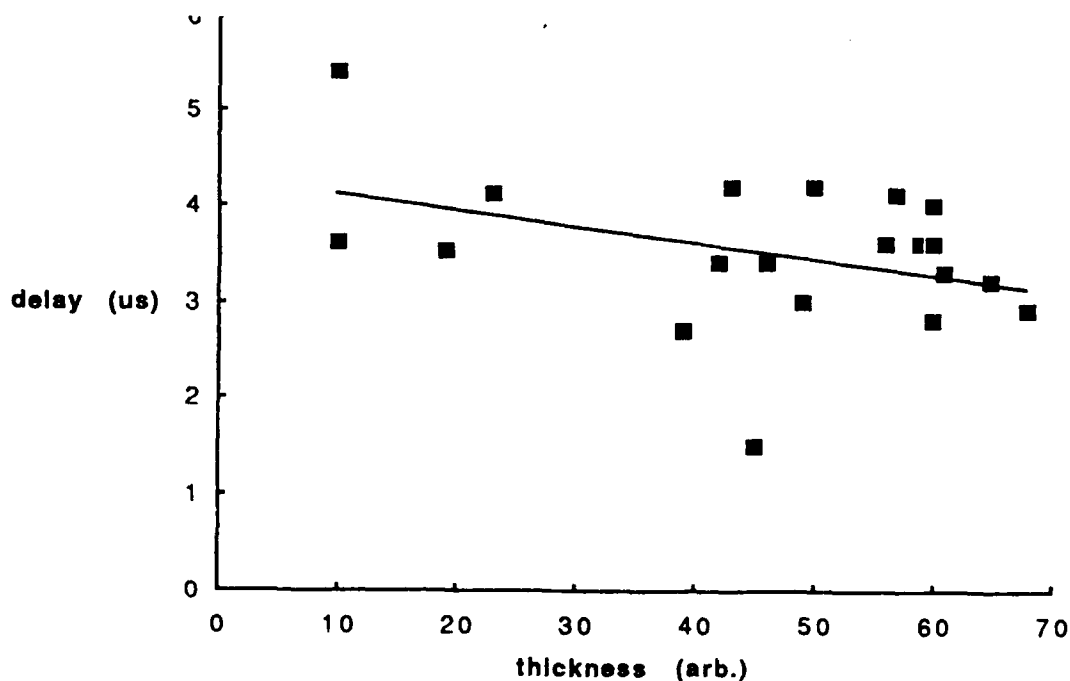


Figure 1 Delay Time vs. Film Thickness

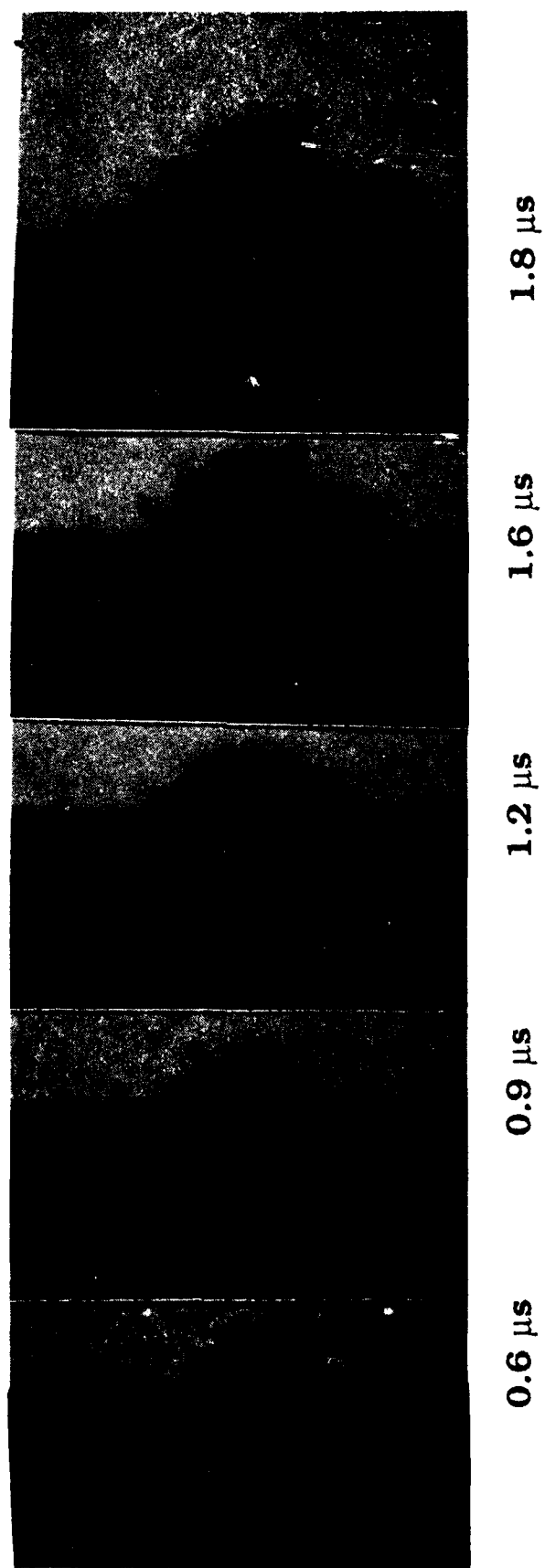


Figure 2 Schlieren Photographs of Plume at Several Times

THEORETICAL STUDIES OF HIGHLY ENERGETIC CBES MATERIALS*

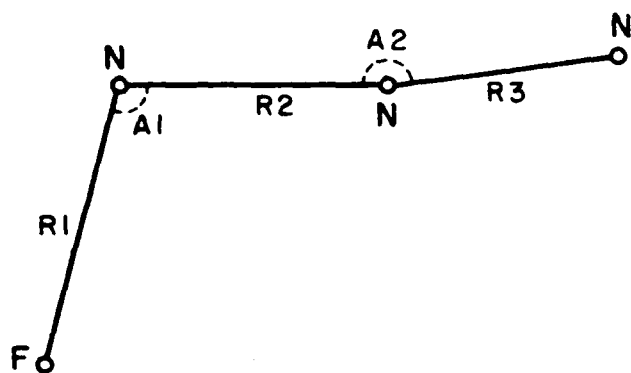
N. E. Brener, J. Callaway, N. R. Kestner, and H. Chen
Louisiana State University
Baton Rouge, Louisiana 70803

A new method of geometry optimization for large clusters of molecules, the simulated annealing procedure, has recently been developed. In this procedure, the molecular geometries are held fixed while inter-atomic potentials are used to describe the interaction between each pair of atoms in the cluster. In the case of FN_3 clusters, N-N, N-F, and F-F inter-atomic potentials are determined from atomic charges computed at the CISD level and from N_2 -NF and NF-NF interactions computed at the MP2 level. This method, which simulates the process of gradually cooling the cluster from an initial high temperature, is fast and enables one to study clusters that are large enough to simulate the solid. Optimized geometries and average molecular volumes have been obtained for FN_3 clusters containing up to 9 molecules. As shown in Table I, the volume per molecule was found to quickly reach a nearly constant value as the size of the cluster increases. This converged value of the molecular volume has been used to compute the density and the energy density of solid FN_3 , yielding values of 1.3 g/cm^3 and $.9 \text{ kcal/\AA}^3$ respectively. The energy density calculation is based on an energy content of 3.26 eV per FN_3 molecule, as described below. Due to its speed and flexibility, this simulated annealing program can be applied to many energetic molecules of interest.

Recent studies have also focused on identifying new high energy density materials that are possible candidates for advanced propellants. A large number of new materials and structures have been investigated computationally in order to select those that are promising and warrant further study. In these initial calculations, geometry optimizations were done at the SCF 6-31G* level in order to screen these materials in regard to energy content. A number of potentially highly energetic materials have been found. One of these, N_6 , is described in detail below.

For purposes of comparison, we first give the energy content (at the SCF 6-31G* level) of fluorine azide (FN_3), which is at the level of current state of the art propellants but is not in the category of advanced propellants. Thus a material with significantly more energy than fluorine azide would be considered a candidate for an advanced propellant.

Fluorine Azide (FN₃)



R1 = 1.3819 Å
R2 = 1.2536 Å
R3 = 1.0995 Å
A1 = 104.33°
A2 = 173.99°

	<u>Total Energy (Hartrees)</u>
FN ₃ singlet	- 262.6024876
N ₂ singlet + NF triplet	- 262.7222201

Energy Content = .1197325 Hartrees = 3.2567 eV
(the total energy of FN₃ minus the
total energy of the components)

We now give the SCF optimized geometry and energy content of trans N₆ (Fig. 1) and the N₆ ring (Fig. 2). The energy content is defined as the total energy of a molecule of N₆ minus the total energy of three N₂ molecules. Total energies are given in Hartrees and distances are given in Angstroms. In the geometry optimizations for trans N₆, all of the bond lengths and angles were allowed to be different, as shown in Fig. 3, but the geometry still converged to the symmetric structure given in Fig. 1. In order to check the possibility of non-planar geometries, a vibrational frequency calculation was done for the Fig. 1 structure in which all possible degrees of freedom were allowed. The computed frequencies were all positive, indicating that the planar, symmetric structure of Fig. 1 is the ground state. In the case of the N₆ ring, non-planar structures, including a boat and a chair, were also considered, but these all converged to the planar ring structure of Fig. 2. Since this ring structure is .71 eV higher in energy than the Fig. 1 structure, trans N₆ is the global minimum of the N₆ system.

According to Fig. 1, the energy content of trans N₆ is 9.71 eV, which is approximately three times the energy content of FN₃. Even though N₆ is heavier, with six atoms instead of four, its energy content per atomic mass unit is still more than twice that of FN₃.

In order to investigate its stability with respect to dissociation into fragments, we computed the activation barrier of trans N_6 at the SCF 6-31G* level. Three different dissociation pathways, $N_6 \rightarrow N_2 + N_2 + N_2$, $N_6 \rightarrow N_4 + N_2$, and $N_6 \rightarrow N_3 + N_3$ were considered in the calculations. The third one, $N_6 \rightarrow N_3 + N_3$, was found to be the actual path as the other two both exhibited two negative frequencies. Table II gives the results of the SCF barrier calculation for $N_6 \rightarrow N_3 + N_3$. Although the total energy continues to increase, the closed shell singlet (RHF) state becomes unstable for $R1 \geq 1.65$ and therefore the point $R1 = 1.645$ was taken to be the location of the top of the barrier. This gives a barrier height of .41 eV, which is comparable to the FN_3 SCF barrier of .47 eV.

The above results, which were obtained at the SCF 6-31G* level, can be summarized as follows:

- 1) Trans N_6 is the global minimum (ground state) of the N_6 system.
- 2) Trans N_6 has more than twice as much energy per atomic mass unit as does FN_3 .
- 3) The activation barrier of trans N_6 is comparable to that of FN_3 .

The next step is to check these results, particularly the barrier size, at higher (correlated) levels of calculation. If correlation causes the computed barrier height to increase, as is the case for FN_3 , then trans N_6 would appear to be stable as well as highly energetic and would therefore be considered a candidate for an advanced propellant.

*Supported by the Air Force Astronautics Laboratory (AFAL) under Contract F04611-87-K-0026.

Table I. FN_3 Clusters

<u>Number of Molecules</u>	<u>Volume per Molecule (\AA^3)</u>
3	82.7
4	82.2
5	80.7
6	79.7
7	79.1
8	80.5
9	80.6

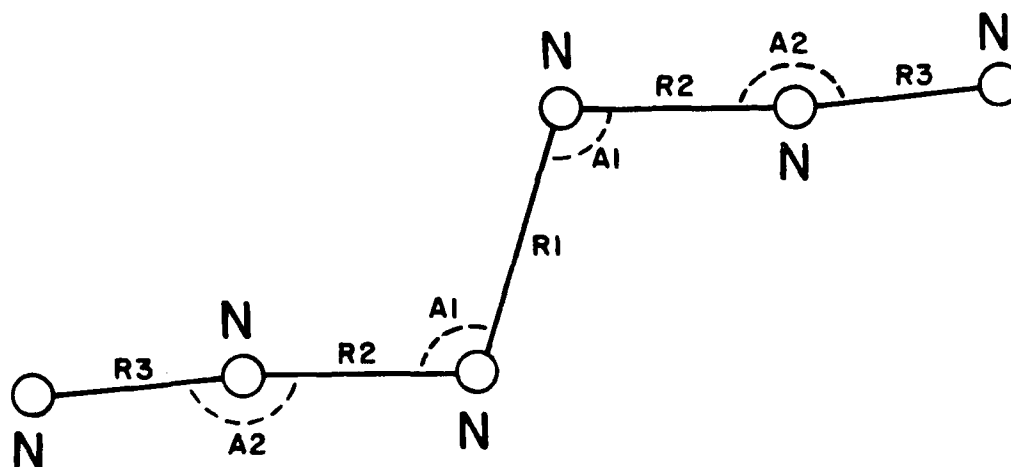
Density of Solid $FN_3 = 1.3 \text{ g/cm}^3$

Energy Density of Solid $FN_3 = .2 \text{ kcal/\AA}^3$

Table II. SCF Optimized Geometry for $N_6 \rightarrow N_3 + N_3$

<u>R1</u>	<u>R2</u>	<u>R3</u>	<u>A1</u>	<u>A2</u>	<u>Total Energy</u>
1.42981	1.23572	1.10107	107.3782°	174.8077°	-326.4750476
1.60	1.23799	1.10002	103.1844°	175.6693°	-326.4647266
1.62	1.23793	1.10005	102.7613°	175.7734°	-326.4626330
1.63	1.23790	1.10007	102.5497°	175.8254°	-326.4615460
1.645	1.23786	1.10010	102.2324°	175.9035°	-326.4598712
1.70	1.23737	1.10034	101.0990°	176.1931°	-326.4533663
1.75	1.23649	1.10073	100.1840°	176.3977°	-326.4471104
1.80	1.23566	1.10115	99.2942°	176.5741°	-326.4406748
1.85	1.23438	1.10169	98.4749°	176.7335°	-326.4341618
1.90	1.23289	1.10237	97.7157°	176.8551°	-326.4276452
2.00	1.22928	1.10394	96.3715°	177.0171°	-326.4147940

Figure 1. Trans N_6

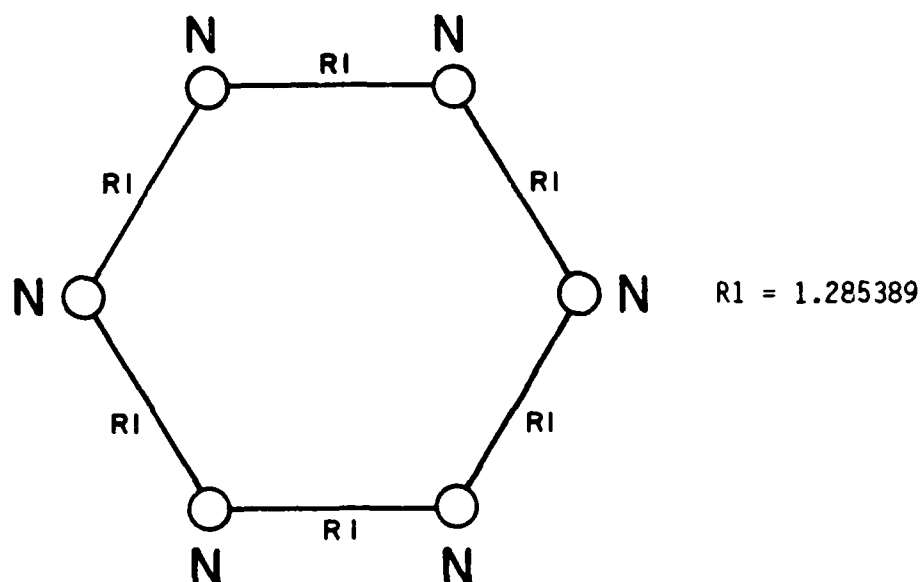


$R1 = 1.429808$
 $R2 = 1.235724$
 $R3 = 1.101074$
 $A1 = 107.378173^\circ$
 $A2 = 174.807741^\circ$

	<u>Total Energy</u>
Trans N_6 singlet	-326.4750476
N_2 singlet + N_2 singlet + N_2 singlet	-326.8318485

ENERGY CONTENT = .3568009 Hartrees = 9.705 eV

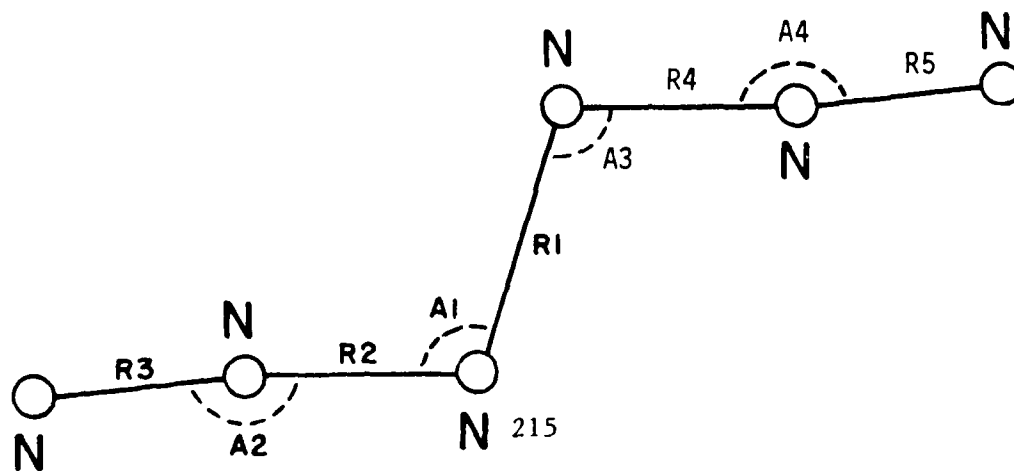
Figure 2. N_6 Ring



	<u>Total Energy</u>
N_6 Ring singlet	-326.4489642
N_2 singlet + N_2 singlet + N_2 singlet	-326.8318485

ENERGY CONTENT = .3828843 Hartrees = 10.4145 eV

Figure 3. Trans N_6



Theoretical Studies of Spin-Forbidden and Electronically Nonadiabatic Processes: Decay Processes in Energetic Materials

David R. Yarkony
Department of Chemistry
The Johns Hopkins University
Baltimore, MD 21218

In the following we consider questions related to the decay of two energetic materials $\text{He}(2^3\text{S})$ and $\text{N}_3\text{H}(1^1\text{A}')$. For the $\text{He}(2^3\text{S})$ system we study decay mechanisms involving nonadiabatic and radiative couplings induced by the interaction with a second helium atom. For $\text{N}_3\text{H}(1^1\text{A}')$ we report preliminary results of an, in progress, study of the spin-forbidden decomposition process $\text{N}_3\text{H}(1^1\text{A}') \rightarrow \text{NH}(\text{X}^3\Sigma^-) + \text{N}_2$. The results of this study are compared with calculations of relativistic effects in the NH moiety and we also report *ab initio* electronic transition moments for the $\text{A}^3\Pi \rightarrow \text{X}^3\Sigma^-$ and $\text{c}^1\Pi \rightarrow (\text{b}^1\Sigma^+, \text{a}^1\Delta)$ transitions which are of interest as probes of the NH molecule.

The quantities reported here are based on *ab initio* electronic structure calculations using a recently developed system of programs BROOKLYN 89. These programs are based entirely on the symbol matrix element approach.¹ The starting point is a large scale (10^5 – 10^6 term) direct CI wavefunction developed from a state averaged MCSCF reference space. Using these wavefunctions relativistic effects are incorporated within the Breit-Pauli approximation. Our approach^{2,3} enables us to treat both \hat{H}^{so} , the spin-orbit and the spin-other-orbit operator, and \hat{H}^{ss} the dipolar spin-spin operator in an equivalent manner. The first order perturbations, $\Psi^1(\text{I})$, with

$$\Psi(\text{I}) = \Psi^0(\text{I}) + \Psi^1(\text{I}) \quad 1.1$$

required for the description of spin-forbidden radiative decay problems are determined *exactly* within large (10^5 – 10^6 term) configuration state function spaces by direct solution of

$$[\hat{H}^0 - E^0(\text{I})]\Psi^1(\text{I}) = -\hat{H}^{\text{BP}}\Psi^0(\text{I}) \quad 1.2$$

where $\hat{H}^{\text{BP}} = \hat{H}^{\text{so}} + \hat{H}^{\text{ss}}$. When the states in the zeroth order space are quasidegenerate (as in the He_2 system discussed below) a generalization of eqs. 1.1–1.2 based on partitioning theory is used.⁴ Perturbed zeroth order states, referred to as dressed diabatic states

$$\Psi^{\text{d}}(\text{I}) = \Psi^0(\text{I}) + \Psi^1_{\text{Q}}(\text{I}) \quad 1.3$$

are obtained as the solution of

$$[\hat{H}^0 - E^0(\text{I})]\Psi^1_{\text{Q}}(\text{I}) = -\hat{Q}\hat{H}^{\text{BP}}\Psi^0(\text{I}) \quad 1.4$$

where \hat{Q} projects onto the orthogonal complement of the quasidegenerate state. The final electronic eigenstates of the system are the eigenfunctions of $\hat{H}^0 + \hat{H}^{\text{BP}}$ in the basis of the Ψ^{d} .

Electronically nonadiabatic processes are characterized within an adiabatic states approach. This approach is enabled by the exact (for a given set of CI wavefunctions) computation of the nonadiabatic coupling matrix elements

$$g_{\alpha}(\text{J}, \text{I}) = \langle \Psi^0(\text{J}) | \frac{\partial}{\partial R_{\alpha}} \Psi^0(\text{I}) \rangle$$

and

$$k_{\alpha,\beta}(\text{J}, \text{I}) = \langle \frac{\partial}{\partial R_{\alpha}} \Psi^0(\text{J}) | \frac{\partial}{\partial R_{\beta}} \Psi^0(\text{I}) \rangle \quad 1.5$$

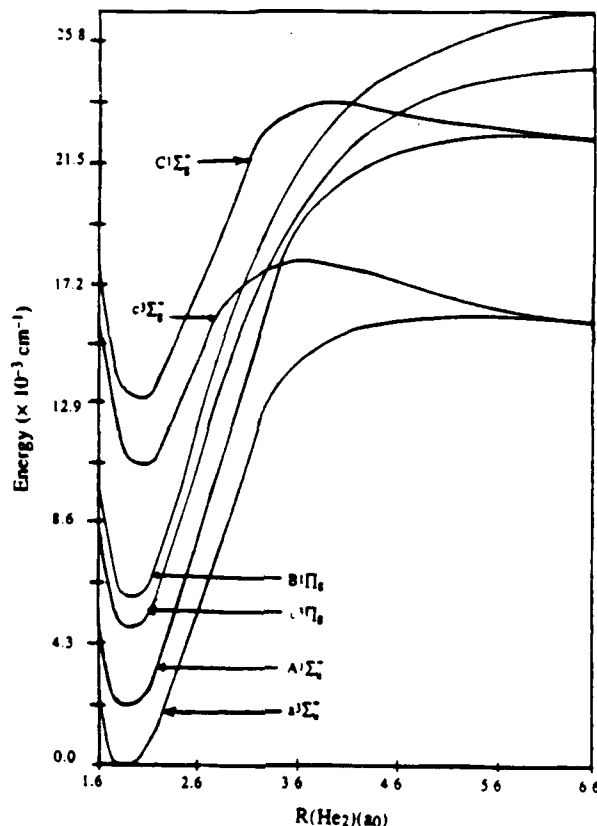
using analytic gradient techniques.⁵ Our computational methods are summarized in the figure which accompanies this abstract.

A: Decay of Metastable $\text{He}(2^3\text{S})$

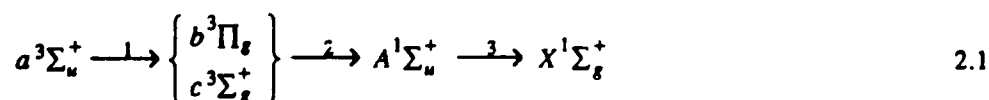
The first excited state of helium, $\text{He}(2^3\text{S})$, is highly metastable in an isolated environment as its radiative decay to the ground state is both spin and dipole forbidden. Since this state has over 19 eV of energy relative to the ground state it is of interest in this program. Our studies are aimed at describing the electronic structure aspects of the decay of $\text{He}(2^3\text{S})$ induced by interactions with other helium atoms.

Previously at these meetings Chabalowski⁶ reported on the spin-forbidden dipole-allowed radiative decay process $\text{He}_2(\text{a}^3\Sigma_u^+; v = n) \rightarrow \text{He}_2(\text{X}^1\Sigma_g^+)$ and found $\tau(v=0) = 18\text{s}$, $\tau(v=9) = 6\text{s}$. Here⁷ we consider the electronic structure aspects of a nonadiabatic-radiative decay mechanism in which motion of $\text{He}(2^3\text{S}) + \text{He}$ on the $\text{a}^3\Sigma_u^+$ potential energy curve is coupled by relativistic, rotational and radiative interactions to the $\text{A}^1\Sigma_u^+$ state which serves as a gateway to the $\text{X}^1\Sigma_g^+$ (electronically quenched) state of He_2 through the spin-allowed dipole-allowed bound-free transition $\text{A}^1\Sigma_u^+ \rightarrow \text{X}^1\Sigma_g^+$. State averaged MCSCF/second order CI wavefunctions for the ground $\text{X}^1\Sigma_g^+$ state, and the excited, $\text{a}^3\Sigma_u^+$, $\text{A}^1\Sigma_u^+$, $\text{b}^3\Pi_g$, $\text{B}^1\Pi_g$, $\text{c}^3\Sigma_g^+$, and

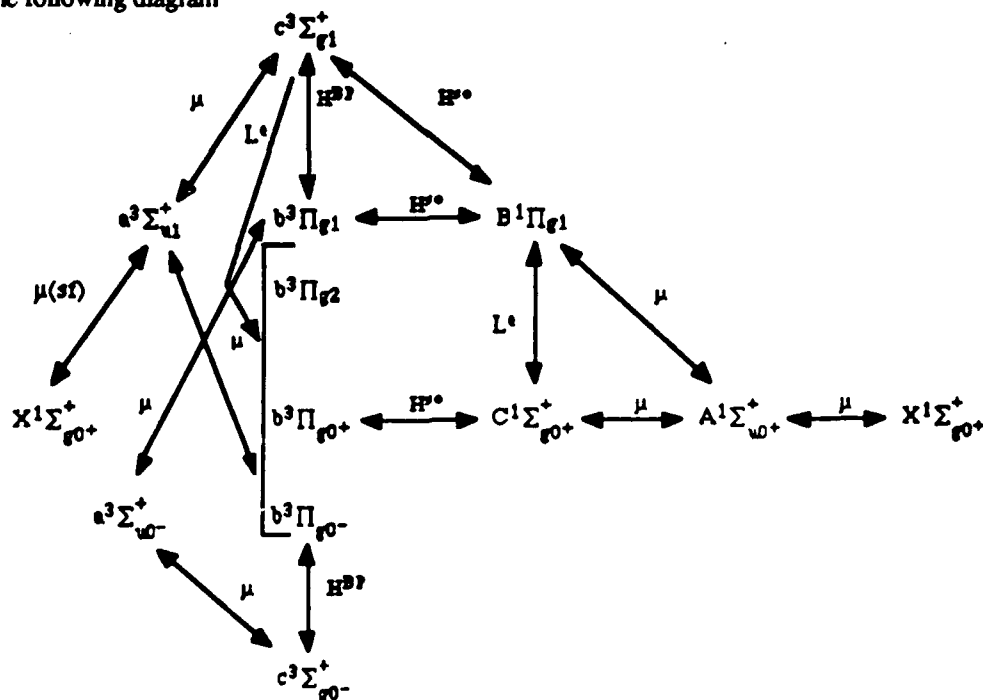
$C^1\Sigma_g^+$ states (referred to here as the primary space) of He_2 were determined. The potential energy curves for these states are given below.



Using these wavefunctions all interstate matrix elements of the form $\langle \Psi^0(J) | \hat{O} | \Psi^0(I) \rangle$ were determined for (i) $\hat{O} = \hat{H}^{BP}$, (ii) $\hat{O} = \hat{L}^2$, where \hat{L}^2 is the total electronic orbital angular momentum operator and (iii) $\hat{O} = \hat{\mu}$ where $\hat{\mu}$ is the dipole moment operator. These interactions, which describe, in phenomenological sense the following sequential decay process



are depicted in the following diagram



As indicated in step 2 of 2.1, in the nonrotating molecule these interactions give rise to the spin-forbidden dipole-allowed radiative transitions ($b^3\Pi_g, c^3\Sigma_g^+ \rightarrow A^1\Sigma_u^+$). However a complete description of these radiative decay processes requires consideration of interactions originating outside the primary space. Thus the spin-forbidden, dipole-allowed perpendicular, $\mu_\perp(J, A^1\Sigma_{u0}^+)$, $J = c^3\Sigma_g^+, b^3\Pi_{g1}$ and parallel, $\mu_\parallel(b^3\Pi_{g0}^+, A^1\Sigma_{u0}^+)$, transition moments attributable to interactions outside the primary space were determined using quasidegenerate perturbation theory.

In this approach the zeroth order wavefunctions for the $c^3\Sigma_g^+$, $b^3\Pi_{g1}$ and $b^3\Pi_{g0}^+$ states are replaced with following dressed diabatic wavefunctions (eq. 1.3)

$$\Psi^d(c^3\Sigma_g^+) = \Psi^0(c^3\Sigma_g^+) + \Psi_Q^1(^1\Pi_{g1}, c^3\Sigma_g^+) \quad 2.2$$

$$\Psi^d(b^3\Pi_{g1}) = \Psi^0(b^3\Pi_{g1}) + \Psi_Q^1(^1\Pi_{g1}, b^3\Pi_{g1}) \quad 2.3a$$

$$\Psi^d(b^3\Pi_{g0}^+) = \Psi^0(b^3\Pi_{g0}^+) + \Psi_Q^1(^1\Sigma_{g0}^+, b^3\Pi_{g0}^+) \quad 2.3b$$

Then with the zeroth order $A^1\Sigma_{u0}^+$ state replaced by its counterpart through first order in perturbation theory (eq. 1.1)

$$\Psi(A^1\Sigma_{u0}^+) = \Psi^0(A^1\Sigma_{u0}^+) + \Psi^1(^3\Pi_{u0}^+, A^1\Sigma_{u0}^+) + \Psi^1(^3\Sigma_{u0}^-, A^1\Sigma_{u0}^+) \quad 2.4$$

the following intrinsic or diabatic state transition moments were determined

$$\mu_\perp^d(c^3\Sigma_g^+, A^1\Sigma_{u0}^+) \equiv \langle \Psi^d(c^3\Sigma_g^+) | \hat{\mu}_\perp | \Psi(A^1\Sigma_{u0}^+) \rangle \quad 2.5a$$

$$= \langle \Psi^0(c^3\Sigma_g^+) | \hat{\mu}_\perp | \Psi^1(^3\Pi_{u0}^+, A^1\Sigma_{u0}^+) \rangle + \langle \Psi_Q^1(^1\Pi_{g1}, c^3\Sigma_g^+) | \hat{\mu}_\perp | \Psi^0(A^1\Sigma_{u0}^+) \rangle \quad 2.5b$$

$$\mu_\perp^d(b^3\Pi_{g1}, A^1\Sigma_{u0}^+) \equiv \langle \Psi^d(b^3\Pi_{g1}) | \hat{\mu}_\perp | \Psi(A^1\Sigma_{u0}^+) \rangle \quad 2.6$$

$$= \langle \Psi^0(b^3\Pi_{g1}) | \hat{\mu}_\perp | \Psi^1(^3\Sigma_{u0}^-, A^1\Sigma_{u0}^+) \rangle + \langle \Psi_Q^1(^1\Pi_{g1}, b^3\Pi_{g1}) | \hat{\mu}_\perp | \Psi^0(A^1\Sigma_{u0}^+) \rangle$$

and

$$\mu_\parallel^d(b^3\Pi_{g0}^+, A^1\Sigma_{u0}^+) \equiv \langle \Psi^d(b^3\Pi_{g0}^+) | \hat{\mu}_\parallel | \Psi(A^1\Sigma_{u0}^+) \rangle \quad 2.7$$

$$= \langle \Psi^0(b^3\Pi_{g0}^+) | \hat{\mu}_\parallel | \Psi^1(^3\Pi_{u0}^+, A^1\Sigma_{u0}^+) \rangle + \langle \Psi_Q^1(^1\Sigma_{g0}^+, b^3\Pi_{g0}^+) | \hat{\mu}_\parallel | \Psi^0(A^1\Sigma_{u0}^+) \rangle$$

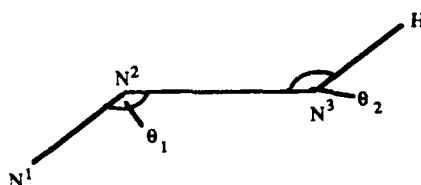
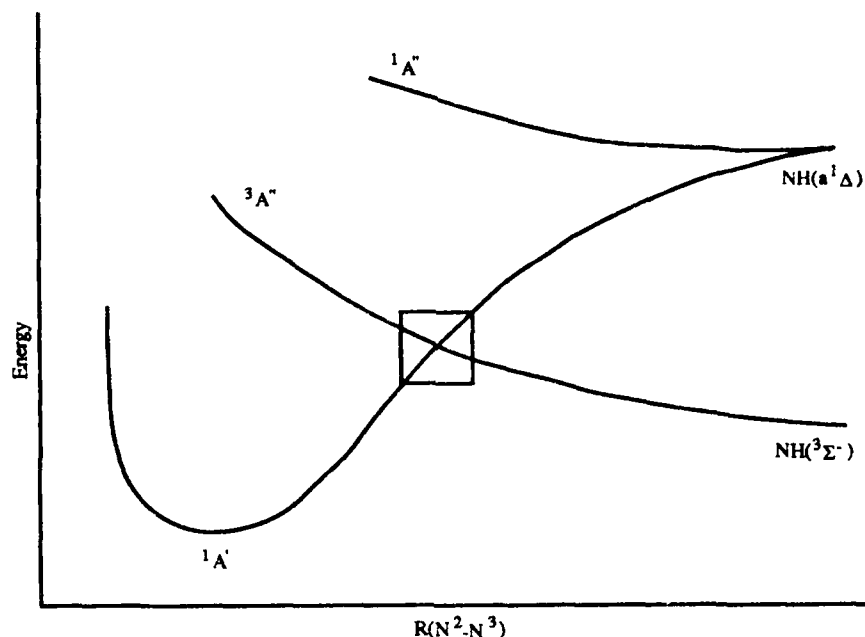
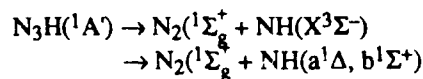
These spin-forbidden transition dipole moments represent additional couplings not included in the preceding diagram. Note that the use of quasidegenerate perturbation theory is essential here since it permits effects within the primary space to be partitioned from extraprimary space interactions.

In order to obtain a qualitative estimate of the efficiency of this quenching mechanism the probability for the spontaneous emission processes represented by step 2 in 2.1 were determined. For the $c^3\Sigma_g^+ \rightarrow A^1\Sigma_{u0}^+$ transition approximately 30% of the radiative rate is attributable to extraprimary space interactions. For the $(b^3\Pi_{g1}, b^3\Pi_{g0}^+) \rightarrow A^1\Sigma_{u0}^+$ transitions extraprimary space effects are negligible. The maximum total radiative rate for the (absolutely) bound levels of the $c^3\Sigma_g^+$, $b^3\Pi_{g1}$, and $b^3\Pi_{g0}^+$ states were found to give lifetimes of 60s, 40s and 2700s respectively. Thus it is likely that this step will represent a significant bottleneck to the mechanism 2.1.

B: The Decomposition Reaction $N_3H \rightarrow N_2 + NH$

At the last HEDM contractors meeting considerable attention was devoted to the photochemical decomposition of the azide N_3H . King and coworkers⁸ reported experimental observations of the distinct fine-structure states of $NH(X^3\Sigma^-)$ and Alexander et al.⁹ provided an explanation of an observed fine structure state preference based on *ab initio* electronic structure calculations and a dynamical symmetry analysis. While these studies have provided considerable insight into the photochemical decomposition a key factor, the branching ratio between the spin-allowed production of $NH(a^1\Delta)$ and the spin-forbidden production of $NH(X^3\Sigma^-)$ has yet to be explained. The computational determination of this quantity requires an analysis of the spin-orbit induced coupling of the lowest singlet and triplet PES's in the vicinity of the (minimum energy) curve crossing followed by an analysis of the propensity for electronic nonadiabaticity, that is spin-conserving behaviour. The situation is summarized in the following figure.

Spin-Forbidden Decomposition of N₃H



Here we report preliminary results from an ongoing study of this process, which focuses on a determination of the singlet-triplet couplings in the region \boxtimes . In C_s symmetry the coupling of the $1^1\text{A}'$ and $1^3\text{A}''$ potential energy surfaces is characterized by these distinct matrix elements which are:

$$\langle 1^1\text{A}'(0) | \hat{H}^{\text{so}} | 3^3\text{A}''(0) \rangle = \langle 1^1\text{A}'(0) | \hat{H}_z^{\text{so}}(0) | 3^3\text{A}''(0) \rangle \quad 3.1$$

$$\langle 1^1\text{A}'(0) | \hat{H}^{\text{so}} | 1/\sqrt{2} (3^3\text{A}''(1) + 3^3\text{A}''(-1)) \rangle = 0 \quad 3.2$$

and

$$\langle 1^1\text{A}'(0) | \hat{H}^{\text{so}} | 1/\sqrt{2} (3^3\text{A}''(1) - 3^3\text{A}''(-1)) \rangle = \sqrt{2} \langle 1^1\text{A}'(0) | \hat{H}_x^{\text{so}}(1) | 3^3\text{A}''(-1) \rangle \quad 3.3$$

On the right hand side of eqs. 3.1, 3.3 the nonvanishing space and spin contribution from the \hat{H}^{so} operator have been indicated explicitly.

The matrix elements in eqs. 3.1, 3.3 were evaluated at the minimum energy crossing point determined by Alexander et al.⁹, that is $R(\text{N}^1-\text{N}^2) = 2.064a_0$, $R(\text{N}^2-\text{N}^3) = 3.597a_0$, $R(\text{NH}) = 1.958a_0$, $\theta_1 = 180^\circ$, $\theta_2 = 90^\circ$. A large contracted gaussian basis set which consists of an (11s7p2d16s4p2d) basis on nitrogen and a (7s2p4s2p) basis on hydrogen was used. For this initial study the $3^3\text{A}''$ and $1^1\text{A}'$ wavefunctions were described in flexible first order configuration state function spaces of dimension 61626 and 41404 respectively. We find $\langle 1^1\text{A}'(0) | \hat{H}^{\text{so}} | 3^3\text{A}''(0) \rangle = 37.6 \text{ cm}^{-1}$ and $\langle 1^1\text{A}'(0) | \hat{H}^{\text{so}} | 1/\sqrt{2} (3^3\text{A}''(1) - 3^3\text{A}''(-1)) \rangle = 1.37 \text{ cm}^{-1}$. Thus the M_x components of the $3^3\text{A}''(M_x)$ state will be produced with significantly different probabilities. Since $R(\text{N}^2-\text{N}^3)$ is large it is useful to compare these matrix elements with those in the isolated NH moiety. We find

$$\langle X^3\Sigma_{0+}^- | \hat{H}^{\text{so}} | b^1\Sigma_{0+}^+ \rangle = 65 \text{ cm}^{-1} \quad 3.4a$$

$$\langle X^3\Sigma_{0+}^- | \hat{H}^{\text{so}} | d^1\Sigma_{0+}^+ \rangle = 10 \text{ cm}^{-1} \quad 3.4b$$

$$\langle X^3\Sigma_1^- | \hat{H}^{\text{so}} | c^1\Pi_1 \rangle = 25 \text{ cm}^{-1} \quad 3.4c$$

Matrix elements 3.4a, b can contribute to 3.1 while matrix element 3.4c contributes to 3.3. Then to the extent that an isolated molecule description is appropriate from 3.4 and 3.1, 3.3 we conclude that the $^1A'$ state has no $c^1\Pi$ character and at most 60% $b^1\Sigma^+$ character.

C: Spin-Forbidden and Spin-Allowed Radiative Transitions in NH

As noted in the introduction recent interest in the spectroscopy of NH has been motivated in part by its importance for the detection of NH produced in the decomposition, or reactions, of azides. There is little reliable *ab initio* data on the relevant electronic transition moments. In the course of our recent studies of the spin-forbidden dipole-allowed ($b^1\Sigma^+, a^1\Delta$) \rightarrow $X^3\Sigma^-$ transitions we have obtained transition moments for the dipole-allowed $A^3\Pi \rightarrow X^3\Sigma^-$, $c^1\Pi \rightarrow (b^1\Sigma^+, a^1\Delta)$ transitions. These calculations were performed with large flexible gaussian basis sets on nitrogen, 8s6p4d and hydrogen 5s4p using second order configuration state function spaces of $180-250 \times 10^3$ terms. The transition moments determined to date are summarized in the following table (Atomic Units used throughout).

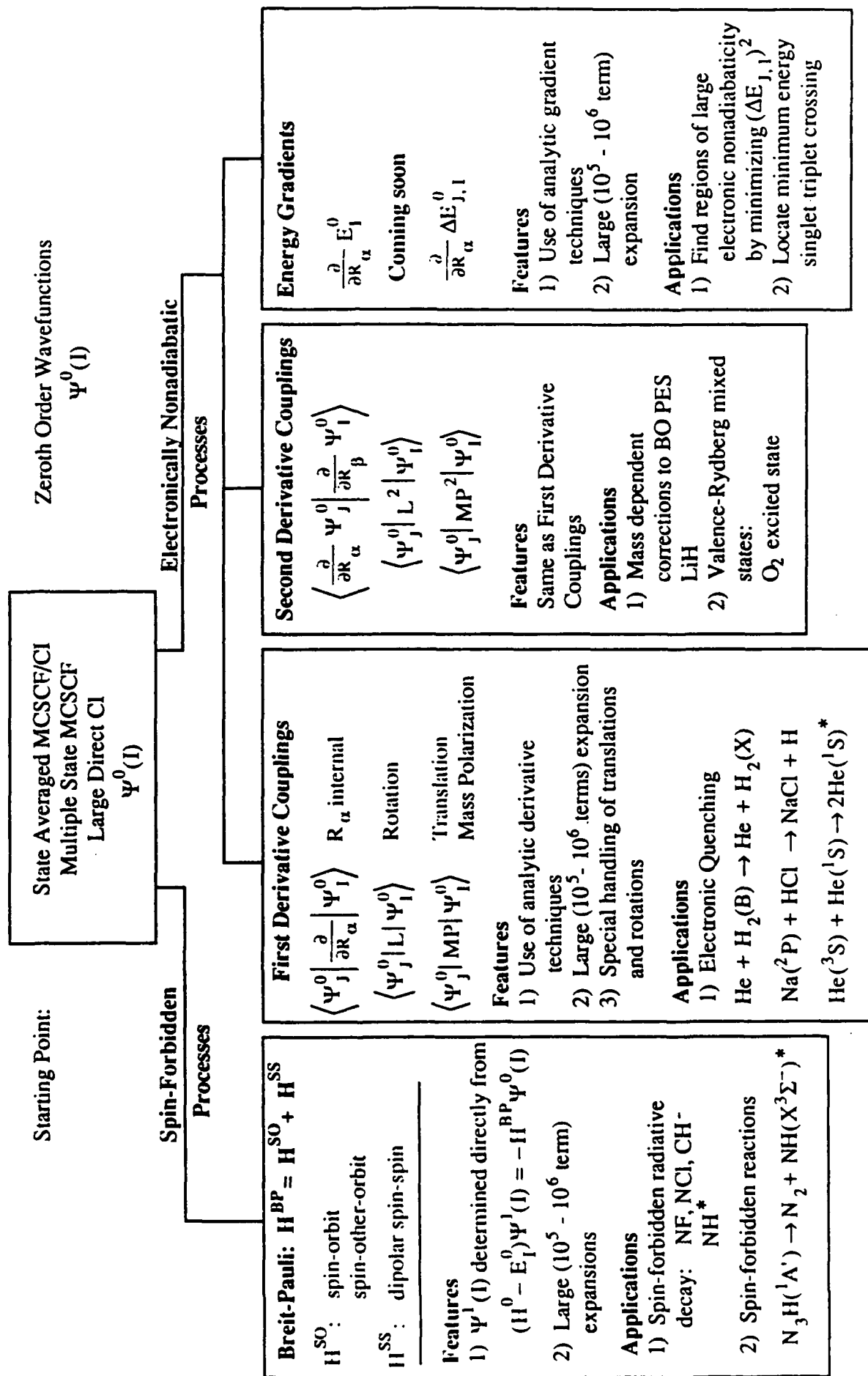
R	$\mu_1(c^1\Pi, a^1\Delta)$	$\mu_1(c^1\Pi, b^1\Sigma^+)$	$\mu_1(A^3\Pi, X^3\Sigma^-)$	$\mu_1(a^1\Delta, X^3\Sigma^-)$	$\mu_1(b^1\Sigma^+, X^3\Sigma^-)$	$\mu_0(b^1\Sigma^+, X^3\Sigma^-)$
1.80	0.2773	0.0950	0.2565	0.3991(-3) ^a	-0.6116(-3)	0.1471(-3)
1.975	0.2242	0.0740	0.2212	0.3375(-3)	-0.4964(-3)	0.1544(-3)
2.10	0.1882	0.0603	0.1964	0.2993(-3)	-0.4229(-3)	0.1560(-3)
2.40	0.1066	0.0345	0.1360	0.2198(-3)	-0.2663(-3)	0.1421(-3)

^aCharacteristic base 10 given parenthetically

References

1. B. Liu and M. Yoshimine, J. Chem. Phys. **74**, 612 (1981).
2. D. R. Yarkony, J. Chem. Phys. **84**, 2075 (1986).
3. J. O. Jensen and D. R. Yarkony, Chem. Phys. Lett. **141**, 391 (1987).
4. D. R. Yarkony, J. Chem. Phys. **89**, 7324 (1989).
5. (a) B. H. Lengsfeld, P. W. Saxe and D. R. Yarkony, J. Chem. Phys. **81**, 4549 (1984).
(b) P. W. Saxe, B. H. Lengsfeld and D. R. Yarkony, Chem. Phys. Lett. **113**, 159 (1985).
(c) B. H. Lengsfeld and D. R. Yarkony, J. Chem. Phys. **84**, 348 (1986).
(d) J. O. Jensen and D. R. Yarkony, J. Chem. Phys. **89**, 975 (1988).
6. C. F. Chabalowski, J. O. Jensen, D. R. Yarkony and B. H. Lengsfeld, J. Chem. Phys. **90**, 2504 (1989).
7. D. R. Yarkony, J. Chem. Phys., in press.
8. J. C. Stephenson, M. P. Casassa and D. S. King, J. Chem. Phys. **89**, 1378 (1988).
9. M. H. Alexander, H.-J. Werner and P. J. Dagdigan, J. Chem. Phys. **89**, 1388 (1988).

SYMBOLIC MATRIX ELEMENT BASED QUANTUM CHEMISTRY PROGRAMS FOR
CHARACTERIZING SPIN-FORBIDDEN AND ELECTRONICALLY NONADIABATIC PROCESSES



*High Energy Density Systems in Cryogenic Media:
The Production and Reaction of Atoms and Radicals*

Eric Weitz
Department of Chemistry
Northwestern University
Evanston, IL 60208

The overall aim of our program is to investigate the effect of a condensed phase rare gas environment on the photochemistry, photophysics and subsequent chemistry of reactive species. Within the context of this overall goal the major areas of investigation in our AFOSR supported work will center on:

- Investigations of the influence of low temperature condensed phase media on dynamical processes including photodissociation and energy transfer.
- Measurements of diffusion coefficients in low temperature condensed phase media
- The effect of low temperature condensed phase media on the rates and pathways of chemical reactions.

Our work to date has concentrated on the first two areas. This report will summarize the results of our work in these two areas in the last year.

Energy Transfer

Isolated binary collision (IBC) models of vibrational energy transfer and relaxation processes in dense media have been developed in an effort to obtain a predictive ability for rates for these process in dense media based on rates for the corresponding processes in a dilute gas phase environment. In its simplest form an IBC picture of vibrational relaxation in dense media assumes that vibrational relaxation is due to binary interactions which are well separated in time (time between encounters that leads to energy transfer \gg vibrational period) and that the probability of relaxation per collision event is independent of phase. Then

$$1/\tau = 1/\tau_c \cdot P \quad (1)$$

where P can be determined from gas phase experiments. In this picture, the problem boils down to a calculation of $1/\tau_c$, the collision rate in the dense media (condensed phase). A variety of approaches have been used to calculate $1/\tau_c$. The simplest is the cell model of Madigosky and Litovitz¹ where

$$\frac{1}{\tau_c} = \frac{\bar{v}}{(\rho^{-1/3} - \sigma)} = \left[\frac{8kT}{\pi\mu} \right]^{1/2} (\rho^{1/3} - \sigma)^{-1} \quad (2)$$

Current treatments typically employ radial distribution functions and derive formulas of the type

$$\frac{1}{\tau_c} = \frac{1}{\tau_g} \frac{\rho_l}{\rho_g} \quad (3)$$

here various methods are used to evaluate $g_l(R^*)$, the radial distribution function at R^* , the effective distance for vibrational energy transfer.²

We have been interested in the applicability of IBC models to systems undergoing V-V energy transfer and those involving polar molecules.³⁻⁵ As will be discussed below, in polar systems strong

interactions may lead to complex formation in dense media which could lead to significant deviations from the predictions of IBC models.

In an effort to investigate these questions we have been studying relaxation and energy transfer processes for HF and HCl in rare gas media.

We have been able to produce vibrationally excited species in condensed media via any of three processes. They are

- 1) Photodissociation and recombination of a diatomic. This has been applied with success to HCl photolyzed by ArF radiation.³
- 2) Direct excitation of the desired species with a pulsed tunable infrared laser. This has also been applied with success to HCl.⁴
- 3) Photoelimination of a vibrationally excited species from an appropriate precursor. This has also been successfully applied to HCl⁵ and HF*. Vibrationally excited HF can be produced via ArF photolysis of C₂HF₃.

To obtain a data base from which the gas phase probability of relaxation of a species can be extracted, we have measured the vibrational relaxation of HF by Xe, Kr and Ar at room temperature and at temperatures that correspond to convenient temperatures for studies of relaxation processes in the corresponding liquid rare gas. Vibrational relaxation is monitored by following the infrared emission of HF ($v=1$) with an InSb detector. The HF($v=1$) emission is isolated from emission from higher vibrational states using an interference filter which primarily views the R branch of the $v=1 - v=0$ transition. The signal from the InSb detector is digitized and averaged with a LeCroy digital oscilloscope. The averaged signal is fed to a computer for analysis. This data is presented in table 1 and is shown plotted versus the square root of reduced mass in figure 1.

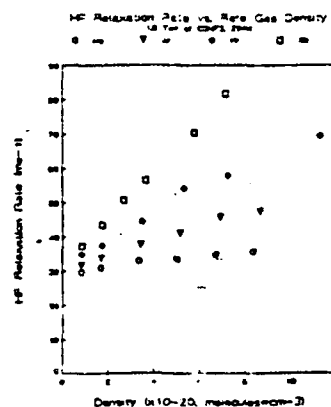
RELAXATION RATE CONSTANTS ($\text{cm}^3\text{molec}^{-1}\text{s}^{-1}$)

T(k)	$k_{\text{HF-He}}$	$k_{\text{HF-Ar}}$	$k_{\text{HF-Kr}}$	$k_{\text{HF-Xe}}$	$k_{\text{HF-C}_2\text{HF}_3}$
294	0.76×10^{-17}	2.1×10^{-17}	3.4×10^{-17}	6.9×10^{-17}	2.3×10^{-13}
204		4.9×10^{-17}	4.6×10^{-17}	17.6×10^{-17}	
193		5.0×10^{-17}	4.9×10^{-17}		
$\text{Probability/Collisions } P_{AB} = \frac{k_{AB}}{z_{AB}}$					
294	0.23×10^{-7}	0.94×10^{-7}	1.6×10^{-7}	3.0×10^{-7}	0.98×10^{-3}
204		2.7×10^{-7}	2.6×10^{-7}	9.2×10^{-7}	
193		2.8×10^{-7}	2.8×10^{-7}		

The hydrogen halides have been shown to relax via V-R energy transfer processes. Therefore it is not surprising that a plot of the rate of relaxation versus $\mu^{1/2}$ is not linear. A linear plot, where the probability of relaxation decreased dramatically with reduced mass, would be predicted by SSH theory which attempts to describe V-T relaxation processes.⁶ A relatively constant probability of relaxation as a function of reduced mass would be expected by simple theoretical descriptions of V-R energy transfer processes.⁷ What is seen in figure 1 is a significant increase in the probability of relaxation as a function of the mass of the collision partner. This type of behavior is indicative of the

Figure 1.

HF-M relaxation at
294 K. Typical
error limits are
 $\pm 10\%$.



involvement of attractive forces in the relaxation process.⁸ Rates of relaxation of HF in liquid Xe and liquid Kr have been measured and this data has been previously reported⁹.

The compatibility of these two sets of data with IBC predictions can be determined by evaluation of the radial distribution function in equation 3. To do this, we have used a treatment by Chesnoy¹⁰. For HF in liquid Xe and liquid Kr this predicts that,

$$\frac{\tau_g \rho_g}{\tau_l \rho_l} \quad (4)$$

When we compare the ratio for the rate of relaxation of HF in liquid Xe, scaled for the density of liquid Xe, versus gas phase Xe at 204 K we find it is 0.1 rather than approximately 1 which would be predicted by the treatment in equation (4). Similarly, the rate of relaxation of HF by liquid Kr, scaled for the density of liquid Kr, versus gas phase Kr at 193 K is 0.15 rather than the predicted 1.0! Thus HF relaxes significantly more slowly in liquid Kr or liquid Xe than expected. Two possible related explanations for this behavior involve:

- 1) Formation of a transient HF-M complex which increases the effective moment of inertia of the HF which would lead to a decrease in the rotational velocity in an HF - rare gas collision and thus a decrease in the probability of vibration-rotation energy transfer; the process by which HF is known to relax in the gas phase or,
- 2) Formation of a transient HF-M complex which may be a multicentered complex where the complexed rare gas atoms shield the HF from impulsive collisions with the remainder of the rare gas atoms thus also decreasing the probability of vibration-rotation energy transfer.

Our recent work on HF relaxation in liquid Ar also implies that complexes are involved in the relaxation process¹¹.

Our HF is produced "in situ" by photolysis of C_2HF_3 because it is very difficult to work with HF particularly at low temperature where dimerization is an important process. However, because HF is produced via photoelimination, we have C_2HF_3 molecules and photofragments present in our system. To minimize the effect of photofragments we use only one or two photolysis pulses before changing samples. However, there is still the possibility of effects due to the presence of the parent molecule and photofragments. Since we can produce HCl^* in a cleaner fashion by either method 1 or 2 described above, we decided to see if similar effects were observed with HCl .

Figure 2 shows data for the relaxation of HCl by Xe at both room temperature and at 204K. Note that the room temperature rate for the relaxation of HCl is within experimental error of that determined by Schramm¹². Clearly, however, the behavior of the low temperature data is quite anomalous. An explanation for this behavior could be based on the same grounds as that discussed

above for the slow relaxation of HF in the liquid rare gases. The method of production of HCl^* we used for these measurements still involves some potential chemistry. For this reason we are going to repeat these experiments using our IR-WEX excitation source where the only species present in the cell will be HCl , HCl^* , Xe and possibly HCl-Xe complexes. Since we have already reproduced the literature rate of relaxation of Xe at room temperature with the photolysis method and we have previously checked the photolysis method of products of HCl^* versus the WEX method of products,⁴ we are confident the two experiments will give the same results. Nevertheless, we want to be absolutely sure that the very surprising data we have obtained is not due to an artifact associated with the photolysis process.

Figure 2a.
HCl-Xe relaxation
at 294 K.

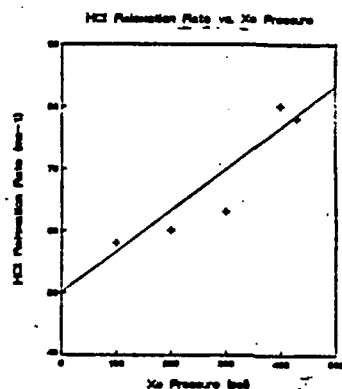
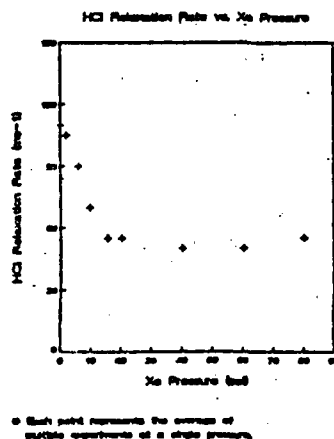


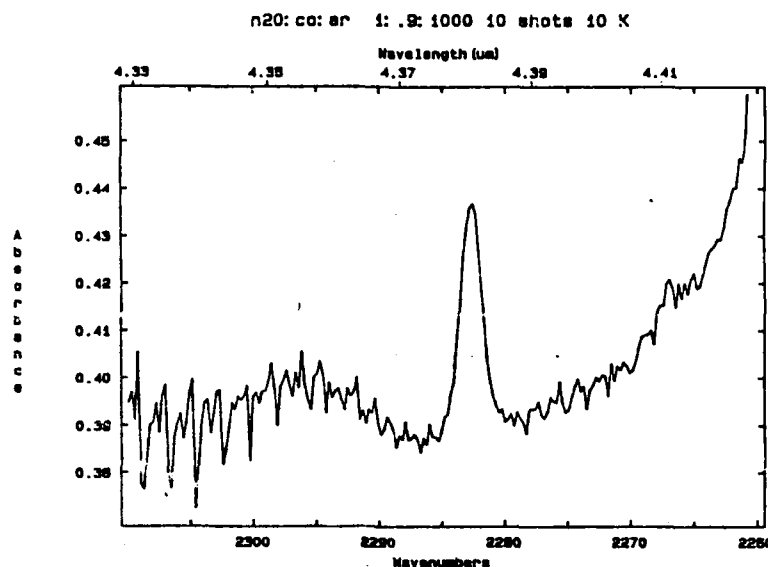
Figure 2b.
HCl-Xe relaxation
at 204 K.



Diffusion

We have devised an experimental procedure to measure diffusion coefficients of species in low temperature condensed phase systems. The procedure involves the photolytic production of the species of interest and the measurement of the diffusion coefficient of the species by monitoring the rate of a diffusion controlled reaction of the species. We are currently investigating diffusion of O atoms. The O atoms are produced via photolysis of N_2O using ArF laser radiation and the reaction of the O atoms with CO is monitored by observing the production of CO_2 . Figure 3 shows a CO_2 signal that has been generated via photolysis of N_2O in a rare gas crystal.

Figure 3.



For technical reasons the actual reaction that is being monitored is



Photolysis was done in a crystal that had the composition: Ar:N₂O:CO of 1000:1:0.9. At present we are not prepared to draw definite conclusions regarding O atom diffusion in this system or related systems.

References

1. W. M. Madigosky and T. A. Litovitz, J. Chem. Phys. **34**, 489 (1961).
2. J. Chesnoy, Ann. Phys. Fr. **9**, 893 (1984).
3. J.T. Knudtson and Eric Weitz, Chem. Phys. Letters **104**, 71 (1984)
4. Y. P. Vlahoyannis, H. Krueger and E. Weitz, J. Chem. Phys. **86**, 3311 (1987)
5. J. T. Knudtson, Y. P. Vlahoyannis, H. Krueger and E. Weitz, J. Chem. Phys. **82**, 4381 (1985)
6. R. N. Schwartz, Z. I. Slawsky and K. F. Herzfeld, J. Chem. Phys. **20**, 1591 (1952).
7. C. B. Moore, J. Chem. Phys. **43**, 2979 (1965).
8. E. Weitz and G. W. Flynn, Ann. Rev. of Phys. Chem. **25**, 275 (1974).
9. E. Weitz, Proceedings of the 1988 Conference on High Energy Density material.
10. J. Chesnoy, Chem. Phys. **83**, 283 (1984).
11. A. Moustakas and E. Weitz, unpublished data.
12. H. Schwahn and B. Schramm, Chem. Phys. Letters **130**, 29 (1986).

CHEMICALLY BOUND EXCITED CLUSTERS. II *

PS 27

C.A.Nicolaides

Theoretical and Physical Chemistry Institute,

National Hellenic Research Foundation,

48, Vas.Constantinou Ave., Athens 116 35, Greece

Contents

- I. On the Stability of Molecules at Avoided Crossings of Dissociating Ground States
- II. An Estimate of the Lifetime of H_4^+
- III. A MIES Geometry for $(H_2O)_2^+$
- IV. Molecular Electronic States in Ionic Crystals
- V. References
- VI. Tables and Figures

*Lecture presented at the 3rd annual contractors conference on High Energy Density Materials, March 1989, New Orleans organized by the AFOSR, AFAL and the National Research Council.

*Research supported by grant AFOSR 87-0342

I. On the Stability of Molecules at Avoided Crossings of Dissociating Ground States

In ref.1, results of configuration-interaction calculations on H_4 and other hydrogen clusters were presented which showed that at certain nonstandard geometries the adiabatic ground and first excited energy surfaces along a reaction coordinate have the features depicted in fig.1.

The distinguishing feature of the avoided crossing of fig.1 is that the lowest-curve (1) represents a slice of a ground state dissociating hypersurface. This implies that, in principle, the minimum -if it is real- can trap energy whose decay is allowed only via tunneling. In the case of $(H_2)_2$ and of other clusters, the minimum on (1) turns out to be virtual /1-6/. In other species, this need not occur.

Curve (2) represents a chemically bound excited state hypersurface which goes asymptotically into products one of which is excited. Calculations on $(H_2)_2$ and on other clusters /1,2,6-8/ show that this minimum is real in C_s symmetry. The energy which is trapped here dissipates into the ground state dissociative products via nonadiabatic coupling. In the case of $(H_2)_2$, this fragmentation rate is of the order of 10^{13} sec^{-1} /ref.9 and Table 1/.

The prediction - for a class of molecules- of the avoided crossing-induced binding which is shown in fig.1, was made possible by the maximum ionicity of excited state (MIES) theory /1,2/. This theory has suggested the existence of chemically bound excited clusters (CBEC) whose prediction is guided by the ionic character of excited molecular moieties which appear in one of the dissociation channels. Symmetry considerations and orbital overlap effects are also taken into account. For a number of important clusters, the relevant excited molecular moiety is the $H_2^+ B^1\Sigma_u^+$ state /1,2/. This state changes from covalent to ionic and back to covalent character as a function of the internuclear distance. Its ionic character is maximized around 4.0 a.u./10/. This information was used as input to explain and predict the MIES bonding and structure of noble gas dihydrides and of hydrogen clusters /1,2/. The intramolecular charge transfer is imprinted on the electronic energy spectrum as an avoided crossing between the

dissociating ground and the first excited hypersurfaces along a geometrical coordinate which emerges naturally as a fragmentation reaction coordinate. E.g., in $(H_2)_2$, this coordinate represents the distance of one hydrogen atom from the center of the isosceles triangle H_3 .

The charge transfer which occurs at the avoided crossing of fig.1 is reflected in the character of the wavefunctions. This is of a mixed valence-Rydberg type and is revealed from CI calculations with multireference zeroth order vectors and large basis sets with diffuse functions /1,11/. On the other hand, the extreme proximity of the adiabatic hypersurfaces in CBEC and the absence of covalent multiple bonding has allowed a diabatic (crossing) representation to be constructed at an approximate MIES geometry, by state-specific SCF calculations of closed and open shell single configurations of the same symmetry /7/.

The ground state tunneling characteristics of fig.1 which are caused by intramolecular charge transfer in neutral, dissociating clusters, can also be identified in positively or negatively charged species from their dissociation products which involve ionic fragments. For example, the lowest state of $^2\Sigma^+$ symmetry in He_2^+ , which is a result of valence-Rydberg mixing $(1\sigma_g 1\sigma_u^2 \leftrightarrow 1\sigma_g^2 n\sigma_g)$, has the tunneling form of curve 1 of fig. 1 /12/. However, it is radiatively unstable due to the $^2\Sigma_g^+ \rightarrow ^2\Sigma_u^+ (1\sigma_g^2 1\sigma_u)$ transition. On the other hand, as we reach the ionization threshold of the $He_2^+ \ ^2\Sigma_g^+$ Rydberg series, the bound, lowest $He_2^{++} \ ^1\Sigma_g$ state is obtained, whose potential energy keeps a similar tunneling form (See fig.4 and Table 5 of ref.12), while its wave-function is a mixture of $1\sigma_g^2$, $1\sigma_g n\sigma_g$ and $1\sigma_u^2$ configurations /13/. Given the existence of ground state tunneling surfaces with real, chemical minima, it is important to know the fragmentation rates. In the case of certain dications whose potential energy curve is similar to that of He_2^{++} , these rates are of the order of 10^6 sec^{-1} or larger /14/.

II. An Estimate of the Lifetime of H_4^+

The geometry of H_4^+ has been found to be that of a pyramidal structure with a C_{2v} triangular basis and a C_s overall symmetry belonging to the A' irreducible

representation, near a very narrow avoided crossing with the dissociative A' ground state /1,2/. In order to explore the degree of stability of this CBEC state, the zeroth vibrational level for the local mode involving motion of the H atom at the apex of the pyramid, towards and away from the triangular basis (R coordinate), has been determined assuming all other nuclear motions frozen. This level is about 518 cm^{-1} lower than a nearby conical intersection, which occurs when the triangular base acquires a C_{3v} symmetry /2/.

Within this $\text{H}_3\text{-H}$ diatom approximation, H_4^* ($v=0$) can make a transition to the dissociative ground state (H_2+2H) either non-radiatively, via the vibronic coupling in the region of the avoided crossing, or radiatively (a much slower process). We have computed the H_4^* lifetime due to the vibronic coupling between the two surfaces in the region of avoided crossing to be of the order of 10^{-13} sec /9/.

Analytic as well as numerical methods have been employed for the computation of the golden-rule expression for the predissociation rate

$$W = \frac{2\pi}{h} \left| \left\langle X_f \left| B(R) + 2A(R) \frac{\partial}{\partial R} \right| X_i \right\rangle \right|^2$$

X_i and X_f are the initial and final nuclear wavefunctions and

$$B(R) = - \frac{\hbar^2}{2\mu} \left\langle \Psi_f \left| \frac{\partial^2}{\partial R^2} \right| \Psi_i \right\rangle$$

$$A(R) = - \frac{\hbar^2}{2\mu} \left\langle \Psi_f \left| \frac{\partial}{\partial R} \right| \Psi_i \right\rangle$$

$B(R)$ is very small and was ignored. $A(R)$ was computed by a finite differences method.

For the analytic method, which discretizes the continuum with the same basis functions used for the bound X_i and uses special provisions (such as the Stieltzes derivative formula) for the determination of the normalization factor, box normalized sin and cos functions were used, which were shown to be convenient as well as effective in the study of predissociation of HeH^* by Petsalakis et al /15/.

For reasons of comparison, the vibrational functions were also obtained numerically. The results are shown in Table 1.

The extreme instability of the $(\text{H}_2)_2^+$ cluster is probably characteristic of other such singlet CBECs. Although their study is still of great interest from the point of view of intramolecular energy transfer, as regards the question of stability it is useful to extend the theoretical search for CBECs which have higher spin symmetries or are embedded in crystals.

III. A MIES Geometry for $(\text{H}_2\text{O})_2^+$

We /16/ have applied the MIES analysis to the understanding of excited hypersurfaces of $(\text{H}_2\text{O})_2$. The semifinal results -obtained from large MCHF with CI calculations- demonstrate the diabatic crossing /7/ as well as the adiabatic avoided crossing along the coordinate which separates " H^- " from " $(\text{H}_2\text{O}_2)\text{H}^+$ ". The results are depicted in Figures 2 and 3. Tables 2 and 3 show our results from three types of computational methods for the geometry and vibrational frequencies of $(\text{H}_2\text{O}_2)\text{H}^+$.

It would be of interest to subject these intramolecular charge-transfer phenomena to experimental analysis using ultrafast spectroscopic methods (eg. ref.17).

IV. Molecular Electronic States in Ionic Crystals.

Although this research direction is not part of our grant proposal, I incorporate the results of our related work, since they are very relevant to the theme of the conference.

As regards the question of flow of vibronic energy, it has recently been determined theoretically /18/ that the excited electronic spectra of molecules and clusters are perturbed strongly by certain solid state environments. This finding has important implications for energy absorption, transfer and dissipation. For example, under suitable conditions, situations which are related to that of fig.1

can lead to an increase of the lifetime of autofragmenting molecular states embedded in solids .

Table 4 and Fig.4 demonstrate the influence of specific crystals on the spectrum of H_2 and on the MIES avoided crossing in H_4 .

V. References

1. C.A.Nicolaides, I.D.Petsalakis and G.Theodorakopoulos, J.Chem.Phys. 81, 748 (1984); 80, 1705 (1984).
2. A.Metropoulos and C.A.Nicolaides, J.Phys.B21, L77(1988)
3. J.A.Montgomery, Jr. and H.H.Michels, J.Chem.Phys. 86 5882 (1987)
4. E.M.Evleth and E.Kassad, J.Chem.Phys.89, 3928 (1988)
5. J.A.Montgomery, Jr. and H.H.Michels, J.Chem.Phys. 89 3929 (1988)
6. S.Yu Huang, Z.Sun and W.A.Lester, Jr., First meeting on High Energy Density Matter, supported by the AFOSR and the AFAL, Rosslyn, Va.(1987).
7. C.A.Nicolaides and A.Zdetsis, J.Chem.Phys. 80, 1900 (1984)
8. J.K.Perry and D.R.Yarkony, J.Chem.Phys. 89, 4945(1988)
9. I.D.Petsalakis, A.Metropoulos, J.Theodorakopoulos and C.A.Nicolaides, Chem.Phys.Lett., to be published.
10. W.Kolos and L.Wolniewicz, J.Chem.Phys. 45, 509 (1966); P.Karafiloglou, G.Theodorakopoulos and I.D.Petsalakis, J.Mol.Stru.(Theochem) 180, 31(1988).
11. In general, charge transfer situations in molecular excited states are characterized by a few, chemically meaningful state-specific configurations, whose contribution to the phenomenon can be computed very effectively via nonorthonormal CI (I.D.Petsalakis, G.Theodorakopoulos, C.A.Nicolaides and R.J.Buenker, J.Chem.Phys. 81, 3161(1984); *ibid*, 81, 5952(1985)).
12. A.Metropoulos, C.A.Nicolaides and R.J.Buenker, Chem.Phys.114, 1(1987)
13. The tunneling form of the He_2^{++} potential was first computed by L.Pauling J.Chem.Phys.1, 56 (1933). He explained this remarkable feature in a valence bond picture, in terms of covalent-ionic mixing of the structures $\text{He}:\text{He}:$ (repulsive) and $\text{He}:\text{He}^+:$ (attractive).
14. E.g. JM Curtis, AG Brenton and RK Boyd, Chem.Phys.116, 241 (1987); RW Wetmore and RK Boyd, J.Phys.Chem. 90 6091 (1986) and refs. therein.
15. I.D.Petsalakis, G.Theodorakopoulos and R.J.Buenker, Phys.Rev. A38 4004 (1988).
16. C.A.Nicolaides and P.Valtazanos, unpublished.
17. M.Dantus, M.S.Rosker and A.H.Zewail, J.Chem.Phys. 87, 2395(1987).
18. C.A.Nicolaides, P.Valtazanos and N.C.Bacalis, Chem.Phys.Lett. 151, 22(1988).

Table 1

Lifetime of H_4^+

Results of the analytic and numerical calculations /9/.

	Analytic	Numerical
Width(cm^{-1})	72.54	16.40
Trans.rate(s^{-1})	0.1366×10^{14}	0.0309×10^{14}
Lifetime(s)	0.73×10^{-13}	3.2×10^{-13}

Table 2. Optimized geometries for the protonated hydrogen peroxide cation and for Hydrogen Peroxide in the SCF, FORS-MCSCF and MP2 approximations. Bond lengths are in Å and bond and torsion angles are in degrees. The FORS-MCSCF calculation involves 5992 configurations while the the MP2 calculation involves 48932. The experimental geometry of Hydrogen peroxide is also given for comparison.

H₂O₂				
	<u>SCF</u>	<u>MCSCF</u>	<u>MP2</u>	<u>Expt</u>
R(O ₁ -O ₂)	1.39084	1.48768	1.46615	1.452
R(O ₁ -H ₁)	0.94663	0.97372	0.97005	0.965
R(O ₂ -H ₂)	0.94663	0.97372	0.97005	0.965
O ₂ -O ₁ -H ₁ bend	102.84	98.67	99.20	100.0
O ₁ -O ₂ -H ₂ "	102.84	98.67	99.20	100.0
H ₁ -O ₁ -O ₂ -H ₂ torsion	114.22	119.05	119.01	119.1
Energy (Hartree)	-150.82239	-150.92639	-151.20179	

H₃O₂⁺			
	<u>SCF</u>	<u>MCSCF</u>	<u>MP2</u>
R(O ₁ -O ₂)	1.39975	1.48080	1.45446
R(O ₁ -H ₁)	0.96567	0.99225	0.98922
R(O ₁ -H ₂)	0.96567	0.99225	0.98922
R(O ₂ -H ₃)	0.96128	0.98555	0.98240
O ₂ -O ₁ -H ₁ bend	108.51	103.54	104.11
O ₂ -O ₁ -H ₂ "	108.51	103.54	104.11
O ₁ -O ₂ -H ₃ "	101.94	99.43	99.96
H ₁ -O ₁ -O ₂ -H ₃ torsion	118.88	123.33	122.54
H ₂ -O ₁ -O ₂ -H ₃ "	118.88	123.33	122.54
Energy (Hartree)	-151.09350	-151.22354	-151.46618

Table 3 Vibration Frequencies (in cm^{-1}) for the protonated hydrogen peroxide cation and for Hydrogen Peroxide in the SCF, FORS-MCSCF and MP2 approximations. The FORS-MCSCF calculation involves 5992 configurations while the MP2 calculation involves 48932. The experimental frequencies for Hydrogen peroxide are also given for comparison.

		H₂O₂			
		<u>SCF</u>	<u>MCSCF</u>	<u>MP2</u>	<u>Expt</u>
a	ν_1 (OH symm. stretch)	4175	3752	3859	3877 \pm 3
	ν_2 (OOH symm. bend)	1605	1437	1432	1424 \pm 10
	ν_3 (OO stretch)	1167	829	924	911 \pm 2
	ν_4 (internal rotations)	410	343	369	
b	ν_5 (OH asym. stretch)	4172	3754	3856	3888 \pm 2
	ν_6 (OOH asym. bend)	1470	1308	1296	1278 \pm 6

		H₃O₂⁺		
		<u>SCF</u>	<u>MCSCF</u>	<u>MP2</u>
a'	ν_1 (OH sym. stretch)	4003	3655	3730
	ν_2 (OH ₂ sym. stretch)	3861	3527	3568
	ν_3 (OH ₂ bend)	1804	1675	1661
	ν_4 (OOH bend)	1613	1479	1478
	ν_5 (OH ₂ wag)	1056	1096	1078
	ν_6 (OO stretch)	1001	830	920
a''	ν_7 (OH ₂ asym. stretch)	3956	3625	3673
	ν_8 (OH ₂ asym. wag)	1289	1188	1196
	ν_9 (internal rotations)	471	398	444

Table 4

Full CI calculations on H_2 T_e for H_2 singlet states (in cm^{-1})^{a)}

State	Experimental [11]	This work	
		free molecule	molecule in AgF(+) molecule in AgF(-)
X	0.0	0.0	0.0
B	91700.0	91171.3	40242.6 95269.3
C	100089.8	100159.0	60080.6 121917.7
E	100082.3	99846.7	41001.3 125176.8
F	100911.0	100735.8	49595.1 105928.9

Figure 1

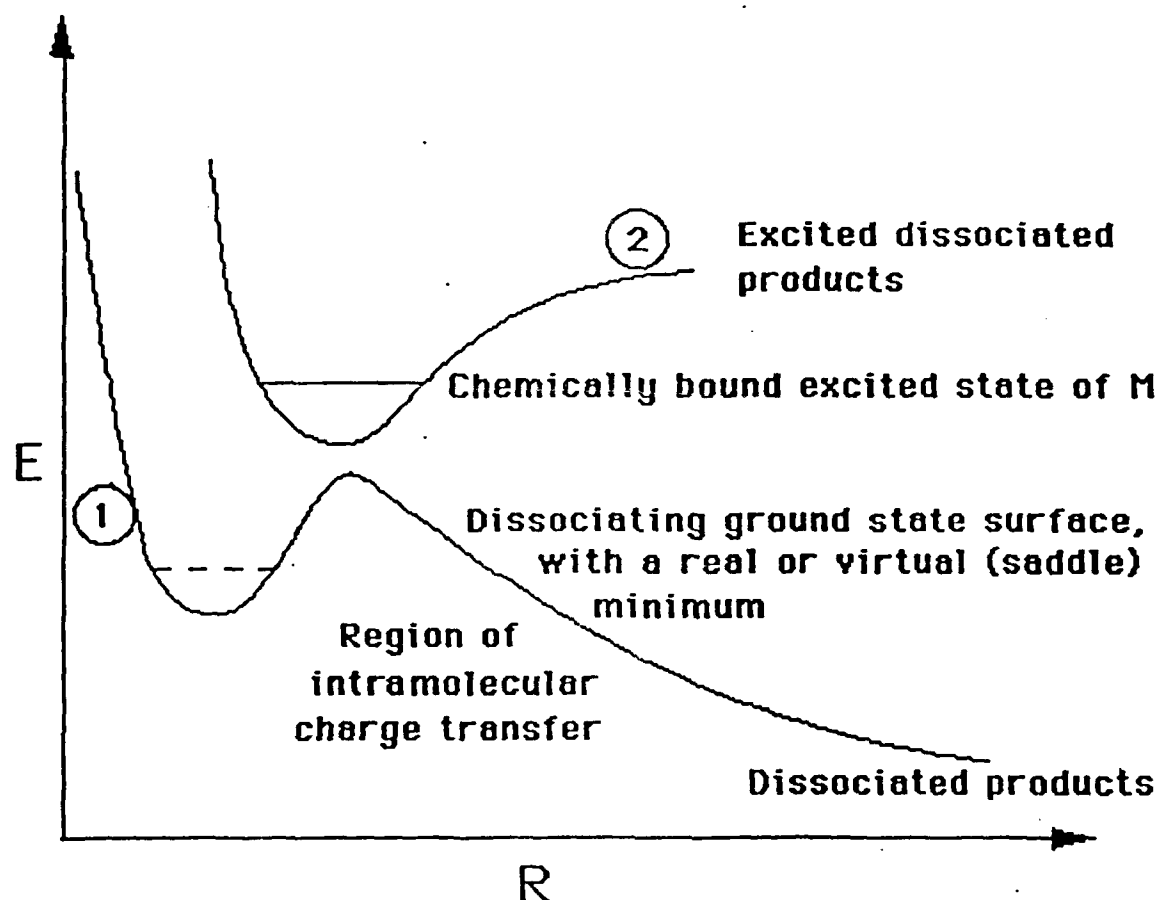


Figure 1

Potential energy surface characteristics along the reaction coordinate R as revealed from the calculations of ref.1. The ground state surface, (1), has a tunneling form and leads to molecular dissociation. The excited state, (2), is chemically bound. It decays via nonadiabatic coupling with the ground state. The molecule, M , may be neutral or charged. If the dissociated products for upper and lower curves are charged differently, the charge transfer is physically identifiable from them (e.g. $A^+ + B^+ \leftrightarrow A + B^{++}$). If they are not, the charge transfer must be understood from properties of M at the crossing region (e.g. case of the H_4 cluster).

Fig. 2

Water Dimer $(\text{H}_2\text{O})_2^*$

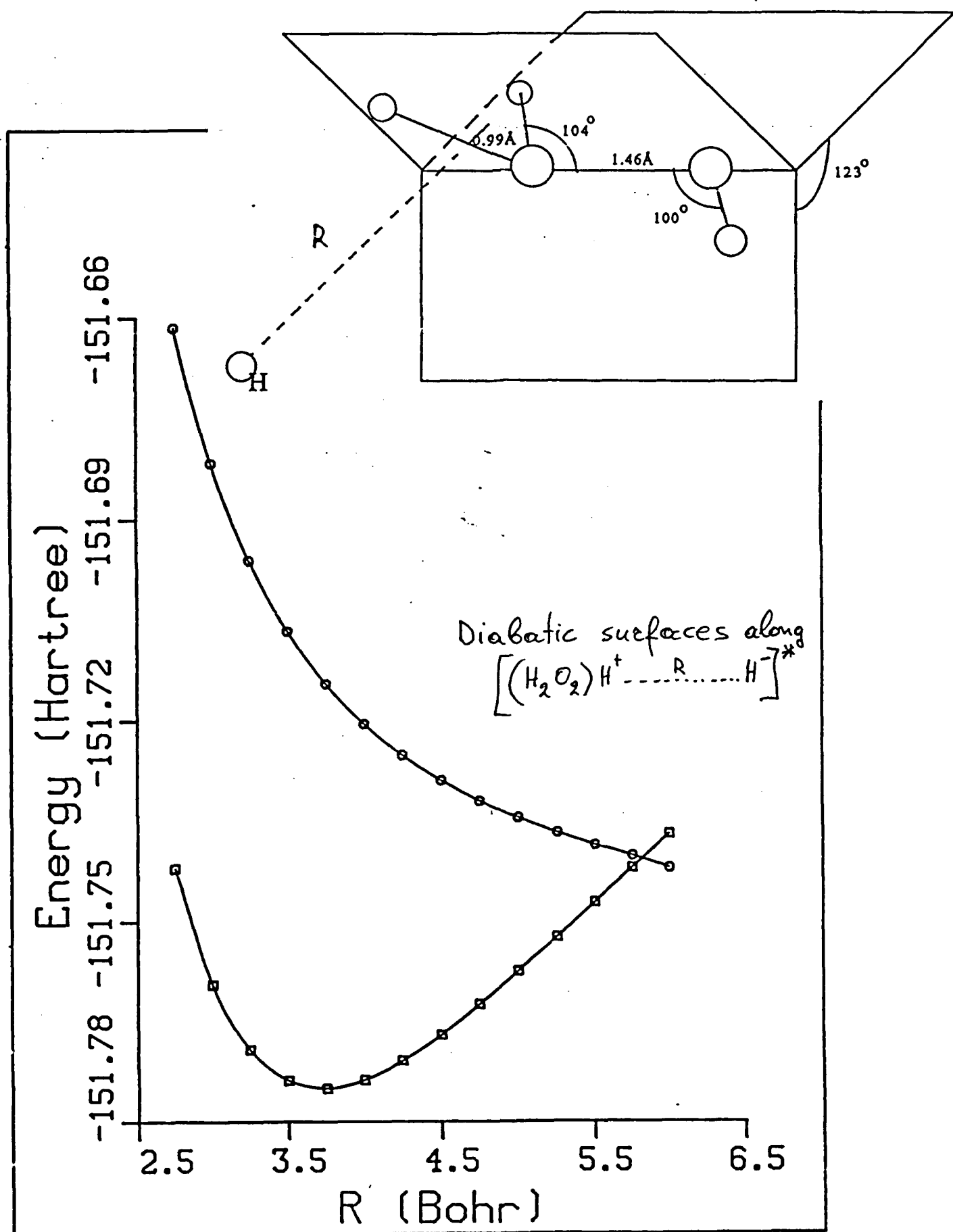
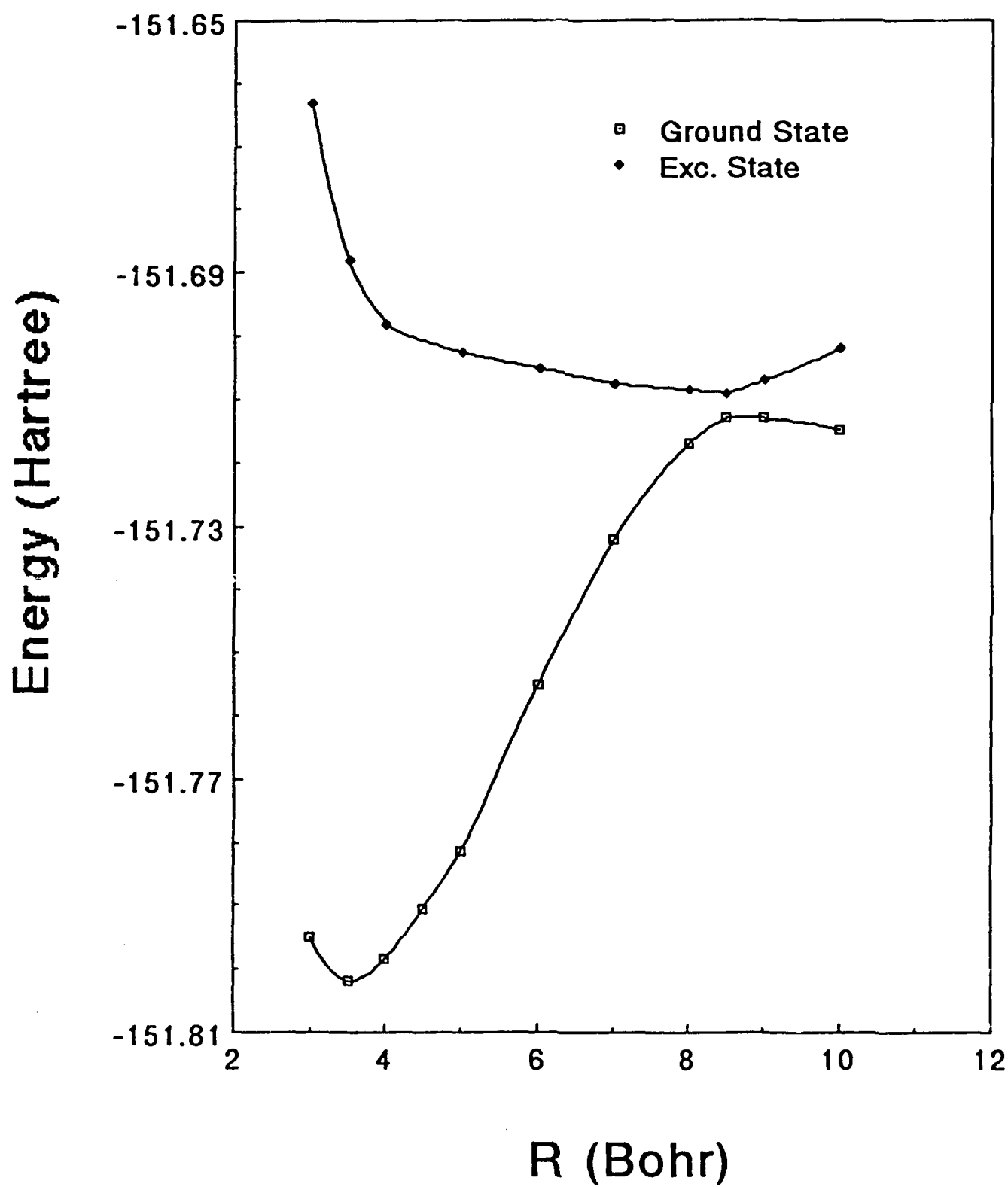


Fig.3. Water Dimer-MIES Configuration



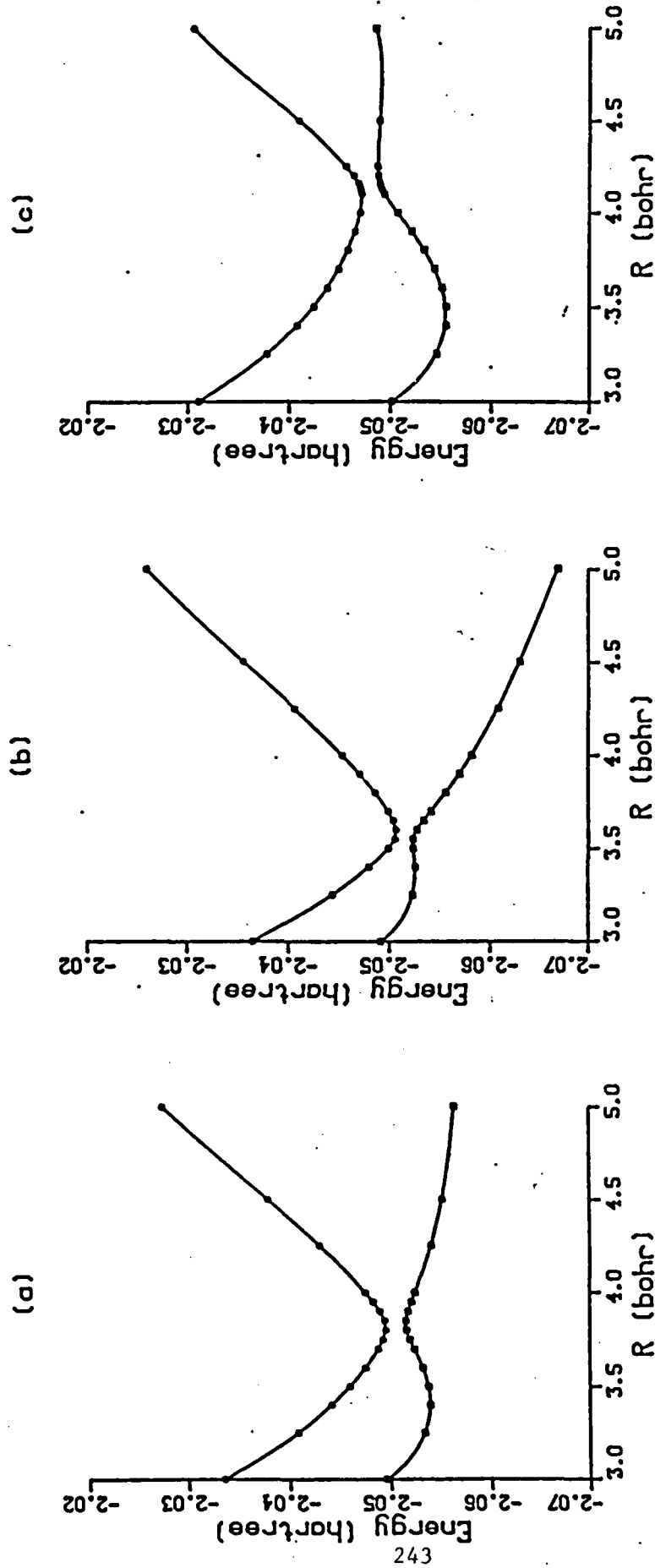


Fig. 4. Full CI calculations of the potential energy surface of the two lowest A' states of free $(H_2)_2$ (a), as well as of $(H_2)_2$ in a RbI crystal treated as a cluster of four hydrogens surrounded by suitably placed point charges. The geometry of H_4 is that of a trigonal pyramid [2,9] with R being the distance of the fourth hydrogen atom from the triangle. The avoided crossing is typical of the MIES clusters and determines their stability. (b) corresponds to a geometry where the ions surrounding $(H_2)_2$ are negative. In (c) the surrounding ions are positive. The lattice electrostatic energy has been subtracted out. The effect of the ionic medium on the characteristics of the avoided crossing is large.

Figure 4.

Limitations on Atom Densities in Cryogenic Matrices

A. T. Pritt, Jr., N. Presser, and R. R. Herm

*Infrared Science Department
Chemistry and Physics Laboratory
The Aerospace Corporation*

INTRODUCTION

Reaction of low mass metal atoms with liquid oxygen or liquid fluorine are highly exothermic and represent a potentially significant improvement to the specific impulse of currently available rocket fuels. Entrapping these low mass atoms in cryogenic matrices would provide the energy storage required since the energy between the metal atoms and the host material is relatively weak, typical of Van der Waal attractions. This weak attraction accounts for the close agreement of electronic and vibrational spectra observed for species in both the gas phase and trapped in matrices.¹ The degree to which these atoms can be trapped, therefore, is a gauge of how much the specific impulse can be improved. The purpose of our program with the ARIES office is to experimentally determine the ultimate densities of low mass metals which can be deposited into matrices in the form of monomers, dimers, trimers, and higher order clusters.

The concept of storing energy in cryogenic matrices by trapping atoms or radicals is not new. In the late 1950's as part of the AFOSR Free Radicals Program, it was recognized that energy associated with atomic recombination was much greater than the typical difference between the bond energies associated with chemical reactions. Researchers at that time investigated both experimentally and theoretically the limitation to trapping atoms and radicals in cryogenic matrices.² Jackson and Montroll³ calculated the maximum monomer concentration for an atom trapped in a matrix. In their approach they considered that the atom could recombine with itself once. For example, hydrogen, nitrogen, or oxygen atoms could recombine to form the diatomic species. For these atoms which only exist as a monomer or a dimer, Jackson and Montroll calculated that as much as 17% of the atoms could exist as monomers in a linear chain, and for a three dimensional crystal lattice on the order of 10% could be achieved.

In this report we have developed a simple model to estimate possible maximum monomer concentrations in which clustering does not stop at the dimer level but continues as long as the atoms occupy nearest neighbor positions, bonding to one another. This simple model is based only on site statistics to determine monomer, dimer, and trimer concentrations for a given metal atom fraction. Using the results of this model to estimate the ultimate monomer densities, we have calculated specific impulses for these atoms trapped in a hydrogen matrix and burned with either oxygen or fluorine.

MODEL

In this model we consider a case in which a gas stream containing both the metal atom and the matrix specie strike a cold surface and are trapped on lattices associated with the surface. We assume that the trapped atoms are immobile and therefore do not have an opportunity to recombine unless by chance they are positioned at nearest neighbor lattice sites. Metal atoms, if they occupy neighboring sites, recombine to form dimers, trimers, and higher order clusters. In addition, only one metal atom occupies a lattice site. The deposited matrix, consequently, is representative of the random distribution present in the gas phase. In addition we only consider the probability that any particular site is occupied by either a metal atom or a matrix atom or molecule. The matrix atom or molecules do not form any chemical bonds and only occupy sites.

Monomers. The probability that any particular site is occupied by a metal atom is equal to the fraction, f , of metal atoms available; consequently, the probability that a matrix specie occupies a given site is $1-f$. A monomer is defined as a metal atom surrounded by the matrix species at its nearest neighboring sites. Of the metal atoms trapped in the matrix the probability that any metal atom exists as a monomer is,

$$P_m = (1 - f)^n \quad (1)$$

where n is the number of nearest neighbors. Since all the matrix atoms are indistinguishable, only one configuration satisfies the monomer requirement of all nearest neighbor sites occupied by the matrix specie. As the fraction of metal atoms becomes diminishingly small, the probability that all the metal atoms exist as monomers approaches unity. The fraction of sites X_m (mole fraction) which are occupied by metal atoms as monomers is,

$$X_m = f P_m = f (1 - f)^n. \quad (2)$$

The maximum number of sites which can be occupied by a metal monomer can be derived by differentiating equation (2), setting it to zero, and solving for f .

Dimers. The probability that any metal atom is adjacent to one and only one other metal atom can be constructed in a manner similar to that for the monomer. The probability that one of the nearest neighbors of a metal atom contains only one other metal atom with the remaining nearest neighbor sites occupied by indistinguishable matrix atoms or molecules is $nf(1-f)^{n-1}$. The multiplicative factor of n is required since there are n ways (configurations) to position the second metal atom about the first metal atom. A dimer is defined as one in which not only are the nearest neighbors to the first metal atom occupied by matrix species but also the second metal atom must have all its nearest neighbors occupied by matrix species. Hence the probability any particular metal atom exists in the form of a dimer, P_d , as a function of the fraction of metal atoms present is,

$$P_d = n f (1-f)^{n-1} (1-f)^{n-s-1} \quad (3)$$

The last factor in the expression determines that the probability that the second metal atom has only matrix species for its nearest neighbors (exclusive of the first metal atom). The exponent s represents the number of nearest neighbor sites which are shared by both metal atoms since these are already counted when considering the first metal atom. The fraction of sites S_d which are occupied by metal atoms in the form of dimers is,

$$S_d = f P_d = n f^2 (1-f)^{2n-s-2}. \quad (4)$$

The maximum number of sites which can be occupied by a metal dimer (consisting of two sites for a dimer), therefore, can be derived by differentiating equation (4), setting it to zero, and solving for f . The dimer concentration is half the fraction of lattice sites occupied by metal atoms in the form of dimers. Calculating the probability for a given atom to appear in the form of a trimer and higher order cluster is also straight forward but requires determining various possible configurations and summing them.

The maximum fractions of monomers and dimers which can be obtained based on this model for various crystal types is presented in Table I. In figure 1 is plotted the fraction of metal atoms which appear as monomers and dimers as a function of the mole percent of metal atoms in a face center crystal. Martin and Welker⁴ have experimentally determined the fraction of lithium monomers and dimers which were deposited in a xenon matrix. Their experimental results agree reasonably with the predictions of this model. A similar plot for the deposition of sodium monomers in xenon (see figure 1), however, does not agree with the results presented here.

Table I. Maximum Mole Fraction of Monomers and Dimers for Various Crystals

Crystal	n	Monomer		Dimer	
		$f(\text{max})^a$	X_m	$f(\text{max})$	X_d
cubic	6	0.143	0.067	0.167	0.0135
bcc	8	0.111	0.049	0.125	0.0096
fcc	12	0.077	0.032	0.100	0.0090
hcp	12				

^a The metal atom fraction which produces the maximum mole fraction of monomers or dimers.

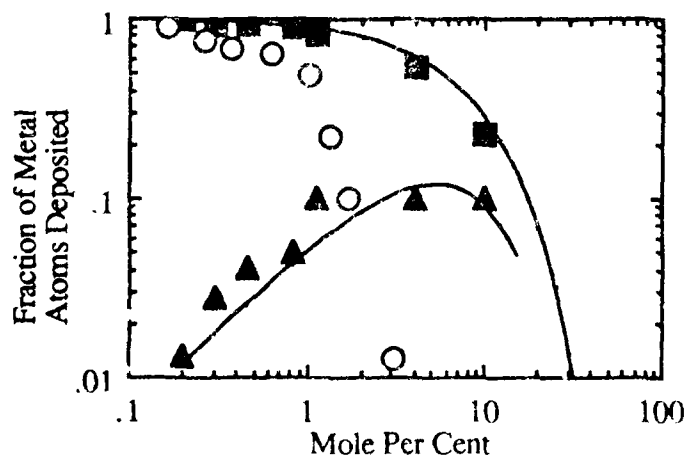


Figure 1. Fraction of Metal Atoms Deposited in the form of monomers and dimers as a function of the total mole percent of the metal atom in an fcc crystal. The solid line refers to that predicted by the model presented here, the solid symbols to Li, (\blacksquare) monomer and (\blacktriangle) dimer, the open symbol (\bigcirc) to sodium monomer, each deposited in an Xe matrix (see reference 4).

Isp CALCULATIONS

Using the limitation imposed by this simple model on the maximum monomer concentration that can be obtained, we have calculated the specific impulse (Isp) for various fuel/oxidizer mixtures in which the fuel consist of a metal trapped in a hydrogen matrix, and the oxidizer is either liquid oxygen or fluorine. Since the crystal lattice of solid hydrogen is in a hexagonal closed pack arrangement, we can estimate the maximum monomer as well as dimer concentrations from the above model. All remaining metal atoms are assumed to be in their standard state. The heat of formation for the hydrogen fuel with its additive metal atom is estimated by weighting the heats of formation of the individual components by their mole fraction in the matrix,

$$\Delta H_f (\text{mixture}) = \sum_i X_i \Delta H_f (i), \quad (5)$$

where X_i is the mole fraction for each component. The Edwards EDCONV code was used to calculate the Isp, the temperature, and product specie distribution at the rocket nozzle exit. Calculations assumed a chamber pressure of 10 atm and an exhaust pressure of 11 atm. Isp's were calculated for the reaction of only hydrogen and oxygen (fluorine) to provide a baseline comparison to the metal additive cases. The metal percent is 7.7%, representing the greatest monomer concentration as calculated by the model. Of the metal atom concentration 38% are monomers, ~7% are dimers, and the rest is considered as solid metal in their standard state.

For all but one case the metal additive reacted preferentially with the oxidizer. As the fuel to oxidizer (F/O) ratio was increased all the metal atoms formed new products at the expense of hydrogen reactions. The remaining hydrogen consumed whatever oxidizer that was left and the remaining unreacted hydrogen represented a heat sink. Lowering of the temperature in many cases resulted in the formation of condensed reaction products from which the heat of condensation increases the Isp. Figure 2 presents a sample calculation for the case of boron trapped in a hydrogen matrix. The maximum Isp is 476 s, representing an increase of 16% over that for the baseline case. At this F/O ratio the oxygen mole fraction is stoichiometric with the boron to produce B_2O_3 (s).

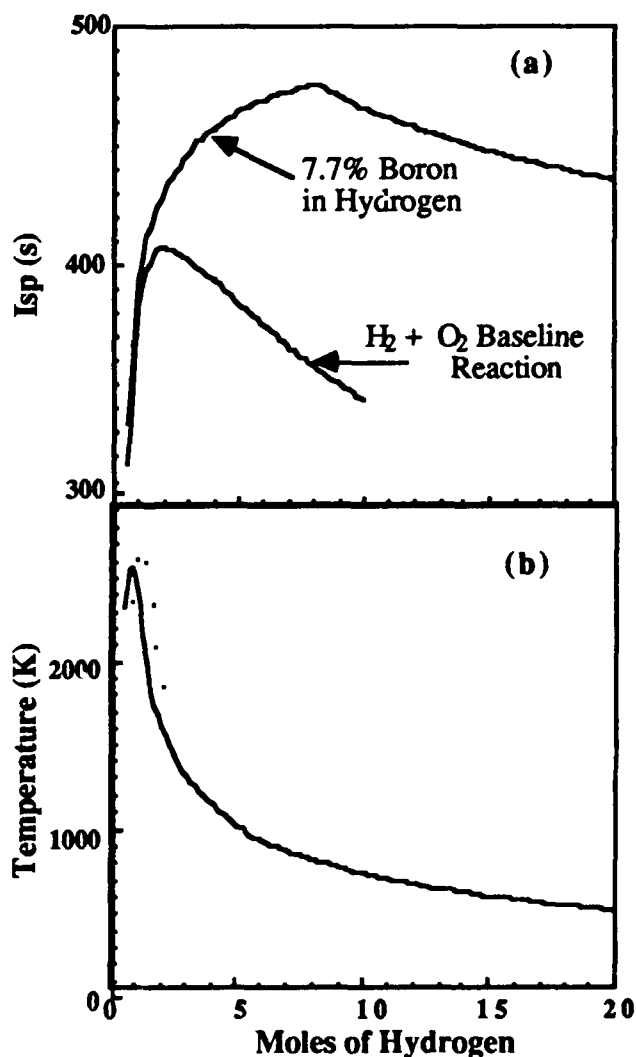


Figure 2. Plots of Isp (a) and Temperature (b) vs. the moles of hydrogen burned. A hydrogen fuel is burned with 0.5 moles of liquid oxygen; hence the x axis is equivalent to the F/O ratio.

Isp calculations were performed for other low mass atoms in hydrogen matrices reacting with oxygen and fluorine. Table 2 presents the results of these calculations, reporting the peak Isp's and the corresponding major products. Beryllium produced the highest Isp followed by boron, the next highest. Carbon was the only atom which did not preferentially react with the oxidizer. Burning oxygen with the hydrogen/carbon mixture produced CO and CO_2 at the maximum Isp, but as the F/O was increased further, the major carbon product was methane and water. The reaction of H_2/C with fluorine at the maximum Isp produced CH_4 and HF.

Table II. Results of the Isp Calculations

Fuel	Oxidizer			
	Oxygen		Fluorine	
Additive	Isp (s)	Products	Isp (s)	Products
None	408	H ₂ O	424	HF
Li	424	Li ₂ O (c)	457	LiF (c)
Be	490	BeO(c)	466	BeF ₂ (l)
B	476	B ₂ O ₃ (c)	463	BF ₃
C	435	CO, CO ₂ , H ₂ O	440	CH ₄ ,
Na	378	Na ₂ O(c)	413	HF
Mg	414	MgO (c)	436	NaF (l)
Al	438	Al ₂ O ₃ (c)	428	MgF ₂
Si	437	SiO ₂ (c)	432	AlF ₃
				SiF ₄

In these calculation it has been assumed that the maximum monomer concentration yields the greatest Isp. To verify this assumption, Isp calculations were performed for varying amounts of metal fraction in the hydrogen matrix using the monomer and dimer concentrations as predicted by the model. For these calculations stoichiometric amounts of the oxidizer was used to react all the metal present in the matrix. Hydrogen remained unreacted. At low metal atom fractions the temperature at the nozzle was low and increased as the metal mole fraction increased. The Isp vs the total boron mole fraction entrapped in hydrogen is presented in figure 3. The results of these calculations show that a peak in the Isp corresponded to a mole fraction of the total metal present of ~8% which is reasonably close to the value of 7.7% calculated for maximum monomer concentration.

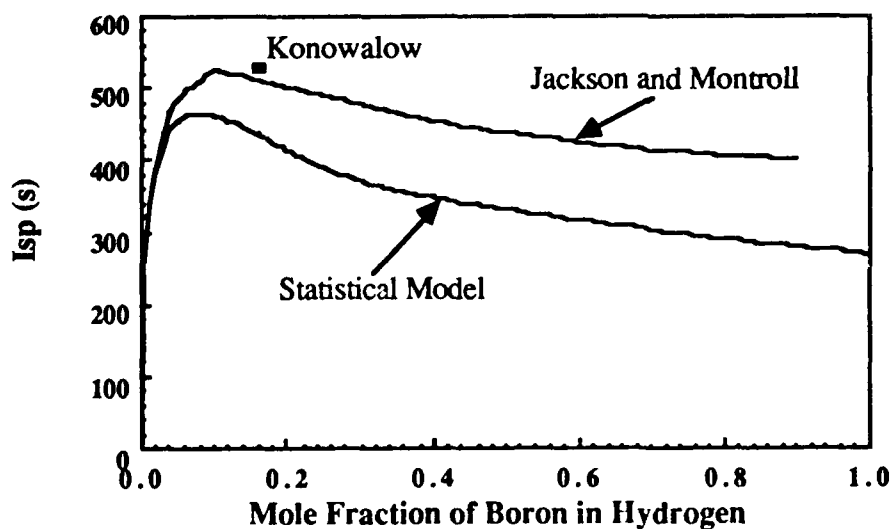


Figure 3. Calculated Isp as a function of total boron metal in a hydrogen matrix. The statistical model refers to one in which higher order clustering continues according to the model present here. The Jackson and Montroll model limits the clustering to to dimers only. The point marked Konowalow refers to a matrix in which the boron atoms are regularly positioned in a six co-ordinated matrix.

In a similar manner we have calculated the Isp for a fuel in which boron is trapped in a hydrogen matrix but one in which the boron atoms stop recombination at the dimer level. The distribution of monomer and dimers was estimated using the results of Jackson and Montroll. As shown in figure 3 the Isp for this fuel is greater since only monomers and dimers are present. However, it should be noticed that the peak in the Isp curve occurs near the 10% boron mole fraction value. At this value the Isp is nearly 523 sec or 28% improvement over the O₂ + H₂ reaction. At higher mole fractions the temperature of the nozzle is greater, and the product distribution does not favor the most exothermic channel, that of the producing B₂O₃. For boron mole fractions greater than 50%, boron does not burn completely and some water is produced. In addition, a significant fraction of the hydrogen molecules are dissociated to atoms. This energy in dissociating the hydrogen is absorbed, reducing the available chemical energy.

CONCLUSIONS

This simple statistical model is based on a source in which the metal atoms and matrix specie are completely randomized as in a mixed gaseous flow, and this random distribution is frozen in a solid matrix. A fuel prepared in this manner indicates that monomer concentrations can be sufficient to increase the Isp when added to a hydrogen matrix.

Improvements to the maximum concentration of monomer metal atoms in a matrix may be possible. In this model it is assumed that there is no activation energy to the metal bonding process. For the metal atoms considered in this report, the formation of their dimers from two metal monomers is likely to have no or small activation barriers and, therefore, would proceed at any temperature. The formation of a trimer from a monomer and dimer, however, may have an activation barrier substantially greater than kT . *Ab initio* calculations for the low mass metal atom dimers and trimers would aid in identifying those systems for which higher concentrations of monomers and dimers may be stabilized. In the case that the formation of a trimer has a substantial activation energy, the statistics would follow the prescription of Jackson and Montroll.

Dan Konowalow has calculated the energy for the Van der Waals interaction ($\sim 80 \text{ cm}^{-1}$) between lithium and hydrogen.⁵ In addition, he indicated that the structure of the cluster would involve a central lithium atom surrounded by six hydrogens, four equatorial hydrogens and two in axial positions. If a means of isolating such clusters and depositing them in a matrix were found, the ultimate monomer concentration might be increased over that predicted by this model. In fact such a monomer concentration would exceed that predicted by the Jackson and Montroll model since each of the atoms are selectively located rather than positioned by chance. If atomic boron follows a six coordination as predicted for lithium, the Isp would be on the order of 527 sec (see figure 3), slightly greater than the peak of the Jackson and Montroll model.

REFERENCES

1. M. E. Jacox, "Comparison of Ground State Vibrational Fundamentals of Diatomic Molecules in the Gas Phase and in Inert Solid Matrices," *J. Mol. Spectrosc.* **113**, 286-301 (1985) and M. E. Jacox, "Comparison of the Electronic Energy Levels of Diatomic Molecules in the Gas Phase and in Inert Solid Matrices," *J. Mol. Struct.* **157**, 43-59 (1986).
2. For a review of the Free Radicals Program sponsored by AFOSR see A. M. Bass and H. P. Broida, *Formation and Trapping of Free Radicals* (Academic Press, New York, 1960).
3. J. L. Jackson and E. W. Montroll, "Free Radical Statistics," *J. Chem. Phys.* **28**, 1101-1109 (1958).
4. T. Welker and T. P. Martin, "Optical Absorption of Matrix Isolated Li, Na, and Ag Clusters and Microcrystals," *J. Chem. Phys.* **70**, 5688-5691 (1979).
5. D. Konowalow, *Proceedings of 3rd High Energy Density Matter Contractors' Conference*, March, 1989, New Orleans, LA.

WEAK INTERACTIONS

Daniel D. Konowalow

Applied Research in Energy Storage Office
Air Force Astronautics Laboratory/LSX
Edwards Air Force Base, CA 93523-5000

INTRODUCTION

Several aspects of the HEDM program depend on an accurate treatment of weak interactions. They include studies of high-spin molecules and of van der Waals clusters. Here, I discuss quintet states of CO and van der Waals clusters of Li and Li₂ with H₂.

Quintet States of CO (with M. E. Rosenkrantz and J. E. Bohr)

For the purpose of energy storage we seek a molecule such as N₂ or CO which has one or more weakly bound yet possibly stabilizable upper states and a very deeply bound ground state. Fig. 1 illustrates the concept: it shows for example, that one might be able to extract about 11 eV for each transition of a weakly bound excited state of CO to the ground state.

High spin state molecules corresponding to the interaction of ground state atoms are particularly likely candidates for the upper state since they typically will exhibit mainly electrostatic, induction, and dispersion type van der Waals interactions at long-range but no short-range "chemical" binding. Furthermore, such high spin states will have no dipole-allowed transitions to the ground state and, thus, are potentially long-lived states so long as spin-orbit and spin-spin decay modes do not cause them to have an unacceptably short lifetime.

Bussery, Rosenkrantz, Konowalow and Aubert-Frecon (BRKAF) [1] studied the interaction of ground state C(³P_J) and O(³P_J) atoms. They find that the long-range interaction energy may be represented by the multipole expression

$$E(R) \approx C_5 R^{-5} + C_6 R^{-6} + C_8 R^{-8} + C_{10} R^{-10} + \dots \quad (1)$$

The $C_5 R^{-5}$ term represents the energy contribution due to the electrostatic interaction of the permanent quadrupole in C with that in O; that term may be either positive, negative or zero depending on the coupling of the atomic angular momenta to produce a particular molecular state. The remaining terms in Eq. (1) represent the various components of the dispersion interaction energy which corresponds to the interaction of mutually induced multipoles. For example, the term $C_6 R^{-6}$ represents the interaction of an induced dipole on C with an induced dipole on O. The magnitude of C_6 depends on the particular state which results from the interaction of the atoms, but its sign is intrinsically negative (thus, the interaction is always attractive) only so long as both interacting atoms are in their ground electronic states. The higher order terms correspond to the interactions involving higher order induced multipoles. The long-range analysis suggests that the $1^5\Sigma^+$ will be by far the most deeply bound of the quintets corresponding to C(³P_J)+O(³P_J). The

interaction curves will be in the order $1^5\Sigma^+ < 1^5\Delta < 2^5\Sigma^+, 1^5\Sigma^-, 1^5\Pi, < 2^5\Pi$ at sufficiently large separations.

In order to carry out accurate configuration interaction (CI) computations we modified the basis set of McLean and Liu (ML) [2] to include an s and a p Rydberg function. We optimized the most diffuse 3d functions of the original ML bases for the dipole polarizability; we optimized an added 4f function for the quadrupole polarizability and we optimized an added 5g function for the octupole polarizability. Our computed polarizabilities agree nicely with literature values [3, 4]. Thus, we obtain a basis set which can reproduce accurately the terms in Eq. (1).

Using the ALCHEMY [5] scheme, we carried out multiconfiguration self consistent field (MCSCF) calculations which correlated just the six p electrons and used the MCSCF orbitals in a second-order configuration interaction (SOC) calculations in which eight electrons were correlated. The latter comprised between 385,000 and 706,000 configuration state functions depending on the electronic state under consideration. The results are shown in Fig. 2.

It is clear that the $1^5\Sigma^+$ state of CO is sufficiently deeply bound to be thermally stable at reasonably low temperatures. Its dissociation energy of $\sim 750 \text{ cm}^{-1}$ (about 1100 K) is about 4kT at 0° C and about 14 kT at 77 K. The $1^5\Sigma^+$ state has over ten bound vibrational energy levels; its fundamental frequency ω_e is 123 cm^{-1} . The $2^5\Sigma^+$ and $1^5\Delta$ states, which are nearly degenerate, have dissociation energies under 100 cm^{-1} ($\sim 140 \text{ K}$); the remaining quintets are even more weakly bound.

This suggests a way to populate the $1^5\Sigma^+$ state selectively. If a mixture of ground state carbon and oxygen atoms are kept at about 140 K in a magnetic field so that their spins are kept aligned, all quintets but the $1^5\Sigma^+$ state will be thermally unstable. Thus, any atom recombination will form the $1^5\Sigma^+$ state preferentially. There may, of course, be other ways to form the CO quintets.

It remains to be learned the radiative lifetimes of the quintet states and to learn whether there are ways to control the various decay processes. A preliminary version of our work on CO has been published in *Forefronts*, 4, 2-6 (1988). (*Forefronts* is a publication of the Cornell University Center for Theory and Simulation in Science and Engineering.)

Li_nH_m Clusters

It has long been known that finely divided metals may enhance the performance of rocket fuels. Consider the following set of optimized specific impulse values calculated by Rodgers [6].

Reaction	Isp (sec)
$12.6 \text{ H}_2 + 2.3 \text{ O}_2 \rightarrow$	434
$5.0 \text{ H}_2 + 0.5 \text{ O}_2 + \text{Li}_{(s)} \rightarrow$	447
$8.5 \text{ H}_2 + 0.5 \text{ O}_2 + \text{Li}_{2(g)} \rightarrow$	480
$6.5 \text{ H}_2 + 0.5 \text{ O}_2 + \text{Li}_{(g)} \rightarrow$	509

It is evident that the more finely divided the Li the greater the boost in Isp over the standard H₂/O₂ fuel. Pritt's [7], statistical model suggests a maximum loading of about 7% Li in solid H₂. This assumes that H₂ will undergo no reactions and Li will react only with neighboring Li atoms or molecules. It is intriguing that predicted maximum loading corresponds very nearly to the optimum mixture of Li and H₂ calculated by Rodgers. A cryogenic solid fuel of H₂ with admixed Li and H₂ could certainly be prepared. The questions I wish to address here is: Can one do better? Is it possible to make weakly bound molecules of the sort pictured in Fig. 3 which would be sufficiently stable to be used as a cryogenic liquid fuel?

In initial studies of the LiH₂ molecule I used a compact basis that was double zeta in s and p functions and included one d and one f function on each atom to help describe the quadrupole- and octupole-polarizability. A SOCI calculation of the interaction energy of ground state Li on a line with ground state H₂ (itself held fixed with a bond length of 1.4 a₀) gave an equilibrium separation (of Li from bond center) of 9.5 a₀ and a well depth of about 25 cm⁻¹ (ca~ 36K). I confirmed that there was a substantial barrier (> 4eV) in the reaction H₂+Li → H+HLi. I prepared a substantially more complete basis, but found the computations to be too time consuming and so I switched to a rather different approach to this problem.

Finally, I turned to a sequence of calculations in which the excitations and thus the correlations are carefully restricted to those which are important in relaxing the Li core and those responsible for describing the dispersion interactions commonly called van der Waals interactions. This was the interacting Hartree-Fock (IHF) and interacting correlated fragment (ICF) approach of Liu and McLean [8-10]. In the IHF scheme the separated fragments are described at the HF level, while in the ICF scheme the separated fragments are described at the multiconfiguration self consistent field level. It is known that the IHF scheme will produce a binding energy too deep while the ICF scheme will give about 85-90% of the correct binding energy. I also relax the Li core which is fairly polarizable (α_D ~ 0.19 au) in both IHF and ICF computations.

The results are given in Table 1. Our first basis (#1) comprised a 6-31G basis on Li and a DZP basis on each H atom. I augmented the H basis to TZP level and optimized an additional p

function for the dipole polarizability and added a polarizability-optimized d and f function to Li to form basis set #2. The substantial increase in D_e (dissociation energy) shows the importance of the added polarizability (not polarization) basis functions. For the ICF calculations I describe the H_2 molecule with a two-configuration wave function $c_1 \sigma_g^2 + c_2 \sigma_u^2$. The ICF binding of Li to H_2 is less than predicted by the IHF scheme (as expected). The difference in binding with angle of approach of Li to the center of H_2 shown in Table 1 is anomalous, since H_2 is more polarizable along the bond than perpendicular to it. This is probably because I haven't fully optimized the basis set on H_2 . In any case the $ca \sim 90 \text{ cm}^{-1} \approx 130 \text{ K}$ binding suggests that LiH_2 would be thermally stable at liquid H_2 temperatures and certainly so at solid H_2 temperatures. I've performed a crude calculation on $Li-H_2$ treated as a diatomic molecule, i.e., with H_2 as a single particle. Those calculations show that the $Li-H_2$ diatomic has at least two vibrational energy levels.

Table 1 also shows that Li_2H_2 is even more deeply bound than LiH_2 as expected (since Li_2 is more polarizable than Li).

These results encourage me to pursue the question of the properties of larger $Li(H_2)_n$ and $Li_2(H_2)_m$ clusters as potential rocket fuels.

REFERENCES

1. B. Bussery, M. E. Rosenkrantz, D. D. Konowalow and M. Aubert-Frecon, "Semiempirical Determination of the Long-Range Molecular States Dissociating to $C(^3P_J) + O(^3P_J)$ ", Chem. Phys. **132**, 0000 (1989).
2. B. Liu and A. D. McLean, private communication.
3. H. J. Werner and W. Meyer, Phys. Rev. A, **13** 13 (1976).
4. E.-A. Reinsch and W. Meyer, Phys. Rev. A **18** 1793, (1978).
5. B. Liu and M. Yoshimine, J. Chem. Phys. **74**, 612 (1981).
6. S. L. Rodgers, private communication.
7. A. T. Pritt, previous paper in this meeting.
8. B. Liu and A. D. McLean, J. Chem. Phys. **72**, 3418 (1980).
9. B. H. Lengsfeld, A. D. McLean, M. Yoshimine and B. Liu, J. Chem. Phys. **79**, 1891 (1983).
10. A. D. McLean, B. Liu and J. H. Barker, J. Chem. Phys. **89**, 6339 (1988).

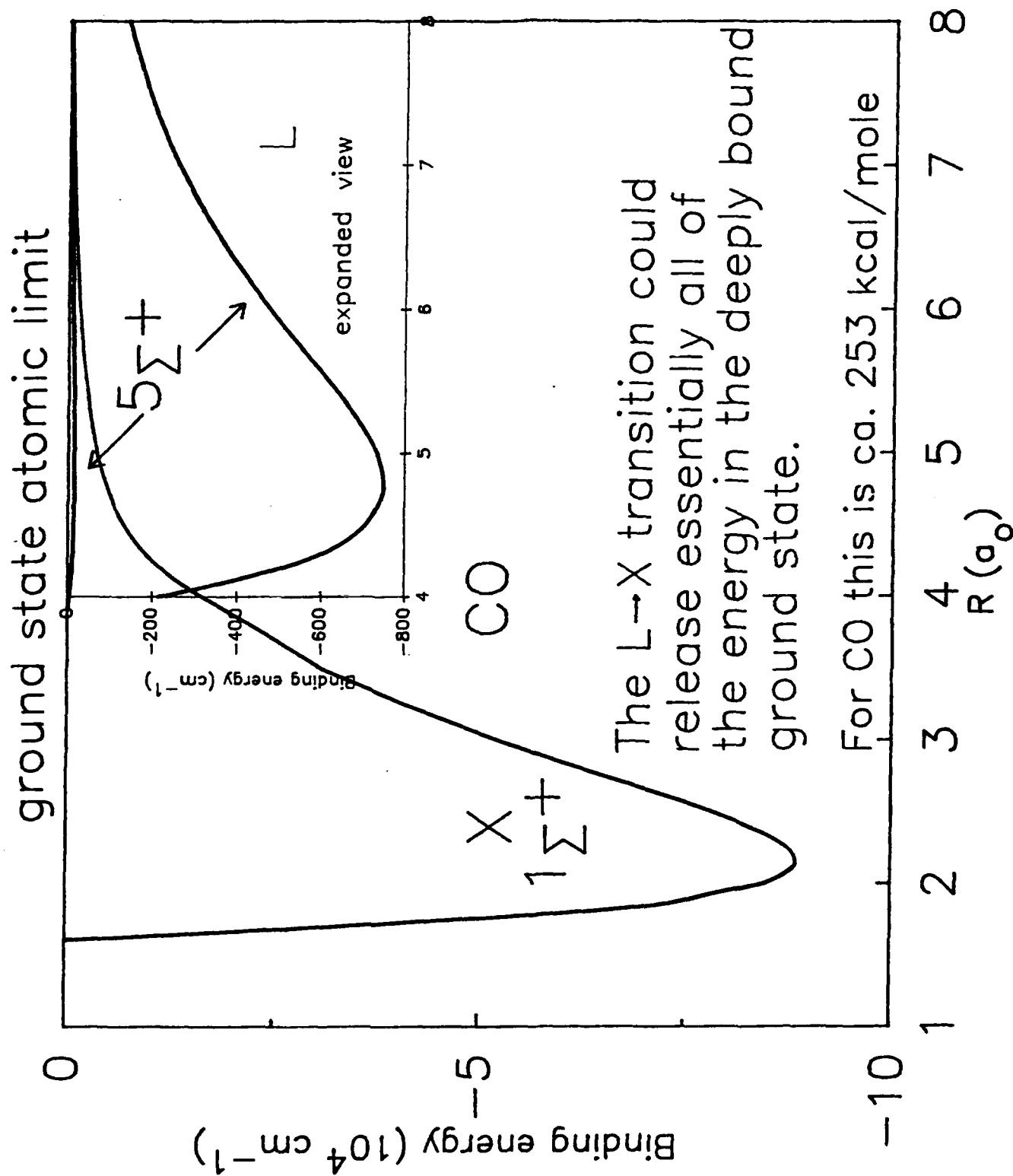


Fig. 1: The concept

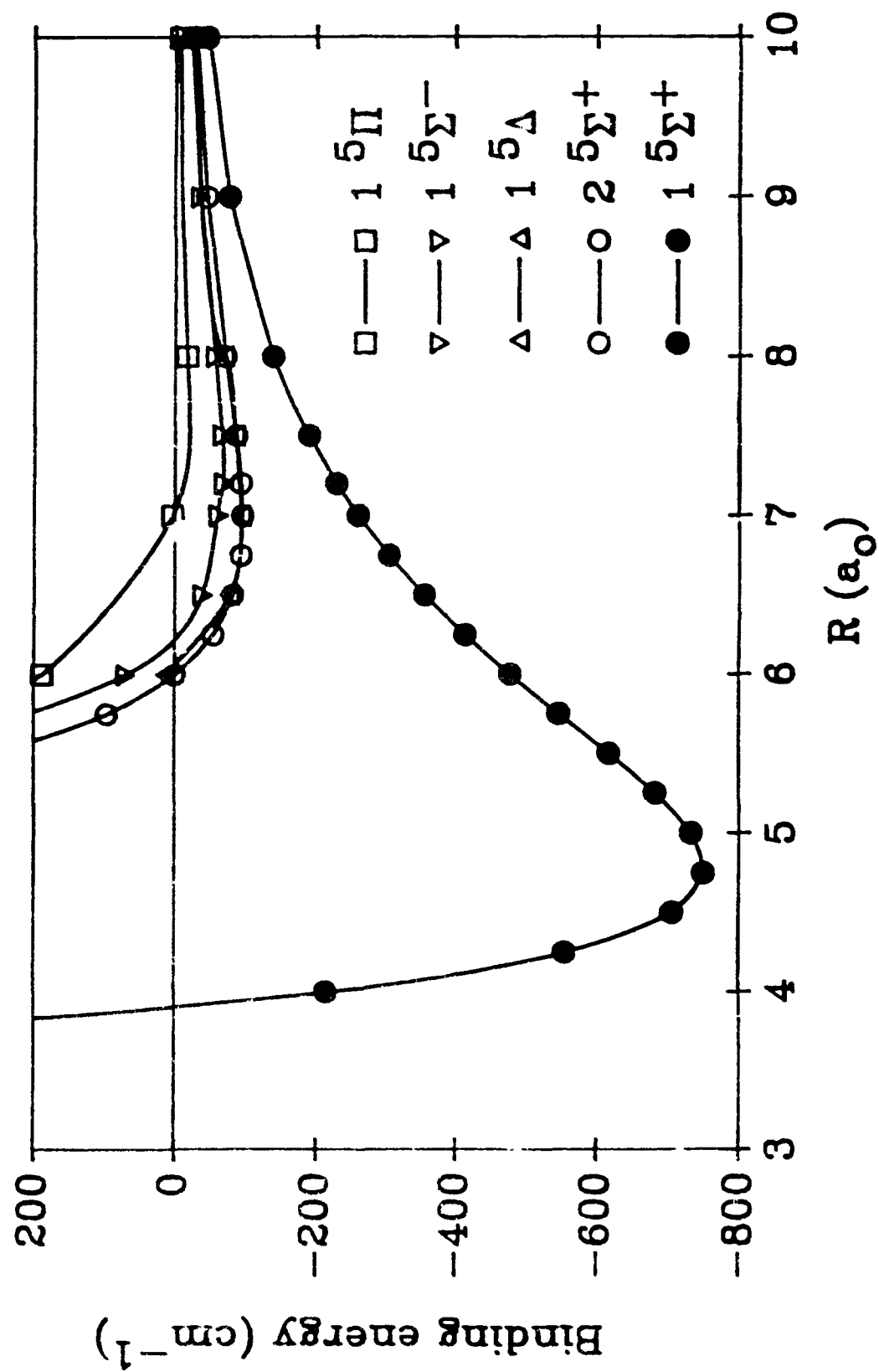


Fig. 2 Binding energy curves for quintet states of CO

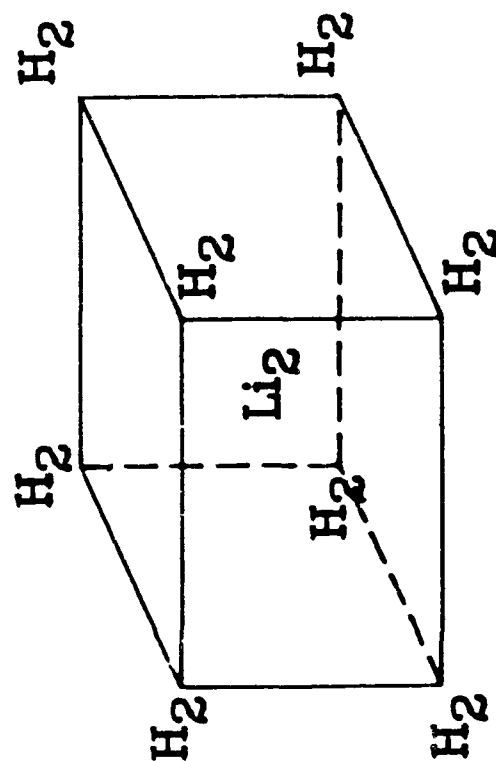
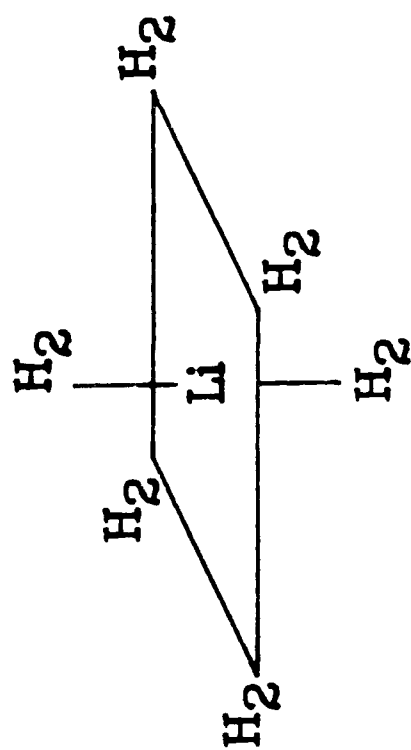


Fig. 3: Are these "stoichiometric clusters" stable?

Table 1: van der Waals binding in LiH_2 and Li_2H_2

LiH_2 SCHEME	BASIS	ANGLE^a	R_e (a_0)	D_e (cm^{-1})
IHF:	6-31G;dzp	0°	9.63	26.2
IHF:	6-31G+d+f; tzp	0°	8.59	138.0
ICF:	basis #2;	0°	9.47	82.4
ICF:	basis #2	45°	9.22	93.6
ICF:	basis #2;	90°	9.17	93.5
Li_2H_2				
IHF:	basis #1	0°	8.5	52.1
ICF:	basis #2	0°	9.43	114.0

^a Angle of approach of Li to the center of the H_2 molecule.

HIGH ENERGY DENSITY MATERIALS CONTRACTORS CONFERENCE

12 March - 15 March 1989

Matrix Isolation Spectroscopy of Metal Atoms Generated by Laser Ablation: the Li/Ar System

Mario E. Fajardo
University of Dayton Research Institute
ARIES Office
Air Force Astronautics Laboratory/LSX
Edwards AFB, CA 93523-5000

ABSTRACT

Results of preliminary experiments on lithium doped argon matrices prepared by laser ablation of solid lithium are presented, including near UV/VIS absorption spectra, and photobleaching and annealing studies of the matrices, as well as visible emission spectra of the laser ablated Li plume.

The UV/VIS absorption spectra of the matrices are dominated by a new absorption feature not observed in previously published studies on Li/Ar matrices. This new feature is attributed to absorption by Li atoms in novel trapping sites in the Ar solid; sites not accessible to Li atoms generated by the conventional Knudsen effusion technique.

A simplified calculation of the potential energy surface experienced by a ground state Li atom trapped in fcc solid Ar yields approximate values for trapping site energies and barriers to mobility. These values are consistent with the above interpretation of the novel spectroscopic features.

EXPERIMENTAL

The argon solids doped with lithium impurities are prepared in a closed cycle cryostat by co-condensing a slow stream of argon gas (0.5 to 5 mmol/hr) and the products of a laser ablated lithium plume onto a thin sapphire window cooled to 13 K. Sample thicknesses ranged from 5 to 100 microns, with typical molar Li atom concentrations estimated as 0.1 %. The temperature at the cryotip is measured with a carbon resistor and can be controlled to within ± 1 K by a 25 W heater.

The lithium ablation source consists of a thin disk of lithium metal onto which is focussed the output of a XeCl excimer laser at 308 nm. Incident intensities are in the 10^7 to 10^9 W/cm² range, with total pulse energies of 1 to 10 mJ, and a pulse duration of about 20 ns. With each pulse some lithium metal is vaporized and then ionized adjacent to the metal surface, creating a visibly bright plume. The disk is rotated about its axis, and as the experiment proceeds a round track is cut into its surface. The rotation serves to improve the shot-to-shot reproducibility of the plumes which is checked by monitoring their fluorescence.

The matrices are then interrogated by UV/VIS absorption spectroscopy. A quartz-halogen lamp is run at its maximum rating of 600W to get a useful UV flux down to 350 nm. The transmission of the lamp is recorded with an OMA using an unintensified silicon photodiode array. File manipulations are performed using the OMA's onboard computer.

LIF and photobleaching experiments can also be performed by focussing the output of an excimer pumped dye laser, or Ar⁺ pumped CW dye laser, onto the matrix, then detecting the fluorescence with the OMA using a more sensitive intensified diode array.

RESULTS

Figure 1 shows the first microsecond of the fluorescence from a laser ablated Li plume. The incident laser intensity was approximately 10^8 W/cm², which is typical of the intensities used in the matrix deposition experiments. All of the major emissions can be assigned to atomic Li transitions [1]; there is no evidence in the nascent fluorescence of any excited molecular species. An analysis of the electron temperature in the plasma has not been attempted, rather, these spectra are used as "fingerprints" of each plume in order to help correlate results of different experiments.

Figure 2 shows the UV/VIS absorption spectrum of a Li/Ar matrix generated using the laser ablation technique. The spectrum shows a strong triplet feature at 612, 625, and 639 nm which is interpreted as a matrix perturbed variant of the atomic Li 2s to 2p

transition at 670.8 nm in the gas phase. Previously reported spectra of Li/Ar samples prepared by Knudsen effusion of lithium [2-5] have shown from three to five peaks in the region around the atomic transition, but these peak positions have not been observed before.

Figure 3 shows the results of a photobleaching experiment on a Li/Ar matrix. The lower trace shows the transmission of the sample prior to irradiation with a CW dye laser tuned to the triplet absorption feature. This sample was prepared with a higher flow rate of Ar gas than was used in making the sample from Figure 2, and a shoulder can be seen to the red of the main absorption. The top trace shows the remaining absorption after the irradiation.

DISCUSSION

The data presented above clearly indicate that Li/Ar matrices deposited using a laser ablation source of Li atoms differ from those deposited using a more conventional Knudsen effusion Li source. This discussion will focus on the differences between the two metal atom sources, and on how these differences are manifested in the final matrix isolated products. A brief preliminary review of previous work done on systems of alkali metals trapped in rare gas solids will help to motivate and direct the discussion.

The absorption spectra of the heavier alkali metals (Na, K, Rb, Cs) trapped in rare gas matrices were recognized early on [6,7] to consist primarily of pairs of triplet absorption features, one centered around the free atom absorption wavelength and the other shifted to the blue. Variations in deposition conditions produced changes in the relative intensities of the two triplets. Studies which included LIF experiments [8] firmly established that each of the triplets arises from alkali atoms trapped in a single site; two sets of triplets implying two trapping sites.

In contrast, experiments on Li doped rare gas matrices showed only one unambiguous triplet absorption. Spectra published by different groups [2-5,9,10] differed significantly, and sometimes showed as many as seven peaks in the region around the free atom Li absorption, but no clear "doublet of triplets" structure was reported. Calculations of possible trapping sites [11] for Li atoms in solid Ar indicated that a four Ar atom vacancy is required to accommodate a single Li atom; this trapping site was assigned to the unshifted triplet emission.

In this light, the spectrum shown in Figure 2 can be seen as the missing blue-shifted triplet absorption of Li in Ar, in analogy with the spectra of the other matrix isolated alkali metals. The photobleaching behavior of the blue-shifted triplet depicted in Figure 3 is

in agreement with photobleaching experiments on Na doped rare gas solids [8]. The residual absorption from 650 to 680 nm in the upper trace of the same figure then corresponds to the unshifted triplet reported in earlier studies. The question still remains as to the identity of the Li atom trapping site to be associated with the blue-shifted triplet, and as to how this site is accessed by laser ablated Li atoms and not by Knudsen oven generated Li atoms.

The most obvious difference between Li atoms generated by Knudsen effusion at 500 C, and those generated by laser ablation of solid lithium, is the much higher kinetic energy content of the laser ablated atoms. Laser ablation of opaque solids using incident intensities near the threshold for plasma production yields neutral atoms and molecules with kinetic energies in the 0 to 20 eV range, with typical energies of a few eV [12,13]. The kinetic energy of atoms issuing from a Knudsen oven is described by a Maxwell-Boltzmann energy distribution characterized by the oven temperature; in the case of lithium the typical kinetic energy is of order 0.1 eV.

Considering now the matrix deposition process, the major heat load on the matrix is due to the accommodation of the room temperature kinetic energy of the rare gas host atoms. Due to the poor thermal conductivity of the matrix material, this heat load causes local heating and hence increased mobility of all species on the accreting surface of the matrix [14,15]. Thus, during the cooling and crystallization process, slow Li atoms from a Knudsen effusion source will be stopped in this layer and have the opportunity to create large, stable trapping sites. However, the much faster laser ablated Li atoms may be able to burrow their way into existing crystalline structures and trap in tighter sites. Note also that mobility in this surface layer during deposition implies the possibility of recombination of the Li atoms to form molecules or clusters, lowering isolation yields. Other groups have reported unsuccessful attempts at isolating Li atoms in solid Ne at 2 K [4,5]; the failures may be due to such surface recombination.

In an attempt to evaluate the plausibility of this model of laser ablated Li atoms penetrating close-packed solid Ar structures, a calculation was performed on the potential energy surface experienced by a ground state Li atom trapped in solid Ar. The assumptions used in the calculation are as follows. The Li atom is taken to be trapped in a substitutional site in an fcc Ar solid. The Ar atoms are kept rigidly at their undistorted fcc lattice positions; no relaxation by the trapping cage is allowed for. Contributions from 248 Ar atoms are included, corresponding to the first 12 coordination shells around the substitutional site; no use is made of periodic boundary conditions, more in the spirit of a cluster rather than a solid state calculation. The potential surface is calculated as a pairwise sum over the gas phase Li-Ar ground state pair potential [16,17], with the zero of energy

defined at infinite separation of the Li atom and the cluster. Only part of the potential surface was calculated, in the form of "cuts" with the Li atom starting at the cage center and moving outwards along four major symmetry directions. These directions correspond to moving the Li atom from the cage center: first along a line directly at a nearest neighbor Ar atom (the 110 direction), second along a line which bisects a pair of nearest neighbors (the 122 direction), third along the C_3 cage axis between three nearest neighbors (the 111 direction), and finally along the C_4 axis between four nearest neighbors and directly at a second nearest neighbor (the 100 direction).

The results of this calculation are shown in Figure 4. The four directions can be distinguished by inspection near the cage wall (approximately 2 Å from the center): for a mostly repulsive pair potential like the Li-Ar ground state, the steepest repulsion arises from motion of the Li atom directly at a nearest neighbor Ar atom (solid curve), the next steepest from motion between two Ar neighbors (dotted curve), and so on. The most notable feature of the potential surface is that the energy at the center of the cage is repulsive by approximately 0.1 eV. Similar calculations have shown that at least a four Ar atom vacancy is required to accommodate a Li atom [11]. Following these curves outwards from the cage center, other metastable trapping sites are encountered. The minima at 1.2 eV correspond to Li atoms in octahedral interstitial sites; the minima at 1.9 eV to tetrahedral interstitial sites. Note also that the barriers between all of these sites are typically between 1 to 3 eV; these barriers are calculated in the impulsive limit of no Ar atom recoil imposed by the constraints mentioned above. Therefore, within the limits of validity of the model, it is reasonable to expect that Li atoms with several eV of kinetic energy will be mobile in solid Ar.

CONCLUSIONS

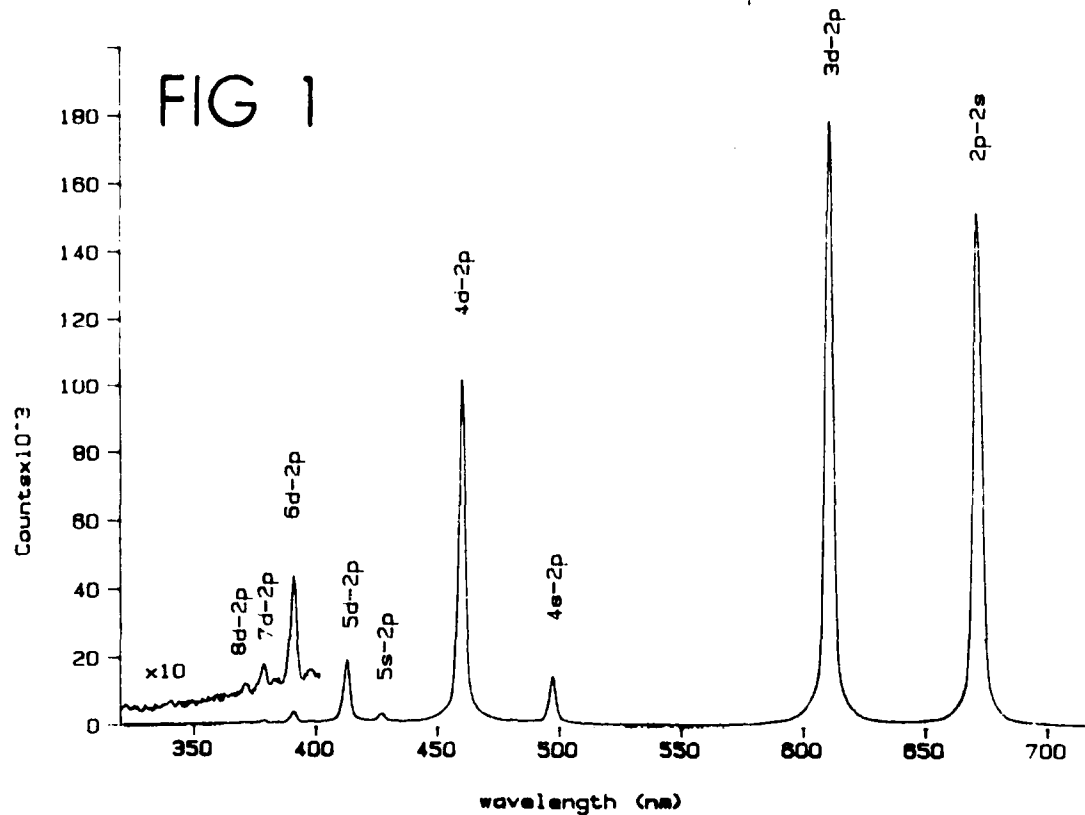
Lithium atoms generated by laser ablation and lithium find different trapping sites in solid Ar than do Li atoms generated by Knudsen effusion. This difference is attributed to the penetration into previously deposited close-packed Ar structures by the kinetically hot laser ablated Li atoms. In contrast, the relatively slow Knudsen generated Li atoms impinging upon an accreting matrix surface are stopped in the still cooling surface layer and ultimately trap in larger, multi-substitutional sites. Li atom recombination due to mobility in the accreting surface layer may be responsible for previous unsuccessful attempts at isolating Li atoms in solid Ne; if such is the case, the laser ablation technique may provide improved isolation yields by avoiding surface recombination.

Future efforts in this lab will include the characterization of laser ablated Li/Ar samples by LIF. Experimental modifications will be made to allow for pulse deposition of the Ar host gas, as well as for Knudsen effusion of the Li guest. The laser ablation technique will be applied to "difficult" systems, e.g. matrix isolation of Li atoms in solid Ne and H₂. Eventually, attempts will be made to ablate directly into condensed phases such as liquid rare gases and liquid hydrogen. Observation of the Li atom recombination dynamics will provide information about predicted [18] cluster species such as Li(H₂)_n.

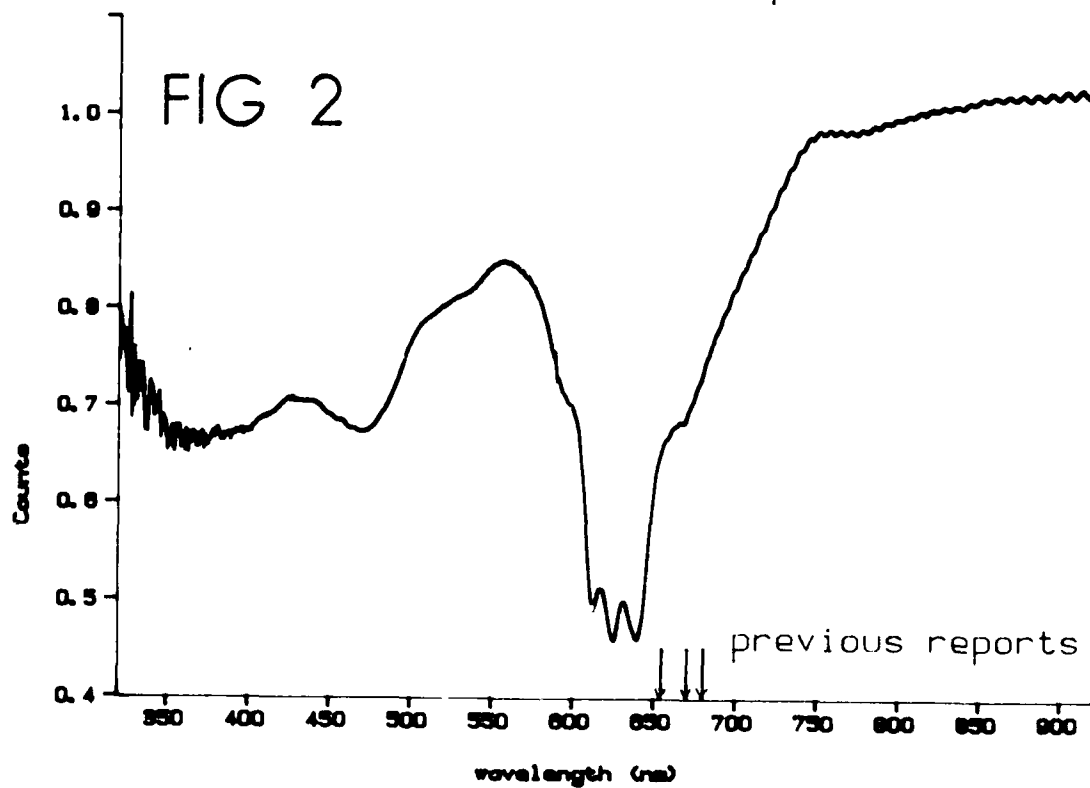
REFERENCES

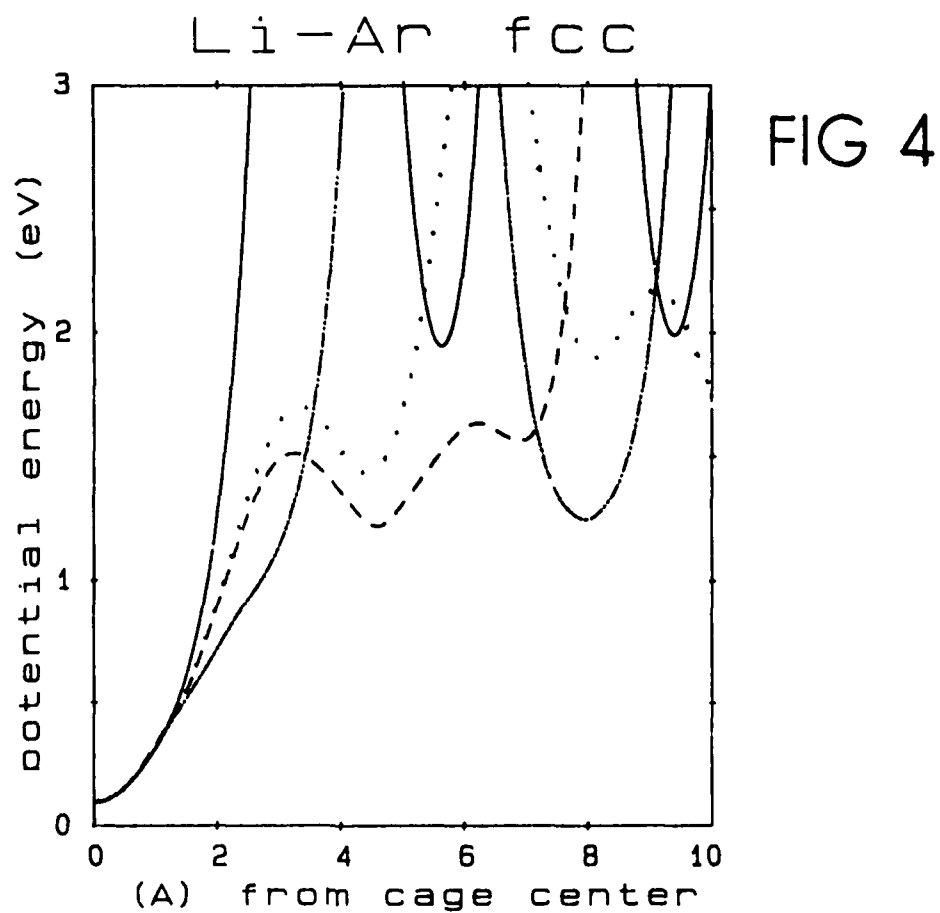
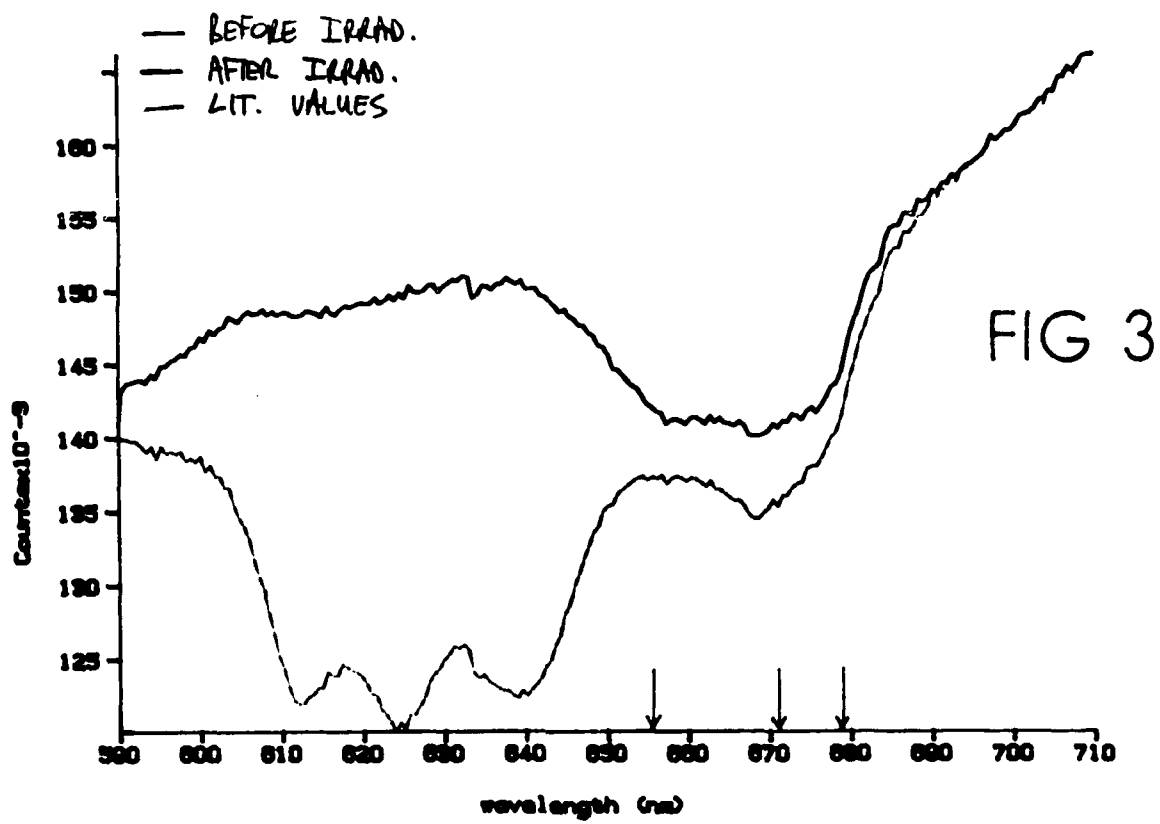
- 1.) H.G. Kuhn, Atomic Spectra, (Academic Press, 1969).
- 2.) L. Andrews; G.C. Pimentel, J. Chem. Phys., 47(8), 2905-10 (1967).
- 3.) A.A. Belyaeva; Yu.B. Predtechenskii; L.D. Shcherba, Opt. Spektrosk., 24(3), 449-51 (1968).
- 4.) A.A. Belyaeva; Y.B. Predtechenskii; L.D. Shcherba, Opt. Spektrosk., 34(1), 40-5 (1973).
- 5.) J.J. Wright; L.C. Balling, J. Chem. Phys., 73(7), 3103-6 (1980).
- 6.) W. Weyhmann; F.M. Pipkin, Phys. Rev. A, 137(2A), A490-6 (1965).
- 7.) B. Meyer, J. Chem. Phys., 43(9), 2986-92 (1965).
- 8.) L.C. Balling; M.D. Havey; J.F. Dawson, J. Chem. Phys., 69(4), 1670-5 (1978).
- 9.) R.B. Merrithew; G.V. Marusak; C.E. Blount, J. Mol. Spectr., 29, 54-65 (1969).
- 10.) T. Welker; T.P. Martin, J. Chem. Phys., 70(12), 5683-91 (1979).
- 11.) S. Ossicini; F. Forstmann, Nuovo Cimento Soc. Ital. Fis., D, 1D(5), 688-96 (1982).
- 12.) J.F. Friichtenicht, Rev. Sci. Instrum., 45, 51 (1974).
- 13.) J.F. Ready, Effects of High-Power Laser Radiation, (Academic Press, 1971).
- 14.) G.C. Pimentel, Angew. Chem. internat. edit., 14(4), 199-206 (1975)
- 15.) H.E. Hallam; editor, Vibrational Spectroscopy of Trapped Species, (Wiley Interscience, New York, 1973).
- 16.) R. Scheps; C. Ottinger; G. York; A. Gallagher, J. Chem. Phys., 63(6), 2581-90 (1975).
- 17.) J. Pascale; J. Vandeplanque, J. Chem. Phys., 60(6), 2278-89 (1974).
- 18.) D.D. Konowalow, "Weak Interactions" paper presented at HEDM Contractors' Conference, New Orleans, March 1989.

Fluorescence from Li plume



Li/Ar transmission spectrum





Metastable Metals in Matrix Materials

N. Presser, A. T. Pritt, Jr., and R. R. Herm

*Infrared Science Department
Chemistry and Physics Laboratory
The Aerospace Corporation*

INTRODUCTION

Trapping metal atoms in cryogenic matrices is not new. Reports in the literature date back to 1959 when Robinson reported trapping mercury atoms and shortly thereafter sodium atoms in rare gas matrices.¹ Since then a number of studies have been reported on trapping sodium atoms in rare gas matrices. Visible absorption spectroscopy typically is used to monitor the presence of free atoms (monomers), dimers, trimers, and higher order clusters in the matrix. Recent reports on the spectroscopy of sodium atoms in rare gases has been directed toward understanding the electronic structure of these atoms in their environment. The goal of this work, however, is to determine those factors which influence the ultimate monomer concentration which can be deposited in a matrix. Reported here is our initial work in trapping sodium in xenon, argon, and a mixture of hydrogen and xenon matrices.

EXPERIMENTAL DETAILS

A schematic of the apparatus is shown in figure 1. Cryogenic samples were produced on a transparent substrate at 4.5 K using a He cryostat (Janis, Model 10DT). The substrate was attached to a cold finger via copper flange and indium metal seals for good thermal contact. A calibrated Si diode monitored the temperature of the indium seal. The substrate sat inside two cold shields, the inner one at ~6 K, the outer, at ~80 K. Pressure in the chamber was 2×10^{-8} Torr.

The metal atoms were generated in an effusive quartz oven approximately 15 cm from the substrate. The oven was heated by two separate ovens, keeping the temperature of the oven above the liquid melt slightly higher than the melt. In all cases the mean free path in the oven was ten times greater than the 3 mm dia. orifice through which the gas effused. Metered flows of the matrix gas entered the chamber at a 45° angle to the sodium flow. The pressure in the chamber under these flow condition never exceeded 1×10^{-5} Torr.

Visible absorption spectroscopy has been used to determine concentration levels of various free atom and clusters in the matrix. Radiation from a tungsten-halogen lamp (100 watt) was focused through a small aperture, and collimated by lens, passed through a longpass filter to eliminate the uv radiation, through several neutral density filters, through the vacuum chamber containing the substrate and cryogenic matrix and refocused onto the entrance slit of a 1/3 meter

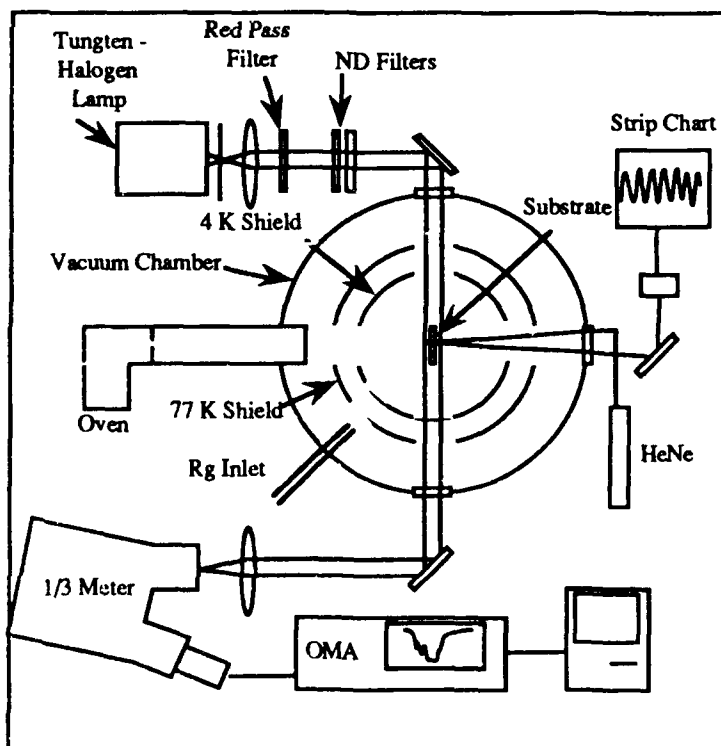


Figure 1. Schematic of the Cryogenic Apparatus. The substrate is attached to a copper heat sink in contact with a liquid helium dewar. The substrate rotates between the deposition position shown above and a position perpendicular to the lamp beam path.

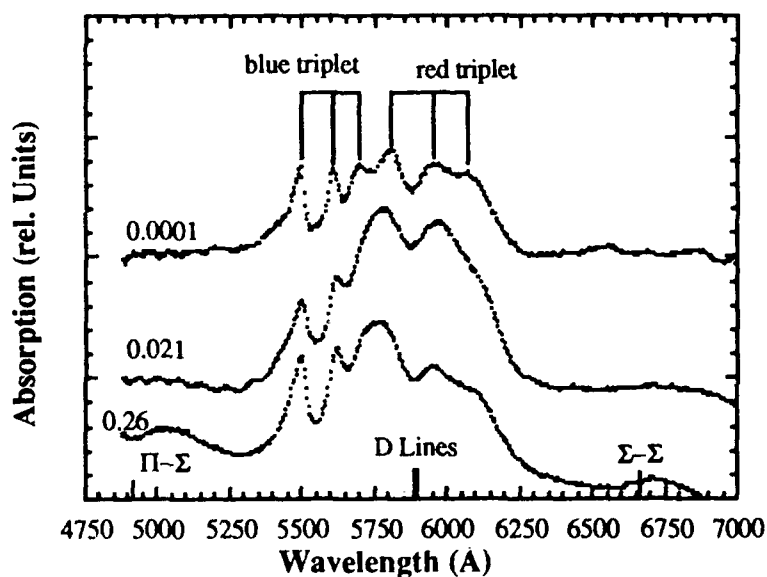
McPherson monochromator. A grating of 150 lines/mm blazed at 6 μm was used in 1st order. The output was detected by a silicon diode array which was attached to an optical multichannel analyzer (PAR OMA I system). The dispersion across the 500 element array was ~ 200 nm.

RESULTS AND DISCUSSION

Sodium - Xenon System

Monomers. Trapping sodium atoms in a xenon matrix was the first system to be investigated since, sodium atoms are easily vaporized in a quartz oven, the xenon matrix has high optical transparency, and this system has been studied most in the literature. We trapped sodium atoms in a fixed flow of xenon at 4.5 K for several settings of the oven temperature, hence several flowrates. Typical spectra for the trapped atoms are shown in figure 2. The spectra exhibit the usual two sets of triplets, the narrower bands 720 cm^{-1} to the blue and the broader bands 200 cm^{-1} to the red of the gas phase atomic sodium transition (D lines). Balling and Wright² have shown that although absorption for these two triplet sets produce different fluorescence spectra, the lifetimes are similar, corresponding to the lifetime of the free atom. This result led to the conclusion that both sets of triplets are monomer species corresponding to different trapping sites. A number of models have confirmed this interpretation.³ The ratio of the absorption intensity for the blue triplet to that for the red triplet varied from one spectra to another. The variation of this ratio is not understood but may be related to deposition parameters.

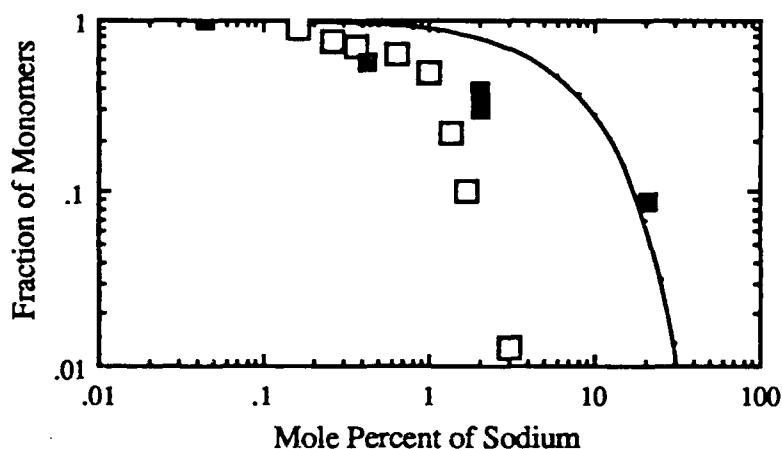
Figure 2. Visible absorption spectra of sodium trapped in a xenon matrix. The mole fraction of sodium in the xenon matrix is given by the values above each spectra. The position of the sodium dimer transitions, $B^1\Pi_u-X^1\Sigma_g$ and $A^1\Sigma_u-X^1\Sigma_g$ as well as that of the sodium atom D lines are shown along the bottom scale.



The goal of this project is to determine the maximum monomer concentrations which can be deposited in a given matrix. In figure 3 is presented the fraction of sodium which appear as atoms as a function of the mole fraction of sodium in the xenon matrix. The fraction of monomers is determined by integrating the blue and red triplet bands and normalizing them to the sodium flowrate and total deposition time. At the lowest sodium mole fraction we have assumed that only monomers exist, thus determining the absorption coefficient for the sum of the three bands. Since the relative absorption intensities of the red and blue triplets varied from experiment to experiment, we also assumed that the absorption coefficients for each triplet are equal. The solid line in figure 3 corresponds to the a statistical model presented previously by A. T. Pritt et al.⁴ and the open symbols are the experimental results of Welker and Martin.⁵ Errors in the determining the fraction of monomers reside solely in assuming that the at near infinite dilution all the sodium appears in its monomer form and is directly proportional to the integrated absorption of the red and blue triplets. Errors associated with determining the mole fraction of Na stem from two assumptions: first the sodium flowrate can be determined by assuming effusive flow from the oven to the substrate, and second the sticking coefficient for sodium is unity. Systematic errors in these assumptions translate into moving the collection of data points equally along the abscissa since the data are presented in log-log form. If these assumptions are reasonable, more sodium in its monomer form has been trapped in the xenon matrix than was reported by Welker and Martin. The deposition rates used by

Martin and Welker were approximately 40 times greater than ours. Although at intermediate mole per cent the fraction of monomers does not agree with the statistical model, we are encouraged that the monomer fractions at higher mole per cent do agree.

Figure 3. Plot of the fraction of metal monomers as a function of the mole per cent of sodium in a xenon matrix. The closed squares are experimental values from this work, and the open squares are taken from reference 5.



Dimers. At low mole fractions of sodium, only the two sets of triplets were observed. In our spectra only when the mole fraction of sodium atoms exceeds 0.2 does a new absorption feature appear at 496 nm with no accompanying band near 666 nm. Currently the assignment of this spectral feature is in doubt. Martin and Welker noted that the magnitude of this 496 nm band, corresponding in position to the $\text{Na}_2 \ ^1\Pi_u - ^1\Sigma_g$ transition, increased quadratically with the sodium mole fraction. Furthermore, these authors found that photolysis of the 666 nm band decreased intensity of both the 666 nm and 496 nm bands and enhanced the absorptions associated with the monomer bands, implying that dimers were dissociated and redistributed in the matrix as monomer species. Hormes and Karrasch,⁶ however, have assembled a beam apparatus in which the sodium atoms pass through a magnet in which the atoms are deflected and the dimers pass through a second orifice. The dimer beam, ~95% pure, was co-deposited with xenon on a substrate at 10 K. Their absorption spectra contained neither the 496 nm nor the 666 nm bands. The 496 nm band, therefore, may be associated with perhaps another monomer trapping site. Additional arguments against assigning the 496 nm band to sodium dimers are: its shape which is much broader than that predicted from gas phase spectra and upon annealing this band disappears.

Annealing Experiments. The annealing experiments indicate temperatures at which perceptible diffusion takes place in these matrices. As the temperature is raised for sodium trapped in the xenon matrices, the red triplet absorption intensity decreases. For a mole fraction of 0.0001 sodium in xenon the red triplet disappeared after the system was raised to 42 K, henceforth referred to as the annealing temperature. The blue triplet increase about 50 % in the peak intensity and upon cooling the matrix to 4.5 K the individual peaks narrowed. The intensity lost in the red triplet did not fully reappear in the blue triplet, indicating loss of sodium monomer species in the matrix. This loss is puzzling: either the sodium monomers form higher order clusters which do not have features in this region of the spectrum or the sodium atoms are rapidly diffusing through grain boundaries forming a sodium film on the surface. In addition, the absorption baseline increases toward lower wavelengths, suggesting that scattering in the matrix has increased. For matrices containing increased fractions of sodium atoms, the annealing temperature decreased. Mole fractions greater than 0.2 resulted in annealing temperatures less than 10 K. The 496 nm band shown in the spectrum labeled 0.26 in figure 2 also disappeared upon annealing near 8 K.

Sodium - Argon System

We have generated absorption spectra of sodium deposited in argon matrices. The spectral features depend strongly on the rate of deposition. When the deposition rate is high ($\sim 10^{15}$ molecules/cm²/s) the absorption features are so broad that the triplet signature is difficult to discern. On the other hand when the deposition rate is low ($\sim 10^{13}$ molecules/cm²/s) the absorption features are also broad. Only at intermediate deposition rates are the spectra sufficiently narrow that the triplet structure is observable.

Sodium - Xenon/Hydrogen System

At 4.5 K the optical density of hydrogen matrices is high presumably due to a high concentration of scattering centers in the matrix. Our initial experiments, therefore, to obtain visible absorption spectra of sodium in hydrogen were to prepare matrices of 12 % hydrogen in xenon as the host material for the sodium. Under these conditions sodium atoms have a high probability of having at least one hydrogen molecule in a nearest neighbor site. The visible absorption spectrum is shown in figure 4. In addition the spectrum for the same sample annealed to 16 K is also presented. A triplet structure appears but at wavelengths differing from the pure xenon case. The annealed spectrum shows the same triplet structure but with one of the red features disappearing. Since this study we have found that deposition of pure hydrogen at lower temperatures produce reasonable optically clear matrices. Hence this study will continue in the pure hydrogen system.

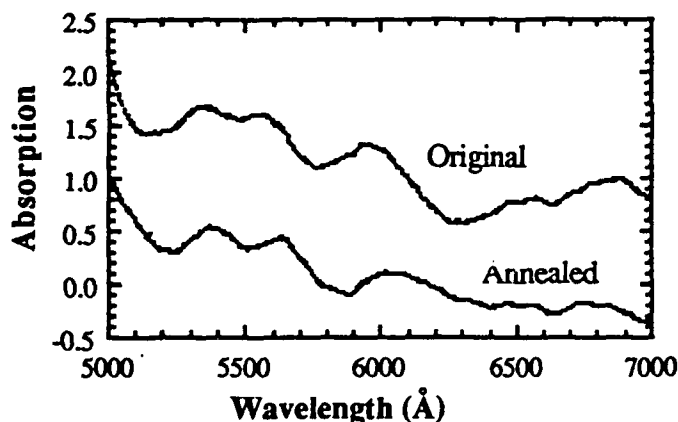


Figure 4. Absorption spectra of sodium deposited in a mixed matrix of hydrogen and xenon. The Na/H₂/Xe ratio was 1/12/87

SUMMARY

That the fraction of sodium monomers in the xenon matrix for the higher total mole fraction of sodium agrees well with what would be predicted for a statistical distribution indicates that the deposition procedures and not any physical restrictions govern the success of storing sodium monomers in xenon matrices. The degree by which other light mass metal atoms can be stored in cryogenic matrices, principally hydrogen, constitutes the thrust of our future work. The use of absorption spectroscopy may not be sufficient for tracking dimers and higher order clusters as evidenced by the controversy surrounding the identification of sodium dimers. Our development of additional diagnostic tools such as laser induced fluorescence and FTIR spectroscopy is designed to aid in determining cluster distributions of metals in cryogenic matrices.

REFERENCES

- 1 M. McCarty and G. W. Robinson, *Mol. Phys.* **2**, 415 (1959)
- 2 L. C. Balling, M. D. Harvey, and J. F. Dawson, *J. Chem. Phys.* **69**, 1670 (1978).
- 3 L. C. Balling and J. J. Wright, *J. Chem. Phys.* **81**, 675 (1984) and the references cited therein.
- 4 A. T. Pritt, N. Presser, and R. R. Herm, *Proceedings of the 3rd High Energy Density Matter Contractors' Conference*, March, 1989, New Orleans, LA.
- 5 T. Welker and T. P. Martin, *J. Chem. Phys.* **70**, 5683 (1979).
- 6 J. Hormes and B. Karrasch, *Chem. Phys.* **70**, 29 (1982).

Energy Transfer Processes in Rare Gas Solids

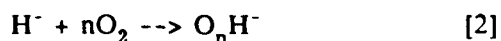
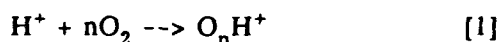
H. Helvajian, L. Wiedeman, B. Koffend
Laser Chemistry & Spectroscopy Department
Aerospace Corporation
Los Angeles, Ca.

The HEDM program goal as understood is to identify viable concepts for developing new propellants with the potential for increasing the ISP beyond current capabilities. To be of any practical use, these new propellants must be storable (several hours) and should be environmentally safe. This criteria under strict interpretation leads to the consideration of specific chemical reactions which release large enthalpy per product unit mass (\propto ISP). In this regard, chemical reactions with ground state reactants have limited ISP potential. As an example, the highly exoergic H_2/F_2 chemical reaction has a theoretical ISP near 528 sec, and even neglecting the product toxicity, has only slightly larger ISP than the H_2/O_2 chemical reaction. Comparatively, chemical reactions involving excited state (electronic) reactants or radical species have by their nature the potential for much higher energy release, though their storability in large densities pose formidable problems. The notion that there exist simple means for trapping these neutral highly electronically excited species runs contrary to common chemical principles. However, one can conceive of trapping radical species in cage like cells as found in cryogenic matrices.

Our proposal and experimental program has been to develop the necessary expertise for trapping of charged species in similar cryogenic cells. An ion impregnated cryogenic solid would release significant energy upon each charge neutralization reaction, and since such reactions are more exoergic than most neutral state chemical reactions, the potential exists for developing a high density (10^{19} - 10^{21} ions/cm³), high ISP (470 - 600 sec) fuel. The major difficulty in our proposal is that space charging (10^9 - 10^{10} ions/cm³) sets an inherent limitation to the maximum charge density which can essentially be trapped. This rather severe restriction may be partly assuaged if we allow the trapping of species having an opposite charge. Furthermore, in such a charge impregnated and energized solid

atomic diffusion and premature charge neutralization can be controlled if the charged species are in fact chemically bound to specific matrix lattice sites. This final requirement that the ionic species be, in essence, "anchored" rather than "caged" greatly increases the potential limit for trapping the maximum ion density. Oppositely charged but chemically bound species can be maintained in a cryogenic matrix, if relative to the trapped anion, the host material has a lower electron affinity and also if the ionization potential of the host is greater than the affinity of the cation to an electron.

The idea of trapping oppositely charged species in some cryogenic matrix is not in itself sufficient for making a high ISP propellant, unless the matrix host material can itself serve as a source of fuel. Therefore, our proposal incorporates a bipropellant scheme consisting of two cryogenic solid species, each impregnated with charges with the added requirement that when both solids come in contact they in themselves react. As a simple example we present the H_2/O_2 chemical reaction but now require that solid H_2 and O_2 be used. If we could impregnate solid O_2 with H^+ and H^- species, the trapped ions may stabilize in a form as given by the equations below.



If $n = 1$, the electron affinity and ionization potential of the species are such that no charge migration via electron hopping should occur. Using just equations (1) and (2), the addition of 1.4 eV/(H^-) which is sufficient energy to detach the electron, releases nearly 8.5 eV/(H^+) following charge neutralization. For $n \gg 1$, the energy released would be lower. Experiments are necessary to determine the conditions for making n small. One could also consider impregnating solid O_2 with F^- and HeH^+ species. Some reasons might be the necessity for a larger electron affinity anion and that perhaps the He rare gas atom would shield the cation during the deposition process.

We used the bipropellant (solid H_2/O_2^{**}) example above to calculate the ISP given that the solid oxidizer is impregnated with charges. The calculations were conducted using the one dimensional

isentropic equilibrium program written at AFAL (Beckman, and Acree). For a given set of input parameters (e.g. exhaust and chamber pressures), the program optimizes for maximum ISP. We adjusted the parameters such that using a liquid H_2/O_2 bipropellant fuel gave a calculated ISP of 400 sec. The exhaust pressure was set at one atmosphere (14.7 PSI), while the chamber pressure was set at 1000 PSI. Plotted on Figures 1 and 2 are the results of these calculations for implanting in solid O_2 the charged species described in the example above. The plots represent the (%) increase in ISP above that for the optimized liquid H_2/O_2 system (400 sec) as a function of (%) ion mole fraction trapped. In Figure 1, we also show the effect of increasing n value on ISP. The results in Figure 1 show that for $n = 1$ or 2, a 6% ion mole fraction trapped in solid O_2 results in a 13% increase in the ISP above that for liquid H_2/O_2 . If similar ISP increases could be achieved from energizing the solid hydrogen with the same ion mole fraction (%), then a potential 25% ISP increase could be obtained in a H_2^{**}/O_2^{**} fuel system. A 6% ion mole fraction trapping means that each charge is on the average surrounded by eight matrix atoms. The $n = 3$ example shows the effect of trace concentrations of trapped H_2O , which react with the proton to form the hydronium (H_3O^+) ion. The net ISP increase is roughly 1/3 that for the $n = 1$ or 2 case. Figure 2 compares the increase in ISP if atomic fluorine is the negative charge carrier and the proton is deposited in the solid while chemically bound to a rare gas atom. These results also show that greater than 10% ISP can be achieved by depositing a 6% mole fraction in the oxidizer alone. In general, these calculations show that *for ion deposition of a few (%)*, a potential ISP increase of 10 - 25% can be achieved by utilizing a bipropellant scheme based on solid H_2/O_2 . For the Figures 1 and 2, we also calculated the ISP change as a function of the chamber/exhaust pressure. In general we found that for a factor of two increase in the chamber pressure, the ISP increased by an additional 5%.

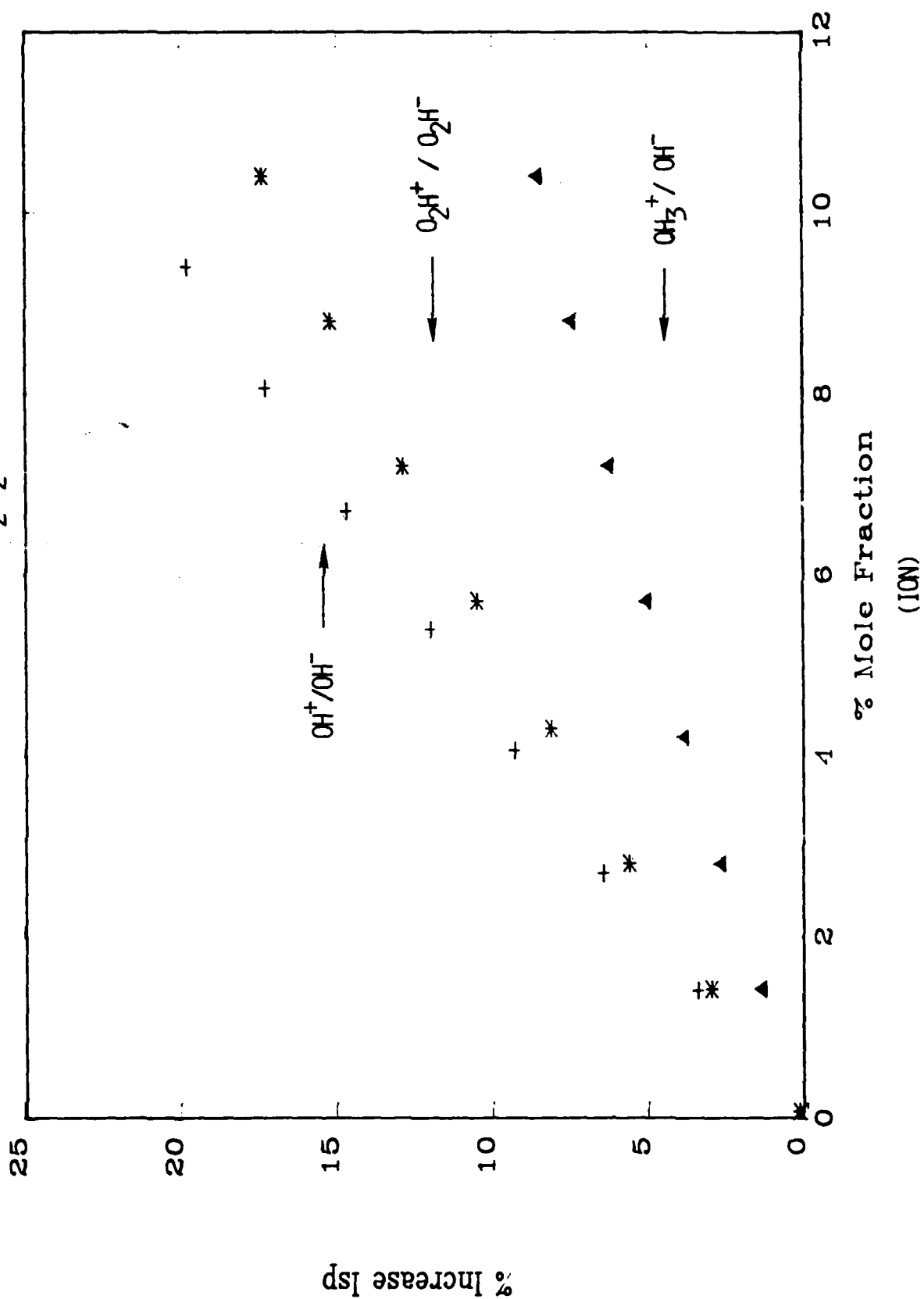
In effect, Figures 1 and 2 are only calculations and whether separated charges can be actually stored, at useful percentages, will depend on the results found in experiments. We have built an experimental chamber where we can prepare mass selected cations and anions insitu for deposition on to a rotatable cryogenically cooled target (10 K). The experimental chamber is also designed to allow monitoring of the reaction products (mass, species internal and translational energy) upon prompt (nanosecond) initiation of the charge neutralization. Figure 3 shows a schematic drawing of our exper-

imental facility. The gas handling is all teflon insulated which also allows safe handling of corrosive gases. A computer data acquisition system measures various parameters depending on the deposition or the reaction phase of the experiment. A short pulse laser is used to initiate the charge neutralization process in the energized solid. Another pulsed laser which is wavelength tuned to generate $L\alpha$ probes the arrival of matrix ejected atomic hydrogen at a known distance above the target surface. We use resonant multiphoton ionization ($L\alpha + h\nu$) and quadrupole detection to probe the ejected hydrogen atoms. By delaying the probe laser relative to the charge neutralizing initiation pulse, the kinetic energy distribution of the ejected H atoms can be measured. Similarly, other wavelength tuned probe lasers can monitor the trapped product distributions by laser induced fluorescence or measure specific trapped product densities via laser absorption spectroscopy. Figure 4a shows the mass spectrum from the cation source as measured by the quadrupole with H_2 and Ar gases. The hot filament discharge creates ions which are extracted by applying a 200 eV potential field. Initially a high extraction voltage is necessary for maximizing the current, however depositing of ions moving with these kinetic energies becomes more difficult. The fast ions impacting on the surface may generate thermal electrons which could prematurely neutralize the both incoming and previously trapped ions. We get around this problem by incorporating an ion decelerator which reduces the ion kinetic energy to less than 1 eV. The decelerator exit port sits 2 cm from the target surface to insure linearity in the electric field and to reduce the loss of ions from space charge spreading. Figure 4b shows a mass selected spectrum of low kinetic energy ArH^+ ions.

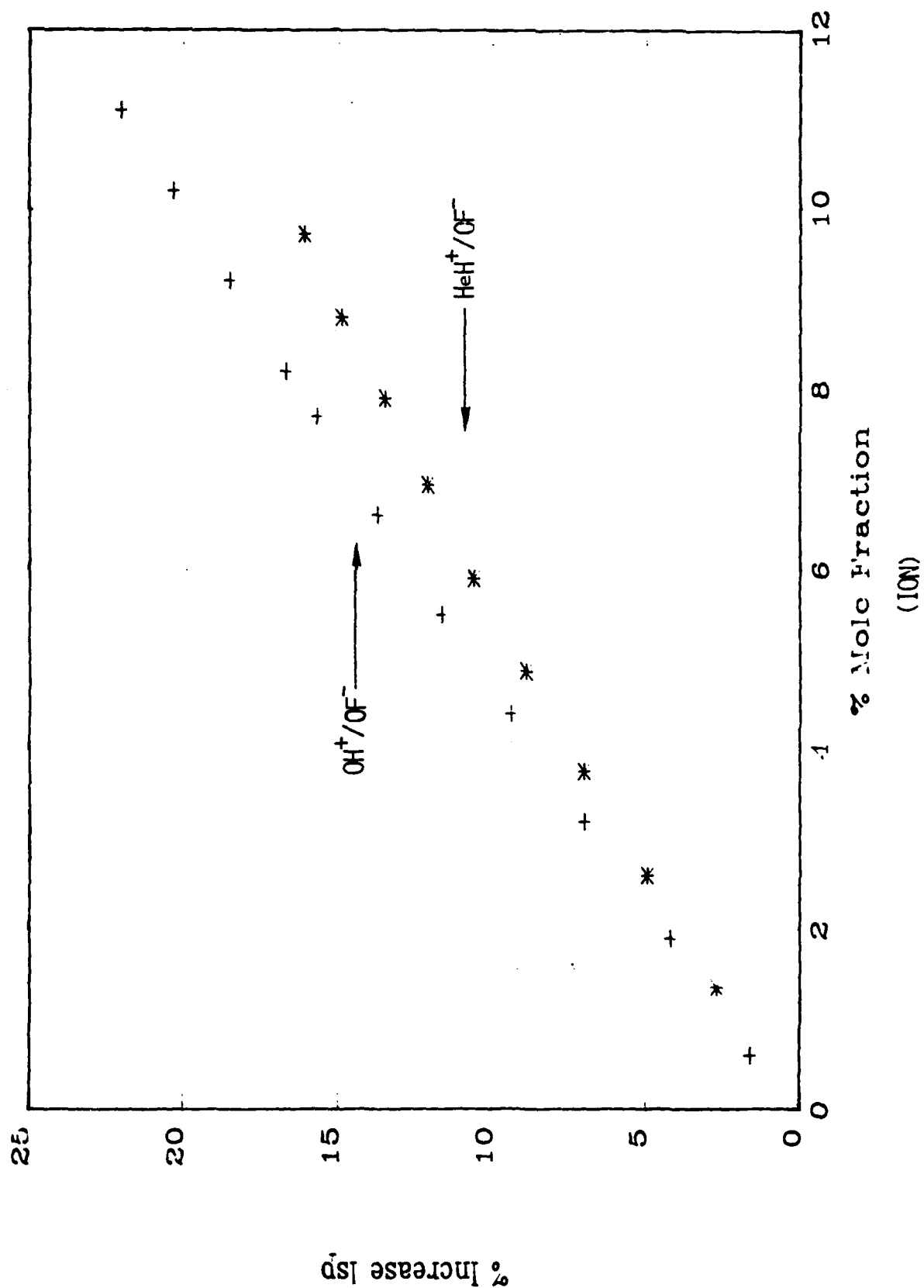
We have prepared a sequence of experiments which allow us to understand the chemistry and to test the feasibility of storing charged species at useful densities. In our initial experiment we hope to study the charge neutralization reaction in a non reactive Ar rare gas matrix. Using a reverse bias target we hope to initially trap ArH^+ species by co-condensing it with Ar gas. In this experiment the electrons will be delivered from a source not on the target, thus alleviating problems potentially resulting from chemistry with the negative charge carrier species. In a following experiment, a fraction of the matrix host will be replaced with oxygen and the reaction products will be measured. A similar set of experiments are planned for trapping of OH^- , and F^- . The final experiment will be to trap both

positive and negative ions, the charge density in this electroneutral solid can be measured by spectroscopic absorption if one can find a neutral product "tracer" compound which forms with known branching fraction upon charge neutralization. Since we specify that both the positive and negative charges be bound to the matrix host, if their spectroscopy and absorption cross section are known one may be even able to measure their density directly.

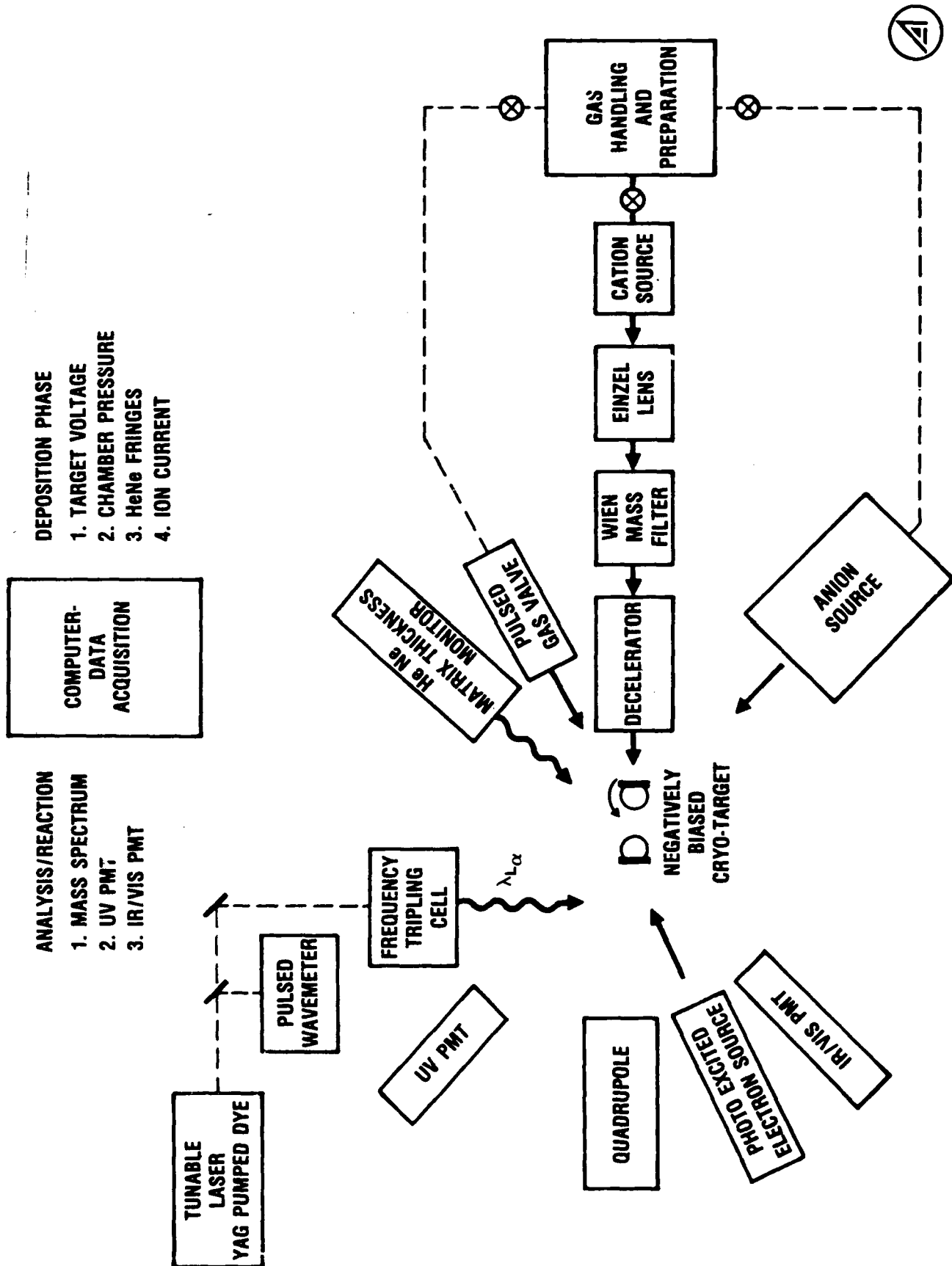
% ISP INCREASE ABOVE THAT FOR (H₂/O₂) REACTION

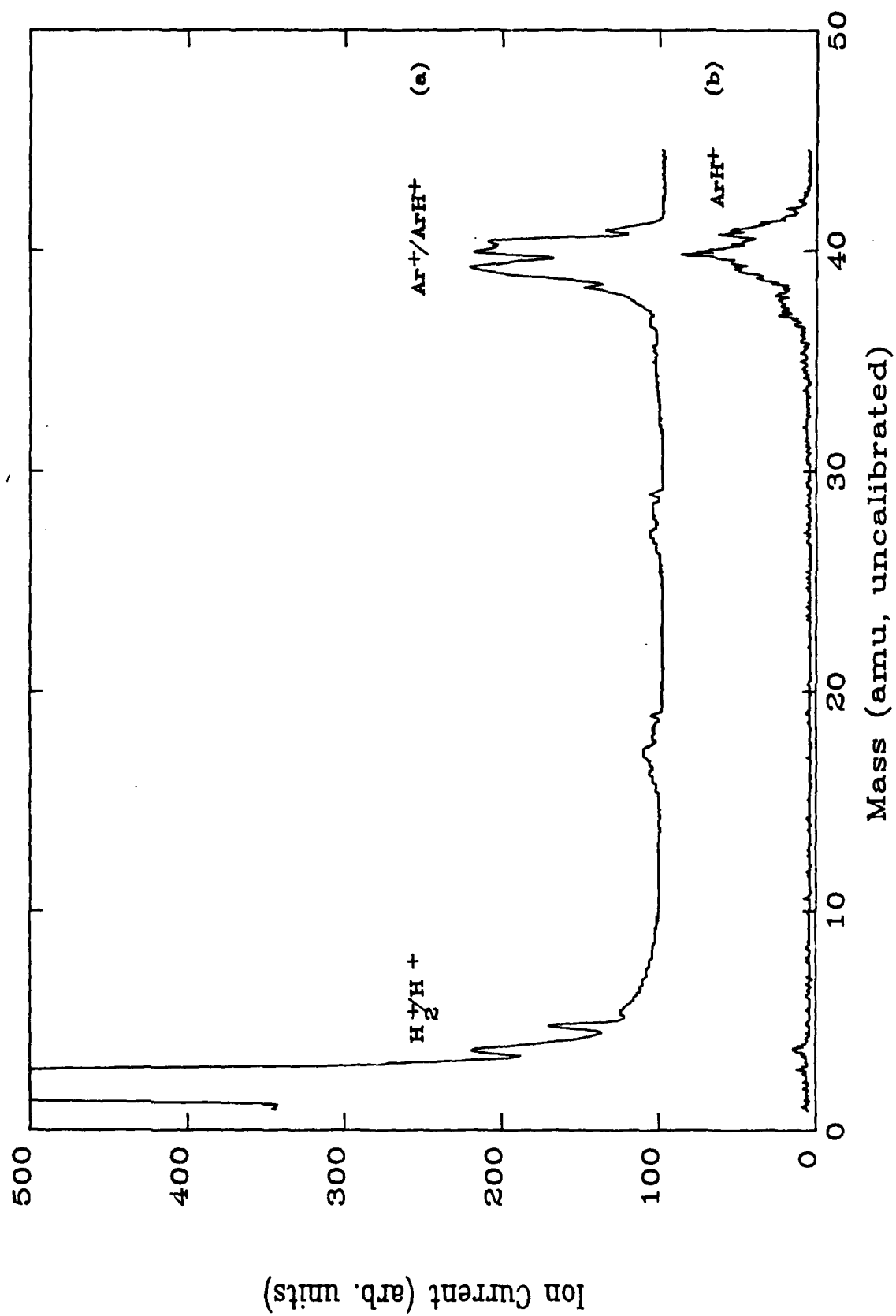


% ISP INCREASE ABOVE THAT FOR (H₂/O₂) REACTION



Experimental Schematic





Rydberg Holes and Solid State Exciplex Lasers
presentation at
High Energy Density Materials
Contractors Meeting
New Orleans, 1989

V.A. Apkarian
Department of Chemistry
University of California
Irvine, California 92717

We have previously reported on energy storage via charge separation and self-trapping in solid xenon doped with atomic halogens.¹ The scheme relies on two key ingredients: the existence of delocalized charge transfer states that can be optically accessed, and efficient subsequent self-trapping of holes. It is well known that holes are more deeply self-trapped in the lighter rare gases due mainly to their narrower valence bands.² Yet we have failed to store any significant energy in halogen doped solid krypton. While in such solids the triatomic krypton halides can be efficiently photogenerated, see figure 1, only a very weak thermoluminescence can be observed. The key to this apparent discrepancy is sought in the nature and extent of delocalization of the optically accessed charge transfer states:

The excitation spectra of halogen doped solid xenon were recently treated by us as a Rydberg progression of hole states.³ In this picture, the charge transfer states correspond to an electron localized on the impurity halogen center and an orbiting hole in the extended solid. The binding energies for the stationary states of such a system are given as:

$$B_n = 13.6\mu / \epsilon^2 n^2 \quad (1)$$

$$\text{in which } 1/\mu = 1/M_e + 1/M_h = 1/M_h \quad (2)$$

where μ is the reduced mass of the electron hole pair and well approximated as the mass of the hole since the electron is assumed to be stationary. ϵ in eq. 1 is the dielectric constant of solid xenon (2.18), and n is the effective principal quantum number for this many electron system. The effective mass of the hole is taken from band structure calculations to be $2.1M_e$, where M_e is the mass of a free electron. The effective quantum numbers are taken from gas phase values for the Rydberg states of the alkali atoms which are isoelectronics with the present system (K, Rb, Cs for Cl^- , Br^- , and I^- respectively). This simple treatment gives an excellent reproduction of the observed excitation spectra as shown in figure 2.

The validity of this model, in which a continuum dielectric is assumed, rests on the extent of delocalization of the charge transfer state. This can be gauged by calculating the Rydberg orbits for a given state:

$$r_n = n^2 \epsilon a_0 / \mu \quad (3)$$

In table 1, radii, r_n , and the radii of successive shells for progressions of I in Ne, Ar, Kr and Xe are summarized. In Xe, the 7s state is already commensurate with the radius of the nearest neighbor shell, in Ar the 9s state is the first that can be sustained while in Ne it should not be possible to sustain Rydberg holes. Based on these analyses, it would seem that Rydberg holes should be possible to sustain in solid Kr since states with small principal quantum numbers (7S) retain orbits comparable to the nearest neighbor shell radii. A charge transfer excitation spectrum of F in krypton is shown in figure 3. The absorption shows a sharp feature which can not be ascribed to molecular states for which an extensive vibrational progression is to be expected. The expected Rydberg progression is not seen either. The causes for the collapse of this progression is not at present understood. Studies are underway to resolve this issue. If indeed the collapse is due to insufficient delocalization, it should be possible to broaden the valence -- hence increase mobility of the hole -- by resorting to high pressures. Our preliminary studies in diamond anvil cells have been encouraging. We have to date observed dissociation of Cl_2 in xenon and very efficient production of Xe_2Cl at estimated pressures of 20kbar. An emission spectrum from the cell is shown in figure 4. Note the emission peak has now shifted to 600nm from its \emptyset pressure value of 572nm in solid xenon (485nm in the gas phase).

While the absence of delocalization has negative implications with respect to long term energy storage, the generation of high densities of localized (molecular) charge transfer states can be used as compact, efficient lasers. This we have recently demonstrated for the case of XeF doped crystalline argon.^{4,5} When pumped at 351nm, laser action on both the B \rightarrow X and C \rightarrow A transitions (purple and green) are observed.⁴ When pumped at 243nm, laser action on the D \rightarrow X transition at 286nm is observed. Some of the fascinating attributes of these lasers can be gauged from demonstrated characteristics:

- Broad tunability; the C \rightarrow A band, due to its bound-to-repulsive nature is broad with a FWHM of \sim 70nm. Single pass gain in excess of 100% over the 6mm path length of the active volume was measured from 520 - 590nm.

- Gain saturation measurements on the $C \rightarrow A$ band yielded a photon conversion efficiency of $\sim 30\%$.
- Multipass gain in a flat-flat resonator, of $\sim 100\text{cm}^{-1}$ for $B \rightarrow X$ and $C \rightarrow A$ lasers are inferred from the spectral collapse. (7cm^{-1} for the case of $D \rightarrow X$ measured without cavity mirrors).
- Excited state number densities in excess of 10^{19}cc^{-1} are observed, which imply energy densities in excess of 10KJ/L .

These extremely high energy densities (>3 orders of magnitude higher than gas phase excimer lasers) are achieved without introducing nonradiative loss channels. It should be possible to extend these principles to several other members of the rare gas halide family, to generate compact tunable lasers in the entire VUV to far red spectral range.

References

1. M.E. Fajardo and V.A. Apkarian, J. Chem. Phys. 89, 4124 (1988), and references therein.
2. M. Umehara, Phys. Rev. B 33, 4237, 4245 (1986).
3. N. Schwentner, M.E. Fajardo, and V.A. Apkarian, Chem. Phys. Lett. 154, 237 (1989).
4. N. Schwentner and V.A. Apkarian, Chem. Phys. Lett. 154, 413 (1989).
5. A. Katz, J. Feld and V.A. Apkarian, Optics Lett. 14, xxxx (1989).

Table 1. Calculated term values B_n^C and exciton radii r_n compared with experimental term values B_n (in eV) and successive radii a_n (in Å) of shells in a fcc lattice for I^- in Ne, Ar, Kr and Xe matrices. n.o. means no progressions observed.

		6S	6P	7S	7P	8S	8P	9S	9P
Ne	B_n^C	71.9	46.3	29.4	22.0	16.2	13.0	10.3	8.62
	B_n	n.o.							
	r_n	0.07	0.11	0.17	0.23	0.30	.39	.49	0.58
Ar	B_n^C	7.5	4.83	3.07	2.30	1.69	1.36	1.07	0.90
	B_n	n.o.							
	r_n	0.59	0.92	1.45	1.94	2.63	3.27	4.15	4.95
	a_n							3.755	
Kr	B_n^C	2.36	1.52	.97	.73	0.53	0.43	.34	0.28
	B_n	n.o.							
	r_n	1.64	2.55	4.01	5.35	7.27	9.05	11.47	13.68
	a_n			3.992	5.646	6.914	7.984	8.927	
Xe	B_n^C	1.72	1.11	0.70	0.53	0.39	0.31	0.25	0.21
	B_n			0.73	0.54	0.40	0.32	0.22	
	r_n	1.92	2.98	4.69	6.26	8.51	10.59	13.42	16.01
	a_n			4.340	6.138	7.517	8.680	9.705	

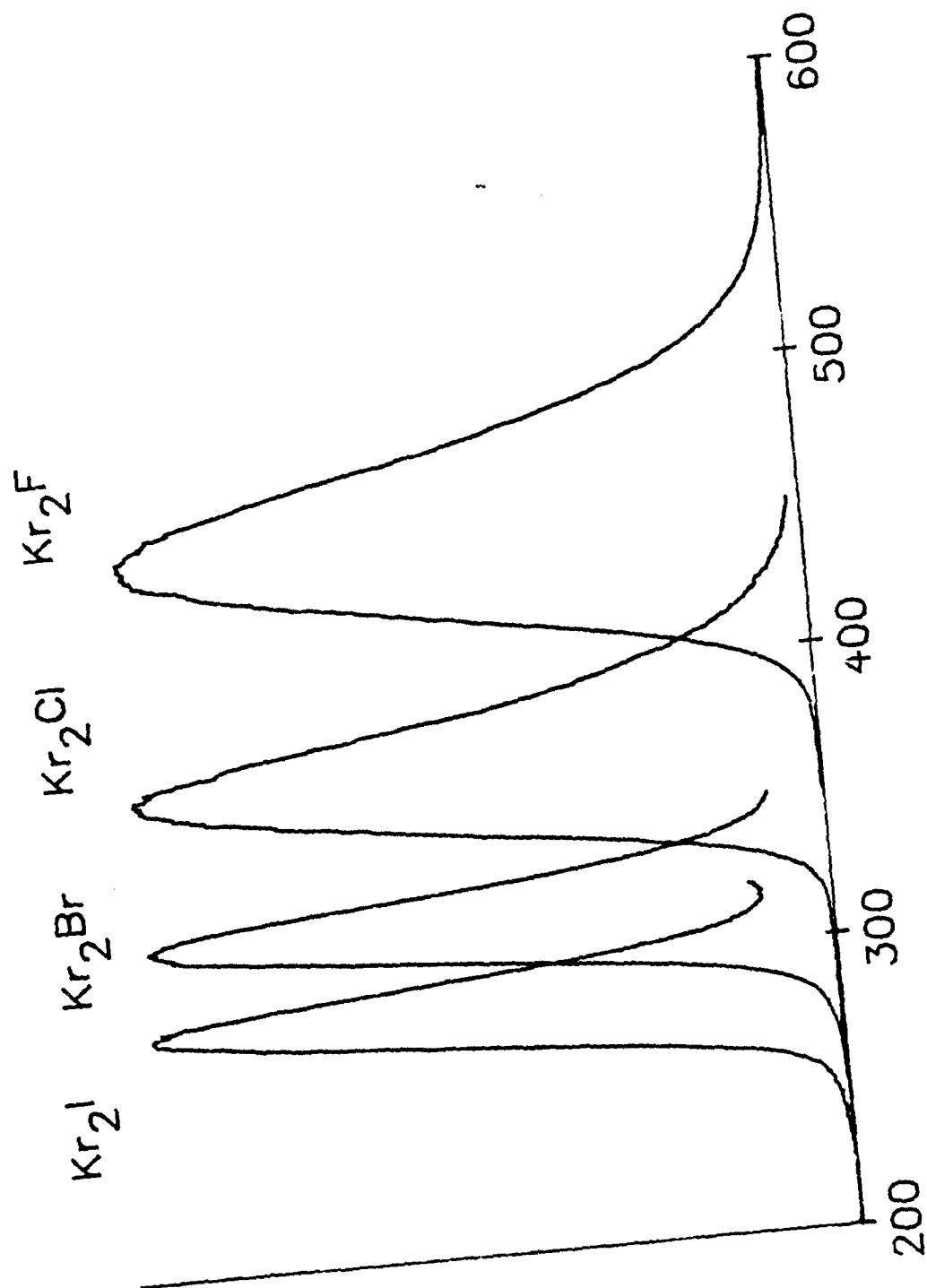
Figure Captions:

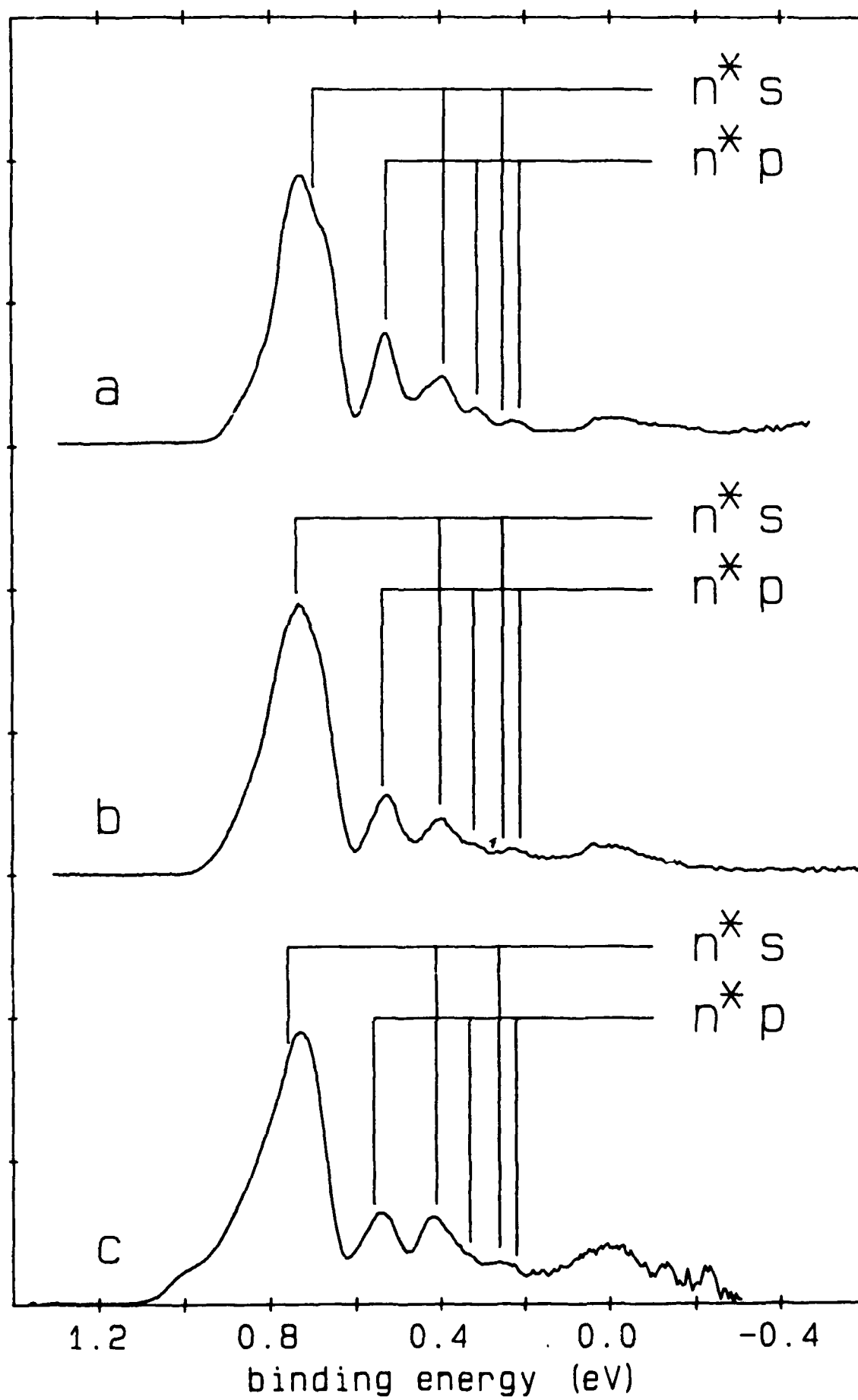
Fig. 1: Emission spectra of krypton halides, Kr_2^+X^- ($\text{X} = \text{I}, \text{Br}, \text{Cl}, \text{F}$) in solid krypton, at 15K.

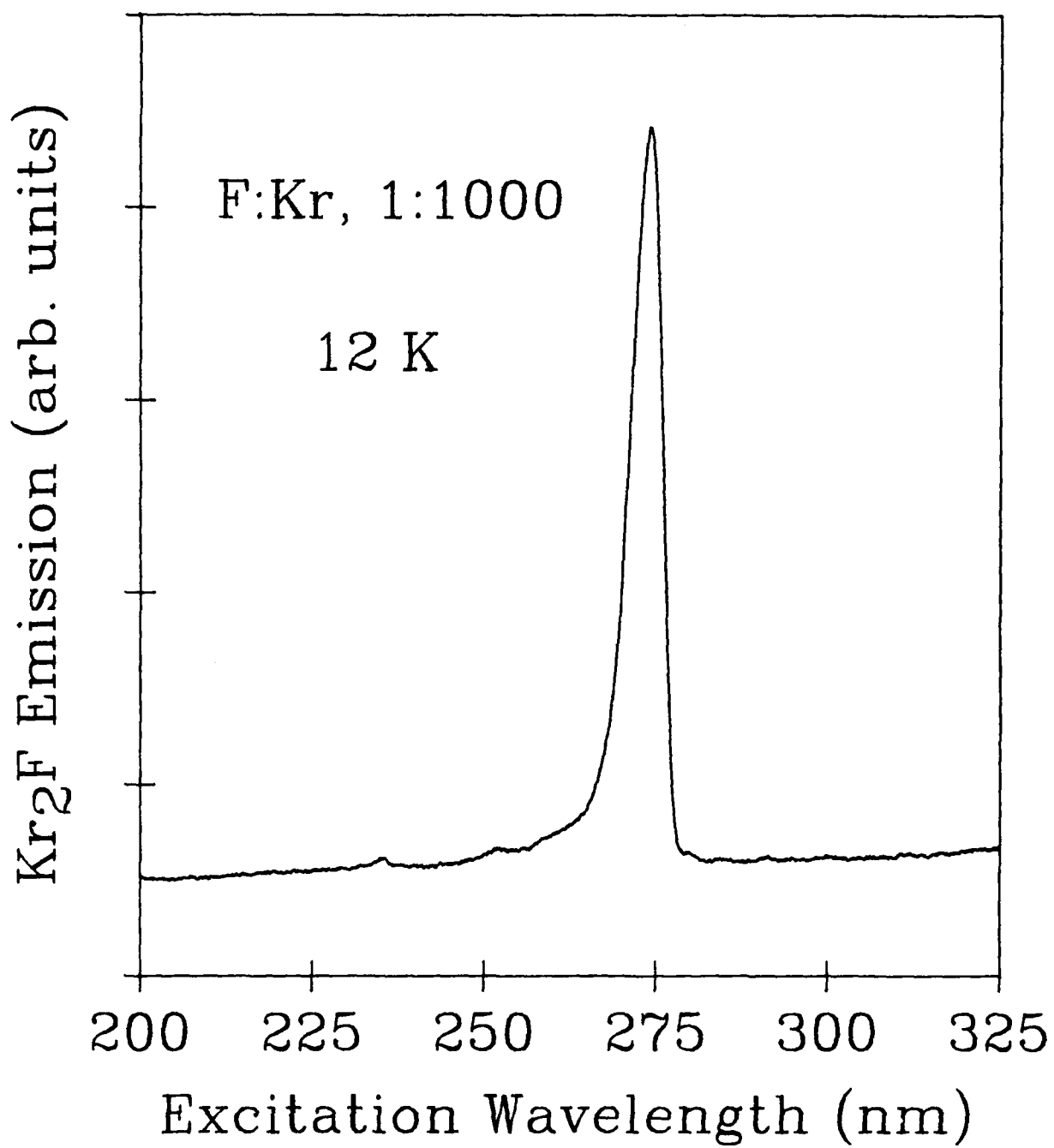
Fig. 2: Excitation spectra of halogen doped solid xenon, a) iodine, b) bromine, c) chlorine. The assignment to the Rydberg progressions are marked, six members of the progression are quite well observed and reproduced. ($n^* = n - \delta$, where δ is the quantum defect).

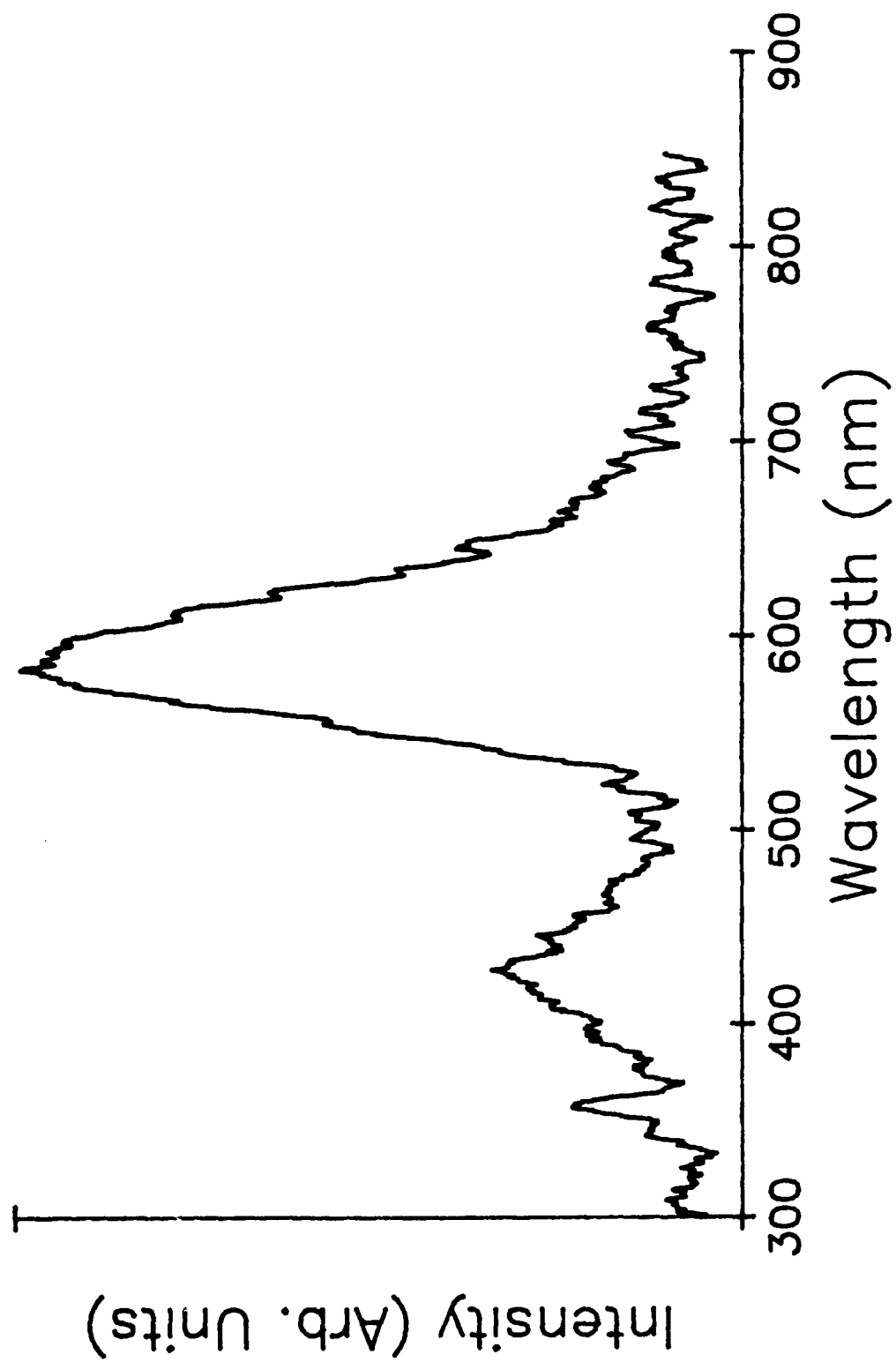
Fig. 3: Excitation spectrum of F doped solid krypton. The observed resonance cannot be assigned to molecular states.

Fig. 4: Emission spectra of Xe_2Cl in solid xenon under 20Kbar of pressure in a diamond anvil cell. The emission at $\sim 400\text{nm}$ is due to fluorescence of the diamonds.









Ab Initio Study of ArH, ArH⁺, Ar₂H, Ar₂H⁺, and Ar₄H⁺ Molecules

Marcy E. Rosenkrantz

University of Dayton Research Institute

Air Force Astronautics Laboratory, ARIES Office

Our goal is to store energy for use in novel propulsion systems. As an example we wish to consider the reaction



Therefore, if we can stabilize protons in a matrix, and then induce the recombination reaction we could obtain about 13.6 eV.

Our test of the feasibility of this approach is to characterize the behavior of protons in an argon matrix. We have investigated ArH, ArH⁺, Ar₂H, Ar₂H⁺ and Ar₄H⁺ using *ab initio* techniques. Both Pimentel and Bondybey¹ as well as Milligan and Jacox² have investigated condensed Ar/H₂ mixtures, experimentally. The IR spectra of the photolysis products of these mixtures show an absorption at 905 cm⁻¹. The deuterated mixtures have absorption bands at 644 cm⁻¹. Bondybey and Pimentel attribute this band to a hydrogen atom in an octahedral interstitial site of Argon. Milligan and Jacox, however, attribute this absorption to the presence of species of the type Ar_nH⁺ (n=2,4).

Our goals in this study were several-fold:

1. To characterize the potential curve of ArH in its ground and low-lying excited states.

2. To characterize the potential curve of ArH^+ .
3. To characterize the potential surfaces of several Ar_nH^+ clusters.

The initial two parts of this investigation would serve to test our ability to use the MESA codes of Lengsfeld, Saxe, Page and Martin⁷ on the Cray-2 at the Air Force Weapons Laboratory as well as give us an introduction to the simplest Ar_nH system. The third part would give us an indication of the behavior of a system approaching that found in an argon matrix.

We present in tables 1-3 the results of our calculations of the ground and first three excited states of ArH and of the ground state of ArH^+ . For these calculations, we used the 12s9p/6s4p argon basis of McLean and Chandler⁴ augmented by a diffuse s function with ζ value of 0.08, a diffuse p function ($\zeta=0.05$) and three d functions ($\zeta=1.0, 0.3, 0.1$). This is the argon basis used by Simandiras, Gaw and Handy⁵ in their calculations of several conformers of ArH_3^+ . For the hydrogen atom, we used the 6s/4s basis of Meyer⁶ augmented by an s function ($\zeta=0.02$), three p functions ($\zeta=0.7, 0.2, 0.4$), and a d function ($\zeta=0.2$). We do not understand why our second order CI (SOC1) calculations on the ground state of ArH give a potential curve so much deeper than that determined by other methods and by experiment. We are currently investigating the degree of basis set superposition included in our calculations. An Interacting Hartree-Fock (IHF) fragment calculation yields characteristic constants for this system in excellent agreement with experiment and other calculations.

The results of both our SOC1 and first order CI (FOCI) calculations on ArH^+ are in excellent agreement with those of other calculations and experiment. The excited states of ArH form a Rydberg series which approaches the ArH^+ curve. At small separations, these states can be thought of as an ArH^+ core with a H Rydberg electron. As a result, the characteristic constants of these curves closely resemble those of the ion. These results are also in good agreement with those of other calculations.

We have completed geometry optimization calculations for Ar_2H and Ar_2H^+ . These were performed using the Compact Effective Core Potentials and Shared Exponent Basis set for Ar, determined by Stevens, *et al'*. The Ar_2H molecule has a bent arrangement of the atoms with the Ar-H-Ar angle equal to 61.65° and the Ar-H distances equal to 3.62\AA . This arrangement yields an Ar-Ar distance of 3.72\AA which is very close to that of the Ar_2 molecule.

In contrast, the Ar_2H^+ molecule is linear and asymmetric. One of the Ar-H distances is 1.396\AA and the other is 1.800\AA . The former distance is 0.1\AA larger than the R_e of the ArH^+ ion. The latter distance is very close to that found by Simandiras, Gaw and Handy⁷ for the ArH distance in a planar arrangement of ArH_3^+ , with the argon directly above the apical hydrogen. Matcha and Milleur⁸ confined their calculations for this system to a symmetric geometry and found the ArH distances to be $2.999a_0$. The frequencies for this system are 33.9 cm^{-1} , 1018.0 cm^{-1} , and 1327 cm^{-1} , for the asymmetric stretch, bending and symmetric stretch modes, respectively. They were determined at the MCSCF optimized geometry using an STO-3G basis for Argon at the SCF level. This was done because the MESA codes do not as yet support the computation of derivatives of effective core potential integrals.

The asymmetric stretching frequency is very close to that found for the Ar-HCl system. Since ArH^+ is isoelectronic with HCl, this similarity is not surprising. The fact that this system is asymmetric can be understood purely on the basis of electrostatic arguments. The ArH^+ system is strongly bound and attracts the other argon atom predominantly via a charge induced dipole interaction. The frequencies determined at the SCF level are usually too large by approximately 10%. Thus the bending frequency tends to support the contention of Milligan and Jacox² that the 905 cm^{-1} absorption found in their matrix studies of Ar/ H_2 mixtures is due to the presence of Ar_nH^+ species ($n=2,4$) in the matrix. The geometries of Ar_2H and Ar_2H^+ indicate that the recombination of an electron to Ar_2H^+ causes the hydrogen atom to be pushed away from the argon atoms which themselves also move slightly apart.

Thus far we have completed only a preliminary geometry optimization of the Ar_4H^+ system at the SCF level using the basis set and ECP for argon described above. We determined the

geometry to be that of a tetrahedron with Ar-H distances of 1.99Å and Ar-Ar distances of 3.25Å. The ArHAr angles are all 109.47°. We are currently determining the optimized square planar geometry of Ar_4H^+ and will report results of these calculations and those of the frequencies at a later time.

Table 1. Characteristic Constants for ArH.

Source	$R_e (a_0)$	$D_e (cm^{-1})$
Present SOCI	6.77	67.9
IHF	6.79	41.3
Das, Wahl and Wagner ¹ (MCSCF + dispersion)	6.59	38.7
	6.59	39.16
Theodorakopoulos, et al ^{1, 2} (MRD-CI)	6.99	36.65
Expt (Bickes, et al ^{1, 3})	6.69	38.15
(Bassi, et al ^{1, 2})	6.84	33.55
Semi-empirical (Braga & Murrell ^{1, 3})	6.85	30.72

Table 2. Characteristic Constants for ArH^{*}.

Source	$R_e(a)$	$D(cm^{-1})$	$\omega_e(cm^{-1})$	$\omega_e x_e(cm^{-1})$
$2^2\Sigma^+ Ar^1S + H 2s^2S$				
Present FOCl	2.44	2977	77.87	
MCVB (Vance & Gallup ^{1,4})	2.8	28528		
SCF-CI (Olson and Liu ^{1,5})	2.40	19649		
		31102		
$3^2\Sigma^+ Ar^1S + H 2p_\sigma^2S$				
Present FOCl	2.43	2794	81.17	
MCVB (Vance and Gallup ^{1,4})	2.79	23903		
SCF-CI (Olson and Liu ^{1,5})	2.43	15245		
		24529		
$1^2\Pi Ar^1S + H 2p_\pi^2P$				
Present FOCl	2.41	3083	106.62	
MCVB (Vance and Gallup ^{1,4})	2.79	22617		
SCF-CI (Olson and Liu ^{1,5})	2.39	11381		
		24738		

Table 3. Characteristic Constants for ArH^+ .

Source	$R_e (a_0)$	$D_e (\text{cm}^{-1})$	$\omega_e (\text{cm}^{-1})$	$\omega_e \times (\text{cm}^{-1})$
Present SOCI	2.44	33216	2728	56.0
Present FOCI	2.41	31948	2714	57.83
PNO-CI (Rosmus' ⁴)	2.42	32580	2758	56.0
DIM (Roach & Kuntz' ⁷)	2.61	33070	-	-
Expt scattering data	2.41	33633	2711	-

(Chupka and Russell' ⁶ ; Saykally, et al' ⁸)

Table 4. Ar_2H^+ Geometry.

Linear geometry

Ar-H distance: 1.396Å

1.800Å

Vibrational Frequencies:

33.9 cm^{-1}

1018.0 cm^{-1}

1327.3 cm^{-1}

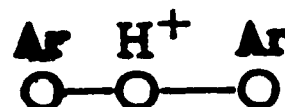


Table 5. Ar_2H Geometry.

Planar geometry

Ar-H distance: 3.62Å

Ar-Ar distance: 3.72Å

ArHAr angle: 61.65°

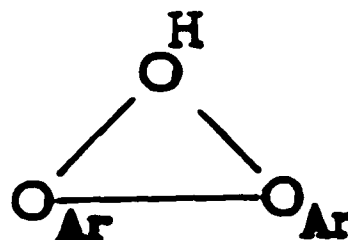


Table 6. Ar_4H^+ Geometry.

Tetrahedral geometry

Ar-H distance: 1.99Å

Ar-Ar distance: 3.25Å

ArHAr angles: 109.47°

References

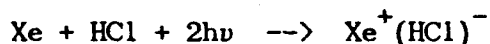
1. V.E. Bondybey and G.C. Pimentel, J. Chem. Phys. 56, 3832 (1972).
2. D.E. Milligan and M.E. Jacox, J. Mol. Spectrosc. 46, 460 (1973).
3. B.H. Lengsfeld, III, P. Saxe, M. Page, and R. Martin, MESA, Molecular Electronic Structure Algorithms, unpublished.
4. A.D. McLean and G.S. Chandler, J. Chem. Phys. 72, 5639 (1980).
5. E.D. Simandiras, J.F. Gaw, and N.C. Handy, Chem. Phys. Lett. 141, 166 (1987).
6. W. Meyer, Chem. Phys. 17, 27 (1976).
7. W. J. Stevens, H. Basch, and M. Krauss, J. Chem. Phys. 81, 6026 (1984).
8. R.L. Matcha, and Mac B. Milleur, J. Chem. Phys. 69, 3016 (1978).
9. A.F. Wagner, G. Das, and A.C. Wahl, J. Chem. Phys. 60, 1885 (1974); G. Das, A.F. Wagner, and A.C. Wahl, J. Chem. Phys. 68, 4917 (1978).
10. G. Theodorakopoulos, S. Farantos, R.J. Buenker, and S.D. Peyerimhoff, J. Phys. B. 17, 1453 (1984).
11. R.W. Bickes, B. Lantzsch, J.P. Toennies, and K. Walaschewski, Faraday Discuss. Chem. Soc. 55, 167 (1976).
12. D. Bassi, M.G. Dondi, F. Tommasini, F. Torello, and U. Valbusa, Phys. Rev. A 13, 584 (1976).
13. J.P. Braga, J.N. Murrell, Mol. Phys. 53, 295 (1984).
14. R.L. Vance, and G.A. Gallup, J. Chem. Phys. 73, 894 (1980).
15. R.E. Olson, and B. Liu, Phys. Rev. A 17, 1568 (1978).
16. P. Rosmus, Theoret. Chim. Acta 51, 359 (1979).
17. W.A. Chupka, and M.E. Russell, J. Chem. Phys. 49, 5426 (1968).
18. K.B. Laughlin, G.A. Blake, R.C. Cohen, and R.J. Saykally, J. Chem. Phys. 90, 1358 (1989).

THE INTERACTION OF HYDROGEN CHLORIDE WITH RARE GAS ATOMS

Cary F. Chabalowski and George F. Adams
US Army Ballistic Research Laboratory
Aberdeen Proving Ground, MD 21005-5066

David R. Yarkony
Department of Chemistry
The Johns Hopkins University
Baltimore, MD 21218

Recently, Fajardo and Apkarian^{1,2,3} have published experimental results documenting long term energy storage (1-2 days) in solid Xenon. The basic principle rests upon the formation (via laser excitation) and separation of a stable, negatively charged exciplex such as Cl^-Xe_2 and a self-trapped positive hole (STH) localized on a Xe_n^+ ($n=2$ or 3) molecule. The first step in the formation of these separated polarons is a cooperative charge transfer excitation involving molecular Cl_2 or HCl and the Xe atoms in the solid to form:



which quickly reacts with another Xe atom to form the more stable triatomic exciplex Xe_2^+Cl^- . This exciplex decays primarily from the 4^2T state through a radiative process with a natural lifetime of 225 ns.² The stability of the STH is related to the stabilization energy associated with crystal relaxation effects. A very recent publication by Schwentner, Fajardo, and Apkarian⁴ gives another description of the charge transfer (CT) excitation as a Rydberg progression of hole states.

As an extension to our earlier studies of rare gas (RG) atomic and molecular interactions,⁵ we begin this preliminary theoretical treatment of the RG halide interactions by studying the interactions of HCl with Xe atoms. Quantum chemical calculations are performed on the ground and excited states of HCl (not reported here), XeCl , and HClXe , including State Averaged-CASSCF⁶ and CI calculations.

Details of Calculations

All calculations were carried out in the C_{2v} point group. The atomic basis sets used are a combination of GTOs and the effective core potentials (ECPs) of Wadt and Hay.⁸ The ability of our codes to handle ECPs allows for the treatment of systems including such heavy atoms as Xe. The gaussian basis consists of a non-contracted set of 4 s-type primitives and one p-type polarization

function($\alpha_p=1.0$) on hydrogen, giving [4s/1p]. The chlorine basis contains 3 non-contracted s- and p-type valence AOs with exponents optimized for their use with the ECPs.⁸ This is augmented by a negative ion function($\alpha_p=0.049$) and a polarization function($\alpha_d=0.50$), for a total basis set of [3s,3p/1p,1d]. Likewise, the Xe basis associated with the ECPs consists of 3 s- and p-type primitives which are contracted to double-zeta⁸ and augmented by a single polarization function($\alpha_d=0.25$), giving [2s,2p/1d].

The orbitals used as expansion vectors in the CI are obtained by state-averaging in a CASSCF, thereby generating orbitals suitable to both the ground and excited states. These preliminary wavefunctions are generated from the ALCHEMY⁷ code by doing all single and double electronic excitations from a set of reference configuration state functions (CSFs). Due to the exploratory nature of these calculations, rather small CI expansions were used. PECs and electronic transition dipole moments are then calculated and used to explicitly include the vibrational motion of the nuclei, enabling us to predict transition probabilities and radiative lifetimes. One potential weakness in these calculations is the neglect of spin-orbit (SO) interactions. But earlier theoretical work done by Hay and Dunning⁹ on XeCl showed that much useful qualitative and semi-quantitative information can be obtained without inclusion of SO effects. Our codes already include these effects for the lighter atoms where use of the Breit-Pauli Hamiltonian is appropriate, and plans have already been laid for including in our codes SO effects in heavy atoms.

Xe-Cl Interactions

To help determine the suitability of the ECPs for studying the HCl-Xe interactions, we have first calculated the PECs and transition probabilities for the Xe-Cl system which has already been studied both theoretically⁹ and experimentally.¹⁰ We calculate the $1,2^2\Sigma^+$ and the $1,2^2\Pi$ states and the strong transitions $2^2\Pi \rightarrow 1^2\Pi$ and $2^2\Sigma^+ \rightarrow 1^2\Sigma^+$, as well as the weak $2^2\Pi \rightarrow 1^2\Sigma^+$ and $2^2\Sigma^+ \rightarrow 1^2\Pi$ transitions, reporting lifetimes for emissions from the $v'=0$ levels. This is believed to be the first time that the lifetimes have been calculated theoretically for the weak transitions.

The PECs can be seen in Fig. 1, and some molecular constants are reported in Table 1 along with values from earlier theoretical work by Hay and Dunning⁹ (HD). HD had calculated the electronic states both with and without SO effects, and both values are reported in Fig. 1. Our equilibrium bondlengths and ω_e 's are in reasonably good agreement with HD's values. It is worth pointing out that the R_e 's and ω_e 's of HD are almost unaffected by the inclusion of SO. Fig. 2 gives the electric transition dipole moments for the strong transitions as a function of $R(\text{Xe-Cl})$. Near the R_e (6.4 bohr) values for the $2^2\Sigma^+$ excited state, the moment for the $\Sigma\text{-}\Sigma$ transition is approximately 4.5 times greater than the $\Pi\text{-}\Pi$ moment. The transition moments and PECs from this work are nearly identical to those calculated by HD when SO is ignored. Table 1 also includes the results of

our vibrational analysis for the radiative lifetimes. Again, our predicted lifetimes for the strong transitions are very similar to HD's without SO effects. But it is here that the SO does make a difference by nearly doubling the natural lifetimes for both the $2\Sigma^+$ and 2Π states. HD's lifetimes with SO are amazingly close to the experimental values. It must be kept in mind that the term symbols $2\Sigma^+$ and 2Π are now only approximations to the correct state descriptions due to mixing of different Λ components of Ω through the spin-orbit operator.

Fig. 3 shows the transition moments for the weak transitions and the resulting lifetimes are listed in Table 1. These excited states are predicted to have lifetimes on the order of 26 μ s and 104 μ s for the $2^2\Pi-1^2\Sigma$ and $2^2\Sigma-1^2\Pi$ transitions respectively. These are several orders of magnitude greater than the lifetimes for the strong transitions.

Xe--HCl Interactions

HCl-Xe is treated as a linear system with the Xe opposite the hydrogen atom. Calculations were performed at nuclear separations of $R=(6.425,7.0,8.0,10.0,15.0,20.0)$ while holding $R(\text{HCl})$ at $R_e(\text{HCl})=1.2689$ bohr. The lowest 2 states of $1A_1$ symmetry and the lowest 3 states of $1B_1 (\Pi_x)$ symmetry were calculated. The states of interest are the $1^1A_1(X^1\Sigma^+)$ and $1^1B_1(A^1\Pi)$ and 2^1B_1 , which turns out to be a charge transfer state with an electron going from the $\text{Xe}(p_x)$ doubly occupied MO to a $\text{H-Cl}(\sigma^*\text{-antibonding})$ MO. This $2^1B_1(\text{CT})$ state could then be responsible for the CT and subsequent breaking of the H-Cl bond. The $2^1B_1(\text{CT})$ lies above the HCl $A^1\Pi$ valence state. The $A^1\Pi$ state is essentially localized on the HCl, and in the isolated HCl the $A^1\Pi$ state is the lowest excited singlet and everywhere repulsive, dissociating to the same asymptote as the ground state^{11,12}. It will be interesting to see if the $2^1B_1(\text{CT})$ state (or its equivalent) becomes the lowest excited state when more Xe atoms are added. These calculations have already been started. The third state of B_1 symmetry in Fig. 4 is a mixture of many CSFs but predominantly described by exciting an electron from the HCl sigma bond to the negative ion $\text{Cl}(p_x)$ MO. This is most likely a state trying to be Rydberg in nature but due to the lack of true Rydberg AOs in the basis it is poorly represented.

And finally we can look at the electric dipole moments for the transitions $A^1\Pi \rightarrow X^1\Sigma^+$ (T1) and $2^1B_1(\text{CT}) \rightarrow X^1\Sigma^+$ (T2) shown in Fig. 5. In isolated HCl, this study calculates T1 to be 0.32 D at $R=2.4$ bohr (near $R_e(\text{HCl})$). The values for the transition moment of T1 is seen to approach this value as $R(\text{HCl-Xe}) \rightarrow 20$ bohr. Its asymptotic value falls short of the .32 D found in HCl, most likely due to a slight difference in the details involved in generating the CI expansion vectors from the state averaged CASSCF. In following calculations using better AO basis sets and larger CI expansions this discrepancy should disappear. What is especially interesting is the increase in the moment for T2 as $R(\text{HCl-Xe})$

approaches what is reported to be near the equilibrium distance of $R(\text{Cl-Xe})=6.4$ bohr in the exciplex Xe_2^+Cl^- . At this point the moment for T2 is about equal to the transition moment for T1. Again it is interesting to speculate what the size of the transition moment will be for the CT transition when more Xe atoms are included. One also notices that the moment for the CT transition is largest at about $R=8.0$ bohr. This is consistent with the notion that the neutral Cl and Xe atoms (at the onset of excitation) will most likely be at a $R(\text{Xe-Cl})$ distance which is larger than $R(\text{Xe}^+\text{Cl}^-)=6.4$ bohr.

Conclusions

It has been shown that much insight into the XeCl interactions can be achieved through the combination of effective core potentials and wavefunctions obtained from state averaged MCSCF and CI. The results compare favorably with earlier ab initio work, although the difference in radiative lifetimes predicted by HD both with and without spin-orbit effects highlight the need for inclusion of such effects.

The results on HCl-Xe found a CT transfer state as the second highest excited state of $^1\Pi$ symmetry, which drops in energy as the R_e for the exciplex is approached. This CT state is represented by promoting an electron into a HCl σ^* -antibonding orbital which could account for the formation of the Cl atom upon excitation in the solid. The changes in transitions moments also predict an enhanced probability for populating this CT state at internuclear distances approximating those in the Xenon solid. More Xe must be included in the model and the level of theoretical treatment will be enhanced.

1. M.E. Fajardo and V.A. Apkarian, J. Chem. Phys. 85, 5660(1986).
2. M.E. Fajardo and V.A. Apkarian, J. Chem. Phys. 89, 4102(1988).
3. M.E. Fajardo and V.A. Apkarian, J. Chem. Phys. 89, 4124(1988).
4. N. Schwentner, M.E. Fajardo, and V.A. Apkarian Chem. Phys. Let 154, 237(1989).
5. C.F. Chabalowski, J.O. Jensen, D.R. Yarkony and B.H. Lengsfeld J. Chem. Phys. 90, 2504(1989); J.K. Perry and D.R. Yarkony J. Chem. Phys. 89, 4945(1988).
6. B.H. Lengsfeld, J. Chem. Phys. 77, 4073(1982).
7. B. Liu and M. Yoshimine, J. Chem. Phys. 74, 612(1981).
8. W.R. Wadt and P.J. Hay, J. Chem. Phys. 82, 284(1985).
9. P.J. Hay and T. Dunning, J. Chem. Phys. 69, 2209(1978).
10. G. Inoue, J.K. Ku and D.W. Setser, J. Chem. Phys. 80, 6006(1984).

Table 1.

	$R_e(\text{\AA})$			$\omega_e(\text{cm}^{-1})$		
	This Study	H+D ^(a) (w/o SO)	H+D (with SO)	This Study	H+D (w/o SO)	H+D (with SO)
$2^2\Sigma^+$	3.20	3.25	3.22	198.	190.	188.
$2^2\Pi$	3.08	3.14	3.14	196.	188.	188.

	Radiative Lifetime (ns) ($v'=0$)			
	This Study	H+D (w/o SO)	H+D (with SO)	Exp. ^(b)
$2^1\Sigma^+-1^2\Sigma^+$	6.0	5.6	11.	11.1
$2^1\Pi-1^1\Pi$	74.	64.	120.	131.
$2^2\Pi-1^2\Sigma^+$	2645			
$2^2\Sigma^+-1^1\Pi$	104.45			

(a) Hay & Dunning, JCP 69, 2207 (1978); DZP+1st Order POL-CI

(b) Inoue, Ku, Setser, JCP 80, 6006 (1984).

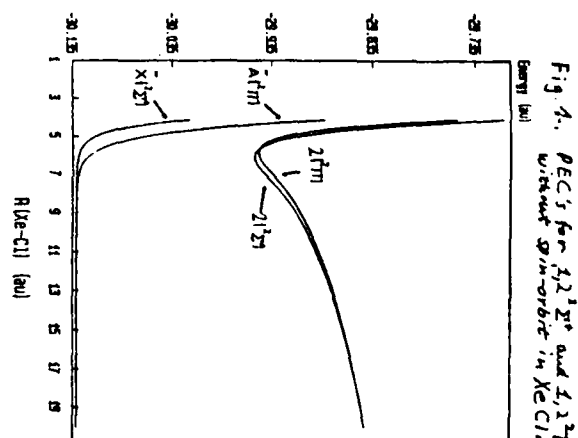


Fig. 1. PEC's for $2^2\Sigma^+$ and $2^2\Pi$ without spin-orbit in XeCl.

Fig. 2

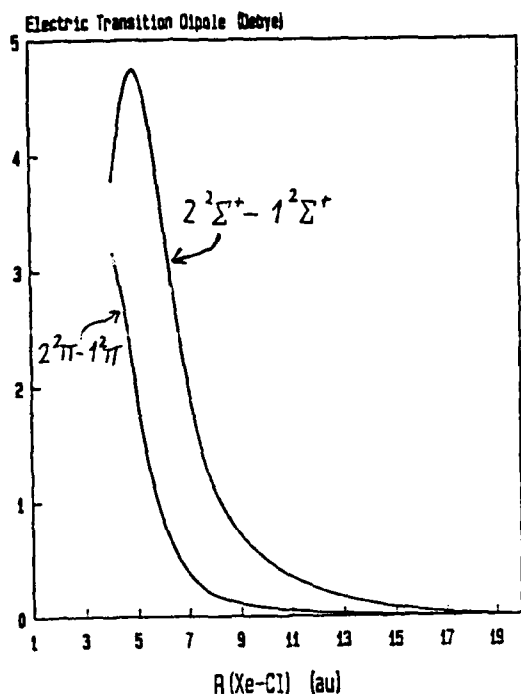


Fig. 3.

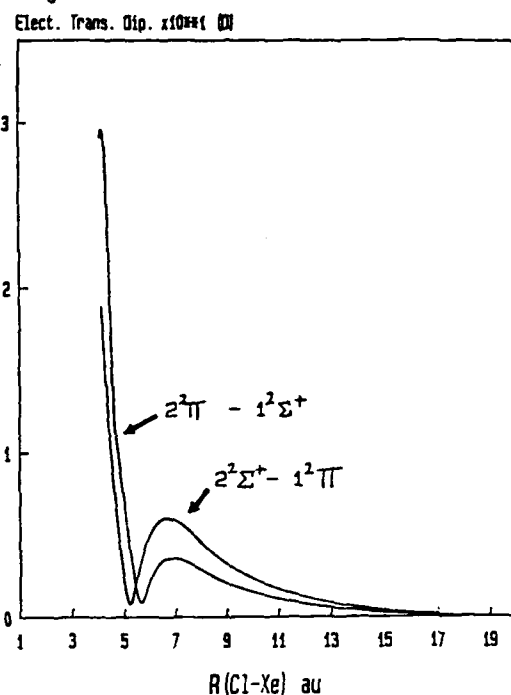


Fig. 4. PECs for the 2 lowest energy states of 2A_1 symmetry and 2B_1 symmetry.

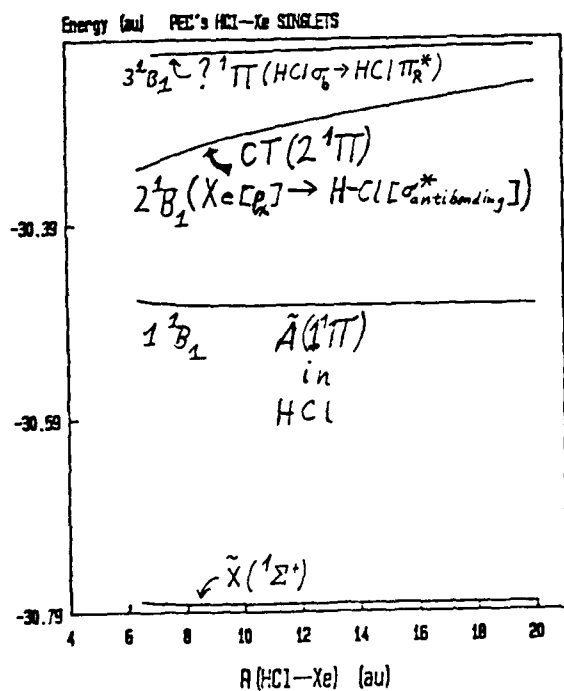
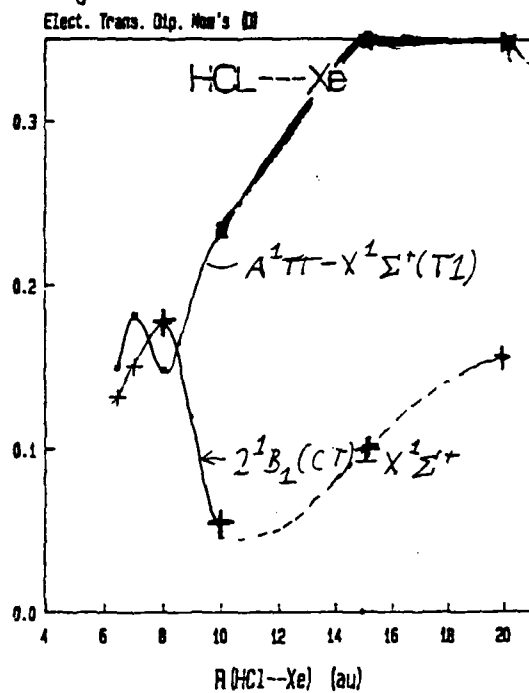


Fig. 5



Experimental Probes of Coupling Between Elementary

Limits in the Higher Excited States of HCl

Kenneth S. Haber, Evdokia Patsilinakou, Yanan Jiang and Edward R. Grant

Department of Chemistry

Purdue University

West Lafayette, IN 47907

The application of ionization-detected ultraviolet multiphoton absorption spectroscopy adds distinct dimensions to the power with which experiment can characterize the electronic structure and intramolecular dynamics of high-lying excited states. We illustrate in part the scope of multiphoton methods by new results on HCl, a system which figures in our initial efforts to prepare charge-transfer molecules from van der Waals precursors.

HCl is a system for which a great deal is known from conventional VUV absorption spectroscopy¹ as well as recent work employing MPI.² We have extended survey spectra of the molecule, jet-cooled in our case, to wavelengths as short as 210 nm. The present report, however, focusses on the longer wavelength region from 242 to 232 nm, and, more particularly, the vibrational levels of three electronic states that fall within that interval, Rydberg $p\pi$ $F^1\Delta$ and $E^1\Sigma^+$ and sub-Rydberg $V^1\Sigma^+$. We characterize these states in terms of the distributions of fragment cations and anions that follow from UV photoionization.

Figure 1 shows the time-of-flight (TOF) mass spectrum following ionization of the two-photon prepared $v=0$ level of the $F^1\Delta$ state. The only ion product observed is HCl^+ . Figure 2 gives a spectrum of this signal, showing the rotational simplicity that accompanies supersonic cooling.

Tuning a short distance to the blue we encounter the $v=13$ band of the $V^1\Sigma^+$ state. The mass spectrum in this case is decidedly different. As shown in Figure 3, HCl^+ is a minor product compared with the fragment ions H^+ and Cl^+ . In the wavelength region of

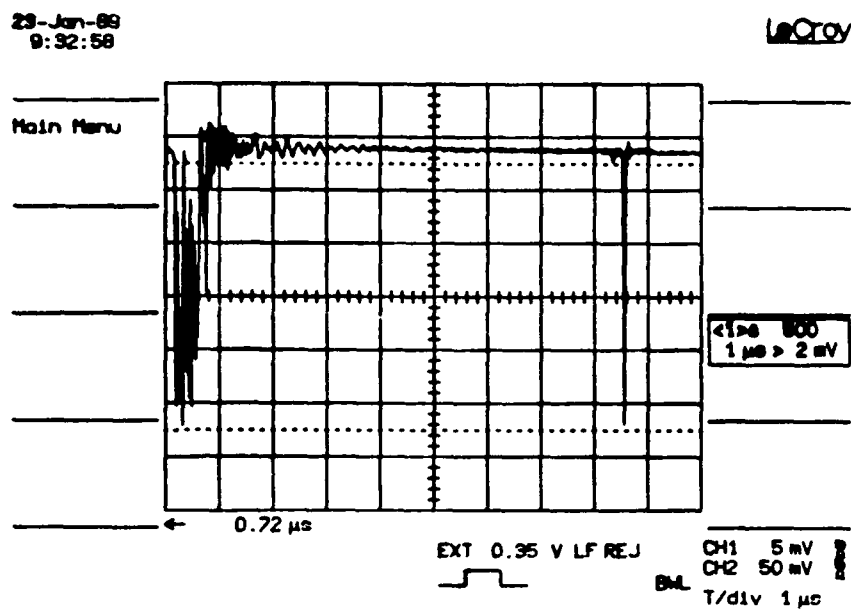


Figure 1. Three-photon ionization TOF mass spectrum of HCl via two-photon resonance with $F^1\Delta$ ($v=0$)

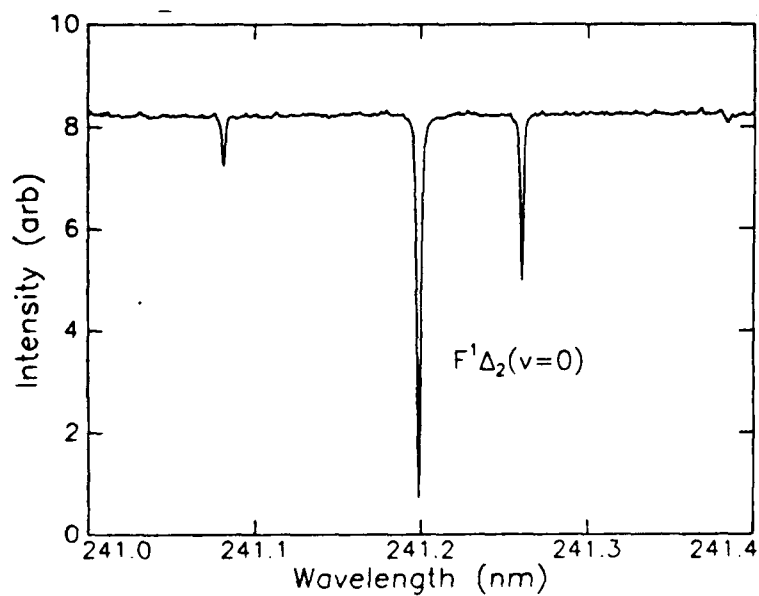


Figure 2. Two-photon spectrum of HCl in the region of the $F^1\Delta$ ($v=0$) state recorded at the $H^{35}Cl$ mass

these scans we have the interesting energetic situation that four photons provide ample energy to exceed appearance thresholds for H^+ and Cl^+ , but the energy of one photon is *insufficient* to fragment an HCl^+ ion formed in its *vibrational ground state* following three-photon ionization.³ Thus, only those ions that retain a significant fraction of the energy of three photons in excess of the ionization threshold are subject to secondary photofragmentation. Apparently, ionization via $V^1\Sigma^+$ leaves excited HCl^+ to undergo such subsequent photofragmentation while ionization via the $F^1\Delta$ state does not.

Figure 4, which compares scans mass resolved on H^{35}Cl^+ and $^{35}\text{Cl}^+$ over the $V^1\Sigma^+ v=13$ state underline this difference in behavior.

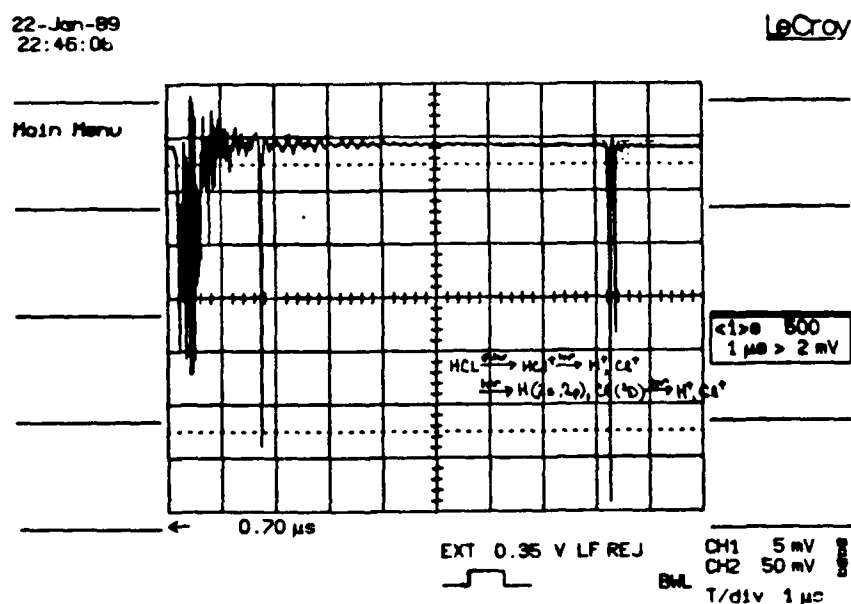


Figure 3. TOF Mass spectrum of HCl ionized via $V^1\Sigma^+ (v=13)$

A similar comparison can be made, over this same wavelength interval, between H^{35}Cl^+ and H^+ . Figure 5 shows the results. Again, ion fragmentation is evident for the V state, where here 35/37 isotope doubling is observed because we collect the H^+ from H^{35}Cl and at a slightly different wavelength, H^{37}Cl . Also interesting in this spectrum is an apparent peak

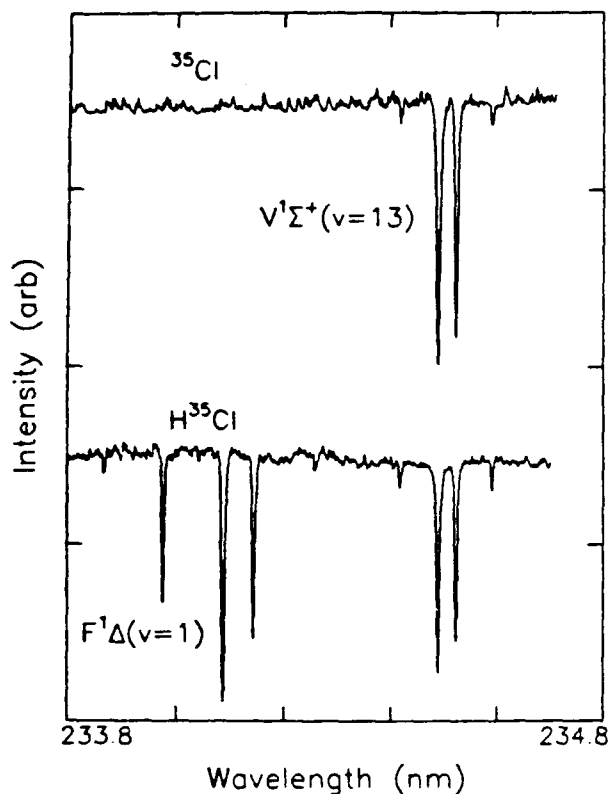


Figure 4. H^{35}Cl^+ versus $^{35}\text{Cl}^+$ scans comparing the behavior of $V' \Sigma^+(v=13)$ with that of $F' \Delta(v=1)$

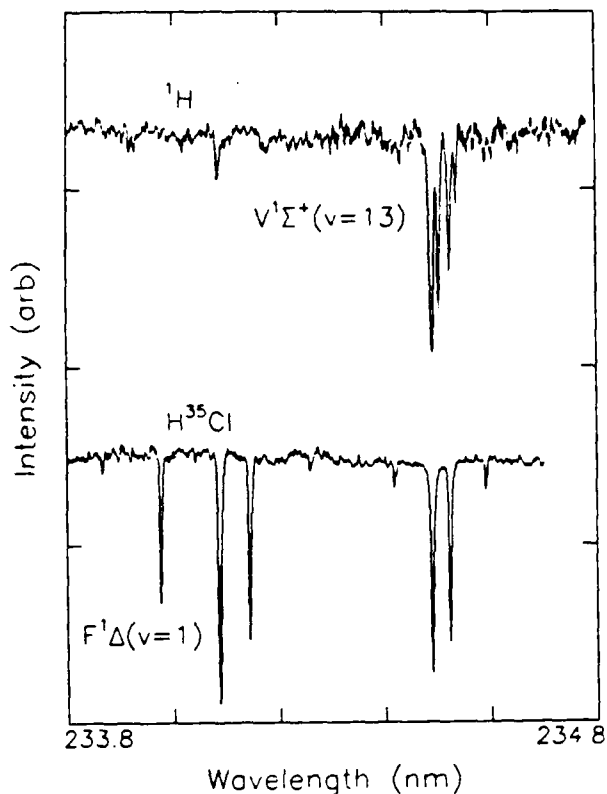


Figure 5. H^{35}Cl^+ versus $^1\text{H}^+$ scans over the region of Figure 4

coincident with the strongest F state resonance. A TOF spectrum presented as Figure 6 confirms that, indeed, H^+ is present, but without the lower energy fragment Cl^+ .

In the absence of Cl^+ , a source that must be considered for this H^+ signal is H^+ , Cl^- ion pairs. Our molecular beam instrument has ion optics and detector which can be configured for anions. Setting it up in this way for the $F' \Delta v=1$ resonance we find the anion mass spectrum shown in Figure 7. Separate experiments reverse the polarity of the ion optics and, using a Cl^+ -producing resonance, show that this flight time corresponds to the Cl^- mass. An intense electron signal produced by ionizing Xe seeded in the present He:HCl beam gives no accompanying Cl^- signal, ruling out $e^- + \text{HCl}$ dissociative attachment.

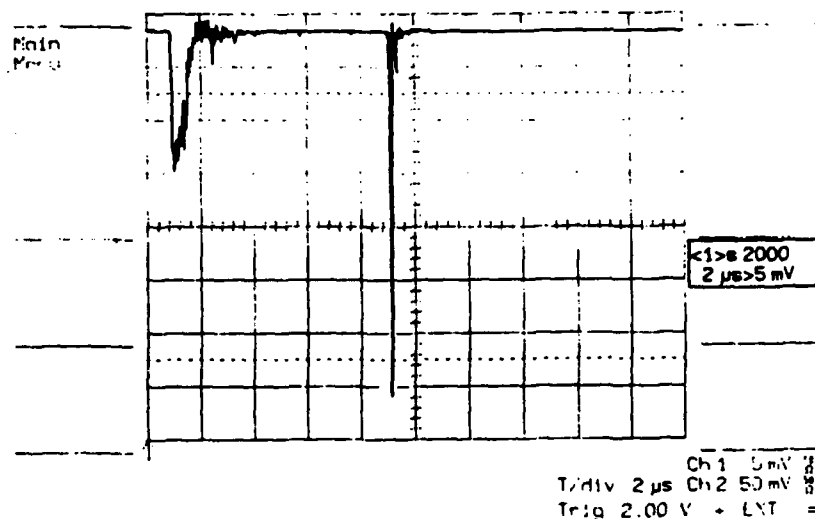


Figure 6. TOF mass spectrum of HCl ionized via $F^1\Delta$ ($v=1$)

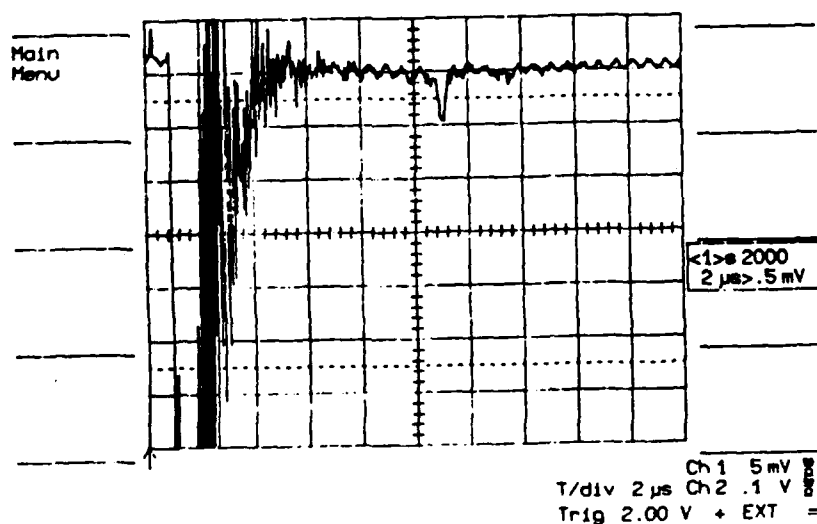


Figure 7. Anion TOF mass spectrum of HCl ionized via $F^1\Delta$ ($v=1$)

With the H^+/Cl^- signal for $F^1\Delta$ ($v=1$) calibrated by observation of both cations and anions we can assign a fractional yield to ion-pair production compared with simple ionization. The results are indicated in Figure 8. From similar anion spectra (for which cation comparisons are obscured by ion fragmentation) we can estimate branching ratios for

V and E $^1\Sigma^+$ states, which are also shown. Most striking, perhaps, is the fact that the extent of charge-transfer character, as measured by ion-pair production, is small for states calculated⁴ to have charge-transfer character (V and E), and is of comparable magnitude for a state regarded to be purely Rydberg.

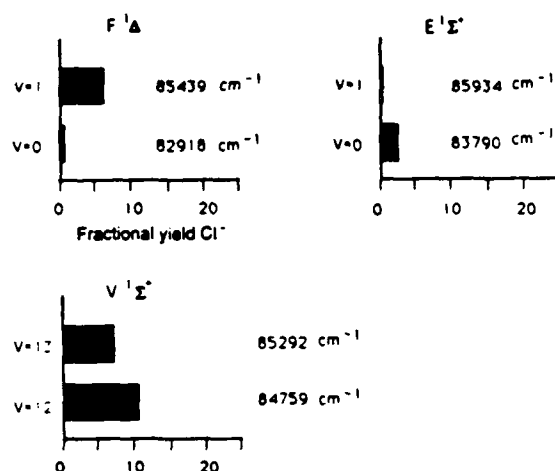


Figure 8. Summary of Cl⁻ yields as a function of selected two-photon resonant intermediate state.

Comparison on the basis of ion fragmentation yields rather stronger contrast. The F state photoejects an electron to produce only HCl. The V state yields mainly fragments H⁺ and Cl⁺. The E state, which is calculated as mixed with the V state is intermediate in its behavior.

It will be useful to extend these categorizations over a broader range of states, acquiring more precise information on product vibrational state distributions by means of photoelectron velocity analysis. It is anticipated that such spectroscopic and dynamical information will exhibit useful correlations with patterns of charge-transfer character in dimers containing HCl.

Research sponsored by the Air Force Office of Scientific Research under Contract F49620-87-C-0092.

References

1. D. S. Ginter and M. L. Ginter, *J. Mol. Spectrosc.* **90**, 177 (1981).
2. R. Callaghan, S. Arepalli and R. J. Gordon, *J. Chem. Phys.* **86**, 5273 (1987); T. A. Spiglanin, D. W. Chandler and D. H. Parker, *Chem. Phys. Lett.* **137**, 414 (1987).
3. S. Daviel, Y. Iida, F. Carnovale and C. E. Brion, *Chem. Phys.* **83**, 319 (1984).
4. M. Bettendorff, S. D. Peyerimhoff, and R. J. Buenker, *Chem. Phys.* **66**, 261 (1982).

GAS PHASE PRODUCTION OF ENERGETIC SPECIES FOR CRYOGENIC TRAPPING

P. G. Carrick

Univ. of Dayton Research Institute

Air Force Astronautics Laboratory

AFAL/LSX

Edwards Air Force Base, CA 93523

INTRODUCTION

An experimental program is underway at the Air Force Astronautics Laboratory to develop high energy materials for propulsion and energy storage. One major focus of this program is in the stabilization of atoms or weakly bound molecules in cryogenic solids and liquids. A number of gas phase production techniques are under consideration, two of which are currently in operation. Gas phase atoms are obtained by excimer laser ablation of the solid metal. Weakly bound energetic molecules are synthesized in essentially collision free conditions in a corona excited supersonic expansion. Other techniques under consideration or construction include effusive oven techniques, hollow cathode sources, and flow discharge reactors.

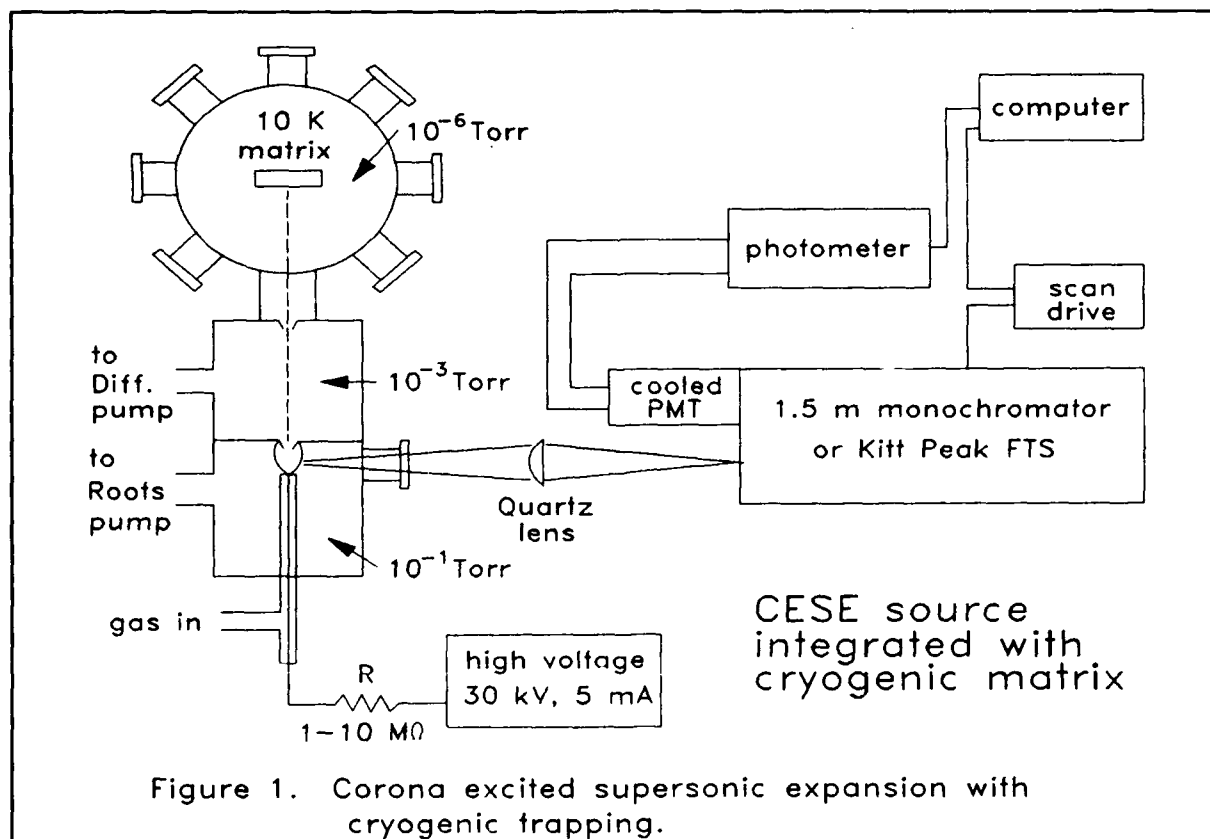
Atomic systems to be studied for potential cryogenic stabilization include lithium, boron, carbon, magnesium, and aluminum. Small clusters of these elements may also be of interest. Lithium was chosen to be studied first, due to the recent calculations by Konowalow (1) that indicate possible stabilization of lithium atoms in solid or liquid hydrogen in the form of LiH_2 or Li_2H_2 .

Energetic molecules and intermediates of energetic molecules that will be studied include high spin state molecules such as CO and N_2 quintet states, small azides such as FN_3 and CH_3N_3 , intermediates such as CH_3N and CF_3N , and weakly bound molecules such as N_2O_2 .

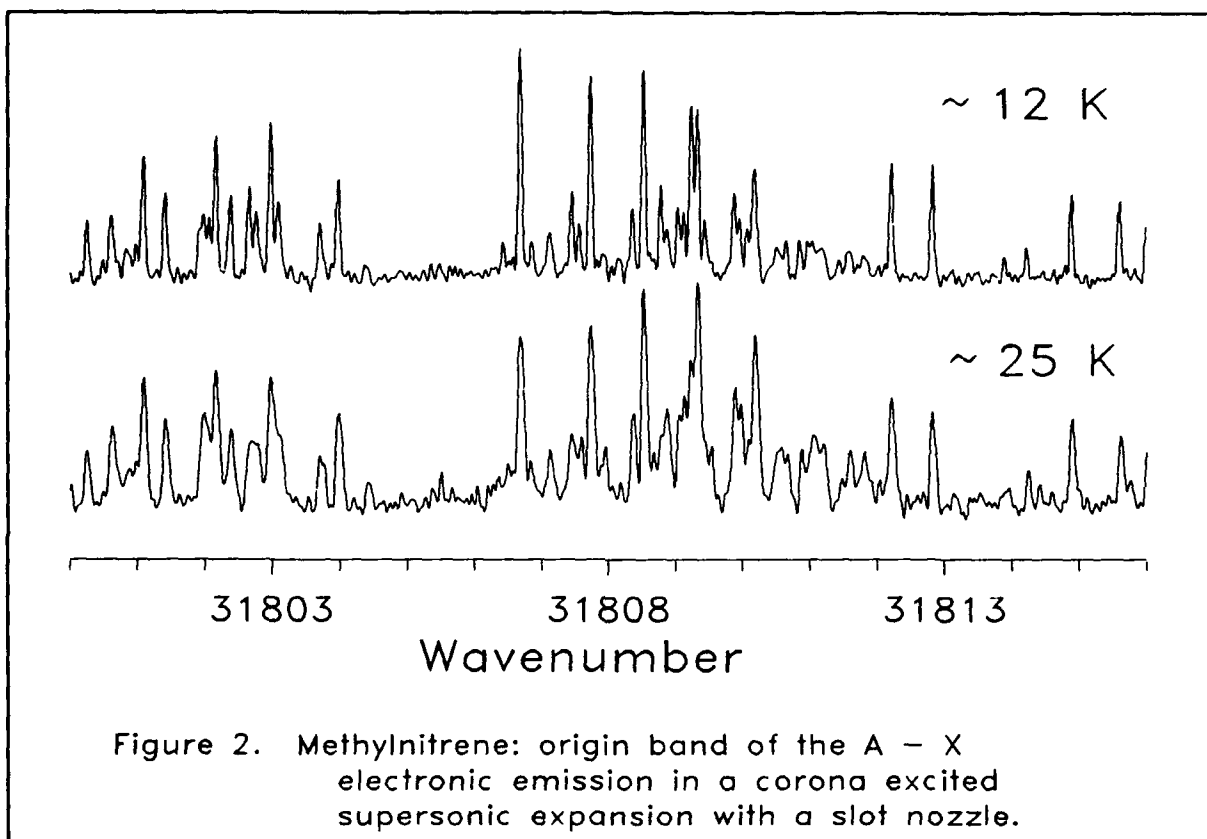
ENERGETIC MOLECULES: JET COOLED METHYLNITRENE

The methylnitrene intermediate (CH_3N) has been made in a corona excited supersonic expansion of a small amount of methylazide (CH_3N_3) mixed in helium or argon (2,3). This technique looks promising for the production of many of the above listed energetic molecules and intermediates. The advantages of this technique are twofold: the rotational cooling of the supersonic expansion provides simplification of complicated spectra, which assists in the assignment of new molecules, and the expanding discharge provides both a mechanism for production of transient or weakly bound molecules and a relatively collision free environment, which reduces reactions that result in the destruction of the target molecules.

The design and operating characteristics of the corona excited supersonic expansion (CESE) have been described previously (4,5). Figure 1 contains a diagram of how this source will be combined with a closed cycle cryogenic refrigerator in order to collect and stabilize molecules produced in the CESE at low temperatures.



This source has also recently been used to obtain rotationally resolved electronic emission from the $A^3E - X^3A_2$ transition of the methylnitrene radical in the ultraviolet by imaging the emission from the jet into the McMath fourier transform spectrometer (FTS) at Kitt Peak National Observatory. Initial experiments utilized a 0.10 mm diameter pinhole nozzle for the expansion, resulting in a somewhat complicated spectrum with resolution of about 0.2 cm^{-1} . This spectrum was partially analyzed to obtain one of the two rotational constants for this symmetric top molecule.

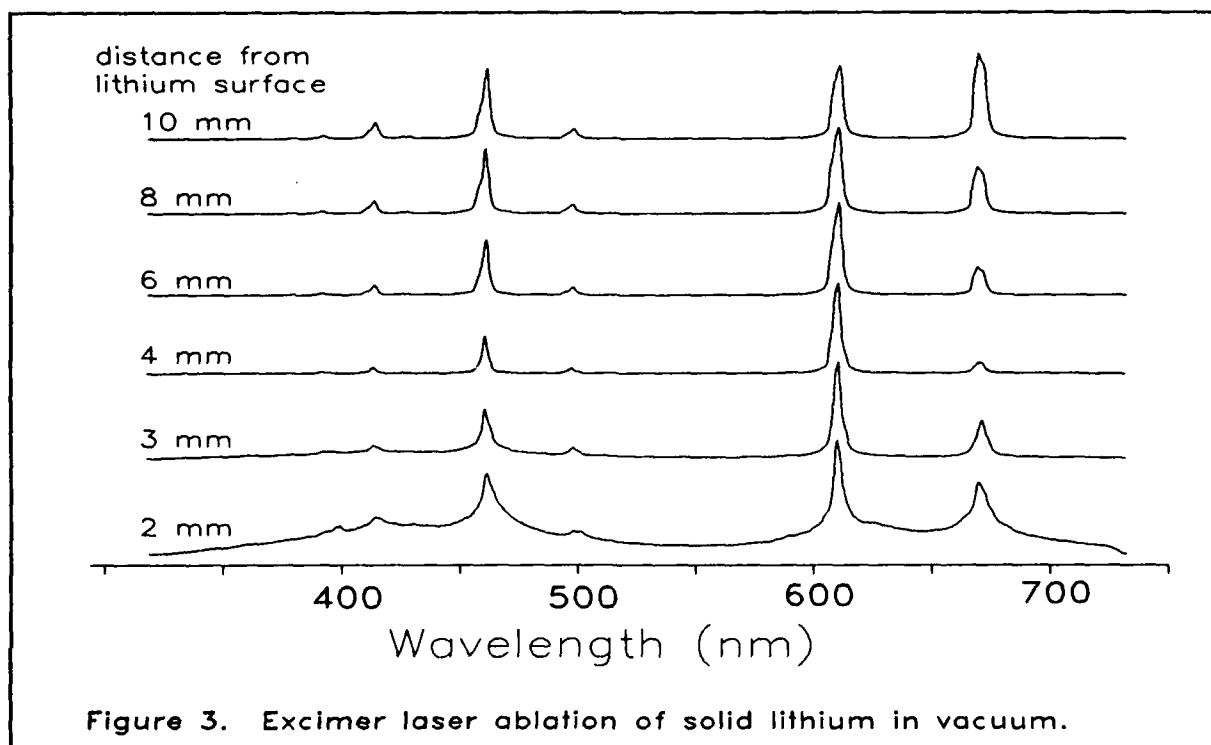


Recently the CESE source was outfitted with a slot nozzle of approximate dimensions 0.050 by 3.0 mm. The use of this nozzle resulted in both an increase in signal to noise ratio and improved resolution when substituted for the pinhole nozzle in the above experiment. Greater control of the expansion conditions was also obtained, resulting in scans of different rotational temperatures. An example of two FTS scans showing different rotational temperatures of methylnitrene made in the slit nozzle is shown in figure 2. The improvement in signal/noise and resolution combined with line intensity data from the different temperature scans provided sufficient information for a more complete assignment of the

methylnitrene spectra. A symmetric top $A^3E - X^3A_2$ Hamiltonian was developed (6) to fit this data and obtain the molecular rotational constants. The analysis of the deuterated methylnitrene is presently underway.

LASER ABLATION OF METALS: LITHIUM

Gas phase atomic lithium can be produced from solid lithium by excimer laser ablation. For laser power densities on the order of 10^8 W/cm^2 , a fraction of the ablated lithium atoms are excited to various electronic states. The emission from these excited states has been observed by an Optical Multichannel Analyzer (OMA). The OMA can also be used to observe different segments of the visible plume as it expands away from the surface of the solid lithium sample, as shown in Figure 3. The progression of scans from just above the level of the surface to 10 mm above the surface indicates that the lithium is relaxing down to lower energy states, but a certain amount of electronic energy remains out to at least 1 cm. Although some amount of electronic energy may remain out at a distance of 2 cm (approximately where the cryogenic surface is placed in our apparatus), most of the energy deposited into the matrix is probably due to the kinetic energy of the lithium atoms in the plume.



REFERENCES

1. Private communication.
2. P. G. Carrick and P. C. Engelking, **J. Chem. Phys.**, 81, 1661 (1984).
3. P. G. Carrick, C. R. Brazier, P. F. Bernath, and P. C. Engelking, **J. Am. Chem. Soc.**, 109, 5100 (1987).
4. A. T. Droege and P. C. Engelking, **Chem. Phys. Lett.**, 96, 316 (1983).
5. P. C. Engelking, **Rev. Sci. Instrum.**, 57, 2274 (1986).
6. C. R. Brazier, P. F. Bernath, and P. G. Carrick, in preparation.

Dynamics of Atomic Hydrogen Trapped in Crystal Lattices

Bruce C. Garrett
Chemical Dynamics Corporation
Upper Marlboro, MD 20772

Condensed phases offer a practical means of storing hydrogen atoms as an energy source. The stability of atomic radicals trapped in condensed phases is determined by their mobility. More rapidly diffusing atoms have a higher probability of recombining with other atoms and, therefore, have a lower stability. For atoms with light masses, such as hydrogen, quantum mechanical effects such as zero-point energies and tunneling can be important. Variational transition state theory (VTST)¹ is a well established method for calculating rates for gas-phase reactions and it incorporates quantum mechanical effects in a reliable yet practical manner. Recently, it has been extended to treat adatom diffusion and chemisorption of H₂ on surfaces,² and more recent applications have been made to diffusion in bulk metals.³ We review the methods for including quantum mechanical effects in VTST, and as an example of the method, present results of its recent application³ to diffusion of H in Ni lattices and on Ni(100) surfaces.

Computational method

For diffusion on a surface or in bulk, in which all binding sites are equivalent, the diffusion coefficient can be related to the hopping rate between adjacent sites provided the following assumptions are true: (1) the concentration of H is sufficiently low so that the hydrogen atoms do not interact with one another; and (2) diffusion occurs through a series of uncorrelated hops from one binding site to another adjacent one. In this random walk model, the diffusion coefficient $D(T)$ is related to the hopping rate constant $k(T)$ by:^{4,5}

$$D(T) = \frac{a^2}{2\gamma} k(T) \quad (1)$$

where a is the hop length and γ is the dimensionality of the system ($\gamma=2$ for surface diffusion, $\gamma=3$ for bulk diffusion).

The rate constant $k(T)$ is calculated by VTST with semiclassical adiabatic ground state transmission coefficients. The computational procedures used here are similar to those used for gas-phase reactions,¹ and details of the modifications needed to treat diffusion on surfaces are outlined in Refs. 2, 3, and 6. In review, the procedure consists of first locating the reactant, product and saddle point geometries (locations at which the gradient vanishes). The reaction path

is generally taken to be the minimum energy path (MEP) which is determined by following the negative of the gradient vector in mass weighted coordinates from the saddle point down into the reactant and product geometries. The generalized transition state theory rate is expressed in terms of the location of the transition state along the reaction coordinate and the canonical variational theory (CVT) rate expression is the one that minimizes the generalized expression with respect to s . The rate expression is given by:

$$k^{\text{CVT}}(T) = \sigma \frac{k_B T}{h} \frac{\tilde{Q}^{\text{CVT}}(T)}{\tilde{Q}^{\text{R}}(T)} \exp\left[-\Delta V_a^{\text{G}}(s_*^{\text{CVT}})/k_B T\right] \quad (2)$$

where σ is a symmetry factor, k_B is Boltzmann's constant, T is the temperature of the system, h is Planck's constant, $\tilde{Q}^{\text{R}}(T)$ is the partition function of the reactant species, $\tilde{Q}^{\text{CVT}}(T)$ is the partition function for the bound degree of freedom at the CVT transition state location s_*^{CVT} , and $\Delta V_a^{\text{G}}(s_*^{\text{CVT}})$ is the change in the ground-state adiabatic potential (described below) between the reactants and s_*^{CVT} . The partition functions are evaluated quantum mechanically and have their zeros of energy at the zero-point energy level.

Eq. (2) for the rate treats all bound vibrational motions quantum mechanical, but the reaction coordinate motion is treated classically. A consistent method for including quantal effects on the reaction coordinate motions is by the vibrationally adiabatic theory of chemical reactions. Within the adiabatic approximation, the effective barrier along the reaction path is given by

$$V_a^{\text{G}}(s) = V_{\text{MEP}}(s) + \epsilon^{\text{GT}}(s, \alpha = 0) \quad (3)$$

where $V_{\text{MEP}}(s)$ is the potential along the minimum energy path and $\epsilon^{\text{GT}}(s, \alpha=0)$ is the ground-state energy level for the bound vibrational modes at the generalized transition state located at s . The probability of tunneling through this effective potential is obtained from the small-curvature semiclassical adiabatic ground-state (SCSAG) method.⁷ For the unimolecular process considered here the reactant and product species correspond to local wells in the adiabatic potential separated by the adiabatic barrier. In this case, tunneling occurs from discrete energy levels in the bound wells of the adiabatic potential and the transmission coefficient is given by^{2,3}

$$\kappa^{\text{QSCSAG}}(T) = \sum_v \kappa_v^{\text{QSCSAG}}(T) + \kappa_c^{\text{QSCSAG}}(T) \quad (4)$$

where the contribution from each bound vibrational state v in the adiabatic potential is given by

$$\kappa_v^{\text{QSCSAG}}(T) = \frac{\exp(V_a^G(s_*^{\text{CVT}}) / k_B T)}{k_B T} \frac{dE_v}{dv} P^{\text{SCSAG}}(E_v) \exp(-E_v / k_B T) \quad (5)$$

and E_v is the energy of vibrational state v and $\kappa_c^{\text{QSCSAG}}(T)$ is the contribution from continuum energies.

The quantized rate $k^{\text{CVT/QSCSAG}}(T)$ is obtained by combined eq. (2) with eq. (4) which reduces in the low temperature limit to

$$\lim_{T \rightarrow 0} k^{\text{CVT/QSCSAG}}(T) = \frac{\sigma}{h} \frac{dE_0}{dv} P^{\text{SCSAG}}(E_0) \quad (6)$$

Consistent with Wigner threshold laws, for this thermoneutral process the hopping rate goes to a finite value which is independent of temperature as the temperature approaches absolute zero.

Application to H diffusion in and on Ni

The calculations reported here employ a potential energy surface based upon the embedded-atom method (EAM) which provides a physically motivated function describing the potential-energy of a solid in terms of the "embedding energy" of each atom in the crystal.⁸ This energy is a function of local electron density that the atom senses due to nearby atoms. The EAM potential used here was empirically adjusted to static bulk properties and refined to reproduce the observed activation barrier of H diffusion on Ni(100).

The equilibrium binding sites of H atoms in bulk Ni are the octahedral sites. Diffusion proceeds from one octahedral site to another through an adjoining tetrahedral site which is bound by less than 0.05 eV. The classical barrier to diffusion is 0.4 eV and the H-atom diffusion requires significant relaxation of the Ni atoms away from the H atom. Although the experimental data for diffusion in bulk varies, Vokl and Alefeld⁹ report a best fit of all the data, with an activation energy of 0.41 eV and pre-exponential factor of 0.0048 cm²/s. The calculated results are in good agreement; the activation energy is 0.44 eV and the calculated pre-exponential factor is 0.007 cm²/s. In addition, H/D kinetic isotope effects (KIEs) also agree well with experiment; calculated H/D KIEs range from 1.2 to 1.3 in the temperature range from 573 to 1273 compared to experimental values from 1.1 to 1.4.⁹ Because of the long diffusion path between the equilibrium octahedral sites, tunneling is found to be negligible for temperatures above about 100 K.

A more detailed analysis of tunneling has been performed for H diffusion on the Ni(100) surface. In this case diffusion occurs between four-fold sites and the tunneling path is shorter than for bulk diffusion. Although the barrier for surface diffusion of 0.17 eV is smaller than for bulk diffusion, tunneling contributes more to surface diffusion. Figure 1 compares our CVT/SCSAG

diffusion coefficients with experimental ones of George, DeSantolo, and Hall (GDH),¹⁰ Mullins, Roop, Costello, and White (MRCW),¹¹ and Mullins, Roop, and White (MRW).¹² In these calculations only the eight Ni atoms below the two four-fold sites are allowed to move. The agreement with experiment is excellent including reproducing an unusually low H/D KIE.

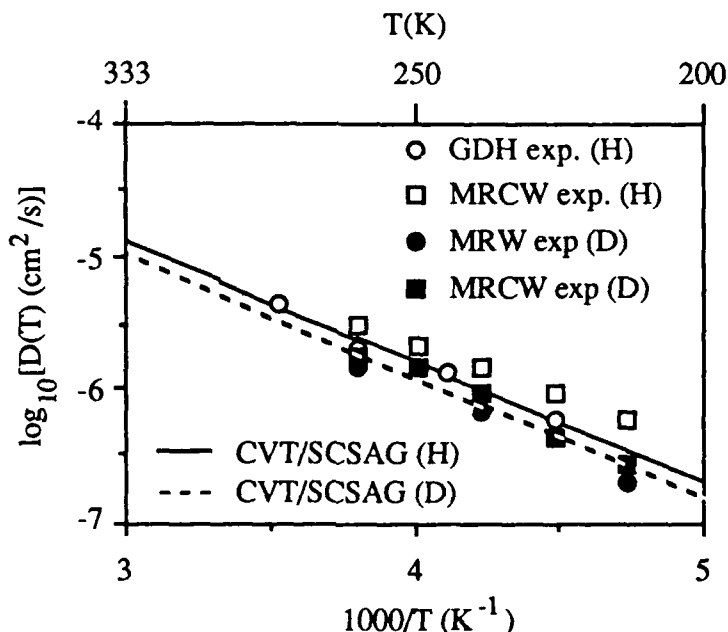


Figure 1. Comparison of computed and experimental diffusion coefficients for H and D on Ni(100).

Over the temperature range shown in figure 1, tunneling contributes less than 50% to the diffusion rate. Although experimental results are not available for lower temperatures, it is interesting to examine the low temperature behavior of the diffusion coefficients where tunneling dominates. Results computed using the CVT/QSCSAG method outlined above are shown in figure 2. As expected, the diffusion coefficient obtains a low temperature limit which is about 1.5×10^{-13} cm²/s in this case. (We note that the calculated results at these low temperatures have not been converged with respect to the number of moving Ni atoms and most likely underestimate the true diffusion coefficient.) The surprising result is that the low temperature limit is obtained at relatively high temperature, near 80 K. This limiting temperature is determined strongly by the spacing between the energy levels and more weakly by the probabilities for tunneling from each bound vibrational level. Although the tunneling probabilities may not be quantitative, the spacings between energy levels are much more accurately calculated, and the qualitative trend observed in figure 2 is correct. This indicates that cryogenic temperatures may not be necessary to obtain the maximum localization of H atoms in crystal lattices.

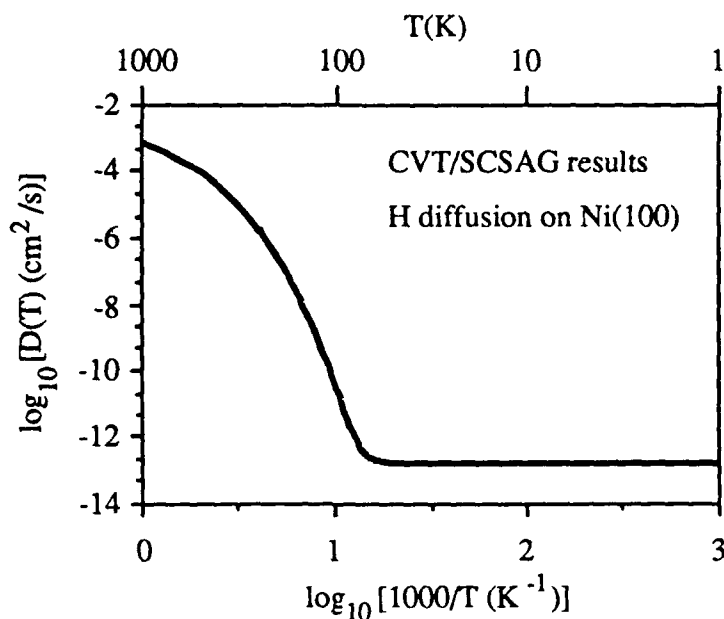


Figure 2. Low temperature behavior of the diffusion coefficient for H on Ni(100).

References

1. D. G. Truhlar, A. D. Isaacson, and B. C. Garrett in *The Theory of Chemical Reaction Rates*, M. Baer, ed. (CRC Press, Boca Raton, FL, 1985), Vol IV, p. 65; D. G. Truhlar and B. C. Garrett, *Ann. Rev. Phys. Chem.* **35**, 159 (1984).
2. J. G. Lauderdale and D. G. Truhlar, *J. Amer. Chem. Soc.* **107**, 4590 (1985); *Surf. Sci.* **164**, 558 (1985); *J. Chem. Phys.* **84**, 1843 (1986); T. N. Truong and D. G. Truhlar, *J. Phys. Chem.* **91**, 6229 (1987); *J. Chem. Phys.* **88**, 6611 (1988); T. N. Truong, G. Hancock, and D. G. Truhlar, *Surf. Sci.*, in press.
3. B. M. Rice, B. C. Garrett, M. L. Koszykowski, S. M. Foiles, and M. S. Daw, in preparation.
4. A. F. Voter and J. D. Doll, *J. Chem. Phys.* **80**, 5832 (1984); **82**, 80 (1985).
5. S. M. Valone, A. F. Voter, and J. D. Doll, *Surf. Sci.* **155**, 687 (1985).
6. A. D. Isaacson, D. G. Truhlar, S. N. Rai, G. C. Hancock, J. G. Lauderdale, T. N. Truong, T. Joseph, B. C. Garrett, and R. Steckler, University of Minnesota Supercomputer Institute Research Report 88/87, September 1988.
7. R. T. Skodje, D. G. Truhlar, and B. C. Garrett, *J. Phys. Chem.* **85**, 3019 (1981); *J. Chem. Phys.* **77**, 5955 (1982).
8. (a) M. S. Daw and M. I. Baskes, *Phys. Rev. Lett* **50**, 1285 (1983); (b) M. S. Daw and M. I. Baskes, *Phys. Rev. B* **29**, 6443 (1984); (c) M. S. Daw, in preparation.
9. J. Volkl and G. Alefeld, *Diffusion in Solids*, ed. A. J. Nowick and J. J. Burton (Academic Press, New York, 1975) and references therein.
10. S. M. George, A. M. DeSantolo, and R. B. Hall, *Surf. Sci.* **159**, L425 (1985).
11. D. R. Mullins, B. Roop, S. A. Costello, and J. M. White, *Surf. Science* **186**, 67 (1987).
12. D. R. Mullins, B. Roop, and J. M. White, *Chem. Phys. Lett.* **129**, 511 (1986).

Acknowledgement. Much of the work reported here was performed by Dr. Betsy M. Rice while she was a postdoctoral associate at Chemical Dynamics. This work also benefitted from collaborations with other staff members at Chemical Dynamics - Drs. P. K. Swaminathan, C. S. Murthy, and M. J. Redmon - and at Sandia National Laboratories, Livermore, CA - Drs. M. L. Koszykowski, S. M. Foiles, and M. S. Daw.

ENERGY STORAGE IN SOLID MOLECULAR HYDROGEN DUE TO TRAPPED ATOMS

James R. Gaines
Department of Physics
University of Hawaii at Manoa
Honolulu, Hawaii 96822

The problem to be treated here is the storage of energy, in the form of free atoms, in a molecular solid host, namely solid molecular H_2 . The relevant properties of the host, methods of producing the atoms, and interesting aspects of their recombination into molecules will be discussed.

I. Introduction to the Properties of Solid Hydrogen Hosts

a. Melting temperature, structure, and density

Hydrogen and its isotopes form a class of molecular solids where the binding forces are very weak resulting in the molecules retaining their individual identities as well as many of their gas phase properties. The binding forces are so weak that the triple point of H_2 is 14 K while the triple point of T_2 is 19 K. The other hydrogen solids, HD, D_2 , DT, and HT have triple point temperatures in between 14 K and 19 K. The density of the hydrogen solids at zero applied pressure ranges from .09 g/cm³ (H_2) to .32 g/cm³ (T_2). The main point regarding the density is that these are the lightest solids and as such are excellent candidates for exotic aviation fuels. Except for one special case, the solid hydrogens crystallize into an HCP lattice. The nearest neighbor distance is between 3.75 Å (H_2) and 3.53 Å (T_2). The one exception involves an ordering of the rotational moments of the molecules where the lattice structure changes from HCP to FCC.

b. Rotation of the molecules

In the solid, the molecules can still rotate almost freely thus the nomenclature "ortho" and "para", used to describe the different molecular symmetries of the homonuclear molecules in the gas phase still apply in the solids. For instance, at room temperature, H_2 consists of 75% ortho and 25% para molecules. When solidified quickly, these fractions still remain and the ortho H_2 slowly decays to the para H_2 ground state.

c. Thermal Properties

Both the thermal conductivity and the heat capacity are influenced by the ratio of rotating to non-rotating molecules in the solid, but we will neglect the complication introduced by the ortho-para question. The heat capacity is that of an insulating solid and is well described by the Debye expression, $C_v = 234 R (T/\theta_d)^3$, where θ_d is the Debye temperature. For all the solid hydrogens, θ_d is approximately 100 K. The thermal conductivity has been measured for nearly all the solid hydrogens. It is very large in the temperature range 1 K to 10 K, peaking in the vicinity of 3 K. The "thermal diffusivity" of solid hydrogen is such that a typical thermal relaxation time at liquid helium temperatures is of order of a few seconds.

Thus the molecular solid hydrogen hosts are well characterized and have well behaved thermal and physical properties. From a scientific standpoint, the system of solid hydrogens (from H_2 through T_2) has the largest relative mass difference of any system of isotopes and provides a rich background for studying free atoms. From the practical standpoint, these are the lightest solids.

II. Production of Atoms in Solid Hydrogen

a. Electron beams

The first study of note, done on hydrogen solid containing H atoms was done by Leach⁽¹⁾ and Fitzsimmons at the University of Wisconsin. They bombarded a solid H₂ sample with 160 KeV electrons from a pulsed source. Using standard EPR techniques, they measured the time decay of the signal from H atoms and deduced the recombination coefficient as a function of temperature.

b. RF discharge

A standard method of producing atoms has been to dissociate molecules, in the gas, with an RF discharge and then condense the atoms along with molecules on a cold surface for later study⁽²⁾. While relatively high atom populations ($> 10^{18} \text{ cm}^{-3}$) have been reported from EPR measurements, these are also transient populations and can decay rapidly. From the measurements of Leach, decay times of minutes would be expected near 4 K.

c. Radioactive decay (beta decay)

The first use of this technique to my knowledge was made by Sharnoff and Pound⁽³⁾. They incorporated about 1% T₂ in D₂ to produce a constant supply of atoms. Once again, EPR techniques were used to detect the atoms. This is the technique that has been used to produce atoms in all the systems that will be described here.

III. Recombination of Atoms in Solid Hydrogen

a. The gain-loss equation for the atom density

The solid molecular hydrogen acts as a host for the atoms and tends to prevent their recombination, once formed. If the atom density obeys a simple "gain-loss" equation, we expect

$$(1) \quad \frac{dm}{dt} = K - \alpha m^2$$

where K is the constant production term that arises from tritium beta decay or a pulsed electron source while α is the recombination coefficient for atoms⁽⁴⁾. In the steady-state, the equilibrium atom density is given by $m_{eq}^2 = K/\alpha$. Simple theories of recombination express the coefficient α in terms of the diffusion coefficient (D). Since D decreases with decreasing temperature, α also decreases and m_{eq} increases.

b. Particular solutions to the gain-loss equation

Two solutions of Eqn. 1 for the atom concentration as a function of time are of interest here: (i) if the source term is removed, the atom concentration m decays in time according to

$$(2) \quad \frac{1}{m} - \frac{1}{m_0} = \alpha t$$

This permits a determination of the recombination coefficient α .

(ii) When the atom concentration starts from zero and builds to the equilibrium value m_0 , the time dependence is

$$(3) \quad m = m_0 \tanh(\alpha m_0 t)$$

The time constant of the build-up, $\tau = (\alpha m_0)^{-1}$, from our work on T₂, has the value $\tau = (0.15 \text{ s})/m_0$ where m_0 is expressed in PPM. Thus for 100 PPM, the atom population builds up in 15 s. The equations given here for the atom time dependence are inadequate in solids containing T₂. A more local theory, that starts with the beta decay event and calculates the spatial average of the atom concentration is "in progress" but not completed.

c. Estimates of the stored energy at the equilibrium density

The internal energy contribution from the atoms can be expressed as

$$(4) \quad U_{\text{atoms}} = \frac{1}{2} q N_s m = E m$$

where q is the energy of a single recombination (4.5 eV) and m is the concentration of atoms. N_s is the number of molecules in the sample. The quantity E defined above has the numerical value, $E = 1.14 \times 10^4 \text{ J/cm}^3$, and represents the energy that would be stored in the atom system if there was one atom per lattice site. We have detected atom concentrations that approach 1000 PPM(5), leading to a stored energy of 11.4 J/cm^3 or 127 J/g at 4 K.

IV. Experimental Detection of Atoms

a. The hyperfine interaction produces a distinct EPR spectrum

Most of the observations have involved electron paramagnetic resonance because the EPR signature of atoms is so distinctive as each hydrogen isotope has its own identifiable hyperfine splitting making it possible to separate the contributions from the different types of atoms.

b. The spin density is obtained by comparison with ruby signal

Central to the determination of the atom densities from their ESR signals is the method of calibration used to extract a "spin count". For this purpose we have used the ESR signal from a doped ruby crystal. At room temperature, by observing the ruby signal and that of a standard DPPH sample of known spin density, we can calibrate the ruby signal in terms of the DPPH standard. Leaving the ruby crystal in its same location inside our EPR cavity, we can use its resonance to transfer the DPPH spin count to the atom signals. From this calibration technique, we can plot the atom density, m , as a function of time at a given temperature and eventually, as a function of temperature.

c. Experimental values of the atom density

In Fig. 1, we show the atom density in "parts per million" (PPM) as a function of time at a few temperatures. Since the density of molecules in H_2 is $2.7 \times 10^{22} \text{ cm}^{-3}$, a concentration of 1 PPM corresponds to an atom density of $2.7 \times 10^{16} \text{ cm}^{-3}$.

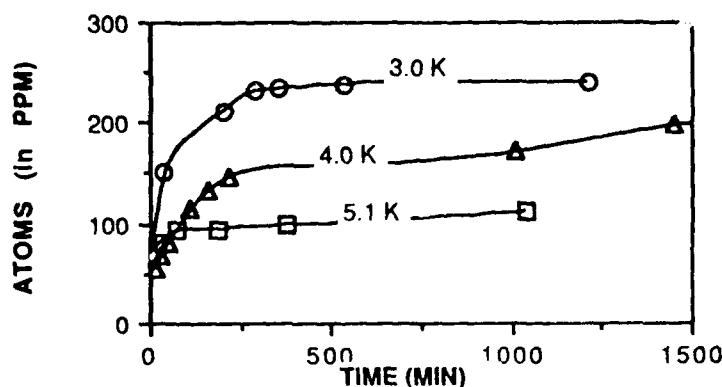


Figure 1

d. Thermal spikes are observed under certain conditions

Two traces are shown in Fig. 2: (a) On the top trace, the temperature of a DT sample is suddenly increased from 3.6 to 5.1 K by changing the "set-point" of a temperature controller. The

indicated temperature "overshoots" to past 8 K, dips to below 5.1 K, and then approaches the temperature "set-point" on the controller of 5.1 K. In trace (b), the same set of conditions are duplicated for an HD sample (that contains no free atoms). Here the temperature rises smoothly from 3.9 K to the set-point temperature of 5.1 K without a heat spike occurring illustrating that without atoms in the sample, there are no heat spikes.

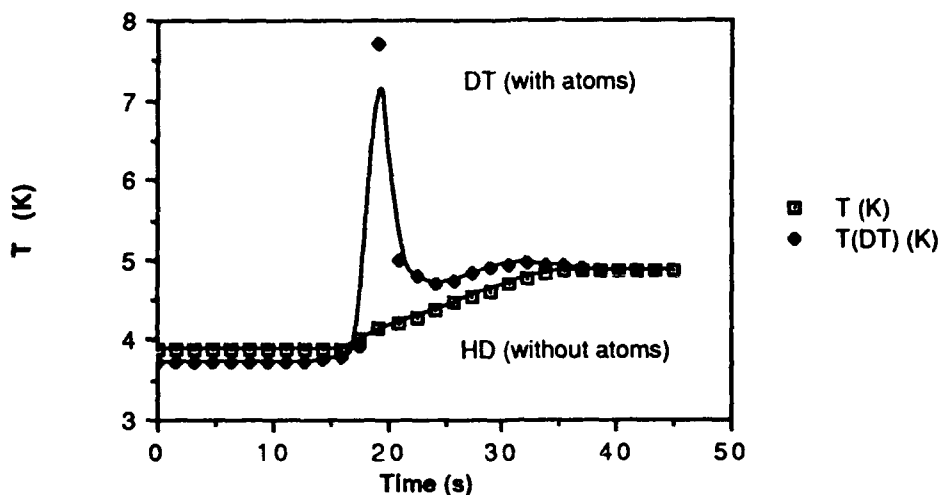


Figure 2

The heat spikes as seen by the germanium resistance thermometer that measures the sample temperature correlate with a decrease in the spin count as measured in the EPR experiments. The EPR experiments are of extreme value in observing the free atoms as each of the hydrogen isotope atoms has a different hyperfine splitting permitting the measurement of the atom concentration for each type of atom. In Figure 3, where DT contains a high atom density, the EPR spin count for T atoms decreases by about 300 PPM after a spike.

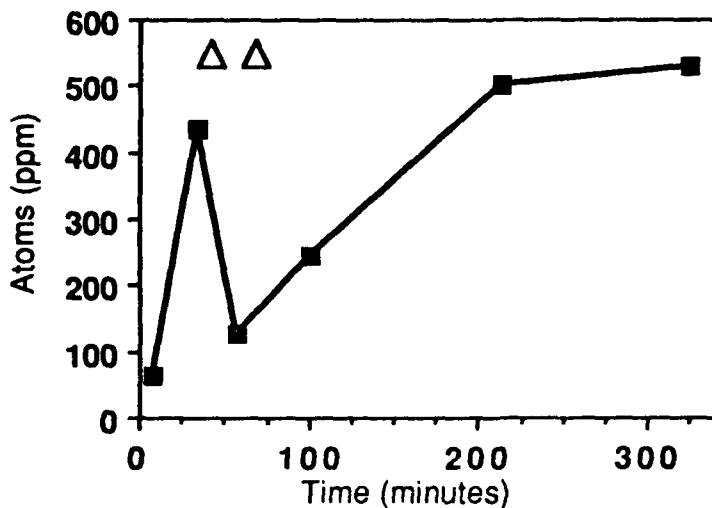


Figure 3

When the sample is T₂, the spin count decrease after a spike can reach 500 PPM. The specific

heat of the hydrogen hosts is not very large below 4 K as all the solid hydrogens have a Debye temperature near 100 K so the heat released by this sudden atom recombination can produce a very large temperature change.

V. Summary and Planned Experimental Extensions

a. The atom density is temperature dependent

The atom density is still increasing with decreasing temperature indicating that we have not saturated the energy storage capacity of the molecular hydrogen hosts. We plan to continue the study to below 1 K in order to find where the density saturates.

b. At high atom densities, the system becomes unstable

Even though heat spikes occur when the atom density is sufficiently large, we have been able to completely suppress the heat spikes by covering the samples with liquid ^4He . We will use ^3He and ^4He to increase the effective heat capacity of the hydrogen host containing atoms.

c. In high magnetic fields, the recombination may be inhibited

We have found two ways to extract the diffusion coefficient for atoms from the data. One way depends on measurements of the atom recombination coefficient while the other depends on an analysis of the EPR linewidths and spin-lattice relaxation times. From this latter approach, we obtain a diffusion coefficient that is appropriate to atom motion that is orders of magnitude larger than that we deduce from recombination. We conclude that recombination is greatly inhibited and that application of even higher magnetic fields may inhibit it even more making possible higher atom densities.

VI. Acknowledgements

The work described here has been done in collaboration with several other scientists, most notably, Clark Souers (LLNL), Gilbert Collins (OSU/LLNL), Evan Mapoles (LLNL), Peter Fedders (Washington University), and my colleagues at the University of Hawaii, Dr. Chester Vause and Dr. Yue Cao. All of the recent experimental results presented here were obtained at LLNL in Clark Souers Laboratory by Gilbert Collins. The project at the University of Hawaii is supported by AFOSR through contract No. F04611-88K-0048.

References

1. R.K. Leach, thesis, University of Wisconsin, 1972 (unpublished), University Microfilms No. 72-23060.
2. A.S. Iskovskikh, A. Ya. Katunin, I.I. Lukashevich, V.V. Sklyarevskii, V.V. Suraev, V.V. Filippov, N.I. Filippov, and V.A. Shevtsov, Sov. Phys. JETP 64 (5), 1085 (1986).
3. M. Sharnoff and R.V. Pound, Phys. Rev. 132, 1003 (1963).
4. James R. Gaines, James D. Sater, Evelyn M. Fearon, P.C. Souers, Fred E. McMurphy, and Evan R. Mapoles, Phys. Rev. Lett. 59, 563 (1987)
5. J.D. Sater, James R. Gaines, Evelyn M. Fearon, P.C. Souers, Fred E. McMurphy, and Evan R. Mapoles, Phys. Rev. B37, 1482 (1988).

High Energy Density Materials Contractors Conference
March 12-15, 1989
New Orleans, LA

PHOTOINITIATED CHAIN REACTIONS IN LOW TEMPERATURE SOLIDS

Charles A. Wight
Department of Chemistry
University of Utah
Salt Lake City, Utah 84112

Abstract

A fundamental understanding of chain reaction processes in low temperature solids is desirable from the standpoint of storing and igniting revolutionary new HEDM propellants. In our laboratory, we have investigated chain reactions in model chemical systems in order to better understand chain reaction initiation, propagation, and termination processes at the molecular level. The experiments are conducted by depositing small quantities of gaseous reagents as a thin amorphous film onto an optical window at 10-77 K. Reactions are initiated by pulsed UV laser photolysis, and photochemical quantum yields for the various products are determined by IR, UV, and/or Raman spectroscopy of the samples before and after laser photolysis. Principal results and conclusions are described for photochlorination of simple alkanes, photopolymerization of solid formaldehyde, and photochemical destruction of solid ozone and mixtures of ozone with ice.

Photochlorination of Alkanes

We have investigated photochemical reactions of simple alkanes codeposited with molecular chlorine as a thin film on the surface of a CsI optical window. In each case, a XeCl excimer laser is used to dissociate a small fraction of the chlorine molecules to Cl atoms, inducing the reaction forming HCl and the corresponding alkyl chloride. For most alkanes (including propane, n-butane, isobutane, n-pentane, cyclopentane, n-hexane, cyclohexane, and n-heptane) there is no conclusive evidence for chain reactions in solid-state mixtures with chlorine at a variety of concentrations. Only cyclopropane and cyclobutane show evidence of chain reactions (i.e., photochemical quantum yields significantly in excess of unity). For these two alkanes, we have identified special chemical mechanisms by which photochemically generated radicals can be separated in the solid state. In the case of cyclopropane, ring opening (with inversion of configuration) accomplishes this, as shown schematically in Figure 1. Radical separation is crucial for chain reaction propagation. In the absence of such a mechanism, radical recombination leads to premature termination of the reaction, as illustrated in Figure 1 for the

case of propane. This is believed to be the case for all of the other simple alkanes listed above.

Photopolymerization of Formaldehyde

A second type of chain reaction we have investigated is the proton-transfer initiated photopolymerization of solid formaldehyde. This chain reaction occurs at temperatures below 10 K, the lowest temperature we have attempted. We reported that initiation of the reaction occurs by creating a strong acid in the interior of the amorphous solid. This has been done three ways:

- 1) by co-depositing the formaldehyde with HCl vapor
- 2) by forming HCl via photochemical reaction of solid Cl_2 in excess formaldehyde
- 3) by proton transfer reactions from electronically excited 2-nitrophenol (a photo-acid) doped into solid formaldehyde.

Most of our efforts on this

system have been directed toward determining the chain length of the polymer formed in the reaction. In our first report, we determined the chain length of the oligomer formed at low temperatures to be 6.4 ± 1.5 monomer units. Upon warming the samples, the chain length grows to about 16 ± 3 monomer units.

Our results are consistent with the following reaction mechanism. Protonation initially occurs at the oxygen atom of a formaldehyde monomer. The HOCH_2^+ ion then forms a new C-O bond with a nearby monomer molecule forming $\text{HOCH}_2\text{OCH}_2^+$. The oligomerization proceeds at low temperatures by repeating this step until the active end of the growing oligomer reaches a site in which none of its neighboring monomer molecules has its oxygen atom near enough to form the next C-O bond in the chain. The reaction stops at that point. When the sample is warmed to its glass transition temperature, movement of the monomer molecules occurs, and the relatively short oligomers may grow into polyoxymethylene (the polymer of formaldehyde). The infrared spectrum of polyoxymethylene is relatively insensitive to chain length, and our estimate of the polymer chain length is made on the basis of quantum yield

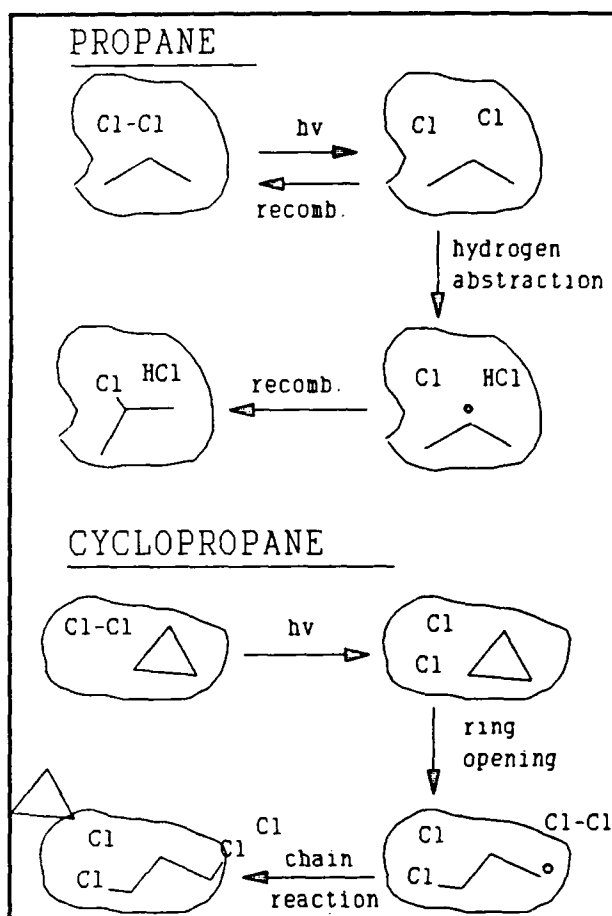


Figure 1

measurements at various concentrations of Cl_2 initiator (the precursor to HCl).

Goldanskii and co-workers have investigated gamma-initiated polymerization of crystalline formaldehyde samples, and have reported chain lengths for polymerization of 10^3 or more depending on the temperature of the crystal. The comparison of their results to ours reveals that the disordered environment of samples formed by vapor deposition strongly limits the extent of chain propagation. This is illustrated schematically in Figure 2.

Photochemistry of Solid Ozone

Photochemical chain reactions of ozone are ubiquitous in the gas phase, and play a key role in the destruction of atmospheric ozone by active forms of chlorine. In a preliminary study, we have investigated the photodissociation of solid ozone deposited as a thin film on the surface of an optical window at 15 K. We have found no evidence for the participation of chain reactions in these experiments.

Instead, we have found a very strong state selectivity for reactions of electronically excited $\text{O}(^1\text{D})$ atoms in the solid state. Experiments were conducted at a number of different photolysis wavelengths in the visible and ultraviolet, as listed in Table I.

The quantum yields for photodestruction of ozone are nearly equal to twice the gas phase quantum yields for production of $\text{O}(^1\text{D})$ atoms in the primary step. For example, 591 nm photolysis (in the Chapuis band of ozone) results in very little destruction of ozone (less than 4 molecules of ozone destroyed per 100 photons absorbed by the sample). On the other hand, at 300 nm where the $\text{O}(^1\text{D})$ yield is reported to be essentially 1.0, we observe 2 molecules of ozone destroyed per photon absorbed by the sample. Our interpretation of this result is that $\text{O}(^3\text{P})$ atoms produced by photolysis in the visible (and to some extent in the UV) undergo simple recombination with its caged O_2 partner photofragment to regenerate the original O_3 molecule. Excited $\text{O}(^1\text{D})$ atoms are extremely reactive toward neighboring ozone molecules, resulting in the net conversion of two ozone molecules to three oxygen molecules.

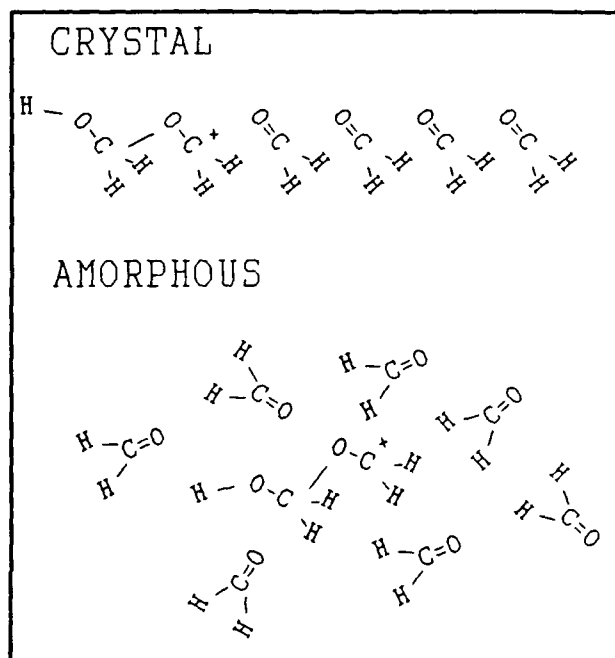
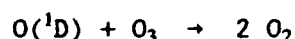
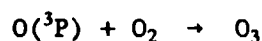
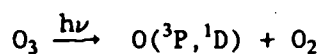
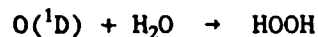


Figure 2



When ozone is co-deposited with water vapor, similar behavior is observed. Photolysis in the visible results in no detectable loss of ozone. Photolysis in the UV, however, results in loss of ozone and formation of hydrogen peroxide.



It is well known that gas phase $\text{O}(^1\text{D})$ atoms are extremely reactive toward both ozone and H_2O molecules. The same is observed in the solid state. By varying the relative concentrations of ozone and water in the samples, we systematically alter the probability of an $\text{O}(^1\text{D})$ atom being formed adjacent to a neighboring water or ozone reaction partner. The observed quantum yield for ozone destruction is a linear function of water concentration, showing that $\text{O}(^1\text{D})$ atoms exhibit no preference for reaction with either O_3 or H_2O in the solid state, in accordance with the gas phase behavior.

Table I. Photolysis cross sections and quantum yields for solid ozone.

λ (nm)	$\sigma_a(10^{-19} \text{ cm}^2)^a)$	$\sigma_d(10^{-19} \text{ cm}^2)^b)$	$\Phi(\text{solid})^c)$	$2\phi(\text{gas})^d)$
591	0.13 ± 0.03	0.0033 ± 0.0005	0.025 ± 0.020	0.0
311	1.2 ± 0.2	1.4 ± 0.1	1.2 ± 0.2	$0.80 \pm 0.04^e)$
308	1.7 ± 0.2	2.43 ± 0.05	1.5 ± 0.2	$1.61 \pm 0.06^e)$
300	4.5 ± 0.5	8.1 ± 0.5	2.0 ± 0.2	$1.95 \pm 0.03^f)$
266	$75. \pm 10.$	$130. \pm 30.$	1.7 ± 0.3	$1.76 \pm 0.07^g)$
240	$70. \pm 30.$	$150. \pm 70.$	2.2 ± 0.3	$2.0^h)$

^{a)} From UV-VIS absorption spectrum of solid ozone at 10 K, this work.

^{b)} From sample depletion vs. laser fluence, this work.

^{c)} Photodepletion quantum yield, σ_d/σ_a , this work.

^{d)} 2.0 times the gas phase $\text{O}(^1\text{D})$ quantum yield from ozone.

^{e)} Arnold, I.; Comes, F.J.; Moortgat, G.K. *Chem. Phys.* 1977, **24**, 21.

^{f)} Brock, J.C.; Watson, R.T. *Chem. Phys.* 1980, **46**, 477.

^{g)} Brock, J. C.; Watson, R. T. *Chem. Phys. Lett.*, 1980, **71**, 371.

^{h)} Kajimoto, O.; Cvetanovic, R. J. *Chem. Phys. Lett.* 1976, **37**, 533.

Publications Acknowledging AFAL Support

1. A. J. Sedlacek and C.A. Wight, "Laser-initiated free radical chlorination of propane in amorphous thin films: Temperature dependence from 15-77 K", J. Phys. Chem. 92, 2821 (1988).
2. E. S. Mansueto, C.-Y. Ju, and C. A. Wight, "Laser-initiated polymerization of solid formaldehyde", J. Phys. Chem. 93, 0000 (1989).
3. A. J. Sedlacek and C. A. Wight, "Free radical chain reactions of chlorine with cyclobutane in the solid state: Evidence for radical migration via H atom transfer", J. Chem. Phys. 88, 2847 (1988).
4. A. J. Sedlacek and C. A. Wight, "Photochemical chain reactions in amorphous solids", Laser Chem. 8, 155 (1988).
5. A. J. Sedlacek and C. A. Wight, "Photochemistry of solid ozone", J. Phys. Chem., 93, 509 (1989).
6. E. S. Mansueto and C. A. Wight, "Excited-state proton transfer polymerization of amorphous formaldehyde", J. Am. Chem. Soc., submitted for publication.
7. A. J. Sedlacek and C. A. Wight, "Solid-state reactions of O(¹D) atoms with ozone and water", J. Phys. Chem., submitted for publication.
8. C. A. Wight, T. W. Tang, and E. S. Mansueto, "Low temperature photochemistry in amorphous films", Proc. SPIE, 1056-30 (1989).
9. C. A. Wight, T. W. Tang and E. S. Mansueto, "Laser-Induced Reaction and Polymerization in Low Temperature Amorphous Solids", Proc. Int. Laser Sci. IV Conf., in press.

Dynamics of Metastables in the Condensed Phase*

by

P. K. Swaminathan
Chemical Dynamics Corporation
Upper Marlboro, MD 20772

In our computational research program on condensed phase dynamics, recent work has involved the problem of electronically nonadiabatic dynamical effects in the quenching of $\text{He}(2^3\text{S})$ to $\text{He}(1^1\text{S})$ in going from the gaseous helium densities to densities characteristic of condensed phase helium environments. The nonadiabatic dynamics involves scattering on multiple electronic surfaces, notably the $a(^3\Sigma_u^+)$, $A(^1\Sigma_u^+)$, $b(^3\Pi_g)$, $B(^1\Pi_g)$, $c(^3\Sigma_g^+)$, and $C(^1\Sigma_g^+)$ states of He_2 and turns an incoming wave on the $a(^3\Sigma_u^+)$ surface into an outgoing branch in the $X(^1\Sigma_g^+)$ channel with possible emission of one or more photons in the process. Dynamical aspects of pathways involving various electronic states and nonadiabatic couplings leading to such a spin-forbidden quenching can now be studied employing Yarkony's new *ab initio* results¹ for the relevant potential energy surfaces and couplings in this metastable system.

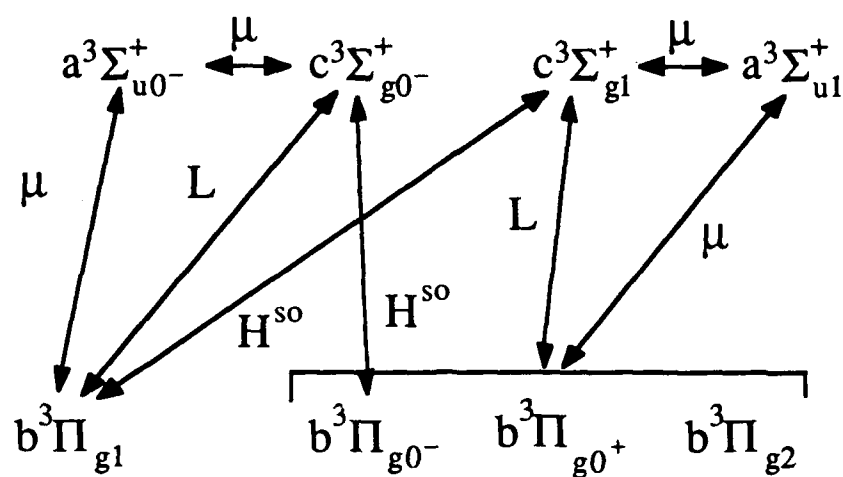
Radiative versus Nonradiative Quenching in the Gas Phase

The diagrams (on the following page) illustrate the important triplet-triplet, singlet-triplet and singlet-singlet dynamical pathways for the a-X quenching process. (Please note that the singlet-triplet diagram suppresses intramultiplet couplings). The solid arrows indicate transition dipoles and electronically nonadiabatic dynamical couplings known from Yarkony's calculations (H^{SO} : spin-orbit, μ_{sf} : spin-forbidden dipole, and L: rotational couplings) and the dashed arrow is a negligible (due to large energy gap) neglected H^{SO} coupling. The diagrams can be employed to identify two distinct possible types of quenching: (1) a direct spin-forbidden route involving a two-state dynamical problem that includes the a-state and an X-state dressed with the photon² (closely on resonance with the atomic $2^3\text{S}-1^1\text{S}$ line) and (2) a more complex nonadiabatic route leading to a multistate dynamical problem incorporating a variety of pathways over to the singlet manifold where strong quenching propensity prevails.

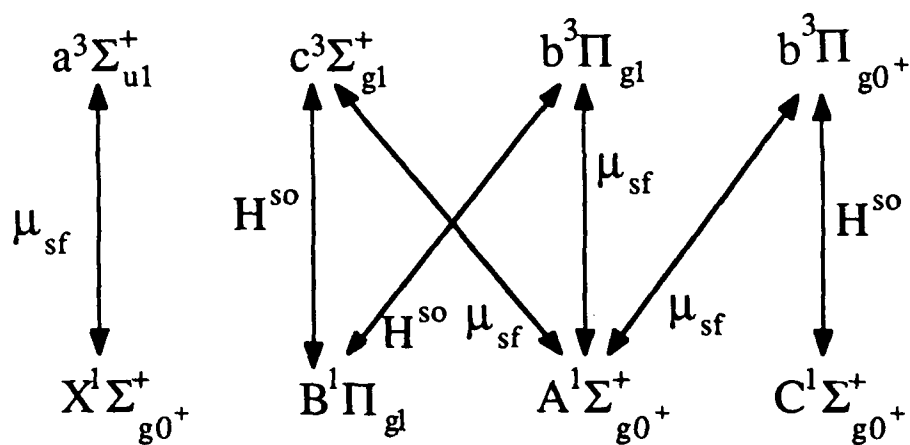
It was found that although the system *can* quench nonradiatively, the probabilities are very low $\sim 10^{-16}$ compared to $\sim 10^{-8}$ for radiative routes. Two-state model studies using the self-consistent eikonal method (SCEM) have yielded the following cross sections (in a_0^2) for collision-induced radiative quenching: $1.23\text{E-}4$ (probability $\sim 1\text{E-}6$), $1.92\text{E-}13$

* The coworkers in this ongoing project are: Drs. C. S. Murthy and B. C. Garrett (CDC), and D. R. Yarkony (JHU).

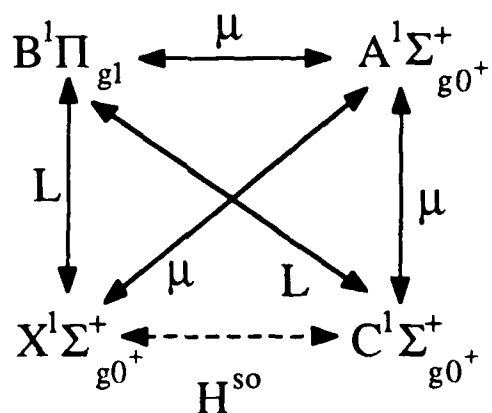
Triplet-Triplet transition pathways



Singlet-Triplet transition pathways



Singlet-Singlet transition pathways



(probability $\sim 1.E-7$) at translational energies 5.4 and .27 eV respectively. Probabilities drop down to $1.E-8$ at .004eV but climb again to $1.E-7$ at .002eV. These numbers are consistent with the experimental³ cross section upper limit of $\sim 1.E-9a_0^2$ which dealt with pressure effects at low translational energies.

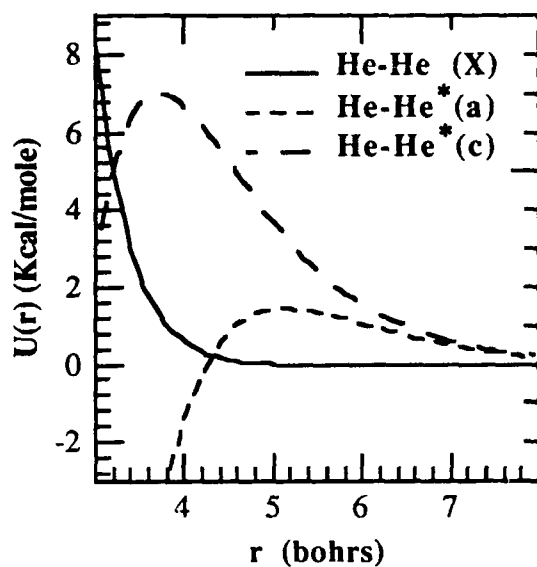
Preliminary results on different choices of possible many-state models indicate some notable features. The nonadiabatic route to the singlet manifold is incapable of competing with the propensities of the above two-state radiative route. This is consistent with Yarkony's anticipation¹ of a bottleneck in the multiplet crossover rate. The dynamical problem, however, becomes very complicated when the photon emitting pathways are included and requires a thorough scan of photon frequency dependence in each dipole coupling: there are 13 dipole couplings, 9 allowed and 4 forbidden. Random examination of several many-state models and trajectories were done for sensitivity to photon frequencies and dependence on keeping or dropping the radiative couplings. Dramatic changes have been found in the relative propensities; hence it is difficult to *a priori* rule out competition from these pathways at this stage.

High Pressure Cluster Formation in Condensed Phase Bubbles

The a-state and c-state characters of solute-bath interactions of a $He^*(2^3S)$ in a high pressure helium liquid lead to quantitatively different stabilities for the metastable atomic species. The pertinent regions of the a, c, and X interaction potentials along with key solvation simulation results⁴ are shown on the next page. The c-state bubble (not shown, see ref. 4) protects the atomic species upto very high pressures whereas the a-state more easily allows reaction with a solvent He atom leading to a pronounced degree of cluster formation that varies with pressure. Average $\langle n \rangle$ values of He_n^* and the thermodynamics are given in a table on the next page. One remarkable feature (seen in the graphs) is the maintenance of a bubble structure despite the cluster formation (the simulation ignores many-body interactions so far). The cluster location is shown in a $g(r)$ plot on an expanded scale. The c- and a-states are radiatively coupled in reality and both states can play a role in determining the metastable atom's bubble. The cluster formation observed here is a neutral excitation trapping process in liquid that is analogous to the charged exciton trapping phenomenon observed⁵ in rare gas halide crystals. These results indicate that stabilization of a metastable by clustering it to a suitable entity may still result in trapping into bubbles in the condensed phase. Since such bubbles can protect the species' energy from dissipation to bulk, it is useful to identify conditions for their formation in different matrices for different species.

Solvent Shift of $2^3S \rightarrow 2^3P$ Absorption Line

One of the key experimental observations on helium bubbles was the blue shifted nature of the above absorption line in contrast to a red shifted nature of the corresponding emission line. This was fruitfully studied in a phenomenological bubble model⁶ using adiabatic line shape theory in the static limit. Solvent static and dynamical effects can in general play a role in shifting spectra. We have characterized the high pressure helium bath and deduced parameters for stochastic dynamics simulations of metastable species trapped in it. However, in the case of the present atomic transition, solvent dynamics can be shown to be less crucial in determining the absorption line at high pressures (a typical bath atom moves only $\sim 0.2a_0$ within a transition dipole relaxation time compared to $\sim 1.5a_0$ for the low pressure cryogenic regime where previous experiments were). We have verified the experimental absorption line blue shifts employing the quantal radial distribution function from Hansen and Pollock⁷ and Yarkony's¹ transition dipole function. We have also performed a similar calculation employing our radial distribution function for the a-bubble

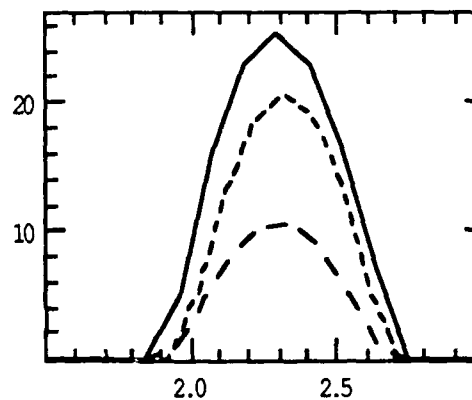
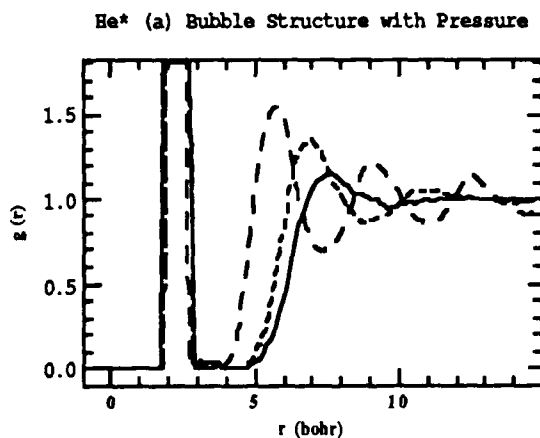


g(r) plots

Solid Line: 0.5GPa

Short Dashed Line: 1.4GPa

Long Dashed Line: 10 GPa



MC Results of $\text{He}^*(2^3\text{S})$ in $\text{He}(1^1\text{S})$ bath at 300K

'n-mer' Structure				
$V_m/\text{cm}^3.\text{mol}^{-1}$	$\langle P \rangle/\text{GPa}$	$\langle U \rangle/\text{kJ}.\text{mol}^{-1}$	r_{bub}/a_0	$\langle n \rangle$
17.95	0.29	0.36	2.29	5.9
13.17	0.55	-2.0	2.29	6
0.57	0.85		0	
9.02	1.4	-0.9	2.32	6-7
1.5	2.2			
4.76	10.1	10.4	2.24	9
10.3	11.9	2.14	3-4	
4.35	13.8	14.2	2.27	10-11
13.9	15.6		4	

(a) First and second row values for each volume correspond to a- and c-states of He-He^* interaction.

and the $a \leftrightarrow b$ transition dipole function to find a large red shift for the high pressure line position by $\sim 29\text{eV}$. This value should be modified by considering contributions due to transitions dictated by the (presently unknown radiative) coupling of c -state to the u -manifold (outside the primary space employed by Yarkony) of the 2^3P asymptote. We have found that the large red shift is predicted even when the contribution from clustering region of a -bubble is subtracted. At slightly lower pressures the complication of reaction may be avoided and the a, c inelasticity characterized via spectroscopic studies (see above).

Summary

The role of our computational technology in analyzing condensed phase energy transfer and reaction attributes is just beginning to be unravelled. Our method development aimed at assembling the required computational technology for studying condensed phase energy transfer and reaction problems has resulted in a powerful toolkit that includes the following codes:

- Gas Phase selfconsistent eikonal method (SCEM) code for up to 4 atoms in an electronically inelastic process.
- Monte Carlo /Molecular Dynamics codes for heatbath modelling with solution Monte Carlo code to include a possible reaction with the solvent.
- SCEM+GLE (Generalized Langevin Equation) condensed phase electronically inelastic dynamics code with radiative and nonradiative couplings included.

In future applications, we plan to focus on calculations interpreting experimental mechanisms and examine chemical and physical requirements of HEDM candidates.

References

1. D. Yarkony, "On the Quenching of Helium 2^3S : Potential Energy Curves for, and Nonadiabatic, Relativistic and Radiative Couplings between the $a(^3\Sigma_u^+)$, $A(^1\Sigma_u^+)$, $b(^3\Pi_g)$, $B(^1\Pi_g)$, $c(^3\Sigma_g^+)$, and $C(^1\Sigma_g^+)$ states of He_2 .", Preprint.
2. μ_{sf} is computed in C. Chabalowsky, J. O. Jensen, D. R. Yarkony, and B. H. Lengsfeld III, *J. Chem. Phys.* **90**, 2504 (1989).
3. H. W. Moos and J. R. Woodworth, *Phys. Rev. Letts.* **30**, 775 (1973).
4. C. S. Murthy and P. K. Swaminathan, *J. Chem. Phys.* **90**, 2778 (1989).
5. see also contributions from A. Apkarian in this program.
6. A. P. Hickman, W. Steets and N. F. Lane, *Phys. Rev. B* **12**, 3705, 1975.
7. J. P. Hansen and E. L. Pollock, *Phys. Rev. A* **5**, 2214 (1972).

SPECIFIC IMPULSE ENHANCEMENT VIA PRESSURE STABILIZED EXCITED ELECTRONIC STATES OF HIGH ENERGY DENSITY PROPELLANTS

John W. Kenney, III
Department of Physical Sciences-Chemistry
Eastern New Mexico University
Portales, New Mexico 88130

Introduction

Straightforward thermodynamic considerations indicate that the I_{sp} of a given rocket fuel/oxidizer couple may be increased significantly by preparing one or both of these energetic reactants in excited electronic states. A number of promising propellant systems based upon metastable electronically excited reactants are currently under investigation (1). In all of these systems, the exothermicity of the rocket propulsion reaction (and hence the I_{sp}) is enhanced as this excess stored electronic energy is converted to additional exothermic reaction energy. The idea is to design high energy chemical propellants into which additional electronic energy can be pumped and to develop conditions that act to stabilize the electronically excited propellant prior to reaction in the rocket nozzle. It should be noted that electronic excitation energies (ΔH_{ex}) from 100-1000 nm (1196 kJ mol^{-1} - $119.6 \text{ kJ mol}^{-1}$) are on the order of exothermic propulsion reaction energies (ΔH^*). By adding this excitation energy the specific impulse is enhanced as $I_{sp}^* = I_{sp}^*[1 + \chi_{ex}f_{ex}]^{1/2}$ where χ_{ex} is the fraction of excited reactants and $f_{ex} = \Delta H_{ex}/\Delta H^*$ is the excitation figure of merit. Since f_{ex} is on the order of unity, substantial enhancements are possible if χ_{ex} can be increased to a substantial fraction. For example, a 25% I_{sp} enhancement is predicted if $\chi_{ex} = 3/4$ and $f_{ex} = 3/4$.

Pressure Effects in Excited Electronic States

Our research effort has focused on chemical and physical modifications of high-energy-content organometallic and metallocene systems with the objective of increasing the lifetimes of their low-lying excited electronic states into a metastable time regime. Of particular interest to us are excited electronic states based upon the promotion of one or more electrons from filled antibonding ϕ^* or non-bonding ϕ^{nb} molecular orbitals into empty bonding molecular orbitals ψ : i.e., $(\phi^*)^n(\psi)^0 \rightarrow (\phi^{nb})^{n-m}(\psi)^m$ or $(\phi^*)^n(\psi)^0 \rightarrow (\phi^*)^{n-m}(\psi)^m$. The excited states thus produced are (or have the potential to be) squeezed or geometrically contracted relative to their corresponding ground states since they have higher formal bond orders (2). An electronically excited molecule that is smaller in its excited state than in its ground state has the potential be stabilized by high pressure. The high pressure environment acts as a perturbation on the vibronic Hamiltonian of the system. This perturbation increases the steepness of the potential well by forcing greater overlap between the bonding orbitals in the excited state and by providing an electrostatic barrier to large deviations

from the equilibrium geometry. The excited-state-to-ground-state transition probability is diminished because the pressure perturbation inhibits expansion into the larger ground state geometry. The objective is to use the pressure perturbation to produce low Franck-Condon factors and badly mismatched vibrational levels to minimize radiative and non-radiative transition probabilities. The use of the diamond anvil cell (DAC) to investigate the effects of pressure on excited state lifetimes is discussed (3). Also of interest to us are molecules that exhibit manifolds of closely spaced excited electronic states with varying spin multiplicities and orbital symmetries. In this case, electronic excitation energy storage may be achieved by thermally tuning the excited manifold to an excited state that does not couple efficiently with the ground state through either radiative or non-radiative decay pathways. A desirable excited electronic manifold for energy storage is one in which the lowest state within the manifold is the forbidden state. Very low (cryogenic) temperatures favor the preferential population of this lowest forbidden state. Dramatic lengthening of the excited state lifetime with decreasing temperature is often observed for such systems. A high energy propellant that possesses a forbidden excited electronic state--a state that originates from bond-order-increasing electron promotions relative to the ground state and that also happens to be poised at the bottom of an excited electronic manifold--has the potential to be stabilized by a combination of cryogenic temperatures and high pressures. Several representative systems are discussed.

Practical Realizations of High Pressure Environments

A pressurization scheme that uses a massive pressurization device to compress small amounts of fuel (e.g., ~250 g DAC used to pressurize microgram quantities of energetic material) is not practical for rocket propulsion applications. What is needed is a pressurization strategy that does not add significant mass over and above the fuel/oxidizer mass. Several possibilities exist for significantly improving this mass ratio that are within the capabilities of existing chemical and engineering technology: (1) high pressure molecular micro-encapsulation, (2) high pressure mini-encapsulation with shrink-wrapped fuel/oxidizer pellets, (3) magnetostriction, (4) centrifugal compression with fuel/oxidizer flywheels (5) cryocompression.

References

1. "Proceedings of the Air Force High Energy Density Materials Conference", 28 February - 2 March 1988, Newport Beach, California.
2. Many binuclear d^8 -- d^8 transition metal complexes contract upon excitation by forming a metal metal bond in the excited state that is not present in the ground state. See, for example, Kenney, M.I.S.; Kenney, J.W., III; Crosby, G.A., *Organometallics* **1986**, 5, 230-234.
3. Hemley, R.J.; Bell, P.M.; Mao, H.K., *Science* **1987**, 236, 605-612.

THEORETICAL STUDIES OF METASTABLE MOLECULAR SYSTEMS

K. Kirby

Harvard-Smithsonian Center for Astrophysics

Metastable States of CO (with M. Rosenkrantz and D. L. Cooper)

Carbon monoxide is an interesting molecule in which to look for metastability because it is easy to obtain, and well-studied in the laboratory both in the gas-phase and in matrices. Recently we reported ab initio multiconfiguration self-consistent field (MCSCF) and configuration interaction (CI) calculations of the $I^1\Sigma^-$ and $D^1\Delta$ states of CO^1 which lie more than 8 eV above the $X^1\Sigma^+$ state. The $I^1\Sigma^-$ and $D^1\Delta$ states arise from different couplings of the same electron occupation, $\dots 5\sigma^2 1\pi^3 2\pi$ and consequently the potential curves (as shown in figure 1) and dipole moments of these states are extremely similar. Although electric dipole transitions directly to the ground state are forbidden, transitions to lower-lying vibrational levels of the $A^1\Pi$ state are allowed for the vibrational levels lying above $v'=0$ in both states. Decay to the $A^1\Pi$ is very slow due to the small transition energy involved and the radiative lifetimes vary greatly with v' , from .13s for $v'=1$ to 8×10^{-5} s for $v'=15$ of $I^1\Sigma^-$. The $v'=0$ level of the $I^1\Sigma^-$ state lies below $v=0$ of the $A^1\Pi$ and thus the radiative lifetime is infinite, whereas $v'=0$ of the $D^1\Delta$ lies just above $v=0$ ($A^1\Pi$) and the radiative lifetime is 1.6s. These $v'=0$ levels of the I and D states are the focus of our study due to their extraordinarily long radiative lifetimes.

The $I^1\Sigma^-$ and $D^1\Delta$ states have been observed as perturbors of the strong fourth positive system ($A^1\Pi-X^1\Sigma^+$)² and in two-photon transitions from the $v''=0$ of the $X^1\Sigma^+$ state.^{3,4} These states have also been seen in very weak absorption from the ground state due to interactions with the $A^1\Pi$ state. Only particular bands appear, depending on the proximity and vibrational overlap of levels in the I or D state with levels in the $A^1\Pi$ state.^{5,6} In all the above observations, the $v'=0$ levels of the I and D states have never been observed. The evidence for the population of the $I^1\Sigma^-$ and $D^1\Delta$ in electron impact experiments is somewhat conflicting. Although these states were not observed in electron energy loss measurements by Swanson et al.,⁷ recent work by Mason and Newell⁸ notes an appearance threshold at 10eV and a lifetime of approximately $80 \pm 10 \mu s$ in general agreement with Wells et al.⁹ We find that

lifetimes for vibrational levels >10 in both the I and D state are consistent with the experiments.¹

In order to measure experimentally the lifetimes of the $v'=0$ levels of the $I^1\Sigma^-$ and $D^1\Delta$ states a number of ways of populating these levels may be considered. Because the Franck-Condon overlaps of $v''=0(X^1\Sigma^+)$ and $v'=0(I^1\Sigma^-, D^1\Delta)$ are vanishingly small, direct population through electron impact or two-photon transitions is not effective. Franck-Condon factors ≥ 0.1 may be achieved by first pumping $v''=8$ through 12 of the ground state. This kind of procedure has been used by several experimenters^{10,11} to study other transitions in CO.

We have also investigated the possibility of population of the $v'=0$ levels through cascade from higher-lying vibrational levels within the I and D states.¹ In every case (except for $v=1$ of the $I^1\Sigma^-$ state) the excited vibrational levels decay preferentially through transitions to the $A^1\Pi$ state (pathway 1) rather than through vibrational cascade within the I and D states (pathway 2). However the ratio of the lifetimes of pathway 2 vs. pathway 1 varies from 4 (for $I^1\Sigma^- v'=2$) to 90 (for $I^1\Sigma^- v'=15$), and thus, over time, significant population can build up in $v'=0$ through cascade from higher v' .

Another mechanism for producing $v'=0$ in both $I^1\Sigma^-$ and $D^1\Delta$ is through pumping of the $W^1\Pi$ Rydberg state. This state lies 12.76 eV above the $X^1\Sigma^+$ state and is the first in the Rydberg series converging to the $A^2\Pi$ state of CO^+ . The transition $W^1\Pi-X^1\Sigma^+$ has a very large oscillator strength.¹² Spontaneous radiative decay takes place predominantly to the X state, but from $v=2$ of the W state, 1.8% (2.5%) of decay leads to the $I^1\Sigma^-$ ($D^1\Delta$) and one third of those transitions populate $v'=0$ (I or D) directly. Stimulated emission specific to the $v'=0$ levels would change these percentages radically.

Finally, as in the production of the $c^3\Pi_u^-$ state of H_2 , charge transfer of CO^+ in an appropriately chosen gas should be considered as a possible way of making CO $v'=0$ ($D^1\Delta$ and $I^1\Sigma^-$).

High Spin States of CN and NO (with F. Penotti and D. L. Cooper)

Sextet states of CN and NO can be formed from ground state atoms, $C(^3P) + N(^4S)$ and $N(^4S) + O(^3P)$. The goal in looking at such states is to quantify any binding that may be present and to identify possible decay mechanisms. A basic set of Slater type orbitals (6s/4p/3d/3f/1g) of McLean, as modified by M. Rosenkrantz was used for C, N, and O.

Calculations of the ${}^6\Sigma^+$ states of both CN and NO have been completed. For CN, molecular orbitals were obtained from an SCF calculation on the ${}^6\Pi$ state. For NO, the molecular orbitals were obtained from a multiconfiguration SCF (MCSCF) on the ${}^6\Sigma^+$ state.

The configuration interaction wavefunctions for both systems included two core orbitals (1σ , 2σ) which remained doubly-occupied and two sets of valence orbitals: (3σ , 4σ) and (5σ , 6σ , 1π , 2π), as well as the virtual orbitals. All excitations within the valence space and single and double excitations into the virtual space were allowed, with the restriction that two or more electrons always occupied the (3σ , 4σ) space. For CN(NO) ${}^6\Sigma^+$ the wavefunction included 435,470 (197,094) configuration state functions.

As can be seen in Figures 2 and 3, the two states are very different, with the CN ${}^6\Sigma^+$ exhibiting a double minimum structure. The outer well of CN ($R_{\min} \approx 5.0a_0$) and the single well of NO ($R_{\min} \approx 5.9a_0$) are van der Waals minima, with well depths of 384 cm^{-1} and 294 cm^{-1} , respectively. The origin of the inner well ($R_{\min} = 3.35a_0$ and $D_e = 623 \text{ cm}^{-1}$) in CN can be found by examining the dipole moment function, which attains maximum ionicity ($\sim .3ea_0$, C^-N^+) near $R = 3.5a_0$. The ion pair state $C^-(4S) + N^+(3P)$ can give rise to a sextet state. However in the NO system the analogous ion pair $O^-(2P) + N^+(3P)$ cannot give rise to a sextet, and there is no inner well. The CN and NO ${}^6\Sigma^+$ states support 10 and 4 vibrational levels, respectively. The spin-orbit interactions of these sextets with lower-lying quartet states of both systems must be examined to determine the lifetimes of these high-spin states.

References

1. M. E. Rosenkrantz and K. Kirby, J. Chem. Phys. to be published 1 June 1989.
2. J. D. Simmons, A. M. Bass and S. G. Tilford, Ap. J. **155**, 345 (1969).
3. C. Kittrell, S. Cameron, L. Butler, R. W. Field and R. F. Barrow, J. Chem. Phys. **78**, 3623 (1983).
4. B. A. Garitz and C. Kittrell, Phys. Rev. Lett. **53**, 156 (1984).
5. J. D. Simmons and S. G. Tilford, J. Chem. Phys. **45**, 2965 (1966).

6. G. Herzberg, J. D. Simmons, A. M. Bass, and S. G. Tilford, Can. J. Phys. 44, 3039 (1966).
7. N. Swanson, R. J. Celotta, C. E. Kuyatt, and J. W. Cooper, J. Chem. Phys. 62, 4880 (1975).
8. N. J. Mason and W. R. Newell, J. Phys. B. 21, 1293 (1988).
9. W. C. Wells, W. L. Borst and E. C. Zipf, Phys. Rev. A8, 2463 (1973).
10. G. L. Wolk and J. W. Rich, J. Chem. Phys. 79, 12 (1983).
11. R. L. DeLeon, J. Chem. Phys. 89, 20 (1988).

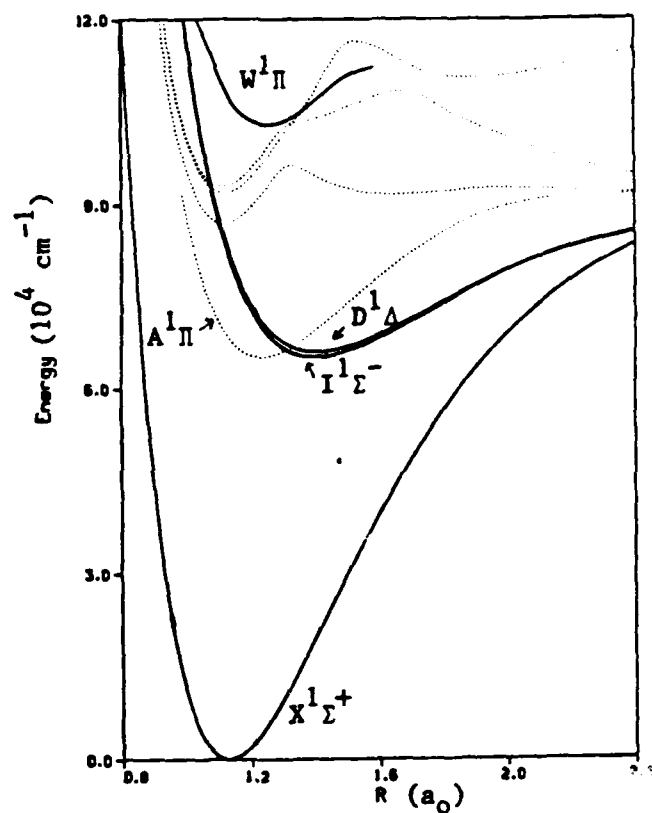


Fig. 1. Potential energy curves for CO.

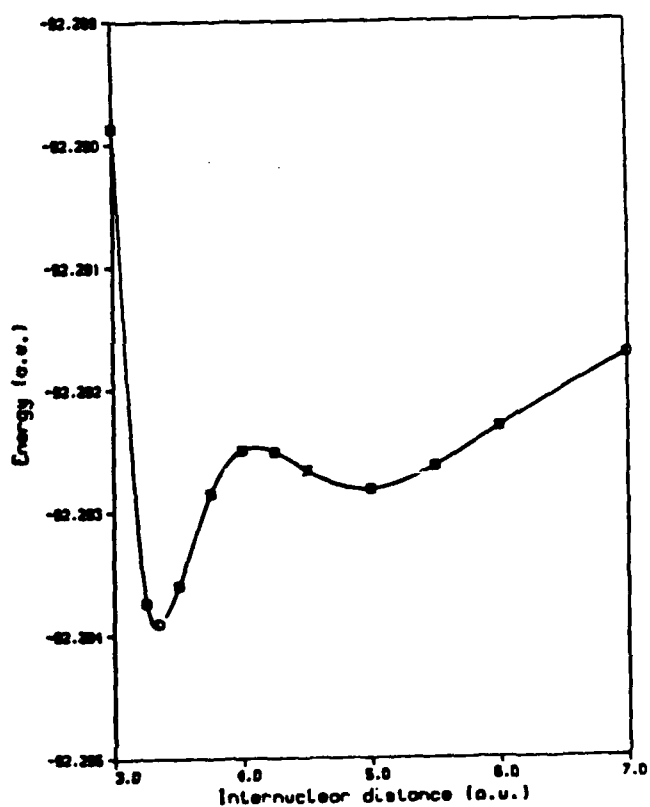


Fig. 2. Potential energy curve for lowest ${}^6\Sigma^+$ state of CN.

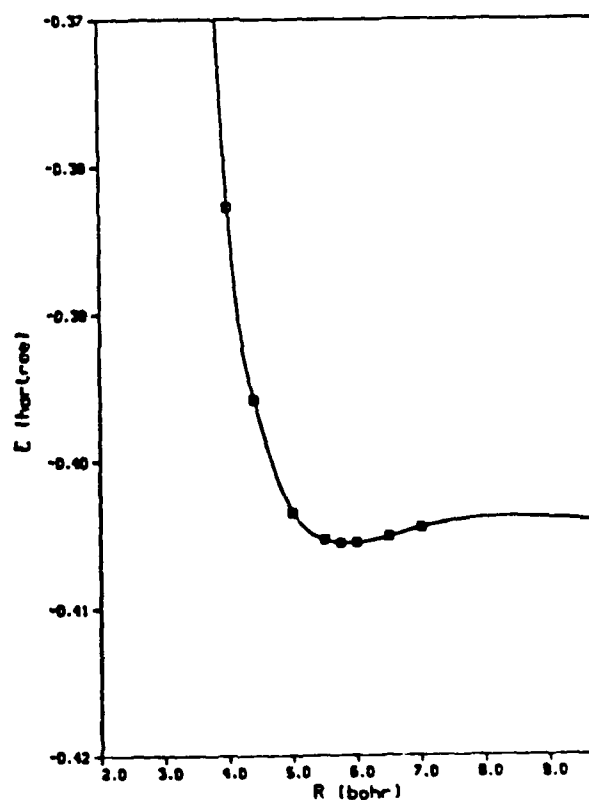


Fig. 3. Potential energy curve for lowest ${}^6\Sigma^+$ state of NO.

The Stability of $N_2(A'^5\Sigma_g^+)$

W.J. Marinelli, W.J. Kessler, A.M. Woodward,
and W.T. Rawlins
Physical Sciences Inc.
Research Park, P.O. Box 3100
Andover, MA 01810

INTRODUCTION

Experimental investigations of "active" nitrogen have long postulated the existence of a high-energy metastable electronic state of N_2 responsible for the excitation of many species. Various reports indicate the state has a low heterogeneous deactivation probability on glass and metal surfaces and lives for several milliseconds in the gas phase. Matrix isolation studies have shown that chemiluminescence from "active" nitrogen trapped at 10 to 35 K may radiate for many seconds.¹ The existence of such a long-lived metastable state would have important consequences for our understanding of upper atmospheric chemistry, chemical lasers, energy storage and high voltage switching.

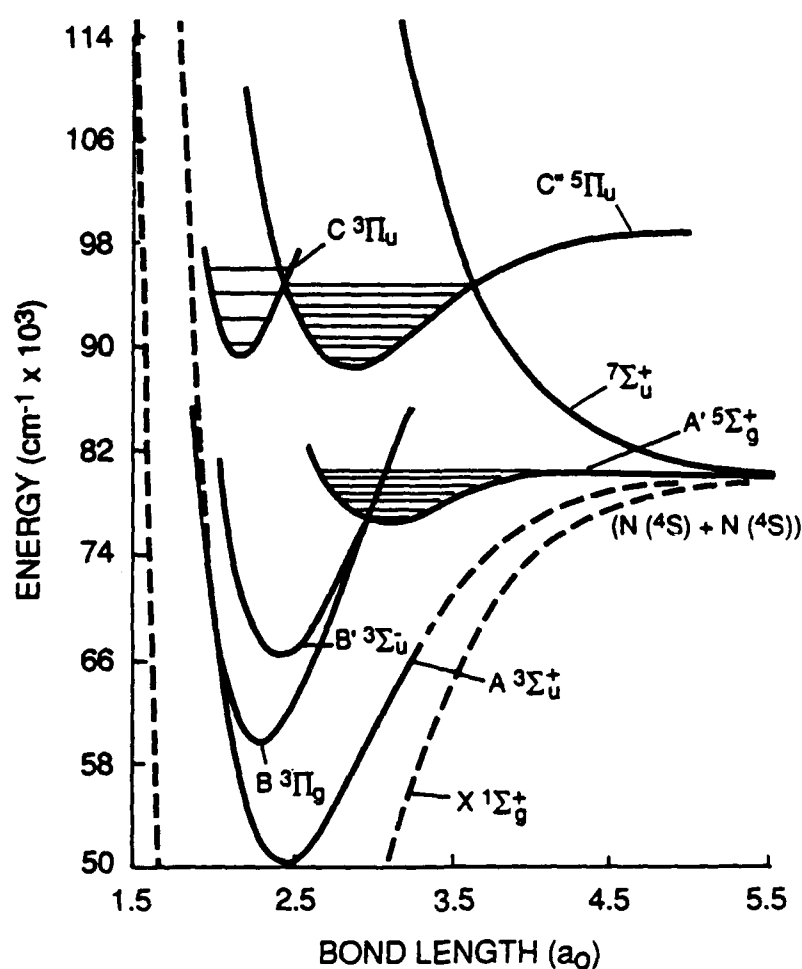
Recently, several theoretical efforts have focussed on the stability of the "high spin" $^7\Sigma_g^+$ and $^5\Sigma_g^+$ electronic states of N_2 . These states arise from the pairing of two $N(^4S)$ atoms to form an N_2 molecule in which all or all but two of the electron spins remain unpaired in the resulting molecular orbitals. These states are characterized by the formation of a weakly-bound (several cm^{-1}) van Der Waals minimum at long r_e and a somewhat more strongly covalently bound minimum at shorter r_e . Since these configurations are the lowest energy of each of the spin multiplicities, they should be stable with respect to decay via dipole radiation and perhaps metastable with respect to collisional deactivation. Curve-crossing to the $^5\Sigma$ state has been postulated by Berkowitz, Chupka, and Kistiakowsky² as the mechanism for predissociation of the $B^3\Pi_g$ state.

The potential of the $^5\Sigma_g^+$ state was initially investigated by Mulliken,³ who predicted a covalent well depth of $\sim 2300\text{ cm}^{-1}$. Subsequent calculations by Krauss and Neumann⁴ predicted a shallower potential with a well depth much closer to 850 cm^{-1} . Siegbahn⁵ calculated that D_e was approximately 1450 cm^{-1} . Experimental evidence for the existence of a stable $^5\Sigma$ state is limited to the effects it may have on the predissociation of the $B^3\Pi_g$ and $a^1\Pi_g$ states. The proposition advanced by Berkowitz et al.,² that the $^5\Sigma$ state is responsible for these predissociations, is bolstered by the evidence of Carroll,⁶ who derived a well depth of 850 cm^{-1} from predissociation and airglow data.

Recently, Partridge and coworkers⁷ performed CASSCF/MRCI ab initio calculations on the $^5\Sigma_g^+$ and $^5\Pi_u$ states of N_2 . Their calculations for the $^5\Sigma$ state (designated A') revealed a covalent well depth of approximately 3450 cm^{-1} and a van der Waals minimum with a binding energy of 47 cm^{-1} . A barrier of

approximately 500 cm^{-1} with respect to dissociation to form two $\text{N}(^4\text{S})$ atoms further enhances the stability of the covalently-bound state. Recombining $\text{N}(^4\text{S})$ atoms, a primary mechanism for formation of the A' -state, must traverse this barrier to enter the covalently bonded well. The potential supports 7 bound vibrational levels with a spacing of approximately 630 cm^{-1} . The potential for the $^5\Pi_u$ state (designated C'') was also found to be more deeply bound than previously estimated. The C'' -state well depth is calculated to be $10,505\text{ cm}^{-1}$ with a vibrational spacing of approximately 925 cm^{-1} . A potential energy diagram of these states is shown schematically in Figure 1.

Perhaps the most important result from the Partridge study was the assignment of the previously unassigned Herman Infrared (HIR) band system of N_2 to the $\text{C}''^5\Pi_u\text{-A}'^5\Sigma_g^+$ transition. This assignment was subsequently confirmed by FTIR studies of Huber and Vervloet.⁸ The HIR bands are observed in the



B-0752a

Figure 1. Potential energy diagram for the excited quintet and triplet states of N_2 . The vibrational levels of the $\text{C}''^5\Pi_u$ and $\text{A}'^5\Sigma_g^+$ states are indicated.

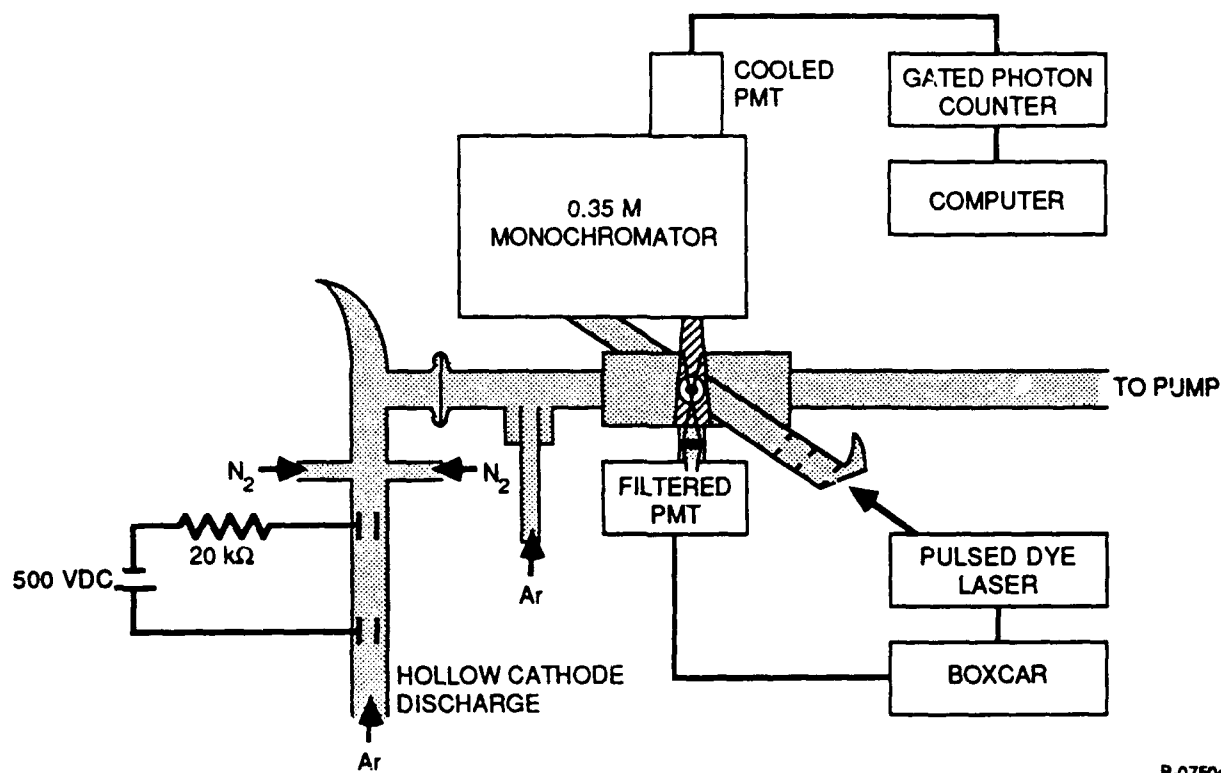
650 to 900 nm region as a result of an energy pooling reaction between two $N_2(A^3\Sigma_u^+)$ molecules.⁹⁻¹¹ Emission from the $C^3\Pi_u$ and $B^3\Pi_g$ states is also observed from the energy pooling process. The calculated radiative lifetime of the C'' -state is 4.3 μ s; similar to the $B^3\Pi_g-A^3\Sigma_u^+$ First-Positive bands.¹² The calculated lifetime is in conflict with experimental observations that the ratio of C''/C state emission intensities is unchanged over a pressure range of a few torr. This would place the lifetime of the C'' -state nearer the 37 ns lifetime of the C -state and raises the possibility that the C'' -state derives its lifetime from coupling to the C -state.

The assignment of the N_2 HIR bands to the $C''^5\Pi_u-A'^5\Sigma_g^+$ transition coupled with the 3450 cm^{-1} well depth establishes a means of production and indirect evidence for the stability of the A' -state. The 9.45 eV electronic term energy of the A' -state is more than sufficient to excite many of the states observed in "active" nitrogen. However, the magnitude of the intersystem collisional transfer processes and non-radiative spin-orbit and spin-spin couplings to other electronic states in the N_2 manifold, which decrease the A' -state lifetime, have not been addressed. The experiments reported in this paper employ a discharge-flow laser induced fluorescence technique to quantitatively explore the stability of the A' -state in the gas phase.

RESULTS AND DISCUSSION

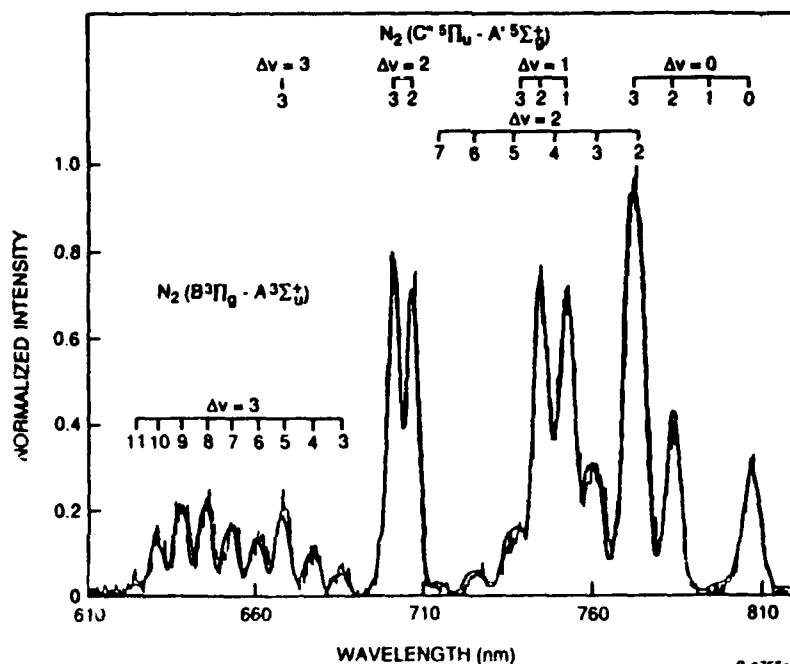
Our approach to determining the collisional stability of the $A'^5\Sigma_g^+$ state of N_2 was as follows. We employed energy pooling of two $N_2(A^3\Sigma_u^+)$ molecules to produce the $C''^5\Pi_g$ state. Radiative cascade through the $C''-A'$ HIR bands results in production of the A' -state. The production rate can be determined absolutely via quantitative observation of the HIR band emission intensity. LIF on the $C''-A'$ transition was employed to probe for the presence of the A' -state. Calibration of the LIF detection system was accomplished approximately by comparison with LIF signals from the nearby $B^3\Pi_g-A^3\Sigma_u^+$ transition. The $N_2(A^3\Sigma)$ population may be inferred from HIR band emission intensities using the HIR energy pooling rate coefficient or directly using $N_2(A-X)$ Vegard-Kaplan band emission intensities. A simple kinetic model, tied to absolute population measurements, is used to predict the A' -state population. The HIR band LIF intensities were compared with intensities predicted by the calibrated computer model. The gas phase $N_2(A')$ lifetime required to explain the observed signal level was then determined from the model. A schematic diagram of the experiment is shown in Figure 2.

Initial experiments were conducted using Ar as a buffer gas at pressures of approximately 4 Torr. Observation of N_2 HIR emission showed that the intensity was maximized under these conditions at N_2 mole fractions of approximately 0.05. An emission spectrum of the region from 560 to 820 nm, recorded at a point 5 ms downstream of the $N_2(A)$ generator, is shown in Figure 3. The spectrum includes the data and a fit to the data indicating the presence of both the $N_2(C''-A')$ HIR bands and the $N_2(B-A)$ First Positive bands. The transition probabilities calculated by Partridge et al.⁷ were used in calculating the fitted spectrum.



B-0750a

Figure 2. Schematic diagram of the discharge flow reactor and LIF detection system used in the experiments.



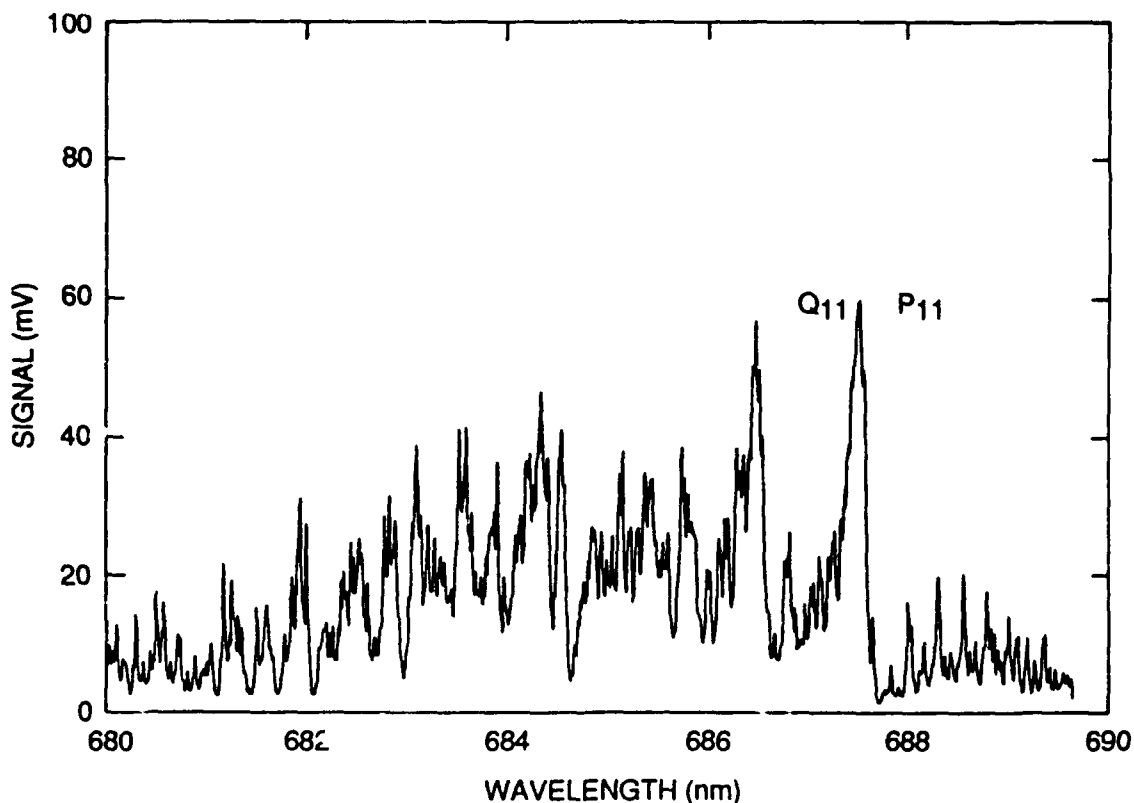
B-0755a

Figure 3. Visible emission spectrum of N_2 resulting from the $N_2(A)$ energy pooling reaction. The important $C''-A'$ and $B-A$ transitions are indicated.

A lower limit on the $N_2(A')$ production rate is given by the $C''-A'$ emission intensity. This emission intensity can also be used to determine the $N_2(A)$ concentration at that point in the flow reactor. The total $N_2(A')$ concentration at any point in the flow reactor is the integral of $N_2(A')$ production and loss processes from the $N_2(A)$ generator to that location. Initially, we assume that only quenching at the walls of the flow reactor is responsible for the loss of $N_2(A')$. Under typical experimental conditions the HIR band emission measurement gives an $N_2(A)$ density of 9×10^9 molecules cm^{-3} 5 ms downstream of the generator.

Given the initial $N_2(A)$ concentration determined from their spectra, the concentration of $N_2(A')$ can be calculated at any point in the flow reactor using a simple numerical model. The model predicted that $N_2(A')$ concentrations on the order of 4×10^7 molecules cm^{-3} could be expected in the observation region, 5 ms downstream of the injector if only wall loss was considered.

Approximate calibration of the LIF detection system was accomplished by observing the LIF produced by pumping the $N_2(B^3\Pi_g-A^3\Sigma_u^+, 3-0)$ band. The origin of the band is at 685.83 nm. This is a spectral region where no absorption is expected from the $N_2(C''-A')$ transition. A typical spectrum of LIF from the 3-0 band is shown in Figure 4.

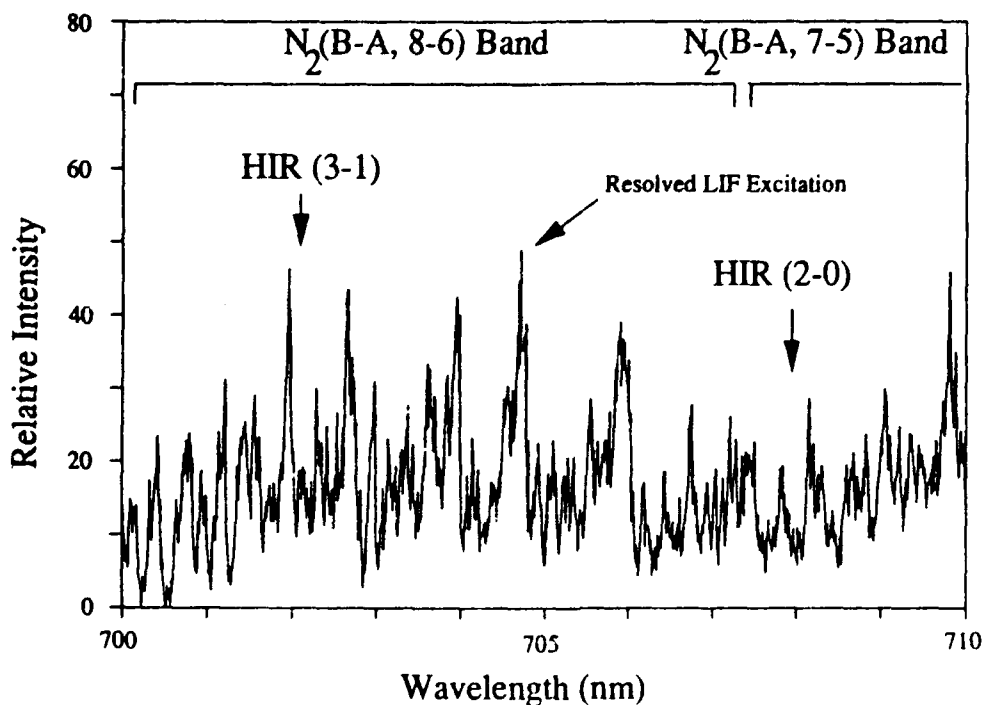


B-1095

Figure 4. LIF excitation spectrum of the $B^3\Pi_g-A^3\Sigma_u^+, 3,0$ band transition observed in the discharge flow reactor. The Q_{11} and P_{11} branch band heads are indicated in the figure.

Several issues must be considered in using this method to determine the sensitivity of the LIF technique for detecting the A"-state. The primary issue is the actual oscillator strength of the C"-A' transition relative to the B-A transition. As mentioned in the introduction, the calculated radiative lifetime for the C"-A' transition, 4.3 μ s, conflicts with some of the data on quenching of C"-state emission. The quenching data suggests that the lifetime of the C"-state is closer to 40 ns. This lifetime would imply a much stronger absorption oscillator strength for the transition. The discrepancy will be addressed further in the discussion session; however, the primary effect of an increased oscillator strength for the C"-A' transition would be a lowering of the detection limit for the A'-state by approximately a factor of one hundred. Thus, our measurements would expect to give a result which was an upper limit on the A'-state concentration and hence a lower bound on the effective loss rate.

An LIF spectrum of the region from 700 to 710 nm is shown in Figure 5. The 2-0 and 3-1 bands of the C"-A' transition should be excited in this wavelength region. Though absorption features are observed in this region, they can be assigned to the N₂(B-A, 8-6) transition. Comparison of the noise levels observed in this spectrum with the signal levels obtained in the spectrum of Figure 4, corrected for the differences in the absorption strengths for the B-A, 3-0 and C"-A', 2-0 bands, establishes a detection sensitivity of approximately 1×10^6 molecules cm⁻³.

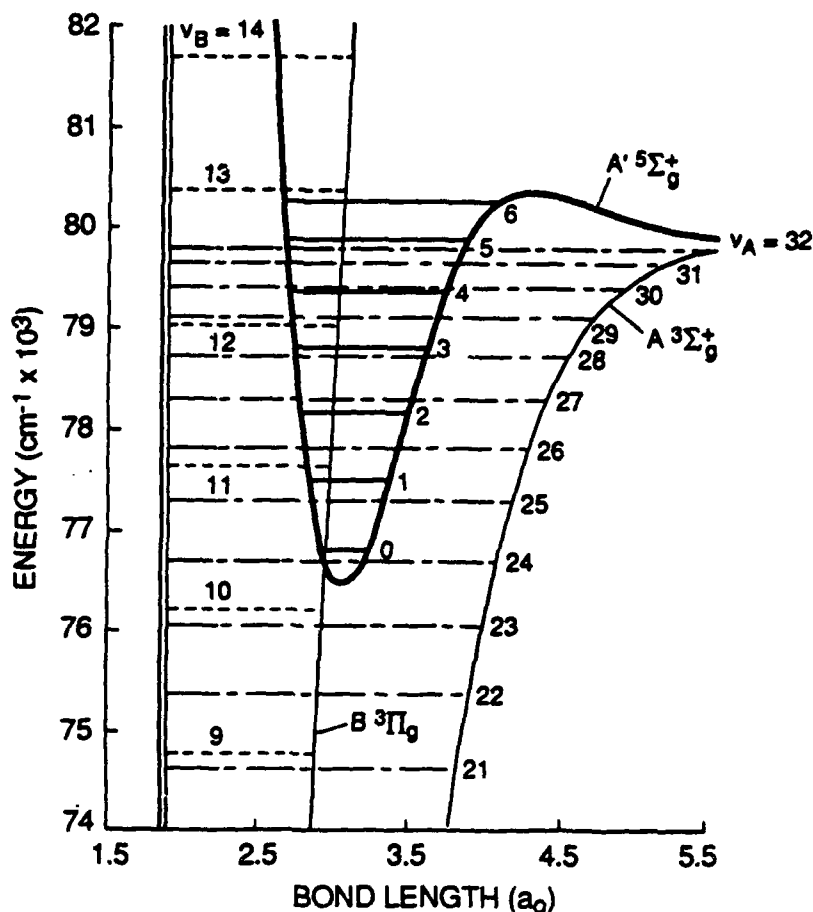


B-1201

Figure 5. LIF excitation spectrum for the region from 700 to 710 nm. Features of the B-A, 8,6 and 7,5 transition are identified. Arrows show the expected location of the HIR 3,1 and 2,0 bands. The excitation point for the spectrum of Figure 7 is shown.

The simple numerical model used to predict the expected $N_2(A')$ densities at the observation point in the discharge flow reactor can be used to determine a lower limit on the loss rate for $N_2(A')$ consistent with a concentration at our detection limit. When the loss rate of 3200 s^{-1} is incorporated in the model an $N_2(A')$ concentration equivalent to the estimated detection limit is predicted at the detection point. Hence, we can place an upper limit on the A' -state lifetime of approximately 0.3 ms.

An expanded potential energy diagram for the A' -state and near isoenergetic levels of the $B^3\Pi$ and $A^3\Sigma$ state is shown in Figure 6. The diagram shows that the lowest vibrational level of the A' -state is near-resonant with $v=10$ of the $B^3\Pi_g$ state. Also, the barrier to predissociation for the A' -state occurs at $v'=13$ of the B-state. The latter observation provides evidence for invoking curve crossing to the A' -state as the mechanism for predissociation of the B-state. Thus both collisional and spin-orbit coupling to the B-state might be evident in the spectrum of levels 10-12. A recent study of the high-resolution LIF spectrum from the $N_2(B^3\Pi_g-A^3\Sigma_u^+, 10-6)$ transition revealed no apparent

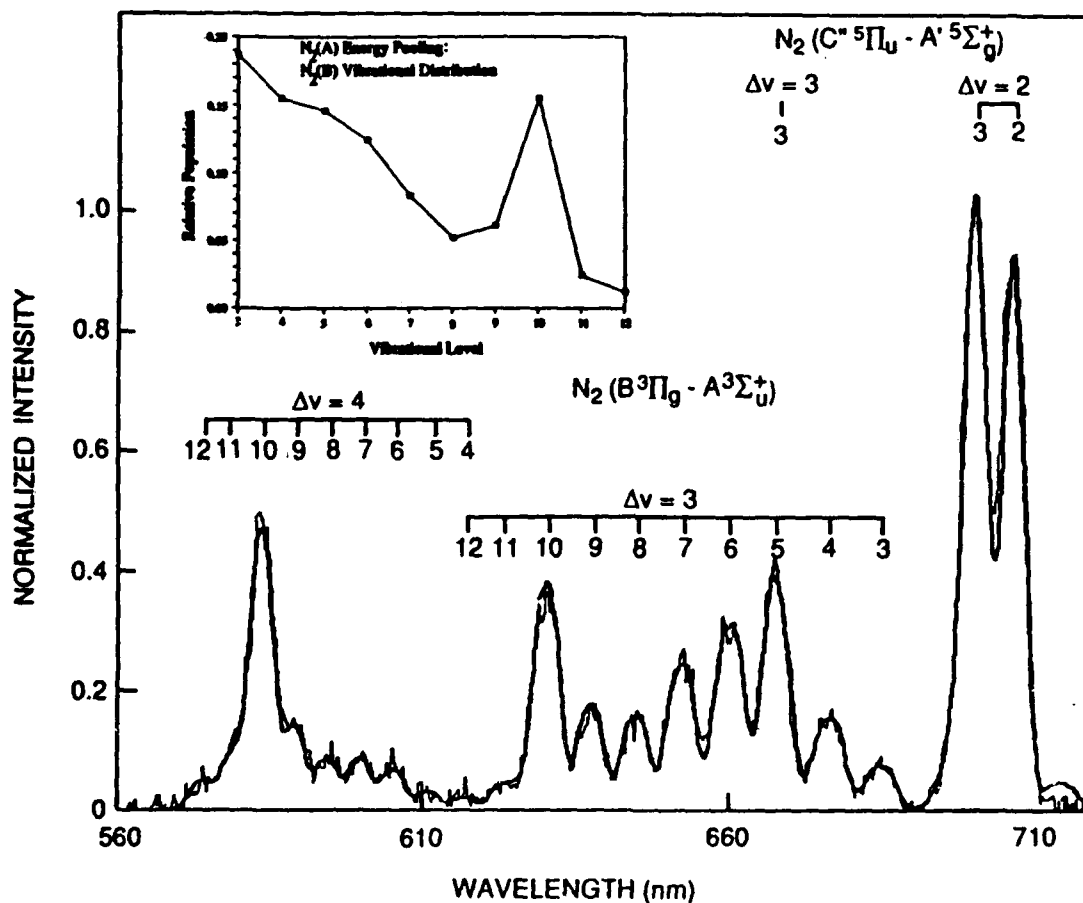


B-0751a

Figure 6. Expanded energy level diagram of the A' -state redrawn from the results of Partridge et al.¹² The figure illustrates the potential for coupling of the A' and B states.

perturbations in the rotational levels of the B-state. In addition, no other studies have reported any perturbations in the spectra of levels 10-12.¹⁴ Thus, there appears to be no direct evidence from the spectroscopy of the B-state to indicate spin-orbit coupling to the A'-state.

If the energy pooling reaction is studied using an Ar buffer gas much of the information on the distribution of vibrational levels populated in the B-state is washed-out by rapid vibrational relaxation. If He is employed as a buffer gas vibrational relaxation is less efficient and much of the nascent vibrational distribution is preserved in the emission spectrum. A typical spectrum of emission from the energy pooling reaction from 560 to 720 nm using He as a buffer gas is shown in Figure 7. In contrast to the spectrum of Figure 3, a strong enhancement in the population of $v=10$ of the B-state is observed. Thus, it would appear that collisional coupling from the A'-state to the B-state may be a mechanism for the decay of the A'-state.



B-0756a

Figure 7. Visible emission spectrum of N_2 due to $N_2(A)$ energy pooling in a dominantly He buffer gas. The enhancement of the population of $v=10$ of the B-state is indicated in the inset plot of the vibrational distribution.

Our experiments in which we vary the N_2 concentration indicate that N_2 is not primarily responsible for coupling of the two manifolds. At the lowest N_2 concentrations employed a gas-kinetic coupling rate coefficient would be required to couple the levels and significant variations in the B-state, $v=10$ enhancement would have been observed. It would appear more likely that Ar or He, which are both present in much greater concentrations, may be responsible for the coupling. The production of $N_2(A')$ in either a supersonic jet or in a rare gas matrix may reduce the collisional coupling to the B-state and enable a more rigorous determination of the lifetime of this state.

REFERENCES

1. See, for example, Formation and Trapping of Free Radicals, edited by A.M. Bass and H.P. Broida (Academic, New York, 1960).
2. J. Berkowitz, W.A. Chupka, and G.B. Kistiakowsky, J. Chem. Phys. 25, 457 (1956).
3. R.S. Mulliken, J. Chem. Phys. 37, 809 (1962).
4. M. Krauss and D.B. Neumann, Mol. Phys. 32 101 (1976).
5. P.E.M. Siegbahn, Int. J. Quantum Chem. 23, 1869 (1983).
6. P.K. Carroll, J. Chem. Phys. 37, 805 (1962).
7. H. Partridge, S.R. Langhoff, and C.W. Bauschlicher, Jr., J. Chem. Phys. 88, 3174 (1988).
8. K.P. Huber and M. Vervloet, J. Chem. Phys. 89, 5957 (1988).
9. I. Nadler, D.W. Setser, and S. Rosenwaks, Chem. Phys. Lett. 72, 536 (1980).
10. I. Nadler, A. Rotem, and S. Rosenwaks, Chem. Phys. 69, 375 (1982).
11. L.G. Piper, J. Chem. Phys. 88, 231 (1988).
12. E.E. Eyler and F.M. Pipkin, J. Chem. Phys. 79, 3654 (1983).
13. H. Geisen, D. Neuschäfer, and Ch. Ottinger, Z. Phys. D - Atoms, Molecules and Clusters 4, 263 (1987).
14. A. Lofthus and P.H. Krupenie, J. Phys. Chem. Ref. Data 6, 113 (1977).

The Phase Diagram of Hydrogen: Prospects for Metallization

Isaac F. Silvera
Lyman Laboratory of Physics
Harvard University
Cambridge, MA 02138

The pressure-temperature-density structural phase diagram of hydrogen and the prospects for attaining atomic metallic hydrogen at ultra-high pressure are discussed. At zero pressure hydrogen occurs naturally as a diatomic molecule. There are two species: ortho and para, which have surprisingly different properties and different structural forms in the solid state at very low temperatures.

Concentrating on the simpler para species, this solidifies at about 14 K and remains in the hexagonal close packed (hcp) structure down to 0 K with the molecules having spherical symmetry in their ground state. With increasing pressure the melting temperature rises (300 K at about 5.5 GPa). Somewhat above 100 GPa (1 megabar) the molecules are expected to go into an orientationally ordered state. At still higher pressures, in the 300-400 GPa pressure region, hydrogen is predicted to become metallic. Metallic hydrogen has been predicted to be a high temperature superconductor, and possess many fascinating properties. The density is more than an order of magnitude higher than at zero pressure, providing a compact high energy content material.

Hydrogen is the simplest atom in the periodic table. On earth it occurs in the molecular state as H_2 . A many body system of molecular H_2 has many unique and fascinating properties. It condenses into a liquid at ~ 20.4 K with a pressure of 1 bar and solidifies at its triple point at just under 14 K. As the temperature is lowered, at low pressure, the behavior depends upon the ortho-para concentration, which we briefly discuss.

Due to the protons of H_2 having nuclear spin $1/2$, the molecular wavefunction must be antisymmetric under permutation of the protons. A careful consideration shows that the total nuclear spin states can be either $I=1$ or 0 . The triplet ($I=1$) can only occur with rotational levels having odd rotational quantum number J ; these are ortho molecules. The singlets ($I=0$) combine with even J states and are called para molecules. Transitions between ortho and para states are strongly forbidden in the isolated molecule. However, in the solid state this takes place at about 2%/hour for a pure ortho- H_2 sample. One of the unique features of hydrogen is that the molecules remain in free rotor states in the low pressure solid. Due to the large splitting between rotational levels, only the ground rotational states, $J=0$ for para and $J=1$ for ortho, are populated at the temperatures of the solid state. Solids of almost pure ortho or para- H_2 , or any mixture, can be made and studied for metastable ortho-para concentration, due to the slow conversion rate.

In fig. 1 we show a tentative phase diagram of pure ortho in para- H_2 . At pressure $P=0$ both species form hcp solids. Para, being in the spherically symmetric $J=0$ state, remains hcp down to $T=0$ K. Ortho has a

threefold ($2J+1=3$) orientational degeneracy; this is lifted when it orientationally orders on a Pa3 lattice¹ at 2.8K. For the remainder of our considerations of the phase diagram with increasing pressure, we shall concentrate mainly on para-H₂ at T=0K.

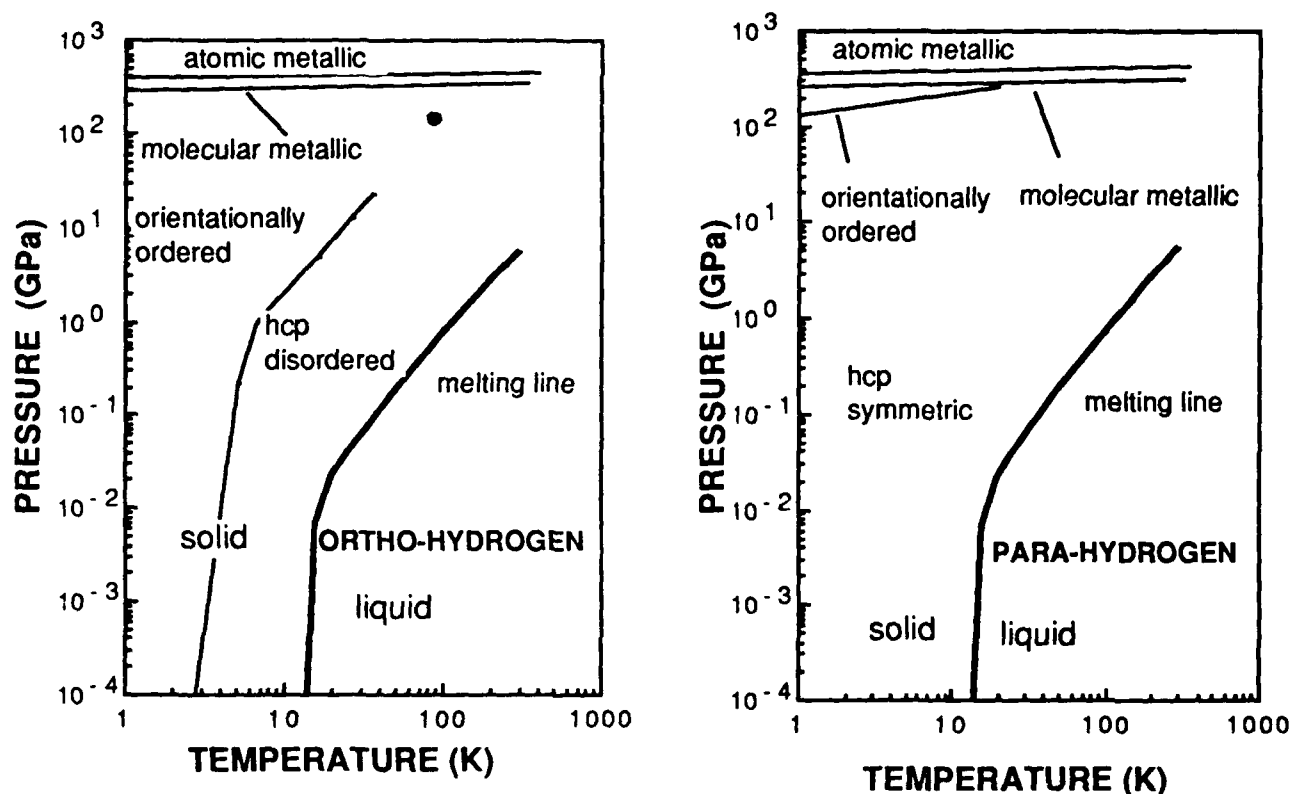


Fig. 1. The phase diagram of para-H₂ and ortho-H₂. The lines for the metallic phase are speculations based on theory.

As pressure is increased to the one megabar range, no change takes place in the lattice structure of para-H₂. However the density changes by about a factor of more than 10, and the intermolecular nearest neighbor distance is reduced from $\sim 3.8\text{\AA}$ to $\sim 1.7\text{\AA}$. At this distance, the anisotropic interactions, which are very small at zero

¹For further details, see the review by I.F. Silvera, Rev. Mod. Physics **52**, 393 (1980).

pressure, grow to be a considerable fraction of the splitting of the rotational levels. As a consequence the rotational levels become mixed and J is no longer a good quantum number. The single molecule distributions are no longer spherical and the molecules are expected to orientationally order. Indeed, this has been observed at a pressure of 28 GPa in ortho-D₂ (the analogue of para-H₂).¹ The transition pressure for the orientational ordering of para-H₂ has been tentatively predicted to be 100 GPa, based on the quantum Monte-Carlo calculation of Ceperley and Alder.² However, in our experiments up to 160 GPa at 5K, this has not yet been observed.⁴

Returning to the phase diagram of ortho-H₂, the critical temperature between the hcp disordered and the ordered phase increases rapidly with pressure. Recently Hemley and Mao⁵ have observed an abrupt change in a spectral feature at 145 GPa and $T=77\text{K}$ which was interpreted as an orientational order transition, shown in fig. 1. However Barbee et al.⁶ have recently presented a new calculation of the high density phases of H₂. They do not support the interpretation of Hemley and Mao, suggesting a structural phase transition for the molecular centers from a possibly already orientationally ordered hcp lattice. We believe that Hemley and Mao are correct, based on the continuity of the phase line shown in fig. 1.

Returning to the phase diagram of para-H₂, as pressure is increased further to the 300-400 GPa region, hydrogen is expected to have an

¹ I.F. Silvera and R.J. Wijngaarden, Phys. Rev. Lett. **47**, 39 (1981).

² D.M. Ceperley and B.J. Alder, Phys. Rev. B **36**, 2092 (1987).

⁴ H. Lorenzana, K. Goettel and I.F. Silvera, unpublished.

⁵ R.J. Hemley and H.K. Mao, Phys. Rev. Lett. **61**, 857 (1988).

⁶ T.W. Barbee, III., A. Garcia, M.L. Cohen and J.L. Martins, Phys. Rev. Lett. **62**, 1150 (1989).

insulator-to-metal (IM) transition - metallic hydrogen. This is expected to take place in two steps: first a transition to a conducting molecular state and then, at a higher pressure, a structural transition to a conducting atomic state.

Metallic hydrogen is predicted to have many special properties, including high T_c superconductivity.⁷ As a possible high specific impulse rocket propellant fuel, the question of metastability is of great importance, i.e. when the pressure is lifted from metallic hydrogen will it remain in the high density phase. An early calculation indicates that metallic hydrogen will be dynamically stable.⁸ However, Salpeter⁹ has shown that it will probably decay to the molecular phase by a tunneling mechanism.

We intend to study hydrogen by pressurizing it in a diamond anvil cell (DAC). By using specially selected and shaped diamonds, as well as special gaskets, we believe that pressures in the 300-400 GPa pressure range can be achieved. The IM transition can be detected by studying the optical absorption and reflection of the hydrogen. This has recently been demonstrated as a very useful technique for the study of very small samples by Goettel et al.¹⁰ who pressurized xenon to 200 GPa at room temperature. An IM transition was observed at $P=133$ GPa by fitting the spectra to a modified Drude model of a metal.

We acknowledge the Air Force (AFAL) for support of this research.

⁷ N.W. Ashcroft, Phys. Rev. Lett. 21, 1748 (1968).

⁸ G.A. Neece, F.J. Rogers, and W.G. Hoover, Comput. Phys. 7, 621 (1971).

⁹ E.E. Salpeter, Phys. Rev. Lett. 6, 229 (1972).

¹⁰ K.A. Goettel, J.H. Eggert, I.F. Silvera and W.C. Moss, Phys. Rev. Lett. 62, 665 (1989).

The *ab initio* Determination of the Damped Dispersion Energy of Interaction
Between an Atom and a Diatomic Molecule

James E. Bohr
National Research Council Resident Research Associate
ARIES Office
Air Force Astronautics Laboratory/LSX
Edwards Air Force Base, CA 93523-5000

The potential energy surface (PES) of a molecular system provides insight into its stability and structure. An *ab initio* calculation of the PES of a candidate high energy density material (HEDM) is usually necessary since typically no experimental data are available to characterize such novel compounds. However, highly accurate quantum mechanical computations can quickly become prohibitively expensive, even for "small" molecular systems. This is especially true at the configuration interaction (CI) level of theory. On the other hand, high accuracy is essential when a compound of interest is only slightly bound, since the relatively small binding energy is actually a difference between the large absolute energy computed at infinite fragment separation and the large absolute energy computed in the binding region. One method of providing a realistic approximation to a CI calculation is to carry out an inherently less expensive self-consistent field (SCF) calculation, to which is added the damped dispersion interaction energy. Koide [1] pioneered an *ab initio* method of determining the damped dispersion energy of two interacting hydrogen atoms; this method was applied by Krauss and co-workers [2] to the interaction of other atomic pairs. Rosenkrantz [3] used the method to derive equations for the damped dispersion energy of an atom interacting with a diatomic molecule, and calculated the induced dipole-induced dipole interaction energy for several atom-diatom systems. The current effort has been to extend the Rosenkrantz code to include higher order induced multipole interactions; specifically, induced dipole-induced quadrupole, induced dipole-induced octupole, and induced quadrupole-induced quadrupole effects. Computational results of the damped dispersion energy of a hydrogen molecule interacting with different rare gas atoms will be given, with comparison to semi-empirical calculations. Preliminary results of SCF plus damped dispersion calculations of lithium interacting with molecular hydrogen, a potential HEDM, will also be presented.

- [1] A. Koide, J. Phys. B 9, 3173 (1976).
- [2] M. Krauss, D. B. Neumann, and W. J. Stevens, Chem. Phys. Lett. 66, 29 (1979); M. Krauss, W. J. Stevens, and D. B. Neumann, *ibid.* 71, 500 (1980); M. Krauss and W. J. Stevens, *ibid.* 85, 423 (1982).
- [3] M. E. Rosenkrantz and M. Krauss, Phys. Rev. A 32, 1402 (1985).

New Orleans, LA, March 12-15, 1989

SYNTHESIS OF NOVEL, SUBSTITUTED POLYCYCLIC CAGE SYSTEMS

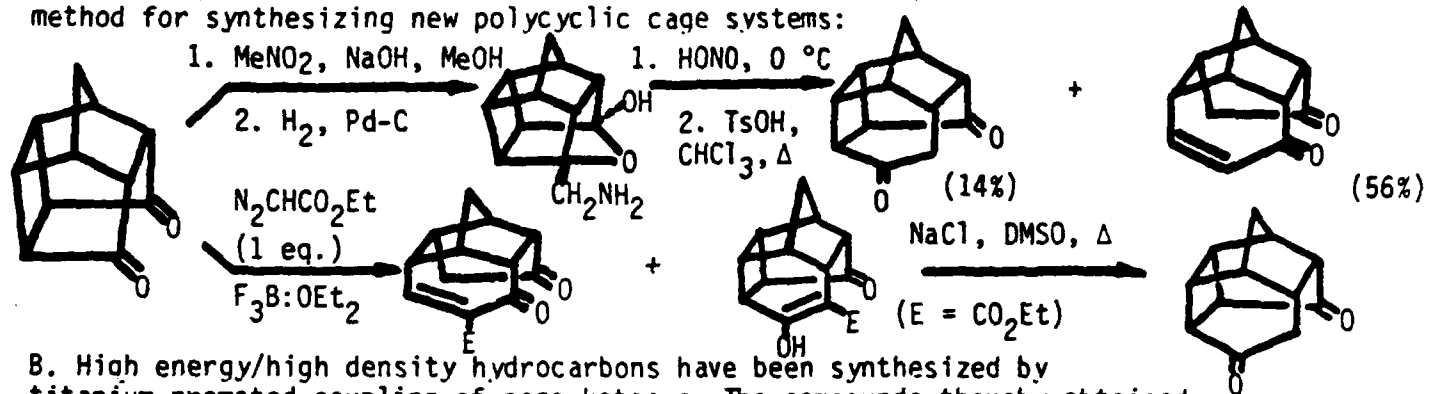
Principal Investigator: Dr. Alan P. Marchand

Department of Chemistry, University of North Texas, Denton, TX 76203-5068

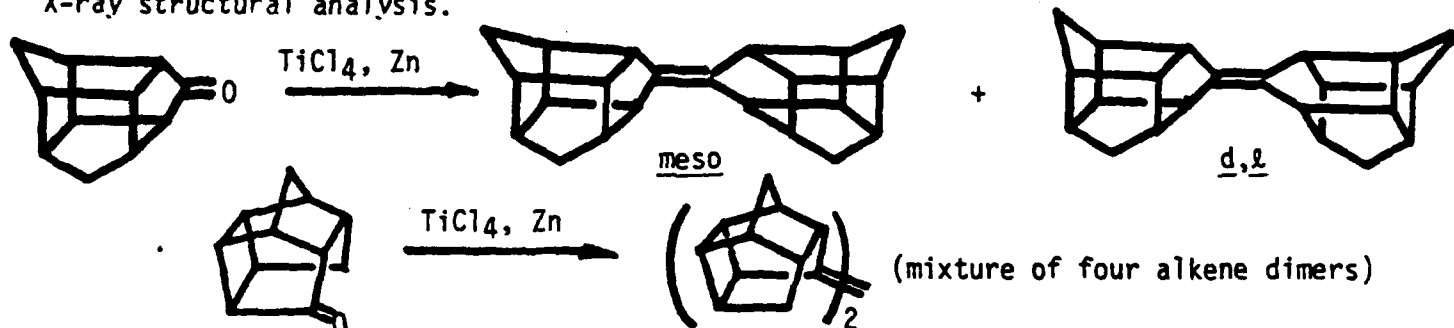
ABSTRACT

I. Synthesis of new high energy/high density polycyclic cage hydrocarbon systems

A. Ring expansions of substituted pentacyclo[5.4.0.0^{2,6}.0^{3,10}.0^{5,9}]-undecane-8,11-diones have been studied. These reactions provide a convenient method for synthesizing new polycyclic cage systems:

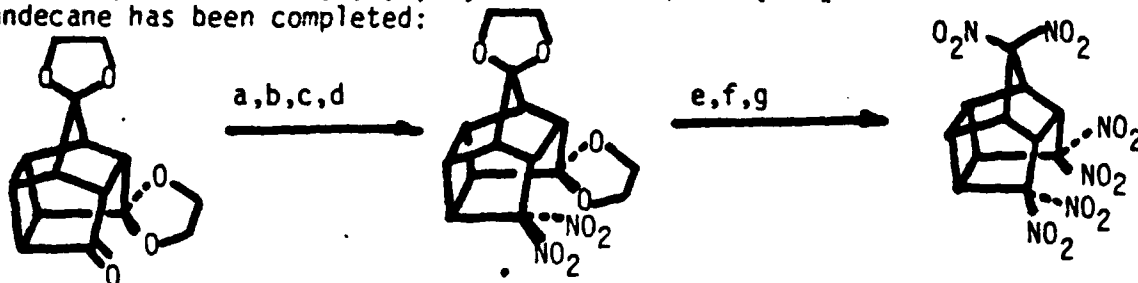


B. High energy/high density hydrocarbons have been synthesized by titanium-promoted coupling of cage ketones. The compounds thereby obtained possess unusually high crystal densities as determined by single crystal X-ray structural analysis.



II. Synthesis of polynitropolycyclic cage compounds, members of a new class of energetic materials

A. The synthesis of 4,4,8,8,11,11-hexanitropentacyclo[5.4.0.0^{2,6}.0^{3,10}.0^{5,9}]-undecane has been completed:



(a) $\text{NH}_2\text{OH}\cdot\text{HCl}$, K_2CO_3 , EtOH , Δ (79%); (b) NBS, dioxane, room temp., overnight (62%); (c) NaBH_4 , 60% aq. EtOH , $0^\circ\text{C} + 25^\circ\text{C}$, 1 h (84%); (d) $\text{K}_3\text{Fe}(\text{CN})_6$, NaNO_2 , aqueous MeOH , 25°C , 2 h (83%); (e) concd H_2SO_4 , CH_2Cl_2 , 25°C , 24 h (50%); (f) $\text{NH}_2\text{OH}\cdot\text{HCl}$, NaOAc , MeOH , reflux 2 h (75%); (g) 98% red HNO_3 , NH_4NO_3 , urea, dry CH_2Cl_2 , reflux 30 min., then 30% aq. H_2O_2 , reflux 15 min. (19%).

RESEARCH OPPORTUNITIES IN THE FIELD OF ENERGETIC MATERIALS

The High Explosives Research and Development (HERD) facility, Energetic Materials Branch, Air Force Armament Laboratory, Eglin Air Force Base, Florida, was established in 1970. It is laid out on a 45 acre plot and consists of 29 buildings/bunkers. The facilities consist of laboratories, processing buildings, equipment and storage buildings, instrumented detonation chamber/instrumentation building and offices. The HERD is currently staffed with 28 multi-disciplined civilian and military scientists, engineers and technicians. It has an annual budget of around \$5M. The mission of the HERD is to provide energetic materials expertise and developmental and processing skills necessary to meet munitions requirements unique to the USAF. A full spectrum of in-house energetic materials research is conducted at the HERD, that includes basic chemistry and thermal characterization, detonation physics, processing and filling warheads. The laboratories within the HERD complex are equipped with the latest in analytical instrumentation and the standard equipment used to characterize, formulate, process and test energetic materials and formulations. Instrumentation/equipment available for use at the HERD includes differential scanning calorimeters, accelerating rate calorimeter, thermogravimetric analyzers, high performance liquid and ion chromatographs, tandem gas chromatograph/mass spectrometer, gas chromatographs, nuclear magnetic spectrometers, inert atmosphere chamber, Fourier transform infrared spectrophotometer, streak and framing cameras, impact machine and computational capabilities. There are opportunities available to faculty, graduate students and post docs for carrying out research projects at the HERD during one year and 10-week programs. These opportunities are made available through the Universal Energy Systems, Inc. under the sponsorship of the Air Force Office of Scientific Research and the National Research Council. The High Explosives Research and Development facility is looking for qualified scientists interested in participating in these programs. Interested parties are encouraged to contact Dr. Robert L. McKenney, Jr. at (904) 882-4212 for further information regarding the aforementioned research opportunities.